UNIVERSIDAD COMPLUTENSE DE MADRID
FACULTAD DE CIENCIAS QUÍMICAS

TESIS DOCTORAL

Mejora de las propiedades de Redes Metal-Orgánicas mediante la asociación de nano-especies activas

Enhancement of Metal-Organic Frameworks properties by the association of active nano-species

MEMORIA PARA OPTAR AL GRADO DE DOCTOR

PRESENTADA POR

Ana Arenas Vivo

Directora

Patricia Horcajada Cortés

Madrid

© Ana Arenas Vivo, 2021

UNIVERSIDAD COMPLUTENSE DE MADRID

FACULTAD DE CIENCIAS QUÍMICAS

Departamento de Química Inorgánica

TESIS DOCTORAL

Mejora de las propiedades de Redes Metal-Orgánicas mediante la asociación de nano-especies activas

Enhancement of Metal-Organic Frameworks properties by the association of active nano-species

MEMORIA PARA OPTAR AL GRADO DE DOCTOR

PRESENTADA POR

Ana Arenas Vivo

Directora: **Patricia Horcajada Cortés**

Tutor académico: **David Ávila Brande**

Instituto Madrileño de Estudios Avanzados en Energía, Madrid

Ed. Electrónica 2021

Enhancement of Metal-Organic Frameworks properties by the association of active nano-species

TESIS DOCTORAL

Ana Arenas Vivo

Departamento de Química Inorgánica

Facultad de Ciencias Químicas

Universidad Complutense de Madrid

Instituto Madrileño de Estudios Avanzados en Energía

Julio 2021

A mis padres, por darme las herramientas para la vida,
y a Rafa, por querer compartirla conmigo.

"I am a great believer in luck. The harder I work,
the more luck I seem to have"

Acknowledgements

"If I have seen further is by standing
on the shoulders of giants"

Sir Isaac Newton

Quiero agradecer en primer lugar a mi directora de tesis, la Dra. Patricia Horcajada. Gracias a ti he conocido el apasionante mundo de los MOFs y sus múltiples aplicaciones, que hasta 2017 eran desconocidos para mí y ahora son mis mejores amigos. Confiaste en mí tras nuestra única entrevista y me ofreciste incorporarme al grupo directamente como investigadora predoctoral. Contigo no sólo he aprendido sobre estos asombrosos materiales, además he aprendido a desarrollarme cómo científica, a cultivar el pensamiento crítico y a supervisar a otros trabajadores. También me brindaste la oportunidad de conocer a grandes investigadores al proponerme para colaborar con tus múltiples contactos, y espero haber sido una gran embajadora de la Unidad de Materiales Porosos Avanzados (APMU). Gracias de veras por todo tu apoyo, por tu ejemplo como líder de grupo, por las enriquecedoras discusiones en tu despacho (profesionales y personales) y por facilitarme continuar con esta tesis doctoral incluso tras haber dejado IMDEA. Espero haber cambiado tu opinión sobre los ingenieros para la investigación de laboratorio y haber abierto las puertas a otros apasionados de la ciencia como yo.

Me gustaría extender este agradecimiento a mi tutor académico, el Dr. David Ávila, que no sólo has sido mi vínculo con la Universidad Complutense, sino que siempre has estado dispuesto a colaborar y ayudar en los proyectos que te presentábamos con una gran sonrisa. Me has hecho sentirme acogida en la Facultad de Químicas a pesar de no desarrollar mi investigación allí de forma presencial. Y me has contagiado tu pasión por la microscopía electrónica. ¡Qué gran herramienta!

También quiero agradecer a los organismos responsables de la financiación de estos años de investigación: a la Comunidad de Madrid por sus becas de Garantía

juvenil (CAM PEJD-2016/IND-2828) y a la Fundación Iberdrola por sus becas de investigación de 2017.

La mayor parte de esta tesis se ha desarrollado en la APMU de IMDEA Energía (Móstoles, Madrid) y en esta sección quería extender el agradecimiento a mis compañeros. Gracias a Pablo por acogerme bajo tu ala cuando me incorporé y por terminar de enseñarme todos esos equipos y montajes en vitrina que desconocía de un laboratorio de química. Comenzamos siendo compañeros y terminamos siendo grandes amigos. Hemos compartido horas de laboratorio, de limpiezas, alegrías y frustraciones, congresos y viajes, noches de trabajo hasta medianoche a ritmo del Rumadai y noches de fiesta. Espero que te vaya genial en tu postdoc en Francia. Espero visitarte, COVID mediante, y siempre te espero en Madrid. Gracias Sara por ser un gran ejemplo como investigadora y demostrarme que se puede con todo, trabajo, familia e incluso con un HPLC que no para de romperse. Tanía, que haría un Zipi sin su Zape, te agradezco que me hayas adentrado más en el mundo biológico. Agradecer a Artem y Sergio todos vuestros consejos y vuestra disponibilidad. Giacomo, aunque siempre has sido el último en enterarte de las cosas con tu despiste siempre has sido el primero en luchar a mi lado para solucionar los problemas. Miriam, a ti te agradezco tu amabilidad, tu detallismo, tus insaciables ganas de aprender y estar siempre ahí para echar una mano, y para cotillear conmigo en los descansos. Muchos de estos resultados han salido gracias a tu trabajo, Iván, mi becario. No sabes la suerte que he tenido de cruzarnos en el camino. Sin ti no habrá podido acabar esta tesis. Gracias por ese magnífico año en IMDEA. Eres un gran profesional y estoy segura de que te va a ir genial en la vida. Acuérdate de mí cuando llegues lejos. También quiero dar gracias a las nuevas incorporaciones, Yolanda y Gabriel, porque, aunque no hemos coincidido tanto por la APMU, continuáis con mis líneas de investigación y mantenéis vivo el camino que inicié.

En IMDEA no todo se vivía en la APMU y también quiero agradecer a otros compañeros. En especial quiero mencionar al equipo de laboratorios centrales por toda vuestra paciencia analizando mis muestras y buscando soluciones específicas para mis materiales. Fernando, Laura, Maria Eugenia, nunca os he agradecido lo suficiente el mimo que habéis puesto a mis muestras y al cuidado de los equipos. Muchos de los resultados que presento no estarían aquí si no fuese por vuestro trabajo y buen hacer. También mencionar a todas las chicas de administración, gracias por vuestra ayuda en la gestión de los proyectos, la compra de materiales, y la organización de los eventos de divulgación, entre otros. Sois ese mecanismo que se engrana silencioso para que el motor de IMDEA siga teniendo producción científica. El reconocimiento de IMDEA Energía como Unidad de Excelencia María de Maeztu no es sólo por el mérito de los investigadores sino también reflejo de vuestro trabajo. Por último, agradecer a las generaciones de doctorandos de otras

Unidades con los que he convivido en mi paso por el centro. Vosotros llenabais mi día a día con una sonrisa y he aprendido mucho de otros campos de la energía gracias a las presentaciones de vuestros trabajos.

No me quiero olvidar tampoco de mis colaboradores durante mis años de tesis. Quería agradecer a "mi primo", el ahora Dr. Daniel Arenas, por el amor con el que me enseñaste a trabajar con el TEM (seguro heredado de David). Gracias al equipo del Departamento de Ingeniería Química de la Universidad de Alcalá de Henares, por acogerme tan bien y poner todos los recursos a mi disposición. En especial agradecer a Georgiana y Laura por adentrarme en el mundo de las bacterias y enseñarme todo lo que sé. Habéis hecho a mi madre feliz por volverme a acercar a la biología, que dejé de lado en la E.S.O. Gracias al departamento de Química Inorgánica y Bioinorgánica de la Facultad de Farmacia de la Complutense, a Marita y a Isabel, por ayudarme a afianzar mis conocimientos sobre biofilm bacteriano y enseñarme el cultivo celular. Gracias al grupo del Dr. Pablo del Pino del Centro Singular de Investigación en Química Biológica y Materiales Moleculares (CiQUS). Colaborar con vosotros ha sido un regalo. Todo ha sido fácil con vosotros y todas las ideas eran estudiadas y llevadas a buen puerto. Me hubiese gustado compartir con vosotros mucho más de una semana presencial en Santiago, no sabéis lo que aprendí en tan poco tiempo. A los estudiantes que estuvieron de estancia y que dejaron un poco de ellos conmigo, Silvia, Sara, Vanessa, también gracias.

Me parece pertinente también dar las gracias al Dr. Joaquín Martínez Urreaga y la Dr. Maria Ulagares de la Orden Hernández, mis primeros tutores y mentores. Los años con vosotros en el grupo de "Polímeros: Caracterización y aplicaciones", del Departamento de Química Industrial y Medioambiente de la Escuela Técnica Superior de Ingenieros Industriales de Madrid, alimentaron mi vocación científica y mi pasión por el campo de los materiales. Sin vuestro ejemplo, vuestros consejos y vuestro apoyo en mis inicios profesionales no habría llegado hasta aquí, casi 8 años después de esa beca de colaboración y ese Trabajo Fin de Grado.

Por supuesto quiero dar las gracias a mis padres. Me habéis puesto todo en bandeja para que fuese exitosa y lograse mi meta de ser investigadora. Gracias por entender mis ausencias, los retrasos por los horarios de experimentos interminables y soportar convivir con todos los días encerrada en mi cueva trabajando. Ojalá os pueda devolver todo lo que habéis hecho por mí. Mamá, estos años de doctorado hemos hablado más que nunca de tu vida académica, tu tesis, tu investigación y además pude conocer por fin el ISCIII. Me encanta poder compartir esta faceta de mi vida contigo y que el fin de tu carrera profesional marque el inicio de la mía. Papá, todos reconocen en mi trabajo tu buen hacer y tu criterio, he aprendido muchísimo de tan gran ingeniero. Gracias por tus curiosas preguntas para comprender mejor lo que estaba haciendo, ya que al buscar las respuestas tenía que

comprender verdaderamente mi trabajo. También quiero dar gracias a mis hermanos, Diego y Antonio, por admirarme y ser fuente de inspiración a partes iguales. Por apoyarme a pesar de no entender mis ganas de seguir estudiando. Gracias por enviarme todos esos artículos que encontrabais y darme ideas para vender mis resultados. Gracias a mis amigos de la universidad y del colegio, por preguntarme siempre cómo iba la tesis, por alegrarse de mis triunfos y perdonar mis faltas en las quedadas. Gracias por acompañarme en la distancia con todas esas videollamadas y mensajes. Sara, me has cuidado mucho desde tan lejos. Fer, a ti te debo regresar a Madrid, eres un gran amigo.

Por último, y no por ello menos importante, mi agradecimiento es para ti, Rafa. Mi roca frente al oleaje del mundo y mis alas para llegar a cumplir mis sueños, gracias por apoyarme en todo. Gracias por entender que la ciencia y la investigación son mi vocación y por animarme a dedicarme a ello, aunque quizá no parezca lo más sensato. Gracias por ir de la mano conmigo y vivir también los momentos de doctorando juntos, por compartir conmigo todos esos sábados en la biblioteca. Gracias por recordarme todos los días que soy inteligente y que tengo capacidad para esto y mucho más, por no permitirme abandonar en los momentos duros y por celebrar conmigo todos los artículos y premios. Gracias por estar orgulloso de mi y de mi trabajo. Tú eres la razón que me anima a superarme cada día, que me invita a ser una gran profesional y mejor persona. No creo merecerme todo lo que me das y te estaré siempre agradecida.

Gracias a todos de corazón, una pequeña parte de vosotros también está en este trabajo.

Resumen

Las Redes Metal-Orgánicas o MOFs (por sus siglas en inglés: *Metal-Organic Frameworks*) son sólidos cristalinos formados a partir de unidades inorgánicas (átomos, clúster, cadenas, …) y ligandos orgánicos polidentados (carboxilatos, fosfonatos, azolatos, ...) creando una red tridimensional (3D) con una importante porosidad. Desde las primeras publicaciones en los años 90, ha crecido exponencialmente el interés en los MOFs, su química y sus aplicaciones. Muestra de ello son las más de 13300 publicaciones registradas tan sólo en 2020 (Web-of-Science: "Metal-Organic Frameworks"). Los MOFs destacan frente a otros materiales porosos debido a su composición híbrida versátil (ligando fácilmente modificable, presencia de centros metálicos insaturados), su riqueza estructural (multitud de topologías, familias isoreticulares) y su porosidad excepcional (áreas superficiales-S_{BET} de hasta 8000 $m^2 \cdot g^{-1}$), convirtiéndolos en candidatos prometedores en diversas aplicaciones de relevancia social e industrial.

Aunque su porosidad se ha explotado tradicionalmente en separación y almacenamiento de fluidos (ej.: CH_4, H_2), la encapsulación de otras especies para la obtención de materiales compuestos con propiedades mejoradas es más reciente y de gran interés. Siguiendo esta novedosa tendencia, en esta tesis se han asociado a diversos MOFs dos tipos de nano-especies activas (nano-EAs): i) metales (nanoclústeres, NCs, y nanopartículas, NPs) y ii) biomoléculas (lipasas). Algunas ventajas de estos materiales compuestos son: i) protección de la especie encapsulada (prevenir agregación, oxidación y/o degradación), ii) efectos de confinamiento, iii) adsorción selectiva, y iv) reactividad complementaria y/o sinérgica, entre otras.

El principal reto de esta tesis es el desarrollo de métodos sintéticos adaptados para lograr una asociación estable de las nano-EAs al MOF, teniendo en cuenta su distinta naturaleza, que consiga: i) distribución homogénea de las nano-EAs, ii) mantener/promover la actividad (ej.: catalítica, biocida) y iii) reproducibilidad. Actualmente, los métodos utilizados para la obtención de composites tipo *core@shell* (nano-EAs@MOF) podrían agruparse en dos: i) difusión de las nano-EAs o sus precursores en el MOF previamente sintetizado, "*ship-in-a-bottle*" (SiB) y ii) síntesis *in situ* del MOF poniendo en contacto sus precursores (ligando, catión)

con las nano-EAs, "*bottle-around-a-ship",* (BaS). Debido al gran interés en el desarrollo de composites nano-EAs@MOF, esta tesis busca aportar un mayor conocimiento sobre este tema, aún en desarrollo, contribuyendo con nuevos protocolos de asociación empleando ambos métodos de asociación, que superen los obstáculos sintéticos encontrados hasta la fecha. Adicionalmente, se ha estudiado la aplicación de los materiales compuestos resultantes en diversos campos de interés.

En Capítulo 3 se presenta la asociación de NPs de Ag al conocido MOF microporoso y fotoactivo aminotereftalato de titanio MIL-125-NH_2 empleando un sencillo proceso SiB en dos pasos. El protocolo de síntesis diseñado en esta tesis ha sido probado para la asociación de AgNPs tanto al MIL-125-NH_2 con tamaño micropartícula como nanopartícula. Da lugar a NPs de Ag de 5 ± 3 nm, distribuidas por toda la partícula, incluso en la superficie exterior del MOF. La fuerte interacción entre la Ag y el grupo -NH_2 del ligando confieren al MOF de unas propiedades optoelectrónicas mejoradas (siendo el ancho de banda del composite de E_g= 2 eV *vs.* 2.6 eV el del MOF). Adicionalmente, la presencia de Ag aumenta la capacidad biocida intrínseca del MOF, mejorando su actividad antimicrobiana. Los estudios realizados con recubrimientos delgados del composite obtenido AgNP@nanoMIL-125-NH_2 han revelado la capacidad del material para inhibir la adhesión bacteriana de *Staphyilococcus aureus* y *Escherichia coli,* proporcionando un tratamiento frente al biofilm bacteriano, así como su elevado carácter biocida.

Aunque con la síntesis del Capítulo 3 se consigue una asociación estable de AgNPs al MIL-125-NH_2, no se había logrado tener control sobre la polidispersidad del tamaño de partícula, así como su localización en la partícula del MOF. Es por ello que en el Capítulo 4 se buscó optimizar la síntesis SiB, siguiendo un procedimiento de fotorreducción para la obtención de NCs de Ag. El proceso ultrarrápido (15 s de irradiación, con un total 20 min de preparación y recuperación) conduce a la formación de NCs de 1.01 ± 0.36 nm (con sólo 28 átomos de Ag) distribuidos únicamente en el interior del MOF, como ha sido demostrado por tomografía realizada en microscopia electrónica de transmisión (TEM). Este composite AgNC@MIL-125-NH_2 tiene una mayor absorción en el rango visible (E_g=2.4 eV) y se ha estudiado su eficacia como fotocatalizador en la degradación de contaminantes orgánicos emergente como son el tinte azul de metileno (MB) y el antibiótico sulfametazina (SMT). Cabe destacar que los ensayos de degradación se han hecho con agua real con concentraciones de contaminantes similares a las encontradas a la entrada de las plantas de tratamiento de aguas. También, por primera vez se ha analizado la capacidad de degradación por oxidación con luz visible en un reactor continuo diseñado en el laboratorio, pudiendo tratar 6.50 $L \cdot h^{-1} \cdot g^{-1}$ de agua contaminada con SMT, flujo comparable al de las plantas de tratamiento.

Para la asociación de NPs metálicas por métodos BaS se ha considerado el uso de la radiación microondas para promocionar la nucleación y crecimiento del MOF en torno a la NP, que actuaría como punto caliente para la síntesis. En el Capítulo 5 se presenta en primer lugar un estudio sistemático sobre diversos parámetros de reacción y como afectan a la obtención final de una determinada fase cristalina formada por aminotereftalato de hierro. La síntesis solvotermal asistida por microondas, en función del disolvente empleado (agua, etanol, dimetilformamida) entre otros parámetros, da lugar a uno de los distintos polimorfos MIL-53-NH_2, MIL-68-NH_2, MIL-88B-NH_2 o MIL-101-NH_2. Es importante enfatizar que durante esta tesis se ha obtenido por primera vez mediante síntesis microondas empleando agua cristales de MIL-53-NH_2. Una vez analizados los parámetros de reacción, la segunda parte del Capítulo 5 presenta los resultados preliminares obtenidos de la asociación AgNPs, previamente sintetizadas, a la familia de aminotereftalatos de hierro. Las micrografías de TEM demuestran que, aunque lejos de estar optimizados, es posible obtener composites AgNP@Fe-MOFs por la síntesis BaS asistida por microondas.

Considerando la naturaleza frágil de las lipasas, en el Capítulo 6 se llevó a cabo un estudio para preservar la actividad de la misma una vez inmovilizada mediante un proceso BaS en el fumarato de hierro flexible MIL-88A. Las lipasas son un tipo de enzimas que se caracterizan por ser catalizadores naturales muy específicos. Su asociación a la estructura de los MOFs permite su heterogeneización y recuperación y reciclado del medio de reacción, así como su protección. En el capítulo 6 se demuestra que las lipasas de *Pseudomonas fluorescens* y *Candida rugosa* siguen siendo activas una vez encapsuladas en el MIL-88A frente a pH extremos. Así mismo, se estudió la actividad catalítica del biocatalizador lipasa@MIL-88A en una reacción modelo de relevancia: la transesterificación de aceite de soja en biodiesel. Una vez optimizados los parámetros de reacción, se observó una selectividad extra del composite lipasa@MIL-88A, comparada con la lipasa libre (visto de forma cualitativa por cromatografía de gases-espectroscopia de masas). Este resultado abre la puerta para considerar un papel activo del MOF en la inmovilización de lipasas y enzimas, pudiendo potenciar si actividad.

Las síntesis aquí presentadas suplen algunas deficiencias de los protocolos del estado del arte (ej.: amplían las estructuras MOFs empleadas, proponen nuevos procedimientos SiB y BaS, controlan el tamaño y localización de los clústeres). Así mismo, la gran variedad de aplicaciones estudiadas con los composites obtenidos en esta tesis demuestran el potencial de los MOFs en múltiples campos. Aunque en el marco de la investigación básica, los resultados aquí obtenidos son de relevancia y sobre todo demuestran la capacidad de investigación de la doctoranda. Es decir, manifiestan su capacidad de: i) plantear un proyecto científico que responda una necesidad, ii) dividirlo en tareas simples para lograr el objetivo, iii) conducir

experimentos, iv) analizar resultados, así como su presentación y comunicación de forma ordenada, y v) colaborar con otros investigadores.

Abstract

Metal-Organic Frameworks (MOFs) are crystalline solids composed by inorganic units (atoms, clusters, chains, …) linked by ionocovalent bonds to organic polydentate ligands (carboxylates, phosphonates, azolates, …) procuring a highly porous three-dimensional (3D) network. From the first reports in the early 90s, interest in MOFs, their chemistry and their applications have increased exponentially. Proving so, are the >13,300 publications registered only in 2020 (Web-of-Science: "Metal-Organic Frameworks"). MOFs outstand from other porous materials due to their hybrid versatile organic-inorganic composition (tunable ligands, presence of unsaturated metallic centers…), their structural richness (multiple topologies, isoreticular families…) and their exceptional porosity (with specific surface areas-S_{BET} up to 8000 $m^2 \cdot g^{-1}$). As consequence, they have become an ideal candidate for relevant industrial and societal applications.

Even traditionally their porosity has been mostly exploited for fluid separation and storage (*e.g.*: CH_4, H_2), the encapsulation of other species for the synthesis of composite materials with improved properties is more recent. Following this interesting trend, this thesis looks after the association of two types of active species (AS) to the structure of various MOFs: i) metallic nanoparticles (NPs) and nanoclusteres (NCs) and ii) biomolecules (lipases). Some of the advantages of these composite materials are: i) AS protection (as MOF prevents aggregation, oxidation and/or degradation), ii) confinement within the porosity, iii) selective adsorption and iv) complementary and/or synergic reactivity, among others.

According to this, the main challenge of this thesis is the development of synthesis protocols that will procure a stable association of AS to MOFs by: i) homogeneous distribution of the AS, ii) preserving/promoting the activity of their individual constituents (*e.g.*: catalytic, biocide) and iii) ensuring reproducibility. Up to date, the main strategies for the attainment of core@shell (AS@MOF) composites could be resumed in two: i) ship-in-a-bottle, SiB, by diffusion of the AS, or its precursors, through the presynthesized MOF and ii) bottle-around-a-ship, BaS, by the *in situ* growth of the MOF crystal surrounding the AS. Due to the great interest in the development of AS@MOF composite, this thesis pursues to

increase the knowledge in this ongoing field and contribute with new protocols, based on both association strategies, that will overcome the limitations found in the state-of-the-art. In addition, the application in multiple relevant fields of the resulting composites has also been studied.

In Chapter 3 is presented the association of AgNPs to the benchmarked mircoporous photoactive titanium aminoterephthalate MIL-125-NH_2, using a simple two-step SiB procedure. The synthesis protocol designed in this thesis has been proven for the association of AgNPs of both MIL-125-NH_2 micro and nanocrystals. The attained NPs of 5 ± 3 nm were distributed on all the MOF, even being associated to their surface. The strong interaction between the -NH_2 labile group of the ligand and the AgNPs provide the MOF with enhanced photoelectronic properties (being the electronic bandgap, E_g, of the composite of 2 eV *vs.* 2.6 eV of the pristine MOF). In addition, the presence of AgNPs increments MIL-125-NH_2 intrinsic antimicrobial activity. The studies here carried out revealed that AgNP@nanoMIL-125-NH_2 thin films exhibited an anti-adherent behavior against *Staphyilococcus aureus* and *Escherichia coli*, procuring a treatment against bacterial biofilm, as well as demonstrated its biocide character.

Despite the synthesis presented in Chapter 3 achieved a strong association of AgNPs to MIL-125-NH_2, control on particle size polydispersity and their location within the MOF was still lacking. Therefore, in Chapter 4, the SiB association was optimized with a photoreduction protocol to procure AgNCs. The ultrafast method (just 15 s of irradiation, 20 min in total of preparation and recuperation), produced tiny Ag NCs (1.01 ± 0.36 nm, just 28 atoms) located solely within the MOF, as demonstrated by transmission electron microscopy (TEM) tomography. The AgNC@MIL-125-NH_2 composite has an enhanced absorption in the visible range (E_g= 2.4 eV) and has been studied as photocatalyst for the degradation of emerging organic contaminants as the methylene blue dye (MB) and the antibiotic sulfamethazine (SMT). It is important to outstand that the experiments were carried out with real water with contaminant concentration close to that reaching wastewater treatment plants. What is more, for the first time has been used a continue reactor for the visible light oxidation of contaminants using MOF as catalysts. The lab designed continuous flow reactor was able to treat 6.50 $L \cdot h^{-1} \cdot g^{-1}$ of SMT contaminated water, in range with wastewater treatment plants real flow.

Considering BaS association of metal NPs, it has been considered the use of microwave irradiation for the nucleation and growth of the MOF surrounding the presynthesized NP. In chapter 5, firstly is presented a systematic study of the influence of different reaction parameters in the attainment of a particular MOF phase constituted by iron aminoterephthalate. Microwave assisted solvothermal synthesis, depending on the solvent used (water, ethanol, dimethylformamide) among other parameters, procure one of the polymorph family MIL-53-NH_2, MIL-

68-NH_2, MIL-88B-NH_2 or MIL-101-NH_2. Emphasis should be made to the result obtained in this thesis, as MIL-53-NH_2 crystals were obtained for the first time by microwave synthesis using water as solvent. After analysis of the reaction parameters, second part of Chapter 5 presents the preliminary results of BaS associated AgNPs to the iron aminoterephthalate family. TEM micrographs showed that, despite of being optimized, was possible to synthesize AgNP@Fe-MOFs with microwave BaS assisted solvothermal synthesis.

As lipases are prone to denaturalization, Chapter 6 also starts with a study carried to optimize their BaS immobilization in the flexible iron fumarate MIL-88A, in order to preserve their activity. Lipases are a type of enzymes considered as natural catalyst with high specificity. Their association to MOF structures enable their heterogenization and recuperation and recyclability from reaction media, as well as their protection. In Chapter 6 has been proven that *Pseudomonas fluorescens* and *Candida rugosa* lipases are still active at extreme pH after their encapsulation in MIL-88A. Even more, the activity of the biocatalyst was studied in a representative reaction of relevance: the transesterification of soybean oil to biodiesel. Once optimized the reaction parameters, an extra selectivity of the lipase@MIL-88A composites was qualitatively identified by gas chromatography-mass spectrometry, compared to the free lipase. These results open the door to consider the active role of the MOF in the immobilization of lipases and enzymes, as it could promote the composite catalytic activity.

The synthesis here reported overcome some deficiencies of the state-of-the-art (*e.g.*: present new MOF structures, promote new SiB and BaS protocol, control the size and location of NCs). Additionally, the obtained composites were studied in a great variety of applications, proving MOF potential in many fields. Even the research here developed is considered as basic, the obtained results are relevant and, above all, evidence the research ability of the PhD. student. What is the same, exemplify her capability to: i) propose a scientific project that answers to a specific need/requirement/, ii) divide it into simpler tasks to achieve the objective, iii) conduct experiments, iv) analyze results, as well as their presentation and communication in an orderly manner and v) collaborate with other researchers.

Abbreviations

4-NA	*p*-nitroaniline or 4-nitroaniline
AAV	Ana Arenas Vivo
AC	Acetylacetone
AgC	Silver nanoparticles coated with citrate
AgNC	Silver nanoclusters
AgNPs	Silver nanoparticles
AgPVP	Silver nanoparticles coated with polivynilpirrolidona
APMU	Advanced Porous Materials Unit
AS	Active species
ATR	Attenuated total reflectance
BaS	Bottle-around-a-ship
BSA	Bovine serum albumin
BTC	Bencene-1,3,5-tricarboxylic acid or trimesic acid
C16:0 A	Palmitic acid
C16:0 E	Methyl palmitate
C17:0 E	Methyl margarate
C18:0 A	Stearic acid
C18:0 E	Methyl stereate
C18:1 A	Oleic acid
C18:1 E	Methyl oleate
C18:2 A	Linoleic acid
C18:2 E	Methyl linoleate
C18:3 A	Linolenic acid
C18:3 E	Methyl linolenate
CFU	Colony forming units
CLSM	Confocal laser scanning microscopy
C-r-lipase	*Candida rugose* lipase
CVD	Chemical vapor deposition
DFT	Density functional theory
DLS	Dynamic light scattering

DMF	*N,N*-dimethylformamide
DMSO	Dimethylsulfoxide
EDS	Energy dispersive X-ray spectroscopy
E_g	Energy bandgap
EOCs	Emerging organic contaminants
EPS	Extracellular polymeric substances
ESH	Environmental, safety and health
FAME	Fatty acid methyl ester
fcc	Face centered cubic
FDA	Fluorescein diacetate
FTIR	Fourier transform infrared
GC-MS	Gas chromatography-mass spectrometry
$H_2BDC\text{-}NH_2$	4-Amino terephthalic acid
HK	Horvath-Kawazoe
HKUST	Hongkong University of Science and Technology
HPLC	High performance liquid chromatography
I-2959	2-hydroxy-4′-(2-hydroxyethoxy)-2-methylpropiophenone (Irgacure-2959)
ICP-OES	Inductively coupled plasma-optical emission spectrometer
IEF	IMDEA Energy Framework
IF	Impact factor
IUPAC	International Union of Pure and Applied Chemistry
MB	Methylene blue
MeOH	Methanol
MIC	Minimum inhibitory concentration
microMOF	MIL-125-NH_2 microparticles
MIL	Material from Institut Lavoisier
MNP	Metallic nanoparticles
MOF	Metal-organic framework
MO_x	Metal oxides
mp	Melting point
nanoMOF	MIL-125-NH_2 nanoparticles
NB	Nutrient broth
NIR	Near-infrared
NLDFT	Non-localized density functional theory
NP	Nanoparticle
OD_{600}	Optical density at 600 nm
PBS	Phosphate buffered saline
PCP	Porous coordination polymer
PdI	Polydispersity index
PEG	Polyethyleneglycol

P-f-lipase	*Pseudomonas fluorescens* lipase
PMAA	Poly(methaacrylic acid)
PMMA	Polymethylmethacrylate
p-NPP	*p*-nitrophenyl palmitate
PPCPs	Pharmaceutical and personal care products
PPD	*p*-phenylendiamine
PSM	Post-synthetic modification
PTFE	polytetrafluoroethylene
PVP	Poly(vinylpyrodidone)
Q1	Frist quartile
Q2	Second quartile
QD	Quantum dots
RhB	Rhodamine B
ROS	Reactive oxygen species
RT	Room temperature
S_{BET}	Brunauer-Emmett-Teller surface
SBU	Secondary building units
SEM	Scanning electron microscopy
SiB	Ship-in-a-bottle
SMT	Sulfamethazine
SPR	Surface plasmon resonance
STY	Space-time yield
TEM	Transmission electron microscopy
TGA	Thermogravimetric analysis
UAH	Universidad de Alcalá de Henares
UiO	Universitetet i Oslo
UV	Ultraviolet
Vis	Visible
V_p	Pore volume
XRPD	X-ray powder diffraction
ZIF	Zeolitic imidazolate framework
ZP	ζ-potential

Index

Index of Figures

Index of Tables

Chapter 1

Introduction

"It's a magnificent field, it's a dream come true, to be able to put building units of various geometries together and make an entirely new family of materials."

Omar Yaghi, BBVA Fronteras del Conocimiento Award 2017

1.1. Metal-Organic Frameworks (MOFs)

Metal-organic frameworks (MOFs), also commonly known as porous coordination polymers (PCPs), are a relatively recent family of crystalline solids conformed by, inorganic secondary building units (SBU; atoms, clusters, chains, etc.) connected *via* ionocovalent bonds to polydentate organic ligands or linkers (carboxylates, phosphonates, azolates, etc.) developing a 3D network with important microporosity (see Figure 1. 1).[1] Since the first references to these type of materials in the early 90's, the number of MOFs and their applications have incredibly increased, mainly due to the contributions of the research groups of O.M. Yaghi,[2] G. Férey,[3] R. Robson,[4] and S. Kitagawa,[5] reaching more than 13,300 publications on the topic just in 2020 (according to Web of Science; accessed December 2020).[6] The vast number of metal ions and organic linkers available, as well as their diverse assemblies, opens an incredible playfield to researchers to design and tailor many different structures. Due to the relevance of this continuously expanding interdisciplinary field in the verge of inorganic and organic chemistry, even the IUPAC (International Union of Pure and Applied Chemistry) gave in 2013 a recommended definition to MOFs: "A Metal-Organic Framework is a coordination network with organic ligands containing potential voids".[7]

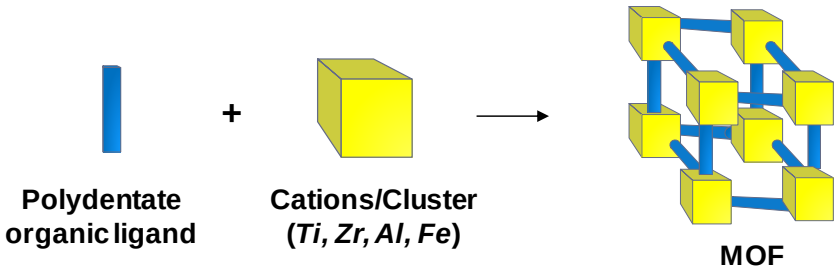

Figure 1. 1: Schematic view of MOF structure assembly with their secondary building units represented as blue sticks (ligand) and yellow cubes (inorganic unit).

As stated before, one of the main characteristics of MOFs is their exceptional porosity, up to record Brunauer-Emmett-Teller surfaces-S_{BET} of 7000-8000 m^2 g^{-1} and pore diameter in the wide range of 3-90 Å (see Figure 1. 2).[8,9] This results in the lowest density for crystalline materials, in other words, their wide-open structure provides free space that can reach up to 90% of their total volume. In comparison with other porous materials such as zeolites, mesoporous silica or carbonaceous materials, MOFs offer several advantages: i) chemical diversity and compositional tuneability, tailored for a specific application, ii) reactivity of the organic ligand (presence of unsaturated coordination sites, *e.g.*: $-NH_2$, -OH, $-SO_3H$, -Br), iii) mild synthetic conditions (due to moderate coordination bond energies), iv) structural versatility and richness of geometry (tuneability of the pore architecture), v) capacity of porosity expansion preserving crystalline structure (MOF isoreticular families), vi) possibility of change in void porosity under external stimuli (pressure, temperatures, solvents), vii) designable surface potential, and viii) some present high chemical and thermal stability.[1,10–15]

It is indeed in MOFs nature where their potential resides. This has promoted their use in a plethora of applications with both industrial and societal interest.[16–18] For mentioning some: catalysis,[19–21] molecule sequestration, separation and storage,[22–24] sensing and imaging, [25–28] energy conversion and storage,[29–31] biomedicine,[32–34] and pollutant degradation, among others.[35–37] This is resumed along with MOF synthesis and properties in Figure 1. 3. Even traditionally MOF porosity has been exploited in fluid capture, separation and storage of small molecules (*e.g.*: CH_4, CO_2, H_2), their large surface area, along with the other above mentioned unique properties, has opened the door for researchers to use MOFs as structural hosts for loading significant amounts of other active species (AS).[38] These AS could be other functional materials such as metallic nanoparticles (MNPs), quantum dots (QD), ceramics (metal oxides, MO_x), or, polymers, as well as biomolecules (enzymes, nucleic acids, antibodies, peptides). Their combination in a core@shell structure (referred as AS@MOF hereafter) leads to the synthesis of novel composites with advanced properties, that could not only overcome MOF limitations but also endow significant improvements to MOFs inherent functions.[39]

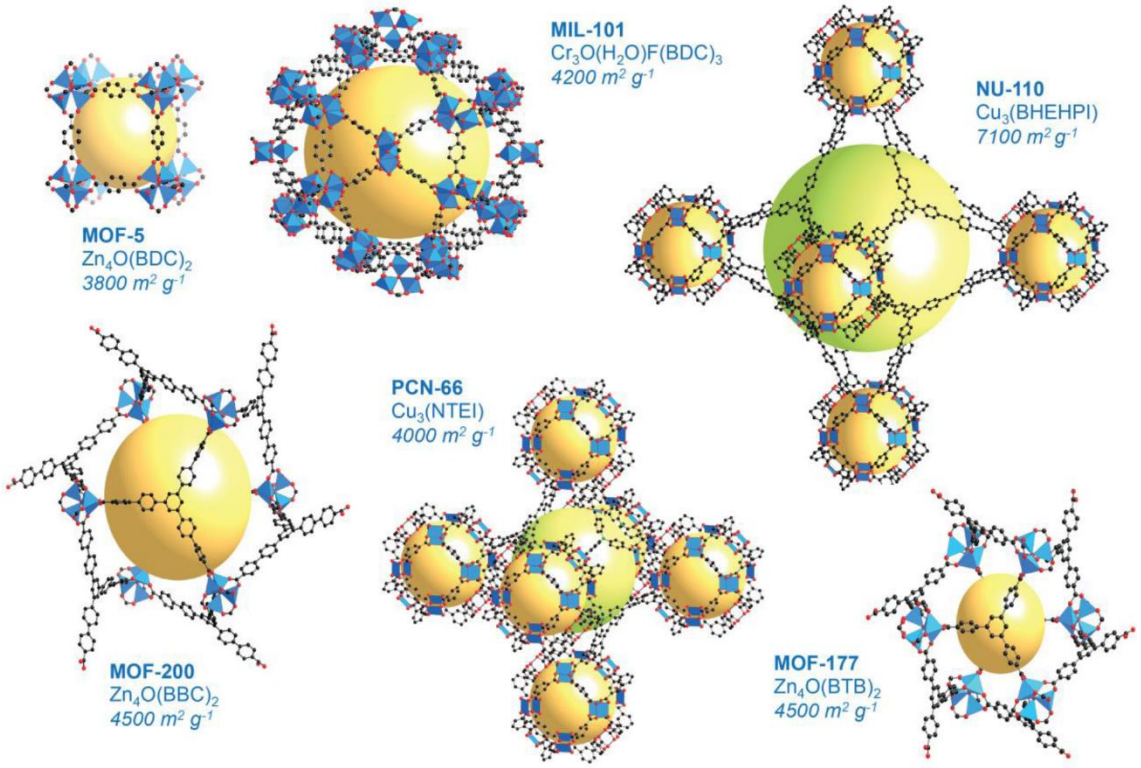

Figure 1. 2: Crystal structure of selected MOFs providing also chemical formula and surface area (S_{BET}). Yellow and green spheres indicate free space in the framework. Reproduced with permission of [40].

1.2. Synthesis of MOFs

As previously stated, MOFs are formed by two major parts: the inorganic node and the organic ligands. The inorganic node can consist of a single metal atom, a metal cluster or a metal-oxocluster (even 1D, 2D or 3D). Starting metallic salts can have mono-, di-, tri- or tetravalent cations. The ligands coordinate with the inorganic SBU by their complexing moieties and they can have di-, tri- or multiple functional groups such as -COOH or - NH. The unlimited combination of different organic ligands and metallic clusters results in a large variety of different topologies, porosities and dimensionalities.[15] This SBU building approach, named reticular synthesis by Yaghi and coworkers,[41] enables rational pore design and orientation of the network. This chemistry has as an outcome the isoreticularity: families of MOFs that maintain the same topology, but they have different functionality/porosity. Such is the example of MOF-5[42] or MOF-74[43] isoreticular families, that with increasing the length of the organic ligand, resulted in increased MOF porosity preserving the geometry. The new synthesized materials are usually named after their chemical structure (MOF, metal-organic framework) or the laboratory where they were created (MIL, Material from Institut Lavoisier;[44] HKUST, Hong Kong

University of Science and Technology;[45] UiO, Universitetet i Oslo;[46] IEF, IMDEA Energy Framework,[47] etc.) and a number indicating generally chronologic order of report.

Not only the choice of its raw chemical constituents determines the final crystallographic phase and topology of MOFs but also the reaction conditions. Some pertinent parameters are pH, temperature (boiling point, dielectric properties), solvents polarity, concentration and nature of starting metallic precursor (acid-basic or redox character).[1] Minor adjustment of these parameters can lead to inferior quality crystals and even to an entirely different phase besides having same starting reagents. For MOF synthesis it is generally required to provide energy, as they are endothermic reactions.[48] This energy can be supported to the reaction mixture in several manners. Traditional synthetic methods include non-solvothermal,[49] hydrothermal[50] and solvothermal synthesis.[51] Other methods explored involve mechanochemical synthesis,[52] sonochemical synthesis,[53] electrochemical synthesis,[54] microwave assisted synthesis,[55] high-throughput,[56] and the use of ionic liquids[57] or supercritical CO_2,[58] among others.[40] A brief introduction to some of them is depicted below.

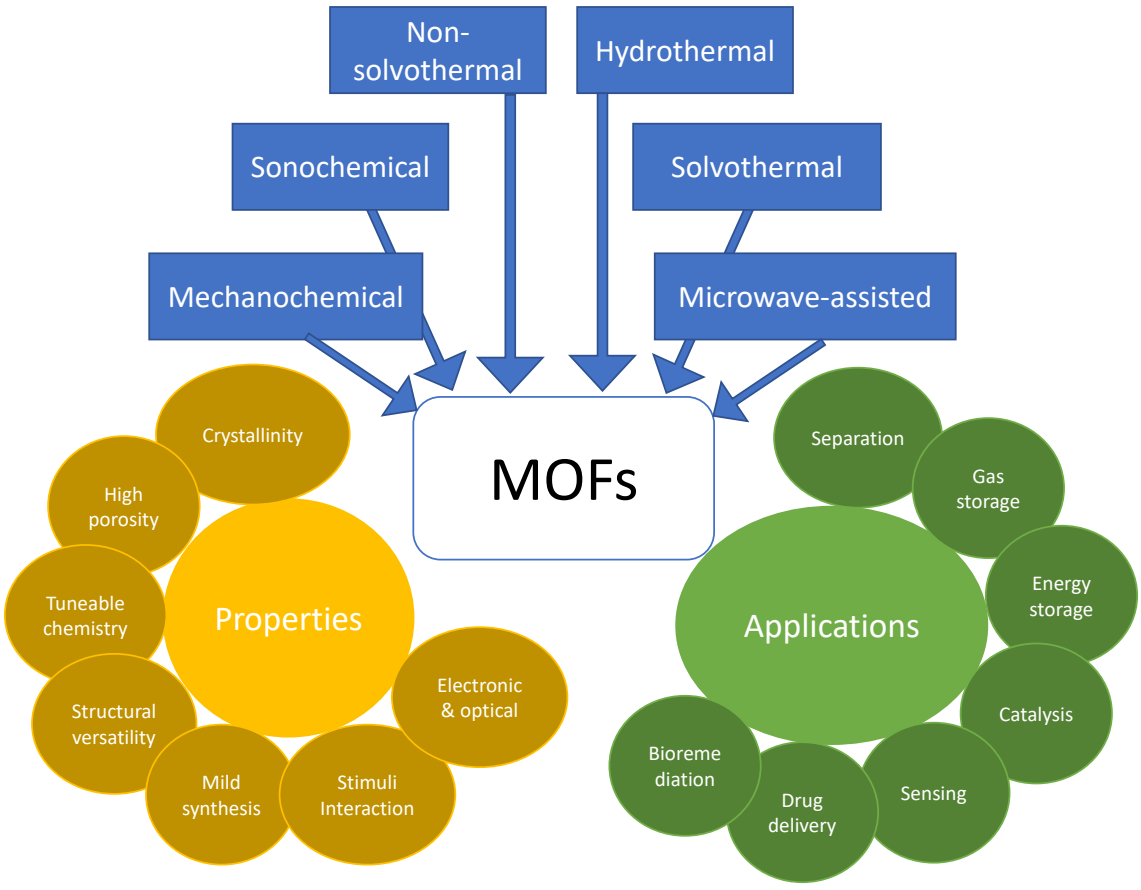

Figure 1. 3: Schematic overview of MOF synthesis, properties and applications.

A) Non-solvothermal synthesis

Non-solvothermal reactions take place below or at the boiling point under ambient pressure, which simplifies the synthetic requirements. Therefore, low temperature (even room temperature, RT, in occasions) and reflux routes enable facile, faster and greener processes comparing to traditional hydrothermal/solvothermal methods. Precipitation reaction followed by recrystallization or slow solvent evaporation are examples of low temperature reactions. Often large MOF crystals suitable for structure determination are obtained by these methods. Nevertheless, a higher reaction temperature by conventional heating and reflux setups are required in some systems to attain suitable reaction rates. Non-solvothermal methods are preferred for scaling up as they present less safety issues and they are cheaper as they do not require pressure resistant equipment.

B) Hydro- and solvothermal synthesis

Both hydro- and solvothermal strategies are well-stablished methodologies for MOF synthesis that involve high temperature (above boiling point) and autogenous pressure in closed vessels. They require the combination of a metallic precursor and an organic ligand in an adequate solvent. Beside water, the main solvents used are alcohols, dialkyl formamides or pyridines. Solvent selection is based on the solubility of the SBU precursors, among other parameters. After reaction is completed, precipitation of the crystalline MOF product from the solution takes place. Often MOF crystals are recovered by filtration after reaction. This relatively simple procedure enables scalability of the reaction, besides security problems related to the high pressure involved in the reaction, and produces relatively large crystals. Even well-known chemistry companies as BASF are commercializing MOFs following this synthetic procedures (*e.g.*: Basolite A520, equivalent to MIL-53(Al), or Basolite C300, equivalent to HKUST-1).[59] It must be taken into account that MOFs synthesized in the presence of solvents often require a subsequent activation step, to remove the excess of solvent remaining in the MOF porosity. Therefore activation is required in both solvothermal and non-solvothermal syntheses.

B1.High throughput solvothermal synthesis

It involves the miniaturization and parallelization of the solvothermal method, allowing to reduce the use of reactants, optimize the synthetic conditions and speed up the discovery of new phases.[60] In a general experiment 12-48 autoclaves are filled within the same "reactor system" (see Figure 1. 4). Requires careful experiment design, reagent and solvent dosage, characterization and data

evaluation. Nowadays there even are automated equipment for small scale synthesis such as the FLEX ISYNTH of Chemspeed© to ease the work of researchers.[56] The large amount of information obtained in short time enables a better understanding of the role of the different reaction parameters in the formation of new phases.

Figure 1. 4: High throughput solvothermal autoclave reactors at IMDEA Energy.[60]

C) Microwave-assisted solvothermal synthesis

The combination of heat and pressure produced by the microwave irradiation due to the polarization of the molecules under electromagnetic irradiation reduces the reaction time compared with traditional solvothermal synthesis. The interaction of the electromagnetic waves with the soluble molecules promotes faster reaction rates, which in addition to the very homogeneous heating, lead to a better control of the particle, with low polydispersity and good crystallinity. In addition, microwave irradiation can mediate preferential crystal growth controlling the morphology of the final MOF crystal. Conjunction of this all, microwave-assisted synthesis can reduce reaction time up to few minutes, a huge advantage compared to solvothermal synthesis that involves several hours or even days. It is an important route as it can be scaled up and is compatible with continuous synthesis and industrial production times, opening the door towards MOF commercialization.

D) Mechanochemical synthesis

This involves solvent-less solid-state grinding, avoiding the need of toxic solvents such as dimethylformamide (DMF). In this case both MOF inorganic and organic precursors are place in a stainless-steel vessel with ball bearings. Even simpler and more accessible, reagents also can be mixed by mortar grinding. The mechanical energy supplied enables the interaction between ligand and metallic salts in the absence of heating.

E) Sonochemical synthesis

The use of ultrasound waves at an intensity of 20 kHz to 10 MHz is also a straightforward MOF synthetic procedure. The sonication of the reaction mixture produces local solvent cavity regions that without the need of extra heat instantly

generates monodisperse crystals. During cavitation the effective temperature can rise as much as 5000 K promoting rapid crystal nucleation and growth, resulting in high quality crystals, which final size depends on exposure time to ultrasound waves.

1.3. Association of active species

MOFs are outstanding scaffolds for the development of new composite materials due to their ultrahigh porosity ranging from micro- to mesopore and their robustness. They can present a passive role, being a support for the AS just enabling their uniform dispersion and preventing their agglomeration and leaching. Moreover, their pore size can define and limit the growth of AS synthesized within their framework and procure confinement effects. In addition, the size of the accessible windows endows selective adsorption among AS.[61] Nevertheless, as MOFs consists of metal ions and organic ligands, they offer the extra possibility of promoting chemical bonds, as for instance metal-metal and coordination interactions, with the embedded AS.[62] In that case, MOFs exhibit an active role in the composite synthesis, avoiding the use of other stabilizing or binding agents. Furthermore, these strong interactions could lead to remarkable functionalities of the composite, widening the MOF active role up to the final properties (*e.g.*: increase catalytic activity, selective adsorption of species).

1.3.1. Association strategies

The different core@shell (AS@MOF) synthetic strategies can be resumed in two big groups (Figure 1. 5). The first, the infiltration of AS through the porosity of a pre-formed MOF host. This approach is commonly known as “Ship-in-a-bottle” (SiB), diffusive or *ex situ* synthesis. As a counterpart, the seconds entails MOF synthesis around an AS that acts as the nucleation seed for the MOF crystal growth surrounding it. This method is referred to as “Bottle-around-a-ship” (BaS).[63] In some cases is also called as “one-pot”, *in situ* or *de novo* synthesis. While both routes lead to the assembly of a composite with the AS embedded within the MOF, different parameters such as AS size and chemical nature or their final desired distribution and accessibility within the AS@MOF composite, will dictate the selected synthetic route. In addition, it should be mentioned that AS could be also associated to MOFs by anchoring to their external surface.[61] This facile strategy enables the association of AS bigger than the pore size and opens the door to the synthesis of composites with dense MOFs. Even though, it presents greater

drawbacks than SiB and BaS strategies, for instance, the amount of AS associated is lower (surface attachment *vs.* pore or defect accommodation), and AS are highly exposed to the environment and at higher risk of leaching.[63,64] Thus, only the assets and the limitations of both the SiB and BaS protocols, as well as their state-of-the-art laboratory procedures, will be further analyzed below.

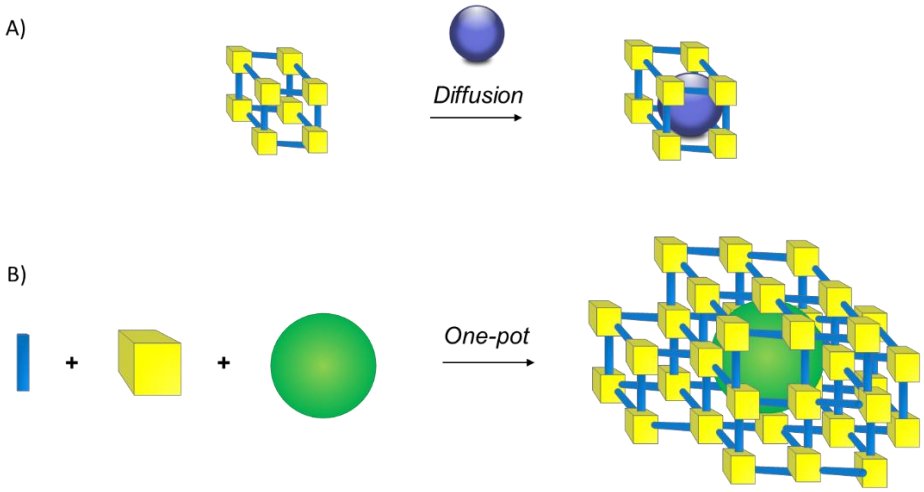

Figure 1. 5: Schematic representation of the AS@MOF association strategies. A) Ship-in-a-Bottle, B) Bottle-around-a-Ship.

1.3.1.1. Ship-in-a-bottle (SiB)

In the case of the SiB approach, a pre-synthesized MOF is used as scaffold for the formation of the AS@MOF composite. Traditionally, the SiB immobilization of MNPs entails a two-step procedure: i) infiltration of the AS precursors through the porosity (either by gas or liquid impregnation) and ii) chemical transformation of the precursors (reduction, hydrolysis, oxidation) to lead to the desired AS. For doing so, the selected MOF should be stable and compatible with the sequential reactions of the AS transformation. SiB is characterized by its simplicity and its potential straight scale-up. In addition, MOF confinement enables high-loading without agglomeration and the control of the final AS size, limited by the pore diameter. That said, SiB procedure has limited constraint on spatial distribution of the AS. As there is an important diffusion resistance through the framework than onto the exterior surface, AS might additionally coat the outer surface. Another limitation is the control of the final morphology of the AS.[63] Below are presented some of the most common methodologies followed:

A) Solution impregnation

Solution impregnation is the most extensively used SiB procedure as it enables the encapsulation of AS of different nature (biomolecules, MNPs) in a single step. It is a facile method where the presynthesized MOF is impregnated a by an aqueous or organic dispersion/solution of the AS or their precursor. This strategy

is restricted by the MOF accessible pore diameter, limiting the size of AS, ruling out the possibility of its use in large biomolecules. Capillary forces and electrostatic interactions rule the wetting of the microstructure. Generally, stirring and/or heating the mixture favors the diffusion of AS across the network.[63] Nevertheless, it should not be forgotten to ensure MOF stability under encapsulation conditions. Also, selecting MOF with available active groups (able to specifically interact with the AS, *e.g.*: amines) could assists in the anchoring of the AS. The final concentration of the AS depends on the mass-transfer conditions, as a competition between guest and solvent molecules takes place. To prevent the deposition of active species on the MOF outer surface it is important to thoroughly wash the composite after the impregnation to remove excessive or unbounded AS. The solution impregnation could be extrapolated also to supercritical fluid impregnation such as supercritical CO_2 impregnation. In this case, the superficial tension is avoided, and uniform coatings can be ensured.

In the case of depositing precursor metal ions instead of already formed MNP or inorganic polymers, a further reaction step (*e.g.*: reduction, hydrolysis, oxidation) is required. For instance, reduction of the AS precursor can be reached using chemicals (*e.g.*: hydrogen, hydrazine, sodium borohydride, ethanol, methanol), or light (UV, visible) as reducing agents.[62] Even limited by the pore size, it is difficult to achieve a homogeneous particle size distribution after reaction. It is important that the MOF withstand the reaction conditions, otherwise it will induce defects in the framework, particle agglomeration and even MOF collapse. In this thesis, different reduction reaction procedures have been followed for the association of MNPs.

B) Chemical vapor deposition

Chemical vapor deposition (CVD) is a well-known method for the deposition of metals on substrates.[65,66] Following the same principle, volatile organometallic precursors could be embedded in MOF pores and channels by sublimation under static vacuum. Fischer's research group was one of the pioneers in the use of CVD in the synthesis of MNP@MOF composites.[67,68] Typically, the MNP precursors are located in a tube with the MOF present downstream. After heating to a certain temperature to induce sublimation and vapor pressure, the volatile compounds are carried by an inert gas towards the MOF, were they diffuse through the channels and are finally deposited in the porous structure. This solvent free method ensures high loading, compared to liquid impregnation, avoiding competitive adsorption of the solvent. After deposition, a gaseous reducing agent such as H_2 is used to finally obtain the MNP and the MNP@MOF composite.[63] As high temperature and pressure are required for sublimation and diffusion through the framework, special attention has to be paid to MOF stability when selecting a scaffold for CVD. [62]

There are many publications in which MOF-5,[69,70] MOF-177,[71] and ZIF-8 [72,73] are usually selected due to their thermal stability and pore accessibility to small gases diffusion.[74]

C) Mechanical grinding

Also using volatile organometallic compounds, mechanical grinding is an effective, but less commonly used, approach to promote a solid-state reaction at moderate temperature. The milling process enables the precursor sublimation and the rapid vapor diffusion through the porosity leading to a well distribution of AS after further chemical transformation (*e.g.*: H_2 reduction).[62]

1.3.1.2. Bottle-around-a-ship (BaS)

Another approach for the synthesis of AS@MOF composites is the self-assembly of MOF surrounding an AS, answering to the symbolism of the BaS strategy. In other words, the AS do not occupy the porosity but instead act as a seed for MOF nucleation and growth around it. This is typically done by dispersing the AS in the reaction media along with the MOF organic and inorganic SBUs. In contrast to the infiltration methods previously mentioned, this approach has no limitation on the AS size as the MOF shell develops wrapping the AS, opening the door for the encapsulation of molecules larger than the pore size. In addition, it gives better control and homogeneity of the AS, as it is already predefined before the composite synthesis (*e.g.*: particle size, shape, activity) ensuring better performance in future applications. However, the subsequent MOF growth around an AS normally exhibit difficulties derived from the high energy barrier between the AS and the MOF building blocks. Consequently, synthesis could result in AS aggregation outside self-nucleated MOF crystals. For preventing this, the AS could be protected by stabilizer such as surfactants or capping agents. During the synthesis, the organic ligands can interact with surfactant/capping agents, forming specific bonds, therefore anchoring to the AS promoting the crystallization around it. This surfactant/capping agents most of the times should be removed after synthesis for preventing the blockage of active sites and particle shielding reducing the performance of the composite. Another difficulty is the control over the spatial distribution of the encapsulated AS as well as achieving the so desired one-AS-in-one-MOF configuration.[74] An example of the complexity of control can be seen in Figure 1. 6, of the transmission electron microscopy (TEM) micrographs of zinc-based zeolitic imidazolate framework ZIF-8 composites, where Lu and his group[75] followed a strategy of successive addition of MNPs on the growing MOF crystals.

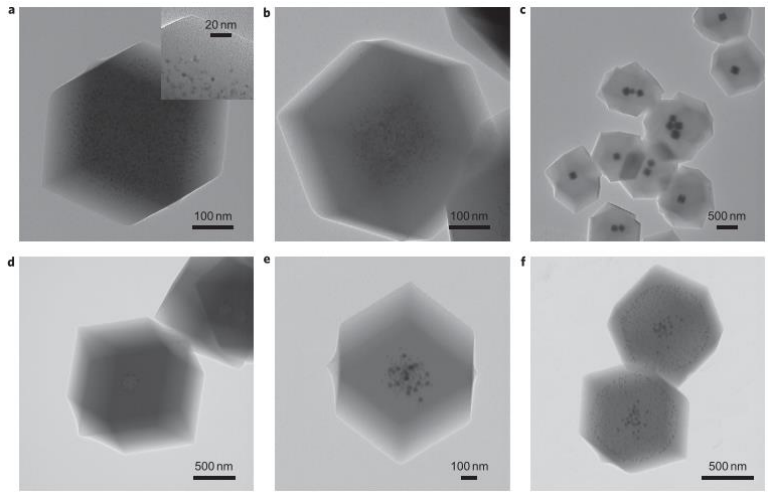

Figure 1. 6: TEM micrographs of MNP@ZIF-8 a) and b) Pt NP, c) Ag cubes, d) Au NP caped by polymers, e) Au NPs and f) Au NPs of 34 nm in the core surrounded by 13 nm Au NP. Reproduced with permission of ref [75].

Recapitulating, in Table 1. 1 is summarized a comparison between the association strategies presented in this manuscript.

Table 1. 1: Comparison between SiB and BaS association strategies. Code: (+) advantage; (-) disadvantage, (~) neither advantage nor disadvantage.

Ship-in-a-Bottle		Bottle-around-a-Ship	
Presynthesized MOF	(+)	MOF nucleation and growth surrounding AS	(-)
Diffusion through MOF porosity	(~)	Allocation inside framework defects	(~)
Limited by accessible pore size	(-)	No size limit	(+)
Simple synthesis	(+)	Many reaction parameters to control	(-)
Several steps required	(-)	One-pot	(+)
Self-stabilized in MOF framework	(+)	Need of surfactants or capping agents	(-)
MOF compatible with AS impregnation/synthesis conditions	(~)	AS compatible with MOF synthesis conditions	(~)
Risk of surface attachment	(-)	Risk of AS aggregation	(-)

1.3.2. Active Species

The availability of several strategies towards association of AS is another advantage of MOFs over other porous supports such as zeolites. In addition, the topological variety of MOFs allows the encapsulation of AS of a broader nature. For instance, MOF milder synthesis conditions enable the BaS association of fragile organic molecules.[38] However, MNP and enzymes are among the most widely studied AS for the development of AS@MOF composites due to their great interest in heterogeneous catalysis and sensing, among others.[74,76] Accordingly, greater attention will be paid to them in following sections.

1.3.2.1. Metallic nano-objects: Ag

In recent years, there has been a growing interest in the synthesis of nanocrystals with different shape and size. While bulk crystal properties merely rely on the elemental composition, decreasing the size to the nanoregion induce unique changes on the material properties. As size decreases, the number of atoms located on the surface of a MNP increases, giving a higher surface-to-volume ratio and affecting to properties such as phase transition behavior or the catalytic activity and selectivity (ability to bind foreign atoms more tightly due to lower coordination with bulk). In addition, MNPs can be considered as an aggrupation of atoms or superatoms that experience quantum size effects that affect to their ionization potential and electron affinities. The combination of both surface and quantum effects explains the size-sensitive behavior of MNPs, affecting to optoelectronic properties (shift in bandgap), magnetic properties (orbital momentum of unpair electrons) or biological properties (size-related cell toxicity).[77] Because of this special behavior, they are widely used in applicative fields such as catalysis, optoelectronics, chemical sensing and data storage, among others.

MNPs can be prepared following two categories: Top-down or Bottom-up. Top-down approach in the nanoworld involves the use of bulk materials and reduce them to the nanoscale normally by means of physical or mechanical transformation, whereas Bottom-up starts from atoms or molecules following chemical transformation to obtain NPs.[78] Some examples of fabrication classified as Top-down methods are laser ablation, arc discharge and radio frequency sputtering. The bottom-up chemical production of NPs can also be classified by the reducing agent in classical chemical and radiation chemical [79] However, free MNPs, due to their high reactivity, are thermodynamically unstable and prone to aggregate losing their favorable activity. Generally, to better control shape, size and size-distribution. the use of stabilizers is extended, particularly in the classical chemical reduction. One option is to achieve electrostatic stabilization by the coordination of anionic species

(*e.g.*: carboxylates, halides) forming an electrical outer layer that generates coulombic repulsion within the surrounding NPs. Another mean of repulsion is achieving steric stabilization protecting the NPs with bulky molecules such as organic molecules (dodecathienol) or polymers (poly(vinylpyrolidone) (PVP), poly(ethylene glycol) (PEG), poly(methacrylic acid) (PMAA), polymethylmethacrylate (PMMA) are the most common).[79]

An interesting alternative to prevent MNPs aggregation is their stabilization in porous materials, such as the here studied MOFs. Their encapsulation not only prevent their aggregation and growth, but also presents a beneficial synergy between both constituents for catalysis. MOFs offer spatial confinement, limit particle growth in the framework, increment reaction selectivity (limiting the direct interaction of reagents with the MNP due to access restrictions controlled by accessible pore size) and offer a transfer path for the reaction products. MNPs increase the number of actives sites available in the network (*e.g.*: acidic (-OH, -SO_3H) or basic (-NH_2) functional groups in the organic linker and/or the unsaturated metal center of the inorganic SBU) and present an opportunity to increase reactivity (limit electron-hole recombination due to ligand-to-metal electron transfer mechanisms). That is, the rational combination of MNP-MOF pair effectively enhances their strengths and counter their deficiencies.

Among other transition metals, silver (Ag) outstands for the variation of the optical and electronic properties with size, modulating the energy gap (E_g). When particles size decreases below 6-8 nm, there is a change of lattice contraction that favors electron confinement and E_g of the semiconductor abruptly increases.[62] This optical properties mainly rely on Ag surface plasmon resonance (SPR, free electron collective oscillation within the NP). AgNPs (see Figure 1. 7), as other metals, support many SPR modes in the visible and near-infrared region (NIR): from 300-1200 nm. While spherical particles exhibit a single scattering peak, anisotropic prims or rods exhibit multiple scattering peaks in the visible region as a result of highly localized polarization on edges.[80] In particular Ag plasmon is close to five times that of Au, reason of its preferential selection along with its moderate prize compared to other precious metals (reference ounce in US $: Ag-15$; Au-950$, Pt-1300$, Pd-300$).[81,82] Furthermore, this variation with size of the electronics properties also modify the fluorescent emission of the AgNPs, feature already explored as biological label. Silver also has the highest electrical and thermal conductivity among all metals, being perfect for electrical connections.[83] In addition AgNPs have been extensively used since ancient times due to their antibacterial activity in health industry, food storage, coatings and other environmental remediation applications.[84,85] Even not fully understood, its antibacterial activity is often explained by two mechanisms: the slow release of Ag^+ ions that interfere with the bacteria membrane causing permeability and leakage of cellular content, and

the reactive oxygen mechanism that produces reactive oxygen species (ROS) that interfere with the bacterial DNA replication causing its death.[86]

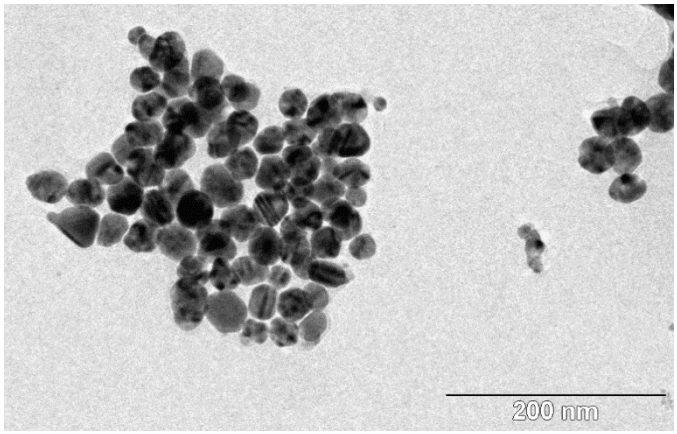

Figure 1. 7: TEM micrograph of citrate caped AgNPs.

An extended method for the preparation of AgNPs is via chemical reduction of its cationic precursors. This reaction is also known as co-precipitation and involves several steps: reduction, nucleation, growth, and agglomeration. Generally, this reaction is carried out using water or organic solvents in which different silver salts are dispersed and the reduction of Ag^+ ions leads to the formation of Ag^0 atoms, which is followed by agglomeration into clusters, which eventually yield colloidal silver with normally a particle size of nanometers.[79] This reaction is governed by the redox potential. In the case of silver, the reduction potential in water for the $Ag^+ \rightarrow Ag^0$ reaction is $E^0 = +0.799$ V. This relatively large potential enables the use of several reducing agents such as sodium citrate ($E^0 = -0.180$ V), sodium borohydride ($E^0 = -0.481$ V), hydrazine ($E^0 = -0.230$ V) or hydroquinone ($E^0 = -0.699$ V).

Another possibility is to induce the reduction of the metal cation by direct or indirect photolysis. The photoreduction mechanism is based on the electron transfer from the solvent to the Ag^+ excited state to form Ag^0, normally by solvent deprotonation. For doing so ultraviolet (UV) irradiation should be used as excitation source, according to the metal salt absorbing spectral region. The use of photosensitizers in the reaction media can increment the absorption range to the UVA-Visible region. In this case, the sensitizer will absorb the radiation generating an intermediate (free radical, anion) that afterwards reacts with the metallic cation to form Ag^0. The light-assisted reduction of AgNPs is a promising approach that exhibits a better control on the final AS particle size, as interrupting the irradiation holds up the progress of the redox reaction.[78]

Due to the relevance of AgNP is not unexpected to find previous works that consider the formation of AgNP@MOF. As a summary, Table 1. 2 enunciates a compilation of the current state-of-the-art.

Table 1. 2: List of Ag@MOF composites and their applications

Composite	Association strategy	Ag content (wt.%)	Application	Ref
Au-Ag@ZIF-8	Impregnation and reduction	*Not reported*	Catalytic reduction of *p-nitrophenol*	[87]
Ag@ZIF-8	*In situ* encapsulation	*Not reported*	*Not reported*	[75]
Ag@MOF-74(Ni)	Impregnation and reduction	1.5-6.5	Noble gas adsorption	[88]
Ag@MIL-53(Al)	Impregnation and reduction	10-15	CO oxidation	[89]
Ag@MIL-101(Cr)	Impregnation and reduction	1.5-7	CO_2 conversion into carboxylic acids	[90]
Ag@MIL-125	Impregnation and photored.	0.5-5	Degradation Rhodamine B	[91]
Ag@Rb/Cs-CDMOFs	Impregnation and reduction	1.2-4	*Not reported*	[92]
Ag@MOF-5	*In situ* encapsulation	*Not reported*	*Not reported*	[93]
Ag@Zn-TSA	Impregnation and reduction	8	Biosensing	[94]
Ag/RGO/MIL-125	Impregnation and photored.	*Not reported*	*Not reported*	[95]
Ag@CO-MOF	Physical adsorption	*Not reported*	Carboxylation from CO_2 fixation	[96]
Ag⊂$Al_2(OH)_2$TCPP	Encapsulation by Atomic Layered deposition on	*Not reported*	*Not reported*	[97]

	Presynthesized AgNP			
Ag@MIL-100(Fe)	Impregnation and reduction	*Not reported*	CO_2 conversion into carboxylic acids	[98]
Ag@UiO-66(Zr)	Impregnation and reduction	*Not reported*	CO_2 conversion into carboxylic acids	[98]
Ag/g-C_3N_4/MIL-125	Impregnation and photored.	*Not reported*	Photooxidation of alcohols	[99]
Ag@IRMOF-3	One-pot synthesis	0.09-2	Formaldehyde conversion	[100]
Ag/MOF(Ag)	One-pot synthesis	*Not reported*	Sensing of trinitrophenol	[101]
Ag@MIL-125-AC	Impregnation and reduction	*Not reported*	*Not reported*	[102]
Ag@MOF-5(Zn)	One-pot synthesis	*Not reported*	Catalytic reduction of *p-nitrophenol*	[103]
Au@Ag/MIL-101(Cr)-S	Impregnation and reduction	*Not reported*	Catalytic reduction of *p-nitrophenol*	[104]
Ag@Ni-MOF	Impregnation and reduction	*Not reported*	A^3 coupling reaction	[105]
Ag@Zn-MOF	Impregnation and reduction	*Not reported*	Sensor H_2O_2	[106]
Ag@MIL-101(Cr)	Impregnation and photoreduction	1.5-2	Catalytic reduction of *p-nitrophenol*	[107]
Ag@MIL-68(In)	Impregnation and reduction	31	*Not reported*	[108]
Ag-Ag_3PO_4@HKUST-1	Impregnation and photored.	*Not reported*	Photodegradation of dye	[109]

Ag/AgCl@Co-Fe-MIL-125-NH_2	*Not reported*	*Not reported*	*Not reported*	[110]
Ag/AgCl@MIL-53(Fe)	One-pot synthesis	*Not reported*	Photodegradation Rhodamine B	[111]
Ag-MIL-101(Cr)	Impregnation and reduction	2	Photocatalytic CO_2 reduction	[112]
Ag@ZIF-9(Co)	Impregnation and photored.	2-9	Photocatalytic CO_2 reduction	[113]
Ag@ZIF-67	Impregnation and reduction	0.1-0.8	Sensor for glucose	[114]
Ag@MOF-5@chitosan	Impregnation and reduction	*Not reported*	Degradation of sulfur mustard	[115]

Besides works presented in Table 1. 2, the synergistic combination of AgNP is far from being fully explored and further studies are required considering the possibilities of Ag-MOF pairs, different association strategies, and their combined activity and thus, this thesis will promote further development of this field. Taking this into account, the amino-substituted titanium terephthalate MIL-125-NH_2 or $[Ti_8O_8(OH)_4(BDC\text{-}NH_2)_6]$ has been selected as support, as it has been less studied for the SiB association of Ag nanospecies compared with its isoreticular parent, MIL-125 (see Table 1. 2). Yet more reasons for the selection of MIL-125-NH_2 will be presented in section 3.2 MOF selection: MIL-125-NH_2. In addition, both nano- and micro-crystals of MIL-125-NH_2 will be considered. Furthermore, special attention will be placed to achieve a modulable amount of Ag associated, as well as its determination (not always reported); and to procure a homogeneous distribution of Ag nanospecies. As a result, it is expected that the resulting Ag@MIL-125-NH_2 composites will exhibit enhanced optoelectrical properties in the visible range, higher catalytic activity and promoted biocidal character (application explored for the first time for Ag@MIL-125-NH_2 in this thesis). On the other side, due to the scarce BaS association procedures on the current state-of-the-art, microwave assisted synthesis will be explored in this thesis for the one-pot association of Ag nanospecies to MOFs and preliminary results are presented in section 5.3 Preliminary AgNP@Fe-MOF composites.

1.3.2.2. Enzymes: lipases

Enzymes are important biomacromolecules naturally present in life systems such as plants, animals and microorganisms. They are of great interest as they facilitate the transformation of biological and chemical substances, in other words, they are natural catalysts. As other catalysts, they decrease the activation energy of the reaction without interfering in the equilibrium and without being consumed. In addition, they can procure tandem catalytic reactions. Even more, enzymatic catalysis is considered a typical green technology that exhibit excellent selectivity (chemo-, stereo- and regio-selectivity).[116] In the last decades enzymes have been explored in biochemical industries as they offer advantages over traditional catalysts related to sustainability (*e.g.*: mild reaction conditions, low environmental impact and low toxicity) and process efficiency. They have been used as catalysts for organic synthesis in healthcare, food, beverages and pharmaceuticals.[117] Despite of this, free enzymes have still limited use in industry due to their fragile nature as they easily denaturalize and lose their catalytic activity under harsh conditions such as high temperatures, extreme pH, mechanical stress or organic solvents. In addition, due to their solubility they present problems for their recovery and further reusability, incrementing the purification steps required after the reaction.[118]

Several strategies have been considered to overcome the above mentioned limitations of free enzymes, such as immobilization, artificial modification, enzyme engineering and directed evolution of enzymes.[118] Enzyme immobilization considers the enzyme being fixed or embedded within a support and is a facile strategy to improve their stability while preserving their activity. Immobilization not only shields the enzyme from the surrounding media but additionally enables enzyme separation, recovery and recycling. Even in some cases, they can exhibit enhanced selectivity due to modification of enzyme conformation, interaction with their supports and the generation of favorable microenvironments.[119]

In recent years MOFs have drawn attention as novel supports for enzyme immobilization due to their advantageous properties previously mentioned: tunable and ordered high porosity and topology, and the possibility of stabilization *via* host-guest interaction with the metal clusters and ligands (*i.e.*: Van der Walls, force, hydrogen bonding, $\pi - \pi$ interaction, electrostatic interaction). The combination of all makes MOFs suitable for encapsulation of varieties of enzymes with different dimensions, morphologies and pensile groups. Moreover, lipases are the most used enzymes in synthetic organic chemistry, catalyzing the chemo-, regio- and/or stereoselective hydrolysis of carboxylic acid esters or the reverse reaction in organic solvents.[120]

Lipase@MOF composites can be synthesized following SiB strategies such as adsorption or covalent linkage. They offer high enzyme loadings with structural

conformation to adapt to the MOF topology. In this case, substrates offer also an extra selectivity. Nevertheless, lipases also tend to attach to the outer surface, they are limited by size compatibility requirements and are prone to enzyme leaching after catalyst reusability. More interestingly, as some MOF exhibit mild synthetic conditions, enzymes can be encapsulated following a BaS procedure. This *in situ* procedures can be distinguished in co-precipitation, that involves the use of co-precipitation agents and surfactants,[121] and biomineralization, in which enzyme molecules also help to MOF nucleation by chemical interactions with the organic SBU.[49] Using one-pot embedding the number of reactions is reduced (MOF synthesis takes place while encapsulating the lipase) and there is no dimensional compatibility required. Even more, leaching is reduced as the network grows surrounding the lipase not being directly allocated in the porosity. However this might partially decrease the catalytic activity due to hindered accessibility to the active nodes and might limit the mass transfer efficiency of reagents and products.[122]

Great efforts have been put into the synthesis of enzyme@MOFs composites worldwide trying to expand the biocatalyst application.[118,119,123] Presented below are summarized some of the enzyme@MOF composites, not only lipases, reported up to date as well as their catalytic reactions.

Table 1. 3: List of enzyme@MOF composites and their catalyzed reactions

MOF	Enzyme	Type of association	Application	Ref
MIL-100(Fe)	Porcine pancreatic lipase	SiB diffusion	Esterification of cinnamic acid	[124]
ZIF-67	*Candida rugose* lipase	BaS *in situ* encapsulation	Transesterification of soybean oil	[125]
ZIF-90	Bovine liver catalases	BaS *in situ* encapsulation	Peroxidase decomposition	[126]
PCN-333(Al)	HRP, Cytochrome c, microperoxidase-11	SiB diffusion	Oxidation of o-Phenylenediamine, oxidation of 2-2'-azino-bis(3-ethylbenzthiazoline-6-sulfonic acid)	[127]
ZIF-8	Glucose oxidase	BaS *in situ* encapsulation	Detection of glucose	[128]

MIL-53(Al), MIL-53-NH_2(Al), MOF-74(Mg)	β-glucosidase	BaS *in situ* encapsulation	Hydrolysis of *p*-nitrophenyl-β-D-glucuronide	[129]
UiO-66-NH_2	Soybean epoxide hydrolase	Covalent linkage	hydrolysis of 1,2-epoxyoctane to (R)-1,2-octanediol	[130]
MIL-100(Fe)	Glucose oxidase	Physical adsorption	Detection of glucose	[131]
ZIF-7, ZIF-8, ZIF-67, ZIF-68, ZIF-70	Glucose dehydrogenase	Physical adsorption	Detection of glucose	[132]
UiO-66, Uio-66-NH_2, MIL-53 (Al)	Porcine pancratitic lipase	Physical adsorption	Warfarin synthesis	[133]
HKUST-1	*Bacilus subtilis* lipase	Physical adsorption	Esterification of lauric acid and benzyl alcohol	[134]
NU-1000	Cutinase	SiB diffusion	Hydrolysis of *p*-nitrophenyl acetate, *p*-nitrophenyl butyrate and *p*-nitrophenyl octanoate	[135]
MIL-88A	Glycerol dehydrogenase	Encapsulation inside hollow MIL-88A spheres	Oxidation of glycerol to dihydroxyacetone	[136]
UiO-66	*Apergilus niger* lipase	Physical adsorption	Transesterification biodiesel production	[137]

UiO-66-NH_2	Amidase	Covalent linkage	Transamination of (S)-4-fluorophenylglycine	[138]
Ni-BTC	S-adenosylmethionine synthease	Physical adsorption	Synthesis (S)-adenosylmethionine	[139]
ZIF-8	NADH, reduced pyridine nucleotide	BaS *in situ* encapsulation	Reduction of CO_2 to CH_4	[140]
ZIF-8	Horseradish peroxidase	BaS *in situ* encapsulation	Peroxidase decomposition	[141]

As depicted from the Table 1. 3, most of the reported examples used SiB procedures such as enzyme diffusion, due to the simplicity of the SiB strategy, that ensures enzyme adsorption within the MOF, and surface immobilization *via* physical adsorption or covalent linkage. On the other hand, many of the examples for BaS *in situ* encapsulation are based on ZIF-8 and ZIF-90, as both structures could be easily synthesized at RT using only water as solvent, and therefore are synthetic procedures compatible with the enzymes. This emphasizes the need of further research applying BaS synthesis procedures with other MOF families. Therefore, this thesis will focus on providing new BaS routes of enzyme immobilization, more precisely lipases. Following an *in situ* strategy enables the association of bigger lipases and the lipase@MOF composites obtained prevent the biomolecule leaching ensuring a longer life of the biocatalysts, compared to those synthesized *via* SiB. In addition, extending the knowledge towards other MOF matrices besides ZIFs, with different topologies and stabilities, presents a great opportunity to extend the use of lipase@MOF heterogenous biocatalyst in further reactions of interest. Consequently, a flexible iron(III) fumarate, MIL-88A, was selected (further information in section 6.1 **Preamble**).

Bibliography

(1) Férey, G. Hybrid Porous Solids: Past, Present, Future. *Chem. Soc. Rev.* **2008**, *37* (1), 191–214. https://doi.org/10.1039/B618320B.

(2) Yaghi, O. M.; Li, G.; Li, H. Selective Binding and Removal of Guests in a Microporous Metal–Organic Framework. *Nature* **1995**, *378* (6558), 703–706. https://doi.org/10.1038/378703a0.

(3) Riou, D.; Roubeau, O.; Férey, G. Composite Microporous Compounds. Part I: Synthesis and Structure Determination of Two New Vanadium Alkyldiphosphonates (MIL-2 and MIL-3) with Three-Dimensional Open Frameworks. *Microporous Mesoporous Mater.* **1998**, *23* (1–2), 23–31. https://doi.org/10.1016/S1387-1811(98)00042-0.

(4) Hoskins, B. F.; Robson, R. Infinite Polymeric Frameworks Consisting of Three Dimensionally Linked Rod-like Segments. *J. Am. Chem. Soc.* **1989**, *111* (15), 5962–5964. https://doi.org/10.1021/ja00197a079.

(5) Kondo, M.; Yoshitomi, T.; Matsuzaka, H.; Kitagawa, S.; Seki, K. Three-Dimensional Framework with Channeling Cavities for Small Molecules:{[M2(4, 4′-Bpy)3(NO3)4] · xH2O}n(M= Co, Ni, Zn). *Angew. Chemie Int. Ed. English* **1997**, *36* (16), 1725–1727. https://doi.org/10.1002/anie.199717251.

(6) Web of Science. Web of Science [v.5.34] - Search Engine www.webofknowledge.com (accessed Dec 28, 2020).

(7) Batten, S. R.; Champness, N. R.; Chen, X.-M.; Garcia-Martinez, J.; Kitagawa, S.; Öhrström, L.; O'Keeffe, M.; Suh, M. P.; Reedijk, J. Terminology of Metal-Organic Frameworks and Coordination Polymers (IUPAC Recommendations 2013). *Pure Appl. Chem.* **2013**, *85* (8), 1715–1724. https://doi.org/10.1351/PAC-REC-12-11-20.

(8) Farha, O. K.; Eryazici, I.; Jeong, N. C.; Hauser, B. G.; Wilmer, C. E.; Sarjeant, A. A.; Snurr, R. Q.; Nguyen, S. T.; Yazaydın, A. Ö.; Hupp, J. T.

Metal–Organic Framework Materials with Ultrahigh Surface Areas: Is the Sky the Limit? *J. Am. Chem. Soc.* **2012**, *134* (36), 15016–15021. https://doi.org/10.1021/ja3055639.

(9) Hönicke, I. M.; Senkovska, I.; Bon, V.; Baburin, I. A.; Bönisch, N.; Raschke, S.; Evans, J. D.; Kaskel, S. Balancing Mechanical Stability and Ultrahigh Porosity in Crystalline Framework Materials. *Angew. Chemie Int. Ed.* **2018**, *57* (42), 13780–13783. https://doi.org/10.1002/anie.201808240.

(10) Zhou, H.-C.; Long, J. R.; Yaghi, O. M. Introduction to Metal–Organic Frameworks. *Chem. Rev.* **2012**, *112* (2), 673–674. https://doi.org/10.1021/cr300014x.

(11) Meek, S. T.; Greathouse, J. A.; Allendorf, M. D. Metal-Organic Frameworks: A Rapidly Growing Class of Versatile Nanoporous Materials. *Adv. Mater.* **2011**, *23* (2), 249–267. https://doi.org/10.1002/adma.201002854.

(12) Farrusseng, D. *Metal-Organic Frameworks : Applications from Catalysis to Gas Storage*; Farruseng, D., Ed.; Wiley-VCH, 2011.

(13) Gangu, K. K.; Maddila, S.; Mukkamala, S. B.; Jonnalagadda, S. B. A Review on Contemporary Metal–Organic Framework Materials. *Inorganica Chim. Acta* **2016**, *446*, 61–74. https://doi.org/10.1016/j.ica.2016.02.062.

(14) Zhou, H.-C. "Joe"; Kitagawa, S. Metal–Organic Frameworks (MOFs). *Chem. Soc. Rev.* **2014**, *43* (16), 5415–5418. https://doi.org/10.1039/C4CS90059F.

(15) Griffin, S. L.; Champness, N. R. A Periodic Table of Metal-Organic Frameworks. *Coord. Chem. Rev.* **2020**, *414*, 213295. https://doi.org/10.1016/j.ccr.2020.213295.

(16) Pettinari, C.; Marchetti, F.; Mosca, N.; Tosi, G.; Drozdov, A. Application of Metal-Organic Frameworks. *Polym. Int.* **2017**, *66* (6), 731–744. https://doi.org/10.1002/pi.5315.

(17) Furukawa, H.; Cordova, K. E.; O'Keeffe, M.; Yaghi, O. M. The Chemistry and Applications of Metal-Organic Frameworks. *Science* **2013**, *341* (6149), 1230444. https://doi.org/10.1126/science.1230444.

(18) Jiao, L.; Seow, J. Y. R.; Skinner, W. S.; Wang, Z. U.; Jiang, H. L. Metal–Organic Frameworks: Structures and Functional Applications. *Mater. Today* **2019**, *27*, 43–68. https://doi.org/10.1016/j.mattod.2018.10.038.

(19) Wasson, M. C.; Buru, C. T.; Chen, Z.; Islamoglu, T.; Farha, O. K. Metal–Organic Frameworks: A Tunable Platform to Access Single-Site Heterogeneous Catalysts. *Appl. Catal. A Gen.* **2019**, *586*, 117214. https://doi.org/10.1016/j.apcata.2019.117214.

(20) Shen, L.; Liang, R.; Wu, L. Strategies for Engineering Metal-Organic Frameworks as Efficient Photocatalysts. *Chinese J. Catal.* **2015**, *36* (12), 2071–2088. https://doi.org/10.1016/S1872-2067(15)60984-6.

(21) Zhu, J.; Li, P. Z.; Guo, W.; Zhao, Y.; Zou, R. Titanium-Based Metal–Organic Frameworks for Photocatalytic Applications. *Coord. Chem. Rev.* **2018**, *359*, 80–101. https://doi.org/10.1016/j.ccr.2017.12.013.

(22) Li, W.; Zhang, Y.; Li, Q.; Zhang, G. Metal−organic Framework Composite Membranes: Synthesis and Separation Applications. *Chem. Eng. Sci.* **2015**, *135*, 232–257. https://doi.org/10.1016/J.CES.2015.04.011.

(23) Nandi, S.; De Luna, P.; Daff, T. D.; Rother, J.; Liu, M.; Buchanan, W.; Hawari, A. I.; Woo, T. K.; Vaidhyanathan, R. A Single-Ligand Ultra-Microporous MOF for Precombustion CO2 Capture and Hydrogen Purification. *Sci. Adv.* **2015**, *1* (11), e1500421. https://doi.org/10.1126/sciadv.1500421.

(24) Xiao, C.; Silver, M. A.; Wang, S. Metal–Organic Frameworks for Radionuclide Sequestration from Aqueous Solution: A Brief Overview and Outlook. *Dalt. Trans.* **2017**, *46* (47), 16381–16386. https://doi.org/10.1039/C7DT03670A.

(25) Kempahanumakkagari, S.; Vellingiri, K.; Deep, A.; Kwon, E. E.; Bolan, N.; Kim, K. H. Metal–Organic Framework Composites as Electrocatalysts for Electrochemical Sensing Applications. *Coord. Chem. Rev.* **2018**, *357*, 105–129. https://doi.org/10.1016/j.ccr.2017.11.028.

(26) Fang, X.; Zong, B.; Mao, S. Metal–Organic Framework-Based Sensors for Environmental Contaminant Sensing. *Nano-Micro Lett.* **2018**, *10* (4), 64. https://doi.org/10.1007/s40820-018-0218-0.

(27) Peller, M.; Böll, K.; Zimpel, A.; Wuttke, S. Metal-Organic Framework Nanoparticles for Magnetic Resonance Imaging. *Inorg. Chem. Front.* **2018**, *5* (8), 1760–1779. https://doi.org/10.1039/c8qi00149a.

(28) Lu, K.; Aung, T.; Guo, N.; Weichselbaum, R.; Lin, W. Nanoscale Metal-Organic Frameworks for Therapeutic, Imaging, and Sensing Applications. *Adv. Mater.* **2018**, *30* (37), 1707634. https://doi.org/10.1002/adma.201707634.

(29) Ke, F.-S.; Wu, Y.-S.; Deng, H. Metal-Organic Frameworks for Lithium Ion Batteries and Supercapacitors. *J. Solid State Chem.* **2015**, *223*, 109–121. https://doi.org/10.1016/j.jssc.2014.07.008.

(30) Bon, V. Metal-Organic Frameworks for Energy-Related Applications. *Curr.*

Opin. Green Sustain. Chem. **2017**, *4*, 44–49. https://doi.org/10.1016/j.cogsc.2017.02.005.

(31) Zhao, Y.; Song, Z.; Li, X.; Sun, Q.; Cheng, N.; Lawes, S.; Sun, X. Metal Organic Frameworks for Energy Storage and Conversion. *Energy Storage Mater.* **2016**, *2*, 35–62. https://doi.org/10.1016/j.ensm.2015.11.005.

(32) Horcajada, P.; Gref, R.; Baati, T.; Allan, P. K.; Maurin, G.; Couvreur, P. Metal - Organic Frameworks in Biomedicine. *Chem. Rev.* **2012**, *112*, 1232–1268. https://doi.org/10.1021/cr200256v.

(33) Wuttke, S.; Lismont, M.; Escudero, A.; Rungtaweevoranit, B.; Parak, W. J. Positioning Metal-Organic Framework Nanoparticles within the Context of Drug Delivery – A Comparison with Mesoporous Silica Nanoparticles and Dendrimers. *Biomaterials* **2017**, *123*, 172–183. https://doi.org/10.1016/J.BIOMATERIALS.2017.01.025.

(34) Giménez-Marqués, M.; Hidalgo, T.; Serre, C.; Horcajada, P. Nanostructured Metal–Organic Frameworks and Their Bio-Related Applications. *Coord. Chem. Rev.* **2015**, *307*, 1–19. https://doi.org/10.1016/j.ccr.2015.08.008.

(35) Rojas, S.; Horcajada, P. Metal-Organic Frameworks for the Removal of Emerging Organic Contaminants in Water. *Chem. Rev.* **2020**, *120* (16), 8378–8415. https://doi.org/10.1021/acs.chemrev.9b00797.

(36) Zhu, L.; Meng, L.; Shi, J.; Li, J.; Zhang, X.; Feng, M. Metal-Organic Frameworks/Carbon-Based Materials for Environmental Remediation: A State-of-the-Art Mini-Review. *J. Environ. Manage.* **2019**, *232*, 964–977. https://doi.org/10.1016/j.jenvman.2018.12.004.

(37) Drout, R. J.; Robison, L.; Chen, Z.; Islamoglu, T.; Farha, O. K. Zirconium Metal–Organic Frameworks for Organic Pollutant Adsorption. *Trends Chem.* **2019**, *1* (3), 304–317. https://doi.org/10.1016/j.trechm.2019.03.010.

(38) Juan-Alcaniz, J.; Gascon, J.; Kapteijn, F. Metal-Organic Frameworks as Scaffolds for the Encapsulation of Active Species: State of the Art and Future Perspectives. *J. Mater. Chem.* **2012**, *22* (20), 10102–10118. https://doi.org/10.1039/C2JM15563J.

(39) Li, S.; Huo, F. Metal–Organic Framework Composites: From Fundamentals to Applications. *Nanoscale* **2015**, *7* (17), 7482–7501. https://doi.org/10.1039/C5NR00518C.

(40) Alshammari, A.; Jiang, Z.; Cordova, K. E. Metal Organic Frameworks as Emerging Photocatalysts. In *Semiconductor Photocatalysis - Materials, Mechanisms and Applications*; Cao, W., Ed.; IntechOpen, 2016; pp 302–341.

https://doi.org/10.5772/63489.

(41) Yaghi, O. M.; O'Keeffe, M.; Ockwig, N. W.; Chae, H. K.; Eddaoudi, M.; Kim, J. Reticular Synthesis and the Design of New Materials. *Nature* **2003**, *423* (6941), 705–714. https://doi.org/10.1038/nature01650.

(42) Eddaoudi, M.; Kim, J.; Rosi, N.; Vodak, D.; Wachter, J.; O'Keeffe, M.; Yaghi, O. M. Systematic Design of Pore Size and Functionality in Isoreticular MOFs and Their Application in Methane Storage. *Science (80-.).* **2002**, *295* (5554), 469–472. https://doi.org/10.1126/science.1067208.

(43) Deng, H.; Grunder, S.; Cordova, K. E.; Valente, C.; Furukawa, H.; Hmadeh, M.; Gándara, F.; Whalley, A. C.; Liu, Z.; Asahina, S.; et al. Large-Pore Apertures in a Series of Metal-Organic Frameworks. *Science (80-.).* **2012**, *336* (6084), 1018–1023. https://doi.org/10.1126/science.1220131.

(44) Dan-hardi, M.; Serre, C.; Frot, T.; Rozes, L.; Maurin, G.; Sanchez, C.; Férey, G. A New Photoactive Crystalline Highly Porous Titanium (IV) Dicarboxylate. *J. Am. Chem. Soc. Commun.* **2009**, *131*, 10857–10859. https://doi.org/10.1021/ja903726m.

(45) Chiericatti, C.; Basilico, J. C.; Zapata Basilico, M. L.; Zamaro, J. M. Novel Application of HKUST-1 Metal-Organic Framework as Antifungal: Biological Tests and Physicochemical Characterizations. *Microporous Mesoporous Mater.* **2012**, *162*, 60–63. https://doi.org/10.1016/j.micromeso.2012.06.012.

(46) Cavka, J. H.; Jakobsen, S.; Olsbye, U.; Guillou, N.; Bordiga, S.; Lillerud, K. P. A New Zirconium Inorganic Building Brick Forming Metal Organic Frameworks with Exceptional Stability. *J. Am. Chem. Soc.* **2008**, *130* (42), 13850–13851. https://doi.org/10.1021/ja8057953.

(47) Salcedo-Abraira, P.; Vilela, S. M. F.; Babaryk, A. A.; Cabrero-Antonino, M.; Gregorio, P.; Salles, F.; Navalón, S.; García, H.; Horcajada, P. Nickel Phosphonate MOF as Efficient Water Splitting Photocatalyst. *Nano Res.* **2020**, *14*, 450–457. https://doi.org/10.1007/s12274-020-3056-6.

(48) Stock, N.; Biswas, S. Synthesis of Metal-Organic Frameworks (MOFs): Routes to Various MOF Topologies, Morphologies, and Composites. *Chem. Rev.* **2012**, *112*, 933–969. https://doi.org/10.1021/cr200304e.

(49) Liang, K.; Ricco, R.; Doherty, C. M.; Styles, M. J.; Bell, S.; Kirby, N.; Mudie, S.; Haylock, D.; Hill, A. J.; Doonan, C. J.; et al. Biomimetic Mineralization of Metal-Organic Frameworks as Protective Coatings for Biomacromolecules. *Nat. Commun.* **2015**, *6* (1), 7240. https://doi.org/10.1038/ncomms8240.

(50) Lin, K.-S.; Adhikari, A. K.; Ku, C.-N.; Chiang, C.-L.; Kuo, H. Synthesis and

Characterization of Porous HKUST-1 Metal Organic Frameworks for Hydrogen Storage. *Int. J. Hydrogen Energy* **2012**, *37* (18), 13865–13871. https://doi.org/10.1016/J.IJHYDENE.2012.04.105.

(51) Horcajada, P.; Chevreau, H.; Heurtaux, D.; Benyettou, F.; Salles, F.; Devic, T.; Garcia-Marquez, A.; Yu, C.; Lavrard, H.; Dutson, C. L.; et al. Extended and Functionalized Porous Iron(Iii) Tri- or Dicarboxylates with MIL-100/101 Topologies. *Chem. Commun.* **2014**, *50* (52), 6872–6874. https://doi.org/10.1039/c4cc02175d.

(52) Quaresma, S.; André, V.; Antunes, A. M. M.; Vilela, S. M. F.; Amariei, G.; Arenas-Vivo, A.; Rosal, R.; Horcajada, P.; Duarte, M. T. Novel Antibacterial Azelaic Acid BioMOFs. *Cryst. Growth Des.* **2020**, *20* (1), 370–382. https://doi.org/10.1021/acs.cgd.9b01302.

(53) Azad, F. N.; Ghaedi, M.; Dashtian, K.; Hajati, S.; Pezeshkpour, V. Ultrasonically Assisted Hydrothermal Synthesis of Activated Carbon–HKUST-1-MOF Hybrid for Efficient Simultaneous Ultrasound-Assisted Removal of Ternary Organic Dyes and Antibacterial Investigation: Taguchi Optimization. *Ultrason. Sonochem.* **2016**, *31*, 383–393. https://doi.org/10.1016/J.ULTSONCH.2016.01.024.

(54) Sánchez-Sánchez, M.; Getachew, N.; Díaz, K.; Díaz-García, M.; Chebude, Y.; Díaz, I. Synthesis of Metal–Organic Frameworks in Water at Room Temperature: Salts as Linker Sources. *Green Chem.* **2015**, *17* (3), 1500–1509. https://doi.org/10.1039/C4GC01861C.

(55) García Márquez, A.; Demessence, A.; Platero-Prats, A. E.; Heurtaux, D.; Horcajada, P.; Serre, C.; Chang, J. S.; Férey, G.; De La Peña-O'Shea, V. A.; Boissière, C.; et al. Green Microwave Synthesis of MIL-100(Al, Cr, Fe) Nanoparticles for Thin-Film Elaboration. *Eur. J. Inorg. Chem.* **2012**, *100* (32), 5165–5174. https://doi.org/10.1002/ejic.201200710.

(56) Padial, N. M.; Castells-Gil, J.; Almora-Barrios, N.; Romero-Angel, M.; Da Silva, I.; Barawi, M.; García-Sánchez, A.; De La Peña O'Shea, V. A.; Martí-Gastaldo, C. Hydroxamate Titanium-Organic Frameworks and the Effect of Siderophore-Type Linkers over Their Photocatalytic Activity. *J. Am. Chem. Soc.* **2019**, *141* (33), 13124–13133. https://doi.org/10.1021/jacs.9b04915.

(57) Ermer, M.; Mehler, J.; Kriesten, M.; Avadhut, Y. S.; Schulz, P. S.; Hartmann, M. Synthesis of the Novel MOF Hcp UiO-66 Employing Ionic Liquids as a Linker Precursor. *Dalt. Trans.* **2018**, *47* (41), 14426–14430. https://doi.org/10.1039/c8dt02999g.

(58) Rasmussen, E. G.; Kramlich, J.; Novosselov, I. V. Scalable Continuous Flow

Metal-Organic Framework (MOF) Synthesis Using Supercritical CO2. *ACS Sustain. Chem. Eng.* **2020**, *8* (26), 9680–9689. https://doi.org/10.1021/acssuschemeng.0c01429.

(59) Yilmaz, B.; Trukhan, N.; Müller, U. Industrial Outlook on Zeolites and Metal Organic Frameworks. *Cuihua Xuebao/Chinese Journal of Catalysis*. Elsevier January 1, 2012, pp 3–10. https://doi.org/10.1016/s1872-2067(10)60302-6.

(60) Bauer, S.; Serre, C.; Devic, T.; Horcajada, P.; Marrot, J.; Férey, G.; Stock, N. High-Throughput Assisted Rationalization of the Formation of Metal Organic Frameworks in the Iron(III) Aminoterephthalate Solvothermal System. *Inorg. Chem.* **2008**, *47* (17), 7568–7576. https://doi.org/10.1021/ic800538r.

(61) Falcaro, P.; Ricco, R.; Yazdi, A.; Imaz, I.; Furukawa, S.; Maspoch, D.; Ameloot, R.; Evans, J. D.; Doonan, C. J. Application of Metal and Metal Oxide Nanoparticles@MOFs. *Coord. Chem. Rev.* **2015**, *307* (2), 237–254. https://doi.org/10.1016/j.ccr.2015.08.002.

(62) Kim, C. R.; Uemura, T.; Kitagawa, S. Inorganic Nanoparticles in Porous Coordination Polymers. *Chem. Soc. Rev.* **2016**, *45* (14), 3828–3845. https://doi.org/10.1039/c5cs00940e.

(63) Railey, P.; Song, Y.; Liu, T.; Li, Y. Metal Organic Frameworks with Immobilized Nanoparticles: Synthesis and Applications in Photocatalytic Hydrogen Generation and Energy Storage. *Materials Research Bulletin*. Elsevier Ltd December 1, 2017, pp 385–394. https://doi.org/10.1016/j.materresbull.2017.04.020.

(64) Lian, X.; Fang, Y.; Joseph, E.; Wang, Q.; Li, J.; Banerjee, S.; Lollar, C.; Wang, X.; Zhou, H.-C. Enzyme–MOF (Metal–Organic Framework) Composites. *Chem. Soc. Rev.* **2017**, *46*, 3386–3401. https://doi.org/10.1039/C7CS00058H.

(65) Manawi, Y.; Ihsanullah; Samara, A.; Al-Ansari, T.; Atieh, M. A Review of Carbon Nanomaterials' Synthesis via the Chemical Vapor Deposition (CVD) Method. *Materials (Basel).* **2018**, *11* (5), 822. https://doi.org/10.3390/ma11050822.

(66) Dinata, A. A.; Rosyadi, A. M.; Hamid, S.; Zainul, R. A review-Chemical vapor deposition: process and application https://osf.io/preprints/inarxiv/yfeau/ (accessed Dec 28, 2020). https://doi.org/10.31227/osf.io/yfeau.

(67) Hermes, S.; Schröter, M. K.; Schmid, R.; Khodeir, L.; Muhler, M.; Tissler, A.; Fischer, R. W.; Fischer, R. A. Metal@MOF: Loading of Highly Porous

Coordination Polymers Host Lattices by Metal Organic Chemical Vapor Deposition. *Angew. Chemie - Int. Ed.* **2005**, *44* (38), 6237–6241. https://doi.org/10.1002/anie.200462515.

(68) Hermes, S.; Schröder, F.; Amirjalayer, S.; Schmid, R.; Fischer, R. A. Loading of Porous Metal-Organic Open Frameworks with Organometallic CVD Precursors: Inclusion Compounds of the Type [LnM]A@MOF-5. *J. Mater. Chem.* **2006**, *16* (25), 2464–2472. https://doi.org/10.1039/b603664c.

(69) Chen, L.; Chen, H.; Li, Y. One-Pot Synthesis of Pd@MOF Composites without the Addition of Stabilizing Agents. *Chem. Commun.* **2014**, *50* (94), 14752–14755. https://doi.org/10.1039/c4cc06568a.

(70) Zhou, Q.; Lei, M.; Li, J.; Liu, Y.; Zhao, K.; Zhao, D. Magnetic Solid Phase Extraction of N- and S-Containing Polycyclic Aromatic Hydrocarbons at Ppb Levels by Using a Zerovalent Iron Nanoscale Material Modified with a Metal Organic Framework of Type Fe@MOF-5, and Their Determination by HPLC. *Microchim. Acta* **2017**, *184* (4), 1029–1036. https://doi.org/10.1007/s00604-017-2094-6.

(71) Proch, S.; Herrmannsdörfer, J.; Kempe, R.; Kern, C.; Jess, A.; Seyfarth, L.; Senker, J. Pt@MOF-177: Synthesis, Room-Temperature Hydrogen Storage and Oxidation Catalysis. *Chem. - A Eur. J.* **2008**, *14* (27), 8204–8212. https://doi.org/10.1002/chem.200801043.

(72) Villajos, J. A.; Orcajo, G.; Calleja, G.; Botas, J. A.; Martos, C. Beneficial Cooperative Effect between Pd Nanoparticles and ZIF-8 Material for Hydrogen Storage. *Int. J. Hydrogen Energy* **2016**, *41* (42), 19439–19446. https://doi.org/10.1016/j.ijhydene.2016.05.143.

(73) Ciprian, M.; Xu, P.; Chaemchuen, S.; Tu, R.; Zhuiykov, S.; Heynderickx, P. M.; Verpoort, F. MoO3 Nanoparticle Formation on Zeolitic Imidazolate Framework-8 by Rotary Chemical Vapor Deposition. *Microporous Mesoporous Mater.* **2018**, *267*, 185–191. https://doi.org/10.1016/j.micromeso.2018.03.028.

(74) Hu, P.; Morabito, J. V.; Tsung, C. K. Core-Shell Catalysts of Metal Nanoparticle Core and Metal-Organic Framework Shell. *ACS Catal.* **2014**, *4* (12), 4409–4419. https://doi.org/10.1021/cs5012662.

(75) Lu, G.; Li, S.; Guo, Z.; Farha, O. K.; Hauser, B. G.; Qi, X.; Wang, Y.; Wang, X.; Han, S.; Liu, X.; et al. Imparting Functionality to a Metal-Organic Framework Material by Controlled Nanoparticle Encapsulation. *Nat. Chem.* **2012**, *4* (February), 310–316. https://doi.org/10.1038/nchem.1272.

(76) Majewski, M. B.; Howarth, A. J.; Li, P.; Wasielewski, M. R.; Hupp, J. T.;

Farha, O. K. Enzyme Encapsulation in Metal–Organic Frameworks for Applications in Catalysis. *CrystEngComm* **2017**, *29*, 4082–4091. https://doi.org/10.1039/C7CE00022G.

(77) Roduner, E. Size Matters: Why Nanomaterials Are Different. *Chem. Soc. Rev.* **2006**, *35* (7), 583–592. https://doi.org/10.1039/b502142c.

(78) Pacioni, N. L.; Borsarelli, C. D.; Rey, V.; Veglia, A. V. Synthetic Routes for the Preparation of Silver Nanoparticles. In *Silver Nanoparticle Applications in the fabrication and design of medical and biosensing devices*; Alarcon, E., Griffith, M., Udekwu, K. I., Eds.; Springer International Publishing: Switzerland, 2015; pp 13–46. https://doi.org/10.1007/978-3-319-11262-6_2.

(79) Abou El-Nour, K. M. M.; Eftaiha, A.; Al-Warthan, A.; Ammar, R. A. A. Synthesis and Applications of Silver Nanoparticles. *Arab. J. Chem.* **2010**, *3* (3), 135–140. https://doi.org/10.1016/j.arabjc.2010.04.008.

(80) Gao, M.; Sun, L.; Wang, Z.; Zhao, Y. Controlled Synthesis of Ag Nanoparticles with Different Morphologies and Their Antibacterial Properties. *Mater. Sci. Eng. C* **2013**, *33* (1), 397–404. https://doi.org/10.1016/j.msec.2012.09.005.

(81) Stamplecoskie, K. Silver Nanoparticles: From Bulk Material to Colloidal Nanoparticles. In *Silver Nanoparticle Applications. Engineering Materials*; Alarcon, E., Griffith, M., Udekwu, K. I., Eds.; Springer, Cham, 2015; pp 1–12. https://doi.org/10.1007/978-3-319-11262-6_1.

(82) Rycenga, M.; Cobley, C. M.; Zeng, J.; Li, W.; Moran, C. H.; Zhang, Q.; Qin, D.; Xia, Y. Controlling the Synthesis and Assembly of Silver Nanostructures for Plasmonic Applications. *Chem. Rev.* **2011**, *111* (6), 3669–3712. https://doi.org/10.1021/cr100275d.

(83) Tao, A. R.; Habas, S.; Yang, P. Shape Control of Colloidal Metal Nanocrystals. *Small* **2008**, *4* (3), 310–325. https://doi.org/10.1002/smll.200701295.

(84) Meng, X. K.; Tang, S. C.; Vongehr, S. A Review on Diverse Silver Nanostructures. *J. Mater. Sci. Technol.* **2010**, *26* (6), 487–522. https://doi.org/10.1016/S1005-0302(10)60078-3.

(85) Chernousova, S.; Epple, M. Silver as Antibacterial Agent: Ion, Nanoparticle, and Metal. *Angew. Chemie - Int. Ed.* **2013**, *52* (6), 1636–1653. https://doi.org/10.1002/anie.201205923.

(86) Wyszogrodzka, G.; Marszałek, B.; Gil, B.; Dorożyński, P. Metal-Organic Frameworks: Mechanisms of Antibacterial Action and Potential

Applications. *Drug Discov. Today* **2016**, *21* (6), 1009–1018. https://doi.org/10.1016/j.drudis.2016.04.009.

(87) Jiang, H. L.; Akita, T.; Ishida, T.; Haruta, M.; Xu, Q. Synergistic Catalysis of Au@Ag Core-Shell Nanoparticles Stabilized on Metal-Organic Framework. *J. Am. Chem. Soc.* **2011**, *133* (5), 1304–1306. https://doi.org/10.1021/ja1099006.

(88) Liu, J.; Strachan, D. M.; Thallapally, P. K. Enhanced Noble Gas Adsorption in Ag@MOF-74Ni. *Chem. Commun.* **2014**, *50* (4), 466–468. https://doi.org/Doi 10.1039/C3cc47777k.

(89) Qian, X.; Zhong, Z.; Yadian, B.; Wu, J.; Zhou, K.; Teo, J. S. K.; Chen, L.; Long, Y.; Huang, Y. Loading MIL-53(Al) with Ag Nanoparticles: Synthesis, Structural Stability and Catalytic Properties. *Int. J. Hydrogen Energy* **2014**, *39* (26), 14496–14502. https://doi.org/10.1016/j.ijhydene.2013.11.052.

(90) Liu, X. H.; Ma, J. G.; Niu, Z.; Yang, G. M.; Cheng, P. An Efficient Nanoscale Heterogeneous Catalyst for the Capture and Conversion of Carbon Dioxide at Ambient Pressure. *Angew. Chemie - Int. Ed.* **2015**, *54* (3), 988–991. https://doi.org/10.1002/anie.201409103.

(91) Guo, H.; Guo, D.; Zheng, Z.; Weng, W.; Chen, J. Visible-Light Photocatalytic Activity of Ag@MIL-125(Ti) Microspheres. *Appl. Organomet. Chem.* **2015**, *29* (9), 618–623. https://doi.org/10.1002/aoc.3341.

(92) Wei, Y.; Han, S.; Walker, D. A.; Fuller, P. E.; Grzybowski, B. A. Nanoparticle Core/Shell Architectures within Mof Crystals Synthesized by Reaction Diffusion. *Angew. Chemie - Int. Ed.* **2012**, *51* (30), 7435–7439. https://doi.org/10.1002/anie.201202549.

(93) Liu, Y.; He, L.; Liu, Y.; Liu, J.; Xiong, Y.; Zheng, J.; Tang, Z. Core-Shell Noble-Metal@metal-Organic-Framework Nanoparticles with Highly Selective Sensing Property. *Angew. Chemie - Int. Ed.* **2013**, *52* (13), 3741–3745. https://doi.org/10.1002/anie.201209903.

(94) Dong, S.; Zhang, D.; Suo, G.; Wei, W.; Huang, T. Exploiting Multi-Function MOF Nanocomposite Ag@Zn-TSA as Highly Efficiente Immobilization Matrixes for Sensitive Electrochemical Biosensing Supplementary Material. *Anal. Chim. Acta* **2016**, *934*, 1–7. https://doi.org/10.1172/JCI44752.288.

(95) Yuan, X.; Wang, H.; Wu, Y.; Zeng, G.; Chen, X.; Leng, L.; Wu, Z.; Li, H. One-Pot Self-Assembly and Photoreduction Synthesis of Silver Nanoparticle-Decorated Reduced Graphene Oxide/MIL-125(Ti) Photocatalyst with Improved Visible Light Photocatalytic Activity. *Appl. Organomet. Chem.* **2016**, *30* (5), 289–296. https://doi.org/10.1002/aoc.3430.

(96) Molla, R. A.; Ghosh, K.; Banerjee, B.; Iqubal, M. A.; Kundu, S. K.; Islam, S. M.; Bhaumik, A. Silver Nanoparticles Embedded over Porous Metal Organic Frameworks for Carbon Dioxide Fixation via Carboxylation of Terminal Alkynes at Ambient Pressure. *J. Colloid Interface Sci.* **2016**, *477*, 220–229. https://doi.org/10.1016/j.jcis.2016.05.037.

(97) Zhao, Y.; Kornienko, N.; Liu, Z.; Zhu, C.; Asahina, S.; Kuo, T. R.; Bao, W.; Xie, C.; Hexemer, A.; Terasaki, O.; et al. Mesoscopic Constructs of Ordered and Oriented Metal-Organic Frameworks on Plasmonic Silver Nanocrystals. *J. Am. Chem. Soc.* **2015**, *137* (6), 2199–2202. https://doi.org/10.1021/ja512951e.

(98) Zhu, N.-N.; Liu, X.-H.; Li, T.; Ma, J.-G.; Cheng, P.; Yang, G.-M. Composite System of Ag Nanoparticles and Metal–Organic Frameworks for the Capture and Conversion of Carbon Dioxide under Mild Conditions. *Inorg. Chem.* **2017**, *56* (6), 3414–3420. https://doi.org/10.1021/acs.inorgchem.6b02855.

(99) Yang, Z.; Xu, X.; Liang, X.; Lei, C.; Cui, Y.; Wu, W.; Yang, Y.; Zhang, Z.; Lei, Z. Construction of Heterostructured MIL-125/Ag/g-C3N4 Nanocomposite as an Efficient Bifunctional Visible Light Photocatalyst for the Organic Oxidation and Reduction Reactions. *Appl. Catal. B Environ.* **2017**, *205*, 42–54. https://doi.org/10.1016/j.apcatb.2016.12.012.

(100) Li, D.; Dai, X.; Zhang, X.; Zhuo, H.; Jiang, Y.; Yu, Y.-B.; Zhang, P.; Huang, X.; Wang, H. Silver Nanoparticles Encapsulated by Metal-Organic-Framework Give the Highest Turnover Frequencies of 10 5 h −1 for Three Component Reaction by Microwave-Assisted Heating. *J. Catal.* **2017**, *348*, 276–281. https://doi.org/10.1016/j.jcat.2017.02.013.

(101) Guo, H.; Zhang, Y.; Zheng, Z.; Lin, H.; Zhang, Y. Facile One-Pot Fabrication of Ag@MOF(Ag) Nanocomposites for Highly Selective Detection of 2,4,6-Trinitrophenol in Aqueous Phase. *Talanta* **2017**, *170* (March), 146–151. https://doi.org/10.1016/j.talanta.2017.03.096.

(102) Abdelhameed, R. M.; Simões, M. M. Q.; Silva, A. M. S.; Rocha, J. Enhanced Photocatalytic Activity of MIL-125 by Post-Synthetic Modification with Cr ^{III} and Ag Nanoparticles. *Chem. - A Eur. J.* **2015**, *21* (31), 11072–11081. https://doi.org/10.1002/chem.201500808.

(103) Yadav, D. K.; Ganesan, V.; Marken, F.; Gupta, R.; Sonkar, P. K. Metal@MOF Materials in Electroanalysis: Silver-Enhanced Oxidation Reactivity Towards Nitrophenols Adsorbed into a Zinc Metal Organic Framework???Ag@MOF-5(Zn). *Electrochim. Acta* **2016**, *219*, 482–491. https://doi.org/10.1016/j.electacta.2016.10.009.

(104) Huang, P.; Ma, W.; Yu, P.; Mao, L. Dopamine-Directed In-Situ and One-Step Synthesis of Au@Ag Core-Shell Nanoparticles Immobilized to a Metal-Organic Framework for Synergistic Catalysis. *Chem. - An Asian J.* **2016**, *11* (19), 2705–2709. https://doi.org/10.1002/asia.201600469.

(105) Wang, S.; He, X.; Song, L.; Wang, Z. Silver Nanoparticles Supported by Novel Nickel Metal-Organic Frameworks: An Efficient Heterogeneous Catalyst for an A3 Coupling Reaction. *Synlett* **2009**, *2009* (3), 447–450. https://doi.org/10.1055/s-0028-1087540.

(106) Arul, P.; John, S. A. Silver Nanoparticles Built-in Zinc Metal Organic Framework Modified Electrode for the Selective Non-Enzymatic Determination of H 2 O 2. *Electrochim. Acta* **2017**, *235*, 680–689. https://doi.org/10.1016/j.electacta.2017.03.097.

(107) Chang, S.; Liu, C.; Fu, H.; Li, Z.; Wu, X.; Feng, J.; Zhang, H. Preparation of Well-Dispersed Nanosilver in MIL-101(Cr) Using Double-Solvent Radiation Method for Catalysis. *Nano* **2018**, *13* (12), 1850145. https://doi.org/10.1142/S179329201850145X.

(108) Houk, R. J. T.; Jacobs, B. W.; Gabaly, F. El; Chang, N. N.; Talin, A. A.; Graham, D. D.; House, S. D.; Robertson, I. M.; Allendorf, M. D. Silver Cluster Formation, Dynamics, and Chemistry in Metal-Organic Frameworks. *Nano Lett.* **2009**, *9* (10), 3413–3418. https://doi.org/10.1021/nl901397k.

(109) Sofi, F. A.; Majid, K.; Mehraj, O. The Visible Light Driven Copper Based Metal-Organic-Framework Heterojunction:HKUST-1@Ag-Ag3PO4 for Plasmon Enhanced Visible Light Photocatalysis. *J. Alloys Compd.* **2018**, *737*, 798–808. https://doi.org/10.1016/j.jallcom.2017.12.141.

(110) Mahmoodi, N. M.; Taghizadeh, A.; Taghizadeh, M.; Abdi, J. In Situ Deposition of Ag/AgCl on the Surface of Magnetic Metal-Organic Framework Nanocomposite and Its Application for the Visible-Light Photocatalytic Degradation of Rhodamine Dye. *J. Hazard. Mater.* **2019**, *378*, 120741. https://doi.org/10.1016/j.jhazmat.2019.06.018.

(111) Liu, Q.; Zeng, C.; Ai, L.; Hao, Z.; Jiang, J. Boosting Visible Light Photoreactivity of Photoactive Metal-Organic Framework: Designed Plasmonic Z-Scheme Ag/AgCl@MIL-53-Fe. *Appl. Catal. B Environ.* **2018**, *224*, 38–45. https://doi.org/10.1016/j.apcatb.2017.10.029.

(112) Guo, F.; Yang, S.; Liu, Y.; Wang, P.; Huang, J.; Sun, W. Y. Size Engineering of Metal-Organic Framework MIL-101(Cr)-Ag Hybrids for Photocatalytic CO2 Reduction. *ACS Catal.* **2019**, *9* (9), 8464–8470. https://doi.org/10.1021/acscatal.9b02126.

(113) Chen, M.; Han, L.; Zhou, J.; Sun, C.; Hu, C.; Wang, X.; Su, Z. Photoreduction of Carbon Dioxide under Visible Light by Ultra-Small Ag Nanoparticles Doped into Co-ZIF-9. *Nanotechnology* **2018**, *29* (28), 284003. https://doi.org/10.1088/1361-6528/aabdb1.

(114) Meng, W.; Wen, Y.; Dai, L.; He, Z.; Wang, L. A Novel Electrochemical Sensor for Glucose Detection Based on Ag@ZIF-67 Nanocomposite. *Sensors Actuators, B Chem.* **2018**, *260*, 852–860. https://doi.org/10.1016/j.snb.2018.01.109.

(115) Liu, L.; Ping, E.; Sun, J.; Zhang, L.; Zhou, Y.; Zhong, Y.; Zhou, Y.; Wang, Y. Multifunctional Ag@MOF-5@chitosan Non-Woven Cloth Composites for Sulfur Mustard Decontamination and Hemostasis. *Dalt. Trans.* **2019**, *48* (20), 6951–6959. https://doi.org/10.1039/c9dt00503j.

(116) Lian, X.; Fang, Y.; Joseph, E.; Wang, Q.; Li, J.; Banerjee, S.; Lollar, C.; Wang, X.; Zhou, H.-C. Enzyme-MOF (Metal-Organic Framework) Composites. *Chem. Soc. Rev.* **2017**, *46* (11), 3386–3401. https://doi.org/10.1039/c7cs00058h.

(117) Chapman, J.; Ismail, A.; Dinu, C. Industrial Applications of Enzymes: Recent Advances, Techniques, and Outlooks. *Catalysts* **2018**, *8* (6), 238. https://doi.org/10.3390/catal8060238.

(118) Liang, S.; Wu, X.-L.; Xiong, J.; Zong, M.-H.; Lou, W.-Y. Metal-Organic Frameworks as Novel Matrices for Efficient Enzyme Immobilization: An Update Review. **2019**. https://doi.org/10.1016/j.ccr.2019.213149.

(119) Cui, J.; Ren, S.; Sun, B.; Jia, S. Optimization Protocols and Improved Strategies for Metal-Organic Frameworks for Immobilizing Enzymes: Current Development and Future Challenges. *Coord. Chem. Rev.* **2018**, *370*, 22–41. https://doi.org/10.1016/J.CCR.2018.05.004.

(120) Reetz, M. T. Lipases as Practical Biocatalysts. *Curr. Opin. Chem. Biol.* **2002**, *6* (2), 145–150. https://doi.org/10.1016/S1367-5931(02)00297-1.

(121) Lyu, F.; Zhang, Y.; Zare, R. N.; Ge, J.; Liu, Z. One-Pot Synthesis of Protein-Embedded Metal–Organic Frameworks with Enhanced Biological Activities. *Nano Lett.* **2014**, *14* (10), 5761–5765. https://doi.org/10.1021/nl5026419.

(122) Nadar, S. S.; Vaidya, L.; Rathod, V. K. Enzyme Embedded Metal Organic Framework (Enzyme–MOF): De Novo Approaches for Immobilization. *Int. J. Biol. Macromol.* **2020**, *149*, 861–876. https://doi.org/10.1016/j.ijbiomac.2020.01.240.

(123) Bilal, M.; Adeel, M.; Rasheed, T.; Iqbal, H. M. N. Multifunctional Metal-

Organic Frameworks-Based Biocatalytic Platforms: Recent Developments and Future Prospects. *J. Mater. Res. Technol.* **2019**, *8* (2), 2359–2371. https://doi.org/10.1016/j.jmrt.2018.12.001.

(124) Nobakht, N.; Faramarzi, M. A.; Shafiee, A.; Khoobi, M.; Rafiee, E. Polyoxometalate-Metal Organic Framework-Lipase: An Efficient Green Catalyst for Synthesis of Benzyl Cinnamate by Enzymatic Esterification of Cinnamic Acid. *Int. J. Biol. Macromol.* **2018**, *113*, 8–19. https://doi.org/10.1016/j.ijbiomac.2018.02.023.

(125) Rafiei, S.; Tangestaninejad, S.; Horcajada, P.; Moghadam, M.; Mirkhani, V.; Mohammadpoor-Baltork, I.; Kardanpour, R.; Zadehahmadi, F. Efficient Biodiesel Production Using a Lipase@ZIF-67 Nanobioreactor. *Chem. Eng. J.* **2018**, *334*, 1233–1241. https://doi.org/10.1016/J.CEJ.2017.10.094.

(126) Shieh, F. K.; Wang, S. C.; Yen, C. I.; Wu, C. C.; Dutta, S.; Chou, L. Y.; Morabito, J. V.; Hu, P.; Hsu, M. H.; Wu, K. C. W.; et al. Imparting Functionality to Biocatalysts via Embedding Enzymes into Nanoporous Materials by a de Novo Approach: Size-Selective Sheltering of Catalase in Metal-Organic Framework Microcrystals. *J. Am. Chem. Soc.* **2015**, *137* (13), 4276–4279. https://doi.org/10.1021/ja513058h.

(127) Feng, D.; Liu, T.-F.; Su, J.; Bosch, M.; Wei, Z.; Wan, W.; Yuan, D.; Chen, Y.-P.; Wang, X.; Wang, K.; et al. Stable Metal-Organic Frameworks Containing Single-Molecule Traps for Enzyme Encapsulation. *Nat. Commun.* **2015**, *6* (1), 5979. https://doi.org/10.1038/ncomms6979.

(128) Wang, H.; Yuan, X.; Wu, Y.; Zeng, G.; Chen, X.; Leng, L.; Wu, Z.; Jiang, L.; Li, H. Facile Synthesis of Amino-Functionalized Titanium Metal-Organic Frameworks and Their Superior Visible-Light Photocatalytic Activity for Cr(VI) Reduction. *J. Hazard. Mater.* **2015**, *286*, 187–194. https://doi.org/10.1016/j.jhazmat.2014.11.039.

(129) Gascón, V.; Castro-Miguel, E.; Díaz-García, M.; Blanco, R. M.; Sanchez-Sanchez, M. In Situ and Post-Synthesis Immobilization of Enzymes on Nanocrystalline MOF Platforms to Yield Active Biocatalysts. *J. Chem. Technol. Biotechnol.* **2017**, *92* (10), 2583–2593. https://doi.org/10.1002/jctb.5274.

(130) Cao, S. L.; Yue, D. M.; Li, X. H.; Smith, T. J.; Li, N.; Zong, M. H.; Wu, H.; Ma, Y. Z.; Lou, W. Y. Novel Nano-/Micro-Biocatalyst: Soybean Epoxide Hydrolase Immobilized on UiO-66-NH2 MOF for Efficient Biosynthesis of Enantiopure (R)-1, 2-Octanediol in Deep Eutectic Solvents. *ACS Sustain. Chem. Eng.* **2016**, *4* (6), 3586–3595.

https://doi.org/10.1021/acssuschemeng.6b00777.

(131) Patra, S.; Hidalgo Crespo, T.; Permyakova, A.; Sicard, C.; Serre, C.; Chaussé, A.; Steunou, N.; Legrand, L. Design of Metal Organic Framework-Enzyme Based Bioelectrodes as a Novel and Highly Sensitive Biosensing Platform. *J. Mater. Chem. B* **2015**, *3* (46), 8983–8992. https://doi.org/10.1039/c5tb01412c.

(132) Ma, W.; Jiang, Q.; Yu, P.; Yang, L.; Mao, L. Zeolitic Imidazolate Framework-Based Electrochemical Biosensor for in Vivo Electrochemical Measurements. *Anal. Chem.* **2013**, *85* (15), 7550–7557. https://doi.org/10.1021/ac401576u.

(133) Liu, W.-L.; Yang, N.-S.; Chen, Y.-T.; Lirio, S.; Wu, C.-Y.; Lin, C.-H.; Huang, H.-Y. Lipase-Supported Metal-Organic Framework Bioreactor Catalyzes Warfarin Synthesis. *Chem. - A Eur. J.* **2015**, *21* (1), 115–119. https://doi.org/10.1002/chem.201405252.

(134) Cao, Y.; Wu, Z.; Wang, T.; Xiao, Y.; Huo, Q.; Liu, Y. Immobilization of Bacillus Subtilis Lipase on a Cu-BTC Based Hierarchically Porous Metal–Organic Framework Material: A Biocatalyst for Esterification. *Dalt. Trans.* **2016**, *45* (16), 6998–7003. https://doi.org/10.1039/C6DT00677A.

(135) Li, P.; Modica, J. A.; Howarth, A. J.; Vargas L., E.; Moghadam, P. Z.; Snurr, R. Q.; Mrksich, M.; Hupp, J. T.; Farha, O. K. Toward Design Rules for Enzyme Immobilization in Hierarchical Mesoporous Metal-Organic Frameworks. *Chem* **2016**, *1* (1), 154–169. https://doi.org/10.1016/J.CHEMPR.2016.05.001.

(136) Jeong, G. Y.; Ricco, R.; Liang, K.; Ludwig, J.; Kim, J. O.; Falcaro, P.; Kim, D. P. Bioactive MIL-88A Framework Hollow Spheres via Interfacial Reaction In-Droplet Microfluidics for Enzyme and Nanoparticle Encapsulation. *Chem. Mater.* **2015**, *27* (23), 7903–7909. https://doi.org/10.1021/acs.chemmater.5b02847.

(137) Hu, Y.; Dai, L.; Liu, D.; Du, W. Rationally Designing Hydrophobic UiO-66 Support for the Enhanced Enzymatic Performance of Immobilized Lipase. *Green Chem.* **2018**, *20* (19), 4500–4506. https://doi.org/10.1039/c8gc01284a.

(138) Lin, C.; Xu, K.; Zheng, R.; Zheng, Y. Immobilization of Amidase into a Magnetic Hierarchically Porous Metal-Organic Framework for Efficient Biocatalysis. *Chem. Commun.* **2019**, *55* (40), 5697–5700. https://doi.org/10.1039/c9cc02038a.

(139) He, J.; Sun, S.; Zhou, Z.; Yuan, Q.; Liu, Y.; Liang, H. Thermostable Enzyme-Immobilized Magnetic Responsive Ni-Based Metal-Organic Framework

Nanorods as Recyclable Biocatalysts for Efficient Biosynthesis of: S - Adenosylmethionine. *Dalt. Trans.* **2019**, *48* (6), 2077–2085. https://doi.org/10.1039/c8dt04857f.

(140) Zhu, D.; Ao, S.; Deng, H.; Wang, M.; Qin, C.; Zhang, J.; Jia, Y.; Ye, P.; Ni, H. Ordered Coimmobilization of a Multienzyme Cascade System with a Metal Organic Framework in a Membrane: Reduction of Co2 to Methanol. *ACS Appl. Mater. Interfaces* **2019**, *11* (37), 33581–33588. https://doi.org/10.1021/acsami.9b09811.

(141) Ricco, R.; Wied, P.; Nidetzky, B.; Amenitsch, H.; Falcaro, P. Magnetically Responsive Horseradish Peroxidase@ZIF-8 for Biocatalysis. *Chem. Commun.* **2020**, *56* (43), 5775–5778. https://doi.org/10.1039/c9cc09358c.

Chapter 2

Objectives

"A scientist is not a person who gives the right answers,
is the one who asks the right questions"

Claude Levi-Strauss

The main objective of this thesis is the association of active nanospecies of different nature (silver nanoparticles and lipases) to the structure of benchmarked metal-organic frameworks to obtain new composite materials with advantageous properties, applicable in a plethora of applications (catalysis, environmental remediation, surface decontamination). For doing so, both ship-in-a-bottle and bottle-around-a-ship synthetic strategies will be followed to obtain the desired core@shell AS@MOF composites. The originally designed protocols in this thesis also aim to overcome some of the previously detected limitations in the state-of-art.

2.1. Specific objectives

1. Development of composite materials based on microporous MOFs, with micro and nano particle crystal size, compatible with the SiB association of silver nano-objects via diffusion of the metallic salt precursor through the windows and posterior reduction.

1.1. Design and optimize a synthetic protocol for obtaining composite materials with embedded Ag nanoparticles with biocidal activity (***Chapter 3***).

- Characterization of the AgNP@MOF by different solid-state techniques, including transmission electron microscopy, to analyze the interaction of the Ag with the structure.
- Preparation of thin films of the resulting AgNP@MOF.
- Validation of the biocide activity of AgNP@MOF thin films under irradiation for the treatment of challenging biofilms. Analysis of the chemical stability of the thin film under the conditions of study.

1.2. Design and optimize the association of Ag nanoclusters to microporous MOFs induced by photochemical reduction for environmental remediation (***Chapter 4***).

- Characterization of the AgNC@MOF by different solid-state techniques, including transmission electron microscopy, to analyze the interaction of the Ag with the structure.
- Validation of the AgNC@MOF photoelectronic properties in the degradation of emerging organic contaminants from water under visible light irradiation.

2. Analysis of the use of microwave irradiation as heating source for the BaS association of silver nanoparticles to MOFs (***Chapter 5***).

- Optimization of the microwave assisted synthesis of a polymorphic MOF family to obtain high purity crystals.
- Synthesis of stable silver nanoparticles compatible with the previously determined protocols for MOF synthesis with microwave heating.
- Procure the *in situ* synthesis of AgNP@MOF.

3. Immobilization of enzymes on biocompatible MOFs using BaS association procedures (***Chapter 6***).

- Design and optimization of a one-pot association of enzymes and MOFs with a green procedure for the attainment of lipase@MOF biocomposites.
- Characterization of the material paying special attention to the MOF role (*i.e.*: protective effect, selective catalytic activity).
- Validate the catalytic activity of the lipase@MOF composite in a relevant reaction as the transesterification of soybean oil for the biodiesel production, considering the lipase-MOF interaction.

Chapter 3

SiB: Antimicrobial AgNP@nanoMIL-125-NH_2

"Never has the threat of antimicrobial resistance been more immediate and the need of innovative solutions more urgent."

Tedros Adhanom Ghebreyesus, 8th World Health Organization Director-General

3.1. Preamble

The first attempts for the association of AS during this thesis research were following the simple SiB procedure, as it enables the synthesis and growth of MNPs within the network of MOFs limiting *a priori* the final particle size by the porosity without the need of surfactants or capping agents. This chapter presents the synthesis of AgNPs within the previously synthesized microporous photoactive titanium terephthalate MIL-125-NH_2 following an impregnation-reduction strategy to conform the AgNP@nanoMIL-125-NH_2 composite (see APPENDIX I I.II SiB association of AgNPs *via* chemical reduction for details).

Taking into account the antimicrobial character of silver, the resulting AgNP@nanoMIL-125-NH_2 composite was further studied as a bactericide coating to mitigate the biofilm contamination of surfaces, still a demanding issue, as they are associated to severe disease spread. Biofilms associated infections are related to the contamination of surgical devices, food preparations, water distribution pipes, conventional air recirculation and cooling systems, and high touch surfaces (*e.g.:* doorknobs, pressing buttons, rail bars, shopping carts). One possible solution is the

development of antifouling and antibacterial surface coatings. In this work, we originally propose the use of photoactive MOFs for biofilm treatment.

The novelty of this work relies on the following:

i) The treatment of strongly contaminated surfaces, as previous studies with MOFs have exclusively addressed biofilm prevention;
ii) This pioneering work reports both antiadherent effect, which removes the biofilm, and bacterial inhibition; and
iii) Our original successful strategy involve the multi-active combination of 1) intrinsic antibacterial effect of a photoactive titanium-based nanoMOF, 2) immobilization of biocide silver nanoparticles, and 3) improved anti-bioadherent effect upon irradiation of the composite coating.

This original research work is compiled in the publication "An Ag-loaded photoactive nano-metal organic framework as a promising biofilm treatment", A. Arenas-Vivo, G. Amariei, S. Aguado, R. Rosal, P. Horcajada, Actabiomaterialia, **2019**, *97*, 490-500 (Q1, IF: 7.242) reproduced here with the journal format.[1] This article has also been featured in the news section of Materials Today.[2] It is important to highlight that this article has been selected by the Spanish Association of Bioinorganic (Asociación Española de Bioinorganica, AEBIN) in their II Edition of best publication published by young researchers awards as the best publication by a predoctoral researcher.[3]

Despite the active contribution of all the authors to this article, we consider important to clearly describe the contribution of the PhD candidate. Conceptualization of this work is attributed to Dr. Patricia Horcajada and Ana Arenas Vivo (AAV). The synthesis of the nanoMIL-125-NH_2 was carried out by this thesis author, AAV, at IMDEA Energy following a previously reported protocol by our research group, the Advanced Porous Materials Unit (APMU).[4] The impregnation-reduction protocol for AgNPs encapsulation was also developed and optimized by AAV. Full material characterization was carried out at IMDEA Energy installations with the exception of TEM observations. For this, with the help of Dr. Daniel Arenas and Dr. David Ávila, samples were analyzed in the Centro Nacional de Microscopía Electrónica. Antimicrobial characterization of the AgNP@nanoMIL-125-NH_2 composite, as well as its precursors, was carried out at the University of Alcalá de Henares (UAH) with the collaboration of Dr. Roberto Rosal team in the Department of Chemical Engineering. Experimental design and training in the bioanalytical design was led by Dr. Georgiana Amariei, while experiments were being carried out both by AAV and Dr. G. Amariei. Result analysis and discussion and original draft preparation was done by AAV. Review and editing of the publication were done by Dr. P. Horcajada and rest of coauthors.

Finally, as the use of MOFs as antimicrobial agents is a recent field with primary reported evidences in 2010-2012,[5–8] to better understand their potential and antibacterial properties, the review of the state-of-the-art of MOFs applied in this field has also been included as annex to the present manuscript. This review was previously published as the book chapter "Antimicrobial Metal Organic Frameworks" by AAV and P. Horcajada, (see APPENDIX II II.I Book Chapter: Antimicrobial MOFs) comprised in the book **Metal Organic Frameworks (2019)**, of central West Publishing (edited by D.V Mittal), pp.:1-34.[9]

Conceptualization of this boom chapter is attributed to AAV and Dr. P. Horcajada. Literature review and current state-of-the-art compilation and selection were carried out by AAV. Original book chapter preparation was done by AAV. Review and editing of the publication were done by Dr. P. Horcajada and AAV.

3.2. MOF selection: MIL-125-NH_2

For SiB experiments, the MIL-125-NH_2 or $[Ti_8O_8(OH)_4(BDC\text{-}NH_2)_6]$ was selected as support (Figure 3. 1). MIL-125-NH_2 is built from Ti-oxo-clusters coordinated to the 2-aminoterephthalate ligand ($H_2BDC\text{-}NH_2$) and typically synthesized *via* solvothermal route. It has a large surface area and high pore volume (S_{BET} ~1500 $m^2 \cdot g^{-1}$, V_p ~0.65 $cm^3 \cdot g^{-1}$) and its structure is ordered with octahedral ~12.5 Å and tetrahedral cavities ~6 Å, accessible via triangular windows ~5—7 Å. It is photochromic as the clusters experience the reduction of Ti^{IV} to Ti^{III} under UV irradiation.[10] In addition, this amino-substituted isoreticular version of the parent MIL-125 extends its light absorption from the UV to the visible region producing a red shift on its E_g from 3.6 to 2.6 eV (375 to 475 nm) due to the electron dislocation from the nitrogen to the ligand aromatic ring.[11] MIL-125-NH_2 has proven good catalytic activity in several reactions such as: cycloaddition,[12] oxidative desulfurization,[12] oxidation of alcohol to aldehydes,[10] photocatalytic degradation of dyes,[13,14] photocatalytic reduction of CO_2[15] and photocatalytic H_2 generation, among others.[16]

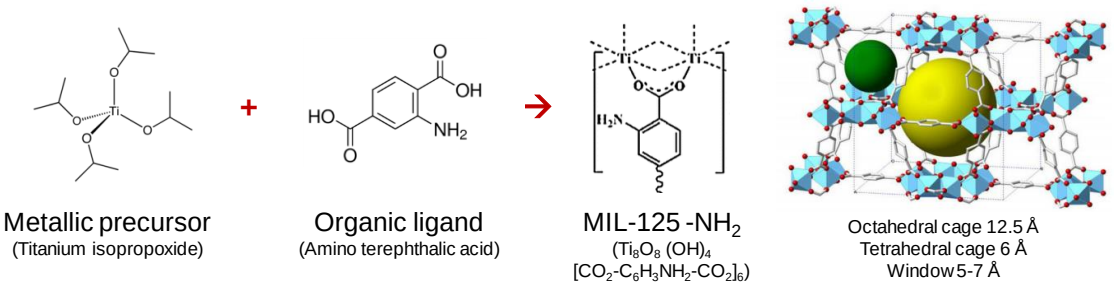

Figure 3. 1: Schematic representation of MIL-125-NH_2

Besides its photoactive properties and its high porosity, MIL-125-NH_2 was selected also for: i) its organic ligand bearing -NH_2 groups able to interact with guest species and prevent their leakage (*i.e.* AgNPs), ii) its *a priori* biocompatible character (rat oral 50% lethal dose (LD_{50}) > 2000 $mg \cdot kg^{-1}$ for TiO_2 ,[17] and 50% inhibitory concentration (IC_{50}) in HeLa and J774 cells = 600 and 20 $\mu g \cdot mL^{-1}$, respectively,[18] and studies have proven its application as robust and biosafe oral therapheutic agent),[19] iii) its very good aqueous stability,[12] and iv) its tunable particle size, enabling the modulation of the surface interactions between the material and surrounding media.[20]

In the APPENDIX I there is complementary information to this chapter. Both the synthetic protocol of pristine MIL-125-NH_2, with micro- and nano-particle size are section I.I Synthesis of MIL-125-NH_2. The protocol optimization for the attainment of AgNPs@MIL-125-NH_2 composites, with MIL-125-NH_2 micro- and nano- crystals, *via* an original two-step SiB impregnation & chemical reduction procedure developed in this thesis is also presented in the APPENDIX I section I.II SiB association of AgNPs *via* chemical reduction SiB association of AgNPs *via* Chemical reduction

The applicability as bactericide material of the synthesized AgNP@nanoMIL-125-NH_2 composite in the form of thin films coating was explored in the original publication, “An Ag-loaded photoactive nano-metal organic framework as a promising biofilm treatment”, presented below in section 3.3 and further it is further discussed in Chapter 7 . The article supporting information, as published, is included in APPENDIX III

.

3.3. An Ag-loaded photoactive nano-metal organic framework as a promising biofilm treatment

Ana Arenas-Vivo [a,b], Georgiana Amariei [c], Sonia Aguado [c], Roberto Rosal [c], Patricia Horcajada [a,*]

[a] *Advanced Porous Materials Unit (APMU), IMDEA Energy Institute, Avda. Ramón de la Sagra 3, E-28935 Móstoles, Madrid, Spain*

[b] *Department of Inorganic Chemistry I, Chemical Sciences Faculty, Complutense University of Madrid, 28040 Madrid, Spain*

[c] *Department of Chemical Engineering, University of Alcalá, E-28871 Alcalá de Henares, Madrid, Spain*

**Corresponding author. E-mail address: patricia.horcajada@imdea.org*

Acta Biomaterialia, 2019, *97*, 490-500 (Q1, IF: 7.242)

Keywords: nano-MIL-125NH_2, Ag nanoparticles, photoactive, biofilm treatment biocide

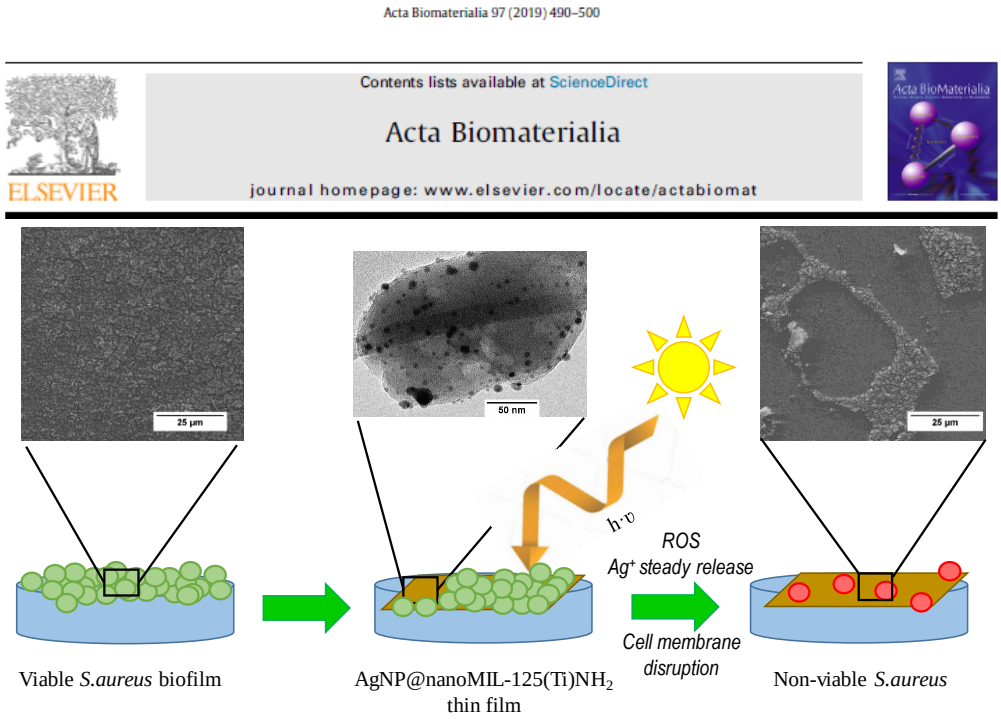

Acta Biomaterialia 97 (2019) 490–500

Contents lists available at ScienceDirect

Acta Biomaterialia

journal homepage: www.elsevier.com/locate/actabiomat

Full length article

An Ag-loaded photoactive nano-metal organic framework as a promising biofilm treatment

Ana Arenas-Vivo [a,b], Georgiana Amariei [c], Sonia Aguado [c], Roberto Rosal [c], Patricia Horcajada [a,*]

[a] Advanced Porous Materials Unit (APMU), IMDEA Energy Institute, Avda. Ramón de la Sagra 3, E-28935 Móstoles, Madrid, Spain
[b] Department of Inorganic Chemistry I, Chemical Sciences Faculty, Complutense University of Madrid, 28040 Madrid, Spain
[c] Department of Chemical Engineering, University of Alcalá, E-28871 Alcalá de Henares, Madrid, Spain

ARTICLE INFO

Article history:
Received 13 May 2019
Received in revised form 11 July 2019
Accepted 2 August 2019
Available online 06 August 2019

Keywords:
Nano-MIL-125NH_2
Ag nanoparticles
Photoactive
Biofilm treatment
Biocide

ABSTRACT

Surface biofilm inhibition is still currently a considerable challenge. Among other organisms, *Staphylococcus aureus* is notable for its ability to form a strong biofilm with proved resistance to chemotherapy. Contamination of high-touch surfaces with *S. aureus* biofilm not only promotes disease spread but also generates tremendous health-associated costs. Therefore, development of new bactericidal and antiadhesive surface coatings is a priority. Considering that metal-organic frameworks (MOFs) have recently emerged as promising antibacterial agents, we originally report here the synthesis of a multi-active silver-containing nanoscaled MOF composite as a potential surface coating against *S. aureus* biofilm owing to a triple effect: intrinsic bactericide activity of the MOF, biocidal character of silver nanoparticles (AgNPs), and photoactivity after UVA irradiation. AgNPs were successfully entrapped within the benchmarked nanoscaled porous photoactive titanium(IV) aminoterephthalate MIL-125(Ti) NH_2 using a simple and efficient impregnation-reduction method. After complete characterization of the composite thin film, its antibacterial and anti-adherent properties were fully evaluated. After UVA irradiation, the composite coating exhibited relevant bacterial inhibition and detachment, improved ligand-to-cluster charge transfer, and steady controlled delivery of Ag^+. These promising results establish the potential of this composite as an active coating for biofilm treatment on high-touch surfaces (e.g., surgical devices, door knobs, and rail bars).

Statement of Significance

Surface contamination due to bacterial biofilm formation is still a demanding issue, as it causes severe disease spread. One possible solution is the development of antifouling and antibacterial surface coatings. In this work, we originally propose the use of photoactive metal-organic frameworks (MOFs) for biofilm treatment. The novelty of this work relies on the following: i) the treatment of strongly contaminated surfaces, as previous studies with MOFs have exclusively addressed biofilm prevention; ii) this pioneering work reports both antiadherent effect, which removes the biofilm, and bacterial inhibition; iii) our original successful strategy has never been proposed thus far, involving the multi-active combination of 1) intrinsic antibacterial effect of a photoactive titanium-based nanoMOF, 2) immobilization of biocide silver nanoparticles, and 3) improved anti-bioadherent effect upon irradiation of the composite coating.
© 2019 Acta Materialia Inc. Published by Elsevier Ltd. All rights reserved.

1. Introduction

Attainment of bacteria-free surfaces and disease spread control is still currently a great challenge [1]. The issue starts with the formation of biofilms over surfaces, which consist of a bacterial microenvironment involving strong interaction of microorganisms and extracellular polymeric substances (EPS) with the substrate [2]. The resulting biofilm is an irreversibly bounded complex microbial aggregation that contaminates surfaces [3].

Biofilm-associated infections are the cause of 80% of hospital-acquired or nosocomial infections. In particular, *Staphylococcus aureus,* is notable among other species as the major cause of these infections [4]. *S. aureus*, a gram-positive cocci frequently found in the human respiratory tract and skin, is known for its persistence on host tissues and surfaces owing to its developed multidrug resistance [5,6]. Contamination of surgical devices, food preparations, and high-touch surfaces (e.g., door knobs, pressing buttons,

* Corresponding author.
E-mail address: patricia.horcajada@imdea.org (P. Horcajada).

https://doi.org/10.1016/j.actbio.2019.08.011
1742-7061/© 2019 Acta Materialia Inc. Published by Elsevier Ltd. All rights reserved.

rail bars, and shopping carts) with *S. aureus* biofilm is the cause of the spread of many diseases, thereby causing high economic loss [7]. Therefore, there is an urgent need for the development of bioactive surface coatings that both limit bacterial adhesion, hence attaining the so-called "antifouling surfaces," and provide efficient antibacterial properties for biofilm treatment.

Herein, we assess the use of metal-organic framework (MOF) coatings in the treatment of infections due to *S. aureus* biofilm. MOFs are a new class of hybrid crystalline materials [8] consisting of inorganic units connected to polydentate organic ligands, forming a porous 3D framework. Because of their exceptional porosity and their compositional and structural versatility, MOFs are prominent as ideal candidates for several industrial and societal applications (*e.g.,* separation, detection, catalysis, energy) [9]. However, the use of MOFs as antibacterial agents (based on biocide cations) was not reported until 2010 [10]. In particular, MOFs present some advantages when compared with other antibacterial materials: i) both their organic and inorganic components can exhibit bactericidal activity by the generation of reactive oxygen species (ROS); ii) they have an uniform and ordered distribution of active sites; iii) release of antibacterial species to the medium during degradation tends to be more controlled and homogeneous [11].

The antibacterial activity of MOF was widely evaluated against bacterial suspensions (known as planktonic state bacteria) [11] as either powdered [12] or shaped MOFs (fibers, membranes) [13,14]. To the best of our knowledge, there are only three studies analyzing the antimicrobial activity of MOFs against bacterial biofilm. First, Cu-SURMOF-2 deposited on gold substrates was proposed as an antifouling coating against *Cobetia marina* [15]. Another Cu-based MOF dispersed in a chitosan film exhibited a remarkable biocidal effect against *Pseudomonas aeruginosa* biofilm, combining the antibacterial action of chitosan and Cu [16]. Finally, an Ag-based MOF was incorporated into a thin-film polyamide membrane to mitigate membrane biofouling of *S. aureus* and *Escherichia coli* [17]. Although these previous studies exhibited considerable inhibition of bacterial viability (>80%), it is important to note the following observations: i) the very short contact times used (1–2 h) might not be representative of biofilm treatment, as longer contact times are required to develop a mature biofilm (>18 h) [18] and ii) the antiadherent properties of the surfaces were not evaluated. These interesting studies, together with the commonly known irradiation biocidal effect [19], prompted us to develop antifouling photo-bactericidal surfaces based on nanoscaled microporous photoactive titanium(IV) aminoterephthalate MIL-125(Ti)NH_2 [20] loaded with silver nanoparticles (AgNPs). Very recently, two Ag-loaded MOFs with antibacterial properties, namely, AgNPs inside Cu-porphyrin spheres [21] and Ag nanowires covered by ZIF-8 [22], have emerged; their studies were limited to planktonic state bacteria, not biofilm. Similarly, although irradiation was able to enhance the bactericidal effect of a MOF-5 composite in suspension, this was solely proved against a planktonic suspension of *E. coli*, again without considering the defying bacterial biofilm infections [23]. Therefore, herein, we originally present a triple multi-action nanocomposite for the challenging anti-adherent treatment of mature *S. aureus* biofilm; which combines the intrinsic bactericidal activity of MOF, immobilized AgNPs, and photoactivity after UVA irradiation in a thin film surface coating.

Specifically, the benchmarked MIL-125(Ti)NH_2 [24,25] was selected for the first time for this application for several reasons: i) its photoactive properties, which are already proven in different catalytic reactions; [26,27] ii) its high porosity (S_{BET}: 1500 $m^2\ g^{-1}$ with tetra- and octahedral cavities of *ca.* 6.1 and 12.5 Å, respectively); iii) its organic ligand (2-aminoterephthalate, BDC-NH_2), bearing –NH_2 groups, able to interact with guest species (*e.g.*, AgNPs); iv) its *a priori* biocompatible character (rat oral 50% lethal dose (LD_{50}) >2000 $mg{\cdot}kg^{-1}$ for TiO_2 [28] and 50% inhibitory concentration (IC_{50}) in HeLa and J774 cells = 600 and 20 $\mu g\ mL^{-1}$, respectively) [29]; v) its very good aqueous stability [27]; and vi) its tunable particle size, enabling the modulation of the surface interactions between the material and the bacteria [11]. Thus, the AgNP@nanoMIL-125(Ti)NH_2 (AgNP@nanoMOF) composite was synthesized using a simple impregnation-reduction protocol and fully characterized by different solid-state techniques. The combined photo-antibacterial effect of a colloidal suspension of the composite was first assessed against *S. aureus* inoculum. Then, homogeneous drop-casted AgNP@nanoMOF thin films were prepared and investigated for their antifouling and biocidal properties by using a combination of complementary techniques. The influence of the presence of AgNPs and photoactivation by UVA irradiation on biofilm treatment was deeply investigated, paying special attention to the chemical integrity of the composite thin film.

2. Materials and methods

2.1. Synthesis and characterization of AgNP@nanoMIL-125(Ti)NH_2 (AgNP@nanoMOF)

MIL-125(Ti)NH_2 nanoparticles (nanoMOF) were obtained as previously described [20]. The impregnation-reduction methodology with AgNPs was inspired from Liu et al. for MIL-101 [30] and MIL-100(Fe) [31]. As the nanoMIL-125(Ti)NH_2 should be kept in methanol for preventing nanoparticle (NP) aggregation, an initial solvent exchange with CH_3CN by centrifugation previous to the impregnation step with $AgNO_3$ was required. Once exchanged, the wet NPs (equivalent material corresponding to 250 mg of dry MOF) were redispersed in 20 mL of a 22 mM $AgNO_3$ solution (75 mg, Acros Organics, 99.85%, MW: 169.87 g mol^{-1}) in CH_3CN by sonication (2 h) and stirred at room temperature (RT) for 16 h. The silver-impregnated nanoMOF (Ag^+@nanoMOF) was recovered by centrifugation and once again exchanged the solvent to absolute ethanol. After solvent exchange, Ag^+@nanoMOF was stirred under Ar atmosphere with 30 mL of absolute ethanol. For reduction, a 50 mL absolute ethanol solution of 18 mM $NaBH_4$ (33 mg TCI, >95%, MW: 37.83 g mol^{-1}) was added to the previous ethanol mixture dropwise and stirred for 10 min under Ar atmosphere. The composite AgNP@nanoMOF was then recovered by centrifugation (11,000*g* RCF, relative centrifugal force) and preserved in absolute ethanol.

Both materials, that is, nanoMOF and AgNP@nanoMOF, were deposited by simple drop-casting (50 µL of 4 g L^{-1} ethanol suspensions; Supporting Information, SI, Fig. S1) over one side of 13 mm-diameter cover glass discs (VWR, Germany) and dried at RT for analyzing antifouling photo-bactericidal activity (concentration = 1.5 $\mu g\ mm^{-2}$; see scanning electron microscopy (SEM) images of the surface in SI, Fig. S2).

2.2. Synthesis of AgNPs + nanoMOF "physical" mixture

For comparison purposes, a "physical" mixture of 20.5 mL aqueous dispersion of AgNPs (synthesized following [32]: with 139 ± 7 ppm of Ag, as determined by inductively coupled plasma-optical emission spectrometry, ICP-OES; particle size: 2.4 ± 1 nm, PDI: 0.34 and ξ-potential: −38.5 ± 0.7 mV, as determined by dynamic light scattering, DLS) and 50 mg nanoMOF was made (2 h sonication followed by 16 h stirring), resulting in AgNPs + nanoMOF (final Ag^0 content of 5.3 ± 0.8 wt% by ICP-OES).

2.3. Material characterization

All materials were fully characterized by using different solid-state techniques including X-ray powder diffraction (XRPD), Fourier transform infrared spectroscopy (FTIR), UV–Visible spec-

troscopy, thermogravimetric analyses (TGA), N_2 sorption isotherms, scanning and transmission electron microscopy (SEM and TEM, respectively), dynamic light scattering (DLS), and ξ-potential (ZP) (SI section 1.).

2.4. Antifouling photo-bactericidal activity and bioanalytical procedures

The microorganisms used in this study were the gram-positive *S. aureus* (CETC 240, strain designation ATCC 6538P) and gram-negative *E. coli* (CET 516, strain designation ATCC 8739), both representative biofilm-forming bacteria. The microorganisms were reactivated in nutrient broth (NB, SI section 1.1) by incubation at 37 °C under shaking at 100 rpm. Inoculums were diluted with fresh NB to 10^6 cells mL^{-1} (tracked by optical density at 600 nm, OD_{600}) to preserve the exponential growth phase of the microorganisms during the total time of contact (total 20 h: 18 h dark + 2 h UVA irradiation).

For antibacterial experiments performed with material suspensions: nanoMOF and AgNP@nanoMOF, as well as control samples (AgNPs + nanoMOF "physical" mixture, TiO_2 anatase, ligand (BDC-NH_2), $AgNO_3$, Ag^0) were suspended over 2.25 mL of the previously mentioned 10^6 cells mL^{-1} inoculums on a 24-well disposable microplate, at different concentrations (0, 1, 20 ppm; in the case of the individual constituents, the concentration was adjusted to one correspondent in the MOF (BDC-NH_2) 13 ppm, TiO_2 4 ppm, $AgNO_3$ and Ag^0 1.21 ppm) (Scheme S1 in SI).

For antifouling and antibacterial experiments performed with thin films: Cover glasses with nanoMOF, AgNP@nanoMOF, and AgNPs + nanoMOF thin films, as well as clear cover glasses, were placed on 24-well microplates with the active layer facing up in contact with 2.25 mL of the previously mentioned bacterial inoculums (final concentration of the thin film: 88 ppm) (Scheme S1 in SI).

In both cases, the prepared microplates were incubated at 37 °C without stirring for 20 h. When irradiated, this period was divided as 18 h incubation in dark (time selected to enable the formation of a mature *S. aureus* biofilm [18,33]), followed by 2 h UVA irradiation at RT. UVA experiments were performed with three actinic BL TL 6W/10 1FM Hg-lamps (Philips) of 6 W each with spectral emission in the UV region (λ_{max} = 365 nm) with a total irradiance of 40 W m^{-2} under 400 nm. As a conservative assumption, the irradiation time of the UV lamps was adjusted to simulate half of the daylight UV solar irradiation reported for a horizontal surface at the latitude of Madrid during Winter-Fall (~80 Wh m^{-2} according to NASA Surface Meteorology and Solar Energy Database) [34]). Samples were irradiated at a distance of 4 cm from the lamp sleeve so that all wells received a uniform amount of irradiation. Additional experiments under visible light irradiation were carried out with a Heraeus TQ Xe 150 Xe-arc lamp (radiant power in the visible range of 120 W m^{-2}), placing the lamp at a distance of 15 cm from the wells for 4 h to simulate half of the daylight visible solar irradiation reported for a horizontal surface at the latitude of Madrid during Winter-Fall (~500 Wh m^{-2} according to NASA) [34].

The antibacterial effect was quantified by determining colony-forming units (CFU) considering the cells from the supernatant liquid (planktonic bacteria) and the cells removed from the biofilm formed over the cover glasses (sessile bacteria) in both dark and irradiated experiments. For the removal of the sessile bacteria from the cover glasses, a previously reported procedure was followed according to ISO 22196 [35]. Afterwards, the aliquots (of both planktonic and sessile bacteria) were serially diluted in phosphate-buffered solution (PBS), and colony counting was performed after inoculation of Petri dishes containing NB agar medium and incubation of these plates at 37 °C for 24 h (Scheme S2 in SI). For colony number estimations, at least three replicates of at least two serial dilutions were considered. Results are presented as the logarithm of CFU mL^{-1} of culture of each sample.

Bacterial viability was also determined using fluorescein diacetate (FDA), a nonfluorescent compound hydrolyzed by esterases in fully functional cells to a green fluorescent compound, fluorescein. For this purpose, the liquid fraction was analyzed in 96-well black microplates by mixing 5 μL of FDA (0.02% w/w in dimethyl sulfoxide, DMSO) and 195 μL of bacterial suspension in each well. The plate was incubated at 25 °C for 30 min, with readings performed every 5 min (exc. 485 nm; em. 528 nm) using a fluorometer (Fluoroskan FL; Thermo Scientific™, Ascent, Waltham, MA, USA) (Scheme S3 in SI). The possible interference of the culture medium and MOFs with fluorescence measurement was checked [36]. Each sample was measured for quadruple, and results are presented as reduction percentage, calculated as the difference in fluorescence intensity of the sample with regard to one of the control blank assays. The fluorometer was also used for the determination of ROS [37]. In brief, the liquid fraction of samples was incubated for 30 min with 50 μL mol L^{-1} of 2′,7′-dichlorodihydrofluorescein diacetate (H_2DCF-DA), which is sensitive for hydrogen peroxide and other ROS, including hydroxyl and peroxyl radicals, (exc. 495 nm; em. 525 nm).

Confocal laser scanning microscopy (CLSM) was performed for visual and qualitative assessment of antibacterial and antifouling activities. The micrographs were obtained using a Leica Microsystems Confocal SP5 Fluorescence microscope (Germany) and processed with ImageJ software. The bacteria were stained with a LIVE/DEAD kit (Live/Dead BacLight Viability Kit, Thermo Fisher, USA) (Scheme S4 in SI). After biofilm formation on the sample surface, cell bodies were visualized in a CLSM system by using the FilmTracer FM 1–43 Green Biofilm Cell Stain (Molecular Probes, Invitrogen Detection Technologies, Carlsbad, CA, USA) according to the manufacturer's instructions (Scheme S5 in SI).

Antifouling capacity of the materials was also assessed using a SEM system (DSM-950 Zeiss, Oberkochen, Germany).

2.5. Stability test of the MOF thin film in the culture broth

To determine the stability of the thin films under bacteriological experimental conditions, thin films of the nanoMOF and the composite AgNP@nanoMOF (concentration of 1.5 μg mm^{-2}) were placed in contact with 2.25 mL of the NB culture broth and incubated in dark at 37 °C for different time periods (30 min–14 days). In addition, to investigate the long-term stability of the thin films, accelerated degradation tests were carried out following ASTM-D870-15, with immersion of the discs in 2.25 mL NB and incubating them at 70 °C for up to 14 days. Then, aliquots of NB were used to determine the NP detachment and chemical stability of the MOF film in the presence of the media.

Particle detachment was determined by DLS, analyzing both particle size and ξ-potential. Quantitative determination of Ag and Ti release of the samples was done with ICP-OES Optima 3300 DV (PerkinElmer, Waltham, MA, USA; aliquots were dehydrated at 80 °C before digestion with HF and HNO_3).

The amount of organic linker released, BDC-NH_2, was determined using a reversed-phase high-performance liquid chromatography (HPLC) system Jasco LC-4000 series separation module (Jasco, Tokyo, Japan), equipped with a variable photodiode array detector Jasco MD-4015 and controlled by ChromNAV 2.0 software (SI section 1.2). The retention time and absorption maximum (λ) for BDC-NH_2 were 2.7 min and λ = 228 nm.

2.6. Statistical analysis

Data are presented as mean ± standard deviation of at least 3 samples ($n \geq 3$), as experiments were replicated until obtaining

reliable results. Difference between groups was analyzed using one-way ANOVA, with Microsoft Excel® software for the calculations. Differences were considered significant when $p < 0.05$.

3. Results

3.1. Synthesis and characterization of AgNP@nanoMIL-125(Ti)NH_2 (AgNP@nanoMOF)

XRPD patterns of AgNP@nanoMOF (Fig. 1) showed characteristic Bragg reflections of MIL-125(Ti)NH_2, together with the characteristic peaks of the face-centered cubic structure (fcc) structure of Ag^0. The amount of Ag^0 associated with the MOF was 5.7 ± 0.2 wt%, as quantified by ICP-OES and in agreement with the TGA results (Fig. S3). Diffuse reflectance UV–Vis spectroscopy (Fig. 1) exhibited a wider absorption of AgNP@nanoMOF with regard to the substrate.

TEM micrographs confirmed the presence of AgNPs in the MOF (Fig. 1). The starting nanoMOF (Fig. S4) showed a characteristic disc shape with a slightly rough external surface and an average size of 250 ± 80 nm ($n = 80$ particles, Fig. S5). After the impregnation-reduction process, AgNP@nanoMOF exhibited a similar shape (Figs. 1 and S4) and was covered by AgNPs of 5 ± 3 nm average size ($n = 600$ particles), identifiable in the micrograph by their higher contrast. The findings in these images are in agreement with the conclusions reached after XRPD pattern analysis. Although AgNPs are homogeneously distributed over the MOF, it seems that larger AgNPs migrate to the surface, while the smaller ones (<2 nm) remain within the MOF structure after the generation of defects to accommodate the AgNPs inside the framework. Details of further analysis of the particle size (determined by DLS) and colloidal stability in different media are given in Supporting Information (see SI section 2.1 and Table S1). In particular, in view of their specific antibacterial evaluation, the colloidal stability of nanoMOF and AgNP@nanoMOF was assessed in a bacterial NB, and both samples exhibited similar small particle sizes and ζ-potential values (~200 nm and −12 mV, Fig. S6).

Furthermore, a red shift in the FTIR spectra of the bands associated with the symmetric and asymmetric $-NH_2$ stretching (from 3477 and 3374 cm^{-1} in the nanoMOF to 3450 and 3358 cm^{-1} in the AgNP@nanoMOF, Fig. S7) suggests the inclusion of AgNPs in the framework, most likely in defects of the host nanoMOF, and their interaction with the $-NH_2$ groups of the ligand, in agreement with previous results of the encapsulation of cobaloxime into the MIL-125(Ti)NH_2 [38]. FTIR also corroborated that the structure remained stable after the impregnation-reduction process, as the band corresponding to coordination of both carboxylates to the titanium (1550–1450 cm^{-1}) is preserved in the composite. Type I

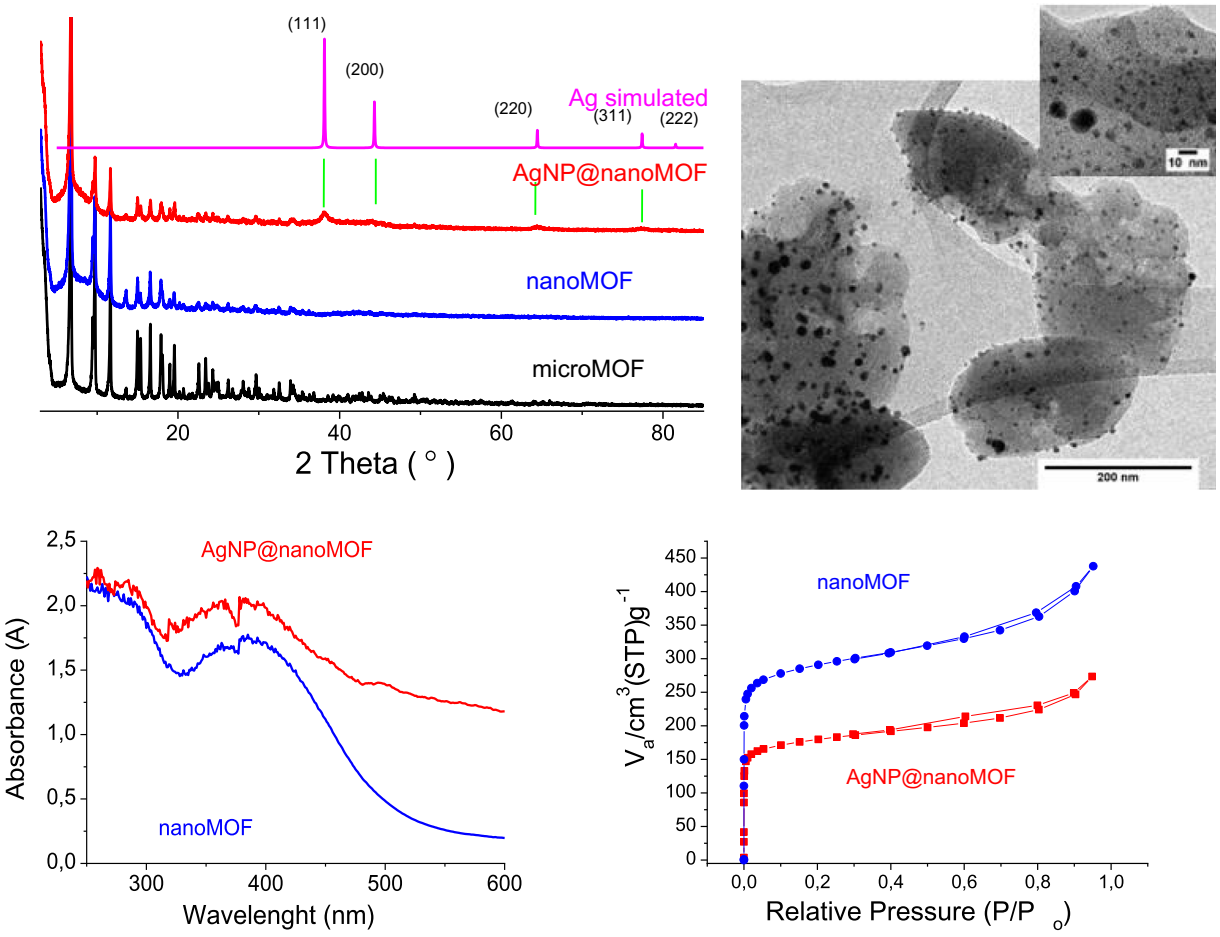

Fig. 1. Characterization of AgNP@nanoMIL-125(Ti)NH_2. Top left: XRPD patterns of microMOF (black), nanoMOF (blue), and AgNP@nanoMOF (red) compared to the simulated XRD pattern of metallic silver (pink). Top right: TEM micrograph of AgNP@nanoMOF (scale bar: 200 nm) with AgNP insert (scale bar 10 nm). Bottom left: Solid UV–Visible spectra of nanoMOF (blue) and the AgNP@nanoMOF (red). Bottom right: N_2 sorption isotherm of nanoMOF (blue) and AgNP@nanoMOF (red) measured at 77° K. (For interpretation of the references to color in this figure legend, the reader is referred to the web version of this article.)Characterization of AgNP@nanoMIL-125(Ti)NH_2. Top left: XRPD patterns of microMOF, nanoMOF and AgNP@nanoMOF compared to the simulated XRD pattern of metallic silver (bottom to top on grey scale). Top right: TEM micrograph of AgNP@nanoMOF (scale bar: 200 nm) with AgNP insert (scale bar 10 nm). Bottom left: Solid UV-Visible spectra of nanoMOF (dark grey) and the AgNP@nanoMOF (light grey). Bottom right: N_2 sorption isotherm of nanoMOF (dark grey) and AgNP@nanoMOF (light grey) measured at 77° K

N_2 sorption isotherms (Fig. 1), characteristic of microporous solids, are associated with lower Brunauer-Emmett-Teller (BET) surface and pore volume after the impregnation-reduction process (1100 ± 20 *vs.* 800 ± 5 $m^2 g^{-1}$ and 0.47 ± 0.02 *vs.* 0.34 ± 0.02 $cm^3 \cdot g^{-1}$, respectively, Fig. S8).

3.2. Antibacterial effect of AgNP@nanoMOF in suspension

For better analysis of the bacterial viability, biocidal activity is represented as $Log_{10}(CFU \cdot mL^{-1})$ due to the bacterial exponential growth. Nevertheless, for analysis of the irradiation effect and better comparison between samples, data are represented as the logarithm ratio as shown in Fig. 2, with C_0 indicating $CFU \cdot mL^{-1}$ of the positive control. In addition, data are also presented in Supporting Information along with the total $CFU \cdot mL^{-1}$ and the inhibition % (Tables S2–S4). Thus, the antibacterial intrinsic effect of nanoMOF was evidenced in suspension first against the gram-positive cocci *S. aureus* and then, against the gram-negative coliform *E. coli*, observing a concentration-dependent activity (Figs. 2, S9). In addition, the biocidal activity of MIL-125(Ti)NH_2 significantly increased ($p < 0.05$) as a NP and further more ($p < 0.01$) during interaction of AgNPs with the framework (Fig. 2). This biocidal activity is further promoted when the AgNP@nanoMOF composite received UVA irradiation for 2 h ($p < 0.01$, Fig. S10). Controls exhibited lower *S. aureus* viability inhibition than the AgNP@nanoMOF composite in all cases (Figs. 2 and S11). These results were further supported

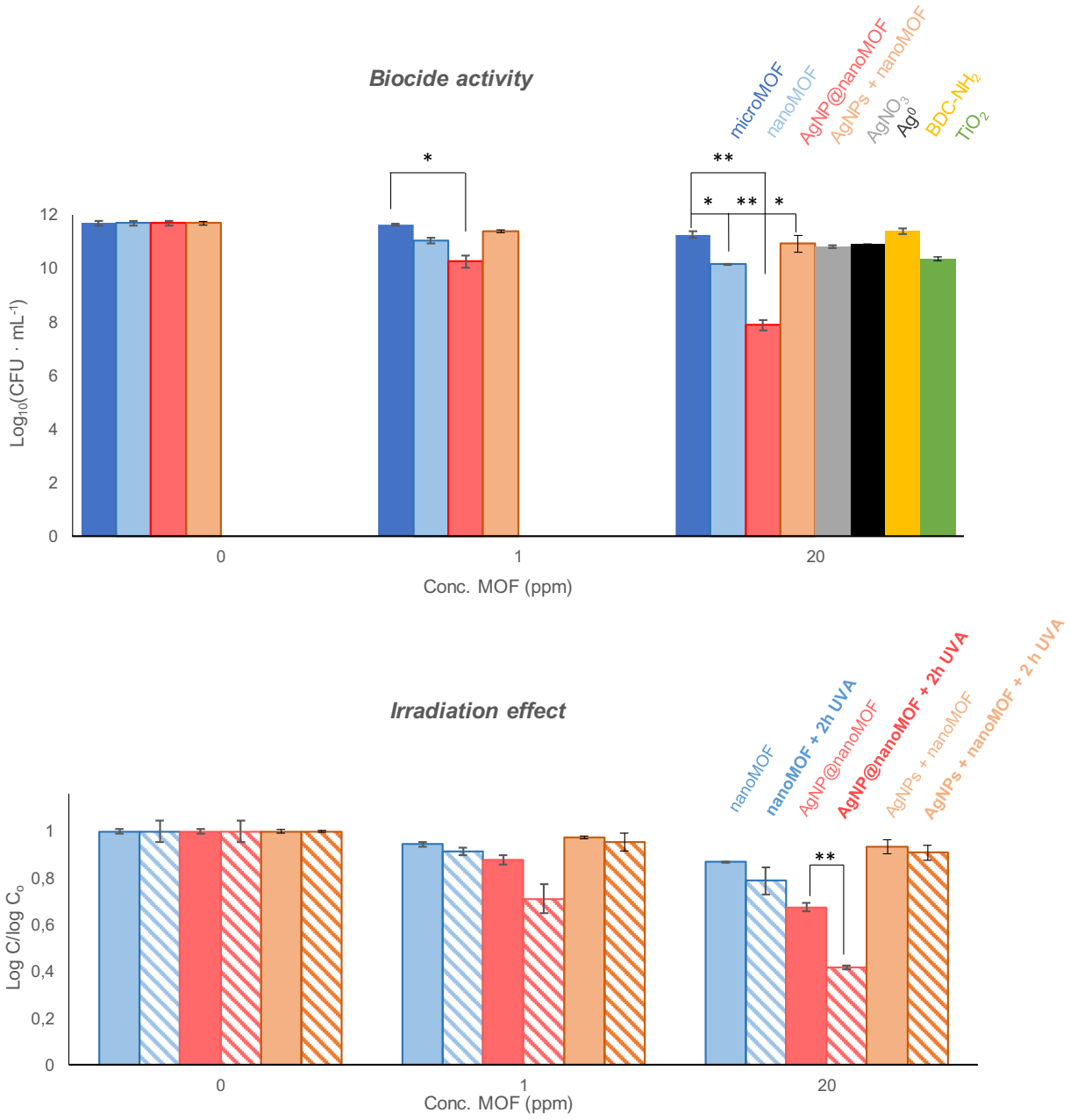

Fig. 2. Colony-forming units mL^{-1} of culture broth of *S. aureus* (represented as the $Log_{10}(CFU)$) in contact with a suspension of microMOF (dark blue), nanoMOF (blue), AgNP@nanoMOF (red), AgNP + nanoMOF (brown), $AgNO_3$ (gray), Ag^0 (black), BDC-NH_2 (yellow), and TiO_2 (green) (biocide activity). *S. aureus* colony-forming units mL^{-1} (represented as the logarithm ratio, being C_0 the $CFU \cdot mL^{-1}$ of the positive control for better comparison) in contact with MOF suspension after 20 h of dark exposure and after 18 h dark + 2 h of UVA irradiation (irradiation effect). *$p < 0.05$; **$p < 0.01$. (For interpretation of the references to color in this figure legend, the reader is referred to the web version of this article.)

by the determination of a reduction in the enzymatic activity of the bacteria (by fluorescence; Fig. S12) and by the discrimination of the live cells from dead cells (by confocal microcopy with LIVE/DEAD staining; Fig. S13).

3.3. Biofilm treatment: antifouling photo-bactericidal activity of AgNP@nanoMOF

The ability of the nanoMOF and AgNP@nanoMOF thin films to hinder *S. aureus* and *E. coli* bacterial attachment was determined by different optical studies [SEM (Fig. 3), confocal microscopy using green staining (Fig. 3) and LIVE/DEAD staining (Fig. S19)] and by different biological assays [bacterial viability *by* plate count of CFU (Figs. 4, S15 and S17), enzymatic activity (Fig. S16), and ROS generation *by* fluorescence staining (Fig. S18)].

SEM images (Fig. 3) revealed higher biofilm formation due to invasive *S. aureus* when in contact with a bare glass disc than when in contact with the nanoMOF and AgNP@nanoMOF thin films. This difference is highly evident in the 18 h dark + 2 h UVA-treated samples, wherein semi-quantitative analysis of the images *by* cell count showed a decrease in bacterial content by 80% in the biofilm after UVA irradiation for the composite thin film. Green staining of viable cell bodies within the biofilm (Fig. 3) revealed that bacterial growth was affected when in contact with nanoMOF and Ag@-nanoMOFs thin films, even after 20 h in dark, as fewer green areas appeared in the images (Fig. S14). After UVA irradiation, both materials showed >90% inhibition of the viable cells. For the control of "physical" mixture AgNPs + nanoMOF thin film, a different behavior is observed: after dark incubation, there is a moderate inhibition of biofilm viability compared to the control, even smaller than that with the pristine MOF, which fairly increased after irradiation, indicating that the "physical" mixture is more inefficient as a biocide antifouling material (Fig. S14).

Although these optical techniques showed information of the anti-adherent (antifouling) properties of the thin film coatings, plate count quantitatively determined cell viability of *S. aureus* in the planktonic state and in the biofilm-forming sessile state, evidencing a significant antibacterial activity against bacteria in both

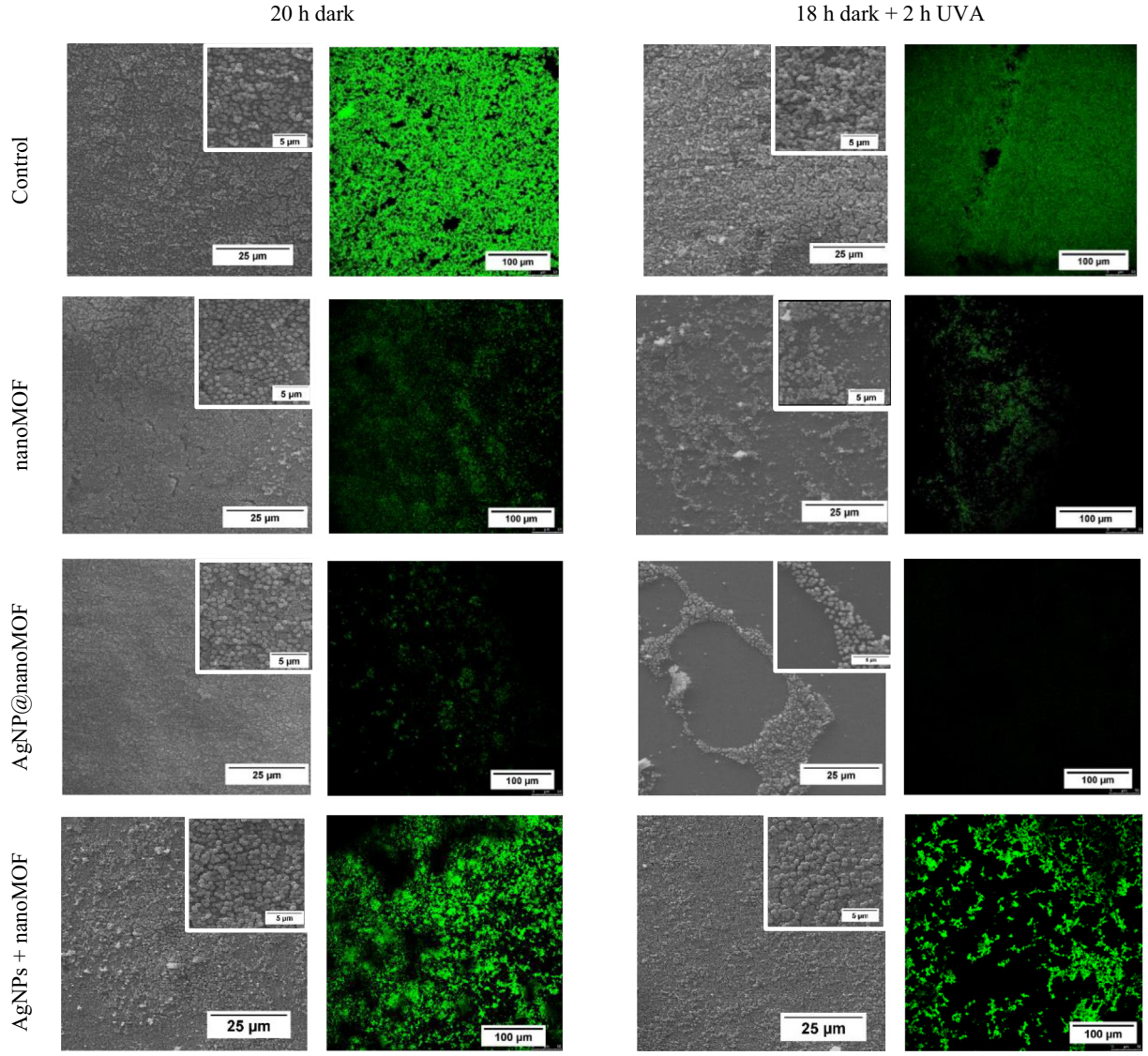

Fig. 3. SEM images (scale bar 25 μm) and green confocal micrographs (scale bar 100 μm) of *S. aureus* biofilm on cover glass surface (left) after biofilm growth for 20 h in dark and (right) 18 h in dark plus 2 h UVA irradiation of the (top to bottom) control cover glass, and the cover glass with nanoMOF thin film, AgNP@nanoMOF and the "physical" mixture AgNPs + nanoMOF thin film deposited on the surface. (For interpretation of the references to color in this figure legend, the reader is referred to the web version of this article.)

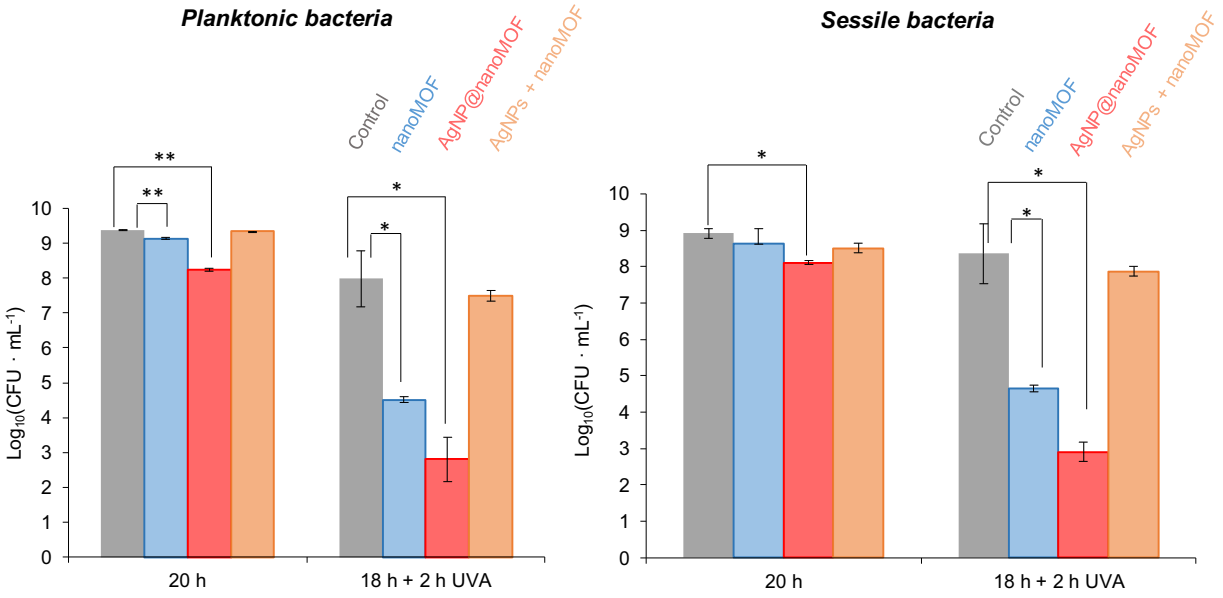

Fig. 4. Colony-forming units·mL^{-1} culture (represented as the Log_{10}(CFU)) of the *S. aureus* suspension (planktonic bacteria; left) and *S. aureus* biofilm detached from the surface (sessile bacteria; right) in contact with nanoMOF (blue), AgNP@nanoMOF (red), and AgNPs + nanoMOF (brown) thin films. *p < 0.05; **p < 0.01. (For interpretation of the references to color in this figure legend, the reader is referred to the web version of this article.)

states (Fig. 4). When irradiated, both planktonic and sessile *S. aureus* bacteria experimented a significant decrease in their viability ($p < 0.05$) when in contact with the nanoMOF and AgNP@nanoMOF, reaching a colony inhibition of 99.9999% in the case of the composite (Table S5). Plate count results are in agreement with the information obtained by SEM (Fig. 3), confirming the important biofilm inhibition activity associated with a biocidal effect of the AgNP@nanoMOF thin film, even further improved upon irradiation. This biocidal effect appeared also after visible light irradiation, reaching 97% of colony inhibition (Table S5, Fig. S15). Finally, additional bacterial viability tests were carried out to better understand these promising results, evidencing a higher ROS generation (Fig. S16) and enzymatic activity reduction (Fig. S18) upon irradiation and an absence of viability in the remaining bacteria (LIVE/DEAD staining, Fig. S19).

3.4. AgNP@nanoMOF thin film chemical stability

For better understanding the biocide and antifouling properties of the nanoMOF and the AgNP@nanoMOF composite, such as the origin of both effects, and for determining the potential use of the materials as antibacterial coatings, the chemical stability of the thin films was investigated under experimental conditions (incubation at 37 °C in NB) and under accelerated degradation conditions (incubation at 70 °C in NB) to assess long-term stability.

Degradation tests at 37 °C (Fig. 5) showed that Ag^+ is continuously and slowly released from the composite to the media. Nevertheless, after 14 days, <6 wt% of the total Ag content was delivered. On the other hand, Ti^{4+} was slowly and progressively delivered from both the nanoMOF and the composite during the first 12 h, reaching a plateau (~2 wt% of the total titanium), which is maintained even after 14 days. The nanoMOF degradation was also assessed by determining the amount of BDC-NH_2 delivered. In the case of nanoMOF, the same degradation trend found for the Ti^{4+} is observed for the ligand: a plateau is reached after 12 h incubation, associated with a release of ~12 wt%. In the case of AgNP@nanoMOF, the amount of released ligand is higher (28 wt%). Finally, particle detachment (determined after 20 h incubation; contact time equivalent to the one of the biocide tests) was ruled out, as only species coming from NB were observed (2.5 ± 1 nm) in both cases, indicating the good stability of the thin film (Fig. S20). These results support good stability of the thin film under the used experimental conditions (optimal for bacterial growth and biofilm formation). In the case of accelerated degradation tests (70 °C), Ti^{4+} was also slowly released from the nanoMOF (only 12 wt% released after 7 days) until burst MOF degradation after 14 days (Fig. S21). In the composite, Ag^+ and Ti^{4+} were continuously released during 14 days, exhibiting a higher degradation rate with the increase in temperature (complete degradation after 14 days at 70 °C).

4. Discussion

4.1. Synthesis and characterization of AgNP@nanoMOF

AgNP@nanoMOF was successfully prepared using a simple and efficient two-step protocol by the impregnation of the mother hosting nanoMOF with the $AgNO_3$ precursor, followed by its controlled reduction within the MOF. While the impregnation-reduction protocol did not significantly affect the MOF crystallinity, XRPD patterns of AgNP@nanoMOF (Fig. 1) revealed a slight peak broadening of AgNP@nanoMOF samples when compared with the nanoMOF, suggesting the generation of defects as a result of the accommodation of an important content of AgNPs (5.7 ± 0.2 wt% of Ag^0). Note here the high efficiency of the process, with 63% efficacy at the impregnation step and an almost complete redox reaction (~100%).

Even the presence of Ag on the AgNP@nanoMOF was appreciable by naked eye because of the macroscopic color change of the sample: brownish compared to pale yellow of the pristine MOF (Fig. S1). UV–Vis spectroscopy provided better understanding of the variation of the optoelectronic properties of the samples. The absorption edge of nanoMOF occurs at slightly higher energies than in the case of AgNP@nanoMOF due to the incorporation of the AgNPs. Moreover, while the nanoMOF bandgap for the direct allowed transitions was 2.3 eV, as determined by Tauc Plot of the Kubelka-Munk function, the composite bandgap was 2 eV. Consequently, AgNP@nanoMOF exhibited a significant increment in the visible range absorbance, which might be beneficial not only for

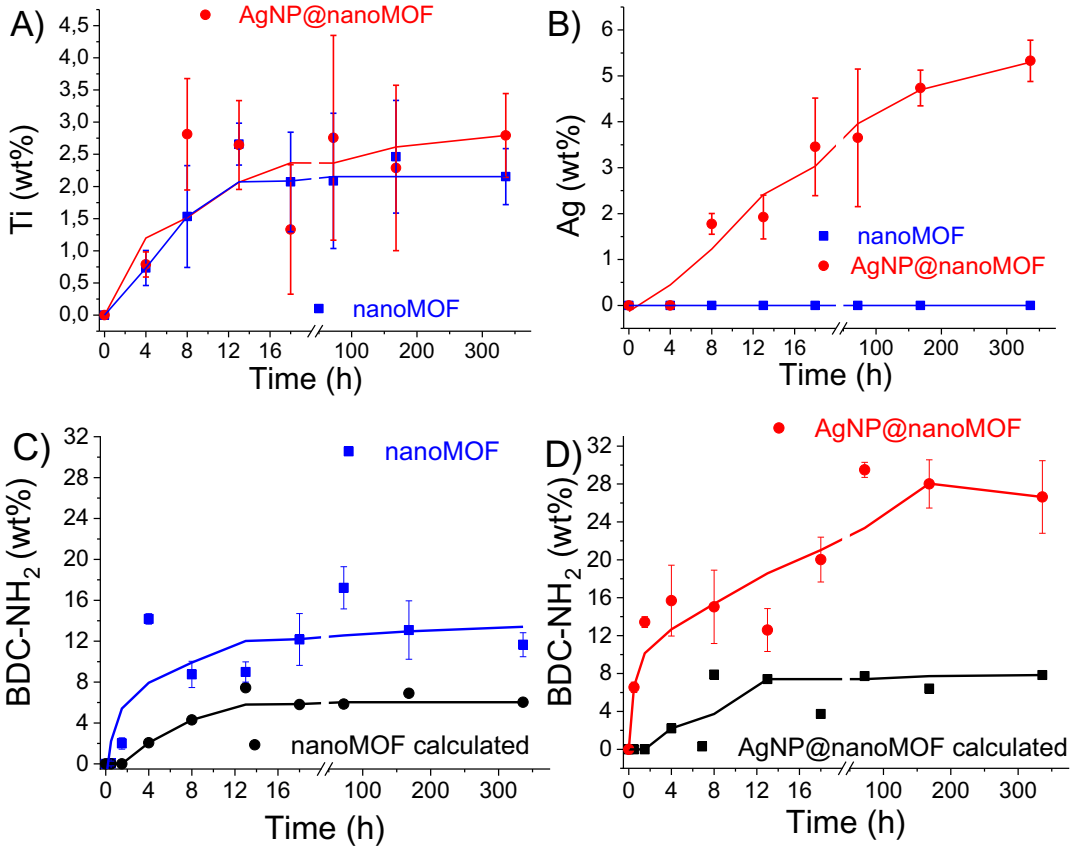

Fig. 5. NanoMOF degradation kinetics and metal release from the nanoMOF and AgNP@nanoMOF thin films on glass substrates in contact with the culture medium NB incubated at 37 °C. Ti (A) and Ag (B) release (expressed as wt% of the total content) determined by ICP-OES. BDC-NH_2 delivery (expressed as wt% of the total content) from the nanoMOF (C) and AgNP@nanoMOF (D). The theoretical BDC-NH_2 degradation, calculated from correspondence with Ti, has been included for comparison.

the photo-biocide application studied in this work but also for other relevant applications (*e.g.*, catalysis, sensing).

Although AgNPs are homogeneously distributed all over the MOF (Fig. 1), it seems that larger AgNPs migrate to the surface, while the smaller ones (<2 nm) remain within the MOF structure after the generation of defects to accommodate the AgNPs inside the framework. N_2 sorption isotherms (Fig. 1) confirmed the presence of AgNPs within the porosity of nanoMOF, showing a significant decrease in de S_{BET} and pore volume values after the impregnation-reduction process. In addition, there was a shift to a smaller pore size distribution as a result of the encapsulation (from 5.6 to 5.0 Å; Fig. S8). Considering the pore size and the particle size distribution of AgNPs (Fig. S5), one can hypothesize that only the AgNPs with dimensions <2 nm (10% as reflected in the histogram) could be located within the cavities. The rest might be associated within the framework, generating extra-defects during the reduction process (in agreement with previously mentioned peak broadening) or on the outer MOF surface.

4.2. Antibacterial effect of AgNP@nanoMOF in suspension

The evidenced antimicrobial activity is particle size dependent (Fig. 2 at 20 ppm, Log_{10}(CFU) = 11.27 *vs.* 10.18 with the 500 nm microMOF and 250 nm nanoMOF, respectively), as it significantly increases with the decrease in particle size ($p < 0.05$). This might be related to the higher reactivity of the smaller nanoMOF due to the increment of surface area available in contact with the bacterial membrane. A similar trend was observed when performing the same experiment for *E. coli* (see SI Fig. S9, Table S3). In addition, taking into account the absence of biocidal activity shown by the ligand and the intrinsic effect of the TiO_2 control (content corresponding to 20 ppm MOF), one can suggest that the intrinsic biocidal character arises from the inorganic component, in agreement with the results of previous minor TiO_2 activity [39]. As expected, considering the well-known antibacterial properties of silver [40], this intrinsic activity was significantly increased ($p < 0.01$) by the presence of AgNPs within the MOF (at 20 ppm, Log_{10}(CFU) = 10.18 *vs.* 7.89 with the nanoMOF and the composite; corresponding to 1.21 ppm of Ag, respectively). This increment was also observed against the suspension of *E. coli* (Fig. S9 and Table S3, at 20 ppm, Log_{10}(CFU) = 9.66 *vs.* 8.20 with the nanoMOF and the composite, respectively). The differences in *S. aureus* and *E. coli* inhibition by the AgNP@nanoMOF composite (99.98 *vs.* 99.5 inhibition %, for each bacterium, respectively) might be due to their different cell wall compositions and the material interaction with the membrane. While the gram-negative bacterial membrane is formed by a double layer, that is, a thin peptidoglycan cell wall surrounded by an outer polysaccharide layer, the gram-positive bacteria lack this outer layer and have a thicker peptidoglycan wall [41].

In contrast, the nanoMOF impregnated with already pre-synthesized AgNPs, the "physical" mixture AgNPs + nanoMOF, exhibited a biocidal activity that was significantly lower than that exerted by AgNP@nanoMOF ($p < 0.05$) and even smaller than that by pristine MOF (at 20 ppm, Log_{10}(CFU) = 10.93 *vs.* 10.18) and seemed to be determined by the action of the individual AgNPs, as seen from the silver blanks (Ag^0 and $AgNO_3$ Log_{10}(CFU) = 10.89 and 10.83, respectively). Hence, these results indicate that the higher bactericidal effect of the AgNP@nanoMOF is not a result of

the combination of its individual components but might be derived from a synergistic effect as a result of the strong interaction between the AgNPs and the nanoMOF.

Remarkably, the bactericidal effect of both nanoMOF and AgNP@nanoMOF was further promoted after 2 h UVA irradiation (see Figs. 2, S10 and S11), preventing >99% of the viable bacterial growth (Table S4). This result is within the same order as those of the Ag@CuTCPP (~6 ppm of MOF) [21] and other Ag-based MOFs reported thus far against *S. aureus* in suspension (see SI Table S7). Additionally, the control experiments, carried out with the "physical" mixture AgNPs + nanoMOF (see Fig. 2), TiO_2, BDC-NH_2, and the silver precursors Ag^0 and $AgNO_3$ (Fig. S11 and Table S4) in the presence of *S. aureus* inoculums after the same UVA irradiation, showed that the individual components of the AgNP@nanoMOF separately did not significantly increase their biocidal activity after irradiation, highlighting the strong interaction of the AgNPs with the $-NH_2$ groups of the nanoMOF structure.

Hence, the combination of complementary techniques (plate count, LIVE/DEAD confocal microscopy, and enzymatic activity; Figs. 2, S12 and S13) fully illustrates the importance of the interaction of AgNPs with the nanoMOF and the potential for the AgNP@nanoMOF composite as a biocidal material: the intrinsic antibiotic effect of nanoMOF is initially enhanced by the presence of silver within its network and further improved under UVA irradiation.

4.3. Biofilm treatment: Antifouling photo-bactericidal activity of AgNP@nanoMOF

Even more important than the control and inhibition of bacteria in their planktonic state is the prevention of bacterial adhesion to surfaces owing to their severe resistance to antibacterial agents, when in biofilms [3]. Whence, the current challenge is both interfering in the adhesion mechanisms by surface modification, attaining the so-called "antifouling surfaces," and providing efficient antibacterial properties.

After 20 h of incubation in dark, nanoMOF, AgNP@nanoMOF, and the AgNPs + nanoMOF "physical" mixture exhibited relatively low activity in the reduction of *S. aureus* biofilm, compared with the positive control (Fig. 3). In contrast, after 2 h UVA irradiation, there was notably less bacterial growth on the thin film of nanoMOF than in the control, evidencing an antifouling effect. Nevertheless, the "physical" mixture seemed to have a similar antiadhesion capacity compared to the nonirradiated sample, not experiencing this increment of the antifouling capacity by UVA, as is the case of pristine nanoMOF. On the other hand, the antifouling effect is considerably enhanced in the composite AgNP@nanoMOF thin film owing to the incorporation of silver in its structure and the stabilization of charges after photon absorption. Semi-quantitative analysis of the images by cell count estimates bacterial detachment of 80% from the biofilm after UVA irradiation in the case of the AgNP@nanoMOF thin film, while it was only 40% in the case of the irradiated pristine nanoMOF and 15% in the case of irradiated AgNPs + nanoMOF. According to Bordi et al. [42] different strategies have been proposed to deal with biofilm formation as a function of their evolution stages: 1) limiting switch from planktonic to biofilm lifestyle, 2) limiting initial adhesion and interaction, 3) interfering in bacterial communication, 4) developing antiadhesive surfaces, and 5) promoting dispersion. Both nanoMOF and AgNP@nanoMOF display two of the previously mentioned actions: first, limiting the initial adhesion (approximately 37% of reduction with regard to the control) and, second, favoring the dispersion of the previously attached bacteria (as promoted by the presence of AgNPs and UVA irradiation; Fig. 3).

The antiadherent properties of the nanoMOF and AgNP@nanoMOF thin films might be associated with the generation of ROS ($HO^{\cdot}$, $O_2^{\cdot-}$, $HO_2^{\cdot}$). It is commonly known that, after UV irradiation, ROS production leads to bacterial death and then, their detachment from the biofilm [19,43]. Consequently, ROS production (quantified by fluorescence emission; Fig. S16) substantially incremented after 2 h UVA irradiation and was more than twice when in contact with nanoMOF and AgNP@nanoMOF thin films than the control. These ROS interfere with the normal bacterial enzymatic activity and induce bacterial death [44]. Generation of ROS after UV excitation of the MIL-125(Ti) analogue was first elucidated by Dan-Hardi et al. [24] and thoroughly explained later for the particular case of its aminated version MIL-125(Ti)NH_2 [45]. Herein, after UV irradiation and photon absorption, charge separation takes place with i) generation of positive holes on the organic ligand (BDC-NH_2) and ii) photogenerated electrons trapped in the Ti^{4+} oxocluster, which leads to the formation of Ti^{3+}, a mechanism known as ligand-to-cluster-charge transfer. In this activated state, the Ti^{IV}/Ti^{III} photoactive redox centers promote reactions with the aqueous culture medium [46], leading to hydroxyl and peroxyl radicals that produce oxidative damage in the bacteria [47]. The inclusion of the AgNPs in the structure might enhance the electron transfer with the media and reduce the electron-hole recombination in the activated state, conducing both mechanisms to a higher inhibition of bacterial colonies [48]. Furthermore, the higher bactericidal activity of AgNP@nanoMOF might also be due to the direct contact of the bacteria with the AgNP, an extensively known antibacterial agent [40], and by its ion release (Ag^+), which is involved in an increase in the membrane permeability, loss of the proton motive force, de-energization of cells and efflux of phosphate, leakage of cellular content, and disruption of DNA replication [11].

Apart from the antifouling properties of an active coating, its bactericidal effect is also of great importance, as detachment of viable bacteria will lead to the continuous formation of biofilm. After 20 h of dark growth, AgNP@nanoMOF thin films were the ones that manifested the highest bacterial inhibition (less than ~10% of bacteria remained viable, in both the planktonic and the sessile state, Table S5). Even the AgNP@nanoMOF suspension in dark had greater bactericidal activity (Table S2), and this reduction can be explained by the lower possibilities of contact in between the bacterial cells and the nanoMOF or the composite when deposited in the thin film. As depicted, the bacterial viability is affected when the nanoMOF is in contact with the cell membrane: the AgNP@nanoMOF thin film has a lower surface area than that of its suspension, hence resulting in lower biocidal activity after 20 h. Upon 2 h UVA irradiation (after the 18 h dark growth), >99.99% and 99.9999% of the colonies were nonviable when in contact with the thin films of the nanoMOF and the AgNP@nanoMOF, respectively (Table S5). However, the "physical" mixture AgNP + nanoMOF exhibited a similar biocidal activity with and without irradiation. According to this, it could be said that the MIC against the *S. aureus* biofilm of the AgNP@nanoMOF composite thin film after irradiation (88 ppm) is in range with some commonly used antibiotics such as cefazolin (MIC = 128 ppm) [49] (see details on other relevant antibiotics in Table S8). For comparison purposes, bacterial viability of both planktonic and sessile *E. coli* bacteria in contact with nanoMOF and AgNP@nanoMOF thin films was also evaluated (Fig. S17). Even the biocidal activity against *E. coli* was slightly higher after UVA irradiation in both materials (Table S6), and cell viability reduction was slightly lower for the gram-negative bacteria (99.95% *vs.* 99.9999% bacterial inhibition, respectively).

Therefore, the compilation of the optical and bioactivity tests demonstrates the potential of the AgNP@nanoMOF composite for *S. aureus* biofilm treatment and that its antifouling and bactericidal properties are the result of a combined effect of the MOF intrinsic activity, the strong interactions of the bactericidal AgNPs with framework, and the photoactivity after irradiation (Scheme S6).

4.4. Chemical stability of the AgNP@nanoMOF thin film

When tested at biofilm-formation experimental conditions (37 °C), analysis of the culture medium in contact with the cover glasses coated with nanoMOF and the AgNP@nanoMOF thin films indicated that the coating is relatively strongly attached to the cover glasses, as no nanoMOF particles were detected in the media (see SI Fig. S20). The variation of the ξ-potential from −9 to −12 mV after 20 h might be a result of the interaction of the salts of the NB medium with the ions released after slow MOF degradation. Similarly, accelerated degradation tests (at 70 °C) revealed a final particle size of ~5 nm after 14 days, also associated with the protein of the NB medium (Fig. S22). This suggested that the degradation of the thin film took place by ion release instead of particle detachment, stressing the strong adhesion of the nanoMOF and AgNP@nanoMOF thin films to the substrate.

The MOF degradation was confirmed by the progressive release of the MOF constituents (Ti and ligand) to the medium. For comparison purposes, the theoretical amount of BDC-NH_2 corresponding to the Ti experimentally released was estimated (Fig. 5). Nevertheless, the experimental amount of BDC-NH_2 is double the calculated amount (12% *vs.* 6%) in terms of Ti release. This divergence could be explained by the presence of residual ligand within the MOF porosity and the outer surface composition, mainly composed of partially coordinated ligands, as previously reported by Vilela et al. [20]. In the case of AgNP@nanoMOF (Fig. 5D), the amount of released ligand is again higher than the expected amount from the measured Ti, observing here differences of 4-fold with the expected release (30% *vs.* 8%, respectively). The lower stability of the composite than that of the nanoMOF (20% *vs*. 12% degradation at 20 h, respectively) could be associated not only with the previously mentioned causes (remaining ligand and ligand at the outer surface) but also with defects generation during the impregnation-reduction process, which might weaken the MOF network (in agreement with the PXRD and N_2 sorption data).

Similarly, the Ag^+ was continuously released over time, following, however, a different profile with an initial induction time (no silver delivered within the first 4 h; Fig. 5B). This suggested the formation of strong interactions between the AgNPs and the nanoMOF, as previously depicted by the biocidal experiments when compared with the results obtained with the "physical" mixture AgNPs + nanoMOF. One could rationally expect the formation of specific interactions between the AgNPs and the amino groups of the BDC-NH_2 ligand, as seen in FTIR from the shift of the symmetric and asymmetric –NH_2 stretching (Fig. S7). Thus, previous nanoMOF degradation is needed for Ag delivery and only 3.5% of the total silver was released after 20 h, with, however, a controlled delivery over extended periods of time (5% after 14 days). Accelerated degradation of the AgNP@nanoMOF at 70 °C likewise revealed the relation between MOF degradation (Ti delivery) with the Ag released into the culture medium (Fig. S21), both following similar kinetics.

Overall, considering the low release of Ti and Ag under experimental conditions (2.5 and 3.5 wt%, respectively) and the fact that the BDC-NH_2 biocidal activity was previously excluded (see Section 4.1), the antifouling bactericidal combined effect of AgNP@nanoMOF might be not only a result of the composite dissolution but also a consequence of the stable association of AgNPs to the MOF. Furthermore, this biocidal effect is promoted by both UVA and visible irradiation. Thus, one could suggest an important role of silver on the ligand-to-cluster charge transfer, which is in agreement with the results of catalytic studies conducted with other noble metal NPs decorated with MIL-125(Ti) [50].

As previously reported studies did not consider biofilm treatment, comparison of the AgNP@nanoMOF thin film stability is not straightforward. As shown in Table S7, the amount of Ag released from the thin film into the NB after 24 h at 37 °C (3.5 wt %) has been compared with the amount of Ag released from other silver-based MOF suspensions. It can be seen that even the stability (referred as Ag wt%) is within the same range, and the delivered Ag amount is lower due to the lower Ag content within AgNP@nanoMOF (only 1.21 ppm of Ag). Furthermore, despite the lower Ag amount, the combination of AgNP, nanoMOF, and irradiation effects led to similar biocidal activity in the planktonic state (Fig. 2 and Table S7). Consequently, this highlights the potential use of the AgNP@nanoMOF composite as an antifouling biocidal coating for biofilm treatment for a long period.

5. Conclusion

AgNPs have been successfully incorporated within a porous photoactive Ti-nanoMOF by a simple two-step impregnation-reduction method. The resulting composite was drop-casted as thin films, exhibiting a remarkable antifouling and photobactericide effect against a strong *S. aureus* biofilm. These results pave the way for the potential use of AgNP@nanoMOF composite-coated surfaces for efficient antiadherent and bactericidal biofilm treatment on high-touch surface-related and nosocomial infections.

Acknowledgments

This work was partially supported by Raphuel project (ENE2016-79608-C2-1-R, MINECOAEI/FEDER, UE). PH acknowledges the Spanish Ramón y Cajal Programme (grant agreement no. 2014-16823) and the People Programme (Marie Curie Actions) of the European Union's Seventh Framework Programme (FP7/2007-2013; REA grant agreement no. 291803). AA-V and PH thank the financial support of Madrid Community (CAM PEJD-2016/IND-2828) and Iberdrola Foundation (2017 Research Grants in Energy and Environment).

Declaration of Competing Interest

The authors declare no conflict of interest.

Appendix A. Supplementary data

Supplementary data to this article can be found online at https://doi.org/10.1016/j.actbio.2019.08.011.

References

[1] K. Liu, L. Jiang, Bio-inspired self-cleaning surfaces, Annu. Rev. Mater. Res. 42 (2012) 231–263, https://doi.org/10.1146/annurev-matsci-070511-155046.
[2] M. Habash, G. Reid, Microbial biofilms: their development and significance for medical device-related infections, J. Clin. Pharmacol. 39 (1999) 887–898, https://doi.org/10.1177/00912709922008506.
[3] L. Townsley, E.A. Shank, Natural-product antibiotics: cues for modulating bacterial biofilm formation, Trends Microbiol. 25 (2017) 1016–1026, https://doi.org/10.1016/J.TIM.2017.06.003.
[4] F. Reffuveille, J. Josse, Q. Vallé, C. Mongaret, S.C. Gangloff, Staphylococcus aureus Biofilms and their Impact on the Medical Field, in: Rise Virulence Antibiot. Resist. Staphylococcus Aureus, InTech, 2017. doi:10.5772/66380.
[5] H.F. Chambers, The changing epidemiology of Staphylococcus aureus?, Emerg Infect. Dis. 7 (2001) 178–182, https://doi.org/10.3201/eid0702.700178.
[6] T.P. Levin, B. Suh, P. Axelrod, A.L. Truant, T. Fekete, Potential clindamycin resistance in clindamycin-susceptible, erythromycin-resistant Staphylococcus aureus: report of a clinical failure, Antimicrob. Agents Chemother. 49 (2005) 1222–1224, https://doi.org/10.1128/AAC.49.3.1222-1224.2005.
[7] C. Even, C. Marlière, J.-M. Ghigo, J.-M. Allain, A. Marcellan, E. Raspaud, Recent advances in studying single bacteria and biofilm mechanics, Adv. Colloid Interface Sci. 247 (2017) 573–588, https://doi.org/10.1016/J.CIS.2017.07.026.
[8] G. Férey, Hybrid porous solids: past, present, future, Chem. Soc. Rev. 37 (2008) 191–214, https://doi.org/10.1039/B618320B.

[9] H. Furukawa, K.E. Cordova, M. O'Keeffe, O.M. Yaghi, The chemistry and applications of metal-organic frameworks, Science 341 (2013) 1230444, https://doi.org/10.1126/science.1230444.
[10] Y. Liu, X. Xu, Q. Xia, G. Yuan, Q. He, Y. Cui, Multiple topological isomerism of three-connected networks in silver-based metal-organoboron frameworks, Chem. Commun. (Camb) 46 (2010) 2608–2610, https://doi.org/10.1039/b923365b.
[11] G. Wyszogrodzka, B. Marszałek, B. Gil, P. Dorożyński, Metal-organic frameworks: mechanisms of antibacterial action and potential applications, Drug Discov. Today 21 (2016) 1009–1018, https://doi.org/10.1016/j.drudis.2016.04.009.
[12] S. Aguado, J. Quirós, J. Canivet, D. Farrusseng, K. Boltes, R. Rosal, Antimicrobial activity of cobalt imidazolate metal–organic frameworks, Chemosphere. 113 (2014) 188–192, https://doi.org/10.1016/j.chemosphere.2014.05.029.
[13] A.R. Abbasi, K. Akhbari, A. Morsali, Dense coating of surface mounted CuBTC metal-organic framework nanostructures on silk fibers, prepared by layer-by-layer method under ultrasound irradiation with antibacterial activity, Ultrason. Sonochem. 19 (2012) 846–852, https://doi.org/10.1016/j.ultsonch.2011.11.016.
[14] W. Miao, J. Wang, J. Liu, Y. Zhang, Self-cleaning and antibacterial zeolitic imidazolate framework coatings, Adv. Mater. Interfaces 1800167 (2018) 1–9, https://doi.org/10.1002/admi.201800167.
[15] M.P. Arpa Sancet, M. Hanke, Z. Wang, S. Bauer, C. Azucena, H.K. Arslan, M. Heinle, H. Gliemann, C. Wöll, A. Rosenhahn, Surface anchored metal-organic frameworks as stimulus responsive antifouling coatings, Biointerphases 8 (2013) 1–35, https://doi.org/10.1186/1559-4106-8-29.
[16] B.H. Neufeld, M.J. Neufeld, A. Lutzke, S.M. Schweickart, M.M. Reynolds, Metal-organic framework material inhibits biofilm formation of *Pseudomonas aeruginosa*, Adv. Funct. Mater. 27 (2017) 1702255, https://doi.org/10.1002/adfm.201702255.
[17] A. Zirehpour, A. Rahimpour, A. Arabi, M.S. Gh, M. Soroush, Mitigation of thin film composite membrane biofouling via immobilizing nano-sized biocidal reservoirs in the membrane active layer mitigation of thin film composite membrane biofouling via immobilizing nano-sized biocidal reservoirs in the membrane active, Environ. Sci. Technol. 51 (2017) 5511–5522, https://doi.org/10.1021/acs.est.7b00782.
[18] E.E. Mann, K.C. Rice, B.R. Boles, J.L. Endres, D. Ranjit, L. Chandramohan, L.H. Tsang, M.S. Smeltzer, A.R. Horswill, K.W. Bayles, Modulation of eDNA release and degradation affects Staphylococcus aureus biofilm maturation, PLoS One 4 (2009), https://doi.org/10.1371/journal.pone.0005822 e5822.
[19] K. Apel, H. Hirt, Reactive oxygen species: metabolism, oxidative stress, and signal transduction, Annu. Rev. Plant Biol. 55 (2004) 373–399, https://doi.org/10.1146/annurev.arplant.55.031903.141701.
[20] S. Vilela, P. Salcedo-Abraira, I. Colinet, F. Salles, M. de Koning, M. Joosen, C. Serre, P. Horcajada, Nanometric MIL-125-NH2 metal-organic framework as a potential nerve agent antidote carrier, Nanomaterials 7 (2017) 321, https://doi.org/10.3390/nano7100321.
[21] G. Ximing, G. Bin, W. Yuanlin, G. Shuanghong, Preparation of spherical metal–organic frameworks encapsulating Ag nanoparticles and study on its antibacterial activity, Mater. Sci. Eng. C 80 (2017) 698–707, https://doi.org/10.1016/j.msec.2017.07.027.
[22] Y.-F. Guo, W.-J. Fang, J.-R. Fu, Y. Wu, J. Zheng, G.-Q. Gao, C. Chen, R.-W. Yan, S.-G. Huang, C.-C. Wang, Facile synthesis of Ag@ZIF-8 core-shell heterostructure nanowires for improved antibacterial activities, Appl. Surf. Sci. 435 (2018) 149–155, https://doi.org/10.1016/J.APSUSC.2017.11.096.
[23] S.R. Thakare, S.M. Ramteke, Fast and regenerative photocatalyst material for the disinfection of E. coli from water: silver nano particle anchor on MOF-5, Catal. Commun. 102 (2017) 21–25, https://doi.org/10.1016/j.catcom.2017.06.008.
[24] M. Dan-hardi, C. Serre, T. Frot, L. Rozes, G. Maurin, C. Sanchez, G. Férey, A new photoactive crystalline highly porous titanium (IV) dicarboxylate, J. Am. Chem. Soc. Commun. 131 (2009) 10857–10859, https://doi.org/10.1021/ja903726m.
[25] R.M. Abdelhameed, O.M.H.M. Kamel, A. Amr, J. Rocha, A.M.S. Silva, Antimosquito activity of a titanium-organic framework supported on fabrics, ACS Appl. Mater. Interfaces 9 (2017) 22112–22120, https://doi.org/10.1021/acsami.7b03164.
[26] K. Meyer, S. Bashir, J. Llorca, H. Idriss, M. Ranocchiari, J.A. van Bokhoven, Photocatalyzed hydrogen evolution from water by a composite catalyst of NH2-MIL-125(Ti) and surface nickel(II) species, Chem. Eur. J. 22 (2016) 13894–13899, https://doi.org/10.1002/chem.201601988.
[27] S.-N. Kim, J. Kim, H.-Y. Kim, H.-Y. Cho, W.-S. Ahn, Adsorption/catalytic properties of MIL-125 and NH 2-MIL-125, Catal. Today 204 (2013) 85–93, https://doi.org/10.1016/j.cattod.2012.08.014.
[28] Material Safety Data Sheet Titanium(IV) oxide, Acros Org. (n.d.). https://www.ch.ntu.edu.tw/~genchem99/msds/exp27/TiO2.pdf. (accessed July 16, 2018).
[29] C. Tamames-Tabar, D. Cunha, E. Imbuluzqueta, F. Ragon, C. Serre, M.J. Blanco-Prieto, P. Horcajada, Cytotoxicity of nanoscaled metal–organic frameworks, J. Mater. Chem. B 2 (2014) 262–271, https://doi.org/10.1039/C3TB20832J.
[30] X.H. Liu, J.G. Ma, Z. Niu, G.M. Yang, P. Cheng, An efficient nanoscale heterogeneous catalyst for the capture and conversion of carbon dioxide at ambient pressure, Angew. Chem. Int. Ed. 54 (2015) 988–991, https://doi.org/10.1002/anie.201409103.
[31] N.-N. Zhu, X.-H. Liu, T. Li, J.-G. Ma, P. Cheng, G.-M. Yang, Composite system of Ag nanoparticles and metal-organic frameworks for the capture and conversion of carbon dioxide under mild conditions, Inorg. Chem. 56 (2017) 3414–3420, https://doi.org/10.1021/acs.inorgchem.6b02855.
[32] M. Gao, L. Sun, Z. Wang, Y. Zhao, Controlled synthesis of Ag nanoparticles with different morphologies and their antibacterial properties, Mater. Sci. Eng. C 33 (2013) 397–404, https://doi.org/10.1016/j.msec.2012.09.005.
[33] B. Jalvo, M. Faraldos, A. Bahamonde, R. Rosal, Antimicrobial and antibiofilm efficacy of self-cleaning surfaces functionalized by TiO_2 photocatalytic nanoparticles against Staphylococcus aureus and Pseudomonas putida, J. Hazard. Mater. 340 (2017) 160–170, https://doi.org/10.1016/j.jhazmat.2017.07.005.
[34] NASA Langley Research Center (LaRC) POWER, NASA Prediction of Worldwide Energy Resources, (n.d.). https://power.larc.nasa.gov/ (accessed July 6, 2019).
[35] G. Amariei, V. Kokol, K. Boltes, P. Letón, R. Rosal, Incorporation of antimicrobial peptides on electrospun nanofibres for biomedical applications, RSC Adv. 8 (2018) 28013–28023, https://doi.org/10.1039/C8RA03861A.
[36] J.M. Clarke, M.R. Gillings, N. Altavilla, A.J. Beattie, Potential problems with fluorescein diacetate assays of cell viability when testing natural products for antimicrobial activity, J. Microbiol. Methods 46 (2001) 261–267, https://doi.org/10.1016/S0167-7012(01)00285-8.
[37] G. Amariei, V. Kokol, V. Vivod, K. Boltes, P. Letón, R. Rosal, Biocompatible antimicrobial electrospun nanofibers functionalized with ε-poly-l-lysine, Int. J. Pharm. 553 (2018) 141–148, https://doi.org/10.1016/J.IJPHARM.2018.10.037.
[38] M.A. Nasalevich, R. Becker, E.V. Ramos-Fernandez, S. Castellanos, S.L. Veber, M. V. Fedin, F. Kapteijn, J.N.H. Reek, J.I. van der Vlugt, J. Gascon, Co@NH_2-MIL-125 (Ti): cobaloxime-derived metal–organic framework-based composite for light-driven H_2 production, Energy Environ. Sci. 8 (2015) 364–375, https://doi.org/10.1039/C4EE02853H.
[39] N.P. Xekoukoulotakis, N. Xinidis, M. Chroni, D. Venieri, E. Hapeshi, D. Fatta-Kassinos, UV-A/TiO_2 photocatalytic decomposition of erythromycin in water: factors affecting mineralization and antibiotic activity, Catal. Today 151 (2010) 29–33, https://doi.org/10.1016/J.CATTOD.2010.01.040.
[40] S. Chernousova, M. Epple, Silver as antibacterial agent: Ion, nanoparticle, and metal, Angew. Chem. Int. Ed. 52 (2013) 1636–1653, https://doi.org/10.1002/anie.201205923.
[41] T.J. Silhavy, D. Kahne, S. Walker, The bacterial cell envelope, Cold Spring Harb. Perspect. Biol. 2 (2010), https://doi.org/10.1101/cshperspect.a000414 a000414.
[42] C. Bordi, S. de Bentzmann, Hacking into bacterial biofilms: a new therapeutic challenge, Ann. Intensive Care. 1 (2011) 19, https://doi.org/10.1186/2110-5820-1-19.
[43] H.-J. Park, J.Y. Kim, J. Kim, J.-H. Lee, J.-S. Hahn, M.B. Gu, J. Yoon, Silver-ion-mediated reactive oxygen species generation affecting bactericidal activity, Water Res. 43 (2009) 1027–1032, https://doi.org/10.1016/J.WATRES.2008.12.002.
[44] H. Schug, C.W. Isaacson, L. Sigg, A.A. Ammann, K. Schirmer, Effect of TiO_2 nanoparticles and UV radiation on extracellular enzyme activity of intact heterotrophic biofilms, Environ. Sci. Technol. 48 (2014) 11620–11628, https://doi.org/10.1021/es502620e.
[45] M. de Miguel, F. Ragon, T. Devic, C. Serre, P. Horcajada, H. García, Evidence of photoinduced charge separation in the metal-organic framework MIL-125(Ti)-NH_2, ChemPhysChem 13 (2012) 3651–3654, https://doi.org/10.1002/cphc.201200411.
[46] M.B. Chambers, X. Wang, L. Ellezam, O. Ersen, M. Fontecave, C. Sanchez, L. Rozes, C. Mellot-Draznieks, Maximizing the photocatalytic activity of metal-organic frameworks with aminated-functionalized linkers: substoichiometric effects in MIL-125-NH_2, J. Am. Chem. Soc. 139 (2017) 8222–8228, https://doi.org/10.1021/jacs.7b02186.
[47] Y. Cai, M. Strømme, K. Welch, Disinfection kinetics and contribution of reactive oxygen species when eliminating Bacteria with TiO_2 induced photocatalysis, J. Biomater. Nanobiotechnol. 05 (2014) 200–209, https://doi.org/10.4236/jbnb.2014.53024.
[48] Z. Li, J. Xiao, H. Jiang, Encapsulating a Co (II) molecular photocatalyst in metal-organic framework for visible-light driven H 2 production: boosting catalytic efficiency via spatial charge separation, ACS Catal. 6 (2016) 5359–5365, https://doi.org/10.1021/acscatal.6b01293.
[49] A. Majidpour, S. Fathizadeh, M. Afshar, M. Rahbar, M. Boustanshenas, M. Heidarzadeh, L. Arbabi, S.S. Moghadam, Dose-dependent effects of common antibiotics used to treat staphylococcus aureus on biofilm formation, Iran. J. Pathol. 12 (2017) 362–370 (accessed June 11, 2019).
[50] L. Shen, M. Luo, L. Huang, P. Feng, L. Wu, A clean and general strategy to decorate a titanium metal-organic framework with noble-metal nanoparticles for versatile photocatalytic applications, Inorg. Chem. 54 (2015) 1191–1193, https://doi.org/10.1021/ic502609a.

Bibliography

(1) Arenas-Vivo, A.; Amariei, G.; Aguado, S.; Rosal, R.; Horcajada, P. An Ag-Loaded Photoactive Nano-Metal Organic Framework as a Promising Biofilm Treatment. *Acta Biomater.* **2019**, *97*, 490–500. https://doi.org/10.1016/j.actbio.2019.08.011.

(2) Sealy, C. Composite could help stop spread of infectious diseases https://www.materialstoday.com/biomaterials/news/composite-could-stop-spread-of-infectious-diseases/#.XacXhQyfDNs.linkedin (accessed Apr 11, 2021).

(3) AEBIN. Best publication awards 2020 to young members of the AEBIN: Best PhD publication award https://www.aebin.es/news/ (accessed Apr 11, 2021).

(4) Vilela, S.; Salcedo-Abraira, P.; Colinet, I.; Salles, F.; de Koning, M.; Joosen, M.; Serre, C.; Horcajada, P. Nanometric MIL-125-NH2 Metal–Organic Framework as a Potential Nerve Agent Antidote Carrier. *Nanomaterials* **2017**, *7* (10), 321. https://doi.org/10.3390/nano7100321.

(5) Slenters, T. V.; Sagué, J. L.; Brunetto, P. S.; Zuber, S.; Fleury, A.; Mirolo, L.; Robin, A. Y.; Meuwly, M.; Gordon, O.; Landmann, R.; et al. Of Chains and Rings: Synthetic Strategies and Theoretical Investigations for Tuning the Structure of Silver Coordination Compounds and Their Applications. *Materials (Basel).* **2010**, *3* (5), 3407–3429. https://doi.org/10.3390/ma3053407.

(6) Brunetto, P. S.; Slenters, T. V.; Fromm, K. M. In Vitro Biocompatibility of New Silver(I) Coordination Compound Coated-Surfaces for Dental Implant Applications. *Materials (Basel).* **2010**, *4* (2), 355–367. https://doi.org/10.3390/ma4020355.

(7) Wang, K.; Yin, Y.; Li, C.; Geng, Z.; Wang, Z. Facile Synthesis of Zinc(II)-

Carboxylate Coordination Polymer Particles and Their Luminescent, Biocompatible and Antibacterial Properties. *CrystEngComm* **2011**, *13* (20), 6231–6236. https://doi.org/10.1039/c1ce05705g.

(8) Tăbăcaru, A.; Pettinari, C.; Marchetti, F.; Di Nicola, C.; Domasevitch, K. V.; Galli, S.; Masciocchi, N.; Scuri, S.; Grappasonni, I.; Cocchioni, M. Antibacterial Action of 4,4′-Bipyrazolyl-Based Silver(I) Coordination Polymers Embedded in PE Disks. *Inorg. Chem.* **2012**, *51* (18), 9775–9788. https://doi.org/10.1021/ic3011635.

(9) Arenas-Vivo, A.; Horcajada, P. Antimicrobial Metal Organic Frameworks. In *Metal Organic Frameworks*; Mittal, D. V., Ed.; Central West Publishing, 2019; pp 1–34.

(10) Dan-Hardi, M.; Serre, C.; Frot, T.; Rozes, L.; Maurin, G.; Sanchez, C.; Férey, G. A New Photoactive Highly Porous Titanium (IV) Dicarboxylate. *J. Am. Chem. Soc.* **2009**, *131*, 10857–10859. https://doi.org/10.1021/ja903726m.

(11) Abdelhameed, R. M.; Simões, M. M. Q.; Silva, A. M. S.; Rocha, J. Enhanced Photocatalytic Activity of MIL-125 by Post-Synthetic Modification with Cr ^{III} and Ag Nanoparticles. *Chem. - A Eur. J.* **2015**, *21* (31), 11072–11081. https://doi.org/10.1002/chem.201500808.

(12) Kim, S.-N.; Kim, J.; Kim, H.-Y.; Cho, H.-Y.; Ahn, W.-S. Adsorption/Catalytic Properties of MIL-125 and NH 2 -MIL-125. *Catal. Today* **2013**, *204*, 85–93. https://doi.org/10.1016/j.cattod.2012.08.014.

(13) Mahmoodi, N. M.; Taghizadeh, A.; Taghizadeh, M.; Abdi, J. In Situ Deposition of Ag/AgCl on the Surface of Magnetic Metal-Organic Framework Nanocomposite and Its Application for the Visible-Light Photocatalytic Degradation of Rhodamine Dye. *J. Hazard. Mater.* **2019**, *378*, 120741. https://doi.org/10.1016/j.jhazmat.2019.06.018.

(14) Emam, H. E.; Ahmed, H. B.; Gomaa, E.; Helal, M. H.; Abdelhameed, R. M. Doping of Silver Vanadate and Silver Tungstate Nanoparticles for Enhancement the Photocatalytic Activity of MIL-125-NH2 in Dye Degradation. *J. Photochem. Photobiol. A Chem.* **2019**, *383*, 111986–111998. https://doi.org/10.1016/j.jphotochem.2019.111986.

(15) Fu, Y.; Sun, D.; Chen, Y.; Huang, R.; Ding, Z.; Fu, X.; Li, Z. An Amine-Functionalized Titanium Metal-Organic Framework Photocatalyst with Visible-Light-Induced Activity for CO 2 Reduction. *Angew. Chemie - Int. Ed.* **2012**, *51* (14), 3364–3367. https://doi.org/10.1002/anie.201108357.

(16) Kampouri, S.; Nguyen, T. N.; Ireland, C.; Valizadeh, B.; Ebrahim, F.; Capano, G.; Ongari, D.; Mace, M.; Guijarro, N.; Sivula, K.; et al.

Photocatalytic Hydrogen Generation from a Visible-Light Responsive Metal-Organic Framework System: The Impact of Nickel Phosphide Nanoparticles. *J. Mater. Chem. A* **2018**, 2476–2481. https://doi.org/10.1039/C7TA10225A.

(17) MATERIAL SAFETY DATA SHEET Titanium(IV) oxide https://www.ch.ntu.edu.tw/~genchem99/msds/exp27/TiO2.pdf. (accessed Jul 16, 2018).

(18) Tamames-Tabar, C.; Cunha, D.; Imbuluzqueta, E.; Ragon, F.; Serre, C.; Blanco-Prieto, M. J.; Horcajada, P. Cytotoxicity of Nanoscaled Metal–Organic Frameworks. *J. Mater. Chem. B* **2014**, *2* (3), 262–271. https://doi.org/10.1039/C3TB20832J.

(19) Rojas, S.; Guillou, N.; Horcajada, P. Ti-Based NanoMOF as an Efficient Oral Therapeutic Agent. *ACS Appl. Mater. Interfaces* **2019**, *11* (25), 22188–22193. https://doi.org/10.1021/acsami.9b06472.

(20) Wyszogrodzka, G.; Marszałek, B.; Gil, B.; Dorożyński, P. Metal-Organic Frameworks: Mechanisms of Antibacterial Action and Potential Applications. *Drug Discov. Today* **2016**, *21* (6), 1009–1018. https://doi.org/10.1016/j.drudis.2016.04.009.

Chapter 4

SiB: Photocatalytic AgNC@MIL-125-NH_2

"I am not in a competition with anyone but myself.
My goal is to improve myself continuously."

Bill Gates

4.1. Preamble

Even in the previous chapter a successful association of AgNPs to MIL-125-NH_2 by impregnation-reduction protocol was achieved, material characterization prompted other questions and concerns: i) particle size was not enough monodispersed, ii) chemical reduction resulted in particles larger that pore size, and in consequence iii) bigger AgNPs allocation resulted in framework defects or even migration to the surface. Therefore, further work was required to improve the SiB association of silver to MIL-125-NH_2.

This chapter explores the photosynthesis of silver nanoclusters (AgNC) stabilized by MOFs. Previous works prepared stable solutions of AgNCs in organic solvents by their interaction with organic molecules such as cyclohexylamine and polymers with pendant -NH_2.[1,2] The creative selection of MIL-125-NH_2 as scaffold for AgNC benefits of the presence of the liable -NH_2 of its organic ligand and the MOF photoactive properties. In consequence, the ultrafast photoreduction protocol here presented leads to the surfactant free photoactive composite AgNC@MIL-125-NH_2, suitable for heterogeneous catalysis.

Considering water scarcity, wastewater treatment has become an inevitable water resource. Nevertheless, the continuously growing chemical product market (12000 new chemicals everyday) raise the concern on the presence of emerging organic contaminants (EOCs) in water, that conventional wastewater treatment plants do not effectively remove.[3] Therefore, more advanced chemical oxidation processes are required and whence, opens the door to the development of new heterogeneous photocatalysts. In consequence, the catalytic activity of the AgNC@MIL-125-NH_2 composite was analyzed for the photocatalytic degradation of EOCs under visible light, with the first example of continuous flow reactors, extending the knowledge of MOF for wastewater treatment. For better understanding of the experimental results, Monte Carlo simulations were carried out to elucidate the interactions of the AgNCs with the MIL-125-NH_2 and with the contaminant molecules. In this application MIL-125-NH_2 played both a passive role, as a scaffold improving stability of catalytic AgNC, and an active role in the photocatalytic degradation of contaminants.

This work was reported in the original publication: "Ultrafast reproducible synthesis of an Agnanocluster@MOF composite and its superior visible-photocatalytic activity in batch and in continuous flow", A. Arenas-Vivo, S. Rojas, I. Ocaña, A. Torres, M. Liras, F. Salles, D. Arenas-Esteban, S. Bals, D. Ávila, P. Horcajada, Journal of Materials Chemistry A, **2021**, *Accepted Manuscript* (Q1, IF: 11.301), repeated here with the journal format.[4] In addition, the steps followed towards the optimization of the ultrafast photosynthesis of AgNC@MIL-125-NH_2 composite is elaborated in APPENDIX IV IV.I SiB association of AgNCs *via* photoreduction: protocol optimization, while the supporting information of the article as published is included in APPENDIX V

.

The singularity of this publication arises from:

- The proposal of a new ultrafast (15 seconds) photoreduction protocol for the synthesis of AgNCs supported on the photoactive titanium carboxylate MOF MIL-125-NH_2 without the need of surfactants.
- The corroboration by electron tomography of the distribution of the AgNCs within MIL-125-NH_2 structure (porosity, defects), compared to previous state-of-the-art protocols that led to surface anchored AgNC.
- The strong interaction between AgNC and MOF, giving enhanced optoelectronic properties to the composite.
- The potential use of AgNC@MIL-125-NH_2 was tested in real applications:
    - the photodegradation of the EOCs methylene blue (MB dye) and sulfamethazine (SMT-antibiotic) in water treatment using tap water (*vs.* reported MilliQ or distilled water studies)

    - the catalytic hydrogenation of *p*-nitroaniline (4-NA) to *p*-phenylenediamine (PPD), reaction with industrial interest.
- The photodegradation of SMT was assessed using a home-made MOF-based photoreactor under continuous flow conditions found in real water treatment plants. No studies of the photodegradation of contaminants under continuous flow have been reported yet.
- The potential degradation of the MOF was deeply investigated not only evaluating its structural robustness (X-ray powder diffraction, XRPD) but also its chemical integrity, monitoring the amount of leached ligand (high performance liquid chromatography, HPLC). Normally, no leaching of metals or ligand is assessed in water remediation or in catalytic studies using MOFs.

Despite the active contribution of all the authors to this article, we consider important to clearly state the contribution of the PhD candidate. Conceptualization of this work involved once more Dr. Patricia Horcajada and AAV, but also Dr. Sara Rojas and Dr. Marta Liras. Experimental works were carried out at IMDEA Energy, using APMU lab installations. Optimization of the photoreduction synthesis was done by AAV and Iván Ocaña (MSc. Student supervised by AAV). Dr. David Ávila contributed again with characterization *via* TEM of the composite. In addition, Dr. Sara Bals and Dr. Daniel Arenas performed TEM tomography to identify the location of AgNCs. Photochemical degradation of MB was completed by AAV and Ivan Ocaña and photochemical degradation of SMT by Dr. S. Rojas and Ana Torres (MSc. Student). Catalytic hydrogenation of (4-NA was performed by AAV. Dr. Fabrice Salles was in charge of Monte Carlo simulations and calculations. Result analysis and discussion and original draft preparation was done by AAV and Dr. S. Rojas and review and editing of the publication was done by Dr. P. Horcajada and Dr. M. Liras, as well as all previously mentioned coauthors.

4.2. Ultrafast reproducible synthesis of an Agnanocluster@MOF composite and its superior visible-photocatalytic activity in batch and in continuous flow

Ultrafast reproducible synthesis of an Agnanocluster@MOF composite and its superior visible-photocatalytic activity in batch and in continuous flow

Ana Arenas-Vivo,[a] Sara Rojas,[a] Iván Ocaña,[a] Ana Torres,[a] Marta Liras,[b,*] Fabrice Salles,[c] Daniel Arenas-Esteban,[d] Sara Bals,[d] David Ávila,[e] Patricia Horcajada[a,*]

[°]*Advanced Porous Materials Unit (APMU), IMDEA Energy Institute, Avda. Ramón de la Sagra 3, E-28935 Móstoles, Madrid, Spain*

[b] *Photoactivated Process Unit, IMDEA Energy. Av. Ramón de la Sagra 3, 28935 Móstoles-Madrid, Spain.*

[c] *ICGM, Univ. Montpellier, CNRS, ENSCM, Montpellier, France.*

[d] *EMAT and NANOlab Center of Excellence, Univ. of Antwerp, Groenenborgerlaan 171, Antwerp 2020, Belgium.*

[e] *Department of Inorganic Chemistry, Chemical Sciences Faculty, Complutense University of Madrid, 28040 Madrid, Spain.*

* *Corresponding author. E-mail address:* patricia.horcajada@imdea.org, marta.liras@imdea.org

Journal of Materials Chemistry A, 2021, *Accepted Manuscript* (Q1, IF: 11.301)

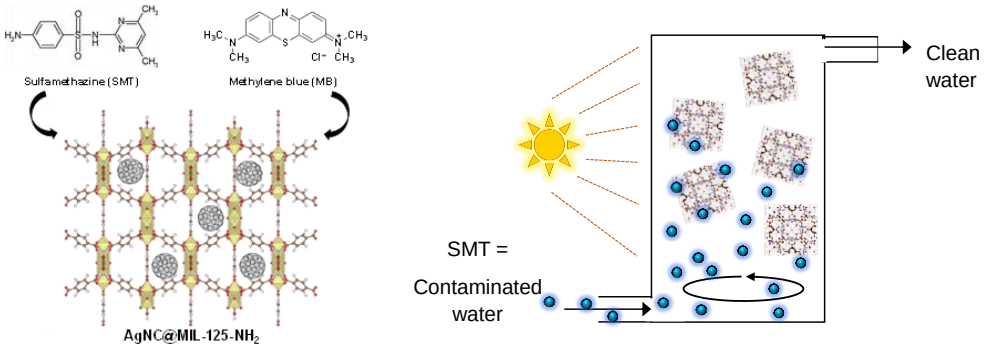

Journal of Materials Chemistry A

ROYAL SOCIETY OF CHEMISTRY

PAPER

Ultrafast reproducible synthesis of a Ag-nanocluster@MOF composite and its superior visible-photocatalytic activity in batch and in continuous flow†

Cite this: DOI: 10.1039/d1ta02251b

Ana Arenas-Vivo, [a] Sara Rojas, [a] Iván Ocaña,[a] Ana Torres,[a] Marta Liras, *[b] Fabrice Salles, [c] Daniel Arenas-Esteban,[d] Sara Bals, [d] David Ávila [e] and Patricia Horcajada *[a]

The (photo)catalytic properties of metal–organic frameworks (MOFs) can be enhanced by post-synthetic inclusion of metallic species in their porosity. Due to their extraordinarily high surface area and well defined porous structure, MOFs can be used for the stabilization of metal nanoparticles with adjustable size within their porosity. Originally, we present here an optimized ultrafast photoreduction protocol for the *in situ* synthesis of tiny and monodisperse silver nanoclusters (AgNCs) homogeneously supported on a photoactive porous titanium carboxylate MIL-125-NH_2 MOF. The strong metal–framework interaction between $-NH_2$ and Ag atoms influences the AgNC growth, leading to the surfactant-free efficient catalyst AgNC@MIL-125-NH_2 with improved visible light absorption. The potential use of AgNC@MIL-125-NH_2 was further tested in challenging applications: (i) the photodegradation of the emerging organic contaminants (EOCs) methylene blue (MB-dye) and sulfamethazine (SMT-antibiotic) in water treatment, and (ii) the catalytic hydrogenation of *p*-nitroaniline (4-NA) to *p*-phenylenediamine (PPD) with industrial interest. It is noteworthy that compared with the pristine MIL-125-NH_2, the composite presents an improved catalytic activity and stability, being able to photodegrade 92% of MB in 60 min and 96% of SMT in 30 min, and transform 100% of 4-NA to PPD in 30 min. Aside from these very good results, this study describes for the first time the use of a MOF in a visible light continuous flow reactor for wastewater treatment. With only 10 mg of AgNC@MIL-125-NH_2, high SMT removal efficiency over 70% is maintained after >2 h under water flow conditions found in real wastewater treatment plants, signaling a future real application of MOFs in water remediation.

Received 17th March 2021
Accepted 20th June 2021

DOI: 10.1039/d1ta02251b

rsc.li/materials-a

Introduction

In recent years, water pollution has become a cause of major concern due to novel and dangerous anthropogenic pollutants.[1] Particularly, hundreds of emerging organic contaminants (EOCs) are found to contaminate water resources, including a wide array of different compounds: pharmaceuticals and personal care products (PPCPs), dyes, pesticides, veterinary products, industrial products, and engineered nanomaterials.[2] EOCs enter the environment from a large variety of sources and pathways (*e.g.*, wastewater treatment plants (WWTPs), hospital effluents, livestock activities, and industrial waste),[3] leading to concentrations in surface waters (even in tap drinking water) capable of causing detrimental effects on living organisms (from ng L^{-1} to μg L^{-1}).[4,5] It is therefore clear that currently used technologies are not equipped to remove them and more effective methods need to be developed.

Among the new processes to eliminate EOCs from water (*i.e.*, ozonization,[6] chlorination,[7] sonodegradation,[8] biodegradation,[9] catalysis,[10] and activated carbon treatment[11]), photocatalysis shows great potential since it could be performed with sunlight illumination under ambient conditions. Metal oxide and chalcogenide semiconductors (*e.g.*, TiO_2, ZnO, Fe_2O_3, CdS, GaP, and

[a]*Advanced Porous Materials Unit, IMDEA Energy, Av. Ramón de la Sagra 3, 28935 Móstoles-Madrid, Spain. E-mail: patricia.horcajada@imdea.org*

[b]*Photoactivated Process Unit, IMDEA Energy, Av. Ramón de la Sagra 3, 28935 Móstoles-Madrid, Spain. E-mail: marta.liras@imdea.org*

[c]*ICGM, Univ. Montpellier, CNRS, ENSCM, Montpellier, France*

[d]*EMAT and NANOlab Center of Excellence, Univ. of Antwerp, Groenenborgerlaan 171, Antwerp 2020, Belgium*

[e]*Department of Inorganic Chemistry, Chemical Sciences Faculty, Complutense University of Madrid, 28040 Madrid, Spain*

† Electronic supplementary information (ESI) available: Details of experimental procedures, characterization (XRPD, N_2 sorption, TGA, FTIR, ICP, TEM, HAADF-STEM, tomography reconstruction, EDX, and DR), HPLC conditions, photocatalytic degradation and catalytic hydrogenation experiments, and simulation studies. See DOI: 10.1039/d1ta02251b

Chapter 5

BaS: Towards microwave-assisted solvothermal synthesis of MNP@MOFs

"It is really inviting to explore microwave irradiation as alternative energy input into chemical reactions in the hope of discovering new products."

Rajender S. Varma, pioneer of microwave-assisted chemistry

5.1. Preamble

The formation of MNP@MOF composites following the BaS method entails the nucleation and growth of the framework surrounding the MNP, that acts as a seed for the growth of the composite. Among other synthetic routes, within AMPU is considered that microwave (MW) heating is a promising tool for the attainment of controlled MNP@MOF.[1,2] Firstly, the inverted temperature gradient inside-out, compared to traditional conductive heating, as reaction mixture absorb MW irradiation instead of being heated from outside the vessel by convection current, leads to faster and scalable (even in continue) synthesis procedures. In addition, selective heating of the different chemical compounds involved in the reaction (MNPs, organic ligand, metallic inorganic salt and solvent) enables crystal phase and shape control.[2]

These advantages are directly related to the interaction of the different molecules with the alternating electric field of the microwaves. Under an applied electric field, molecules and ions tend to orientate in the applied direction. This interaction is defined by the dielectric constant (ε', ability to store energy through polarization) and the dielectric loss (ε'', capacity to transform to heat the stored energy), that depends on the frequency of the microwave irradiation and the temperature. In general, the higher the dielectric loss, the greater their ability to heat. For instance, well-known solvents used in MOF synthesis as water, ethanol and DMF exhibit at RT (25 ± 1 °C) and microwave frequency of 5.8 GHz the dielectric loss of 21, 10 and 4 respectively, directly affecting to the synthesis direct in core heating.[3]

Due to the acknowledged polarizability of MNPs (also called as SPR), it is expected for MNPs to have a strong resonance under MW electromagnetic frequency. Therefore, they will become hot spots in the MOF synthesis liqueur when exposed to MW heating. Intuitively, this seems to be a favorable situation for the BaS synthesis of MNP@MOF composites, as the heating energy of the MNP might help to overcome the activation energy for MOF synthesis becoming preferential nucleation points in the reaction media and facilitating the *in situ* formation of the core@shell composite. This beneficial mechanism is highly dependent on the MNP size, as increasing diameters have higher radiating scattering loses in the form of heat.[4,5]

Given the complexity of the BaS strategy, to better address the synthesis of MNP@MOFs, primarily this thesis chapter focused on the solvothermal MW-assisted synthesis of solely the MOF. Among the great diversity of organic building units, the linear amino terephthalic acid ($H_2BDC\text{-}NH_2$) was selected as ligand, as it leads to highly porous structures and its $\text{-}NH_2$ enables electrochemical interactions with MNPs (as seen in Chapter 4, section 4.2 Ultrafast reproducible synthesis of an Agnanocluster@MOF composite and its superior visible-photocatalytic activity in batch and in continuous flow). The earth abundant non-toxic iron was chosen as inorganic building unit, as in conjunction with $H_2BDC\text{-}NH_2$ can promote the polymorphic series of redox active terephthalates MIL-53,[6] MIL-68,[7] MIL-88B [8] and MIL-101.[9] MIL-53 and MIL-68 are two polymorphs based on iron(III) octahedra chains. While MIL-53 is a flexible network, with 1D diamond shaped channels, MIL-68 presents a rigid orthorhombic structure ($S_{BET} \sim 670\ m^2 \cdot g^{-1}$). The other polymorph pair, MIL-88B and MIL-101, have a different inorganic unit: iron(III) octahedra trimers. Although MIL-53 is able to exhibit a variation of volume of 40%, depending on guest molecules, temperature and pressure; astonishingly the 3D hexagonal network of MIL-88B can reversibly modify its size with a volume variation up to 120%. On the other hand, MIL-101, a rigid 3D cubic MTN-zeotype structure, outstands for its exceptional mesoporosity ($S_{BET} \sim 2500\ m^2 \cdot g^{-1}$).

Previous studies carried by Laybourn *et al.*[10] determined in 20 °C water the dielectric parameters of metal (III) salts (*e.g.*: $FeCl_3$ ε''=42) and terephthalic acid (ε''=0.02) suggesting the preferential heating of the inorganic building unit. Expanding the knowledge, in this thesis has been carried out a systematic study to analyze how modest variations of the MW-assisted method (*i.e.*: temperature, reaction time, concentration, reaction media), could lead to vast different synthetic results such as different crystallographic phases, crystal sizes and reaction yields.

The originality of this work comes from:

- The focus on the influence of the experimental parameters on the on the synthesis of iron(III) aminoterephthalate (Fe-BDC-NH_2) MOFs, with 46 individual reactions carried out.
- The representation of the results obtained by means of crystallization diagrams, that enable the determination of tendencies in the variables.
- The attention on the determination of space time yields (STY), vital for considering industrial scaling up.
- The attainment for the first time of MIL-53-NH_2 under MW assisted hydrothermal conditions.

Main results were presented in the original publication "Phase selective microwave assisted synthesis of iron(III) aminoterephthalate MOFs", A. Arenas-Vivo, D. Ávila, P. Horcajada; Materials, **2020,** *13*, 1469 (Q2, IF:3.057, open access) included below.[11] Supporting information of the publication is also included as published in APPENDIX VI .
In addition, first attempts for the encapsulation of AgNPs are likewise presented in section 5.3 Preliminary AgNP@Fe-MOF composites.

Author contribution: Conceptualization of this work involved Dr. Patricia Horcajada and AAV. Experimental works were carried out at IMDEA Energy, using APMU lab installations. MOF MW assisted synthesis was carried out by AAV with the help of the laboratory technician Ayoub Benckhlafa. Dr. David Ávila performed TEM analysis of the resulting crystalline materials. Result analysis and discussion was done by AAV and Dr. P. Horcajada. Original draft was written by AAV, while manuscript review and editing also involved Dr. P. Horcajada and Dr. D. Ávila.

5.2. Phase selective microwave assisted synthesis of iron(III) aminoterephthalate MOFs

Ana Arenas-Vivo [1], David Ávila[2] and Patricia Horcajada[1]*

[1] *Advanced Porous Materials Unit (APMU), IMDEA Energy Institute, Avda. Ramón de la Sagra 3, E-28935 Móstoles, Madrid, Spain*
[2] *Department of Inorganic Chemistry I, Chemical Sciences Faculty, Complutense University of Madrid, 28040 Madrid, Spain*
**Corresponding author. E-mail address: patricia.horcajada@imdea.org*

Materials, 2020, *13*, 14968 (Q2, IF: 3.057, open access)

Keywords: microwave synthesis; metal-organic frameworks; porous solids; iron; aminoterephthalate; phase selection

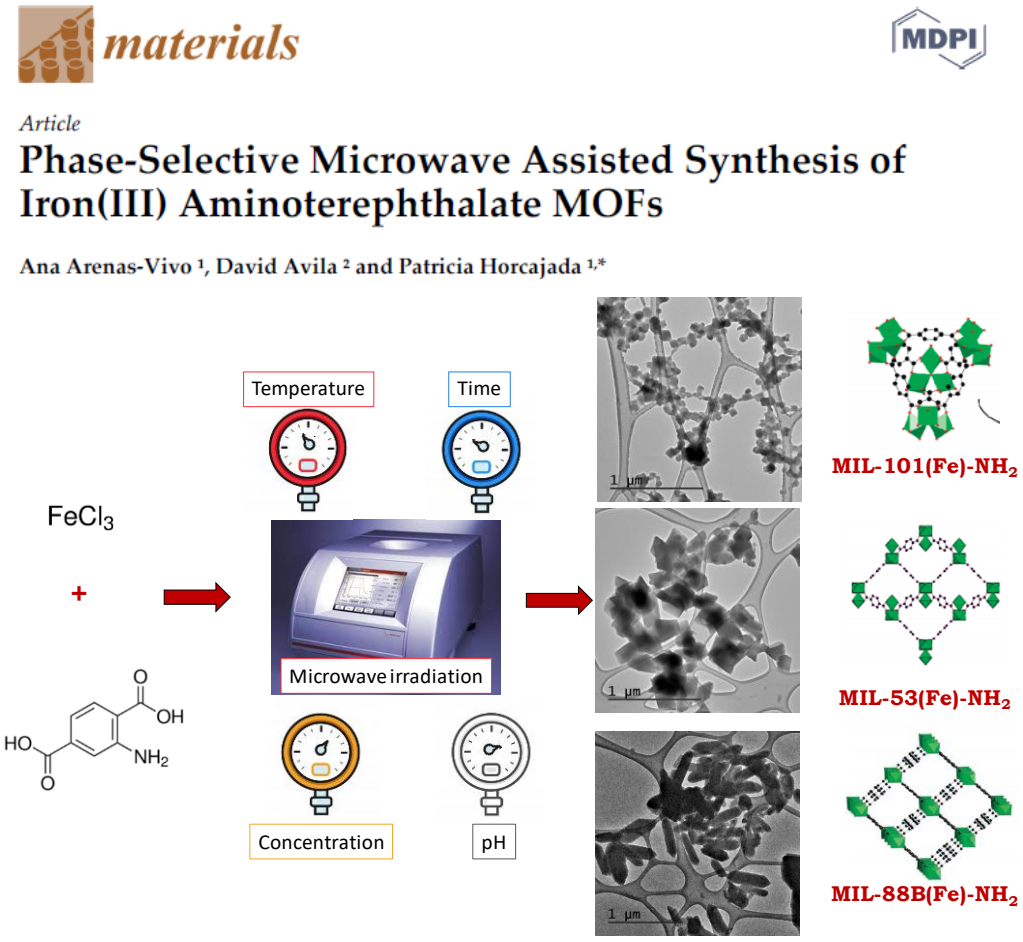

materials

MDPI

Article

Phase-Selective Microwave Assisted Synthesis of Iron(III) Aminoterephthalate MOFs

Ana Arenas-Vivo [1], David Avila [2] and Patricia Horcajada [1,*]

[1] Advanced Porous Materials Unit, IMDEA Energy. Av. Ramón de la Sagra 3, 28935 Móstoles-Madrid, Spain; ana.arenas@imdea.org

[2] Department of Inorganic Chemistry, Chemical Sciences Faculty, Complutense University of Madrid, 28040 Madrid, Spain; davilabr@ucm.es

* Correspondence: patricia.horcajada@imdea.org

Received: 28 February 2020; Accepted: 22 March 2020; Published: 23 March 2020

Abstract: Iron(III) aminoterephthalate Metal-Organic Frameworks (Fe-BDC-NH_2 MOFs) have been demonstrated to show potential for relevant industrial and societal applications (i.e., catalysis, drug delivery, gas sorption). Nevertheless, further analysis is required in order to achieve their commercial production. In this work, a systematic synthetic strategy has been followed, carrying out microwave (MW) assisted hydro/solvothermal reactions to rapidly evaluate the influence of different reaction parameters (e.g., time, temperature, concentration, reaction media) on the formation of the benchmarked MIL-101-NH_2, MIL-88B-NH_2, MIL-53-NH_2 and MIL-68-NH_2 solids. Characterization of the obtained solids by powder X-ray diffraction, dynamic light scattering and transmission electron microscopy allowed us to identify trends to the contribution of the evaluated parameters, such as the relevance of the concentration of precursors and the impact of the reaction medium on phase crystallization. Furthermore, we presented here for the first time the MW assisted synthesis of MIL-53-NH_2 in water. In addition, pure MIL-101-NH_2 was also produced in water while MIL-88-NH_2 was the predominant phase obtained in ethanol. Pure phases were produced with high space-time yields, unveiling the potential of MW synthesis for MOF industrialization.

Keywords: microwave synthesis; metal-organic frameworks; porous solids; iron; aminoterphthalate; phase selection

1. Introduction

Metal-Organic Frameworks (MOFs) are an interesting and recent family of hybrid crystalline solids based on different inorganic units connected with polydentate ligands [1]. Among other properties (e.g., optical, magnetic, electrochemical), they are notable for their impressive porosity [2,3] and their modulable chemical and topological structure [4,5]. As a result, they have an open door for their use in plenty of striking applications, both at industrial and social level, such as fluid storage and separation [6,7], catalysis [8,9], and drug delivery [10,11], among others [12].

Among the great diversity of polydentate ligands, the linear terephthatate derivatives (BDC; including the 1,4-benzene dicarboxylic acid or H_2BDC and its amine substituted form H_2BDC-NH_2) are very popular, leading to the formation of a large variety of highly porous MOF structures based on diverse cations (e.g., Cu, Zn, Al, Cr, Sc) [13]. For instance, based on the earth abundant, non-toxic and redox active iron, the series of polymorphic iron(III) terephthalates MIL-53 [14], MIL-68 [15], MIL-88B [16] and MIL-101 [17] (MIL stands for Matériaux Institut Lavoisier) has been described and widely explored [18]. Briefly, MIL-101 or $[Fe_3O(OH)(BDC)_3(H_2O)_2]$ is based on iron(III) octahedra trimers (Fe_3-μ_3-oxo clusters) and the BDC, creating a rigid three-dimensional (3D) cubic MTN-zeotype structure with exceptional mesoporosity (Brunauer, Emmett & Teller surface (S_{BET}) ~ 2500 $m^2 \cdot g^{-1}$, pore volume (V_P) ~ 2.4 $cm^3 \cdot g^{-1}$) with two mesocages of diameters of 29 and 34 Å, accessible

through pentagonal and hexagonal windows of 12 and 15 × 16 Å, respectively) [17]. A polymorph, also based on iron(III) octahedra trimers, is the flexible microporous MIL-88B structure [$Fe_3O(OH)(BDC)_3(H_2O)_2$] [16] exhibiting a 3D hexagonal network with interconnected cages and pore channel system able to reversibly modify its size (up to 9 Å; with a unit cell volume variation up to 120%) as a function of different external stimuli (e.g., adsorbate, pressure, temperature). Two additional crystalline phases can exist based on the BDC ligand but different inorganic unit, here iron(III) octahedra chains $FeO_4(OH)_2$: MIL-53 and MIL-68, both with the chemical formula [Fe(OH)(BDC)]. MIL-53 is a flexible 3D network with a flexible diamond shaped 1D channels [14]. This structure reaches a variation of a 40% in volume in between open (up to 8.5 Å) and closed form, depending on the guest molecules, pressure and temperature. Finally, MIL-68 is a polymorph of MIL-53, having a rigid orthorhombic structure with hexagonal (~15 Å) and triangular (~5 Å) shaped pores (S_{BET} ~ 670 $m^2 \cdot g^{-1}$) and its amino substituted version has not been reported for iron(III) so far [15]. These benchmarked solids have proven exceptional sorption, catalytic and photocatalytic properties [18].

Consequently, due to the interest of this family of MOFs, subsequent research on Fe-BDC-NH_2 synthesis is fundamental not only for understanding the underlying formation mechanisms but also to promote facile synthetic protocols scalable for commercialization and MOF industrial application [19]. With this is mind, microwave synthesis (MW) of MOFs has been proposed as an alternative to conventional hydro- or solvothermal reactions due to several advantages: (i) energy efficiency, (ii) fast crystallization (increment in number of reaction sites), (iii) phase selectivity, (iv) high yields, (v) variety of morphologies, (vi) particle size control, (vii) lower temperatures and reaction times [20]. The conjunction of this assets dramatically increases production due to the homogeneous energy input, compared to a traditional batch reactor, which can even be enhanced by reaction stirring [21]. In addition, industrial production in the order of $T \cdot year^{-1}$ can be achieved under MW-assisted continuous flow synthesis [22]. In consonance, this technology is efficiently exploited nowadays in the production of several organic chemicals such as drugs or polymers [23,24].

Even at its infancy, MW method has become a resourceful tool for the preparation of MOFs and for their activation/purification (removing pore filling species) [20,25]. Fe-based MOFs have not been an exception and there are previous reports that focus on the MW synthesis of a particular Fe-MOF phase (mostly without substitution of the H_2BDC ligand) [17,26–30]. However, as modest variations of the method lead to vast different synthetic results, a systematic study on the different variables affecting MW synthesis of iron (III) aminoterephthalate phases is still lacking. In this work, a systematic synthetic strategy has been followed, carrying out MW-assisted hydro/solvothermal reactions to rapidly evaluate the influence of different reaction parameters (e.g., time, temperature, concentration, reaction media) on the formation of the benchmarked MIL-101-NH_2, MIL-88B-NH_2, MIL-53-NH_2 and MIL-68-NH_2 solids. Crystallinity analysis as well as phase identification has been carried out by means of powder X-ray diffraction (PXRD), while particle size was investigated by dynamic light scattering (DLS) measurements and transmission electron microscopy (TEM) observation. In addition, important parameters (i.e., reaction yield and space-time yield) have been determined in order to prove the usefulness of MW synthesis for the future high scale production of Fe-BDC-NH_2 MOFs.

2. Materials and Methods

2.1. Synthesis

Fe-BDC-NH_2 MOF structures (for codes see Table S1) were synthesized from iron(III) chloride hexahydrate ($FeCl_3 \cdot 6H_2O$, Sigma Aldrich, 97%, Madrid, Spain), 2-aminoterephthalic acid (H_2BDC-NH_2, Acros Organics, 99%, Geel, Belgium), ethanol (EtOH, Labkem, 96%, Barcelona, Spain), absolute ethanol (Labkem), *N*,*N*-dimethylformamide (DMF, Acros, 99+%, Riad, Saudi Arabia), hydrochloric acid (HCl, J.T. Baker, 37–38%, Loughboroug, United Kingdom) and deionized water.

Different synthetic conditions were investigated (see Tables S2–8) for the microwave (MW) assisted-hydro/solvothermal synthesis of Fe-BDC-NH_2 MOFs. In general, a reaction mixture of 4 mL was loaded in a 10 mL glass vial (G10, Anton Paar GmbH, Graz Austria) and sonicated for 1 min in

an ultrasound bath (Branson 1800, Emerson, St. Louis, Missouri, United States) prior to being sealed and placed in a Monowave-300 MW (maximum power 300 W, Anton Paar GmbH, Graz Austria). The reactor vial in the MW was heated to the reaction temperature as fast as possible with different power impulses, maintained for a predetermined time and cooled down to 65 °C by an air flow prior extraction of the vial from the MW. The mixture was stirred during the MW reaction at 600 rpm at all times. As synthesized samples were recovered by centrifugation (12045 g for 10 min) and washed three times with absolute EtOH (2 $g \cdot L^{-1}$ under stirring) and recovered by centrifugation (12045 g for 10 min; activated sample, *act.*). Samples were stored wet in absolute EtOH prior to further analysis.

2.2. Characterization

Crystal phase of all samples was verified using powder X-ray diffraction (PXRD). PXRD patterns were collected using a conventional PANalytical Empyrean powder diffractometer (PANalytical Lelyweg, Almelo, Netherlands, θ–2θ) using λ_{Cu} $K_{\alpha 1}$, and $K_{\alpha 2}$ radiation (λ = 1.54051 and 1.54433 Å). PXRD diagrams were carried out with a 2θ scan between 3–35° with a step size of 0.013° and a scanning speed of $0.1° \cdot s^{-1}$.

Particle size was monitored via dynamic light scattering (DLS using a Zetasizer Nano series Nano-ZS (Malvern Instruments, Worcestershire, UK). The solids were dispersed in the liquid media (EtOH) at a concentration of 0.1 $mg \cdot mL^{-1}$ using an ultrasound tip (UP400S, Hilscher, Teltow, Germany) at 20% amplitude for 10 s.

Transmission electron microscopy (TEM) images were taken with a JEM 1400 (Jeol, Tokyo, Japan) with a 120 kV acceleration voltage (point resolution 0,38 nm). For TEM studies, 1 mg of sample was dispersed in 10 mL of absolute EtOH and sonicated with an ultrasound tip (UP400S, Hilscher, Teltow, Germany) at 20% amplitude for 10 s. For observation, 1 μL of the prepared solution was dropped over a copper TEM grid coated with holey carbon support film (Lacey Carbon, 300 mesh, copper, approx. grid hole size: 63 μm, TED PELLA Redding, CA, USA). Particle size was monitored via statistic counting (n = 70–100) with ImageJ (Version 1.8.0).

To address the MW assisted reaction performance two parameters have been defined: reaction yield (wt.%, Equation (1) and space-time yield (STY, $kg \cdot m^{-3} \cdot d^{-1}$, Equation (2))

$$Yield\ (\%) = \frac{m_{Fe-BDC-NH_2}}{m_{theoretical}} \times 100 \quad (1)$$

where $m_{FeBDC\text{-}NH2}$ is the experimental mass of the Fe-BDC-NH_2 MOF obtained (determined after drying at 100 °C) and $m_{theoretical}$ is the calculated theoretical amount of the determined phase that could be obtained, according to the metal used (Tables S9-17), both in kg.

$$STY = \frac{m_{Fe-BDC-NH2}}{V \times t} \quad (2)$$

where $m_{FeBDC\text{-}NH2}$ is the experimental mass of the Fe-BDC-NH_2 MOF obtained (kg), V is the reaction volume (m^3) and t is the reaction time (day).

3. Results

H_2O as reaction medium. The $FeCl_3$/H_2BDC-NH_2 system in water was studied under two different temperatures (100 and 150 °C) varying the iron precursor concentration (0.02, 0.05, 0.1 and 0.2 M). As an example, some of these conditions have been resumed in Table 1 (for further information see SI Tables S2 and S3). Under the analyzed reaction conditions, two different phases have been formed: MIL-101-NH_2 and MIL-53-NH_2 (Figure 1, for PXRD see Figures S1–S3). Note that it is typical to find here crystallized unreacted H_2BDC-NH_2 in the as synthesized (*a.s.*) samples due to the poor solubility of the ligand in water. However, the linker excess is removed during the following activation step (see experimental section). As expected, while lower temperature led to the formation of the mesoporous MIL-101-NH_2 (kinetically favored phase), at higher temperature the thermodynamic flexible microporous phase MIL-53-NH_2 was formed. In addition, there is a bisectrix on the T (°C)/[Fe] (M) crystallization diagram in which a mixture of phases is obtained, revealing this concentration dependency: in brief, higher concentrated reactions favor the formation of chains of

corner-sharing $FeO_4(OH)_2$ octahedra leading to MIL-53-NH_2, whereas diluted conditions promote the formation of the trimer Fe_3-μ_3-oxo clusters and, therefore, MIL-101-NH_2 crystallization.

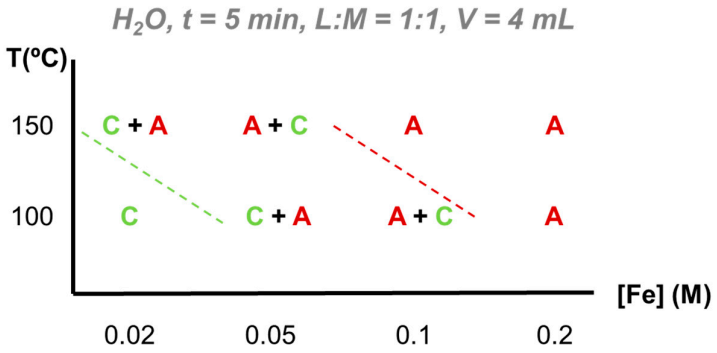

Figure 1. Crystallization diagram for the microwave (MW)-assisted hydrothermal synthesis of the system $FeCl_3$/H_2BDC-NH_2 in water based on powder X-ray diffraction (PXRD) data. Legend: A = MIL-53-NH_2, B = MIL-88B-NH_2, C = MIL-101-NH_2.

Furthermore, to evaluate the influence of the pH on the $FeCl_3$/H_2BDC-NH_2 system, the addition of the strong acid HCl was investigated within the region of the bisectrix, leading to mixture of MIL-53-NH_2 and MIL-101-NH_2 phases (T = 100 °C and [Fe] = 0.05 M, pH variation from 1.5 in the reaction mixture to 1 with HCl). At first glance, HCl presence increased the crystallinity of the Fe-H_2BDC-NH_2 phases (see PXRD in Figure S3). Furthermore, one can qualitatively observe by PXRD that MIL-101-NH_2 proportion seems to decrease (2θ = 4–6°) while MIL-53-NH_2 content seems to increase (2θ = 8.8 and 10.1°) with the addition of HCl, until only MIL-53-NH_2 is produced with higher HCl contents (200 μL).

Table 1. Mass, mol and molar ratios, and dispensed amounts for the MW investigation of the system $FeCl_3$·6 H_2O/H_2BDC-NH_2/HCl in water (V H_2O = 4 mL, T = 150 °C, t = 5 min and (•)t = 30 min). Legend: A = MIL-53-NH_2, B = MIL-88B-NH_2, C = MIL-101-NH_2.

Sample Name	$FeCl_3$ 6H_2O (mg)	$FeCl_3$ 6H_2O (mmol)	H_2BDC-NH_2 (mg)	H_2BDC-NH_2 (mmol)	Ligand: Metal	[Fe] (M)	HCl 1 M (mL)	HCl: Fe	Result *
MW 2-01	21.6	0.08	14.48	0.08	1	0.02	0	0	**C** + **A**
MW 2-02	54	0.2	36.2	0.2	1	0.05	0	0	**A** + **C**
MW 2-03	108	0.4	72.4	0.4	1	0.1	0	0	**A**
MW 2-04 (•)	108	0.4	72.4	0.4	1	0.1	0	0	**A**
MW 2-05	216	0.8	144.8	0.8	1	0.2	0	0	**A**
MW 2-06	54	0.2	36.2	0.2	1	0.05	0.1	0.5	**C** + **A**

* In the case of mixture, the first letter is the major phase.

On the whole, in water, increasing reaction temperature or increasing acidity shifts the equilibrium $FeCl_3$/H_2BDC-NH_2 system to the more favorable thermodynamic phase: MIL-53-NH_2.

EtOH as reaction medium. MIL-88B-NH_2 was the predominant phase observed of the $FeCl_3$/H_2BDC-NH_2 system when using ethanol as reaction medium (see Figure 2 and PXRD in Figures S4–7). All the reaction parameters with EtOH as solvent are resumed in SI Tables S4–6. Although, at lower temperature (100 °C) and longer times (≥20 min), MIL-88B-NH_2 was transformed to a poorly crystalline MIL-101-NH_2. In an attempt to obtain the thermodynamic MIL-53-NH_2 phase as well in ethanol, the reaction temperature was increased to 180 °C. However, except for very short times (5 min), the increment of the reaction temperature only led to the formation of α-Fe_2O_3 (rhombohedral

hematite as identified by PXRD; Figure S7). This indicates that Fe_3-μ_3-oxo clusters are less thermodynamically favored than the iron(III) oxide under high temperatures. In addition, particle size experienced insignificant variation regardless of the conditions (Tables S12–15), remaining below 300 nm with low polydispersity indexes (PdI < 0.3), according to DLS measurements.

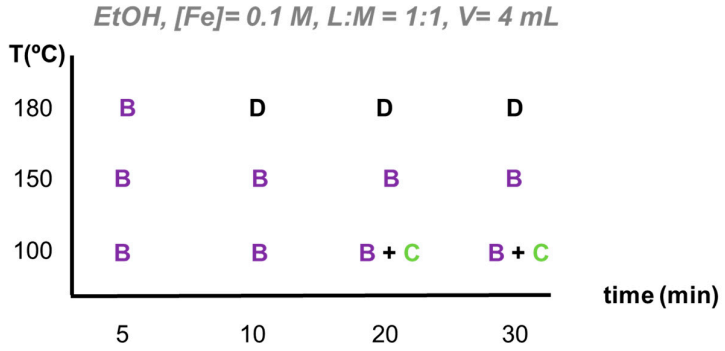

Figure 2. Crystallization diagram for the MW-assisted solvothermal synthesis of the system $FeCl_3$/H_2BDC-NH_2 in EtOH based on PXRD data. Legend: A = to MIL-53-NH_2, B = to MIL-88B-NH_2, C = to MIL-101-NH_2, D = Fe_2O_3.

DMF as reaction medium. The different reaction parameters using DMF can be consulted in SI Tables S7 and S8. In contrast with water and EtOH, the study of the $FeCl_3$/H_2BDC-NH_2 system in DMF in MW-assisted solvothermal synthesis did not lead to the formation of any solid at T = 100 °C. Even at 150 °C, short times under MW (5 min) only led to the formation of poorly crystalline solids. Increasing the time promotes the formation of the MIL-101-NH_2, favored phase in DMF as it was present at all tested concentrations in DMF (see Figure 3 and PXRD Figures S8–10). This need of extra-temperature could be explained because of the higher activation energy for the Fe_3-μ_3-oxo cluster to bond H$_2$BDC-NH_2 in DMF, compared to previously studied solvents (i.e., water and ethanol). Remarkably, at a concentration range 0.05–0.1 M, MIL-101-NH_2 coexists with its polymorph MIL-88B-NH_2, while at higher concentration (0.2 M) chain-based MIL-53-NH_2 appears. Results suggest that DMF is a more complex reaction medium, being the only one in which three Fe-BDC-NH_2 MOF phases were obtained.

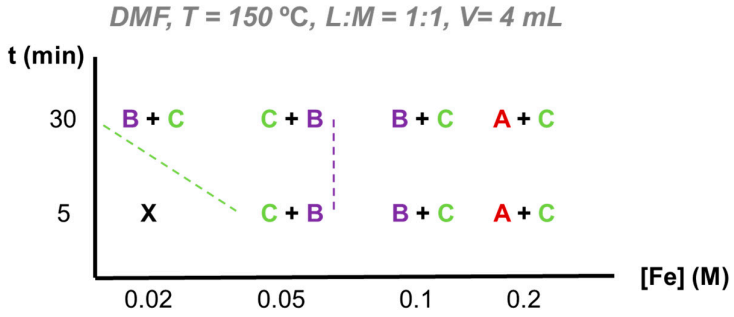

Figure 3. Crystallization diagram for the microwave-assisted solvothermal synthesis of the system $FeCl_3$/H_2BDC-NH_2 in DMF based on PXRD data. Legend: A = to MIL-53-NH_2, B = to MIL-88B-NH_2, C = to MIL-101-NH_2, X = amorphous.

4. Discussion

In the course of this study, 46 individual reaction mixtures (with replicates to ensure reproducibility) were carried out in three different protic and aprotic polar solvents (H_2O, EtOH and DMF) using the MW-assisted solvothermal method. Water and ethanol have been selected as good examples of green chemistry reaction solvents. DMF has been selected as a typical reaction medium

traditionally used in MOF solvothermal synthesis. Remarkably, the MW irradiation is a simple procedure that enables the fast and efficient attainment of three different Fe-BDC-NH_2 crystalline phases by slight modifications on the synthetic conditions, reaching high reaction yields and space-time-yield (STY) comparable to those of industrial process in the market in very short times. Thus, the influence of different parameters (i.e., solvent, temperature, reaction time, molar ratio of metallic precursor and organic ligand, concentration of the reaction mixture and the addition of HCl) on the product formation is here discussed as a function of the sample purity and crystallinity, crystals dimension (including size distribution), reaction yield and STY. The purity and crystallinity of the MW-assisted experiments are discussed on the basis of PXRD (see Supporting information (SI) Section 2) and are schematically represented above in crystallization diagrams. The proportion of the starting reagents and the conditions of synthesis are given in the SI (see Tables S2–8).

H_2O as reaction medium. Using water, pure MIL-101-NH_2 is only obtained at low temperature and concentration (100 °C, 0.02 M), while single MIL-53-NH_2 crystallizes at higher concentrations and temperature (0.1 M; and at 0.2M with both 100 and 150 °C). In addition, the formation of pure MIL-101-NH_2 in water gave to an extremely high reaction yield (almost complete reaction ~100 %) with however, lower STY associated with the diluted starting concentration (3850 $kg \cdot m^3 \cdot d^{-1}$ at 0.02 M). MIL-53-NH_2, besides being the thermodynamically stable phase, was produced as a pure phase in lower yields (<70%; see Table S9). However, considering the higher concentration of the reaction mixture, STY values reached 10400 $kg \cdot m^3 \cdot d^{-1}$, being competitive with the reported production of different MOFs (STY for Basolites© ~3000 $kg \cdot m^3 \cdot d^{-1}$) [19,31].

Particle size determination, by means of DLS, gave a rough estimation of the particle size of 300 ± 100 nm, with no clear dependence with temperature neither with concentration. Here, it should be taken into account that DLS provides information of hydrodynamic size, which can lead to misinterpretation in the case of non-spherical particles, such as MIL-53-NH_2, and with a mixture of different phases, as in this study. In addition, the pure MIL-53-NH_2 phase obtained in water with the highest STY (10400 $kg \cdot m^3 \cdot d^{-1}$; [Fe] = 0.2 M, T = 100 °C) was analyzed by TEM (see Figure S11). There can be seen well-defined submicrometric rhombohedral MIL-53-NH_2 particles. The resulting average particle size was of 330 ± 50 nm (n = 70) with additionally a monodisperse distribution (PdI = 0.11), in accordance with previously observed in DLS (260 ± 70 nm Table S9). To the best of our knowledge, this is the first report of a MW-assisted synthesis of pure submicronic iron(III) aminoterephtalate MIL-53-NH_2 up to date [29,32].

Considering the tests carried out in HCl ([Fe] = 0.05 M, T = 100 °C), the results unveiled the beneficial effect of the strong acid both (Figure S3): (i) on the crystallization of MIL-53-NH_2; higher HCl amounts (≥100 μL) favored the formation of MIL-53-NH_2 over MIL-101-NH_2; and (ii) on modulating and promoting the growth of a better crystallized MIL-101-NH_2 (at lower acidic concentrations; 50 μL). This may be related to the better control of the kinetics rate reaction, associated to the deprotonation equilibrium of the carboxylate ligand (H_2BDC-NH_2 ⇌ H^-BDC-NH_2 + H^+ ⇌ BDC-NH_2 + H^+). For a better analysis of the HCl presence, the water system $FeCl_3$/H_2BDC-NH_2 with and without acid at 100 °C and [Fe] = 0.05 M was further analyzed by TEM (Figure S11). Micrographs revealed that in the absence of HCl, small rounded and undefined octahedra along the quaternary axis (80 ± 10 nm, n =150), corresponding to the MIL-101-NH_2, were the predominant phase (Figure S11A). It is important to outstand the small particle size obtained. A previous report using lower concentrations [Fe] = 0.02, and longer times attained the phase with ~300 nm (seen in TEM) [17]. Upon the addition of 100 μL of acid, although the octahedra of MIL-101-NH_2 seem better defined and well-faceted, its amount significantly decreased, increasing in the meantime the content of larger MIL-53-NH_2 flakes (190 ± 25 nm). Due to the mixture of phases and the absence of spherical particles, DLS measurements determined a high polydispersity (PdI > 0.3) and bigger particle size than the one determined by TEM. Note here that the reaction in presence of HCl was almost complete, with yields of around 100% (see Table S11), but the increment in reaction volumes produces a decrease of the STY (from 8500 to 6500 $kg \cdot m^3 \cdot d^{-1}$, when in the presence of 200 μL of acid). Despite this, a mixture of phases continued to appear up to high HCl volumes (200 μL), which limits the accurate estimation of the proportion of each of them.

EtOH as reaction medium. As previously stated, MIL-88B-NH_2 is the predominant phase in EtOH and might be an interesting candidate for industrial production (see Figure 4). Nevertheless, it is important to notice that increasing MOF precursors concentration did not directly imply higher yields. In the case of reactions at 150 °C, the highest reaction yields were reached at lower concentration (100 and 85% at 0.02 and 0.05 M, respectively), being the more efficient reactions. However, considering the final production, despite the lower yields obtained with higher concentrated solutions (35% at 0.2 M), the maximum STY was performed at higher concentration (6200 $kg \cdot m^3 \cdot d^{-1}$). Therefore, there is a compromise solution to maximize reaction yield and the final product amount, that according to results is achieved at T = 100 °C, [Fe] = 0.1 M and 5 min of reaction. (see reaction yields and STY in Table S14).

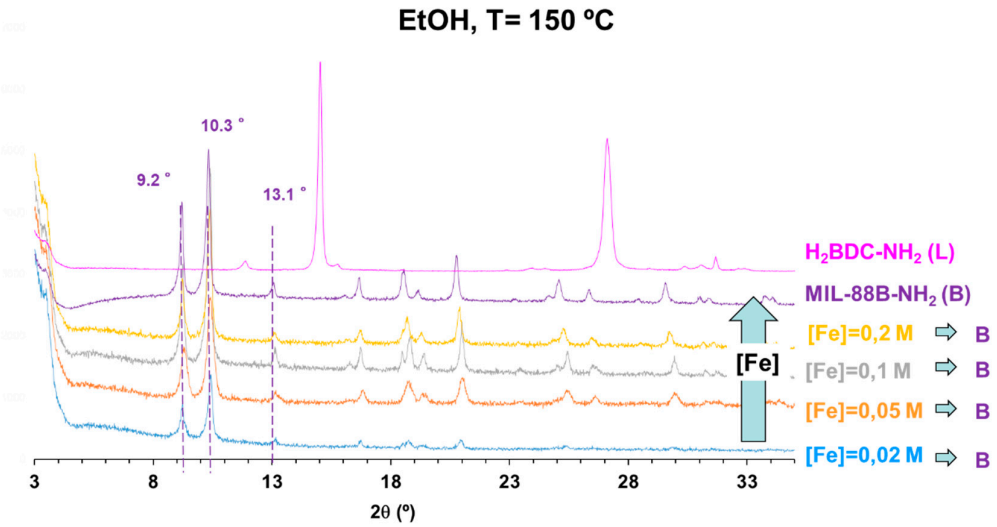

Figure 4. PXRD patterns for the MW investigation of the system $FeCl_3 \cdot 6\ H_2O/H_2BDC\text{-}NH_2$ in ethanol (V EtOH = 4 mL, T = 150 °C, t = 5 min) after activation with EtOH, compared to simulated MIL-88B-NH_2 (purple) and $H_2BDC\text{-}NH_2$ (pink).

Due to its higher STY (16000 $kg \cdot m^{-3} \cdot d^{-1}$) and crystallinity (see PXRD Figure S6), the sample synthetized at T = 100 °C and [Fe] =0.1 M was selected for further analysis with TEM. TEM micrographs (Figure S12) exhibited the characteristic bipyramidal hexagonal prims of MIL-88B-NH_2, confirming the phase determined previously by PXRD. The needles length (l) as determined by TEM, l = 110 ± 20 nm (n = 100), is slightly smaller than the hydrodynamic radius viewed in DLS (210 ± 70 nm). Particles have length: thickness ratio of 1.96 ± 0.65, being relatively symmetrical. Pure MIL-88B-NH_2 has been previously obtained but using DMF as reaction medium [27]. Taking into account DMF toxicity, the protocol proposed in this work for the first time with EtOH provides a safer alternative for industrial production of MIL-88B-NH_2.

Another interesting parameter for improving STY is reaction time. As a consequence, kinetics studies were carried out using two temperatures (100 and 150 °C) to better analyze this variable (see Tables S14 and S15). Results revealed that, although reaction yield grew with incrementing reaction time, maximum STY was performed just after 5 min of reaction (16000 and 3300 $kg \cdot m^3 \cdot d^{-1}$ at 100 and 150 °C, respectively).

DMF as reaction medium. As seen by the variety of phases obtained and characterized by PXRD, DMF is a complex reaction media. At concentrations below 0.2 M, iron trimers-based polymorphs (i.e., MIL-88B-NH_2 and MIL-101-NH_2) were favored, which seems to indicate that the formation of iron chains is only promoted in DMF at high concentrations. Regarding MIL-88B-NH_2, even in mixture, was promoted with incrementing time within the 0.05-0.1 M range (see PXRD Figure S9). Formation of MIL-88B-NH_2 over MIL-101-NH_2 is not only modulated by the concentration, but also by the presence of strong acid as HCl. Reaction time was fixed for this test to be 30 min to maximize

reaction yield (see Table S17) using two different ligand:metal ratios. While the precursors ratio had no significant effect on the MOF formation, the presence of HCl affected the proportion of the resulting polymorphic phases, increasing the formation of MIL-88B-NH_2 over MIL-101-NH_2 (Figure S11). Furthermore, the presence of a strong acid produces MIL-88B-NH_2 in DMF, while promoting MIL-53-NH_2 in water, supporting the important role of the solvent on the nature of the obtained phases.

In addition, HCl modulates the crystal growth, procuring larger well-defined MIL-88B-NH_2 crystals instead of MIL-101-NH_2. (see Figures S10 and S13). Interestingly, MIL-88B-NH_2 needles synthesized in DMF are 8 times longer than those formed in EtOH under similar conditions (without acid) and the length:thickness ratio is twofold times the EtOH ones (4.55 ± 1.42 *vs.* 1.96 ± 0.65, respectively). This indicates once again the important role of the reaction media on the formation of the different phases and its effect on the crystallinity and particle size. Of no less importance is the modulation effect provided by the presence of HCl in the mixture, as not only procured a pure MIL-88B-NH_2 phase, but also modulates particle growth, having a length:thickness ratio of 3.11 ± 0.74, and half the length as in pristine DMF (410 ± 45 nm).

On the other hand, at high concentration (0.2 M), both MIL-53-NH_2 and MIL-101-NH_2 present a good crystallinity, favoring the MIL-53-NH_2 thermodynamic phase with increasing time. Due to its flexible character, this phase could be better identified after drying the sample at 160 °C and removing the remaining EtOH and DMF from the flexible porosity (see Figure S9).

Finally, final yield increases with reaction time (see Table S16). However, the mixture of phases limits further discussion.

Comparison of solvents: From these results, we can conclude that the reaction medium has the most relevant impact on the final phase attained due to several factors: solubility, de-protonation of the ligand (acid-base properties) and boiling T (and therefore final reaction pressure). As in our case, solubility of the H_2BDC-NH_2 ligand is really limited in water, even under reactions conditions (MW-assisted heat and pressure) and seems to decrease the final reaction yield. Nevertheless, H_2O is a particularly interesting solvent as is a cheap, safe and green solvent with no security associated protocols rewarding its storage neither its manipulation, which is of particular interest for commercial protocols. What is more, water has the lower environmental, safety and health (ESH) impact, according to solvent selection guides of companies such as GSK or Pfizer [33]. In addition, under the studied conditions, water was the sole solvent that gave both pure MIL-101-NH_2 and MIL-53-NH_2 phases with highest crystallinity and relatively good STY (3850 and 10400 $kg \cdot m^{-3} \cdot d^{-1}$, respectively). While MIL-53-NH_2 was obtained with water as reaction media for the first time, its polymorph, the MIL-68-NH_2 still remains elusive under the studied variables.

EtOH is another interesting reaction medium, as is less harmful than other organic solvents and its recommended due to its low ESH. Compared to other organic solvents, with tendency to the crystallization of MIL-88B-NH_2. In this work, it has been presented an outstanding STY of 16000 $kg \cdot m^{-3} \cdot d^{-1}$ at soft reaction conditions (T = 100 °C, t = 5 min), which exposes the beneficial use of MW-solvothermal assisted reaction for the industrial production of MIL-88B-NH_2, which has demonstrated efficiency in applications such as photocatalysis, drug delivery and nanomotors [34–37]. In contrast, MIL-88B-NH_2 particles with better crystallinity were produced in DMF, and should not be discarded as reaction medium only due to its known toxicity and cost compared with the previously mentioned solvents.

5. Conclusions

A thorough study has been carried out to analyze the influence of different reaction parameters on the MW assisted hydro/solvothermal synthesis of the $FeCl_3$/H_2BDC-NH_2 isoreticular hybrid compounds. Three pure phases of iron(III) aminoterephthalate MOFs have been obtained, namely: MIL-53-NH_2, MIL-101-NH_2 and MIL-88B-NH_2. Characterization of the MOF phases by different solid-state techniques (PXRD, DLS, TEM) has enabled the identification of the reaction media as the main affecting variable of the MW assisted synthetic process. Importantly, the three different phases were obtained with water or either ethanol, both solvents with low ESH, relevant factor for MOF industrial

production. Concentration of the MOF precursors and reaction temperature are other key parameters for phase selectivity. To the best of our knowledge, here is reported for the first time the MW assisted hydrothermal synthesis of under micron MIL-53(Fe)-NH_2, opening the door for its industrial production.

Supplementary Materials: The following are available online at www.mdpi.com/1996-1944/13/6/1469/s1, **Figure S1.** PXRD patterns for the MW investigation of the system $FeCl_3 \cdot 6H_2O/H_2BDC\text{-}NH_2/HCl$ in water (V H_2O = 4 mL, T = 100 °C, t = 5 min) after activation with EtOH, compared to simulated MIL-101-NH_2 (green), MIL-53-NH_2 (red) and $H_2BDC\text{-}NH_2$ (pink), **Figure S2**. PXRD patterns for the MW investigation of the system $FeCl_3 \cdot 6H_2O/H_2BDC\text{-}NH_2/HCl$ in water (V H_2O = 4 mL, T = 150 °C, t = 5 min) after activation with EtOH, compared to simulated MIL-101-NH_2 (green), MIL-53-NH_2 (red) and $H_2BDC\text{-}NH_2$ (pink), **Figure S3.** PXRD patterns for the MW investigation of the system $FeCl_3 \cdot 6H_2O/H_2BDC\text{-}NH_2/HCl$ in water (V H_2O = 4 mL, T = 100 °C, t = 5 min, [Fe] = 0.05 M) after activation with EtOH, compared to simulated MIL-101-NH_2 (green), MIL-53-NH_2 (red) and H2BDC-NH_2 (pink), **Figure S4.** PXRD patterns for the MW investigation of the system $FeCl_3 \cdot 6H_2O/H_2BDC\text{-}NH_2$ in ethanol (V EtOH = 4 mL, T = 150 °C, [Fe] = 0.2 M, t = 5 min) after activation with EtOH, compared to simulated MIL-88B-NH_2 (purple) and $H_2BDC\text{-}NH_2$ (pink), **Figure S5.** PXRD patterns for the MW investigation of the system $FeCl_3 \cdot 6H_2O/H_2BDC\text{-}NH_2$ in ethanol (V EtOH = 4 mL, T = 100 °C, [Fe] = 0.1 M,) after activation with EtOH, compared to simulated MIL-88B-NH_2 (purple) and MIL-101-NH_2 (green), **Figure S6**. PXRD patterns for the MW investigation of the system $FeCl_3 \cdot 6H_2O/H_2BDC\text{-}NH_2$ in ethanol (V EtOH = 4 mL, T = 150 °C, [Fe] = 0.1 M,) after activation with EtOH, compared to simulated MIL-88B-NH_2 (purple), **Figure S7.** PXRD patterns for the MW investigation of the system $FeCl_3 \cdot 6H_2O/H_2BDC\text{-}NH_2$ in ethanol (V EtOH = 4 mL, T = 180 °C, [Fe] = 0.1 M,) after activation with EtOH, compared to simulated MIL-88B-NH_2 (purple) and Fe_2O_3 (black), **Figure S8.** PXRD patterns for the MW investigation of the system $FeCl_3 \cdot 6H_2O/H_2BDC\text{-}NH_2$ in DMF (V DMF = 4 mL, T = 150 °C, ligand:metal = 1:1) after activation with EtOH, compared to simulated MIL-88B-NH_2 (purple) and MIL-101-NH_2 (green), **Figure S9.** PXRD patterns for the MW investigation of the system $FeCl_3 \cdot 6H_2O/H_2BDC\text{-}NH_2$ in DMF (V DMF = 4 mL, T = 150 °C, ligand:metal = 1:1) after activation with EtOH and dried at 160 °C, for better discriminating between the different Fe-BDC-NH_2 MOF phases, **Figure S10.** PXRD patterns for the MW investigation of the system $FeCl_3 \cdot 6H_2O/H_2BDC\text{-}NH_2/HCl$ in DMF (V DMF = 4 mL, T = 150 °C, t = 30 min) after activation with EtOH, compared to simulated MIL-88B-NH_2 (purple) and MIL-101-NH_2 (green), **Figure S11.** TEM micrographs for PXRD for the MW investigation of the system $FeCl_3 \cdot 6H_2O/H_2BDC\text{-}NH_2/HCl$ in water (V H_2O = 4 mL, t = 5 min) after activation with EtOH: (**A**) T = 100 °C, HCl 0.1 M = 0 μL; (**B**) T = 100 °C, HCl 0.1 M = 100 μL; (**C**) T = 150 °C, HCl 0.1 M = 0 μL, **Figure S12.** TEM micrographs for PXRD for the MW investigation of the system $FeCl_3 \cdot 6H_2O/H_2BDC\text{-}NH_2$ in ethanol (V EtOH = 4 mL, t = 5 min T = 100 °C, [Fe] = 0.1 M) after activation with EtOH scale bar = 1 μm, **Figure S13.** TEM micrographs for PXRD for the MW investigation of the system $FeCl_3 \cdot 6H_2O/H_2BDC\text{-}NH_2/HCl$ in DMF (V DMF = 4 mL, t = 30 min, T = 100 °C, ligand:metal = 1:1) after activation with EtOH: (**A**) HCl 0.1 M = 0 μL (scale bar = 2 μm); (**B**) HCl 0.1 M = 100 μL (scale bar =1 μm), **Table S1**. Letter codes for the resulting products of the following MW synthesis, **Table S2.** Mass, mol and molar ratios, and dispensed amounts for the MW investigation of the system $FeCl_3 \cdot 6H_2O/H_2BDC\text{-}NH_2/HCl$ in water (V H_2O = 4 mL, T = 100 °C, t = 5 min). The resulting phases are indicated by the letter assigned in Table S1, **Table S3.** Mass, mol and molar ratios, and dispensed amounts for the MW investigation of the system $FeCl_3 \cdot 6H_2O/H_2BDC\text{-}NH_2/HCl$ in water (V H_2O = 4 mL, T= 150 °C, t= 5 min and (•) t= 30 min). The resulting phases are indicated by the letter assigned in Table S1, **Table S4.** Mass, mol and molar ratios, and dispensed amounts for the MW investigation of the system $FeCl_3 \cdot 6H_2O/H_2BDC\text{-}NH_2$ in ethanol (V EtOH = 4 mL. T= 150 °C. t= 5 min). The resulting phases are indicated by the letter assigned in Table S1, **Table S5.** Mass, mol and molar ratios, and dispensed amounts for the MW investigation of assigned in Table S1. the system $FeCl_3 \cdot 6H_2O/H_2BDC\text{-}NH_2$ in ethanol (V EtOH = 4 mL. T= 150 °C. t= 5 min). The resulting phases are indicated by the letter assigned in Table S1, **Table S6.** Mass, mol and molar ratios, and dispensed amounts for the MW investigation of the system $FeCl_3 \cdot 6H_2O/H_2BDC\text{-}NH_2$ in ethanol (V EtOH = 4 mL, [Fe] =0.1 M, ligand:metal = 1:1). The resulting phases are indicated by the letter assigned in Table S1, **Table S7.** Mass, mol and molar ratios, and dispensed amounts for the MW investigation of the system $FeCl_3 \cdot 6H_2O/H_2BDC\text{-}NH_2$ in DMF (V DMF = 4 mL. T = 150 °C. ligand:metal = 1:1). The resulting phases are indicated by the letter assigned in Table S1, **Table S8.** Mass, mol and molar ratios, and dispensed amounts for the MW investigation of the system $FeCl_3 \cdot 6H_2O/H_2BDC\text{-}NH_2/HCl$ in DMF (V DMF = 4 mL. T = 150 °C. t = 5 min). The resulting phases are indicated by the letter assigned in Table S1, **Table S9.** Particle size and reaction yield for the MW investigation of the system $FeCl_3 \cdot 6H_2O/H_2BDC\text{-}NH_2$ in water (V H_2O = 4 mL, T = 100 °C, t = 5 min, **Table S10.** Particle size and reaction yield for the MW investigation of the system $FeCl_3 \cdot 6H_2O/H_2BDC\text{-}NH_2$ in water (V H_2O = 4 mL, T = 150 °C, t = 5 min), **Table S11.** Particle size and reaction yield for the MW investigation of the system $FeCl_3 \cdot 6H_2O/H_2BDC\text{-}NH_2/HCl$ in water ([Fe] = 0.05 M, V H_2O = 4 mL, T= 100 °C, t= 5 min), **Table S12.** Particle size and reaction yield for the MW investigation of the system

$FeCl_3 \cdot 6H_2O/H_2BDC\text{-}NH_2$ in ethanol (V EtOH = 4 mL, T = 150 °C, t = 5 min), **Table S13.** Particle size and reaction yield for the MW investigation of the system $FeCl_3 \cdot 6H_2O/H_2BDC\text{-}NH_2$ in ethanol (V EtOH = 4 mL, T = 150 °C, t= 5 min, [Fe] = 0.2 M), **Table S14.** Particle size and reaction yield for the MW investigation of the system $FeCl_3 \cdot 6H_2O/H_2BDC\text{-}NH_2$ in ethanol (V EtOH = 4 mL, T = 100 °C, [Fe] = 0.1 M), **Table S15.** Particle size and reaction yield for the MW investigation of the system $FeCl_3 \cdot 6H_2O/H_2BDC\text{-}NH_2$ in ethanol (V EtOH = 4 mL, T = 150 °C, [Fe] = 0.1 M), **Table S16.** Particle size and reaction yield for the MW investigation of the system $FeCl_3 \cdot 6H_2O/H_2BDC\text{-}NH_2$ in DMF (V DMF = 4 mL, T = 150 °C, ligand:metal = 1:1), **Table S17.** Particle size and reaction yield for the MW investigation of the system $FeCl_3 \cdot 6H_2O/H_2BDC\text{-}NH_2$/HCl in DMF (V DMF = 4 mL, T = 150 °C, t = 30 min, [Fe] = 0.05).

Author Contributions: Conceptualization, P.H. and A.A.V.; methodology, P.H., D.A. and A.A.V.; formal analysis, P.H. and A.A.V.; writing—original draft preparation, A.A.V.; writing—review and editing, P.H., D.A. and A.A.V.; funding acquisition, P.H. All authors have read and agreed to the published version of the manuscript.

Funding: This research was funded by Raphuel project (ENE2016-79608-C2-1-R, MINECO-AEI/FEDER, UE), and the Ramón Areces Foundation project H+MOFs. PH acknowledges the Spanish Ramón y Cajal Programme (2014-15039). DA acknowledges the financial support through the Retos Project from MINECO with reference MAT2017-84385-R for funding. The authors also thank the CNME for the support and facilities.

Acknowledgments: Authors thank to Ayoub Benckhlafa Akil for his technical support in the synthesis and characterization tasks.

Conflicts of Interest: The authors declare no conflict of interest. The funders had no role in the design of the study; in the collection, analyses, or interpretation of data; in the writing of the manuscript, or in the decision to publish the results.

References

1. Férey, G. Hybrid porous solids: Past, present, future. *Chem. Soc. Rev*. **2008**, *37*, 191–214.
2. Maurin, G.; Serre, C.; Cooper, A.; Férey, G. The new age of MOFs and of their porous-related solids. *Chem. Soc. Rev*. **2017**, *46*, 3104–3107.
3. Furukawa, H.; Ko, N.; Go, Y.B.; Aratani, N.; Choi, S.B.; Choi, E.; Yazaydin, A.Ö.; Snurr, R.Q.; O'Keeffe, M.; Kim, J.; et al. Ultrahigh porosity in metal-organic frameworks. *Science* **2010**, *329*, 424–428.
4. Timofeeva, M.N.; Panchenko, V.N.; Khan, N.A.; Hasan, Z.; Prosvirin, I.P.; Tsybulya, S. V.; Jhung, S.H.. Isostructural metal-carboxylates MIL-100(M) and MIL-53(M) (M: V, Al, Fe and Cr) as catalysts for condensation of glycerol with acetone. *Appl. Catal. A Gen*. **2017**, *529*, 167–174.
5. Blandez, J.F.; Santiago-Portillo, A.; Navalón, S.; Giménez-Marqués, M.; Álvaro, M.; Horcajada, P.; García, H.. Influence of functionalization of terephthalate linker on the catalytic activity of UiO-66 for epoxide ring opening. *J. Mol. Catal. A Chem*. **2016**, *425*, 332–339.
6. Furukawa, H.; Cordova, K.E.; O'Keeffe, M.; Yaghi, O.M. The chemistry and applications of metal-organic frameworks. *Science* **2013**, *341*, 1230444.
7. Lin, K.-S.; Adhikari, A.K.; Ku, C.-N.; Chiang, C.-L.; Kuo, H. Synthesis and characterization of porous HKUST-1 metal organic frameworks for hydrogen storage. *Int. J. Hydrog. Energy* **2012**, *37*, 13865–13871.
8. Zhang, T.; Lin, W. Metal-organic frameworks for artificial photosynthesis and photocatalysis. *Chem. Soc. Rev*. **2014**, *43*, 5982–5993.
9. Falcaro, P.; Ricco, R.; Yazdi, A.; Imaz, I.; Furukawa, S.; Maspoch, D.; Ameloot, R.; Evans, J.D.; Doonan, C.J. Application of Metal and Metal Oxide Nanoparticles@MOFs. *Coord. Chem Rev*. **2015**, *307*, doi:10.1016/j.ccr.2015.08.002.
10. Horcajada, P.; Gref, R.; Baati, T.; Allan, P.K.; Maurin, G.; Couvreur, P.; Férey, G.; Morris, R.E.; Serre, C.. Metal-Organic Frameworks in Biomedicine. *Chem. Rev*. **2012**, *112*, 1232–1268.
11. Rojas, S.; Arenas-Vivo, A.; Horcajada, P. Metal-organic frameworks: A novel platform for combined advanced therapies. *Coord. Chem. Rev*. **2019**, *388*, 202–226.
12. Pettinari, C.; Marchetti, F.; Mosca, N.; Tosi, G.; Drozdov, A. Application of Metal-organic Frameworks. *Polym. Int.* **2017**, *66*, 731–744.
13. Zlotea, C.; Phanon, D.; Mazaj, M.; Heurtaux, D.; Guillerm, V.; Serre, C.; Horcajada, P.; Devic, T.; Magnier, E.; Cuevas, F.; et al. Effect of NH2 and CF3 functionalization on the hydrogen sorption properties of MOFs. *J. Chem. Soc. Dalt. Trans*. **2011**, *40*, 4879–4881.

14. Devic, T.; Horcajada, P.; Serre, C.; Salles, F.; Maurin, G.; Moulin, B.; Heurtaux, D.; Clet, G.; Vimont, A.; Grenéche, J.M.; et al Functionalization in flexible porous solids: Effects on the pore opening and the host-guest interactions. *J. Am. Chem. Soc*. **2010**, *132*, 1127–1136.
15. Fateeva, A.; Horcajada, P.; Devic, T.; Serre, C.; Marrot, J.; Grenèche, J.-M.; Morcrette, M.; Tarascon, J.-M.; Maurin, G.; Férey, G Synthesis, Structure, Characterization, and Redox Properties of the Porous MIL-68(Fe) Solid. *Eur. J. Inorg. Chem*. **2010**, *2010*, 3789–3794.
16. Horcajada, P.; Salles, F.; Wuttke, S.; Devic, T.; Heurtaux, D.; Maurin, G.; Vimont, A.; Daturi, M.; David, O.; Magnier, E.; et al.. How linker's modification controls swelling properties of highly flexible iron(III) dicarboxylates MIL-88. *J. Am. Chem. Soc*. **2011**, *133*, 17839–17847.
17. Horcajada, P.; Chevreau, H.; Heurtaux, D.; Benyettou, F.; Salles, F.; Devic, T.; Garcia-Marquez, A.; Yu, C.; Lavrard, H.; Dutson, C.L.; et al. Extended and functionalized porous iron(iii) tri- or dicarboxylates with MIL-100/101 topologies. *Chem. Commun*. **2014**, *50*, 6872–6874.
18. Xia, Q.; Wang, H.; Huang, B.; Yuan, X.; Zhang, J.; Zhang, J.; Jiang, L.; Xiong, T.; Zeng, G.. State-of-the-Art Advances and Challenges of Iron-Based Metal Organic Frameworks from Attractive Features, Synthesis to Multifunctional Applications. *Small*. **2018**, *15*, 1803088.
19. Yilmaz, B.; Trukhan, N.; Müller, U. Industrial outlook on zeolites and metal organic frameworks. *Cuihua Xuebao/Chin. J. Catal*. **2012**, *33*, 3–10.
20. Klinowski, J.; Almeida Paz, F.A.; Silva, P.; Rocha, J. Microwave-assisted synthesis of metal-organic frameworks. *Dalt. Trans*. **2011**, *40*, 321–330.
21. Nüchter, M.; Ondruschka, B.; Bonrath, W.; Gum, A. Microwave assisted synthesis – a critical technology overview. *Green Chem*. **2004**, *6*, 128–141.
22. Morschhäuser, R.; Krull, M.; Kayser, C.; Boberski, C.; Bierbaum, R.; Püschner, P.A.; Glasnov, T.N.; Kappe, C.O. Microwave-assisted continuous flow synthesis on industrial scale. *Green Process Synth*. **2012**, *1*, 281–290.
23. Nagahata, R.; Takeuchi, K. Encouragements for the Use of Microwaves in Industrial Chemistry. *Chem. Rec*. **2019**, *19*, 51–64.
24. Santagada, V.; Frecentese, F.; Perissutti, E.; Fiorino, F.; Severino, B.; Caliendo, G. Microwave Assisted Synthesis: A New Technology in Drug Discovery. *Mini-Rev. Med. Chem*. **2012**, *9*, 340–358.
25. Lee, E.J.; Bae, J.; Choi, K.M.; Jeong, N.C. Exploiting Microwave Chemistry for Activation of Metal-Organic Frameworks. *ACS Appl. Mater. Interfaces* **2019**, *11*, 34989–34996.
26. Haque, E.; Khan, N.A.; Park, J.H.; Jhung, S.H. Synthesis of a Metal-Organic Framework Material, Iron Terephthalate, by Ultrasound, Microwave, and Conventional Electric Heating: A Kinetic Study. *Chem. A Eur. J*. **2010**, *16*, 1046–1052.
27. Ma, M.; Bétard, A.; Weber, I.; Al-Hokbany, N.S.; Fischer, R.A.; Metzler-Nolte, N. Iron-based metal-organic frameworks MIL-88B and NH2-MIL-88B: High quality microwave synthesis and solvent-induced lattice "breathing." *Cryst. Growth Des*. **2013**, *13*, 2286–2291.
28. Dong, W.; Liu, X.; Shi, W.; Huang, Y. Metal-organic framework MIL-53(Fe): Facile microwave-assisted synthesis and use as a highly active peroxidase mimetic for glucose biosensing. *RSC Adv*. **2015**, *5*, 17451–17457.
29. Guo, W.; Sun, W.; Lv, L.-P.; Kong, S.; Wang, Y. Microwave-Assisted Morphology Evolution of Fe-Based Metal–Organic Frameworks and Their Derived Fe $_2$ O $_3$ Nanostructures for Li-Ion Storage. *ACS Nano*. **2017**, *11*, 4198–4205.
30. Taylor-Pashow, K.M.L.; Della Rocca, J.; Xie, Z.; Tran, S.; Lin, W. Postsynthetic modifications of iron-carboxylate nanoscale metal-organic frameworks for imaging and drug delivery. *J. Am. Chem. Soc*. **2009**, *131*, 14261–14263.
31. Farrusseng, D. Metal-Organic Frameworks : Applications from Catalysis to Gas Storage; Farruseng, D., Ed.; Wiley-VCH: Weinheim, Germany, 2011.
32. Soni, A.K.; Dey, R.; Rai, V.K. Metal–organic framework MIL-53(Fe): Facile microwave-assisted synthesis and use as a highly active peroxidase mimetic for glucose biosensing. *RSC Adv*. **2015**, *5*, 34999–35009.
33. Clarke, C.J.; Tu, W.C.; Levers, O.; Bröhl, A.; Hallett, J.P. Green and Sustainable Solvents in Chemical Processes. *Chem. Rev*. **2018**, *118*, 747–800.
34. Dao, X.Y.; Guo, J.H.; Wei, Y.P.; Guo, F.; Liu, Y.; Sun, W.Y. Solvent-free photoreduction of CO2 to CO catalyzed by Fe-MOFs with superior selectivity. *Inorg. Chem*. **2019**, *58*, 8517–8524.

35. Horcajada, P.; Chalati, T.; Serre, C.; Gillet, B.; Sebrie, C.; Baati, T.; Eubank, J.F.; Heurtaux, D.; Clayette, P.; Kreuz, C.; et al.. Porous metal-organic-framework nanoscale carriers as a potential platform for drug delivery and imaging. *Nat. Mater*. **2010**, *9*, 172–178.
36. Claes, B.; Boudewijns, T.; Muchez, L.; Hooyberghs, G.; Van der Eycken, E. V.; Vanderleyden, J.; Steenackers, H.P.; De Vos, D.E. Smart Metal-Organic Framework Coatings: Triggered Antibiofilm Compound Release. *ACS Appl. Mater. Interfaces* **2017**, *9*, 4440–4449.
37. Troyano, J.; Carné-Sánchez, A.; Pérez-Carvajal, J.; León-Reina, L.; Imaz, I.; Cabeza, A.; Maspoch, D. A. A Self-Folding Polymer Film Based on Swelling Metal–Organic Frameworks. *Angew Chem. –Int. Ed*. **2018**, *57*, 15420–15424.

© 2020 by the authors. Licensee MDPI, Basel, Switzerland. This article is an open access article distributed under the terms and conditions of the Creative Commons Attribution (CC BY) license (http://creativecommons.org/licenses/by/4.0/).

5.3. Preliminary AgNP@Fe-MOF composites

After the knowledge developed about the MW assisted synthesis of the iron(III) aminoterephthalate series and the optimization of pure phases in different solvents, the BaS synthesis of AgNP@Fe-MOFs was addressed. It was decided to start with presynthesized AgNPs, that will be dispersed in the MOF synthesis reaction media and act as hot spots for the MOF nucleation. It was expected to have a rapid consumption of reagents due to the selective heating of the MNPs and a narrow control of the composite crystal size distribution.

5.3.1. Bottom-up chemical synthesis of AgNPs

There has been extensive research in the nanoscience field regarding the synthesis of silver nano species by a bottom-up chemical approach, from which silver ions in a solution are reduced in conditions that favor the formation of the Ag^0 small atoms aggregates that lead to metal clusters or nanoparticles.[12,13] Among those, two methods of known reproducibility and simplicity have been selected to produce high quality AgNPs. For further details please refer to

- Hydrophilic 30 nm AgNPs caped with citrate (AgC) were synthesized from the detailed report provided by Parak and colleagues.[14] In brief, a colorless MilliQ water solution of sodium citrate (5 mM) and tannic acid (0.1 mM) was placed in a in a three-neck round bottom flask stirring under reflux. When boiling, 1 mL of a 25 mM $AgNO_3$ solution was added and instantly produced a color change in the solution to bright yellow, manifesting the formation of AgNPs. After recovery by centrifugation, they were stored in 0.25 mM sodium citrate solution until use. Final NP size was assessed by DLS, to also analyze the stability of the AgNP suspension with time. In addition, the suspension was characterized by UV-Vis and TEM.
- Hydrophobic 5 nm AgNPs caped with poly(vinylpyrrolidone) (AgPVP) were synthesize in DMF.[15] In a three-neck round bottom flask, 100 mL of a 0.76 mM PVP solution in DMF (4.18 g PVP, MW:55000 $g \cdot mol^{-1}$) was put under reflux and stirring until reach 156 °C. When boiling, 10 mL of a 0.76 mM $AgNO_3$ MilliQ aqueous solution was injected dropwise and instantly produced a color change in the solution to red/brownish. AgPVP nanoparticles were recovered by centrifugation and redispersed

in DMF until use. This suspension was also characterized by DLS, UV-Vis spectroscopy and TEM.

Table 5. 1: Particle size and ζ-potential values of the AgC and AgPVP nanoparticles with time

NPs	Day	Size (Ø, nm)	PdI	ζ-potential (ZP, mV)
AgC	1	28.3 ± 2.5	0.15 ± 0.02	-39 ± 6
	14	29.8 ± 1.3	0.38 ± 0.09	-41 ± 8
AgPVP	1	6.5 ± 1.1	0.18 ± 0.03	*
	14	7.7 ± 1.3	0.32 ± 0.08	*

* not measured

Hydrodynamic size of the AgNPs was confirmed in dynamic light scattering (DLS) measurements, being the particle diameter within the range of the aimed dimensions (see Table 5. 1). AgC suspension in water was quite stable and presented an adequate electrostatic repulsion provided by the citrate capping (ZP = -39 ± 6 mV).[16] In addition, particle size was relatively monodisperse (PdI = 0.15 ± 0.02). Even after two weeks there was an increment in polydispersity, particle size remained stable within that time, indicating that citrate prevented AgNP aggregation (Figure 5. 1 A). Similar results were observed with the AgPVP nanoparticles in DMF.

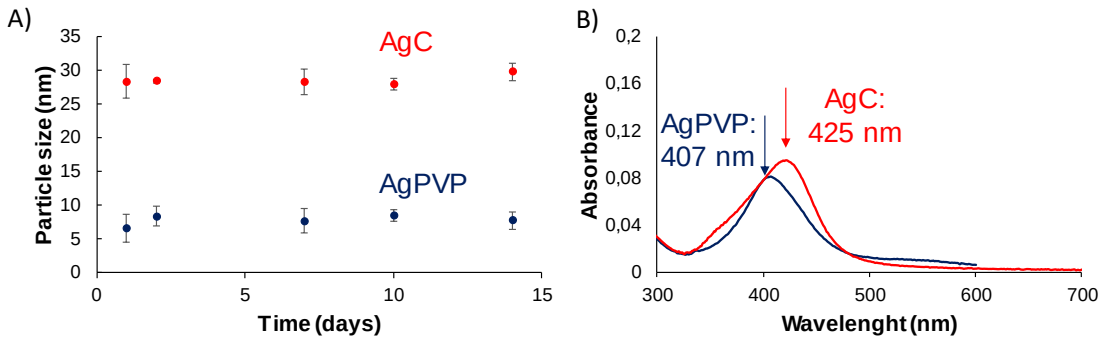

Figure 5. 1: A) Stability of the suspensions of AgC (red) in H_2O and AgPVP (blue) in DMF; B) UV-Vis absorption spectra of AgC (red) in H_2O and AgPVP (blue) in DMF

Observation of the diluted suspension by UV-Vis spectroscopy revealed absorption peaks within the 350-450 nm region, characteristic of plasmonic AgNPs with a shoulder round 500 nm corresponding to the SPR phenomenon. This absorbance explains the distinctive optoelectrical properties of the solutions. As seen from Figure 5. 1 B, there is a red shift of the SPR maximum of AgNPs from 407 nm in the AgPVP coated to 425 nm in the AgC caped, due to the particle size

increment from 5 to 30 nm. In addition, from the broad absorption peak in both suspensions can be said that there is no narrow distribution of particle diameter.[14] This was also observed in TEM micrographs, were particle size analysis measurements with ImageJ determined a mean diameter of 25 ± 6 nm and 5.6 ± 1.7 nm for AgC and AgPVP NPs, respectively (Figure 5. 2).

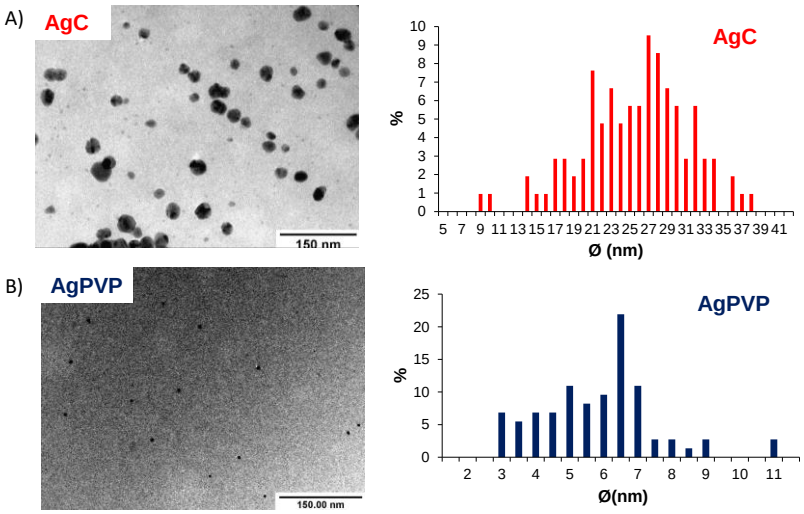

Figure 5. 2: TEM micrographs and particle size distribution histogram (n=100) of A) AgC nanoparticles (red) and B) AgPVP nanoparticles (blue). Scale bar 150 nm

For their use in AgNP@Fe-MOF composite synthesis, suspensions were freshly made, and their composition was determined by ICP-OES being 140 ± 10 and 0.4 ± 0.05 ppm for AgC and AgPVP respectively.

5.3.2. BaS MW assisted synthesis

For the synthesis of AgNP@Fe-MOF composites, optimized phases of the $FeCl_3 \cdot 6\ H_2O$ / $H_2BDC\text{-}NH_2$ system in water and DMF were appointed, in order to preserve the stability of the AS in the reaction media.

MIL-53-NH_2 was chosen as representative for H_2O, as it was the first time the material was obtained under MW irradiation.[11] The reaction parameters selected were those of the MW 2-05 sample ([Fe]=0.2 M, 150 °C, 5 min, see APPENDIX VI Table AVI. 3) due to the high STY (7000 $kg \cdot m^{-3} \cdot d^{-1}$, APPENDIX VI Table AVI. 10). After dispersion of the SBU in H_2O with the help of the ultrasound during 10 min, 10 µL of the AgC suspension were added to the reaction media and placed in the MW. The obtained AgC/MIL-53-NH_2 samples were recovered by centrifugation and characterized by XRPD and TEM.

The synthesized particles, as seen by TEM, had a really nice crystalline structure with rhombohedral cube shape (190 ± 20 nm, n=50, Figure 5. 3 A).

Particles were smaller than those of the previously MW-assisted synthesized sample without AgC (190 *vs.* 300 nm, see TEM micrograph in the supporting information in APPENDIX VI Figure AVI. 12C), and the increment in crystallinity is evident. The modulation on the growth of the MIL-53-NH_2 might have arisen from the citrate present in the reaction media, that interfere procuring finer crystals. This crystallinity was also confirmed by the high intensity XRPD pattern of the AgC/MIL-53-NH_2 composite (Figure 5. 3 C). Unfortunately, observation of the sample, even under high magnification, did not reveal any AgNP associated to the MOF crystals (Figure 5. 3 B). What is the same, the MIL-53-NH_2 self-nucleated without encapsulating the AgNPs.

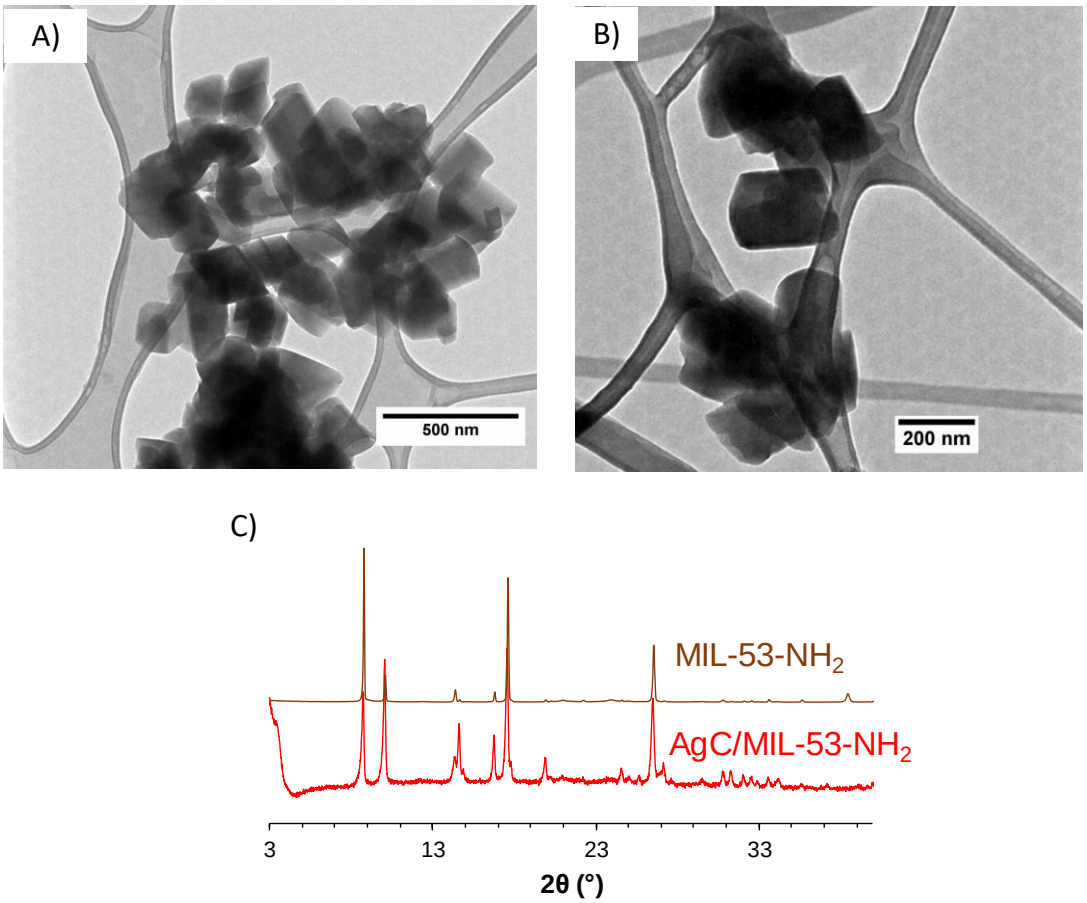

Figure 5. 3: TEM micrographs of the attempted AgC/MIL-53-NH_2 synthesized in water. A) scale bar 500 nm. B) scale bar 200 nm. C) XRPD pattern of AgC/MIL-53-NH_2 (red) compared to the simulated MIL-53-NH_2 (brown)

When using DMF as reaction medium for the association of AgPVP NPs, the selected synthesis procedure was the one corresponding to the MW 4-02 sample ([Fe]=0.05 M, 150 °C, 5 min, see APPENDIX VI Table AVI. 7) as procured the kinetically stable MIL-101-NH_2 with highest STY (1500 *vs.* 600 $kg \cdot m^{-3} \cdot d^{-1}$, APPENDIX VI Table AVI. 16). As in the case of H_2O, 10 µL of the AgPVP suspension was added prior MW irradiation.

Micrographs of the AgPVP@MIL-101-NH_2 composite showed big MOF octahedron (450 ± 100 nm, n=50, Figure 5. 4) with a better crystal definition than those obtained in the absence of AgPVP. It could be depicted that the PVP surfactant might have as well modulated the MOF growth. XRPD confirmed that the MOF crystals corresponded to the MIL-101-NH_2 phase (Figure 5. 4 C). Unlike the previous sample, TEM analysis enabled the identification of AgNPs associated to the MIL-101-NH_2 crystals (in higher contrast in Figure 5. 4 B). Nevertheless, this was not a completely successful attempt as there was a heterogeneous distribution of AgPVP NPs within the sample. Even more, some MIL-101-NH_2 crystals nucleated and grew without NPs. This might be due to the low concentration of AgPVP present in the reaction media (~40 pmol of Ag).

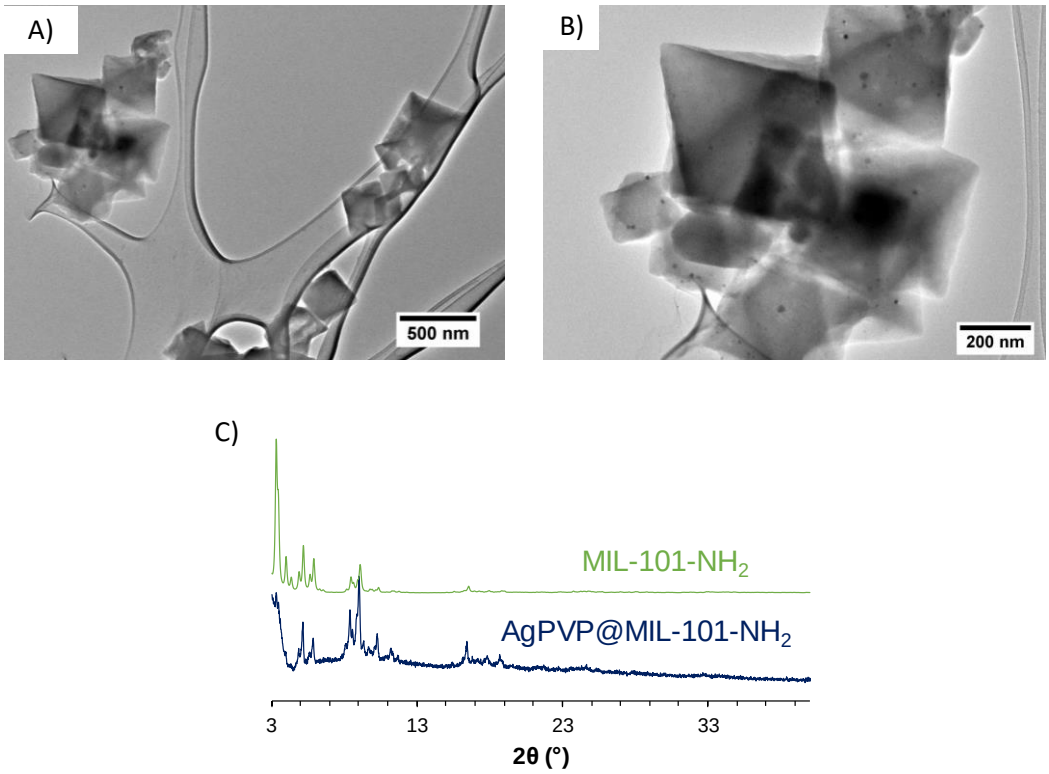

Figure 5. 4: TEM micrographs of the attempted AgPVP@MIL-101-NH_2 synthesized in water. A) scale bar 500 nm. B) scale bar 200 nm. C) XRPD pattern of AgPVP@MIL-101-NH_2 (blue) compared to the simulated MIL-101-NH_2 (green)

Far for being optimized, these preliminary results demonstrate the potential of MW assisted synthesis for the BaS association of MNP to MOFs with a fast and simple methodology. Unfortunately, due to the time limitation for the development of this doctoral thesis, improvement of the AgNP@Fe-MOF composites will not be presented in this manuscript and this research line is going to be continued by other APMU researchers.

Bibliography

(1) Khan, N. A.; Jhung, S. H. Synthesis of Metal-Organic Frameworks (MOFs) with Microwave or Ultrasound: Rapid Reaction, Phase-Selectivity, and Size Reduction. *Coord. Chem. Rev.* **2015**, *285*, 11–23. https://doi.org/10.1016/j.ccr.2014.10.008.

(2) Thomas-Hillman, I.; Laybourn, A.; Dodds, C.; Kingman, S. W. Realising the Environmental Benefits of Metal–Organic Frameworks: Recent Advances in Microwave Synthesis. *J. Mater. Chem. A* **2018**, *6* (25), 11564–11581. https://doi.org/10.1039/C8TA02919A.

(3) Horikoshi, S.; Matsuzaki, S.; Mitani, T.; Serpone, N. Microwave Frequency Effects on Dielectric Properties of Some Common Solvents and on Microwave-Assisted Syntheses: 2-Allylphenol and the C 12-C 2-C 12 Gemini Surfactant. *Radiat. Phys. Chem.* **2012**, *81* (12), 1885–1895. https://doi.org/10.1016/j.radphyschem.2012.07.011.

(4) Jain, P. K.; Huang, X.; El-Sayed, I. H.; El-Sayed, M. A. Review of Some Interesting Surface Plasmon Resonance-Enhanced Properties of Noble Metal Nanoparticles and Their Applications to Biosystems. *Plasmonics* **2007**, *2* (3), 107–118. https://doi.org/10.1007/s11468-007-9031-1.

(5) Yeh, Y. S.; Lue, J. T.; Zheng, Z. R. Measurement of the Dielectric Constants of Metallic Nanoparticles Embedded in a Paraffin Rod at Microwave Frequencies. *IEEE Trans. Microw. Theory Tech.* **2005**, *53* (5), 1756–1760. https://doi.org/10.1109/TMTT.2005.847093.

(6) Devic, T.; Horcajada, P.; Serre, C.; Salles, F.; Maurin, G.; Moulin, B.; Heurtaux, D.; Clet, G.; Vimont, A.; Grenéche, J. M.; et al. Functionalization in Flexible Porous Solids: Effects on the Pore Opening and the Host-Guest Interactions. *J. Am. Chem. Soc.* **2010**, *132* (3), 1127–1136. https://doi.org/10.1021/ja9092715.

(7) Fateeva, A.; Horcajada, P.; Devic, T.; Serre, C.; Marrot, J.; Grenèche, J.-M.; Morcrette, M.; Tarascon, J.-M.; Maurin, G.; Férey, G. Synthesis, Structure, Characterization, and Redox Properties of the Porous MIL-68(Fe) Solid. *Eur. J. Inorg. Chem.* **2010**, *2010* (24), 3789–3794. https://doi.org/10.1002/ejic.201000486.

(8) Horcajada, P.; Salles, F.; Wuttke, S.; Devic, T.; Heurtaux, D.; Maurin, G.; Vimont, A.; Daturi, M.; David, O.; Magnier, E.; et al. How Linker's Modification Controls Swelling Properties of Highly Flexible Iron(III) Dicarboxylates MIL-88. *J. Am. Chem. Soc.* **2011**, *133* (44), 17839–17847. https://doi.org/10.1021/ja206936e.

(9) Horcajada, P.; Chevreau, H.; Heurtaux, D.; Benyettou, F.; Salles, F.; Devic, T.; Garcia-Marquez, A.; Yu, C.; Lavrard, H.; Dutson, C. L.; et al. Extended and Functionalized Porous Iron(Iii) Tri- or Dicarboxylates with MIL-100/101 Topologies. *Chem. Commun.* **2014**, *50* (52), 6872–6874. https://doi.org/10.1039/c4cc02175d.

(10) Laybourn, A.; Katrib, J.; Palade, P. A.; Easun, T. L.; Champness, N. R.; Schröder, M.; Kingman, S. W. Understanding the Electromagnetic Interaction of Metal Organic Framework Reactants in Aqueous Solution at Microwave Frequencies. *Phys. Chem. Chem. Phys.* **2016**, *18* (7), 5419–5431. https://doi.org/10.1039/c5cp05426e.

(11) Arenas-Vivo, A.; Avila, D.; Horcajada, P. Phase-Selective Microwave Assisted Synthesis of Iron(III) Aminoterephthalate MOFs. *Materials (Basel).* **2020**, *13* (6), 1–12. https://doi.org/10.3390/ma13061469.

(12) Abou El-Nour, K. M. M.; Eftaiha, A.; Al-Warthan, A.; Ammar, R. A. A. Synthesis and Applications of Silver Nanoparticles. *Arab. J. Chem.* **2010**, *3* (3), 135–140. https://doi.org/10.1016/j.arabjc.2010.04.008.

(13) Pacioni, N. L.; Borsarelli, C. D.; Rey, V.; Veglia, A. V. Synthetic Routes for the Preparation of Silver Nanoparticles. In *Silver Nanoparticle Applications in the fabrication and design of medical and biosensing devices*; Alarcon, E., Griffith, M., Udekwu, K. I., Eds.; Springer International Publishing: Switzerland, 2015; pp 13–46. https://doi.org/10.1007/978-3-319-11262-6_2.

(14) Hühn, J.; Carrillo-Carrion, C.; Soliman, M. G.; Pfeiffer, C.; Valdeperez, D.; Masood, A.; Chakraborty, I.; Zhu, L.; Gallego, M.; Yue, Z.; et al. Selected Standard Protocols for the Synthesis, Phase Transfer, and Characterization of Inorganic Colloidal Nanoparticles. *Chem. Mater.* **2017**, *29* (1), 399–461. https://doi.org/10.1021/acs.chemmater.6b04738.

(15) Pastoriza-Santos, I.; Liz-Marzán, L. M. Formation of PVP-Protected Metal

Nanoparticles in DMF. *Langmuir* **2002**, *18* (7), 2888–2894. https://doi.org/10.1021/la015578g.

(16) Hunter, R. J. *Zeta Potential in Colloid Science : Principles and Applications*; Ottewi, R. H., Rowell, l R. L., Eds.; Academic Press: London, UK, 1988.

Chapter 6

BaS: Biocatalytic enzyme@MIL-88A

"Biocatalysis is a more environmentally friendly chemistry using enzymes. Our research brings closer this technology to industrial processes."

Paolo Falcaro, RADAR podcast of RAI, September 2020

6.1. Preamble

Apart from MNP, enzymes are also an interesting AS that could benefit from its immobilization in MOFs. Enzymes, as previously presented in Chapter 1 section 1.3.2.2 Enzymes: lipases, are promising green biocatalysts due to their high selectivity (chemo-, regio- and stereo selectivity), excellent efficiency, mild operative conditions (*i.e*: low temperature, atmospheric pressure), and high purity products, when compared with chemical catalysts. Lipases are a type of water soluble enzymes, that are extensively used in organic catalysis due to their ability to hydrolyze or synthesize a great number of carboxylic esters, not only in their natural environment (aqueous solutions) but also in organic solutions.[1] In addition they present broad substrate specificity and great commercial accessibility. For all the above-mentioned reasons, lipases have been selected in this thesis to synthesize lipase@MOF composites with enhanced properties. Heterogenization of the enzymatic biocatalyst by lipase immobilization has already proven to be an effective route to prevent their denaturalization under harsh catalytic conditions and to overcome some of their practical limitations (cyclability, miscibility).[2,3]

As seen in Chapter 1, MOFs have recently emerged as an alternative attractive enzymatic support.[4,5] From Table 1. 3 can be depicted that among the large palette of MOF structures, the zeolitic imidazole frameworks (ZIF-8, ZIF-67, ZIF-70, ZIF-90) stand out as representative framework extensively proposed for enzyme encapsulation. Most likely, these structures have been selected due to their facile synthesis compatible with enzyme stability (*e.g.*: aqueous solutions, RT reaction). In addition, the examples of lipase immobilization based on BaS procedures are still scarce. Therefore, this chapter presents a biofriendly *in situ* strategy for the encapsulation of lipases on the flexible biocompatible iron(III) fumarate MIL-88A (see 6.2 Introduction for further detail on MOF selection). Even the optimized green soft method for the preparation of lipase@MIL-88A biocomposites is here presented, further discussion on the influence of the different parameters of synthesis is also. In addition, present chapter includes full characterization of the optimized composites (*i.e.*: structure, thermal analysis, enzyme loading and enzymatic activity under different pH). Finally, as an interesting model reaction, catalytic activity of the lipase@MIL-88A was evaluated in the transesterification of soybean oil into biodiesel in a solvent-free medium. This illustrative reaction will help to further analyze the role of MOF in the activity of the biocatalyst, and the possible interaction between host and guest lipase.

This work originality comes from:

- The reporting of a new BaS strategy to immobilize lipases validated with two lipases of different size.
- The use of MIL-88A as host for lipases, as representative of alternative MOF support to ZIF structures.
- The verification of the lipase activity after immobilization under harsh conditions.
- The validation of the biocatalyst composites on a relevant reaction such as biodiesel production in the absence of solvents (green reaction).
- The qualitative identification of the reaction products to analyze the possible active role of the MOF in synergy with the lipase on product selectivity.

Author contribution: Conceptualization of this work was performed by Dr. Patricia Horcajada, AAV and Dr. Sara Rafiei. Experimental works were carried out at IMDEA Energy, using APMU, Thermochemical Processes Unit and Biotechnological Processes Unit lab installations. Material synthesis and optimization was done by Dr. S. Rafiei and AAV, with the help of the laboratory technicians, Miriam Bravo and Ayoub Benckhlafa. Lipase@MIL-88A biocomposite was characterised using techniques available at IMDEA Energy. Dr. Tania Hidalgo assisted in the composite scale-up and validation of the enzyme activity after

encapsulation and Dr. Yolanda Pérez aided in the identification of the transesterification reaction products by gas chromatography coupled to mass spectrometry. Result analysis and discussion was done by AAV and Dr. P. Horcajada. This work is pending of publication. Writing of the original draft is being carried out by AAV and manuscript review involves Dr. P. Horcajada and Dr. S. Rafiei.

6.2. Introduction

Lipase-immobilization in MOFs has been traditionally used as an inert heterogeneous support (providing stabilization, easy separation, and recyclability), without paying attention to the potential synergy of both the enzymatic biocatalyst and the MOF. The MOF structure active role on biocatalysis is almost unexplored. Only the recent work of Gkaniatsou *et al.* reports the selective oxidation of model dyes using a microperoxidase-8 immobilized in the robust mesoporous chromium terephthalate MIL-101(Cr) *via* selective electrostatic adsorption of reactants.[6] Moreover, reaction selectivity has been achieved through selective diffusion of the reagents through the MOF porosity.[7] However, although production enhancement[8,9] or perseverance of the free-lipase selectivity[10,11] have been previously reported, there is few information available about synergic product selectivity using immobilized lipases, even in other supports. From the scarce reports, Cabrera *et al.* immobilized *Candida antartica* lipase type B in different hydrophobic supports (butyl agarose and acrylic polymers), finding an enantioselective hydrolysis of (R,S)2-*O*-butyryl-2-phenylacetic acid depending on the acrylic polymer.[12] Recently, Verdasco-Martin research group essayed a battery of biocatalysts, evidencing that the most regioselective towards partial glycerides was based on a *Rhizomucor miehei* lipase immobilized on a porous methacrylic support.[13] On account of that, this chapter not only seeks to immobilize lipases on a MOF *via* a BaS procedure, but also pursues to explore the potential synergic effect between lipase-MOF.

Enzymatic biodiesel production has been selected as model reaction to explore the role of the MOF in the biocomposite catalytic activity. Biodiesel production using enzyme-immobilized MOFs is a very recent topic. Our group originally reported the use of the microporous zinc methylimidazolate ZIF-67 with *Candida rugose* lipase for biodiesel synthesis production via solvent-free transesterification of soybean oil into fatty acid methyl esters (FAMEs).[14] Other authors followed using the benchmarked microporous zinc imidaolate ZIF-8 with the adsorption of *Burkholderia cepacia* lipase, or the *in situ* entrapment of the *Rhizomucor miehei* lipase;[15,16] and the microporous zirconium terephthalate UiO-66 with the surface modified by polydimethylsiloxane to increase the MOF

hydrophobicity, was used for the pore diffusion of *Apergillus niger* lipase for the same biodiesel reaction.[17]

In this work, the biocompatible flexible microporous iron(III) fumarate, MIL-88A was selected as support for lipase immobilization. MIL-88A is based on iron(III) octahedral trimers connected by fumarate anions (*P*-62c) with a reversible pore opening: from an open porosity of 6-7 Å in aqueous solution ($V_{u.c.}$ ~ 2120 Å^3) to a close form dehydrated, unit cell volume ($V_{u.c.}$ ~ 1180 Å^3).[18] MIL-88A is not only interesting for its sorption selectivity and flexibility but also is completely biocompatible since based on abundant, low-cost and endogenous moieties (*i.e.*: iron and fumarate), and can be prepared using a simple and totally green soft synthetic method (ambient pressure, low temperature and aqueous conditions), compatible with the enzyme stability.[19] In the case of the biocatalyst, lipases from *Pseudomonas fluorescens* (*P-f*-lipase) were employed as a model protein (molecular weight of 34 kDa and optimum pH range of 6.5-8.5) with extended use in the bio-transesterification reaction for biodiesel production.[20–23] For comparison purposes, also *Candida rugose* lipase (*C-r*-lipase) was encapsulated, which has a higher molecular weight of 60 kDa and optimum activity in the pH range 6.5-7.5. *C-r*-lipases have a wide range of catalytic activity in both aqueous and water-restricted environments, which include non-specific and stereo-specific hydrolysis, reversal of hydrolysis via esterification, trans-esterification and inter-esterification.[24–26]

6.3. Synthesis

Lipase@MIL-88A biocatalysts were successfully synthesized following an *in situ* simple, rapid and soft green two-step protocol. Different parameters were optimized: i) temperature, to ensure MOF formation and enzyme stability, ii) pH, related with reaction kinetics, enzyme denaturalization and MOF-enzyme electrostatic interactions, iii) time, allied with enzyme immobilization efficiency, and iv) enzyme-MOF ratio, to maximize biocatalyst activity (further discussion on this is included on APPENDIX VII section VII.II.ii Synthetic protocol optimization). Optimal protocol is here resumed (Figure 6. 1).

In the first step, a solution of $FeCl_3.6H_2O$ (1 mmol) and fumaric acid (1 mmol) in 5 mL of distilled water was placed under stirring in a round bottom flask at 65 °C for 10 min. The obtained as-synthesized MIL-88A solid was recovered by centrifugation (5000 rpm, 20 min) and kept in an oven at 100 °C for drying for 1 h. Then, in a typical experiment, 100 mg of as-synthesized MIL-88A solid and 10 mg of lipase (*P-f*-lipase or *C-r*-lipase*)* in 5 mL of distilled water, were added to a round bottom flask, adjusting the pH to 3 by the addition of a 0.1 M NaOH

solution, and kept at 50 °C for 2 h under stirring. The obtained lipase@MIL-88A composite was washed twice with 10 mL of distilled H_2O and recovered by centrifugation (5000 rpm, 10 min). It is important to highlight that the methodology designed enables both the synthesis of the MOF with outstanding crystallinity, while preserving the activity of the lipases.

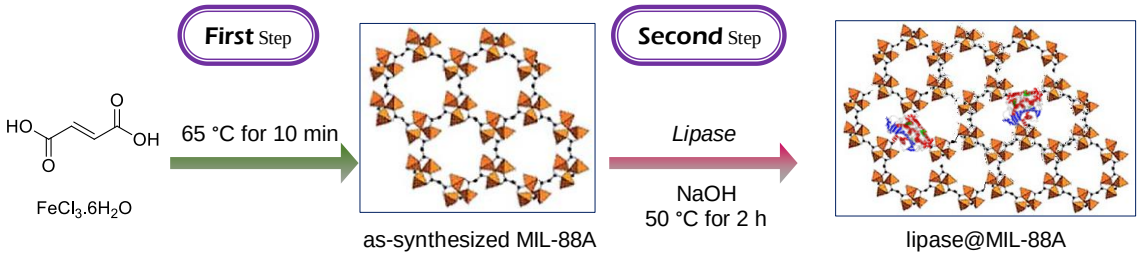

Figure 6. 1: Representation of the preparation of the lipase@MIL-88A biocatalysts, together with the schematic view of the structure of MIL-88A. Iron polyhedral and carbon atoms are in orange and black, respectively. Hydrogen atoms have been omitted for clarity.

6.4. Characterization

Once optimized, both *P-f*-lipase@MIL-88A and *C-r*-lipase@MIL-88A biocatalysts were fully characterized. Crystalline structure of the *P-f*-lipase@MIL-88A and *C-r*-lipase@MIL-88A biocomposites was confirmed by X-ray powder diffraction (XRPD, see Figure 6. 2). Although limited by the flexible character of MIL-88A framework, the direct comparison of these samples by XRPD with a blank MIL-88A (synthesized in absence of enzyme) suggests that the amount of enzyme does not strongly affect the MOF crystallinity.

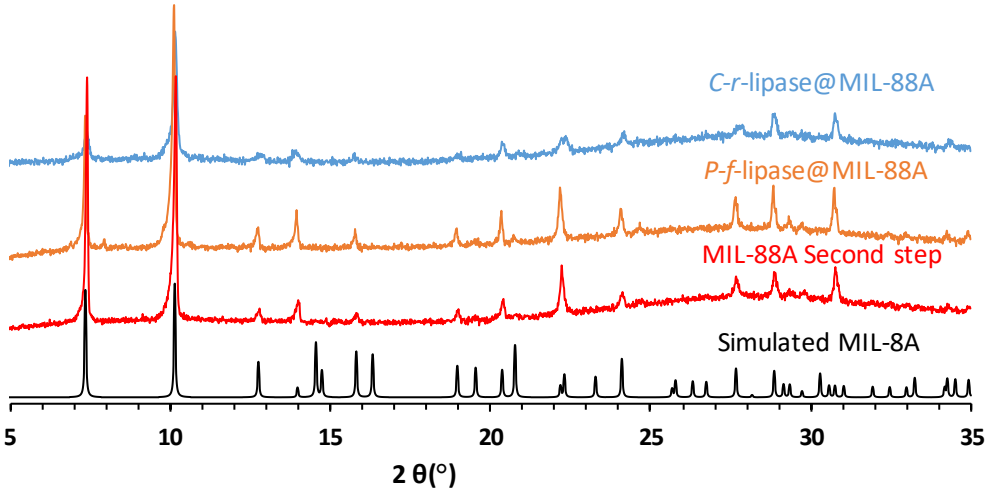

Figure 6. 2: XRPD patterns of simulated MIL-88A (black), MIL-88A second step (in absence of enzyme, red), *P-f*-lipase@MIL-88A(orange) and *C-r*-lipase@MIL-88A (blue)

In addition, scanning electron microscopy (SEM) images,Figure 6. 3, showed micrometric elongated hexagonal needles (length x thickness = 2.0 ± 0.5 x 0.24 ± 0.08 μm), with a significantly increased thickness in the lipase presence (0.6 ± 0.2 and 0.5 ± 0.1 μm for *P-f* and *C-r*-lipase@MIL-88A, respectively, and Table AVII. 3 from APPENDIX VII) suggesting a crystal growth around the enzyme (see Figure 6. 3).

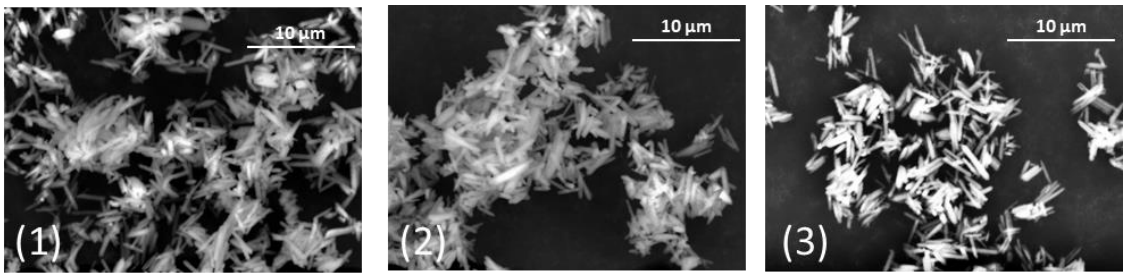

Figure 6. 3: SEM micrographs of MIL-88A (1) (in absence of enzyme), *P-f*-lipase@MIL-88A (2) and *C-r*-lipase@MIL-88A (3).

Quantitative determination of the enzyme encapsulation was carried out both by the Bradford method (UV-Vis spectroscopy) and thermogravimetric analysis (TGA) (see APPENDIX VI section VII.II Biocatalyst preparation for further information on procedures). In the case of *P-f*-lipase, Bradford analysis determined and encapsulation efficiency of 99.1 ± 0.5%, corresponding to a loading of 9.9 ± 0.5 wt.%. Whereas for *C-r*-lipase@MIL-88A, the enzyme loaded and the efficiency was slightly lower (8.6 ± 0.5 wt.% and 95.2 ± 0.6%, respectively, Table AVII. 2). As a complementary quantitative analysis to protein Bradford Method, TGA experiments were done to MIL-88A, *P-f*-lipase@MIL-88A and *C-r*-lipase@MIL-88A. TGA of MIL-88A (see Figure 6. 4) exhibited minor weight loss below 150 °C, associated to water removal from MIL-88A porosity. Thermal decomposition of MIL-88A started at 280 °C and degradation was completed at 500 °C (residual Fe_3O_2 theo. *vs.* exp. = 48 and 45%; in agreement with a small amount of unreacted fumaric acid). TGA curves of *P-f*-lipase@MIL-88A and *C-r*-lipase@MIL-88A exhibited an additional weight loss between 150 and 500 °C, attributed to the decomposition an organic fraction. This extra-organic content was assigned to *P-f*-lipase and *C-r*-lipase molecules, enabling the determination of ~8 and ~7 wt.% of lipase associated to the MOF, which is in agreement with the results obtained from the Bradford method (see Table 6. 1).

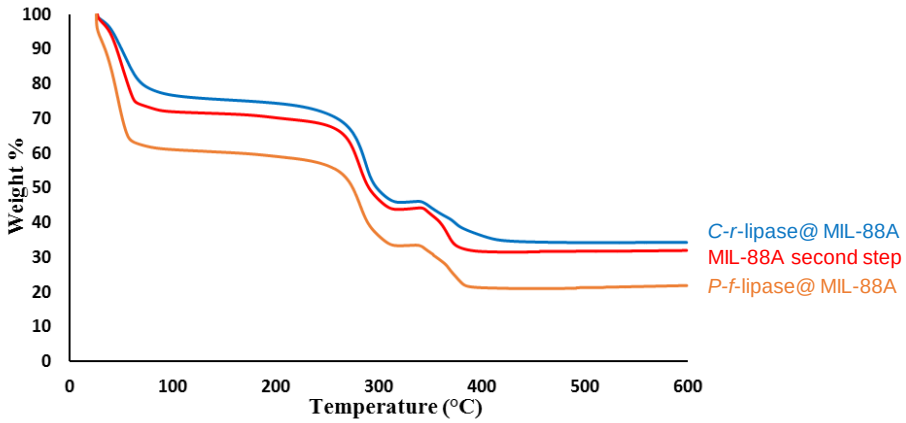

Figure 6. 4: TGA of MIL-88A (red), *P-f-* lipase@MIL-88A (orange) and *C-r*-lipase@MIL-88A (blue).

Table 6. 1: Comparison between TGA and Bradford assay results

	TGA	Bradford method
Sample	Lipase wt.%	Lipase wt.%[a]
P-f-lipase@MIL-88A	8.3 ± 0.5	9.9 ± 0.5
C-r-lipase@MIL-88A	6.7 ± 0.5	8.6 ± 0.5

[a] Theoretical enzyme weight % in the composite corrected by the encapsulation efficiency determined by the Bradford method

Lipase immobilization was also confirmed by Fourier transform infrared (FTIR) spectroscopy (see Figure 6. 5), as both biocatalysts showed an absorption band at about 1050 cm^{-1}, corresponding to C-N stretching vibration mode of amino acids, also present in the free lipase spectra. In addition, there is a slight shift of the 1515 cm^{-1} peak to higher wavenumbers (1523 and 1525 cm^{-1} for *P-f* and *C-r*-lipase respectively), indicating interaction of Fe with the lipases.[27] It should be noted that due to MIL-88A flexible character, exhibiting a closed porosity when outgassed (empty), N_2 sorption analysis was not possible.[18,19]

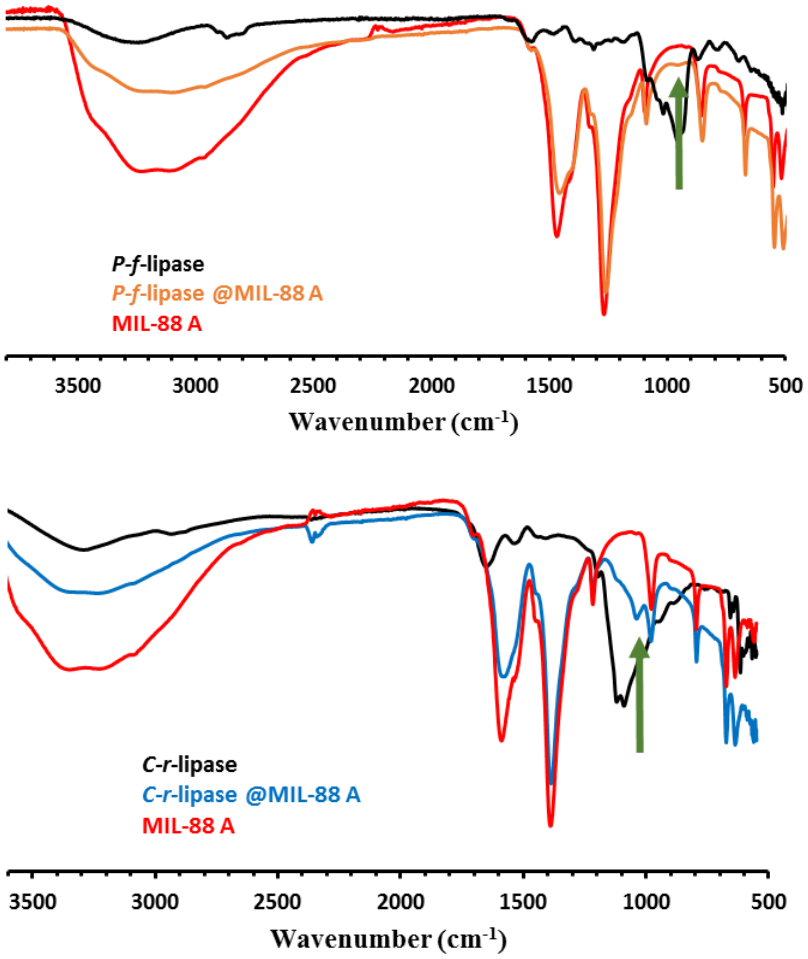

Figure 6. 5: FTIR spectra of MIL-88A (red), free enzymes (black) and lipase@MIL-88A for (top, orange) *P-f*-lipase and (bottom, blue) *C-r*-lipase.

Following, the enzymatic activity of the encapsulated lipases was confirmed by a model reaction, quantifying the relative ester hydrolysis of *p*-nitrophenyl palmitate (*p*-NPP) promoted by the macromolecules (see APPENDIX VII section VII.II.i **Lipase encapsulation and activity assay**). Both *P-f* and *C-r*-lipase@MIL-88A gave similar activity with a production of ~ 7 g *p*-nitrophenol · g^{-1} lipase (see Table AVII. 2). To further confirm the protective effect of the framework on the lipase, preventing its denaturalization, the final activity of the lipase@MOFs was evaluated after exposure to different pH (see procedure on APPENDIX VII section VII.II.iii Biocatalyst characterization). Figure 6. 6 discloses the relative catalytic activities (the maximum observed activity has been defined as 100% for comparison purposes) of native and encapsulated lipases at pH ranging from 2 to 5. Although the relative activity of both the free and encapsulated lipases did not show any considerable difference within the pH 3-4 range, *P-f*-lipase@MIL-88A and *C-r*-lipase@MIL-88A demonstrated a better stability compared with the free lipases at pH 2 and 5. This result emphasizes the improved chemical and structural stability of the embedded lipases within the MIL-88A matrix under punitive

environmental conditions, extending the use of the biocatalyst under a wider pH region (below their optimum pH range). This result fulfills one of the objectives of BaS lipase immobilization, raised at the beginning of the work.

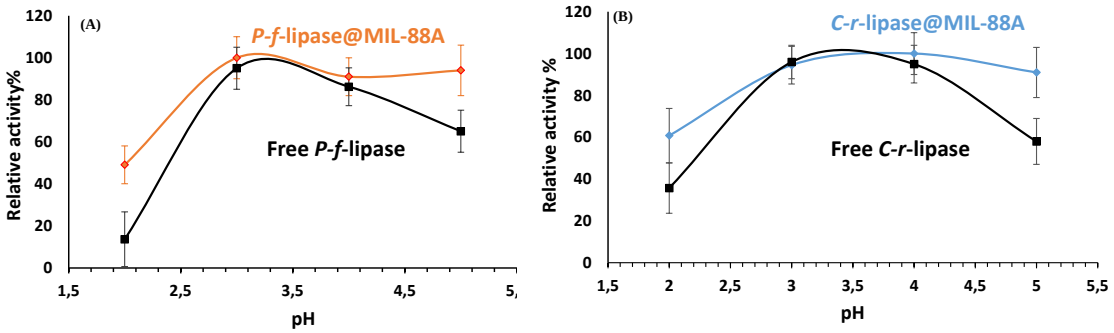

Figure 6. 6: Catalytic activity of (A) *P-f*-lipase@MIL-88A (orange), and (B) *C-r*-lipase@MIL-88A (blue) as a function of pH in comparison with the free enzymes (black).

6.5. Biodiesel production

After full characterization of the biocatalyst proving the immobilization of the lipase, their activity and the protective role of the MOF, they were used as catalyst in an illustrative reaction. The catalytic activity of the biocatalysts towards biodiesel production from soybean oil, was cualitatively evaluated, optimizing the reaction conditions (temperature, time, water content and methanol:oil ratio) for achieving the highest biodiesel selectivity (FAME transesterification *vs.* fatty acid hydrolisis). It is of great importance to highlight that here is pursued a green reaction in absence of solvents, which allows reducing byproducts, pollution and risks to human health, while maximizing the reaction rate. Here, soybean oil, composed mainly by palmitic acid (11 wt.%, C16:0 A), stearic acid (5 wt.%, C18:0 A), oleic acid (24 wt.%, C18:1 A), linoleic acid (49 wt.% C18:2 A) and linolenic acid (7 wt.%, C18:3 A) (APPENDIX VII, section VII.I Materials and characterization techniques, is employed as fatty acid source for the transesterification reaction,[28] and methanol, as the alcohol source. Further details of the biodiesel production can be found in the APPENDIX VII section VII.III Biodiesel production.

6.5.1. Effect of Temperature

Temperature is a key parameter that strongly affects the kinetics of the transesterification reaction and also to the catalytic activity of the encapsulated lipases. Therefore, different temperatures (40, 50 and 60 ºC) were investigated to determine the optimum reaction temperature (Figure 6. 7). While the optimum reaction temperature with *P-f*-lipase@MIL-88A was found to be 50 °C (with a biodiesel selectivity of 69 ± 4%), the statistical hypothesis Student's *t*-test indicated that for the case of *C-r*-lipase@MIL-88A, there was no significant difference in between the different studied temperatures ($t_{(T=40\text{-}50\ °C)} = 0.05$ and $t_{(T=50\text{-}60\ °C)} = 0.10$, being $t_{0.90}(n=4) = 1.5$). In consequence, the lowest temperature (40 °C) was selected as optimum for *C-r*-lipase@MIL-88A (81 ± 1% biodiesel selectivity) since it represents an economic advantage.[29]

6.5.2. Impact of reaction time

Considering the relevance of the biodiesel production at industrial scale, reaction time is an important factor to consider, as it is directly related with the final production cost.[29] For both biocatalysts, 12 h of reaction produced lower biodiesel selectivity than 24 h (50% *vs.* 70% and 75% *vs.* 80%; Figure 6. 7). Once again, the Student's *t*-test was applied to statistically discriminate the data, concluding that no significant differences were found in the biodiesel production at 24 and 48 h. Therefore, the optimum reaction time for *P-f*-lipase@MIL-88A was set to be 24 h (69 ± 4%). Similarly, statistical analysis with the biodiesel produced by *C-r*-lipase@MIL-88A also determined an optimum reaction time of 24 h, for being the shorter reaction time associated with higher reaction selectivity (81 ± 1%).

6.5.3. Role of water content

When using solvent free systems, the water concentration is crucial in lipase-catalyzed FAME production since water content prevents the inactivation of lipase by methanol. Therefore, by decreasing water content, the reaction rate of methanolysis significantly decreases. However, the water excess around lipase covers the polar site of the enzyme, which finally reduces its activity and reaction rate.[30] In this regard, the optimization of the water concentration was examined within the range of 5–15 wt.% of oil weight. While the maximum selectivity was obtained using 5 wt.% of water in the case of *P-f*-lipase@MIL-88A (69 ± 4%; Figure

6. 7), increasing the amount to 10 wt.% led to an 87 ± 2% biodiesel selectivity for *C-r*-lipase@MIL-88A. Therefore, the selected water contents were 5 and 10 wt.% for *P-f*-lipase@MIL-88A and *C-r*-lipase@MIL-88A, respectively.

6.5.4. Influence of molar oil/methanol ratio

The investigation of the methanol to soybean oil molar ratio is of high relevance due to the negative effect that the excess of methanol exerts on the lipase activity.[31] As shown in Figure 6. 7, higher methanol amounts significantly increased the biodiesel selectivity obtained using *P-f*-lipase@MIL-88A biocatalyst, reaching 95 ± 1% with 4:1 methanol:oil molar ratio. Further increments of methanol content did not significantly increase the produced biodiesel. A similar behavior was observed with *C-r*-lipase@MIL-88A, reaching an almost 100% conversion into FAME with a 4:1 methanol:oil molar ratio.

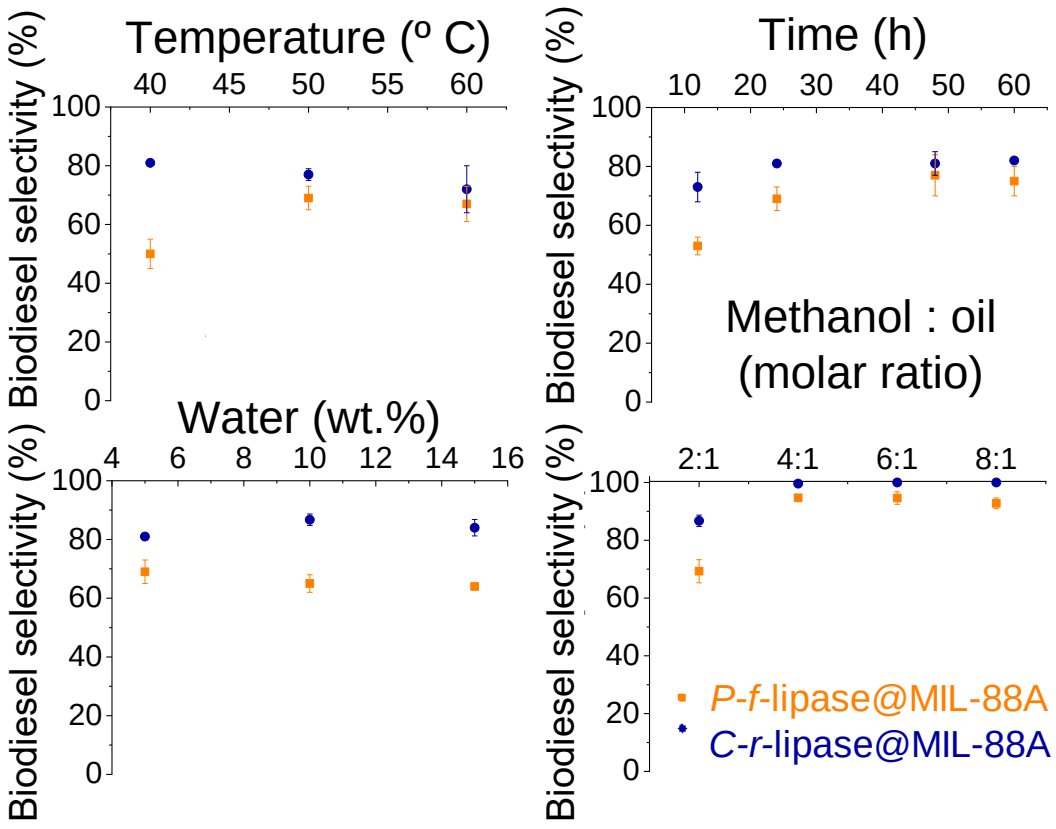

Figure 6. 7: Effect of different reaction parameters in the transesterification of soybean oil with methanol catalyzed by *P-f*-lipase@MIL-88A (orange) and *C-r*-lipase@MIL-88A (blue): Temperature, Time, Water (wt.%) and methanol:oil (molar ratio)..

The optimal reaction conditions found for *P-f*-lipase@MIL-88A with a biodiesel yield of 95% were: 50 °C, 24 h, 5 wt.% H_2O and 4:1 methanol:oil molar ratio. Similarly, the optimum biodiesel yield (99%) for *C-r*-lipase@MIL-88A was reached at 40 °C, 24 h, 10 wt.% H_2O and 4:1 methanol:oil molar ratio.

6.5.5. Biocatalyst recovery and reuse

Considering the promising biodiesel production using *P-f*-lipase@MIL-88A, its reusability and recyclability was further asseseed over sequential transesterification reactions. A progressive decay in the biodiesel selectivity (%) can be observed over time, with a catalytic activity loss from 95 to 60% after 5 consecutive cycles (Figure 6. 8). Despite this decrease, the reciclability of the biocatalyst is an important outcome of lipase immobilization on MIL-88A. The biocatalyst here presented has a reusability in the range of other previously reported lipase@MOF for biodiesel production (5-10 cycles).[14–16,32]

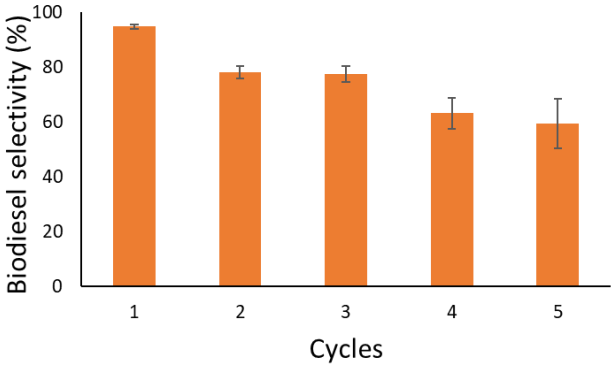

Figure 6. 8: Reusability of *P-f*-lipase@MIL-88A for the soybean oil transesterification into biodiesel under optimum reaction conditions (biodiesel selectivity, %)

This activity loss can be explained by the slight MIL-88A degradation, as observed by XRPD and FTIR (Figure 6. 9). Particullay it can be seen that after 5 cycles the reduction in MOF crystallinity after 5 cycles enabled the release of the immobilized lipase as more bands corresponding to *P-f*-lipase can be seen in FTIR spectra of *P-f*-lipase@MIL-88 A (Figure 6. 9 B, red arrows pointing 300-2800 cm^{-1} and 1100-1000 cm^{-1} C-N vibrations), as upon partial MOF degradation the lipase reaches the MOF surface and could be easily leached.

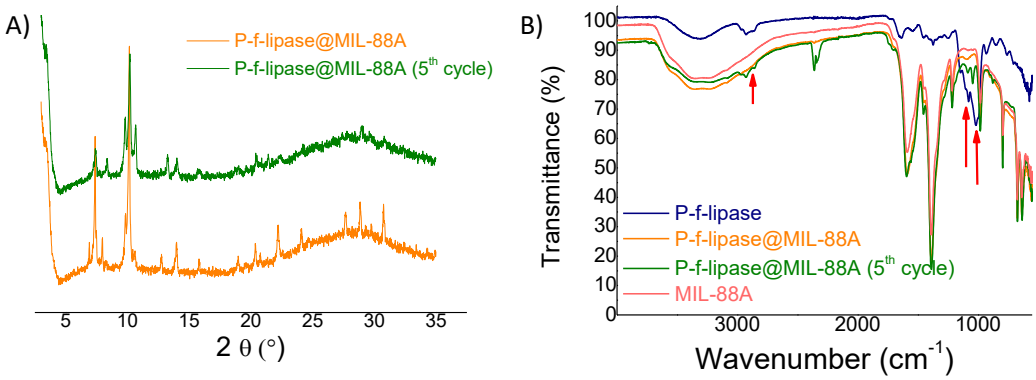

Figure 6. 9: A) XRPD pattern of the *P-f*-lipase@MIL-88A biocatalyst as synthesized (orange) and after 5 biodiesel reaction cycles (green). B) FTIR of MIL-88A (pink), *P-f*-lipase (blue), and *P-f*-lipase@MIL-88A (orange) and *P-f*-lipase@MIL-88A after 5 biodiesel reaction cycles (green)

6.5.6. Qualitative product identification

Interest in the determination of a possible effect of the MOF in the biocomposites activity towards the synthesis of biodiesel, reaction products were identified by means of gas chromatography-mass spectrometry of reference samples of the resultant FAMEs: methyl palmitate (C16:0 E), methyl steareate (C18:0 E), methyl oleate (C18:1 E), methyl linoleate (C18:2 E) and methyl linolenate (C18:3 E).

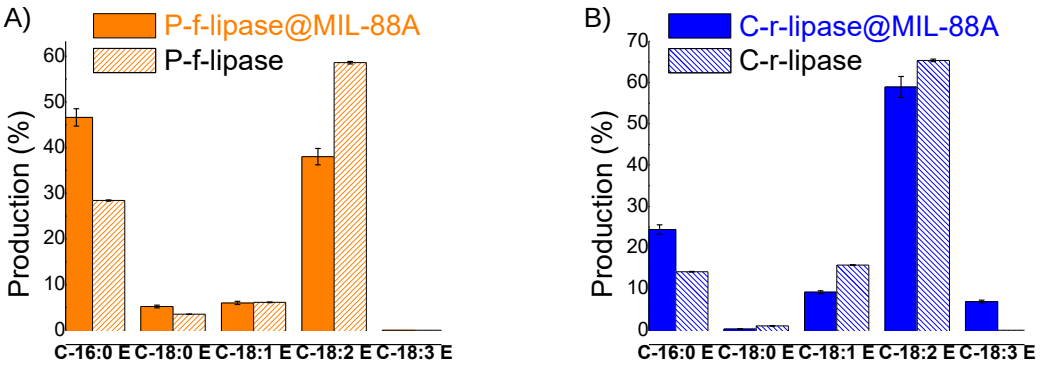

Figure 6. 10: Qualitative assessment of the of the FAMEs produced after transesterification of soybean oil with methanol: A) Production (%) catalyzed by *P-f*-lipase@MIL-88A (orange) and by free *P-f*-lipase (diagonal orange stripes). A) Production (%) catalyzed by *C-r*-lipase@MIL-88A (blue) and by free *C-r*-lipase (diagonal blue stripes). Key of products: methyl palmitate (C16:0 E), methyl steareate (C18:0 E), methyl oleate (C18:1 E), methyl linoleate (C18:2 E) and methyl linolenate (C18:3 E)

Remarkably, different product selectivity was found depending on the lipase immobilized in the MIL-88A (see Figure 6. 10). While *P-f*-lipase@MIL-88A

promotes the attainment of the saturated ester C-16:0 E (besides being only present in the oil in a 11 wt.%), *C-r*-lipase@MIL-88A led primarily to the unsaturated ester methyl linoleate C1-18:2 E as major reaction product (according to the predominant presence of linoleic acid in a 49 wt.%). Interestingly, there is no such selectivity in between the biodiesel products catalyzed by the free enzymes, under same reaction conditions, confirming a remarkable extra selectivity originated by the MOF structure, never described so far for any enzyme@MOF biocomposite.

6.6. Final remarks

From the obtained results in this chapter different conclusions can be deduced. First, BaS methods can be efficiently applied for the synthesis of lipase@MOFs. Second, the green environmentally friendly synthetic procedure presented in this chapter is compatible for the encapsulation of lipases on MIL-88A, presenting the solid as a new host matrix to immobilize enzymes. Third the immobilization of both *P-f* and *C-r*-lipases increases their stability under harsh reaction conditions (extreme pH) and the reusability of the enzyme. Forth, the lipase@MIL-88A biocatalyst is robust on the challenging solvent-free transesterification of soybean oil to biodiesel with almost no byproduct production (undesired fatty acid). Fifth, the qualitative identification of the biodiesel products stresses the relevance of the proper selection of the lipase-MOF pair to promote its active role on the immobilized enzyme selectivity and maximize the composite biocatalytic activity.

Finally, these results demonstrate the potential of lipase@MOF biocatalysts for the application of enzyme catalysis on relevant industrial reactions, leading to a future of environmentally friendly chemical manufacturing processes.

Bibliography

(1) Reetz, M. T. Lipases as Practical Biocatalysts. *Curr. Opin. Chem. Biol.* **2002**, *6* (2), 145–150. https://doi.org/10.1016/S1367-5931(02)00297-1.

(2) Mateo, C.; Palomo, J. M.; Fernandez-Lorente, G.; Guisan, J. M.; Fernandez-Lafuente, R. Improvement of Enzyme Activity, Stability and Selectivity via Immobilization Techniques. *Enzyme Microb. Technol.* **2007**, *40* (6), 1451–1463. https://doi.org/10.1016/j.enzmictec.2007.01.018.

(3) Rodrigues, R. C.; Ortiz, C.; Berenguer-Murcia, Á.; Torres, R.; Fernández-Lafuente, R. Modifying Enzyme Activity and Selectivity by Immobilization. *Chem. Soc. Rev.* **2013**, *42* (15), 6290–6307. https://doi.org/10.1039/C2CS35231A.

(4) Férey, G. Hybrid Porous Solids: Past, Present, Future. *Chem. Soc. Rev.* **2008**, *37* (1), 191–214. https://doi.org/10.1039/B618320B.

(5) Gkaniatsou, E.; Sicard, C.; Ricoux, R.; Mahy, J.-P.; Steunou, N.; Serre, C. Metal–Organic Frameworks: A Novel Host Platform for Enzymatic Catalysis and Detection. *Mater. Horiz.* **2017**, *4* (1), 55–63. https://doi.org/10.1039/C6MH00312E.

(6) Gkaniatsou, E.; Sicard, C.; Ricoux, R.; Benahmed, L.; Bourdreux, F.; Zhang, Q.; Serre, C.; Mahy, J.-P.; Steunou, N. Enzyme Encapsulation in Mesoporous Metal-Organic Frameworks for Selective Biodegradation of Harmful Dye Molecules. *Angew. Chemie Int. Ed.* **2018**, *57* (49), 16141–16146. https://doi.org/10.1002/anie.201811327.

(7) Lian, X.; Fang, Y.; Joseph, E.; Wang, Q.; Li, J.; Banerjee, S.; Lollar, C.; Wang, X.; Zhou, H.-C. Enzyme–MOF (Metal–Organic Framework) Composites. *Chem. Soc. Rev.* **2017**, *46* (11), 3386–3401. https://doi.org/10.1039/C7CS00058H.

(8) Hernandez, K.; Garcia-Galan, C.; Fernandez-Lafuente, R. Simple and

Efficient Immobilization of Lipase B from Candida Antarctica on Porous Styrene–Divinylbenzene Beads. *Enzyme Microb. Technol.* **2011**, *49* (1), 72–78. https://doi.org/10.1016/J.ENZMICTEC.2011.03.002.

(9) Tacias-Pascacio, V. G.; Virgen-Ortíz, J. J.; Jiménez-Pérez, M.; Yates, M.; Torrestiana-Sanchez, B.; Rosales-Quintero, A.; Fernandez-Lafuente, R. Evaluation of Different Lipase Biocatalysts in the Production of Biodiesel from Used Cooking Oil: Critical Role of the Immobilization Support. *Fuel* **2017**, *200*, 1–10. https://doi.org/10.1016/J.FUEL.2017.03.054.

(10) Jung, S.; Kim, Y.; Kim, S.-J.; Kwon, T.-H.; Huh, S.; Park, S. Bio-Functionalization of Metal–Organic Frameworks by Covalent Protein Conjugation. *Chem. Commun.* **2011**, *47* (10), 2904. https://doi.org/10.1039/c0cc03288c.

(11) Bracco, P.; Torrelo, G.; Noordam, S.; de Jong, G.; Hanefeld, U.; Bracco, P.; Torrelo, G.; Noordam, S.; De Jong, G.; Hanefeld, U. Immobilization of Prunus Amygdalus Hydroxynitrile Lyase on Celite. *Catalysts* **2018**, *8* (7), 287. https://doi.org/10.3390/catal8070287.

(12) Cabrera, Z.; Fernandez-Lorente, G.; Fernandez-Lafuente, R.; Palomo, J. M.; Guisan, J. M. Novozym 435 Displays Very Different Selectivity Compared to Lipase from Candida Antarctica B Adsorbed on Other Hydrophobic Supports. *J. Mol. Catal. B Enzym.* **2009**, *57* (1–4), 171–176. https://doi.org/10.1016/J.MOLCATB.2008.08.012.

(13) Verdasco-Martín, C. M.; Garcia-Verdugo, E.; Porcar, R.; Fernandez-Lafuente, R.; Otero, C. Selective Synthesis of Partial Glycerides of Conjugated Linoleic Acids via Modulation of the Catalytic Properties of Lipases by Immobilization on Different Supports. *Food Chem.* **2018**, *245*, 39–46. https://doi.org/10.1016/J.FOODCHEM.2017.10.072.

(14) Rafiei, S.; Tangestaninejad, S.; Horcajada, P.; Moghadam, M.; Mirkhani, V.; Mohammadpoor-Baltork, I.; Kardanpour, R.; Zadehahmadi, F. Efficient Biodiesel Production Using a Lipase@ZIF-67 Nanobioreactor. *Chem. Eng. J.* **2018**, *334*, 1233–1241. https://doi.org/10.1016/J.CEJ.2017.10.094.

(15) Adnan, M.; Li, K.; Wang, J.; Xu, L.; Yan, Y. Hierarchical ZIF-8 toward Immobilizing Burkholderia Cepacia Lipase for Application in Biodiesel Preparation. *Int. J. Mol. Sci.* **2018**, *19* (5), 1424. https://doi.org/10.3390/ijms19051424.

(16) Adnan, M.; Li, K.; Xu, L.; Yan, Y.; Adnan, M.; Li, K.; Xu, L.; Yan, Y. X-Shaped ZIF-8 for Immobilization Rhizomucor Miehei Lipase via Encapsulation and Its Application toward Biodiesel Production. *Catalysts*

2018, *8* (3), 96. https://doi.org/10.3390/catal8030096.

(17) Hu, Y.; Dai, L.; Liu, D.; Du, W. Rationally Designing Hydrophobic UiO-66 Support for the Enhanced Enzymatic Performance of Immobilized Lipase. *Green Chem.* **2018**, *20* (19), 4500–4506. https://doi.org/10.1039/c8gc01284a.

(18) Mellot-Draznieks, C.; Serre, C.; Surblé, S.; Audebrand, N.; Férey, G. Very Large Swelling in Hybrid Frameworks: A Combined Computational and Powder Diffraction Study. *J. Amreican Chem. Soc.* **2005**, *127* (46), 16273–16278. https://doi.org/10.1021/JA054900X.

(19) Horcajada, P.; Chalati, T.; Serre, C.; Gillet, B.; Sebrie, C.; Baati, T.; Eubank, J. F.; Heurtaux, D.; Clayette, P.; Kreuz, C.; et al. Porous Metal-Organic-Framework Nanoscale Carriers as a Potential Platform for Drug Delivery and Imaging. *Nat. Mater.* **2010**, *9*, 172–178. https://doi.org/10.1038/nmat2608.

(20) Kulkarni, N. Studies on Lipase Enzyme from Pseudomonas Fluorescens NS2W, University of Pune (India), 2002.

(21) Kanimozhi, S.; Perinbam, K. Biodesel Production from *Pseudomonas Fluorescens* Lp1 Lipase Immobilized on Amino-Silane Modified Super Paramagnetic Fe $_3$ O $_4$ Nanoparticles. *J. Phys. Conf. Ser.* **2013**, *431* (1), 012010. https://doi.org/10.1088/1742-6596/431/1/012010.

(22) Lima, L. N.; Oliveira, G. C.; Rojas, M. J.; Castro, H. F.; Da Rós, P. C. M.; Mendes, A. A.; Giordano, R. L. C.; Tardioli, P. W. Immobilization of Pseudomonas Fluorescens Lipase on Hydrophobic Supports and Application in Biodiesel Synthesis by Transesterification of Vegetable Oils in Solvent-Free Systems. *J. Ind. Microbiol. Biotechnol.* **2015**, *42* (4), 523–535. https://doi.org/10.1007/s10295-015-1586-9.

(23) Cubides-Roman, D. C.; Pérez, V. H.; de Castro, H. F.; Orrego, C. E.; Giraldo, O. H.; Silveira, E. G.; David, G. F. Ethyl Esters (Biodiesel) Production by Pseudomonas Fluorescens Lipase Immobilized on Chitosan with Magnetic Properties in a Bioreactor Assisted by Electromagnetic Field. *Fuel* **2017**, *196*, 481–487. https://doi.org/10.1016/J.FUEL.2017.02.014.

(24) Domínguez de María, P.; Sánchez-Montero, J. M.; Sinisterra, J. V.; Alcántara, A. R. Understanding Candida Rugosa Lipases: An Overview. *Biotechnol. Adv.* **2006**, *24* (2), 180–196. https://doi.org/10.1016/J.BIOTECHADV.2005.09.003.

(25) Öztürk, B. Immobilization of Lipase from Candida Rugosa on Hydrophobic and Hydrophilic Supports, Izmir Institute of Technology (Turkey), 2001.

(26) Cygler, M.; Schrag, J. D. Structure and Conformational Flexibility of

Candida Rugosa Lipase. *Biochim. Biophys. Acta - Mol. Cell Biol. Lipids* **1999**, *1441* (2–3), 205–214. https://doi.org/10.1016/S1388-1981(99)00152-3.

(27) Liang, K.; Ricco, R.; Doherty, C. M.; Styles, M. J.; Bell, S.; Kirby, N.; Mudie, S.; Haylock, D.; Hill, A. J.; Doonan, C. J.; et al. Biomimetic Mineralization of Metal-Organic Frameworks as Protective Coatings for Biomacromolecules. *Nat. Commun.* **2015**, *6* (1), 7240. https://doi.org/10.1038/ncomms8240.

(28) Baughman, W. F.; Jamieson, G. S. Thechemical Composition of Soya Bean Oil. *J. Am. Chem. Soc.* **1922**, *44* (12), 2947–2952. https://doi.org/10.1021/ja01433a035.

(29) Gebremariam, S. N.; Marchetti, J. M. Economics of Biodiesel Production: Review. *Energy Convers. Manag.* **2018**, *168*, 74–84. https://doi.org/10.1016/J.ENCONMAN.2018.05.002.

(30) Mensah, P.; Carta, G. Adsorptive Control of Water in Esterification with Immobilized Enzymes. Continuous Operation in a Periodic Counter-Current Reactor. *Biotechnol. Bioeng.* **1999**, *66* (3), 137–146. https://doi.org/10.1002/(SICI)1097-0290(1999)66:3<137::AID-BIT1>3.0.CO;2-R.

(31) Lee, D. H.; Kim, J. M.; Shin, H. Y.; Kang, S. W.; Kim, S. W. Biodiesel Production Using a Mixture of Immobilized Rhizopus Oryzae and Candida Rugosa Lipases. *Biotechnol. Bioprocess Eng.* **2006**, *11* (6), 522–525. https://doi.org/10.1007/BF02932077.

(32) Hu, Y.; Dai, L.; Liu, D.; Du, W. Rationally Designing Hydrophobic UiO-66 Support for the Enhanced Enzymatic Performance of Immobilized Lipase. *Green Chem.* **2018**, *20* (19), 4500–4506. https://doi.org/10.1039/c8gc01284a.

Chapter 7
General Discussion

"A quality basic research is essential for further development, because it will produce results that are not predictable a priori"
Margarita Salas

Enhancement of MOF properties

The field of MOFs has been continuously growing since they emerged as a new type of crystalline material. The interest of the research community in MOFs arises from their advantageous properties, already stated in Chapter 1, 1.1 Metal-Organic Frameworks, as the a priori unlimited number of compositions and structures that could be achieved due to the large variety of metal nodes and the countless organic polycomplexing ligands that could be used as SBU.[1] For instance, this has been explored to achieve MOFs of great porosity or to reach targeted functionalities by judiciously selecting the SBU. Although MOFs could be considered as "off-road" materials, in occasions they present limitations (that could be beneficial in certain applications) associated to their ionocovalent bonding structure, such as: i) weak stability (*i.e.*: thermal, mechanical, chemical), ii) moderate activity (*e.g.*: modest electrical conductivity; gradual diffusion and mass transfer limited by pore size, restrained selectivity) and iii) high cost of some of their precursors.[2]

Several strategies have been followed so far to overcome these weaknesses. The first one entails the re-imagination of MOFs and their synthesis to present new structures. A fascinating solution is the entanglement of structures as in the case of interpenetrated MOFs, where two or more networks with the same or different SBU catenate with each other. Contrary to what it might seem, interpenetration cannot prevent the attainment of large surface areas and significantly enhances

their stability.[3] Another example are the multivariate MOFs, that are a class of MOFs that deliberately include heterogeneity in the highly ordered MOF structure by the addition of different metal ions or various linkers in a single structure. This results in a superior performance and activity than combination of single SBU.[4] On the other side are the defective MOFs, in which structural heterogeneity is achieved by the introduction of defects. These defects become functional sites available to enhance the parent MOF properties, such as having a more stable crystal structure.[5]

Another strategy to improve activity and stability entails post-synthetic modification (PSM) of MOFs. This enables the incorporation of other functional groups which a priori are incompatible with traditional MOF solvothermal synthesis. This could be done by modifying the organic ligands with reagents to produce new functional groups (covalent PSM) and/or introducing metal ligating groups onto the inorganic SBU (coordinative PSM).[6] In addition, there could be included as PSM strategies such as MOF surface treatment and/or modification (*e.g.*: coating with hydrophobic polymers to increase MOF stability in water)[7] and the combination of MOFs with other AS to attain advantageous composites.[8] As above stated, this thesis was focused on MOF-based composites to improve their properties.

Among all possible functionalities of MOFs, this research is focused on MOF semiconductor character and the modulation of its optoelectronic properties by compositization. The reader might wonder at this point the reasons behind this election. Why is MOF photoactivity interesting? Could MOFs provide any assets compared to other semiconductors?

Considering that the traditional energy system relies on limited resources as fossil fuels (*i.e.*: carbon, oil and gas), that are scarce for covering the increasing energy consumption demand (with an expected annual demand of $9 \cdot 10^{20}$ J by 2050),[9] it is reasonable to turn to solar radiation as an energy source. Incident solar radiation reaching Earth surface every year is equivalent to more than $3 \cdot 10^{24}$ J, or what is the same, more than 3000 times the expected annual primary energy consumption by 2050.[10] What is more, measurements of solar irradiance in space revealed that the highest energy corresponds to the solar radiation in the visible range of the spectral band (*i.e.*: 400-700 nm).[11]

Hence, for taking advantage of this sustainable, cheap and safe energy source, there are required materials able to interact with solar radiation and use it promoting ionic, redox or radical reactions for different applications (field known as photo-electrochemistry).[12] Those materials belong to semiconductors.[13] Although this technology has been known for many years, is still far from being optimized. Traditional semiconductors such as TiO_2, ZnO, ZnSe, CdS, present some shortcomings: i) limited absorption in the visible range of spectra (energy bandgap,

E_g, > 3 eV), ii) unsuitability of the positions of their conduction and valence bands, iii) poor quantic yield, due to electron-hole pair recombination, iv) poor stability under required reaction conditions, and v) difficult conformability into devices that enable their recovery and reutilization, *inter alia*.[14]

Among other fresh candidates (*e.g.*: perovskites, zeolites, carbonaceous composites based on graphene), MOFs are interesting semiconductors for photo-electrochemistry. Thanks to their tunable composition, they exhibit a E_g between 1 and 5.5 eV, suitable for many reactions. In addition, energy transfer after photon absorption from the ligands to the inorganic SBU (ligand-to-cluster mechanism), enables efficient electron-hole pair stabilization and the metallic centers act as activated quantic entities with high reactivity.[15,16] Besides precise predesign of MOF structures, regular ways to improve MOF optical properties include: the incorporation of the -NH_2 group to the ligand (isoreticular MOFs), the decoration with organic semiconductors and the loading with inorganic semiconductors and metal nanoparticles.[17]

A clear example of amine-functionalized MOFs with extended absorption in the visible range are the zirconium based UiO-66-NH_2,[18] and the titanium based MIL-125-NH_2.[19] MIL-125-NH_2 was selected in the first chapters of this thesis as support for the SiB association of AgNPs (see Chapter 3 section 3.2 MOF selection: MIL-125-NH_2 for the reasons of selection), whence combining two strategies for enhancement of MOF optoelectronical properties. MIL-125-NH_2 comprises Ti oxoclusters that overcome the bandgap limitations of TiO_2 with a reduced E_g of 2.6 eV (with a red-shifted band compared to MIL-125, of 3.6 eV).[20] In recent years, the use of MIL-125-NH_2 as a photocatalyst for the photo-reduction of CO_2, process known as artificial photosynthesis, using H_2O as a sacrificial agent *via* water splitting producing H_2, has gained particular attention.[19,21–30] In fact, the author of this thesis, AAV, was involved in a National project, financed by Fundación Iberdola in 2017, titled "Metallic nano-objects associated to Metal-Organic Frameworks for chemical energy storage" and oriented in the same research line (results not presented in this thesis). In addition to this relevant application, MIL-125-NH_2 photoactivity could be exploited for other uses as environmental remediation,[31,32] photocatalysis of relevant industrial compounds,[33] photochemical vapor generation;[34] or the ones presented in this manuscript: bacterial biofilm inhibition (see section 3.3)[35] and photodegradation of emerging contaminants (see section 4.2),[36] for mentioning some.

Another interesting family of photocatalysts are the polymorphic series of Fe-terephthalate MOFs MIL-53,[37] MIL-68,[38] MIL-88B,[39] and MIL-101,[40] that exhibit bandgaps of 2.7, 2.8, 2.1 and 2.4 eV, respectively, compatible with visible range of solar radiation. This photoactivity is due to their iron(III) oxocluster, that endows

excellent optical properties, excitable both directly by adsorption of incident photons and by ligand-to-cluster mechanism, depending on the photon wavelength.[17] They also have exhibited potential in the photoreduction of CO_2 and in environmental remediation.[41–43] In consequence, these attractive photocatalysts have been selected as scaffold for the microwave assisted BaS association of AgNPs, precisely their aminated version to promote the Ag-NH_2 interaction and charge transfer, and finally achieve enhanced optoelectronic properties in the MOFs (see 5.3).

At this stage -when it has been explained to the reader the relevance of MOFs' photoactivity, their *a priori* assets compared to other semiconductors, the interest behind the enhancement of their optoelectronic properties by association of MNPs, and after enunciation of some of the potential fields of interest for their application- seems opportune to proceed with the discussion of the main results achieved in this thesis, to propose additional research derived from them and to venture some of the future trends.

Photoactive MIL-125-NH_2

Researchers have already associated different semiconductors and MNPs to MIL-125-NH_2 to enhance its optoelectronic properties, by expanding the visible light absorption range and preventing the electron-hole recombination. For instance, Pt,[21] Pd,[24] Co,[23] Au,[33] Ag_3VO_4 and Ag_2WO_4,[44] Ni_2P,[25] CdS,[45] and TiO_2,[46] within others, have been previously associated by SiB strategies to the MIL-125-NH_2.

Focusing on Ag nano-objects, the selected metallic AS in this thesis, there can also been found some references of their association to both MIL-125 and MIL-125-NH_2 (see other AgNP@MOF on Chapter 1 in Table 1. 2). Prior to this thesis, some authors have proposed AgNP photoreduction on presynthesized MIL-125, using different irradiation sources (Xe or Hg lamp). [47–49] The obtained composites resulted on MOFs decorated by AgNPs exclusively on their outer surface and were validated on the photoreduction of Rhodamine B (RhB) dye. Other work also presented a chemical reduction route for the formation of AgNPs (5-10 nm) using a MIL-125-NH_2 with PSM and acetylacetone (AC) as support. The AgNP@MIL-125-AC composite photocatalytic activity was evaluated on the degradation of methylene blue (MB).[20] More recent publications have focused directly on the aminated version MIL-125-NH_2 as scaffold. They include the formation of Ag/AgCl NPs synthesized both by photoreduction[50] and chemical reduction,[32] leading to MIL-125-NH_2 coated by heterogeneous Ag/AgCl NPs. Their photocatalytic activity was

again validated against RhB dye photodegradation under visible light. Similarly, MIL-125-NH_2 was encased among Ag/AgBr NPs (10 nm) with a photoreduction protocol. [51]

Even the studies preceding this thesis formulated composites that exhibited an increment in the photoresponse in the visible range of the spectra and higher catalytic activity than the host MOF, they presented some shortcomings and drawbacks:

- They entailed **difficult synthesis procedures** that required many steps and involved complex laboratory equipment, resulting in time comsuming synthesis (48-72 h). Others required the presence of surfactants or MIL-125-NH_2 covalent PSM for AgNP stabilization, that involved complicated recovery and conservation of the composite.
- Few presented studies regarding the possibility of **association of variable contents of AgNPs** to the MOF, neglecting the possibility to modulate Ag proportion depending on the final application.
- These works did not analyze thoroughly the **interaction between AgNPs and the MOF** (*i.e.*: stability of the composite under reaction conditions, in these cases dye photodegradation).
- Little or no attention was paid to control and/or to determine the **location of the associated AgNPs** (surface, porosity, defects), resulting most of them with AgNPs attached to the outer surface.

In addition, going one step further, current research seems to be focused on the development of **MOF-based devices**, facilitating MOF integration and recovery from their applications, such as Ag/MIL-125-NH_2/cellulose films coated over glasses and Ag/MIL-125-NH_2/TiO_2 photoanodes. [52,53] On account of that, same trend has been followed here with the AgNP@nanoMIL-125-NH_2 biocide thin film coating (publication in Chapter 3 section 3.3).[35] Considering all above mentioned points for improvement, there is plenty of room for improvement and for further research on AgNP@MIL-125-NH_2 composites, in which this thesis is subscribed.

One could resume the two optimized SiB protocols here presented as simple two-step impregnation & reduction procedures. While association of larger AgNPs particles (5 ± 3 nm) was obtained *via* chemical reduction, UVA assisted photoreduction procured smaller AgNCs with narrower polydispersity (1.0 ± 0.4 nm). In both cases, the studies carried out validated the possibility of modulation of the variable Ti:Ag proportion, until saturation with a 70:30 wt.% ratio. The strong interaction between Ag nanospecies and MIL-125-NH_2 determined by extensive characterization (*i.e.*: observed by macroscopic color change, band shift in the FTIR spectra, AgNP leaching analysis, Monte Carlo simulations; see Chapter 4 section 4.2) resulted in an improved absorption in the visible range. The

calculated E_g determined by Tauc Plot for the direct allowed transitions was of 2 and 2.4 eV for the AgNP@nanoMIL-125-NH_2 and the AgNC@MIL-125-NH_2, respectively. In addition, ultrafast photoreduction (15 s) appeared to be more adequate to control the final location of Ag, solely within MIL-125-NH_2 porosity, and to maximize the impregnation yield (80 *vs.* 60% according to TGA, see APPENDIX IV, section IV.I SiB association of AgNCs *via* photoreduction: protocol optimization).

It is important to outstand here the relevance of the ultrafast photoreduction protocol (15 s) presented in Chapter 4, section 4.2.[36] Even UV photoreduction has been previously used in the synthesis of Ag-MIL-125 composites, [47–49] these studies used long irradiation times (2 h) and produced bigger AgNPs instead of AgNC (Ø within the 10-50 nm range), that decorated the MOF outer surface. Hence, to the best of our knowledge, the synthesis of stable AgNCs of controlled size supported on MIL-125-NH_2 porosity by means of photo-induced transformation was pioneeringly pursued. Furthermore, this synthesis, with a total preparation time of only 20 min: i) procures tiny AgNC (just 28 atoms), ii) with a modulable Ag content, iii) allocated merely within the porosity (validated by electron tomography) and iv) strongly interacting with MIL-125-NH_2 (FTIR, Monte Carlo), v) leading to a water stable photocatalyst (possible degradation characterized by high performance liquid chromatography, HPLC, under experimental conditions), vi) optoelectronically active in the visible range (as seen in UV-Vis diffuse reflectance spectroscopy); overpassing the characteristics of previously synthesized Ag-MIL-125-NH_2 composites -including the AgNP@nanoMIL-125-NH_2 presented also here in Chapter 3 section 3.3.

As MIL-125-NH_2 has a tunable particle size, was also ambitioned to extend the SiB simple impregnation & reduction protocol from the microMOF to likewise load AgNPs in the nanoMOF. This is of interest of those applications in which MOF crystal size is important, such as is requested in several bioapplications (*e.g.*: drug delivery, imaging) or for sensing.[54] As seen in APPENDIX I section I.II.ii MIL-125-NH_2 with nanoparticle size (nanoMOF), the extrapolation of the chemical reduction protocol designed for the micrometric MOF was straightforward to its miniaturized counterpart. Even validation of the extension of the ultrafast photoreduction of AgNCs inside the micrometric MOF to the nanoMOF has not been carried out (due to time limitations), it is expected to be easily reproducible, as it has been demonstrated for the case of the AgNPs, and so has been seen so far in the preliminary results of other members of APMU.

Furthermore, the possibility of association of AgNPs to other aminated MOFs, such as UiO-66-NH_2, with impregnation of $AgNO_3$ followed by its chemical reduction was also studied (APPENDIX I, I.II.iii Extension to other MOFs).

Although AgNP distribution was not homogeneous, their association was validated for UiO-66-NH_2 with a micron particle size. These results strengthen the versatility of the simple procedure here presented, even if further optimization is obviously needed. In addition, it would be of interest the extension of these two-step impregnation & reduction procedures to the association of other metallic nanospecies: Au, Cu, Pd, Pt. These AS are also commonly used in catalysis (*e.g.*: chemical, electrochemical) also as bimetallic active centers, and they could benefit from their stabilization in MOFs by simple synthesis. [55] Therefore, even not studied in this thesis, the synthesis here presented might serve as inspiration and first brick for other researchers.

Regardless the merits previously enunciated of the Ag@MIL-125-NH_2 composites here synthesized and their amiable laboratory preparation, it is of convenience to think one step forward and contemplate the viability of their scalability and industrial production. Considering the MOF scaffold here selected, MIL-125-NH_2, both its precursors are commercially available and its production has already been increased at laboratory scale for the attainment of larger amount of powder (multigram, ~ 50 g).[56] In addition, the synthesis protocol was improved, as the work presented a heated reaction (100 °C) at ambient pressure, instead of a solvothermal one. This protocol will simplify the requirements of the vessels needed for its batch production. Nevertheless, as dimethylformamide, DMF, is used as solvent, the chemical resistance of the vessel should be assured selecting materials such as polytetrafluoroethylene (PTFE), polyetheretherketone (PEEK) or stainless steel 1.4401 or 1.4571, that additionally withstand the temperature required. Taking this into account, seems *a priori* viable the large-scale production of MIL-125-NH_2.

Thinking about the association of AgNCs, seems viable to consider a semicontinuous production line. Firstly, the silver precursors and the photoinitiator would be diffused under inert atmosphere into the scaffold inside an opaque stirred vessel. From the vessel, a stream of Ag^+@MIL-125-NH_2 suspension will continuously exit with a controlled flow rate and pass through a transparent section of the pipe where it would be UVA irradiated, to achieve AgNC reduction. The AgNC@MIL-125-NH_2 could be recovered afterwards by means of filtration systems. Accordingly, as no special equipment need to be designed, the photoinduced SiB synthesis procedure here designed is presumably suitable for industrialization. Nevertheless, the proper question that follows is: does it justify the investment? Silver is a relatively expensive raw material, but it should be considered that is only added in a maximum 7 wt.% of the total composite and could be downsized according to the application. Besides, silver is cheaper than gold, that it is used nowadays as catalyst at industrial scale.[57] Furthermore, considering the strong interaction between AgNCs and the structure, might be expected to have an extended lifetime and

procure photocatalyst reusability. Still, even after the end of their lifetime, silver could recovered by similar mechanisms to those already existing for Pt and Pd.[58] In addition, if AgNC@MIL-125-NH_2 composite demonstrate its potential as specific photocatalyst, with an increase in 0.5 to 1.0% in conversion of a desired valuable product, the use of this catalyst could increase the profit margin in millions of dollars *per* day.[59] Therefore, should not be directly discarded the possible industrial production of AgNC@MIL-125-NH_2 composites and further studies should be carried out to better understand their activity and promote its potential application.

Biocide photoactive MOFs

AgNP@nanoMIL-125-NH_2 (AgNP@nanoMOF) was originally proposed as a **multi-action biocide agent with antifouling (antiadherent) properties against biofilm**.[35] For the first time MIL-125-NH_2 was used for this application and its intrinsic bactericidal activity was enhanced by the presence of the AgNPs and even more after UVA irradiation (the novelty of this work was previously highlighted in the Chapter 3, in section 3.1 Preamble).

In this sense, the use of MOFs as bactericide agents is a relatively new field (firsts publications from 2010).[60] They arose as an alternative solution to treat bacterial infections due to the well-known developed multidrug resistant bacterial strains.[61] While MOF antibacterial activity against bacterial suspensions (planktonic bacteria) has been evaluated to a greater extend, reports concerning their activity against challenging bacterial biofilm are still scarce. [60,62]

Compared to other chemical disinfectants proposed against Gram (-) and Gram (+) bacteria (TiO_2, ZnO, I, zeolites, silica based sol-gels), [63,64] MOFs offer the following advantages: i) both their organic and inorganic SBUs can provide bactericidal activity (intrinsic antimicrobial activity), leading to additive, even synergic actions, ii) they have a uniform and ordered distribution of active sites due to their crystalline structure, iii) release of active compounds to the media during degradation tends to be more gradual and homogeneous and iv) not only their framework can be bioactive but they also can entrap diverse bactericidal agents and increase their disinfection power (extrinsic antimicrobial activity). [62] For further details, please refer to the book chapter "Antimicrobial MOFs" in APPENDIX II section II.I.

Several complementary biological techniques were used for the characterization of the biocide and biofouling properties of the AgNP@nanoMOF thin film coatings: colony counting, analysis of reactive oxygen species, ROS, formation and bacterial viability by fluorescent emission, confocal laser scanning

microscopy (CLSM) for visual and qualitative assessment of bactericide (LIVE/DEAD staining) and antiadherent effect (see publication in section 3.3 of Chapter 3 for further detail on experiments and outcomes). Below, there are stated some outstanding deductions derived from the obtained results:

- **Modulable MIL-125-NH_2 particle size is beneficial for biofilm fighting**, as it could enhance interaction with the bacterial membrane. This size dependent intrinsic antimicrobial behavior of the MOF was observed both against Gram (+) *S. aureus* and Gram (-) *E. coli*, and might be related to the increment of surface area available in contact with the bacteria membrane. The control experiments also revealed that this intrinsic activity could come from the inorganic constituent, in agreement with previously reported minor TiO_2 activity.[65]
- The higher **bactericidal effect of the AgNP@nanoMOF** is not a result of the combination of its individual components but **might be derived from a synergistic effect**, as a consequence of the strong interaction between the AgNPs and the nanoMOF framework where are within. This affirmation is supported with lower inhibition results achieved by the control 'physical' mixture of AgNPs + nanoMOF.
- The **AgNP@nanoMOF thin film coating**, combining intrinsic and extrinsic biocide activities and enhanced ligand-to-cluster-charge-transfer upon UVA irradiation, **detached 80% of the bacteria biofilm** from the surface **and inhibited the viability of the 90% of the remaining bacteria**. The possible mechanism of action of the thin films coating might be associated with the generation of ROS that interfere with bacterial enzymatic activity inducing their death (mechanism of ROS generation upon excitation is already discussed in section 4.3 of the Chapter 3 publication).[35]
- The **strong interactions between the AgNPs and the nanoMOF**, as previously depicted with the biocide experiments in comparison with the results obtained with the 'physical' mixture AgNPs + nanoMOF, led to a favorable **chemical stability** under experimental conditions, that ensures **controlled delivery over extended periods of time**.
- Considering that the composite degradation under the conditions of study was not significant (just 2.5 and 3.5 wt.% of Ti and Ag released after 20 h), the **antifouling bactericidal combined effect of AgNP@nanoMOF** might not only be a result of the composite dissolution but mainly a **consequence of the stable association of AgNPs to the MOF and the role of AgNPs in the ligand-to-cluster transfer mechanism upon irradiation**, in agreement with

the catalytic studies done with other noble metal nanoparticles decorating MIL-125.[62]

The knowledge gained after this work, regarding MOFs as potential biocide materials and their biological characterization, opened the door for collaboration with other research groups, with active participation of AAV in experiment design and result analysis. Such is the case of the work published with Dr. Teresa Duarte's group (Universidade de Lisboa), studying the biocide effect of pellets of new five metal biomolecule frameworks (BioMOFs) based on azelaic acid (an antibacterial and antiinflamatory drug) and endogenous cations (*i.e.*: K^+, Na^+, Mg^{2+}). Their potential intrinsic antimicrobial activity was evaluated against two Gram (+) bacteria commonly present in skin, *S. aureus* and *S. epidermis*, analyzing their potential topic use and the increment in solubility of azelaic acid. Inhibition halo results shown that the K-based BioMOF 1 was the most promising candidate for topical formulations.[68] Another work with Dr. Sandra Loera group (Universidad Autónoma Metropolitana de México, to be submitted) analyzed the antibacterial and antifouling effect of thin films prepared by spin coating made of nanocrystals of a Ag-terephthalate MOF, AgBDC. Interestingly, this coating not only has bactericide activity against *E. coli* but also inhibits bacterial adhesion preventing the formation of biofilm up to seven days.

It is expected that researchers interest in the use of MOFs as antimicrobial agents will only grow in the near future, as depicted by some of the recent reviews on the topic. [69–71] Considering the perspective of current state-of-the-art, prospect works more likely will focus on the inhibition of challenging biofilms, not only on surfaces but also in living tissues (*e.g.* prostheses). [72–74] In addition, MOF conformation into membranes for achieving antifouling properties seems a highly probable close to market application, as bacterial membrane clogging is still an unsolved challenge that limits membranes lifecycle. [75] Actually, a recent work followed our lead coating membranes with the photoactive MIL-125 to promote their antibacterial activity with UV irradiation. [76]

Photocatalytic water remediation

The synthesized **AgNC@MIL-125-NH_2 exhibited some appealing properties,**[36] that were considered of interest **for the elimination of EOCs from water**: i) high aqueous stability,[77] ii) the composite preserved an accessible high porosity (S_{BET} = 1430 $m^2 \cdot g^{-1}$) for the adsorption of contaminants, and iii) could play an active role in contaminant degradation due to its photoactive properties, even more enhanced by the incorporated AgNC that extended its visible light

absorption. In conjunction, they make AgNC@MIL-125-NH_2 an interesting candidate for environmental remediation of wastewater by photocatalysis.

Water pollution is becoming a challenge because of the increment of the newly developed anthropogenic substances applied in many sectors (agricultural, industrial, medical), also known as EOCs. These substances end in water streams due to sewage and wastewater production and current technologies in wastewater treatment plants are not able to remove them.[5] Among the different proposed methods to eliminate EOC from water, heterogeneous photocatalysis has the potential of being performed with solar irradiation at ambient conditions, leading to less toxic components.

MOFs, in comparison with other materials used in environmental remediation, can present a dual role for water treatment: their characteristic microporosity is ideal for the adsorption of contaminants, passive role; and they can (photo)catalyze their degradation, active role. Fine selection of the MOF structure can even endow selective adsorption/separation, limited by the pore size; promote interaction with the contaminant molecules, with labile groups of the organic ligand; and foster their degradation with active sites.[78] There is a great interest in the use of MOFs for the elimination of EOCs from water, and most of reported works validated their use in the removal of organic dyes (~75% of the references).[79] Other EOCS entails: pharmaceuticals and personal care products (PPCPs), herbicides and industrial byproducts.

In this work, at first it was assessed the viability of the AgNC@MIL-125-NH_2 as photocatalyst for the visible photodegradation of the model dye MB, under batch conditions. Later, it was addressed the photodegradation of the challenging antibiotic SMT under a continuous flow (see the novelty of these studies in the 4.1 Preamble of Chapter 4). Reaction progress was followed by UV-Vis spectroscopy and/or HPLC, assessing also the photocatalyst stability (see publication in section 4.2 for further information regarding experimental setup, the home made continuous flow reactor and the obtained results). Following, there is a complementary analysis on the highlights of this work:

- **MB photodegradation is enhanced by the association of AgNCs to the MIL-125-NH_2 structure**. Not only the composite exhibited superior photon absorption in the visible range (E_g= 2.40 *vs.* 2.53 eV) but also there was a chemical interaction between -S and -N atoms of MB structure with the AgNC,[80] that mediated a faster mass transfer and dye adsorption.
- Despite this, the kinetic studies indicated that the **limiting stage for the photodegradation** process was not the physisorption of the dye but the reaction of **formation of water radicals ($^{\cdot}OH$, $O_2^{\cdot}$) on the**

AgNC active site.[81,82] These strong oxidants react with MB finally decolorizing the dye.[83]

- Therefore, the superior photocatalytic activity in EOC visible photodegradation is governed by the **enhanced optoelectronic properties of the AgNC@MIL-125-NH_2 composite.**
- A control reaction with AgNP@MIL-125-NH_2 suggested the relevance of the Ag nanospecie size, as the **catalyst activity increased with the decrease in Ag size**, in consonance with previous works.[84,85]
- Analysis of the stability of the photocatalyst are vital in water remediation, for not releasing further contaminants to the treated stream. The **AgNC@MIL-125-NH_2 photocatalyst remained stable** (<2% of ligand leached to the reaction media and perseverance of the crystalline structure) **after decontamination with visible irradiation** of MB and SMT from tap water, with real concentrations.
- The **continuous flow photoreactor presented here for the first time**, working under compatible water treatment flow rates, was able to **treat 6.50 $L \cdot h^{-1} \cdot g^{-1}$ of SMT contaminated water** *via* visible light photocatalytic oxidation.
- Monte Carlo simulations, supported by FTIR analysis, revealed that **SMT were found with the AgNC in the MIL-125-NH_2 octahedral cavities, forming hydrogen bonds** between the -NH_2 groups of both MOF and SMT.
- **Efficiency of photocatalytic water remediation under continuous flow** must be evaluated by its **breakthrough curve** (concentration-time profile), and the use of **AgNC@MIL-125-NH_2 photocatalyst** under visible irradiation **procured a quite good kinetic constant**, compared to other MOFs studied only as adsorbents.[86,87]

This publication is embodied in a greater research line followed by APMU. Its particular interest on the use of MOFs for the elimination of EOC from water has promoted the identification and establishment of collaboration partners to that end. For instance, a collaboration with Canal Isabel II, fresh and wastewater treatment company of Madrid (Spain), is sponsoring the research of a Ph.D. student in a common project to remove chlorides from fresh water.[88] Another examples are the recently launched 3 year National project MOFseidon (Retos investigación 2019, PID2019-104228RB-I00), that aims to develop continuous flow technologies based on MOFs for depollution and disinfection of real wastewaters,[89] or the National project ESENCE (Retos colaboración 2019) in collaboration with Depuración de Aguas del Mediterráneo (DAM) to detect and decontaminate wastewater. Also in this research line is another recently published APMU work

regarding adsorption of atenolol using a robust nickel bispyrazolate MOF-continuous flow column.[90]

Key for the future potential use of MOFs in water treatment is the determination of their stability under wastewater treatment conditions (*e.g.*: real concentration of contaminants in streamed waters, flow rates). Whence, future research should clearly pay attention to this and include these analyses in their studies (for instance simple XRPD characterization after contact with real wastewater and detection of potential metal or ligand leaching). Another important challenge is MOF recyclability and long-term use, specially under continuous flow, which is still almost unexplored. An added concern with photoactive MOFs, in particular those endowing efficient solar harvesting in the visible range and successful EOCs degradation, is the formation of toxic byproducts as result of the photocatalyzed oxidation and their characterization must not be omitted, to ensure they are at least less toxics than the original contaminant.

Finishing this section, enhancement of the optoelectronical properties of MOFs to develop new photocatalysts for wastewater treatment under continuous flow using visible light is a potential solution for EOC removal. Nevertheless, research on this field requires further evaluation of the challenges above mentioned to position photoactive MOFs as truly alternative technology.

Iron(III) aminoterephthalate polymorphs

The series of polymorphic iron(III) aminoterephthalates, MIL-53,[37] MIL-68,[38] MIL-88B[39] and MIL-101,[40] (already presented in 5.1 Preamble of Chapter 5, and in this chapter in the Enhancement of MOF properties section), was selected for: i) their interesting redox and photoactive properties,[41,43] ii) the liable -NH_2 available for MNP interaction and iii) their earth abundant nontoxic inorganic SBU (iron), considering future applications and scalability. Accordingly, they are considered a compelling matrix for MNP association.

The results discussed so far with the photoactive MIL-125-NH_2 showed the merits of the SiB association of AS to presynthesized MOFs, such as the simplicity of impregnation by diffusion through the pores. In addition, some of its limitations have also been lighted, like the difficulty to control the final position of the AS (risk of surface attachment) and their heterogeneous distribution through the framework. Especially, it is difficult to ensure a precise localization of the AS and, even more, to achieve reproducibility in doing so by SiB methodologies. Despite being more complex and difficult to control, BaS strategies appear as ideal routes to ensure

AS@MOF core-shell with the AS really protected by the crystal MOF growth surrounding it (see MNP@ZIF-8 in Figure 1. 6).

Among the many synthetic procedures for MOF synthesis, MW heating has been selected in this thesis for the BaS association of AgNPs to MOF crystals. The different interaction of the molecules with the alternating electric field of the microwaves, depending on their nature, induces selective heating that presumably will be beneficial to promote BaS synthesis of MNP@MOFs.[91] In the case of MNPs, their SPR as result of the polarization with MW irradiation might render them as hot spots in the reaction media, or what is the same, as potential nucleation sites for the MOF to grow.[91] In consequence, it could enhance the one-pot association of the MNPs. In addition, it will imply the reduction of synthesis time (compared to solvothermal BaS encapsulation)[92–95] and better control of the encapsulated particle size.[96] A relatively recent example that benefits of all this is the MW assisted BaS synthesis of Ag@IRMOF-3.[97]

The main progress done in the thesis to achieve this objective (*i.e.*: MW assisted BaS MNP association) is related to the analysis of the compositional factors that can lead to various MOF phases. Due to their distinctive configuration, different MOF phases exhibit different properties, such as different porosity, presence of metal sites or framework flexibility, and therefore is valuable to control their synthesis. For the determination of the optimal conditions for the synthesis of a specific iron(III) aminoterephthalate, a systematic synthetic strategy has been followed carrying out MW-assisted hydro/solvothermal reactions to rapidly evaluate the influence of different reaction parameters (*e.g.:* concentration, temperature, ligand:metal ratio, solvent). It should be acknowledged here the previous work following a similar synthesis strategy presented by Khan & Jhung, analyzing also the MW triggered phase selectivity but on chromium terephthalates MIL-53(Cr) and MIL-101(Cr),[98] and aluminum benzenetricarboxylates MIL-100(Al), MIL-110(Al) and MIL-96(Al).[99]

On the other hand, previous reports considering the iron-based structures, focused solely on the microwave synthesis of a particular polymorph (without considering phase variability), and mostly did not study the amino substituted terephthalate MOFs.[40,100–103] Interestingly, Wang and coauthors considered the influence of MW irradiation time on MIL-53(Fe) morphology, but they did not proceed with further analysis of other parameters, neither extended their investigations to other phases.[104] Therefore, it was pertinent an analysis of the variables affecting MW synthesis iron(III) aminoterephthalate phases. The representation of the results in crystallization diagrams enabled better analysis of the results, as the information of the phases obtained in each reaction iteration was easily visualized. Along with crystal phase determination, STY was determined due

to its significance for large-scale production (see publication in Chapter 5 section 5.2). For guiding the reader over the main results of this work and their positioning among previous state-of-the-art, they are divided below considering the solvent used.

WATER: Under the analyzed reaction conditions, two different phases have been formed using H_2O as solvent: rigid mesoporous MIL-101-NH_2 and flexible microporous MIL-53-NH_2. As anticipated, lower temperature procured the kinetically favored MIL-101-NH_2 phase, while MIL-53-NH_2, the thermodynamically stable phase was formed at higher temperatures. Similar trend was observed in the case of chromium terephthalates.[98] Representation of the attained phases on the T (°C)/[Fe] (M) crystallization diagram revealed a bisector in which a mixture of phases was obtained, evidencing this dependency, both with temperature and concentration. Interestingly, here were **synthesized MIL-101-NH_2 nanocrystals with a 70 % reduction of size compared to previously reported MW synthesis** (Ø~ 80 nm *vs.* 300 nm in previous work, from TEM).[40]

Variation of the pH of the reaction media by the addition of HCl shifted the equilibrium towards the more favorable thermodynamic phase, MIL-53-NH_2, with better crystallinity. This may be related to the better control of the reaction kinetics rate, associated to the deprotonation equilibrium of the carboxylate ligand (H_2BDC-NH_2 ⇌ H^-BDC-NH_2 + H^+ ⇌ BDC-NH_2 + H^+).

It is important to emphasize that this work presented the **first example of microwave assisted synthesis of pure submicronic MIL-53(Fe)-NH_2** of 330 ±50 nm **and what is more, using water as reaction media.** Previous studies reached the MW formation of the non-substituted terephthalate MIL-53 using DMF as solvent, producing crystals of 800-1000 nm. [102,104] H_2O is a particularly compelling solvent as is a cheap, safe and green solvent with no security associated protocols rewarding its storage neither its manipulation, which is of particular interest for commercial protocols. What is more, water has the lower environmental, safety and health impact, according to solvent selection guides of companies such as GSK or Pfizer. [105] Moreover, pure MIL-53-NH_2 crystals were obtained with high STY of 3000-10000 $kg \cdot m^{-3} \cdot d^{-1}$, being competitive with the reported production of different already commercialized MOFs (STY for Basolites© ~3000 $kg \cdot m^{-3} \cdot d^{-1}$).[106,107] When comparing the MW assisted synthesis of MIL-53-NH_2 with the conventional hydrothermal method, the reaction time is reduced in a 99.9 % (from 72 h to 5 min), and STY is increased 1000 fold times (3 *vs.* 3000 $kg \cdot m^{-3} \cdot d^{-1}$ in the conventional and MW heating, respectively).[37] According to all this, the protocol here presented for the MW assisted synthesis in water of MIL-53-NH_2 has strong potential for scaling up to industrial production.

ETHANOL: **MIL-88B-NH_2 was the predominant phase observed when using ethanol** as reaction medium. Pure MIL-88B-NH_2 has been previously obtained under microwave irradiation (l= 1500 nm, thickness ratio=5) but using DMF as reaction medium at higher temperatures (150 °C) and with longer reaction times (10-15 min).[101,103] Taking into account DMF toxicity, the protocol proposed in this work for the first time in microwave with EtOH provides a safer alternative for the production of MIL-88B-NH_2. In addition, comparing this MW-assisted synthesis with the conventional solvothermal with EtOH, MIL-88B-NH_2 reaction time is reduced also a 99.9 % (from 72 h to 5 min).[39]

DIMETHYLFORMAMIDE: Optimization of crystal phases was more complicated using DMF as reaction medium. Interestingly, **MIL-88B-NH_2 needles synthesized in DMF are 8 times longer than those formed in EtOH** under similar conditions (without acid) and the length:thickness ratio is two-fold times the EtOH ones (4.55 ± 1.42 *vs.* 1.96 ± 0.65, respectively). Previous reports also achieved bigger particle size using DMF as solvent.[101,103] This emphasizes once again the important role of the reaction media on the formation of the different phases and its effect on the crystallinity and particle size, due to their different interactions with the alternating MW irradiation. Despite DMF toxicity and higher cost compared to EtOH, might be the preferred reaction media for applications where higher crystallinity is required.

As previously stated, these results represent only the first step into the attainment of MNP@MOF *via* MW assisted BaS synthesis. The viability of the concept has been already published for the Ag@IRMOF-3 composite,[97] yet are few representatives of this powerful synthesis tool (as MW reactions are potentially scalable compared to other BaS methods, as layer by layer MOF growth).[97] Preliminary results unveiled the possibility of AgPVP NPs association to the mesoporous MIL-101-NH_2 (see Chapter 5, section 5.3). This outcome set the grounds for the development of further research at the APMU, within the framework of the European Training Network 'HeatNMof' belonging to Marie Sklodowska-Curie Actions.[108]

Thinking of large-scale production, MW assisted synthesis benefits for being a scalable technology that enables uniform heating, and therefore, uniform reaction *a priori* independent of the vessel volume. Even MWs could be used as batch reactor at industrial scale, MW radiation has a limitation in depth penetration that limits the final reactor size. For avoiding penetration issues, it is a much more interesting strategy to devise a continuous flow tubular reactor with MW heating. Continuous flow microwave (CFMW) reactors have already been exploited in organic synthesis at industrial scale.[109] In addition, the feasibility of CFMW reactors applied to MOF synthesis has been proved by Ranocchiari and his group, with the synthesis of

benchmark structures: zirconium terephthalate UiO-66, aluminum terephthalate MIL-53(Al) and copper benzenetricarboxylate HKUST-1.[110] They obtained high crystalline solids in a multigram scale (~20 g) with extraordinary STY, 4000-6500 $kg \cdot m^{-3} \cdot d^{-1}$, that even surpassed those of commercial Basolites (from BASF).[59] In the last year, the CFMW assisted synthesis was also reported for MIL-100(Fe),[111] and UiO-66-$(OH)_2$.[112] According to all this, it is expected that soon will appear industrial patents regarding this powerful technology. For this reason, further investigation on MOF CFMW assisted synthesis, both on new and already reported phases, as well as with or without association of MNPs; is a really appealing research line, and especially for those applications requiring large scale synthesis of MOFs. Its implantation will reduce MOF production time and energy consumption, and hence, production cost, that will ease MOF penetration into market.

Association of biomolecules to MOFs

Up to this point the discussion was related to the association of MNP to MOFs. Nevertheless, there are other interesting AS, such as **biomolecules, that could be integrated within their structure to enhance MOF properties and even impart new ones**.[113] Biomolecules are AS in organisms, they are ubiquitous and exhibit biological functions that are essential for maintaining basic life activities. Under the umbrella of biomolecules could be included big molecules as carbohydrates, nucleic acids, antibodies, lipids and proteins (oligopeptides, oligonucleotides, enzymes), as well as small molecules as amino acids, fatty acids and drug molecules among others.

It should be mentioned here that this thesis author, AAV, has collaborated with Dr. Pablo del Pino's group (Centro Singular de Investigación en Química Bioloxica e Materiais Moleculares, CiQUS, Spain) in order to associate active biomolecules in MOFs for their NIR-triggered release upon MOF degradation inside living cells. This work presented a MOF-based vehicle for drug delivery. For demonstration of the controlled release, the biocomposite consisted on gold nanostars coated with ZIF-8 and loaded with the blue fluorescent dye Hoeschst H33258, used for DNA staining.[95] Precisely, the collaboration entailed the confirmation of the different AS association by means of thermogravimetric analysis and N_2 sorption measurements. Further, interest in biomolecule association, and more precisely on drug delivery, motivated the redaction of the article review "Metal-organic frameworks: A novel platform for combined advanced therapies" (*Coordination Chemistry Reviews*, **2019,** *388*, 202-226; Q1, IF:14,5), together with Dr. Sara Rojas and Dr. Patricia Horcajada.[114] This review reports complex MOF

bioplatform systems (*i.e.*: two or more AS are encapsulated, controlled delivery at target, monitorization of administration) to pursue more efficient treatments.

Synthesis of biomolecule-embedded MOFs involves biomolecule integration by covalent bonding, physical adsorption, or entrapment within their porous structure (see Chapter 1 section 1.3 for further details about AS association). Another option for biomolecule integration in MOFs is BioMOF synthesis, where biomolecules are directly used as ligands.[115] Such is the case of the K-based azolate biocide BioMOF-1, previously mentioned in this chapter.[68] Due to biomolecule relatively fragile and complex nature, extra requirements are essential for their association, compared to the previously studied MNPs: i) due to biomolecule complicated structure, electrostatic interaction or covalent bonding might become difficult, and a suitable association strategy should be followed for preventing biomolecule leaching, ii) biomolecule functionality must be preserved after association, whence their immobilization conditions ought to be biocompatible, iii) it is pertinent to ensure accessibility to the biomolecule active sites after association, as it might limit its final activity, and iv) conservation and storage of the obtained biocomposites is also important, as disturbances in the environment (*i.e.*: radiation, temperature, dispersion in organic solvents) can degrade sensitive biomolecules. Another point to consider, depending on the final composite application, is the selection of a biocompatible MOF structure with the suitable crystal size (*e.g.*: drug delivery).[116]

In Chapter 6 was presented the BaS immobilization of enzymes into MOFs, (more specifically lipases) to attain highly specific and efficient heterogeneous biocatalysts. Even so, **are enzymes really that attractive? Is it important to invest time in their association to different carriers?** Definitely, yes. Enzymes are able to increase reaction rates a billion times and trigger reactions with high specificity and efficiency, procuring high reaction yield with reactions products of high purity (see more details in Chapter 1 section 1.3.2.2 Enzymes). So much so, that even today they are used at industrial processes for production of food, cosmetics, detergents, pharmaceuticals and several chemicals, as their operation in milder reaction conditions and selectivity is translated in reduced manufacturing costs.[117–120] Even more, industrial demand of enzymes is expected to grow at a compound annual growth rate of 6.4% from 2020 to 2027.[121] Therefore, without doubt enzymes are actually interesting catalysts.

However, all industries suffer from the same common limitation, *i.e.* lack of enzyme stability and recyclability. Several strategies have been followed for overcoming those drawbacks. Here should be acknowledged the extraordinary work of the 2018 Chemistry Nobel Prize Dr. Frances H. Arnold and her contributions to enzyme directed evolution in order to promote commercially viable enzyme

biocatalysts.[122] Nevertheless, biocatalyst optimization should not only consider enzyme activity and functionality, but it should also procure an increase in operational stability and expanded lifetimes. Or what is the same, it is required a multidisciplinary approach to meet industrial market demands.[120] Hence, studies rewarding enzyme immobilization, as the ones here presented in Chapter 6 (that considered lipase heterogenization by their association to MOFs), are still relevant and they will provide more robust biocatalysts for their application in a broader range of industrial reactions.

As seen in Chapter 1 Table 1. 3 SiB postsynthetic encapsulation is at the moment the most utilized strategy for lipase immobilization in MOFs. In spite of the simplicity of using presynthesized MOFs, the large size of some lipases compared to the much smaller aperture of most common MOFs presents limitations to this approach. Here is where BaS association appears as a promising alternative. There are plenty of reports that considered the use of zeolitic imidazolate frameworks, such as ZIF-8 (see Table 1. 3), for the one-pot encapsulation of lipases due to their negligible cytotoxicity and their biocompatible synthetic conditions.Even though, ZIFs structures do not exhibit great stability. Hence, there is interest in the study of alternative MOFs for lipase association, their synthesis and the final lipase@MOF biocomposite properties.

The MW assisted synthesis route previously proposed for BaS MNP association was not suitable for lipases due to their fragile nature and the risk of enzyme denaturalization, losing their biocatalytic activity. It was pursued an alternative route, with an *in situ* soft-heated association at moderate temperatures. The MOF selected for lipase immobilization, iron(III) fumarate MIL-88A, has a water-based synthesis protocol *a priori* compatible with the lipases to be encapsulated. Nevertheless, the previously reported procedures for MIL-88A production were considered harsh for the lipases,[123,124] and they required adaptation for the attainment of lipase@MIL-88A composites. After optimization, it was proposed **a BaS simple, rapid and soft green two-step protocol that first involved MOF crystal seed nucleation and second lipase *in situ* encapsulated by MIL-88A growth**. In contrast with previously reported works, this is a faster procedure (total synthesis and biocomposites recovery time of 4 h compared to the 7 days required for biomimetic mineralization of MIL-88A coating bovine serum albumin)[125] and compromises lipase encapsulation inside the MIL-88A (by comparison to the encapsulation of enzymes inside a hollow sphere shell made of MIL-88A crystals).[126] Therefore, here designed method outstands from previous state-of-the-art. Interestingly, the protocol was used for the association of two lipases of different size: *P-f* and *C-r* lipase (34 and 60 kDa, respectively). This exposes the potential the BaS synthesis MIL-88A as support for lipase@MIL-88A biocomposites.

After material characterization and validation of the biocomposites activity, even under extreme pH (see Chapter 6 6.4 Characterization), its activity for the transesterification reaction of soybean oil into biodiesel was evaluated, one of the industrial reactions that will drive the industrial enzyme market in the following years.[121] In this work, not only a green solvent free reaction was pursued, but whereas previous works rewarding lipase@MOF biocatalyst for biodiesel production, the reaction products were qualitatively determined to analyze possible influence of the MOF in the biocomposite.[127–131] That is to say, the possible active role of the MOF in the biodiesel catalysis was also analyzed for the first time. Qualitative results in Figure 6. 10 evidenced that there was a different FAME production of free and encapsulated enzymes. Consequently, this pioneer work not only **evidences the MOF structure effect on the immobilized enzyme selectivity towards biodiesel production**, as a proof of concept, but also has practical repercussions on the biodiesel chemical nature and its future application. Considering the similar energetic power of both main biodiesel products (standard energy densities = -37 *vs.* -39 kJ · g^{-1} in C-16:0 E and C-18:2 E, respectively) and their different melting point (mp), *P-f*-lipase@MIL-88A would be a more appropriate biocatalyst for biodiesel used under warm weathers (C-16:0 E mp = 29 °C), while the selectivity towards unsaturated acids of *C-r*-lipase@MIL-88A makes it more suitable for winter biodiesel (C-18:2 E mp = -35 °C).[132]

Further analyses are required to determine the source of this possible lipase@MOF chemoselectivity. For instance, determination of MOF adsorption selectivity towards reagents (soybean oil triglycerides) and products (FAMEs), as selectivity might arise from restrictive diffusion through MOF porosity and accessible windows. In addition, complementary characterization to FTIR should be carried out to determine the interaction between lipase and MOF structure, as it could illustrate if, alternatively, selectivity arises from enzyme conformational changes within MOF defects and porosity. For instance, *via* circular dichroism characterization, as it could give information on the secondary structure composition and tertiary structure fingerprints of enzymes, more precisely focusing on the amide I and amide II bands, groups with shifted FTIR peaks (Figure 6. 5).[133] Besides figuring out the cause of the experienced product selectivity, it is interesting to go one step further from qualitative to quantitative determination of FAMEs, as presented by more recent publications on the topic.[129,134,135] This will clarify reaction conversion: the real amount of triglycerides transformed into esters and if there has been produced the unwanted hydrolysis reaction (production off free fatty acids).

On the whole, the identification of the biodiesel products, considered here for first time in contrast with total FAME analysis, stresses the relevance of the proper selection of the MOF substrate to promote its active role on the immobilized lipase selectivity and maximize the composite biocatalytic activity. In addition,

with the aid of the determination of the origin of the extra selectivity, it opens many perspectives to increase selectivity in biocatalysis by finding the appropriate lipase-MOF pair.

Reported works considering association of biomolecules to MOFs have proven their interest in many applications: biosensing, biomedicine (*e.g.*: drug delivery, biolectronic devices), industrial biocatalysis (*e.g.*: food and pharmaceutical production), and separation and pollutant removal (*i.e.*: oxidation-reduction), among others.[136] Nevertheless, present state-of-the-art in the field, even the work here presented, is at its infancy and mostly in the proof-of-concept stage. In consequence, studies concerning industrial conditions, or *in vivo* tests in the cases of biomolecule delivery, are urgently needed to gain knowledge on their practical application. This will implicate collaboration between material scientists, chemists, biologists, and engineers, *inter alia*.

Recapitulation

The main objective of this thesis was to harness MOFs ordered porosity for the association of active species within their crystalline structure to develop new and advantageous composites with enhanced properties. In order to achieve so, in this work were selected previously reported benchmarked structures, whose porosity and accessible windows could match the size of the targeted AS or whose synthetic procedure was compatible with the AS stability (*i.e.*: metallic NPs and enzymes). The selected materials were prepared at IMDEA Energy using APMU laboratory installations. Consequently, knowledge of MOF synthesis, purification and characterization has been acquired during the development of the doctoral thesis. Furthermore, the association strategies here presented that led to the different AS@MOFs were likewise designed during this thesis.

In Chapter 3, AgNPs (~5 nm) were associated to the photoactive microporous titanium terephthalate MIL-125-NH_2 using a SiB two-step protocol, that involved impregnation followed by chemical reduction of the silver salt precursor. An improvement of the association of Ag nanospecies to MIL-125-NH_2 was accomplished in Chapter 4. In this case, much better control on both the Ag nanospecie size, attaining AgNCs of ~1 nm (*i.e.*: 28 atoms), and their location, solely within the MIL-125-NH_2, was achieved by means of ultrafast photoreduction (15 s).

Encapsulation of ASs by growing a MOF shell surrounding them, or what is the same, following BaS synthetic procedures, was also explored in this thesis. MW

assisted solvothermal synthesis has been considered by APMU as a remarkable tool for the BaS association of MNPs into MOFs. For doing so, in Chapter 5 is presented a systematic study on the influence of different reaction parameters for the obtention of pure phases of the polymorphic iron(III) aminoterephthalate family: MIL-53-NH_2, MIL-68-NH_2, MIL-88B-NH_2 and MIL-101-NH_2. Moreover, even not optimized, the MW assisted BaS synthesis of AgNP@MIL-101-NH_2 was presented in this chapter, validating the potential of MW irradiation for BaS composite production.

Due to their fragile nature, MW is not an option for the BaS association of enzymes. Accordingly, in Chapter 6 was developed a green soft method for the immobilization of lipases in the flexible structure of the biocompatible iron(III) fumarate MIL-88A. After heterogenization of lipases of *P. fluorescens* and *C. rugose* on the MIL-88A not only they were available for recovery and recycling, but also were protected in the lipase@MIL-88A composite from harsh environments, as acidic reaction media.

As it has been seen in previous chapters, the different synthesized AS@MOF composites were validated in a plethora of relevant applications: treatment of microbial-contaminated surfaces, water remediation and catalysis of chemical compounds of industrial interest. Due to their diversity, some of these studies were carried out in collaboration with other researchers and institutions, actively participating in the experiment design and result analysis to gain experience and understanding. This versatility in MOF purposes emphasizes once again the numerous fields of interest in which MOFs could have a potential application.[2,137]

Several experiments were carried out to better understand the composite activity in the previously mentioned applications, considering the role of their individual constituents and the AS-MOF interaction in the resulting enhanced properties, and they will be further discussed in this chapter. In addition, special attention has been paid to the analysis of the stability of the AS@MOF under the experimental conditions.

The novelty of this work does not rely on the attainment of new MOF crystals that increment the always growing PCP family. On the contrary, it is based on further exploration of their advantageous properties. In this case, their porosity and tunable structure has been exploited for the association of AS and composite synthesis, in order to enhance their optoelectronic properties. Even the research here presented could be considered as basic and with a low technology readiness level, it is oriented to topics of great interest as the attainment of bacteria free surfaces or water purification. Furthermore, it increases MOF knowledge and promotes their not so future transition from laboratory to the shelf for the general public.

Bibliography

(1) Griffin, S. L.; Champness, N. R. A Periodic Table of Metal-Organic Frameworks. *Coord. Chem. Rev.* **2020**, *414*, 213295. https://doi.org/10.1016/j.ccr.2020.213295.

(2) Jiao, L.; Seow, J. Y. R.; Skinner, W. S.; Wang, Z. U.; Jiang, H. L. Metal–Organic Frameworks: Structures and Functional Applications. *Mater. Today* **2019**, *27*, 43–68. https://doi.org/10.1016/j.mattod.2018.10.038.

(3) Gong, Y.-N.; Zhong, D.-C.; Lu, T.-B. Interpenetrating Metal–Organic Frameworks. *CrystEngComm* **2016**, *18* (15), 2596–2606. https://doi.org/10.1039/C6CE00371K.

(4) Deng, H.; Doonan, C. J.; Furukawa, H.; Ferreira, R. B.; Towne, J.; Knobler, C. B.; Wang, B.; Yaghi, O. M. Multiple Functional Groups of Varying Ratios in Metal-Organic Frameworks. *Science (80-.).* **2010**, *327* (5967), 846–850. https://doi.org/10.1126/science.1181761.

(5) Trickett, C. A.; Gagnon, K. J.; Lee, S.; Gándara, F.; Bürgi, H.-B.; Yaghi, O. M. Definitive Molecular Level Characterization of Defects in UiO-66 Crystals. *Angew. Chemie Int. Ed.* **2015**, *54* (38), 11162–11167. https://doi.org/10.1002/anie.201505461.

(6) Kalaj, M.; Cohen, S. M. Postsynthetic Modification: An Enabling Technology for the Advancement of Metal-Organic Frameworks. *ACS Cent. Sci.* **2020**, *6* (7), 1046–1057. https://doi.org/10.1021/acscentsci.0c00690.

(7) Safy, M. E. A.; Amin, M.; Haikal, R. R.; Elshazly, B.; Wang, J.; Wang, Y.; Wöll, C.; Alkordi, M. H. Probing the Water Stability Limits and Degradation Pathways of Metal–Organic Frameworks. *Chem. – A Eur. J.* **2020**, *26* (31), 7109–7117. https://doi.org/10.1002/chem.202000207.

(8) Li, S.; Huo, F. Metal–Organic Framework Composites: From Fundamentals to Applications. *Nanoscale* **2015**, *7* (17), 7482–7501. https://doi.org/10.1039/C5NR00518C.

(9) World Energy Council. World Energy Scenarios | 2019: European Regional Perspectives https://www.worldenergy.org/publications/entry/world-energy-scenarios-2019-european-regional-perspectives (accessed Apr 3, 2021).

(10) World Energy Council. 2013 Survey www.worldenergy.org (accessed Apr 3, 2021).

(11) Gueymard, C. A. The Sun's Total and Spectral Irradiance for Solar Energy Applications and Solar Radiation Models. *Sol. Energy* **2004**, *76* (4), 423–453. https://doi.org/10.1016/j.solener.2003.08.039.

(12) Klimov, V. I. Mechanisms for Photogeneration and Recombination of Multiexcitons in Semiconductor Nanocrystals: Implications for Lasing and Solar Energy Conversion. *J. Phys. Chem. B* **2006**, *110* (34), 16827–16845. https://doi.org/10.1021/jp0615959.

(13) Bard, A. J. Design of Semiconductor Photoelectrochemical Systems for Solar Energy Conversion. *J. Phys. Chem.* **1982**, *86* (2), 172–177. https://doi.org/10.1021/j100391a008.

(14) Nikokavoura, A.; Trapalis, C. Alternative Photocatalysts to TiO2 for the Photocatalytic Reduction of CO2. *Appl. Surf. Sci.* **2017**, *391*, 149–174. https://doi.org/10.1016/j.apsusc.2016.06.172.

(15) Ryder, M. R.; Tan, J.-C. Nanoporous Metal Organic Framework Materials for Smart Applications. *Mater. Sci. Technol.* **2014**, *30* (13), 1598–1612. https://doi.org/10.1179/1743284714Y.0000000550.

(16) Dhakshinamoorthy, A.; Asiri, A. M.; García, H. Metal-Organic Framework (MOF) Compounds: Photocatalysts for Redox Reactions and Solar Fuel Production. *Angew. Chemie - Int. Ed.* **2016**, *55* (18), 5414–5445. https://doi.org/10.1002/anie.201505581.

(17) Jiang, D.; Xu, P.; Wang, H.; Zeng, G.; Huang, D.; Chen, M.; Lai, C.; Zhang, C.; Wan, J.; Xue, W. Strategies to Improve Metal Organic Frameworks Photocatalyst's Performance for Degradation of Organic Pollutants. **2018**. https://doi.org/10.1016/j.ccr.2018.08.005.

(18) Garibay, S. J.; Cohen, S. M. Isoreticular Synthesis and Modification of Frameworks with the UiO-66 Topology. *Chem. Commun.* **2010**, *46* (41), 7700. https://doi.org/10.1039/c0cc02990d.

(19) Fu, Y.; Sun, D.; Chen, Y.; Huang, R.; Ding, Z.; Fu, X.; Li, Z. An Amine-

Functionalized Titanium Metal-Organic Framework Photocatalyst with Visible-Light-Induced Activity for CO 2 Reduction. *Angew. Chemie - Int. Ed.* **2012**, *51* (14), 3364–3367. https://doi.org/10.1002/anie.201108357.

(20) Abdelhameed, R. M.; Simões, M. M. Q.; Silva, A. M. S.; Rocha, J. Enhanced Photocatalytic Activity of MIL-125 by Post-Synthetic Modification with Cr ^{III} and Ag Nanoparticles. *Chem. - A Eur. J.* **2015**, *21* (31), 11072–11081. https://doi.org/10.1002/chem.201500808.

(21) Toyao, T.; Saito, M.; Horiuchi, Y.; Mochizuki, K.; Iwata, M.; Higashimura, H.; Matsuoka, M. Efficient Hydrogen Production and Photocatalytic Reduction of Nitrobenzene over a Visible-Light-Responsive Metal–Organic Framework Photocatalyst. *Catal. Sci. Technol.* **2013**, *3* (8), 2092. https://doi.org/10.1039/c3cy00211j.

(22) Kampouri, S.; Ebrahim, F. M.; Fumanal, M.; Nord, M.; Schouwink, P. A.; Elzein, R.; Addou, R.; Herman, G. S.; Smit, B.; Ireland, C. P.; et al. Enhanced Visible-Light-Driven Hydrogen Production through MOF/MOF Heterojunctions. *ACS Appl. Mater. Interfaces* **2021**, *13*, 14239–14247. https://doi.org/10.1021/acsami.0c23163.

(23) Nasalevich, M. A.; Becker, R.; Ramos-Fernandez, E. V.; Castellanos, S.; Veber, S. L.; Fedin, M. V.; Kapteijn, F.; Reek, J. N. H.; van der Vlugt, J. I.; Gascon, J. Co@NH $_2$ -MIL-125(Ti): Cobaloxime-Derived Metal–Organic Framework-Based Composite for Light-Driven H $_2$ Production. *Energy Environ. Sci.* **2015**, *8* (1), 364–375. https://doi.org/10.1039/C4EE02853H.

(24) Yan, B.; Zhang, L.; Tang, Z.; Al-Mamun, M.; Zhao, H.; Su, X. Palladium-Decorated Hierarchical Titania Constructed from the Metal-Organic Frameworks NH2-MIL-125(Ti) as a Robust Photocatalyst for Hydrogen Evolution. *Appl. Catal. B Environ.* **2017**, *218*, 743–750. https://doi.org/10.1016/j.apcatb.2017.07.020.

(25) Kampouri, S.; Nguyen, T. N.; Ireland, C.; Valizadeh, B.; Ebrahim, F.; Capano, G.; Ongari, D.; Mace, M.; Guijarro, N.; Sivula, K.; et al. Photocatalytic Hydrogen Generation from a Visible-Light Responsive Metal-Organic Framework System: The Impact of Nickel Phosphide Nanoparticles. *J. Mater. Chem. A* **2018**, 2476–2481. https://doi.org/10.1039/C7TA10225A.

(26) Kampouri, S.; Nguyen, T. N.; Spodaryk, M.; Palgrave, R. G.; Züttel, A.; Smit, B.; Stylianou, K. C. Concurrent Photocatalytic Hydrogen Generation and Dye Degradation Using MIL-125-NH $_2$ under Visible Light Irradiation. *Adv. Funct. Mater.* **2018**, *28* (52), 1806368. https://doi.org/10.1002/adfm.201806368.

(27) Remiro-Buenamañana, S.; Cabrero-Antonino, M.; Martínez-Guanter, M.; Álvaro, M.; Navalón, S.; García, H. Influence of Co-Catalysts on the Photocatalytic Activity of MIL-125(Ti)-NH2 in the Overall Water Splitting. *Appl. Catal. B Environ.* **2019**, *254*, 677–684. https://doi.org/10.1016/j.apcatb.2019.05.027.

(28) Luo, S.; Liu, X.; Wei, X.; Fu, M.; Lu, P.; Li, X.; Jia, Y.; Ren, Q.; He, Y. Noble-Metal-Free Cobaloxime Coupled with Metal-Organic Frameworks NH2-MIL-125: A Novel Bifunctional Photocatalyst for Photocatalytic NO Removal and H2 Evolution under Visible Light Irradiation. *J. Hazard. Mater.* **2020**, *399*, 122824. https://doi.org/10.1016/j.jhazmat.2020.122824.

(29) Mohammadnezhad, F.; Kampouri, S.; Wolff, S. K.; Xu, Y.; Feyzi, M.; Lee, J. H.; Ji, X.; Stylianou, K. C. Tuning the Optoelectronic Properties of Hybrid Functionalized MIL-125-NH2for Photocatalytic Hydrogen Evolution. *ACS Appl. Mater. Interfaces* **2021**, *13* (4), 5044–5051. https://doi.org/10.1021/acsami.0c19345.

(30) Li, Y.; Liu, Y.; Wang, Z.; Wang, P.; Zheng, Z.; Cheng, H.; Dai, Y.; Huang, B. In-Situ Growth of Ti3C2@MIL-NH2 Composite for Highly Enhanced Photocatalytic H2 Evolution. *Chem. Eng. J.* **2021**, *411*, 128446. https://doi.org/10.1016/j.cej.2021.128446.

(31) Wang, H.; Yuan, X.; Wu, Y.; Zeng, G.; Chen, X.; Leng, L.; Wu, Z.; Jiang, L.; Li, H. Facile Synthesis of Amino-Functionalized Titanium Metal-Organic Frameworks and Their Superior Visible-Light Photocatalytic Activity for Cr(VI) Reduction. *J. Hazard. Mater.* **2015**, *286*, 187–194. https://doi.org/10.1016/j.jhazmat.2014.11.039.

(32) Qiu, J.; Li, M.; Wang, H.; Yao, J. Integration of Plasmonic Effect into MIL-125-NH2: An Ultra-Efficient Photocatalyst for Simultaneous Removal of Ternary System Pollutants. *Chemosphere* **2020**, *242*, 125197. https://doi.org/10.1016/j.chemosphere.2019.125197.

(33) Qiu, J.; Yang, L.; Li, M.; Yao, J. Metal Nanoparticles Decorated MIL-125-NH 2 and MIL-125 for Efficient Photocatalysis. *Mater. Res. Bull.* **2019**, *112*, 297–306. https://doi.org/10.1016/j.materresbull.2018.12.038.

(34) Luo, J.; Xu, F.; Tu, J.; Wu, X.; Hou, X. Amine-Functionalized Titanium Metal Organic Framework for Photochemical Vapor Generation for Determination of Selenium by Inductively Coupled Plasma Optical Emission Spectrometry. *Microchem. J.* **2017**, *132*, 245–250. https://doi.org/10.1016/j.microc.2017.02.005.

(35) Arenas-Vivo, A.; Amariei, G.; Aguado, S.; Rosal, R.; Horcajada, P. An Ag-

Loaded Photoactive Nano-Metal Organic Framework as a Promising Biofilm Treatment. *Acta Biomater.* **2019**, *97*, 490–500. https://doi.org/10.1016/j.actbio.2019.08.011.

(36) Arenas-Vivo, A.; Rojas, S.; Ocaña, I.; Torres, A.; Liras, M.; Salles, F.; Esteban, D. A.; Bals, S.; Avila Brande, D.; Horcajada, P. Ultrafast Reproducible Synthesis of an Agnanocluster@MOF Composite and Its Superior Visible-Photocatalytic Activity in Batch and in Continuous Flow. *J. Mater. Chem. A* **2021**. https://doi.org/10.1039/D1TA02251B.

(37) Devic, T.; Horcajada, P.; Serre, C.; Salles, F.; Maurin, G.; Moulin, B.; Heurtaux, D.; Clet, G.; Vimont, A.; Grenéche, J. M.; et al. Functionalization in Flexible Porous Solids: Effects on the Pore Opening and the Host-Guest Interactions. *J. Am. Chem. Soc.* **2010**, *132* (3), 1127–1136. https://doi.org/10.1021/ja9092715.

(38) Fateeva, A.; Horcajada, P.; Devic, T.; Serre, C.; Marrot, J.; Grenèche, J.-M.; Morcrette, M.; Tarascon, J.-M.; Maurin, G.; Férey, G. Synthesis, Structure, Characterization, and Redox Properties of the Porous MIL-68(Fe) Solid. *Eur. J. Inorg. Chem.* **2010**, *2010* (24), 3789–3794. https://doi.org/10.1002/ejic.201000486.

(39) Horcajada, P.; Salles, F.; Wuttke, S.; Devic, T.; Heurtaux, D.; Maurin, G.; Vimont, A.; Daturi, M.; David, O.; Magnier, E.; et al. How Linker's Modification Controls Swelling Properties of Highly Flexible Iron(III) Dicarboxylates MIL-88. *J. Am. Chem. Soc.* **2011**, *133* (44), 17839–17847. https://doi.org/10.1021/ja206936e.

(40) Horcajada, P.; Chevreau, H.; Heurtaux, D.; Benyettou, F.; Salles, F.; Devic, T.; Garcia-Marquez, A.; Yu, C.; Lavrard, H.; Dutson, C. L.; et al. Extended and Functionalized Porous Iron(Iii) Tri- or Dicarboxylates with MIL-100/101 Topologies. *Chem. Commun.* **2014**, *50* (52), 6872–6874. https://doi.org/10.1039/c4cc02175d.

(41) Liu, X.; Zhou, Y.; Zhang, J.; Tang, L.; Luo, L.; Zeng, G. Iron Containing Metal-Organic Frameworks: Structure, Synthesis, and Applications in Environmental Remediation. *ACS Appl. Mater. Interfaces* **2017**, *9* (24), 20255–20275. https://doi.org/10.1021/acsami.7b02563.

(42) Dao, X. Y.; Guo, J. H.; Wei, Y. P.; Guo, F.; Liu, Y.; Sun, W. Y. Solvent-Free Photoreduction of CO2 to CO Catalyzed by Fe-MOFs with Superior Selectivity. *Inorg. Chem.* **2019**, *58* (13), 8517–8524. https://doi.org/10.1021/acs.inorgchem.9b00824.

(43) Xia, Q.; Wang, H.; Huang, B.; Yuan, X.; Zhang, J.; Zhang, J.; Jiang, L.;

Xiong, T.; Zeng, G. State-of-the-Art Advances and Challenges of Iron-Based Metal Organic Frameworks from Attractive Features, Synthesis to Multifunctional Applications. *Small* **2018**, *15* (2), 1803088. https://doi.org/10.1002/smll.201803088.

(44) Emam, H. E.; Ahmed, H. B.; Gomaa, E.; Helal, M. H.; Abdelhameed, R. M. Doping of Silver Vanadate and Silver Tungstate Nanoparticles for Enhancement the Photocatalytic Activity of MIL-125-NH2 in Dye Degradation. *J. Photochem. Photobiol. A Chem.* **2019**, *383*, 111986. https://doi.org/10.1016/j.jphotochem.2019.111986.

(45) Zhang, X.; Chen, Z.; Luo, Y.; Han, X.; Jiang, Q.; Zhou, T.; Yang, H.; Hu, J. Construction of NH2-MIL-125(Ti)/CdS Z-Scheme Heterojunction for Efficient Photocatalytic H2 Evolution. *J. Hazard. Mater.* **2020**, 124128. https://doi.org/10.1016/j.jhazmat.2020.124128.

(46) Yoon, J. W.; Kim, D. H.; Kim, J. H.; Jang, H. W.; Lee, J. H. NH2-MIL-125(Ti)/TiO2 Nanorod Heterojunction Photoanodes for Efficient Photoelectrochemical Water Splitting. *Appl. Catal. B Environ.* **2019**, *244*, 511–518. https://doi.org/10.1016/j.apcatb.2018.11.057.

(47) Yang, Z.; Xu, X.; Liang, X.; Lei, C.; Cui, Y.; Wu, W.; Yang, Y.; Zhang, Z.; Lei, Z. Construction of Heterostructured MIL-125/Ag/g-C3N4 Nanocomposite as an Efficient Bifunctional Visible Light Photocatalyst for the Organic Oxidation and Reduction Reactions. *Appl. Catal. B Environ.* **2017**, *205*, 42–54. https://doi.org/10.1016/j.apcatb.2016.12.012.

(48) Guo, H.; Guo, D.; Zheng, Z.; Weng, W.; Chen, J. Visible-Light Photocatalytic Activity of Ag@MIL-125(Ti) Microspheres. *Appl. Organomet. Chem.* **2015**, *29* (9), 618–623. https://doi.org/10.1002/aoc.3341.

(49) Yuan, X.; Wang, H.; Wu, Y.; Zeng, G.; Chen, X.; Leng, L.; Wu, Z.; Li, H. One-Pot Self-Assembly and Photoreduction Synthesis of Silver Nanoparticle-Decorated Reduced Graphene Oxide/MIL-125(Ti) Photocatalyst with Improved Visible Light Photocatalytic Activity. *Appl. Organomet. Chem.* **2016**, *30* (5), 289–296. https://doi.org/10.1002/aoc.3430.

(50) Mahmoodi, N. M.; Taghizadeh, A.; Taghizadeh, M.; Abdi, J. In Situ Deposition of Ag/AgCl on the Surface of Magnetic Metal-Organic Framework Nanocomposite and Its Application for the Visible-Light Photocatalytic Degradation of Rhodamine Dye. *J. Hazard. Mater.* **2019**, *378*, 120741. https://doi.org/10.1016/j.jhazmat.2019.06.018.

(51) Wu, D.; Han, L. Fabrication of Novel Ag/AgBr/NH2-MIL-125(Ti) Nanocomposites with Enhanced Visible-Light Photocatalytic Activity.

Mater. Res. Express **2019**, *6* (12), 125501. https://doi.org/10.1088/2053-1591/ab540a.

(52) Abdelhameed, R. M.; El-Shahat, M.; Emam, H. E. Employable Metal (Ag & Pd)@MIL-125-NH2@cellulose Acetate Film for Visible-Light Driven Photocatalysis for Reduction of Nitro-Aromatics. *Carbohydr. Polym.* **2020**, *247*, 116695. https://doi.org/10.1016/j.carbpol.2020.116695.

(53) Cui, W.; Shang, J.; Bai, H.; Hu, J.; Xu, D.; Ding, J.; Fan, W.; Shi, W. In-Situ Implantation of Plasmonic Ag into Metal-Organic Frameworks for Constructing Efficient Ag/NH2-MIL-125/TiO2 Photoanode. *Chem. Eng. J.* **2020**, *388*, 124206. https://doi.org/10.1016/j.cej.2020.124206.

(54) Giménez-Marqués, M.; Hidalgo, T.; Serre, C.; Horcajada, P. Nanostructured Metal–Organic Frameworks and Their Bio-Related Applications. *Coord. Chem. Rev.* **2015**, *307*, 1–19. https://doi.org/10.1016/j.ccr.2015.08.008.

(55) Wang, Q.; Astruc, D. State of the Art and Prospects in Metal−Organic Framework (MOF)-Based and MOF-Derived Nanocatalysis. **2019**. https://doi.org/10.1021/acs.chemrev.9b00223.

(56) Moreira, M. A.; Santos, J. C.; Ferreira, A. F. P.; Loureiro, J. M.; Ragon, F.; Horcajada, P.; Yot, P. G.; Serre, C.; Rodrigues, A. E. Effect of Ethylbenzene in P-Xylene Selectivity of the Porous Titanium Amino Terephthalate MIL-125(Ti)-NH 2. *Microporous Mesoporous Mater.* **2012**, *158*, 229–234. https://doi.org/10.1016/j.micromeso.2012.03.039.

(57) Ciriminna, R.; Falletta, E.; Della Pina, C.; Teles, J. H.; Pagliaro, M. Industrial Applications of Gold Catalysis. *Angewandte Chemie - International Edition*. Wiley-VCH Verlag November 7, 2016, pp 14210–14217. https://doi.org/10.1002/anie.201604656.

(58) Dong, H.; Zhao, J.; Chen, J.; Wu, Y.; Li, B. Recovery of Platinum Group Metals from Spent Catalysts: A Review. *International Journal of Mineral Processing*. Elsevier B.V. December 10, 2015, pp 108–113. https://doi.org/10.1016/j.minpro.2015.06.009.

(59) Silva, P.; Vilela, S. M. F.; Tomé, J. P. C.; Almeida Paz, F. A. Multifunctional Metal–Organic Frameworks: From Academia to Industrial Applications. *Chem. Soc. Rev.* **2015**, *44* (19), 6774–6803. https://doi.org/10.1039/C5CS00307E.

(60) Arenas-Vivo, A.; Horcajada, P. Antimicrobial Metal Organic Frameworks. In *Metal Organic Frameworks*; Mittal, D. V., Ed.; Central West Publishing, 2019; pp 1–34.

(61) Okeke, I. N.; Lamikanra, A.; Edelman, R. Socioeconomic and Behavioral Factors Leading to Acquired Bacterial Resistance to Antibiotics in Developing Countries. *Emerg. Infect. Dis.* **1999**, *5* (1), 18–27. https://doi.org/10.3201/eid0501.990103.

(62) Wyszogrodzka, G.; Marszałek, B.; Gil, B.; Dorożyński, P. Metal-Organic Frameworks: Mechanisms of Antibacterial Action and Potential Applications. *Drug Discov. Today* **2016**, *21* (6), 1009–1018. https://doi.org/10.1016/j.drudis.2016.04.009.

(63) Raquez, J.-M.; Habibi, Y.; Murariu, M.; Dubois, P. Polylactide (PLA)-Based Nanocomposites. *Prog. Polym. Sci.* **2013**, *38* (10–11), 1504–1542. https://doi.org/10.1016/j.progpolymsci.2013.05.014.

(64) Wang, Z.; Shen, Y.; Haapasalo, M. Dental Materials with Antibiofilm Properties. *Dent. Mater.* **2014**, *30* (2), e1–e16. https://doi.org/10.1016/J.DENTAL.2013.12.001.

(65) Xekoukoulotakis, N. P.; Xinidis, N.; Chroni, M.; Venieri, D.; Hapeshi, E.; Fatta-Kassinos, D. UV-A/TiO2 Photocatalytic Decomposition of Erythromycin in Water: Factors Affecting Mineralization and Antibiotic Activity. *Catal. Today* **2010**, *151* (1–2), 29–33. https://doi.org/10.1016/J.CATTOD.2010.01.040.

(66) Shen, L.; Luo, M.; Huang, L.; Feng, P.; Wu, L. A Clean and General Strategy To Decorate a Titanium Metal–Organic Framework with Noble-Metal Nanoparticles for Versatile Photocatalytic Applications. *Inorg. Chem.* **2015**, *54* (4), 1191–1193. https://doi.org/10.1021/ic502609a.

(67) Keskin, S.; Kizilel, S. Biomedical Applications of Metal Organic Frameworks. *Ind. Eng. Chem. Res.* **2011**, *50* (4), 1799–1812. https://doi.org/10.1021/ie101312k.

(68) Quaresma, S.; André, V.; Antunes, A. M. M.; Vilela, S. M. F.; Amariei, G.; Arenas-Vivo, A.; Rosal, R.; Horcajada, P.; Duarte, M. T. Novel Antibacterial Azelaic Acid BioMOFs. *Cryst. Growth Des.* **2020**, *20* (1), 370–382. https://doi.org/10.1021/acs.cgd.9b01302.

(69) Shen, M.; Forghani, F.; Kong, X.; Liu, D.; Ye, X.; Chen, S.; Ding, T. Antibacterial Applications of Metal–Organic Frameworks and Their Composites. *Compr. Rev. Food Sci. Food Saf.* **2020**, *19* (4), 1397–1419. https://doi.org/10.1111/1541-4337.12515.

(70) Li, R.; Chen, T.; Pan, X. Metal–Organic-Framework-Based Materials for Antimicrobial Applications. *ACS Nano* **2021**, *15* (3), 3808–3848. https://doi.org/10.1021/acsnano.0c09617.

(71) Liu, J.; Wu, D.; Zhu, N.; Wu, Y.; Li, G. Antibacterial Mechanisms and Applications of Metal-Organic Frameworks and Their Derived Nanomaterials. *Trends Food Sci. Technol.* **2021**, *109*, 413–434. https://doi.org/10.1016/j.tifs.2021.01.012.

(72) Xiao, Y.; Xu, M.; Lv, N.; Cheng, C.; Huang, P.; Li, J.; Hu, Y.; Sun, M. Dual Stimuli-Responsive Metal-Organic Framework-Based Nanosystem for Synergistic Photothermal/Pharmacological Antibacterial Therapy. *Acta Biomater.* **2021**, *122*, 291–305. https://doi.org/10.1016/j.actbio.2020.12.045.

(73) Deng, Q.; Sun, P.; Zhang, L.; Liu, Z.; Wang, H.; Ren, J.; Qu, X. Porphyrin MOF Dots–Based, Function-Adaptive Nanoplatform for Enhanced Penetration and Photodynamic Eradication of Bacterial Biofilms. *Adv. Funct. Mater.* **2019**, *29* (30), 1903018. https://doi.org/10.1002/adfm.201903018.

(74) Liu, Z.; Wang, F.; Ren, J.; Qu, X. A Series of MOF/Ce-Based Nanozymes with Dual Enzyme-like Activity Disrupting Biofilms and Hindering Recolonization of Bacteria. *Biomaterials* **2019**, *208*, 21–31. https://doi.org/10.1016/j.biomaterials.2019.04.007.

(75) Pejman, M.; Firouzjaei, M. D.; Aktij, S. A.; Das, P.; Zolghadr, E.; Jafarian, H.; Shamsabadi, A. A.; Elliott, M.; Esfahani, M. R.; Sangermano, M.; et al. Improved Antifouling and Antibacterial Properties of Forward Osmosis Membranes through Surface Modification with Zwitterions and Silver-Based Metal Organic Frameworks. *J. Memb. Sci.* **2020**, *611*, 118352. https://doi.org/10.1016/j.memsci.2020.118352.

(76) Zhou, S.; Gao, J.; Zhu, J.; Peng, D.; Zhang, Y.; Zhang, Y. Self-Cleaning, Antibacterial Mixed Matrix Membranes Enabled by Photocatalyst Ti-MOFs for Efficient Dye Removal. *J. Memb. Sci.* **2020**, *610*, 118219. https://doi.org/10.1016/j.memsci.2020.118219.

(77) Kim, S.-N.; Kim, J.; Kim, H.-Y.; Cho, H.-Y.; Ahn, W.-S. Adsorption/Catalytic Properties of MIL-125 and NH 2 -MIL-125. *Catal. Today* **2013**, *204*, 85–93. https://doi.org/10.1016/j.cattod.2012.08.014.

(78) Bian, Y.; Xiong, N.; Zhu, G. Technology for the Remediation of Water Pollution: A Review on the Fabrication of Metal Organic Frameworks. *Processes* **2018**, *6* (8), 122. https://doi.org/10.3390/pr6080122.

(79) Rojas, S.; Horcajada, P. Metal-Organic Frameworks for the Removal of Emerging Organic Contaminants in Water. *Chem. Rev.* **2020**, *120* (16), 8378–8415. https://doi.org/10.1021/acs.chemrev.9b00797.

(80) Nair, S.; Tatarchuk, B. J. Supported Silver Adsorbents for Selective Removal

of Sulfur Species from Hydrocarbon Fuels. *Fuel* **2010**, *89* (11), 3218–3225. https://doi.org/10.1016/j.fuel.2010.05.006.

(81) Marcinkowski, D.; Walesa-Chorab, M.; Patroniak, V.; Kubicki, M.; Kadziolka, G.; Michalkiewicz, B. A New Polymeric Complex of Silver(I) with a Hybrid Pyrazine-Bipyridine Ligand - Synthesis, Crystal Structure and Its Photocatalytic Activity. *New J. Chem.* **2014**, *38*, 604. https://doi.org/10.1039/C3NJ01187A.

(82) Hsieh, C. Te; Fan, W. S.; Chen, W. Y.; Lin, J. Y. Adsorption and Visible-Light-Derived Photocatalytic Kinetics of Organic Dye on Co-Doped Titania Nanotubes Prepared by Hydrothermal Synthesis. *Sep. Purif. Technol.* **2009**, *67* (3), 312–318. https://doi.org/10.1016/j.seppur.2009.03.041.

(83) Chambers, M. B.; Wang, X.; Ellezam, L.; Ersen, O.; Fontecave, M.; Sanchez, C.; Rozes, L.; Mellot-Draznieks, C. Maximizing the Photocatalytic Activity of Metal–Organic Frameworks with Aminated-Functionalized Linkers: Substoichiometric Effects in MIL-125-NH $_2$. *J. Am. Chem. Soc.* **2017**, *139* (24), 8222–8228. https://doi.org/10.1021/jacs.7b02186.

(84) Shimizu, K. ichi; Miyamoto, Y.; Satsuma, A. Size- and Support-Dependent Silver Cluster Catalysis for Chemoselective Hydrogenation of Nitroaromatics. *J. Catal.* **2010**, *270* (1), 86–94. https://doi.org/10.1016/j.jcat.2009.12.009.

(85) Lamoth, M.; Plodinec, M.; Scharfenberg, L.; Wrabetz, S.; Girgsdies, F.; Jones, T.; Rosowski, F.; Horn, R.; Schlögl, R.; Frei, E. Supported Ag Nanoparticles and Clusters for CO Oxidation: Size Effects and Influence of the Silver-Oxygen Interactions. *ACS Appl. Nano Mater.* **2019**, *2* (5), 2909–2920. https://doi.org/10.1021/acsanm.9b00344.

(86) Li, H.; He, J.; Chen, K.; Shi, Z.; Li, M.; Guo, P.; Wu, L. Dynamic Adsorption of Sulfamethoxazole from Aqueous Solution by Lignite Activated Coke. *Materials (Basel).* **2020**, *13* (7), 16–20. https://doi.org/10.3390/MA13071785.

(87) Sotelo, J. L.; Ovejero, G.; Rodríguez, A.; Álvarez, S.; García, J. Removal of Atenolol and Isoproturon in Aqueous Solutions by Adsorption in a Fixed-Bed Column. *Ind. Eng. Chem. Res.* **2012**, *51* (13), 5045–5055. https://doi.org/10.1021/ie300334q.

(88) Canal de Isabel II. CÓMO MEJORAR EL TRATAMIENTO DEL AGUA: EN BUSCA DE MATERIALES QUE ACABEN CON LOS CLORATOS https://www.energia.imdea.org/eventos/2020/proyecto-industrial-revista-del-cyii (accessed Apr 4, 2021).

(89) IMDEA Energy. MOFSEIDON: Combined separation and

(photo)degradation of water contaminants using Metal-Organic Framework devices https://www.energy.imdea.org/research/projects/mofseidon (accessed Apr 4, 2021).

(90) Rojas, S.; Navarro, J. A. R.; Horcajada, P. Metal–Organic Frameworks for the Removal of the Emerging Contaminant Atenolol under Real Conditions. *Dalt. Trans.* **2021**, *50* (7), 2493–2500. https://doi.org/10.1039/d0dt03637d.

(91) Thomas-Hillman, I.; Laybourn, A.; Dodds, C.; Kingman, S. W. Realising the Environmental Benefits of Metal–Organic Frameworks: Recent Advances in Microwave Synthesis. *J. Mater. Chem. A* **2018**, *6* (25), 11564–11581. https://doi.org/10.1039/C8TA02919A.

(92) Gu, Z.; Chen, L.; Duan, B.; Luo, Q.; Liu, J.; Duan, C. Synthesis of Au@UiO-66(NH2) Structures by Small Molecule-Assisted Nucleation for Plasmon-Enhanced Photocatalytic Activity. *Chem. Commun. (Camb).* **2015**, *52* (1), 116–119. https://doi.org/10.1039/c5cc07042b.

(93) Lu, G.; Li, S.; Guo, Z.; Farha, O. K.; Hauser, B. G.; Qi, X.; Wang, Y.; Wang, X.; Han, S.; Liu, X.; et al. Imparting Functionality to a Metal-Organic Framework Material by Controlled Nanoparticle Encapsulation. *Nat. Chem.* **2012**, *4* (February), 310–316. https://doi.org/10.1038/nchem.1272.

(94) Hu, P.; Zhuang, J.; Chou, L. Y.; Lee, H. K.; Ling, X. Y.; Chuang, Y. C.; Tsung, C. K. Surfactant-Directed Atomic to Mesoscale Alignment: Metal Nanocrystals Encased Individually in Single-Crystalline Porous Nanostructures. *J. Am. Chem. Soc.* **2014**, *136* (30), 10561–10564. https://doi.org/10.1021/ja5048522.

(95) Carrillo-Carrión, C.; Martínez, R.; Navarro Poupard, M. F.; Pelaz, B.; Polo, E.; Arenas-Vivo, A.; Olgiati, A.; Taboada, P.; Soliman, M. G.; Catalán, Ú.; et al. Aqueous Stable Gold Nanostar/ZIF-8 Nanocomposites for Light-Triggered Release of Active Cargo Inside Living Cells. *Angew. Chemie* **2019**, *131* (21), 7152–7156. https://doi.org/10.1002/ange.201902817.

(96) Klinowski, J.; Almeida Paz, F. A.; Silva, P.; Rocha, J. Microwave-Assisted Synthesis of Metal–Organic Frameworks. *Dalt. Trans.* **2011**, *40* (2), 321–330. https://doi.org/10.1039/C0DT00708K.

(97) Li, D.; Dai, X.; Zhang, X.; Zhuo, H.; Jiang, Y.; Yu, Y.-B.; Zhang, P.; Huang, X.; Wang, H. Silver Nanoparticles Encapsulated by Metal-Organic-Framework Give the Highest Turnover Frequencies of 10 5 h −1 for Three Component Reaction by Microwave-Assisted Heating. *J. Catal.* **2017**, *348*, 276–281. https://doi.org/10.1016/j.jcat.2017.02.013.

(98) Khan, N. A.; Jhung, S. H. Phase-Transition and Phase-Selective Synthesis of

Porous Chromium-Benzenedicarboxylates. *Cryst. Growth Des.* **2010**, *10* (4), 1860–1865. https://doi.org/10.1021/cg901562d.

(99) Khan, N. A.; Lee, J. S.; Jeon, J.; Jun, C. H.; Jhung, S. H. Phase-Selective Synthesis and Phase-Conversion of Porous Aluminum-Benzenetricarboxylates with Microwave Irradiation. *Microporous Mesoporous Mater.* **2012**, *152*, 235–239. https://doi.org/10.1016/j.micromeso.2011.11.025.

(100) Haque, E.; Khan, N. A.; Park, J. H.; Jhung, S. H. Synthesis of a Metal-Organic Framework Material, Iron Terephthalate, by Ultrasound, Microwave, and Conventional Electric Heating: A Kinetic Study. *Chem. - A Eur. J.* **2010**, *16* (3), 1046–1052. https://doi.org/10.1002/chem.200902382.

(101) Ma, M.; Bétard, A.; Weber, I.; Al-Hokbany, N. S.; Fischer, R. A.; Metzler-Nolte, N. Iron-Based Metal-Organic Frameworks MIL-88B and NH2-MIL-88B: High Quality Microwave Synthesis and Solvent-Induced Lattice "Breathing." *Cryst. Growth Des.* **2013**, *13* (6), 2286–2291. https://doi.org/10.1021/cg301738p.

(102) Dong, W.; Liu, X.; Shi, W.; Huang, Y. Metal-Organic Framework MIL-53(Fe): Facile Microwave-Assisted Synthesis and Use as a Highly Active Peroxidase Mimetic for Glucose Biosensing. *RSC Adv.* **2015**, *5* (23), 17451–17457. https://doi.org/10.1039/c4ra15840g.

(103) Taylor-Pashow, K. M. L.; Della Rocca, J.; Xie, Z.; Tran, S.; Lin, W. Postsynthetic Modifications of Iron-Carboxylate Nanoscale Metal-Organic Frameworks for Imaging and Drug Delivery. *J. Am. Chem. Soc.* **2009**, *131*, 14261–14263. https://doi.org/10.1021/ja906198y.

(104) Guo, W.; Sun, W.; Lv, L.-P.; Kong, S.; Wang, Y. Microwave-Assisted Morphology Evolution of Fe-Based Metal–Organic Frameworks and Their Derived Fe $_2$ O $_3$ Nanostructures for Li-Ion Storage. *ACS Nano* **2017**, *11* (4), 4198–4205. https://doi.org/10.1021/acsnano.7b01152.

(105) Clarke, C. J.; Tu, W. C.; Levers, O.; Bröhl, A.; Hallett, J. P. Green and Sustainable Solvents in Chemical Processes. *Chem. Rev.* **2018**, *118* (2), 747–800. https://doi.org/10.1021/acs.chemrev.7b00571.

(106) Farrusseng, D. *Metal-Organic Frameworks : Applications from Catalysis to Gas Storage*; Farruseng, D., Ed.; Wiley-VCH, 2011.

(107) Yilmaz, B.; Trukhan, N.; Müller, U. Industrial Outlook on Zeolites and Metal Organic Frameworks. *Chinese J. Catal.* **2012**, *33* (1), 3–10. https://doi.org/10.1016/S1872-2067(10)60302-6.

(108) EURAXESS. 9 PhD positions in the field of nanomedicine & biotechnology in MSCA European Training Network "HeatNMof" https://euraxess.ec.europa.eu/worldwide/asean/9-phd-positions-field-nanomedicine-biotechnology-msca-european-training-network (accessed Apr 5, 2021).

(109) Bergamelli, F.; Iannelli, M.; Marafie, J. A.; Moseley, J. D. A Commercial Continuous Flow Microwave Reactor Evaluated for Scale-Up. *Org. Process Res. Dev.* **2010**, *14* (4), 926–930. https://doi.org/10.1021/op100082w.

(110) Taddei, M.; Steitz, D. A.; van Bokhoven, J. A.; Ranocchiari, M. Continuous-Flow Microwave Synthesis of Metal-Organic Frameworks: A Highly Efficient Method for Large-Scale Production. *Chem. - A Eur. J.* **2016**, *22* (10), 3245–3249. https://doi.org/10.1002/chem.201505139.

(111) Le, V. N.; Kwon, H. T.; Vo, T. K.; Kim, J. H.; Kim, W. S.; Kim, J. Microwave-Assisted Continuous Flow Synthesis of Mesoporous Metal-Organic Framework MIL-100 (Fe) and Its Application to Cu(I)-Loaded Adsorbent for CO/CO2 Separation. *Mater. Chem. Phys.* **2020**, *253*, 123278. https://doi.org/10.1016/j.matchemphys.2020.123278.

(112) Vo, T. K.; Nguyen, V. C.; Quang, D. T.; Park, B. J.; Kim, J. Formation of Structural Defects within UiO-66(Zr)-(OH)2 Framework for Enhanced CO2 Adsorption Using a Microwave-Assisted Continuous-Flow Tubular Reactor. *Microporous Mesoporous Mater.* **2021**, *312*, 110746. https://doi.org/10.1016/j.micromeso.2020.110746.

(113) Kempahanumakkagari, S.; Kumar, V.; Samaddar, P.; Kumar, P.; Ramakrishnappa, T.; Kim, K.-H. Biomolecule-Embedded Metal-Organic Frameworks as an Innovative Sensing Platform. *Biotechnol. Adv.* **2018**, *36* (2), 467–481. https://doi.org/10.1016/j.biotechadv.2018.01.014.

(114) Rojas, S.; Arenas-Vivo, A.; Horcajada, P. Metal-Organic Frameworks: A Novel Platform for Combined Advanced Therapies. *Coord. Chem. Rev.* **2019**, *388*. https://doi.org/10.1016/j.ccr.2019.02.032.

(115) Zhuang, J.; Young, A. P.; Tsung, C.-K. Integration of Biomolecules with Metal-Organic Frameworks. *Small* **2017**, *13* (32), 1700880. https://doi.org/10.1002/smll.201700880.

(116) Rojas, S.; Carmona, F. J.; Maldonado, C. R.; Horcajada, P.; Hidalgo, T.; Serre, C.; Navarro, J. A. R.; Barea, E. Nanoscaled Zinc Pyrazolate Metal-Organic Frameworks as Drug-Delivery Systems. *Inorg. Chem.* **2016**, *55* (5), 2650–2663. https://doi.org/10.1021/acs.inorgchem.6b00045.

(117) Tewari, Y. B. Thermodynamics of Industrially-Important, Enzyme-

Catalyzed Reactions. *Appl. Biochem. Biotechnol. Part A Enzym. Eng. Biotechnol.* **1990**, *23* (3), 187–203. https://doi.org/10.1007/BF02942054.

(118) Rasor, J. P.; Voss, E. Enzyme-Catalyzed Processes in Pharmaceutical Industry. *Appl. Catal. A Gen.* **2001**, *221* (1–2), 145–158. https://doi.org/10.1016/S0926-860X(01)00804-3.

(119) Schmid, A.; Hollmann, F.; Park, J. B.; Bühler, B. The Use of Enzymes in the Chemical Industry in Europe. *Curr. Opin. Biotechnol.* **2002**, *13* (4), 359–366. https://doi.org/10.1016/S0958-1669(02)00336-1.

(120) Chapman, J.; Ismail, A.; Dinu, C. Industrial Applications of Enzymes: Recent Advances, Techniques, and Outlooks. *Catalysts* **2018**, *8* (6), 238. https://doi.org/10.3390/catal8060238.

(121) Grand View Research. Global Industrial Enzymes Market Share Report, 2020-2027 https://www.grandviewresearch.com/industry-analysis/industrial-enzymes-market (accessed Apr 10, 2021).

(122) Fasan, R.; Kan, S. B. J.; Zhao, H. A Continuing Career in Biocatalysis: Frances H. Arnold. *ACS Catal.* **2019**, *9*, 9775–9788. https://doi.org/10.1021/acscatal.9b02737.

(123) Chalati, T.; Horcajada, P.; Gref, R.; Couvreur, P.; Serre, C. Optimisation of the Synthesis of MOF Nanoparticles Made of Flexible Porous Iron Fumarate MIL-88A. *J. Mater. Chem.* **2011**, *21* (7), 2220–2227. https://doi.org/10.1039/C0JM03563G.

(124) Serre, C.; Millange, F.; Surblé, S.; Férey, G. A Route to the Synthesis of Trivalent Transition-Metal Porous Carboxylates with Trimeric Secondary Building Units. *Angew. Chemie Int. Ed.* **2004**, *43* (46), 6285–6289. https://doi.org/10.1002/anie.200454250.

(125) Liang, K.; Ricco, R.; Doherty, C. M.; Styles, M. J.; Bell, S.; Kirby, N.; Mudie, S.; Haylock, D.; Hill, A. J.; Doonan, C. J.; et al. Biomimetic Mineralization of Metal-Organic Frameworks as Protective Coatings for Biomacromolecules. *Nat. Commun.* **2015**, *6* (1), 7240. https://doi.org/10.1038/ncomms8240.

(126) Jeong, G. Y.; Ricco, R.; Liang, K.; Ludwig, J.; Kim, J. O.; Falcaro, P.; Kim, D. P. Bioactive MIL-88A Framework Hollow Spheres via Interfacial Reaction In-Droplet Microfluidics for Enzyme and Nanoparticle Encapsulation. *Chem. Mater.* **2015**, *27* (23), 7903–7909. https://doi.org/10.1021/acs.chemmater.5b02847.

(127) Zhong, L.; Feng, Y.; Wang, G.; Wang, Z.; Bilal, M.; Lv, H.; Jia, S.; Cui, J. Production and Use of Immobilized Lipases in/on Nanomaterials: A Review

from the Waste to Biodiesel Production. *Int. J. Biol. Macromol.* **2020**, *152*, 207–222. https://doi.org/10.1016/j.ijbiomac.2020.02.258.

(128) Rafiei, S.; Tangestaninejad, S.; Horcajada, P.; Moghadam, M.; Mirkhani, V.; Mohammadpoor-Baltork, I.; Kardanpour, R.; Zadehahmadi, F. Efficient Biodiesel Production Using a Lipase@ZIF-67 Nanobioreactor. *Chem. Eng. J.* **2018**, *334*, 1233–1241. https://doi.org/10.1016/J.CEJ.2017.10.094.

(129) Adnan, M.; Li, K.; Wang, J.; Xu, L.; Yan, Y. Hierarchical ZIF-8 toward Immobilizing Burkholderia Cepacia Lipase for Application in Biodiesel Preparation. *Int. J. Mol. Sci.* **2018**, *19* (5), 1424. https://doi.org/10.3390/ijms19051424.

(130) Adnan, M.; Li, K.; Xu, L.; Yan, Y.; Adnan, M.; Li, K.; Xu, L.; Yan, Y. X-Shaped ZIF-8 for Immobilization Rhizomucor Miehei Lipase via Encapsulation and Its Application toward Biodiesel Production. *Catalysts* **2018**, *8* (3), 96. https://doi.org/10.3390/catal8030096.

(131) Hu, Y.; Dai, L.; Liu, D.; Du, W. Rationally Designing Hydrophobic UiO-66 Support for the Enhanced Enzymatic Performance of Immobilized Lipase. *Green Chem.* **2018**, *20* (19), 4500–4506. https://doi.org/10.1039/c8gc01284a.

(132) National Institute of Standards and Technology. Webbook of chemistry of NIST, SRD 69 https://webbook.nist.gov/chemistry/name-ser/ (accessed Jul 8, 2019).

(133) Secundo, F. Conformational Changes of Enzymes upon Immobilisation. *Chem. Soc. Rev.* **2013**, *42* (15), 6250–6261. https://doi.org/10.1039/c3cs35495d.

(134) Moatamed Sabzevar, A.; Ghahramaninezhad, M.; Niknam Shahrak, M. Enhanced Biodiesel Production from Oleic Acid Using TiO2-Decorated Magnetic ZIF-8 Nanocomposite Catalyst and Its Utilization for Used Frying Oil Conversion to Valuable Product. *Fuel* **2021**, *288*, 119586. https://doi.org/10.1016/j.fuel.2020.119586.

(135) Ben-Youssef, C.; Chávez-Yam, A.; Zepeda, A.; Rivera, J. M.; Rincón, S. Simultaneous Esterification/Transesterification of Waste Cooking Oil and Jatropha Curcas Oil with MOF-5 as a Heterogeneous Acid Catalyst. *Int. J. Environ. Sci. Technol.* **2021**, 1–14. https://doi.org/10.1007/s13762-020-03088-y.

(136) An, H.; Li, M.; Gao, J.; Zhang, Z.; Ma, S.; Chen, Y. Incorporation of Biomolecules in Metal-Organic Frameworks for Advanced Applications. *Coord. Chem. Rev.* **2019**, *384*, 90–106. https://doi.org/10.1016/j.ccr.2019.01.001.

(137) Pettinari, C.; Marchetti, F.; Mosca, N.; Tosi, G.; Drozdov, A. Application of Metal-Organic Frameworks. *Polym. Int.* **2017**, *66* (6), 731–744. https://doi.org/10.1002/pi.5315.

Chapter 8
Conclusions

"Every new beginning comes from
some other beginning's end"

Seneca

In the present thesis, different approaches have been presented for the association of active species to Metal-Organic Frameworks to enhance their inherent properties. From the analysis of the results, the following conclusions have been deduced:

1. The robust and microporous MIL-125-NH_2 is an ideal scaffold for the association of Ag nanospecies following SiB association routes.

2. Small AgNPs (5 nm) have been efficiently associated to MIL-125-NH_2, both with micro- and nano-crystal size, by a simple two-step impregnation-reduction method. Remarkably, as a result of their strong interaction, the AgNP@MIL-125-NH_2 composite exhibited enhanced optoelectronic properties.

3. Thin films of the AgNP@MIL-125-NH_2 exhibited an outstanding antifouling and photobactericide effect against challenging *S. aureus* biofilm, as a result of the combination of its triple complementary biocide activity: MOF inherent antibacterial effect, promoted by the presence of AgNPs and enhanced after UVA irradiation.

4. AgNCs smaller than 1 nm (~28 Ag atoms) have been successfully stabilized within MIL-125-NH_2 porosity by an ultrafast two-step photoreduction protocol.

5. The strong metal-matrix interaction in AgNC@MIL-125-NH_2 leads to a photoactive composite with a 2.4 eV energy band gap, demonstrating a great potential for the visible light assisted degradation of demanding emerging organic contaminants in water, such as the dye methylene blue (MB) and the challenging antibiotic sulfamethazine (SMT).

6. The photodegradation of contaminants under continuous flow using MOFs has been performed here for the first time, enabling the purification of 6.50 $L \cdot h^{-1} \cdot g^{-1}$ of SMT contaminated water.

7. Apart from a photoactive role, MIL-125-NH_2 can also exhibit a passive role for the active AgNCs, providing a support for heterogeneous industrial catalytic processes, as the hydrogenation of 4-nitroaniline.

8. Careful control of the reaction parameters can lead to the efficient preparation of pure phases of the iron(III) aminoterephthalate polymorphic MOF family under microwave-assisted solvothermal reaction with tunable size and high space-time yields, comparable to those of commercial MOFs.

9. The thermodynamic phase MIL-53(Fe)-NH_2 has been obtained for the first time under microwave assisted hydrothermal conditions, opening the door for its industrial production.

10. The beneficial selective heating procured by microwave irradiation enables the BaS association of AgNPs in the MIL-101-NH_2, even further studies are required for achieving a homogeneous core@shell system.

11. An *in situ* simple green two-step protocol has been developed for the efficient association of lipases to the biocompatible and flexible microporous iron(III) fumarate MIL-88A. Besides preserving activity, lipases were protected even under acidic denaturalization conditions.

12. Lipase@MIL-88A composites are efficient biocatalysts on the relevant model reaction of transesterification of soy-bean oil to biodiesel, with a solvent free optimized procedure. *P-f*-lipase@MIL-88A biocatalyst demonstrated enzyme recyclability preserving its activity even after 5 cycles.

13. Determination of the nature of the biodiesel reaction products enabled the identification of an interaction between MOF-lipase pair that procured extra reaction selectivity.

Conclusiones

En esta tesis se han llevado a cabo diversas estrategias para la asociación de nano especies activas a Redes Metal-Orgánicas para la mejora de sus propiedades. Las siguientes conclusiones se derivan de los resultados obtenidos a lo largo de este estudio:

1. La estructura porosa y robusta del MIL-125-NH_2 supone un andamio ideal para la asociación de nano-especies de plata empleando técnicas de asociación del tipo difusión o SiB.

2. Se han asociado pequeñas AgNPs (5 nm) al MIL-125-NH_2, tanto en el caso de micro como de nano cristales de MOF, mediante un proceso simple de impregnación-reducción en dos etapas. Cabe destacar que la fuerte interacción entre las AgNPs y el MOF confieren al composite AgNP@MIL-125-NH_2 propiedades optoelectrónicas mejoradas.

3. Los recubrimientos de tipo film delgados de AgNP@MIL-125-NH_2 exhibieron una destacable actividad antiadherente y fotobactericida frente a los biofilms de *S. aureus*, como resultado de la combinación de su triple efecto biocida complementario: i) la actividad antibacteriana inherente del MOF, ii) la presencia de AgNPs, y iii) la respuesta frente a irradiación UVA.

4. Adicionalmente, se han estabilizado AgNCs menores de 1 nm (~ 28 nm) en la porosidad del MIL-125-NH_2, quedando asociados únicamente en el interior del MOF, mediante una síntesis por fotorreducción ultrarrápida de dos pasos.

5. La fuerte interacción de los AgNCs con el ligando del MOF hacen que el composite AgNC@MIL-125-NH_2 presente una transición de energía mejorada de 2.4 eV, que permite la adsorción de energía en el rango visible. Por ello, se trata de un potencial fotocatalizador para la fotodegradación mediante luz visible de contaminantes emergentes en agua, como son el tinte azul de metileno (MB) y el antibiótico sulfametazina (SMT).

6. Se ha presentado por primera vez la aplicación de MOFs para la fotodegradación de contaminantes en régimen continuo, consiguiendo purificar 6.50 $L \cdot h^{-1} \cdot g^{-1}$ de agua real contaminada con SMT

7. Además de presentar un papel activo, el MIL-125-NH_2 también puede actuar como soporte pasivo que proteja a los AgNCs para su uso en catálisis heterogénea en procesos industriales, como es el caso de la hidrogenación de la 4-nitroanilina.

8. Un control preciso de los parámetros de reacción en la síntesis solvotermal asistida por microondas permite la obtención de fases puras de la familia polimórfica de MOFs basados en aminotereftalato de hierro(III), además de elevados rendimientos espacio-tiempo, comparables con aquellos de MOFs comerciales.

9. La fase termodinámicamente estable MIL-53-NH_2 ha sido obtenida por primera vez mediante síntesis hidrotermal asistida por microondas, permitiendo así una posible producción industrial de la misma.

10. El calentamiento selectivo de los reactivos que se consigue mediante la irradiación microondas permite la encapsulación BaS de AgNPs al MIL-101-NH_2, aunque son necesarios futuros estudios para conseguir una distribución homogénea del tipo núcleo@corteza.

11. Se ha desarrollado un procedimiento *in situ* de química verde para la asociación en dos pasos de lipasas al MIL-88A, un fumarato de hierro(III) flexible y biocompatible. Tras su inmovilización las lipasas no sólo conservaron su actividad, sino que además estuvieron protegidas frente a la desnaturalización en medio ácido.

12. Los composites de tipo lipasa@MIL-88A han demostrado su potencial como biocatalizadores eficientes en una reacción de relevancia: la transesterificación de aceite de soja en biodiesel mediante un proceso optimizado en ausencia de solventes. En concreto, el biocatalizador *P-f*-lipasa@MIL-88A permitió la reciclabilidad de la lipasa, preservando la actividad de esta tras 5 ciclos de reacción.

13. La determinación de los productos de la reacción de obtención de biodiesel ha permitido la identificación de la interacción MOF-lipasa que proporciona una selectividad extra a la reacción.

APPENDIX I

Supporting information Chapter 3

I.I. Synthesis of MIL-125-NH_2

MIL-125-NH_2 solvothermal synthesis was carried out in a round bottom flask according to previously reported experimental procedure, optimized within APMU members.[1] In a typical synthesis, H_2BDC-NH_2 (76 mmol, 13.75 g) was dissolved in a mixture of 200 mL of DMF (2.5 mol) and 50 mL of methanol (MeOH, 1.25 mol) at RT under stirring. The mixture was placed in a round bottom flask equipped with a condenser and was warmed at 100 °C under air. When the mixture reached the temperature of 100 °C, titanium(IV) isopropoxide (50 mmol, 15 mL) was added and then, the MilliQ water (50.56 mmol, 0.91 mL). The mixture was kept under stirring and heated at 100 °C for 72 h under air. The obtained yellow solid was filtered and washed in the filter twice with 100 mL of DMF at RT. For complete activation and release of solvents from the porosity, the as-synthesized solid was dispersed at RT in DMF under stirring overnight (50 mL of DMF *per* 1 g of product). Then, the same procedure was repeated twice using MeOH instead of DMF. The MIL-125-NH_2 bright yellow solid was finally dried at 100 °C. This is material is also called in this manuscript as microMOF, as its particles are ~ 500 nm (see Figure AI. 1).

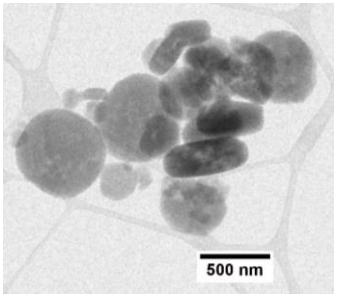

Figure AI. 1: TEM micrograph of MIL-125-NH_2 (microMOF)

Solvothermal synthesis of nanoMIL-125-NH_2 was also fulfilled following a procedure previously reported by APMU,[2] with a similar experimental setup as the microMOF but kept at 100 °C for only 32 h under air. The obtained yellow powder was centrifuged and washed with DMF and methanol. NanoMIL-125-NH_2 should be kept in methanol for preventing nanoparticle aggregation This material is called in the manuscript also as nanoMOF, in comparison with the microMOF, as their particles are below 300 nm (see Figure AI. 2).

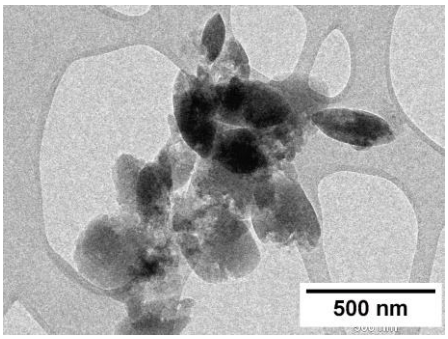

Figure AI. 2: TEM micrograph of nanoMIL-125-NH_2 (nanoMOF)

I.II. SiB association of AgNPs *via* chemical reduction

In the sections below will be presented the synthetic protocol optimization for the SiB attainment of AgNP@MIL-125-NH_2 composites, prepared in this thesis with presynthesized MIL-125-NH_2, with both micro and nano MOF particles and the association of AgNPs by chemical reduction of preimpregnated silver salts.

I.II.i. MIL-125-NH_2 with micron particle size (microMOF)

The SiB association of AgNPs to microMIL-125-NH_2 (microMOF) by chemical reduction was inspired by the methodology presented by Liu *et al.* for MIL-101 [3] and MIL-100(Fe).[4] For the discussion of the optimization of the impregnation-reduction protocol, TEM micrographs will be analyzed (being the AgNPs the ones with higher contrast in the micrographs), as it enables the determination of the resulting AgNP size and distribution as well as the final composite morphology.

First attempts considered an initial step of impregnation of 250 mg of activated MIL-125-NH_2 with 2 mL of a 0.2 M $AgNO_3$ solution (75 mg, 0.44 mmol) in CH_3CN, stirred during 4 h at RT. The recovered material was put under Ar atmosphere for reduction with $NaBH_4$ as reducing agent (E_0=-0.481 V), with 1 mL of a 0.55 M absolute ethanol solution and let stir for 3 h under inert atmosphere. $NaBH_4$ was added in excess to ensure complete reduction from Ag^+ to Ag^0. The final AgNP@microMOF_1 brown solid was recovered by centrifugation and thoroughly washed with absolute ethanol to remove the excess $NaBH_4$ and dried at 100 °C.

Optical inspection indicated association of Ag due to the material color change from yellow to brown. The presence of Ag was additionally confirmed by EDS with a Ti:Ag wt.% of 70:30 (being lower than the starting 55:45 wt.%). From the TEM micrographs can be seen that the reduction process was aggressive with the host MOF as the MIL-125-NH_2 characteristic disc shape was affected and become difficult to recognize (see Figure AI. 3 A). While the protocol presented by Liu *et al.* was suitable for MIL-100, it could not be directly extrapolated to MIL-125-NH_2. The observed AgNPs had a diameter of 7 ± 3 nm (as determined from TEM micrographs, n=245).

In order to diminish MOF degradation during the reduction of the silver salt to AgNPs, a second attempt was carried out decreasing the $NaBH_4$:Ag molar ratio from 2.5 to 2 but still keeping an excess of reducing agent. Therefore, the prepared reducing solution was of 0.4 M $NaBH_4$ in absolute ethanol. Color change from yellow to brown was observed almost right after the addition of the reducing solution and let stir again for 3 h (sample AgNP@microMOF_2). TEM analyses revealed that the shape of MIL-125-NH_2 was better preserved, even though with a rough external surface (see Figure AI. 3 B). The reduction of the $NaBH_4$:Ag molar ratio appeared not to have an effect on the AgNP formation (Ø=10 ± 5 nm, n=100), and was selected for the reduction. In spite of this, better control of the reduction step could produce AgNPs with a lower size dispersion and even be less aggressive with the

MIL-125-NH_2 particles. Again the Ag content determined by EDS was lower than the expected (Ti:Ag wt.%: 70:30 *vs.* experimental 55:45 wt.%). This suggested that impregnation step could also be improved.

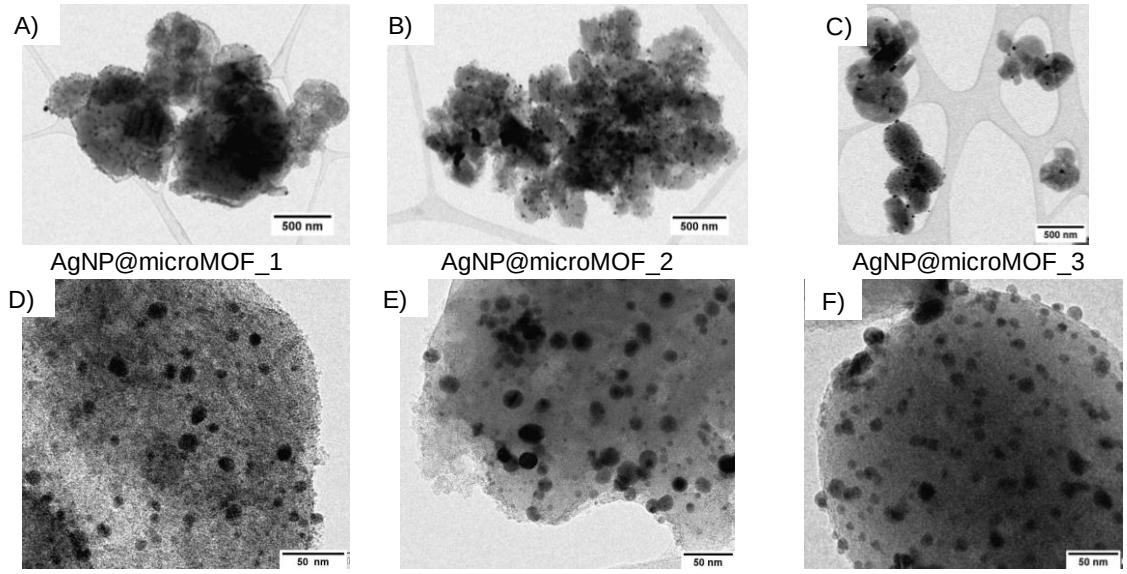

Figure AI. 3: TEM micrographs of different AgNP@MIL-125-NH_2 composites, during the optimization of the synthesis protocol: AgNP@microMOF_1 A) & D), AgNP@microMOF_2 B) & E) and AgNP@microMOF_3 C) & F). Scale bar 500 nm (up) and 50 nm (low)

With the conclusions extracted, a new impregnation-reduction protocol was designed to overcome the previous limitations. In this case, the impregnation of 250 mg of microMOF with 2 mL of a 0.2 M $AgNO_3$ solution in CH_3CN, was first done under sonication for 2 h and stirred during 16 h at RT. The recovered dry solid was dispersed in 2 mL of absolute ethanol prior to the reduction under inert atmosphere. The addition of the 1 mL of the 0.4 M $NaBH_4$ solution in ethanol was done dropwise and only let stirring for just 10 min, shortening the reaction time of the reduction. The sample, AgNP@microMOF_3, was recovered by centrifugation and washed with absolute ethanol to remove the excess $NaBH_4$. Images of the AgNP@microMOF_3 composite (see Figure AI. 3 C) revealed that reducing the time of reduction was beneficial for preserving MIL-125-NH_2 crystallinity and its characteristic disc shape. Even more, 10 min was enough for the formation of AgNPs (Ø= 8 ± 4 nm, n=120). It could be seen that the AgNP were not homogeneously distributed on the sample. Nevertheless, the amount of Ag associated, as determined by EDS, was again a Ti:Ag 70:30 wt.%. despite of the aid of ultrasounds for the infiltration of the $AgNO_3$ salt trough the pores and the longer contact time. It was concluded that the Ag association reached saturation of the MIL-125-NH_2 host as in all synthesized materials (AgNP@microMOF_1,2 and 3) the same weight ratio between Ti:Ag was achieved.

As a consequence, the updated impregnation reduction protocol was attempted reducing significantly the amount of starting $AgNO_3$. For sample

AgNP@microMOF_4, 250 mg of MIL-125-NH_2 were impregnated with 2 mL of a 7 mM $AgNO_3$ solution in CH_3CN (being Ti:Ag wt.% of 97:3) by sonication (2 h) followed by stirring (16 h, RT). For the reduction, 1 mL of a 15 mM solution of $NaBH_4$ in absolute ethanol were added dropwise over a 2 mL absolute ethanol suspension of the impregnated microMOF under Ar atmosphere and stirred for 10 min. The recovered AgNP@microMOF_4, as determined by EDS, matched the expected Ti:Ag wt.% of 97:3, having a 100 % impregnation yield indicating that the protocol was suitable. From the micrographs could be seen that AgNPs were present in all microMOF host particles (see Figure AI. 4 A) and had a Ø=4 ± 2 nm (n=100). Accordingly, the adjustments made appeared to be beneficial for the association of AgNPs.

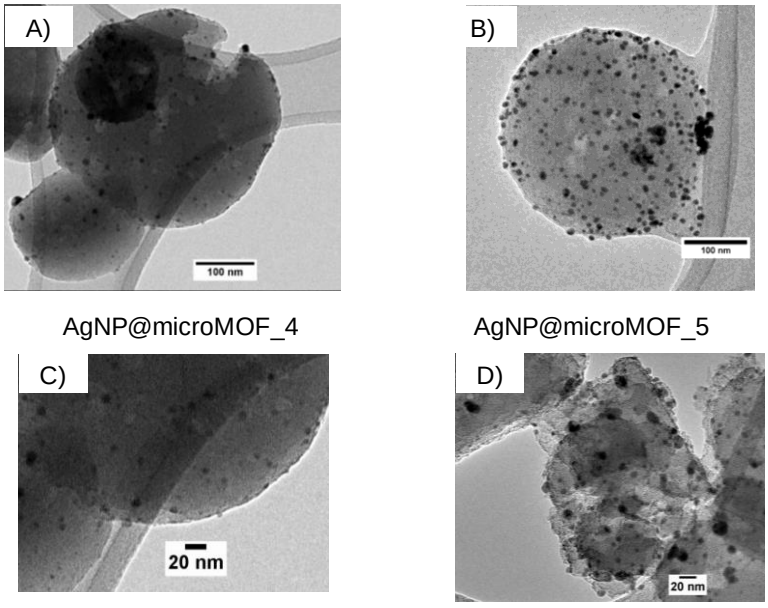

Figure AI. 4: TEM micrographs of different AgNP@MIL-125-NH_2 composites, during the optimization of the synthesis protocol: AgNP@microMOF_4 A) & C) and AgNP@microMOF_5 B) & D). Scale bar 100 nm (up) and 20 nm (low)

After several attempts verifying the impregnation-reduction protocol was appropriate for the SiB association of different contents of AgNPs to the MIL-125-NH_2 scaffold, certain parameters were defined: the concentration of the silver salt solution was settled on 22 mM of $AgNO_3$ in CH_3CN; the concentration of the reducing agent solution was fixed on 18 mM in absolute ethanol, considering 2 molar equivalents of $NaBH_4$ per mol of $AgNO_3$; reduction should be carried in inert atmosphere, adding the reducing solution dropwise and stirring for 10 min. As an example, the composite AgNP@microMOF:5 could be seen in Figure AI. 4 B), prepared under this conditions with a Ti:Ag weight ratio of 92:8 wt.% (Ø=7 ± 3 nm). Low angles tilt of the TEM sample holder revealed that bigger AgNPs were adsorbed on the surface while smaller ones were within the microMOF structure, probably allocated in defects generated by NP growth and agglomeration in the pores.

I.II.ii. MIL-125-NH_2 with nanoparticle size (nanoMOF)

As MIL-125-NH_2 has a tunable particle size, was also ambitioned to extend the SiB simple impregnation-reduction protocol from the microMOF to likewise load AgNPs in the nanoMOF. For better understanding of the SiB synthesis of the AgNP@nanoMOF sample, here is introduced information extracted from the original publication previously presented in Chapter 3.[5]

Briefly, here is presented the impregnation-reduction protocol applied to nanoMIL-125-NH_2 to reach the saturation of AgNPs. As the nanoMOF should be kept in methanol for preventing NP aggregation, an initial solvent exchange with CH_3CN by centrifugation previous to the impregnation was required. Once exchanged, the wet NPs (equivalent material corresponding to 250 mg of dry nanoMOF) were redispersed in 20 mL of a 22 mM $AgNO_3$ solution (Ti:Ag raio 55:45 in wt.%) in CH_3CN by sonication (2 h) and let stir at RT for 16 h. The silver-impregnated nanoMOF (Ag^+@nanoMOF) was recovered by centrifugation and once again exchanged the solvent to absolute ethanol. After solvent exchange, Ag^+@nanoMOF was put under Ar atmosphere stirring with 30 mL of absolute ethanol. For the reduction, a 50 mL absolute ethanol solution of 18 mM $NaBH_4$ was added to the previous ethanol mixture drop by drop and let stir for 10 min under Ar. The composite AgNP@nanoMOF was then recovered by centrifugation and preserved in absolute ethanol. Even the presence of Ag on the AgNP@nanoMOF was appreciable at naked eye due to the macroscopic color change of the sample: brownish compared to the yellow of the pristine nanoMOF (see Figure S 1 in APPENDIX III), additional characterization revealed that AgNP@nanoMOF composite was successfully prepared using the simple and efficient two-step SiB protocol (for further characterization please refer to publication “An Ag-loaded photoactive nano-Metal-Organic Framewrok as a promising biofilm treatment”, and its supporting information in APPENDIX III).

I.II.iii. Extension to other MOFs

Extending the visible range absorbance is of interest of other photoactive MOFs as the zirconium aminoterephthalate UiO-66-NH_2 or $Zr_6O_4(OH)_4[C_8H_5O_4N]_6$.[6,7] It consist of an inner $Zr_6O_4(OH)_4$ core in which the triangular faces of the Zr6-octahedron are alternatively capped by μ3-O and μ3-OH groups. It All of the polyhedron edges are bridged by carboxylates (-CO_2). It

has a significant porosity (S_{BET}=1110 $m^2 \cdot g^{-1}$) accessible through triangular windows of 6 Å. As well as MIL-125-NH_2, has a limited visible absorption with E_g= 2,7 eV. For this reason, the association of AgNP using the above mentioned SiB impregnation-reduction protocol was attempted with UiO-66-NH_2.

UiO-66-NH_2 both in micro and nano particle form were synthesized following previous reports. [8–10] For the association, a low Zr:Ag weight ratio was selected (97:3). Accordingly, 250 mg of UiO-66-NH_2 were put in contact with 1 mL of a 22 mM $AgNO_3$ solution in CH_3CN by sonication (2 h) and let stir for 16 h. The preimpregnated solid was recovered by centrifugation and put under Ar atmosphere with 2 mL of absolute ethanol. Reducing solution consisted of 1,6 mL of a 18 mM $NaBH_4$ solution in absolute ethanol and was added dropwise over the UiO-66-NH_2 dispersion and keep stirring during 10 min in an inert atmosphere. Final AgNP@Uio-66-NH_2 composites were recovered by centrifugation.

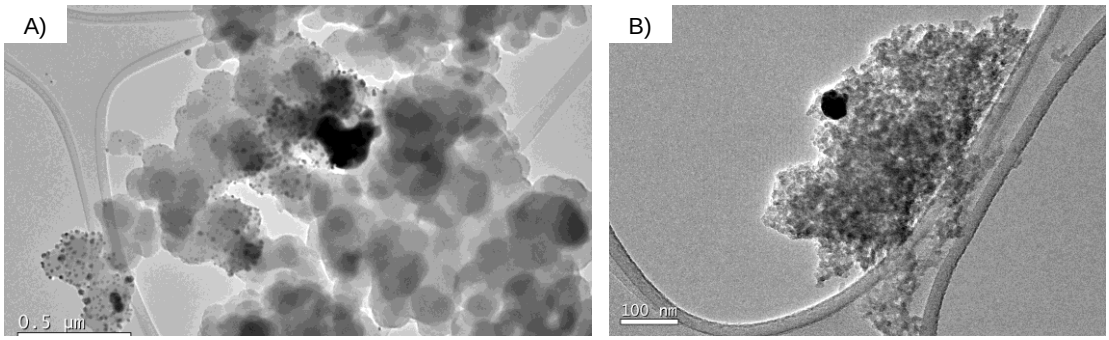

Figure AI. 5: TEM micrographs of: A) AgNP@microUiO-66-NH_2 (scale 0.5 µm) and B) AgNP@nanoUiO-66-NH_2 (scale 100 nm)

Lamentably, as TEM micrographs of Figure AI. 5 showed, the SiB optimized protocol for MIL-125-NH_2 was not successful for the association of AgNPs to UiO-66-NH_2. In the case of the micro UiO-66-NH_2, impregnation was not homogeneous as some crystals had an abundant population of AgNPs while in other silver was completely absent. For the nano UiO-66-NH_2 (MOF particles Ø= 20 ± 3 nm, n=200), the resulting AgNP were surrounded or encased by the MOF particles in an aleatory manner, indicating interaction with the external surface but not with the porosity. What is more, impregnation of nanoUiO-66-NH_2 might have not taken place due to is lower porosity (S_{BET}= 370 *vs.* 1110 $m^2 \cdot g^{-1}$ of the micro) and the lower crystallinity of the MOF.[10] Further studies are being conducted by APMU researchers on optimizing the SiB association of AgNPs to UiO-66-NH_2, but are outside of this thesis.

Bibliography

(1) Moreira, M. A.; Santos, J. C.; Ferreira, A. F. P.; Loureiro, J. M.; Ragon, F.; Horcajada, P.; Yot, P. G.; Serre, C.; Rodrigues, A. E. Effect of Ethylbenzene in P-Xylene Selectivity of the Porous Titanium Amino Terephthalate MIL-125(Ti)-NH2. *Microporous Mesoporous Mater.* **2012**, *158*, 229–234. https://doi.org/10.1016/j.micromeso.2012.03.039.

(2) Vilela, S.; Salcedo-Abraira, P.; Colinet, I.; Salles, F.; de Koning, M.; Joosen, M.; Serre, C.; Horcajada, P. Nanometric MIL-125-NH2 Metal–Organic Framework as a Potential Nerve Agent Antidote Carrier. *Nanomaterials* **2017**, *7* (10), 321. https://doi.org/10.3390/nano7100321.

(3) Liu, X. H.; Ma, J. G.; Niu, Z.; Yang, G. M.; Cheng, P. An Efficient Nanoscale Heterogeneous Catalyst for the Capture and Conversion of Carbon Dioxide at Ambient Pressure. *Angew. Chemie - Int. Ed.* **2015**, *54* (3), 988–991. https://doi.org/10.1002/anie.201409103.

(4) Zhu, N.-N.; Liu, X.-H.; Li, T.; Ma, J.-G.; Cheng, P.; Yang, G.-M. Composite System of Ag Nanoparticles and Metal–Organic Frameworks for the Capture and Conversion of Carbon Dioxide under Mild Conditions. *Inorg. Chem.* **2017**, *56* (6), 3414–3420. https://doi.org/10.1021/acs.inorgchem.6b02855.

(5) Arenas-Vivo, A.; Amariei, G.; Aguado, S.; Rosal, R.; Horcajada, P. An Ag-Loaded Photoactive Nano-Metal Organic Framework as a Promising Biofilm Treatment. *Acta Biomater.* **2019**, *97*, 490–500. https://doi.org/10.1016/j.actbio.2019.08.011.

(6) Zhang, H.; Li, J.; He, X.; Liu, B. Preparation of a G-C3N4/UiO-66-NH2/CdS Photocatalyst with Enhanced Visible Light Photocatalytic Activity for Tetracycline Degradation. *Nanomaterials* **2020**, *10* (9), 1824. https://doi.org/10.3390/nano10091824.

(7) Shen, L.; Liang, S.; Wu, W.; Liang, R.; Wu, L. CdS-Decorated UiO-66(NH2) Nanocomposites Fabricated by a Facile Photodeposition Process: An Efficient and Stable Visible-Light-Driven Photocatalyst for Selective

Oxidation of Alcohols. *J. Mater. Chem. A* **2013**, *1* (37), 11473–11482. https://doi.org/10.1039/c3ta12645e.

(8) Cavka, J. H.; Olsbye, U.; Guillou, N.; Bordiga, S.; Lillerud, K. P. A New Zirconium Inorganic Building Brick Forming Metal Organic Frameworks with Exceptional Stability - Supp. Info. *J. Am. Chem. Soc.* **2008**, *6*, 1–19. https://doi.org/10.1021/ja8057953.

(9) Garibay, S. J.; Cohen, S. M. Isoreticular Synthesis and Modification of Frameworks with the UiO-66 Topology. *Chem. Commun.* **2010**, *46* (41), 7700. https://doi.org/10.1039/c0cc02990d.

(10) Vilela, S. M. F.; Salcedo-Abraira, P.; Micheron, L.; Solla, E. L.; Yot, P. G.; Horcajada, P. A Robust Monolithic Metal-Organic Framework with Hierarchical Porosity. *Chem. Commun.* **2018**, *54* (93), 13088–13091. https://doi.org/10.1039/c8cc07252c.

APPENDIX II

Antimicrobial Metal Organic Frameworks

II.I. Book Chapter: Antimicrobial MOFs

1- Antimicrobial Metal Organic Frameworks

Ana Arenas Vivo and Patricia Horcajada *

Advanced Porous Materials Unit (APMU), IMDEA Energy Institute, Avda. Ramón de la Sagra 3, E-28935 Móstoles, Madrid, Spain
**Corresponding author. E-mail address: patricia.horcajada@imdea.org*

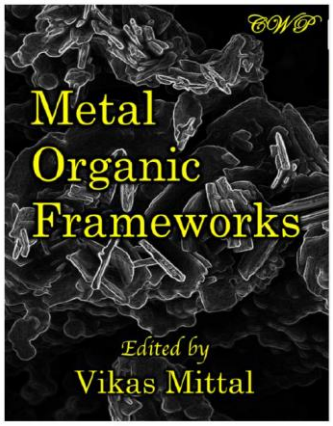

Chapter 1, pp.:1-36, *Metal Organic Frameworks*, edited by V. Mittal, ©2019 Central West Publishing, Australia, ISBN: 978-1-925823-57-8

1

Antimicrobial Metal Organic Frameworks

Ana Arenas Vivo and Patricia Horcajada*

Advanced Porous Materials Unit, IMDEA Energy Institute, Av. Ramón de la Sagra 3, 28935 Móstoles-Madrid, Spain

**Corresponding author*: patricia.horcajada@imdea.org

1.1 Introduction

Bacteria are the most common microorganisms present on Earth and can be found in almost every habitat. While some of these bacteria are beneficial, a great proportion is the cause of the propagation of several diseases and infections [1]. Apart from the direct health care implications, unwanted bacteria colonization is of high relevance in other less obvious industries and applications (food packaging, marine shipping, water treatment, heat exchanging systems, etc.), thus, having a significant environmental and socioeconomic impact [2].

Over the last decades, there has been a radical change in the approach to treat infections. Although infectious diseases have been traditionally treated with antibiotics, their frequent use has led to the prevalence of resistant bacterial strains [3]. While classical evolving infections are believed to entail the free-floating (planktonic) bacteria, the appearance of chronic infections is related with sessile aggregation of microorganisms, known as biofilms [4]. These bacterial micro-environments are formed by irreversibly attached microorganisms and extracellular polymeric substances (EPS) in interaction with a substrate. The biofilm formation process involves the development of a protective environment to the growing colony ideal for bacterial proliferation. It is well known that cells within biofilms experience: i) differentiation in response to the local conditions they are subjected to, ii) cell-to-cell communication (quorum-sensing) and iii) demonstrated resistance to environmental stresses [5]. Therefore, the need for new bactericides is a pressing real chal-

Metal Organic Frameworks, edited by Vikas Mittal
© 2019 Central West Publishing, Australia

lenge and encourages biologists, chemists and materials scientists to develop efficient antibacterial agents. Different strategies have been developed in order to resolve the issue during several stages of biofilm formation (*i.e.* contact, attachment, proliferation, maturation and dispersion), such as 1) limiting switch from planktonic to biofilm lifestyle, 2) limiting initial adhesion and interaction, 3) interfering in bacterial communication, with quorum-sensing autoinducers, 4) developing anti-adhesive surfaces and 5) promoting dispersion [6]. Several chemical disinfectants, both inorganic (TiO_2, ZnO, Ag, NO, I, etc.) and inorganic-organic hybrid materials (montmorillonite, zeolites and silica based sol-gels) [7] have been increasingly used against Gram (-) and Gram (+) bacteria in several consumer products (e.g. catheters, prosthesis, food wrap films, etc.) [8,9].

In recent years, a new type of hybrid materials, called metal organic frameworks (MOFs) (also known as porous coordination polymers (PCPs)), has been developed as promising biocide materials [10]. These crystalline solids consist of inorganic units (e.g. atoms, clusters and chains) connected *via* ionocovalent bonding to polydentate organic ligands (e.g. carboxylates, phosphonates and azolates), leading to porous 3D frameworks (Figure 1.1). Due to their exceptional porosity (up to Brunauer-Emmett-Teller surfaces-S_{BET} = 7000 $m^2\ g^{-1}$; pore diameter = 3-90 Å) [11] and compositional and structural versatility, MOFs stand out as ideal candidates for several strategic applications, both at industrial and social level (e.g. separation, sensing, catalysis, energy, etc.) [12]. More recently, their use has

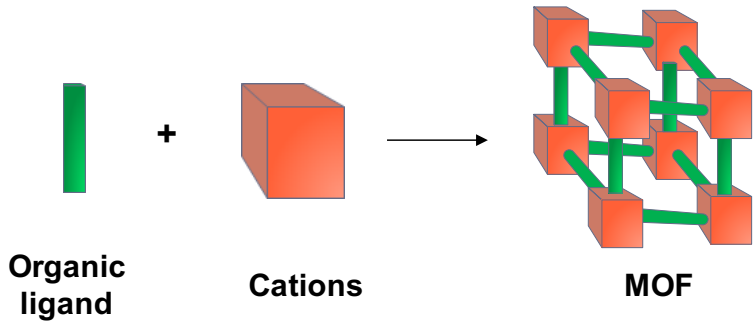

Figure 1.1 Schematic representation of a MOF.

been explored in biomedicine (e.g. diagnosis, drug delivery and cosmetics) [13]. Some of the advantages of MOFs compared to other antibacterial materials are as follows: i) both organic and inorganic

components of MOFs can provide bactericidal activity by the generation of reactive oxygen species (ROS), ii) they have a uniform and ordered distribution of active sites and iii) metal release to the media during degradation tends to be more homogeneous. In addition, not only their framework can be bioactive, but they can also entrap diverse bactericidal agents and increase their disinfection power [14].

Taking into consideration these properties, MOFs as biocide agents can be classified according to the origin of their bioactivity: i) MOFs with intrinsic antimicrobial activity, which comes from the network, or ii) MOFs with extrinsic antimicrobial activity, which arises from a hosting therapeutic agent that is associated to their structure [15]. The first one entails the controlled degradation of the MOF for the liberation of the active components (metal, ligand or both) and these structures are normally referred to as 'ion reservoirs' [16,17]. The second classification requires the release of the active ingredients (AIs, e.g. metallic nanoparticles, NPs, drugs, etc.) *via* diffusion through the MOF porosity or leakage upon MOF dissolution. Since the first reported one dimensional (1D) PCP with biocide properties in 2010-2012 [18,21], diverse studies have explored the use of MOFs as antibacterial agents. Recently, Wyszogrodzka *et al.* [14] also reviewed the topic in greater details.

The aim of this book chapter is to review the development of antimicrobial MOFs (limiting them to porous 3D structures), with either intrinsic or extrinsic activity, including not only some AI immobilization strategies and examples of their integration in several devices (membranes, thin films, etc.), but also their applications.

1.2 Intrinsic Antimicrobial Activity

As mentioned above, the origin of the bactericide effect in MOFs with intrinsic antimicrobial activity relies on the activity of its individual (organic and/or inorganic) components. It is well-known that certain metals (e.g. Cu, Ti, Ag, Zn and Fe) [22-24] possess a bioactive character. As a consequence, these have been selected in several studies as inorganic building units for the formulation of MOFs to obtain antibacterial frameworks. Other strategy is the use of drugs and other therapeutic biomolecules as organic ligands for building metal biomolecules frameworks (or bioMOFs). Some of these 'bioactive ingredients' have been further discussed by Rojas *et al.* [17]. Even more, both the cation and ligand can have disinfectant proper-

ties, and, therefore, the final MOF exhibits an additive or synergistic bactericide effect.

Some of the advantages of intrinsic antimicrobial activity of MOFs over other solids are: i) active antibacterial agents are obtained relatively easily, by just considering the MOF synthesis protocol (e.g. without the need of other impregnation steps), ii) there is no need to achieve high porosity in these frameworks as the bactericidal activity comes from the constituents, iii) they can be synthesized with different particle sizes, which strongly determine their final biodistribution, toxicity and activity [25], iv) they can remain stable in bio-relevant conditions with time to achieve their purpose and v) they have an uniform and ordered distribution of active sites, along with more homogeneous release to the media during degradation.

In this section, 3D MOFs with intrinsic biocidal activity are compiled, organized according to the source of their effect: derived from the metal, ligand or both.

1.2.1 Antimicrobial Activity Derived from Metal

The MOFs studied as 'metal reservoirs' were firstly compiled by Wyszogrodzka *et al.* [14] in 2016 (Table 1.1). In combination with these, an up-to-date compilation is presented here, organized by the nature of the selected metallic cation.

The antibacterial action of silver has been extensively utilized, from consumer products to medical devices. Although its mechanism of action is not completely understood, it is believed that it results from the Ag^+ delivery, which interacts with the bacterial cell membrane and plasma components, thus, affecting their function [22]. Interestingly, Liu *et al*. [26] were the first to report the synthesis of three Ag-based metal organoboron frameworks for use as Ag^+ reservoir against planktonic *Escherichia coli* (facultative aerobic Gram (-)) and *Staphylococcus aureus* (aerobic Gram (+)). The as-prepared micrometric crystals were subjected to the standard disk diffusion method, thus, measuring the bacterial growth inhibition zone to evaluate the biocidal activity. The minimum inhibitory concentration (MIC) for both bacteria was 300 ppm of MOF, Ag content being 12 wt% (36 ppm). The Ag^+ release from the three MOF structures, determined in distilled water by inductively coupled plasma optical emission spectroscopy (ICP-OES), was 3.7, 4.4 and 5.2 10^{-6} g per day. Berchel *et al.* [16] also evaluated the antibacterial activity of

the $Ag_3[C_7H_4O_5P]$ MOF, previously reported by the same group [27], against *S. aureus*, *E. coli* and *Pseudomonas aureginosa* (aerobic Gram (-)). The minimal active bactericidal concentration (MBC) in the culture medium was determined by means of optical density and plate count, with $Ag_3[C_7H_4O_5P]$ displaying interesting bactericidal properties with a broad antibacterial spectrum. Given the proven negligible bactericidal effect of the ligand, 3-phosphonobenzonic acid, the authors concluded that the MOF activity might exclusively come from the Ag^+ released from the MOF.

To further develop new MOFs based on Ag and aromatic–carboxylic acids ligands containing hydroxyl and pyridyl groups, Lu *et al*. [28] generated three new structures, Ag_2(3-NPTA)$(bipy)_{0.5}(H_2O)$ [28] (Figure 1.2), $Ag_2[(O\text{-}IPA)(H_2O)\cdot(H_3O)]$ and $Ag_5[(PYDC)_2(OH)]$ [29], with the ligands 3-/4-nitrophthalic acid and 4,4'-bipyridyl in the first, whereas 5-hydroxyisophthalic acid and pyridine-3,5-dicarboxylic acid in the other two. The developed MOFs exhibited a significant antimicrobial activity against *S. aureus*

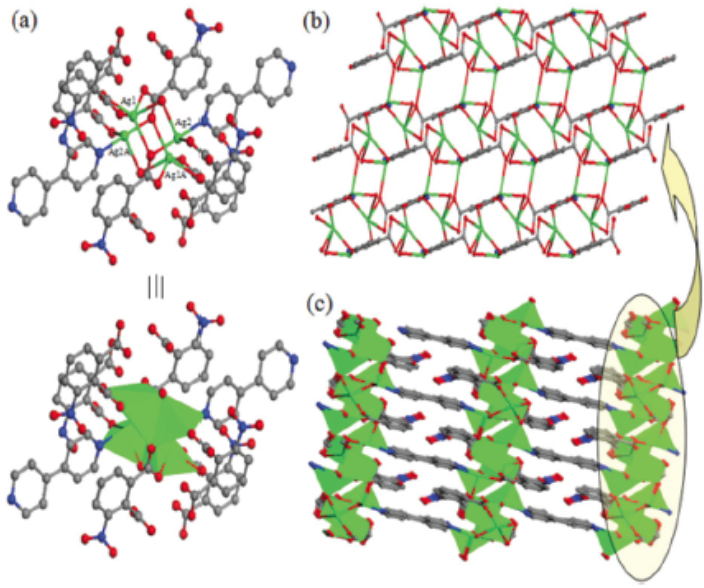

Figure 1.2 Ball and stick representation as well as polyhedral representation of the tetranuclear unit (a), a 2-D layer magnification part of the structure (b) and 3D framework (c) in Ag_2(3-NPTA)$(bipy)_{0.5}(H_2O)$. Reproduced from Reference 28 with permission from Royal Society of Chemistry.

and *E. coli*. Their MICs, estimated by optical density, were in the range of 10-20 ppm of MOF, which indicated relatively higher antibacterial activity in suspension as compared to other MOFs (20 *vs*. 300 ppm [26]). These Ag-based MOFs also showed higher activity in the inhibition zone test as compared to Ag nanoparticles (AgNPs). Based on the findings from ICP-OES and transmission electron microscopy (TEM) images, the authors proposed that the bactericidal mechanism was due to the delivery of Ag^+ and their interference with the cell membrane, resulting in the loss of cellular cohesion (Figure 1.3).

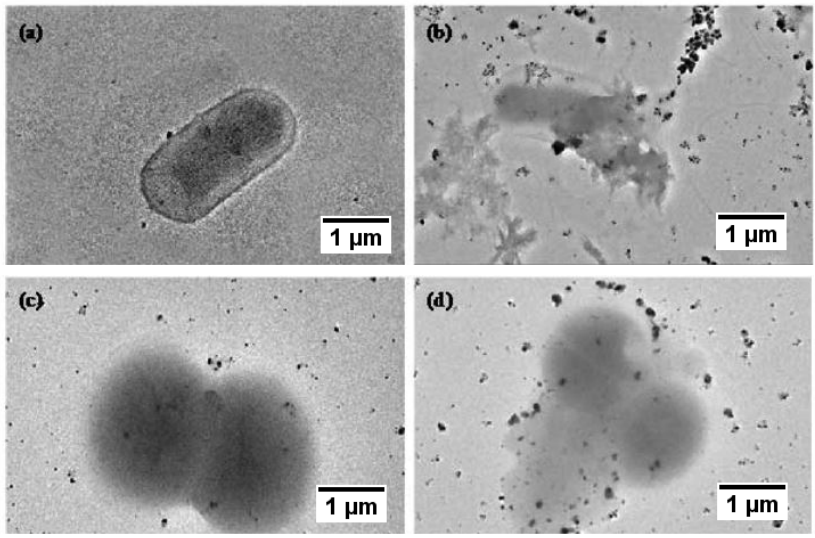

Figure 1.3 TEM morphological images of cell structures: intact and damaged E. coli (a, b); intact and damaged S. aureus (c, d). Reproduced from Reference 28 with permission from Royal Society of Chemistry.

For the development of novel Ag-MOFs based on polyoxometalates (P_2W_{18}), useful for their abundant coordination sites, Wang *et al*. [30] reported three original structures based on Ag as cation. They evaluated their potential biocide properties *via* inhibition zone, observing that the ligands (1,3-bis(1,2,4-triazol-1-y1)propane and 1,4-bis(1,2,4-triazol-1-y1)butane), dimethyl sulfoxide (solvent used for the synthesis) and P_2W_{18} displayed almost no inhibition against *S. aureus* and *E. coli*, while the Ag-MOFs exhibited a similar inhibition as $AgNO_3$ (positive blank used as reference of Ag^+ re-

lease). Zhang *et al*. [31] recently essayed the *S. aureus* viability against the SD/Ag14 open MOF, with cyclopropylacetylene and *p*-toluenesulfonate as building blocks shaping the Ag_{14} cluster. The authors determined a MIC of 5 ppm *via* plate count, which was smaller than the 20 ppm reported for AgMOFs by Lu *et al*. [28,29].

Another group of MOFs with metal-induced intrinsic antimicrobial activity are Cu-based MOFs. Again, the release of Cu^{2+} is the key to promote disinfection. These cations can adhere to bacterial cell membranes and cause their cytolysis and release of intracellular content, resulting in the loss of bacteria viability [32]. With the aim of investigating the effect of MOF morphology on bacterial viability, Wang *et al.* [33] synthesized the Cu-pyridine MOF with different shapes (rhombus layers, rhombus discs, rhombus lumps and bread-like) and determined the MIC against Gram (+) (*Bacillus subtilis* and *S. aureus*) and Gram (-) bacteria (*Salmonella enteriditis*, *E. coli*, *Proteus vulgaris* and *P. aeruginosa*). Overall, the rhombus lumps exhibited the best antibacterial performance (e.g. *E.coli* MIC = 6.25 ppm), although the mechanism of action was not analyzed. The antibacterial activity of the well-known microporous Cu trimesate (CuBTC, also called HKUST-1) [34] was first proved by Abbasi *et al.* [35] on dense coating on silk fibers (see Section: Devices and Applications). Soon afterwards, Chiericatti *et al*. [36] reported the first use of HKUST-1 as an antifungal agent. The material showed higher antifungal activity against *Saccharomyces cerevisae* than *Geotrichum candium* in plate count. The physicochemical characterizations performed after assays determined that HKUST-1 activity resulted from the release of Cu ions upon framework degradation. HKUST-1 fungicidal effect has been further studied recently by Celis-Arias *et al.* [37] against *Aspergillus niger, Fusarium solani* and *Penicillium chrysogenum*, taking into consideration the effect of the MOF particle size. HKUST-1 doped with CuO NPs (2 wt%, HKUST-1-NP) exhibited higher disinfection at lower concentration, particularly against *P. Chrysogenum*, when compared with pristine HKUST-1 and a proportional amount of CuO-NPs. HKUST-1 coated by activated carbon (AC-HKUST-1), generated by an *in-situ* ultrasound assisted synthesis, was also explored as a dye absorbent for water treatment as well as an antibacterial agent against challenging multidrug-resistant *S. aureus* and *P. aeruginosa* by Azad *et al*. [38]. The obtained MIC values were 100 and 50 ppm, respectively, without significant differences in the biocidal activity of the AC-HKUST-1 and blank HKUST-1, thus, ruling out the effect of the AC on the bactericidal effect. Never-

theless, the coated material exhibited higher dye adsorption capacity with a 97% removal as compared to 63% for HKUST-1. Additionally, the copper terephthalate surface-anchored MOF Cu-SURMOF-2 has also been proposed by Sancet *et al*. [39] to treat biofilm formation in the maritime environments against the Gram (-) halophilic *Cobetia marina*. Preliminary stability studies of the layer-by-layer synthesized MOF, carried out with X-ray diffraction (XRD) and ICP-OES, revealed that Cu–SURMOF-2 was stable in water and artificial sea water during the 2 h contact time of study. Nevertheless, the MOF lost its cohesion with *C. marina* present in the medium and had a fast release of 2 ppm of Cu in 2 h. The authors suggested that the EPS delivery affected the MOF integrity after bacterial attachment to the surface, thus, leaching Cu^{+} ions that interfere with the viability of bacteria. Indeed, LIVE/DEAD staining showed 80% of *C. marina* yellow, which indicated initial viability affection. The atomic force microscopy (AFM) and scanning electron microscopy (SEM) micrographs revealed a wrinkled bacterial surface, when in contact with the Cu-SURMOF-2 for 2 h. Figure 1.4 also shows the inhibition zone test analysis.

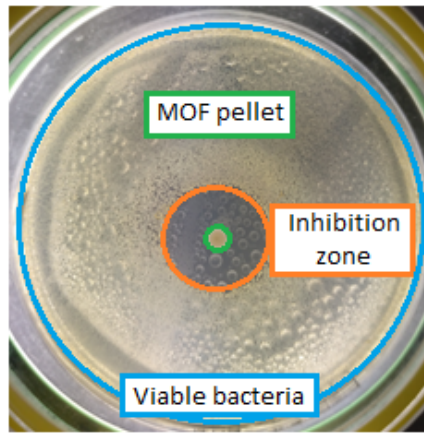

Figure 1.4 Inhibition zone test carried out with a MOF pellet (green circle) on top of a petri dish (inhibition zone (orange circle) and viable bacteria (blue circle)).

In addition, several cobalt complexes have been previously reported with proven antiviral and antibacterial efficacy [40]. In this case, it is believed that these complexes promote the ROS generation when cations are in the culture broth, thus, affecting the function of

the plasma membrane proteins. Hence, it might be reasonable to use Co as a building unit of biocide MOFs. However, one might also consider the potential toxicity of cobalt when compared with, for instance, an endogenous metal such as zinc (oral LD_{50} (rats; considering sulfate salts) = 1710 and 424 mg/kg [41,42] and daily doses = 15 and 0.03 mg, for Zn and Co, respectively) [43]. In this respect, Zhuang *et al*. [44] synthesized the porous Co-TDM MOF with Co and an octa-topic carboxylate ligand, tetrakis[(3,5-dicarboxyphenyl)-oxamethyl] methane, to probe its bactericidal effect against two strains of *E. coli*. Bacterial growth was evidenced *via* optical density at 600 nm (OD_{600}) in contact with 10-15 ppm of Co-TDM over an 8 h period. This bactericidal effect was observed even after 20 minutes in contact with the *E. coli* strains. TEM observations of the damaged bacteria led to the conclusion that the cell death resulted due to the disruption of the cell membrane when in contact with the MOF. Aguado *et al*. [45] selected two cobalt imidazolates, ZIF-67 (ZIF: zeolitic imidazolate frameworks) and Co-SIM-1 (SIM: substituted imidazolate material) as bactericidal materials. The authors conducted agar plate diffusion tests and determined MIC *via* OD measurements against *S. cerevisiae*, *Pseudomonas putida* and *E. coli*, using AgTAZ PCP for comparison purposes, selected for its commercially available ligand (1,2,4-triazole) and the well-known activity of Ag. With a progressive cobalt release (over 3 months) within the range of previously studied Ag-based materials [16,26], the selected Co-based MOFs showed higher activity than AgTAZ. In another study, the authors dispersed Co-SIM-1 in polylactic acid (PLA), a polymer derived from renewable resources with natural hydrophilicity that reduces biofuling tendency, and electrospun into fibers with antimicrobial effect against *P. putida* and *S. aureus* [46] (see Section: Devices and Applications).

Lastly, MOFs constituted by Zn building units have also been reported as biocide materials. Zn, as a biocompatible endogenous cation (daily recommended dose = 15 mg) [43], has attracted the interest of researchers due to its bactericidal and bacteriostatic properties. The mechanism of action has been thoroughly studied and attributed to ROS generation and enhanced membrane permeability, internalization of NPs due to loss of proton motive force and uptake of toxic dissolved zinc ions [47]. Although most of the reported studies are based on the activity of extrinsic AI (see Section: Extrinsic Antimicrobial Activity), a few studies deal with the intrinsic activity of zinc. For instance, Martin-Betancor *et al*. [48] evaluated the bacte-

ricidal activity of the zeolite imidazolate framework, Zn-SIM-1, against suspensions of photosynthetic cyanobacteria (*Anabaena*, *Synechoccocus*) in comparison with Co-SIM-1 and AgTAZ. The biocidal activity of the materials was determined by measuring chlorophyll *a* concentration and performing inhibition zone tests. Co-SIM-1 exhibited slightly superior activity as compared to its Zn MOF analogue. As it was elucidated that the biocidal activity was a result of the dissolved metals present in the culture medium, total ion

Table 1.1 Compilation of the MOFs used as ion reservoir for bactericide applications

Compound	Metal	Ligand	Ref.
$[(AgL)NO_3]\cdot 2H_2O$ $[(AgL)CF_3SO_3]\cdot 2H_2O$ $[(AgL)ClO_4]\cdot 2H_2O$	Ag	L=Tris-(4-pyridylduryl)borane	[26]
$Ag_3[C_7H_4O_5P]$	Ag	3-Phosphonobenzoate	[16]
$[Ag_2(O\text{-}IPA)(H_2O)\cdot(H_3O)]$	Ag	5-Hydroxyisophthalic	[29]
$[Ag_5(PYDC)_2(OH)]$	Ag	Pyridine-3,5-dicarboxylic acid	[29]
$C_{24}H_{39}Ag_7N_{24}O_{65}P_2W_{18}$ $C_{35}H_{53}Ag_7N_{30}O_{63}P_2W_{18}$ $C_{36}H_{60}Ag_4N_{27}O_{64}P_2W_{18}$	Ag	Polyoxometalate: $P_2W_{18}O_{62}^{6-}$ Ligand: bis(triazole) with different spacer lengths	[30]
$C_{171}H_{173}Ag_{42}Cl_9O_{10}S_3$	Ag	p-toluenesulfonate	[31]
$CuC_{12}H_{14}N_2O_8$	Cu	4,4'-dicarboxy-2,2'-bipyridine	[33]
HKUST-1	Cu	Bencene 1,3,5-tricarboxylic acid	[36]
Cu-SURMOF 2	Cu	Benzene 1,4-dicarboxylic acid	[39]
$Co_4(H2O)_2(TDM)(H2O)_8$	Co	tetrakis [(3,5-dicarboxyphenyl)oxamethyl] methane acid	[44]
ZIF-67	Co	2-methylimidazolate	[45]
Co-SIM-1	Co	4-methyl-5-imidazole carboxaldehyde	[45] [48]
AgTAZ	Ag	1,2,4-triazole	[45] [48]
Zn-SIM-1	Zn	4-methyl-5-imidazole carboxaldehyde	[48]
BioMIL-5	Zn	Azelaic acid	[49]
	Ag	Bencene 1,3,5-tricarboxylic acid	[50]

concentration was determined with two experimental techniques (ICP-OES and heavy metal bioreporter) and *via* chemical computational modelling (Visual MINTEQ). The experiments revealed a higher amount of Co dissolved in the medium, occasionally double of the Zn concentration, therefore, explaining the higher activity of the Co-SIM-1 material as compared to Zn-SIM-1.

1.2.2 Antimicrobial Activity Derived from a Cation-Ligand Combined Effect

There are plenty of references in the literature related to the MOFs made of endogenous and/or therapeutically active ligands (also known as bioMOFs) and their applications in biomedicine (drug delivery, imaging and sensing [13,15,17,25,51,52]), however, only a few reports can be found concerning their antibacterial activity.

Occasionally, the combination of different species is required to provide a cooperative therapeutic effect. BioMOFs based on antibacterial cations and bioactive ligands (Figure 1.5) represent this useful combination, as these can be specifically designed for a particular application. Such is the case of the $[Ag(\mu_3\text{-PTA=S})]_n(NO_3)_n{\cdot}nH_2O$ bioMOF [53], which combines the antimicrobial activity of Ag and aminophosphine 1,3,5-triaza-7-phosphaadamantane derivative (PTA=S). The bioMOF was screened against *E. coli*, *P. aeruginosa* and *S. aureus*, determining MIC values of 11, 14 and 56 ppm, respectively. A control with the corresponding amount of silver exhibited MIC values of 37, 368 and 368 ppm, whereas the MIC of the PTA=S ligand alone was over 600 ppm for the three bacteria. This led to the conclusion that the anti-bactericidal effect of $[Ag(\mu_3\text{-PTA=S})]_n(NO_3)_n{\cdot}nH_2O$ was the result of the combination of its constituents.

Tamames-Tabar *et al*. [49] synthesized biocompatible and bioactive Zn azelate, BioMIL-5, which inhibited the growth of *S. aureus* and *S. epidermis* due to its individual components. BioMIL-5 progressively degraded in the culture broth and water, thus, releasing active constituents. Antibacterial activity studies included the determination of MIC and MBC of Zn, azelaic acid and BioMIL-5 (MIC: 0.5, 1.5 and 1.7 ppm; MBC: 2.0, 3.0 and 4.3 ppm), where no synergic but additive activity was found, along with the determination of the duration of the effect under these concentrations. While smaller concentration (0.5 and 1.7 ppm) significantly decreased the growth rate, the inhibitory effect over bacteria was prolonged up to 7 days

at the MBC concentration of 4.3 ppm. Other bioMOF, [Zn(μ-4-hzba)$_2$]$_2$·4(H_2O), based on Zn and hydrazinebenzoate ligands was reported by Restrepo *et al.* [54], along with the assessment of its effective antimicrobial efficiency against *S. aureus*. Diffusion of the powder on the agar plate was observed to produce higher inhibition zones than the ligand alone, whereas both exhibited similar metabolic bacterial activity inhibition, measured through the fluorescein diacetate (FDA) fluorescence staining method. Stability studies indicated that [Zn(μ-4-hzba)$_2$]$_2$·4(H_2O) provided a slower and more controlled release of the ligand, indicating a long-term potential. Although not experimentally proven, the combined antimicrobial activity of a Zn-based MOF, (Zn_2(ppa)$_2$(1,3-bdc)(H_2O)), coordinating to a quinolone-like drug, was also suggested in another study by Duan *et al*. [55].

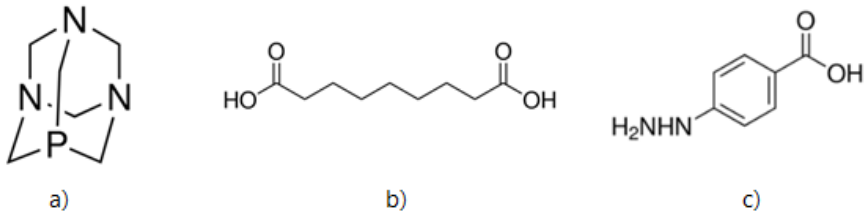

Figure 1.5 Chemical structure of some antimicrobial ligands used in the preparation of bioMOFs: a) 1,3,5-triaza-7-phosphaadamantane (used in [53]), b) azelaic acid (used in [49]) and c) 4-hydrazinobenzoic acid (used in [54]).

Finally, the antibiotic effect of few MOFs based on potentially antimicrobial ligands has been suggested in some literature studies, however, no experimental microbiocidal results have been presented. Bio-MIL-3 [56], a porous calcium 3,3',5,5'-azobenzenetetracarboxylate with accessible metal acid sites, is able to adsorb and deliver significant amounts of NO. As Ca has *a priori* no effect on bacteria, it is suggested that a potential antimicrobial activity could result from the ligand (azobenzene derivative) [57], being further increased by the encapsulation of NO on the metal sites (see Section: Association of Therapeutic Agents). Similarly, a Ba(II) azodibenzoate, Ba(4,4′-ADB), was also reported as a potential antimicrobial MOF based on the bactericidal activity of its ligand [58].

1.3 Extrinsic Antimicrobial Activity

Although the permanent porosity of MOFs has been traditionally exploited for the capture and storage of several fluids (e.g. CO_2, CH_4, H_2, etc.) [59], an interest in the encapsulation of biologically active species (AS: biomolecules, enzymes, metallic nanoparticles, etc.) has also risen. Apart from being allocated within the framework (defects, porosity, etc.), these AS could interact with different functional groups in the ligands (e.g. $-NH_2$, $-OH$, $-SO_3H$, $-Br$, among others) *via* van der Waals forces and/or hydrophobic and electrostatic interactions [60]. In this manner, MOFs can be used as stable carriers of AS, exhibiting an extrinsic activity associated with their cargo.

In the case of MOFs used as antibacterial agents, both metallic nanoparticles and therapeutic agents have been immobilized on their structure to achieve extrinsic antimicrobial activity. Even more, when included in a MOF with intrinsic bactericidal effect, their individual actions can be complemented. The mechanism of action might result from the performance of the composite entity (AS@MOF), while on other occasions, the AS is required to be released to come in contact with the target bacteria, *via* diffusion from the MOF porosity, detachment from its surface or release subsequent to MOF degradation. In literature, the recent efforts seem to move the focus towards the development of MOF composites with extrinsic antimicrobial activity.

1.3.1 Strategies for Immobilization of Active Species

MOFs are commonly proposed as immobilizing supports due to their high surface area, robustness and compositional versatility. Three different synthetic procedures for the immobilization of AS on MOFs can be distinguished: i) diffusion, ii) *in-situ* or *de novo* synthesis and iii) chemical and physical forces [61].

The diffusion protocol, also known as 'ship-inside-a-bottle', is normally achieved in two steps: 1) MOF synthesis and activation, to ensure a free porosity and 2) post-synthetic encapsulation of the AS by diffusion through the porosity (see Figure 1.6(a)). Some limitations of this procedure are: i) the size of the AS to be encapsulated is limited by the pore dimensions, ii) the potential leaching of the encapsulated AS and iii) the precise control on the final location of AS within the framework is challenging to achieve, as a fraction might be interacting with the surface instead of being allocated in the MOF

porosity. These deficiencies can be overcome with the *in-situ* synthetic protocol, as the AS is placed in contact with the MOF precursors (metal and ligand), which serves as a seed for the crystal growth of the framework surrounding them ('bottle-around-a-ship', see Figure 1.6(b)). In this case, the main constraint is the compatibility between the integrity of the AS and the MOF synthetic conditions, in order to preserve their nature and activity.

The third synthetic procedure involves the adsorption of AS on the outer MOF surface *via* different forces, either weak (van der Waals forces and/or hydrophobic and electrostatic interactions) or covalent interactions (see Figure 1.6(c)). As in the diffusion procedure, this strategy involves the use of preformed MOFs *prior* to the post-synthetic surface modification. Considering the high internal/external surface ratio, it is expected that the resulting composite has a lower AS association compared to the other procedures.

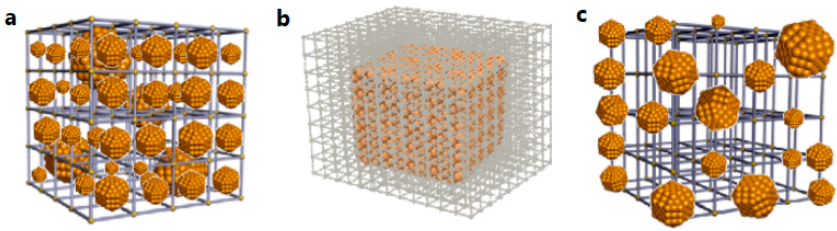

Figure 1.6 Representative structures of the AS@MOF composites achieved using different synthetic approaches. Reproduced from Reference 62 with permission from American Chemical Society.

1.3.2 Association of Metallic Nanoparticles

Noble-metal-nanoparticles@MOF core shell heterostructures have become promising candidates for many relevant applications (e.g. catalysis, imaging and sensing) [63] (Figure 1.7). In the case of antimicrobial MOF composites, Ag nano-species have been widely selected for their extensive biocidal activity [64] to achieve extrinsic bactericidal properties.

Ximing *et al.* [65] used *in-situ* synthesis to generate spherical copper porphyrin derivative MOF, CuTPP, as outer shell for previously prepared AgNPs and provided structural characterization of the composite material. Ag-CuTCPP ion release, determined *via* ICP-OES, indicated that CuTCPP MOF was stable, and the Ag composite

exhibited a steady Ag^+ release. *In vitro* antibacterial tests were carried out against *E. coli*, *S. aureus* and *B. subtilis*. MIC of Ag-CuTCPP against *E. coli* was higher than the control, indicating an inefficient treatment. Nevertheless, MIC for *S. aureus* and *B. subtilis* strains were within the same range as penicillin (even though the MIC values were higher than the Ag^0 and Ag^+ positive controls). After contact with Ag-CuTCPP, the SEM micrographs of planktonic bacteria suggested that the released Ag^+ caused cell disruption and bacterial death by intracellular content leakage. In addition to the bactericidal properties, the potential of Ag-CuTCPP for wound healing was also investigated. For this purpose, cytotoxicity was also determined using a half inhibitory concentration (IC50) value of 50.3 $\mu g \cdot mL^{-1}$. The material exhibited lower cytotoxicity than free AgNPs (6.5 $\mu g \cdot mL^{-1}$). *In vivo* wound healing for infection in mice was then performed, which resulted in higher antibacterial effect of Ag-CuTCPP MOF as compared to penicillin, along with better sustenance of the activity with time (as demonstrated by colony count in heart, lung, liver and kidney).

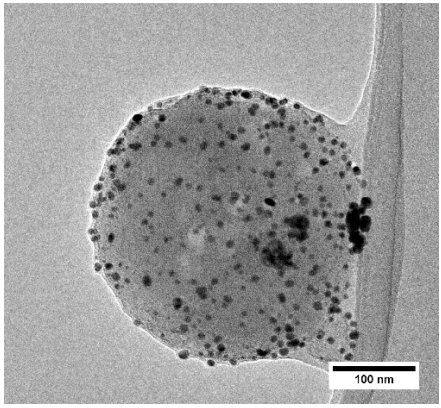

Figure 1.7 Example of a TEM micrograph of a noble-metal-nanoparticles@MOF, with the loaded NPs in higher contrast (scale bar 100 nm).

Thakare and Ramteke [66] also anchored AgNPs on MOF-5 and combined the photo- and bioactive properties against *E. coli,* inactivating 90% of bacteria in 1 h. However, the experimental conditions used for the synthesis of the material (silver content is not specified) and for the biocide experiments (*E. coli* strain, MOF concentration, irradiation λ and W) need to be described in detail.

Mortada *et al*. [67] took advantage of the free pyridyl and dicarboxyl groups present in the Zr-based MOFs UiO-67-bpydc and UiO-66-2COOH (using 2,2′-bipyridine-5,5′-dicarboxylate and 1,2,4,5-benzenetetracarboxylate as ligands) respectively, to metalate silver cations by post-synthetic modification. Metalation was confirmed by a combination of experimental techniques, determining an Ag content of 12 and 13 wt% in UiO-67-bpydc and UiO-66-2COOH respectively. OD measurements enabled the determination of MIC, which was observed to be 50 ppm for UiO-67-bpydc and 75 ppm for UiO-66-2COOH, corresponding to 6.5 and 9.6 ppm of Ag respectively. These results are observed to be comparable to the Ag-based MOFs synthesized by Lu *et al.* [29].

Guo *et al.* [68] employed an *in-situ* procedure to prepare a core-shell composite consisting of pre-synthesized Ag nanowires with Zn-imidazolate ZIF-8 and tested antibacterial activity against *B. subtilis* and *E. coli*. MIC, determined by OD_{600}, indicated that 200 and 300 ppm of Ag@ZIF-8, corresponding to 80 and 120 ppm of Ag respectively, were required to prevent the growth of bacterial colonies of *B. subtilis* and *E. coli* respectively. Positive controls of Ag nanowires and pristine ZIF-8 generated with the same MIC concentrations exhibited lower antibacterial efficacy than Ag@ZIF-8, suggesting a synergistic effect of the Ag core and the ZIF-8 shell, which stabilized the silver release.

1.3.3 Association of Therapeutic Agents

Studies on the cytotoxicity of MOFs [69] have indicated the potential of using MOFs as therapeutic carriers, with potential applications in drug delivery and as antimicrobial agents. Even more, bioMOFs, used as hosting material, can be used for the concomitant administration of more than one therapeutic agent.

Early work in this field considered the encapsulation of NO (an important biological signaling molecule), owing to its antibacterial and wound healing activities [70]. NO adsorption and release was thoroughly studied using MOFs, in particular, metal hydroxyterephthalate M-CPO-27 (M= Co, Ni, Zn; also called MOF-74) and HKUST-1 [71]. McKinlay *et al.* [72] presented the activity of Ni-CPO-27, loaded simultaneously with NO and the antibiotic metronidazole, against *P. aeruginosa* and *S. aureus*. The multi-rate delivery of the bactericidal agents was assessed, with NO release faster than the larger metronidazole molecules. Antibacterial activity tests revealed the relative-

ly effective intrinsic biocidal activity of the pristine MOFs. Encapsulation of metronidazole solely resulted in slight reduction of the intrinsic activity due to the reduced ability to release metal ions, as the channels were blocked with the antibiotic. Nevertheless, the inclusion of NO and metronidazole significantly increased the inhibition of metabolic activity, thus, resulting in bactericidal performance even at shorter durations due to the fast NO release, along with sustenance of the material activity up to 10 days.

Iodine, another known bioactive molecule [73], was successfully encapsulated in ZIF-8 by Au-Duong and Lee [74] to benefit from the MOF degradation under acidic pH for progressive release. Both iodine adsorption and release at pH=6 were studied prior to the biocide tests. Firstly, the activity of iodine and I@ZIF-8 was demonstrated by inhibition zone against *E. coli*, *S. epidermis* and *S. aureus*, and the composite was active in plates with pH preadjusted to 6 (MOF dissolution), but not pH=7. Bacterial viability and growth inhibition, determined by colony counting, showed that the three strains were neutralized with a dosage of 200 ppm of I@ZIF-8 after 3 minutes only. Further, I@ZIF-8 thin films deposited over glass slides were used to determine the inhibition of biofilm formation. After dropping 100 µL of *E. coli* and *S. aureus* bacterial suspensions at pH 6 and 7, slides were observed with only LIVE/DEAD stain under confocal microscope. Images revealed the loss of membrane integrity (red stain) at pH=6, indicating again the pH-controlled iodine liberation.

The use of ZIF-8 for drug encapsulation has also been explored in other studies. Nabipour *et al.* [75] made use of the pH-dependent stability of ZIF-8 to release the antibiotic ciprofloxacin (CIP), previously encapsulated by diffusion. CIP release in pH 7.4 and 5.0 buffers was monitored by UV-vis spectroscopy and the antimicrobial activity against *E. coli* and *S. aureus* was determined by disk diffusion as well as determination of the inhibition zone. At pH 5, almost 70% of the CIP was released within the first 5 h, while at pH 7.4, as ZIF-8 was more stable, 70% release of CIP took 48 h. The larger inhibition zone of CIP-ZIF-8, compared to the free CIP and the pristine MOF, was associated with the gradual degradation of ZIF-8 and the release of Zn^{2+} and CIP. Chowdhuri *et al*. [76] co-encapsulated in one-pot synthesis procedure vancomycin (VAN) and folic acid (FA) in ZIF-8 to treat multi-drug resistant *S. aureus* and *E. coli*. MBC of ZIF-8@FA@VAN against *S. aureus* was 16 ppm and >512 ppm for *E. coli*. With the help of the conjugated carbon dots and the evaluation

of their fluorescent emission by confocal fluorescence microscopy, it was observed that ZIF-8@FA@VAN internalization was significantly higher in the case of *S. aureus*, explaining the greater biocide activity of the composite against this strain. In addition, *S. aureus* bacteria treated with ZIF-8@FA@VAN exhibited a higher ROS generation, indicating it to be the possible mechanism of cell death. SEM images of treated *S. aureus* revealed a damaged surface compared to the control, while no significant change was observed in *E. coli*. These results suggested the potential use of ZIF-8@FA@VAN for the treatment of challenging multi-drug resistant *S. aureus*.

Nabipour and coworkers proposed another Zn-based MOF for the encapsulation of different drugs with antibacterial properties. The authors explored the post-synthetic inclusion of nalidixic acid in the porosity of $Zn_2(bdc)_2(dabco)$ [77], where the Zn cluster was linked to bencenedicarboxylates and diazabicyclooctanate. The activity of the developed MOF against *E. coli* and *S. aureus* was analyzed. Inhibition zone test indicated a higher inhibition in the case of *E. coli*, higher than the inhibition of the pristine MOF and drug alone in both strains. Antibacterial activity revealed a MIC value lower than 0.05 ppm for both strains. More recently, the authors also presented $Zn_2(bdc)_2(dabco)$, loaded with gentamicin [78], immobilized by diffusion. In this case, only the inhibition zone was evaluated, being higher for *S. aureus*. From the results of both studies, it is reasonable to derive the importance of the selection of the drug to be immobilized for attributing extrinsic antimicrobial activity to a MOF composite.

Claes *et al*. [79] explored the stimulus-responsive degradation of the porous iron(III) terephthalate MIL-88B(Fe) to release antibiofilm compounds (Figure 1.8). *Salmonella enterica* subspecies *S. Typhimurium* secretes siderophores that have a high affinity for iron and can produce a controlled release of the inhibitor encapsulated in the MOF lattice by metal complexation. 5-(4-Chlorophenyl)-*N*-(2-isobutyl)-2-aminoimidazole (IMI) was the selected antibiofilm compound, with a 10 wt% encapsulated by diffusion in a previously activated MIL-88B(Fe) solid. MOF degradation in water and in presence of an external chelator (Na_3 citrate) was verified. The results showed that the presence of IMI within the porosity did not affect the stimulus-responsive degradation and that IMI was easily trigger released. To test the inhibition of biofilm, the MIL-88B(Fe) micrometric particles were deposited by drop-casting on polystyrene petri-dishes. Non-loaded MIL-88B(Fe) is non-toxic to biofilm. With 1

mg·cm^{-2} concentration of MOF loaded with 10 wt% of IMI, 70±10 % of *S. Typhimurium* were inhibited without the need of external chelators, compared with the non-coated petri dish. Interestingly, by increasing the MOF coating to 1.25 mg·cm^{-2}, almost no biofilm was grown on the MOF surface.

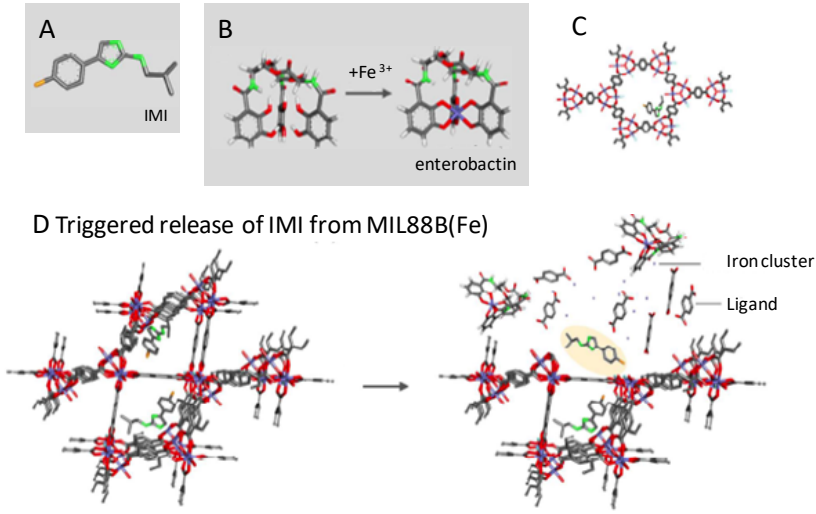

Figure 1.8 Anti-biofilm compound release from MIL-88B(Fe) by competitive metal complexation. Depicted are (A) the chemical structure of the anti-biofilm compound (IMI), (B) chelation of Fe(III) by the siderophore enterobactin, (C) adsorption of IMI in MIL-88B(Fe) visualized from the c-axes and (D) the triggered release of IMI from MIL-88B(Fe). Hydrogen atoms are hided except for the enterobactin molecules in (B) and (D) (C = dark grey; O = red; N = green; Fe = purple; H = light grey; Cl = orange). Reproduced from Reference 79 with permission from American Chemical Society.

Also made from iron, the microporous biocompatible carboxylate MOF-53 NPs were used by Lin *et al*. [80] as platform to encapsulate VAN by physisorption and release it due to the pH-dependent MOF degradation (Figure 1.9). Release studies in PBS revealed that more than 90% of VAN was released at pH 7.4 and 6.5 after 24 h, while at pH 5.5, around 75% VAN was released during the same period. Bacterial inhibition of *S. aureus* suspensions against VAN@MOF-53 with 20 wt% of VAN was determined by CFU plate count, determining that bacteria were no longer viable with 200 ppm of VAN@MOF-53. In addition, the absence of cytotoxicity of VAN@MOF-53 was deter-

mined using an MTT assay carried with calvarial cells of mice. Naseri *et al*. [81] presented a new Cu-based bioMOF with 4,4'-biphenyldicarboxylate as ligand and cytosine as extrinsic antimicrobial. Cytosine was embedded with a simple one-step sonochemical method. MIC and MBC were determined against *Proteus mirabilis* (1600 and 2000 ppm respectively), which were observed to be relatively higher as compared to the other materials presented in this review.

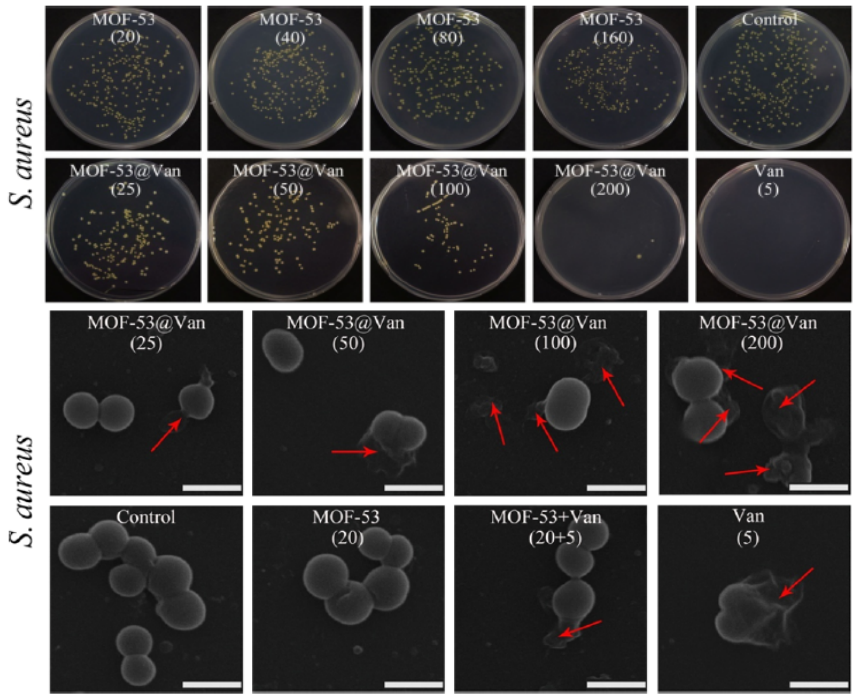

Figure 1.9 (Top): Representative images of viable S. aureus grown on different samples after 24 h of culture ; (Bottom): SEM morphology of S. aureus seeded on various samples after incubation at 37 °C for 24 h. The scale bar is 1 μm. Reproduced from Reference 80 with permission from American Chemical Society.

1.4 Devices and Applications

In most of the literature presented so far, MOFs were handled as powder suspensions in contact with the target bacteria (in the cul-

ture broth suspension or in the agar plate). Nevertheless, polycrystalline powders are unsuitable for industrial applications due to difficulties in processing (dust, clogs, mass loss, challenges during transfer, etc.) [82]. Consequently, it is of great interest to shape MOFs into more application-oriented forms such as pellets and films, along with their inclusion into composite materials [83]. It can be achieved either during the synthesis process (such as monoliths of MOFs [84]) or by the immobilization on already shaped substrates [85]. In this respect, the MOF-shaping strategies followed to date targeting antimicrobial applications are presented in the following sections.

1.4.1 Thin Films and Surface Coatings

Thin films and surface coatings involve different techniques, including drop-casting, spin-coating, layer-by-layer deposition and crystal growth. An example is the previously mentioned Cu-SURMOF-2 [39], prepared layer-by-layer *via* spray deposition over 16-mercaptohexadecanoic acid self-assembled monolayers (MHDA-SAM) on top of gold substrates and proposed as antifouling coating against *C. marina* (Figure 1.10). Bacterial viability, determined by

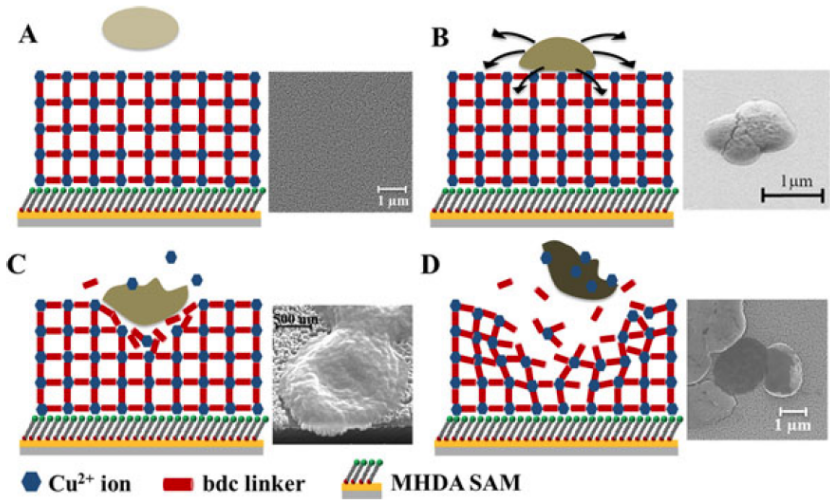

Figure 1.10 Schematic illustration of the active disassembly of the Cu-SURMOF 2 under the influence of *C. marina* and SEM images of the bacteria in contact with the surface. Reproduced from Reference 39 with permission from Springer.

LIVE/DEAD, revealed 8% of yellow stained bacteria, commonly accepted as debilitated bacteria, but still alive. In addition, the authors determined that a Cu-SURMOF coated surface reduced by 50% the necessary shear stress required to remove bacteria biofilm, as compared with a MHDA-SAM positive blank. Other MOFs studied as surface coatings for biofilm inhibition are I@ZIF-8 [74] and IMI@MIL-88B [79], with thin films prepared by simple drop-casting.

In order to obtain antimicrobial textiles for wound healing and surgical procedures, Abbasi *et al*. [35] reported an ultrasonically-assisted synthesis of HKUST-1 as surface coating of silk fibers *via* several dipping cycles. Antimicrobial tests were performed using the inhibition zone test against *E. coli* and *S. aureus*. While the pristine silk fibers showed no inhibition, moderate antibacterial activity was obtained in the composite due to the slow Cu ion release. Rodriguez *et al.* [86] also explored HKUST-1 as antimicrobial surface coating using previously electrospun cellulosic fibers pretreated with carboxylic groups and a layer-by-layer alternative dipping protocol. A preliminary inhibition zone test against *E. coli* indicated that the bacterial inhibition resulted from the Cu ions released from the MOF coating. CFU plate count of *E. coli* bacterial suspensions incubated for 1 h in contact with 2x2 cm^2 cellulosic patches coated with HKUST-1 revealed complete bacterial viability inhibition. Wang *et al.* [87] also exploited the antibacterial activity of HKUST-1/cellulosic fiber (CF) composites as a potential solution to the microorganism favorable environment produced after sweat absorption in cellulosic textiles (Figure 1.11). In comparison with the previous studies, the authors presented a totally green synthesis

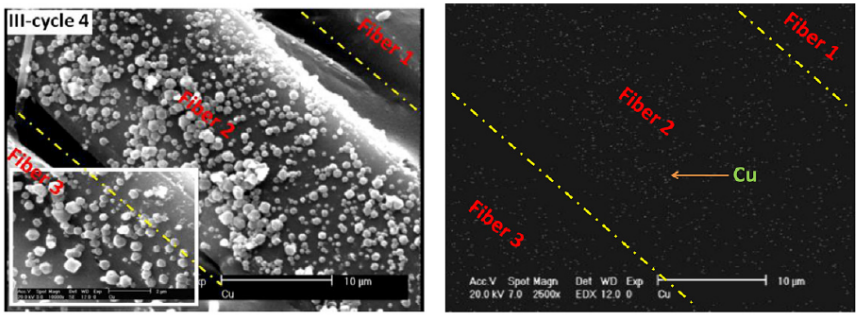

Figure 1.11 SEM image and wavelength-dispersive X-ray (WDX) analysis of group III fibers after 4 cycles of dipping. Reproduced from Reference 35 with permission from Elsevier.

procedure which avoided the use of DMF as solvent. Antibacterial activity was confirmed *via* disk diffusion and inhibition of *E. coli* and *S. aureus*.

Another Cu-based MOF reported as antifouling coating is the water stable copper triazolate Cu-BTTri [88], dispersed in a chitosan film (10 wt% of MOF). The authors explored the combination of the antibacterial action of chitosan and Cu present in the MOF against *P. aureginosa* biofilm. Cell viability of the attached bacteria was determined after 6 and 24 h by means of a spectroscopic assay called CTB, which is an indirect measurement of the metabolic activity of bacteria. While chitosan films inhibited ~55% of bacteria, the addition of Cu-BTTri composite film reached ~85% inhibition, with further sustenance over 24 h period. Reusability test of the films indicated no statistical difference between the first and second cycles. After ligand and copper release studies, it was concluded that the activity of the Cu-BTTri/chitosan film resulted from the constituent leaching. In spite of the interesting bactericidal studies on sessile *P. aureginosa* bacteria in the biofilm, the antifouling properties of the Cu-BTTri/chitosan film were not reported.

Similarly, Co-based MOFs have been mixed with fibers to provide them antimicrobial properties. Recently, Qian *et al.* [89] presented cellulose paper composite with ZIF-67 (CP/CNF/ZIF-67) as a biodegradable biocidal paper for packaging, generated by following an impregnation-crystal growth protocol. The mechanical properties of CP/CNF/ZIF-67 composite evidenced an improved tensile strength, elastic modulus, folding endurance and tear index compared to pristine fibers, thus, suggesting that the MOF NPs acted as crosslinkers, binding to the surrounding cellulose fibers. Antibacterial tests of CP/CNF/ZIF-67 against *E. coli* indicated a promising inhibition zone that increased with the number of ZIF-67 NPs on the fibers' surface. In the study of Quirós *et al*. [46], direct blending of Co-SIM-1 with PLA was employed to produce electrospun mats made of composite fibers, where the MOF microscale particles were completely embedded inside the polymeric fibers. The antimicrobial potential of Co-SIM-1/PLA mats was evaluated against *P. putida* and *S. aureus* biofilm formed on the mat surface. SEM images revealed the biofilm inhibition (up to 30% with composites based on 6 wt% content of Co-SIM-1) and LIVE/DEAD staining confirmed bacterial viability inhibition, being more apparent in the case of *P. putida*. Another imidazolate MOF, ZIF-8, was presented by Miao *et al*. [90] in a mixture with polyvinylidenefluoride (PVDF) and H-

perfluorooctyltriethoxysilane (POTS) to obtain a superhydrophobic self-cleaning and antibacterial coating for different substrates (e.g. membranes, filter paper, non-woven fabrics and textiles). Bacterial inhibition of *E. coli* suspensions in contact with 10 cm^2 of coated substrates, determined by CFU plate count, indicated that the Zn ion release might be the cause of the important biocidal activity of the composite coating.

1.4.2 Membranes

MOF thin film processing in the active layer of microfluid membranes has also been extensively studied. Generally, polymeric or inorganic hollowed or fibred substrates are selected and the MOF particles are grown by solvo/hydrothermal synthesis (*in-situ* or seeded growth), interfacial synthesis in two immiscible solvents and liquid phase epitaxy (layer-by-layer) method [91] (Figure 1.12).

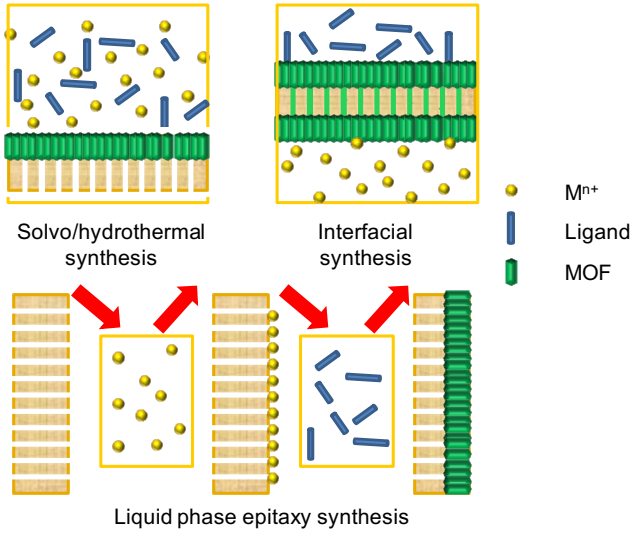

Figure 1.12 Scheme of the synthesis methods for continuous MOF-composite membranes.

Zirehpour *et al.* [50] incorporated silver trimesate MOF nanoparticles (Ag-BTC, 33 nm) in the active layer of a forward osmosis membrane (0.02%) to mitigate biofouling [50]. Characterization of the composite exhibited a good compatibility of the MOF with the active thin-film polyamide matrix of the thin film nanocomposite

(TFN) membrane. Bactericidal activity of the Ag-BTC/TFN membranes was studied against *S. aureus* and *E. coli* biofilms. Bacterial viability was determined from the plate count of the colony forming units of the bacteria detached from the surface after 1 h incubation of the inoculums in contact with the membrane active layer. Results showed a 90% bacterial viability inhibition for both strains with a "fresh" Ag-BTC/TFN membrane as well as with the membrane presoaked in water for 24 h and 6 months, suggesting a remarkable long-term bactericidal activity. It is important to notice that only 1 h contact might not be representative for sessile bacterial inhibition, as longer time is usually required to develop a mature biofilm [92]. In addition, Ag^+ release studies indicated a burst release of silver within the first day that might be responsible for the biocidal effect. Biofouling experiments were determined by passing an *E. coli* solution and analyzing the water flux through the membrane during 24 h. While the flux of the TFN membrane (negative blank) decreased by 20% after 24 h, the Ag-BTC/TFN membrane reduced the flux by 10% only, thus, supporting the antifouling activity of the composite.

Wang *et al.* [93] prepared as well the TFN membranes *via* simple interfacial polymerization, integrating both ZIF-8 and graphene oxide in the active layer (Figure 1.13). The authors demonstrated the antimicrobial properties of the composite membranes (TFN-ZG) against *E. coli*. The presence of graphene oxide prevented the agglomeration of MOF NPs in the active layer. Determination of the inhibition concentration for inoculums in suspension (by plate count) showed the lower bacterial viability when the content of ZIF-8 increased (TFN-ZG1: 50%, TFN-ZG2: 66%, TFN-ZG3: 84% bacterial inhibition). Besides, hydrophilicity, determined by contact angle, had a significant influence over the antifouling and filtration performance of the TFN-ZG membranes. TFN-ZG1 exhibited smaller contact angle (10.7°), and the hydrophobic nature of ZIF-8 prevailed with higher amounts of MOF.

Finally, Ming *et al.* [94] prepared a MOF-polymer mixed matrix membrane (MMMs) based on poly(ε-caprolactone) (PCL) and the Zr porphyrin-MOF MOF-525. This MOF was selected due to its potential to generate ROS after irradiation. The MOF-525/PCL membrane was tested as photodynamic bactericidal agent against *E. coli*. To ensure good compatibility between the MOF particles and polymeric matrix, 10 or 30 wt% of 100 nm MOF NPs (synthesized by optimized solvothermal procedures) were used. The resulting MOF-525/PCL membrane possessed a homogenous red color, character-

istic of porphyrin derivatives. The homogeneous distribution of the MOF NPs was confirmed by SEM and confocal microscopic studies. In addition, a good biocompatibility of the MOF-525/PCL membrane without irradiation was confirmed by plate count. Nevertheless, upon irradiation, a noticeable inhibition effect was evidenced within the first 30 min, increasing with the MOF-525 content in the membrane (reaching even 50% of the bacterial inhibition with 30 wt% MOF content, as determined by the plate count).

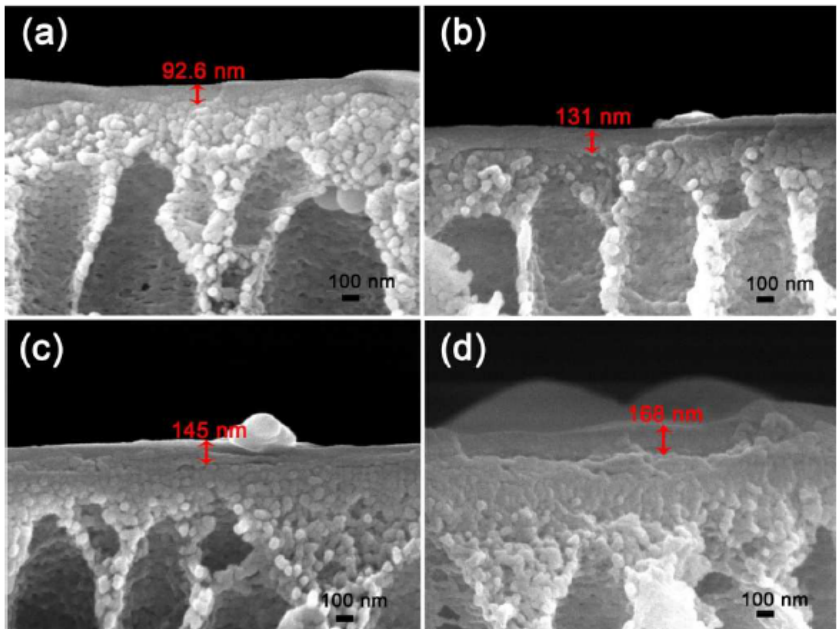

Figure 1.13 FE-SEM images of the cross section of the membranes: pristine (a), TFN-ZG1 (b), TFN-ZG2 (c), and TFN-ZG3 (d). Reproduced from Reference 93 with permission from American Chemical Society.

1.5 Conclusions and Perspectives

MOFs, due to their compositional versatility and porosity, have generated a significant interest as antimicrobial agents. Early attempts studied their intrinsic biocidal activity, by the selection of bioactive cations and/or organic ligands. Due to the extensively known activity of silver, Ag-based MOFs have been widely studied, evidencing their bactericidal properties against both Gram (+) and Gram (-)

bacteria. Other frequently proposed MOFs are the microporous copper trimesate HKUST-1, used as bactericidal and antifungal agents as well as the zinc-imidazolate ZIF-8, easily synthesized at room temperature. Though studied to a lesser degree, some cobalt imidazolates (ZIF-67, Co-SIM-1, etc.) also seem to be promising biocidal materials. Further, the combination of an active cation with a bioactive organic species leads to concurrent bactericidal MOFs, such as the Zn azelate bioMIL-5. In spite of the interest in this multi-target approach, this research direction is at an early stage, and there are plenty opportunities for the development of new MOF structures with combined (additive or even synergistic) antimicrobial activity. Important selection criteria might be the use of endogenous molecules to overcome toxicity when the MOF is degraded to release the bactericidal compounds to the media, particularly in *in vivo* applications.

However, there has been a change of trend towards the integration of bioactive species (e.g. metallic nanoparticles, therapeutic agents, etc.) within the MOF porosity to provide extrinsic antimicrobial activity. Even more, when included in a MOF with intrinsic bactericidal effect, their individual actions can be complemented. Up to now, only metallic silver, in the form of nanoparticles or nanowires, has been employed in different studies. In contrast, a large variety of antimicrobial molecules have been entrapped within MOF porosity (e.g. NO, I, ciprofloxacin and vancomycin). It is envisaged that the low cytotoxicity of some MOFs will enable their use as efficient drug carriers in the near future.

Both intrinsic and extrinsic biocidal MOFs need to be integrated in different application-oriented forms for their final use. Common solutions are the elaboration of thin films or surface coatings and the MOF integration in substrates such as membranes. A good compatibility between the MOF and substrate is the key for the final device integrity. These devices are the ones ultimately in contact with the bacterial environment and should preserve their antimicrobial properties over time to ensure their action. The manufacturing of these devices has lately enabled the study of MOF bactericidal activity not only against bacterial suspensions, but also against sessile bacteria in the challenging biofilms, which exhibit higher resistance against environmental stresses and traditional antibiotics. Therefore, progress in MOF conformation will also guide the successful attainment of the relevant purpose of the bacteria-free surfaces.

There is still a significant leap needed from the lab scale till final biocidal devices. The studies so far have proven the potential of MOFs as effective antimicrobial agents, which needs to be translated to actual devices. Besides biomedical applications (e.g. surgical implants, wound healing, etc.), biocidal MOFs are also promising for water treatment, food packaging, maritime transport and off-shore industries, heat exchangers, electrochemical devices, among others.

References

1. Even, C., Marlière, C., Ghigo, J.-M., Allain, J.-M., Marcellan, A., and Raspaud, E. (2017) Recent advances in studying single bacteria and biofilm mechanics. *Advances in Colloid and Interface Science*, **247**, 573-588.
2. Liu, K., and Jiang, L. (2012) Bio-inspired self-cleaning surfaces. *Annual Review of Materials Research*, **42**(1), 231-263.
3. Okeke, I. N., Lamikanra, A., and Edelman, R. (1999) Socioeconomic and behavioral factors leading to acquired bacterial resistance to antibiotics in developing countries. *Emerging Infectious Diseases*, **5**(1), 18-27.
4. Townsley, L., and Shank, E. A. (2017) Natural-product antibiotics: cues for modulating bacterial biofilm formation. *Trends in Microbiology*, **25**(12), 1016-1026.
5. Stewart, P. S., and William Costerton, J. (2001) Antibiotic resistance of bacteria in biofilms. *Lancet*, **358**(9276), 135-138.
6. Bordi, C., and de Bentzmann, S. (2011) Hacking into bacterial biofilms: a new therapeutic challenge. *Annals of Intensive Care*, **1**(1), 19.
7. Simchi, A., Tamjid, E., Pishbin, F., and Boccaccini, A. R. (2011) Recent progress in inorganic and composite coatings with bactericidal capability for orthopaedic applications. *Nanomedicine: Nanotechnology, Biology and Medicine*, **7**(1), 22-39.
8. Raquez, J.-M., Habibi, Y., Murariu, M., and Dubois, P. (2013) Polylactide (PLA)-based nanocomposites. *Progress in Polymer Science*, **38**(10-11), 1504-1542.
9. Wang, Z., Shen, Y., and Haapasalo, M. (2014) Dental materials with antibiofilm properties. *Dental Materials*, **30**(2), e1-e16.
10. Férey, G. (2008) Hybrid porous solids: past, present, future. *Chemical Society Reviews*, **37**(1), 191-214.
11. Farha, O. K., Eryazici, I., Jeong, N. C., Hauser, B. G., Wilmer, C. E., Sarjeant, A. A., Snurr, R. Q., Nguyen, S. T., Yazaydın, A. Ö., and Hupp, J. T. (2012) Metal-organic framework materials with ultrahigh surface areas: is the sky the limit? *Journal of the American Chemical*

Society, **134**(36), 15016-15021.
12. Furukawa, H., Cordova, K. E., O'Keeffe, M., and Yaghi, O. M. (2013) The chemistry and applications of metal-organic frameworks. *Science*, **341**(6149), 1230444.
13. Horcajada, P., Gref, R., Baati, T., Allan, P. K., Maurin, G., and Couvreur, P. (2012) Metal - organic frameworks in biomedicine. *Chemical Reviews*, **112**, 1232-1268.
14. Wyszogrodzka, G., Marszałek, B., Gil, B., and Dorożyński, P. (2016) Metal-organic frameworks: mechanisms of antibacterial action and potential applications. *Drug Discovery Today*, **21**(6), 1009-1018.
15. Doonan, C., Riccò, R., Liang, K., Bradshaw, D., and Falcaro, P. (2017) Metal-organic frameworks at the biointerface: synthetic strategies and applications. *Accounts of Chemical Research*, **50**(6), 1423-1432.
16. Berchel, M., Gall, T. Le, Denis, C., Hir, S. Le, Quentel, F., Elléouet, C., Montier, T., Rueff, J.-M., Salaün, J.-Y., Haelters, J.-P., Hix, G. B., Lehn, P., and Jaffrès, P.-A. (2011) A silver-based metal-organic framework material as a 'reservoir' of bactericidal metal ions. *New Journal of Chemistry*, **35**(5), 1000-1003.
17. Rojas, S., Devic, T., and Horcajada, P. (2017) Metal organic frameworks based on bioactive components. *Journal of Materials Chemistry B*, **5**(14), 2560-2573.
18. Slenters, T. V., Sagué, J. L., Brunetto, P. S., Zuber, S., Fleury, A., Mirolo, L., Robin. A. Y., Meuwly, M., Gordon, O., Lamdmann, R., Daniels, A. U., and Fromm, K. M. (2010) Of chains and rings: Synthetic strategies and theoretical investigations for tuning the structure of silver coordination compounds and their applications. *Materials*, **3**(5), 3407-3429.
19. Brunetto, P. S., Slenters, T. V., and Fromm, K. M. (2010) In vitro biocompatibility of new silver(I) coordination compound coated-surfaces for dental implant applications. *Materials*, **4**(2), 355-367.
20. Wang, K., Yin, Y., Li, C., Geng, Z., and Wang, Z. (2011) Facile synthesis of zinc(II)-carboxylate coordination polymer particles and their luminescent, biocompatible and antibacterial properties. *CrystEngComm*, **13**(20), 6231-6236.
21. Tăbăcaru, A., Pettinari, C., Marchetti, F., Di Nicola, C., Domasevitch, K. V., Galli, S., Masciocchi, N., Scuri, S., Grappasonni, I., and Cocchioni, M. (2012) Antibacterial action of 4,4′-bipyrazolyl-based silver(I) coordination polymers embedded in PE disks. *Inorganic Chemistry*, **51**(18), 9775-9788.
22. Chernousova, S., and Epple, M. (2013) Silver as antibacterial agent: Ion, nanoparticle, and metal. *Angewandte Chemie - International Edition*, **52**(6), 1636-1653.
23. Raghupathi, K. R., Koodali, R. T., and Manna, A. C. (2011) Size-dependent bacterial growth inhibition and mechanism of antibac-

terial activity of zinc oxide nanoparticles. *Langmuir*, **27**(7), 4020-4028.
24. Hong, R., Kang, T. Y., Michels, C. A., and Gadura, N. (2012) Membrane lipid peroxidation in copper alloy-mediated contact killing of Escherichia coli. *Applied and Environmental Microbiology*, **78**(6), 1776-1784.
25. Giménez-Marqués, M., Hidalgo, T., Serre, C., and Horcajada, P. (2016) Nanostructured metal-organic frameworks and their bio-related applications. *Coordination Chemistry Reviews*, **307**, 342-360.
26. Liu, Y., Xu, X., Xia, Q., Yuan, G., He, Q., and Cui, Y. (2010) Multiple topological isomerism of three-connected networks in silver-based metal-organoboron frameworks. *Chemical Communications*, **46**(15), 2608-2610.
27. Singleton, R., Bye, J., Dyson, J., Baker, G., Ranson, R. M., and Hix, G. B. (2010) Tailoring the photoluminescence properties of transition metal phosphonates. *Dalton Transactions*, **39**(26), 6024-6030.
28. Lu, X., Ye, J., Sun, Y., Bogale, R. F., Zhao, L., Tian, P., and Ning, G. (2014) Ligand effects on the structural dimensionality and antibacterial activities of silver-based coordination polymers. *Dalton Transactions*, **43**(26), 10104-10113.
29. Lu, X., Ye, J., Zhang, D., Xie, R., Feyisa, R., Sun, Y., Zhao, L., Zhao, Q., and Ning, G. (2014) Silver carboxylate metal - organic frameworks with highly antibacterial activity and biocompatibility. *Journal of Inorganic Biochemistry*, **138**, 114-121.
30. Wang, X., Zhao, D., Tian, A., and Ying, J. (2014) Three 3D silver-bis(triazole) metal-organic frameworks stabilized by high-connected Wells-Dawson polyoxometallates. *Dalton Transactions*, **43**(13), 5211-5220.
31. Zhang, S.-S., Wang, X., Su, H.-F., Feng, L., Wang, Z., Ding, W.-Q., Blatov, V. A., Kurmoo, M., Tung, C.-H., Sun, D., and Zheng, L.-S. (2017) A water-stable Cl@Ag $_{14}$ cluster based metal-organic open framework for dichromate trapping and bacterial inhibition. *Inorganic Chemistry*, **56**(19), 11891-11899.
32. Raffi, M., Mehrwan, S., Bhatti, T. M., Akhter, J. I., Hameed, A., Yawar, W., and ul Hasan, M. M. (2010) Investigations into the antibacterial behavior of copper nanoparticles against Escherichia coli. *Annals of Microbiology*, **60**(1), 75-80.
33. Wang, K., Geng, Z., Yin, Y., Ma, X., and Wang, Z. (2011) Morphology effect on the luminescent property and antibacterial activity of coordination polymer particles with identical crystal structures. *CrystEngComm*, **13**, 5100-5104.
34. Chui, S. S.-Y., Lo, S. M.-F., Charmant, J. P. H., Orpen, A. G., and Williams, I. D. (1999) A chemically functionalizable nanoporous material. *Science*, **283**(5405), 1148-1150.

35. Abbasi, A. R., Akhbari, K., and Morsali, A. (2012) Dense coating of surface mounted CuBTC metal-organic framework nanostructures on silk fibers, prepared by layer-by-layer method under ultrasound irradiation with antibacterial activity. *Ultrasonics Sonochemistry*, **19**(4), 846-852.
36. Chiericatti, C., Basilico, J. C., Zapata Basilico, M. L., and Zamaro, J. M. (2012) Novel application of HKUST-1 metal-organic framework as antifungal: Biological tests and physicochemical characterizations. *Microporous and Mesoporous Materials*, **162**, 60-63.
37. Celis-Arias, V., Loera-Serna, S., Beltrán, H. I., Álvarez-Zeferino, J. C., Garrido, E., and Ruiz-Ramos, R. (2018) The fungicide effect of HKUST-1 on *Aspergillus niger* , *Fusarium solani* and *Penicillium chrysogenum*. *New Journal of Chemistry*, **42**(7), 5570-5579.
38. Azad, F. N., Ghaedi, M., Dashtian, K., Hajati, S., and Pezeshkpour, V. (2016) Ultrasonically assisted hydrothermal synthesis of activated carbon-HKUST-1-MOF hybrid for efficient simultaneous ultrasound-assisted removal of ternary organic dyes and antibacterial investigation: Taguchi optimization. *Ultrasonics Sonochemistry*, **31**, 383-393.
39. Arpa Sancet, M. P., Hanke, M., Wang, Z., Bauer, S., Azucena, C., Arslan, H. K., Heinle, M., Gliemann, H., Woll, C., and Rosenhahn, A. (2013) Surface anchored metal-organic frameworks as stimulus responsive antifouling coatings. *Biointerphases*, **8**(1), 1-35.
40. Chang, E. L., Simmers, C., and Knight, D. A. (2010) Cobalt complexes as antiviral and antibacterial agents. *Pharmaceuticals*, **3**(6), 1711-1728.
41. *Zinc Sulfate Heptahydrate Safety Data Sheet*, Fisher Scientific (2010). Online: https://www.fishersci.com/store/msds?partNumber=Z76500andproductDescription=ZINC+SULFA+HEPTA+USP%2FFCC+500GMandvendorId=VN00033897andcountryCode=USandlanguage=en [accessed 6th September 2018].
42. *Cobalt Sulfate Heptahydrate Safety Data Sheet*, Acros Organics (2004). Online: https://www.ch.ntu.edu.tw/~genchem99/msds/exp18/CoSO4.pdf [accessed 6th September 2018].
43. *HERA Biocompatibility Brochure*, Kulzer GmbH (2017). Online: https://www.kulzer.com/media/webmedia_local/downloads_new/hera_11/nichtedelmetalllegierungen_fuer_k_b/Hera_Biocompatibility_Brochure_EN.pdf [accessed 6th September 2018].
44. Zhuang, W., Yuan, D., Li, J.-R., Luo, Z., Zhou, H.-C., Bashir, S., and Liu, J. (2012) Highly potent bactericidal activity of porous metal-organic frameworks. *Advanced Healthcare Materials*, **1**(2), 225-238.

45. Aguado, S., Quirós, J., Canivet, J., Farrusseng, D., Boltes, K., and Rosal, R. (2014) Antimicrobial activity of cobalt imidazolate metal - organic frameworks. *Chemosphere*, **113**, 188-192.
46. Quirós, J., Boltes, K., Aguado, S., de Villoria, R. G., Vilatela, J. J., and Rosal, R. (2015) Antimicrobial metal-organic frameworks incorporated into electrospun fibers. *Chemical Engineering Journal*, **262**, 189-197.
47. Sirelkhatim, A., Mahmud, S., Seeni, A., Kaus, N. H. M., Ann, L. C., Bakhori, S. K. M., Hasan, H., and Mohamad, D. (2015) Review on zinc oxide nanoparticles: antibacterial activity and toxicity mechanism. *Nano-Micro Letters*, **7**(3), 219-242.
48. Martín-Betancor, K., Aguado, S., Rodea-Palomares, I., Tamayo-Belda, M., Leganés, F., Rosal, R., and Fernández-Piñas, F. (2017) Co, Zn and Ag-MOFs evaluation as biocidal materials towards photosynthetic organisms. *Science of the Total Environment*, **595**, 547-555.
49. Tamames-Tabar, C., Imbuluzqueta, E., Guillou, N., Serre, C., Miller, S. R., Elkaïm, E., Horcajada, P., and Blanco-Prieto, M. J. (2015) A Zn azelate MOF: combining antibacterial effect. *CrystEngComm*, **17**(2), 456-462.
50. Zirehpour, A., Rahimpour, A., Arabi, A., Gh, M. S., and Soroush, M. (2017) Mitigation of thin film composite membrane biofouling via immobilizing nano-sized biocidal reservoirs in the membrane active layer mitigation of thin film composite membrane biofouling via immobilizing nano-sized biocidal reservoirs in the membrane active. *Environmental Science and Technology*, **51**(10), 5511-5522.
51. Beg, S., Rahman, M., Jain, A., Saini, S., Midoux, P., Pichon, C., Ahmad, F. J., and Akhter, S. (2017) Nanoporous metal organic frameworks as hybrid polymer-metal composites for drug delivery and biomedical applications. *Drug Discovery Today*, **22**(4), 625-637.
52. Imaz, I., Rubio-Martínez, M., An, J., Solé-Font, I., Rosi, N. L., and Maspoch, D. (2011) Metal-biomolecule frameworks (MBioFs). *Chemical Communications*, **47**(26), 7287-7302.
53. Jaros, S. W., Smoleński, P., Guedes da Silva, M. F. C., Florek, M., Król, J., Staroniewicz, Z., Pombeiro, A. J. L., and Kirillov, A. M. (2013) New silver BioMOFs driven by 1,3,5-triaza-7-phosphaadamantane-7-sulfide (PTA=S): synthesis, topological analysis and antimicrobial activity. *CrystEngComm*, **15**(40), 8060-8064.
54. Restrepo, J., Serroukh, Z., Santiago, J., Aguado, S., Gomez-Sal, P., Mosquera, M. E. G., and Rosal, R. (2017) Antibacterial Zn-MOF with hydrazinebenzoate linkers. *European Journal of Inorganic Chemistry*, **2017**(3), 574-580.
55. Duan, L.-N., Dang, Q.-Q., Han, C.-Y., and Zhang, X.-M. (2015) An interpenetrated bioactive nonlinear optical MOF containing a coordinated quinolone-like drug and Zn(ii) for pH-responsive release.

Dalton Transactions, **44**(4), 1800-1804.
56. Miller, S. R., Alvarez, E., Fradcourt, L., Devic, T., Wuttke, S., Wheatley, P. S., Steunou, N., Bonhomme, C., Gervais, C., Laurencin, D., Morris, R. E., Vimont, A., Daturi, M., Horcajada P., and Serre, C. (2013) A rare example of a porous Ca-MOF for the controlled release of biologically active NO. *Chemical Communications*, **49**(71), 7773-7775.
57. Badawi, A. M., Azzam, E. M. S., and Morsy, S. M. I. (2006) Surface and biocidal activity of some synthesized metallo azobenzene isothiouronium salts. *Bioorganic and Medicinal Chemistry*, **14**(24), 8661-8665.
58. Chen, Z.-F., Zhang, Z.-L., Tan, Y.-H., Tang, Y.-Z., Fun, H.-K., Zhou, Z.-Y., Abrahams, B. F., and Liang, H. (2008) Coordination polymers constructed by linking metal ions with azodibenzoate anions. *CrystEngComm*, **10**(2), 217-231.
59. Pettinari, C., Marchetti, F., Mosca, N., Tosi, G., and Drozdov, A. (2017) Application of metal-organic frameworks. *Polymer International,* **66**(6), 731-744.
60. Juan-Alcaniz, J., Gascon, J., and Kapteijn, F. (2012) Metal-organic frameworks as scaffolds for the encapsulation of active species: state of the art and future perspectives. *Journal of Materials Chemistry*, **22**(20), 10102-10118.
61. Meilikhov, M., Yusenko, K., Esken, D., Turner, S., Van Tendeloo, G., and Fischer, R. A. (2010) Metals@MOFs - Loading MOFs with metal nanoparticles for hybrid functions. *European Journal of Inorganic Chemistry*, (24), 3701-3714.
62. Kobayashi, H., Mitsuka, Y., and Kitagawa, H. (2016) Metal nanoparticles covered with a metal-organic framework: from one-pot synthetic methods to synergistic energy storage and conversion functions. *Inorganic Chemistry*, **55**(15), 7301-7310.
63. Yang, Q., Xu, Q., and Jiang, H.-L. (2017) Metal-organic frameworks meet metal nanoparticles: synergistic effect for enhanced catalysis. *Chemical Society Reviews*, **46**(15), 4774-4808.
64. Marambio-Jones, C., and Hoek, E. M. V. (2010) A review of the antibacterial effects of silver nanomaterials and potential implications for human health and the environment. *Journal of Nanoparticle Research*, **12**(5), 1531-1551.
65. Ximing, G., Bin, G., Yuanlin, W., and Shuanghong, G. (2017) Preparation of spherical metal - organic frameworks encapsulating ag nanoparticles and study on its antibacterial activity. *Materials Science and Engineering C*, **80**, 698-707.
66. Thakare, S. R., and Ramteke, S. M. (2017) Fast and regenerative photocatalyst material for the disinfection of E. coli from water: Silver nano particle anchor on MOF-5. *Catalysis Communications*, **102**, 21-25.

67. Mortada, B., Matar, T. A., Sakaya, A., Atallah, H., Ali, Z. K., and Karam, P. (2017) Postmetalated zirconium metal organic frameworks as a highly potent bactericide. *Inorganic Chemistry*, **56**(8), 4739-4744.
68. Guo, Y.-F., Fang, W.-J., Fu, J.-R., Wu, Y., Zheng, J., Gao, G.-Q., Chen, C., Yan, R.-W., Huang, S.-G., and Wang, C.-C. (2018) Facile synthesis of Ag@ZIF-8 core-shell heterostructure nanowires for improved antibacterial activities. *Applied Surface Science*, **435**, 149-155.
69. Tamames-Tabar, C., Cunha, D., Imbuluzqueta, E., Ragon, F., Serre, C., Blanco-Prieto, M. J., and Horcajada, P. (2014) Cytotoxicity of nanoscaled metal-organic frameworks. *Journal of Materials Chemistry B*, **2**(3), 262-271.
70. Miller, M. R., and Megson, I. L. (2009) Recent developments in nitric oxide donor drugs. *British Journal of Pharmacology*, **151**(3), 305-321.
71. Hinks, N. J., McKinlay, A. C., Xiao, B., Wheatley, P. S., and Morris, R. E. (2010) Metal organic frameworks as NO delivery materials for biological applications. *Microporous and Mesoporous Materials*, **129**(3), 330-334.
72. McKinlay, A. C., Allan, P. K., Renouf, C. L., Duncan, M. J., Wheatley, P. S., Warrender, S. J., Dawson, D., Ashbrook, S. E., Gil, B., Marszalek, B., Düren, T., Williams, J. J., Charrier, C., Mercer, D. K., Teat, S. J., and Morris, R. E. (2014) Multirate delivery of multiple therapeutic agents from metal-organic frameworks. *APL Materials*, **2**, 124108.
73. He, C., Zhang, J., and Shreeve, J. M. (2013) Dense iodine-rich compounds with low detonation pressures as biocidal agents. *Chemistry - A European Journal*, **19**(23), 7503-7509.
74. Au-Duong, A. N., and Lee, C. K. (2017) Iodine-loaded metal organic framework as growth-triggered antimicrobial agent. *Materials Science and Engineering C*, **76**, 477-482.
75. Nabipour, H., Sadr, M. H., and Bardajee, G. R. (2017) Synthesis and characterization of nanoscale zeolitic imidazolate frameworks with ciprofloxacin and their applications as antimicrobial agents. *New Journal of Chemistry*, **41**(15), 7364-7370.
76. Chowdhuri, A. R., Das, B., Kumar, A., Tripathy, S., Roy, S., and Sahu, S. K. (2017) One-pot synthesis of multifunctional nanoscale metal-organic frameworks as an effective antibacterial agent against multidrug-resistant *Staphylococcus aureus*. *Nanotechnology*, **28**(9), 095102.
77. Nabipour, H., Hossaini Sadr, M., and Rezanejade Bardajee, G. (2017) Release behavior, kinetic and antimicrobial study of nalidixic acid from $[Zn_2(bdc)_2(dabco)]$ metal-organic frameworks. *Journal of Coordination Chemistry*, **70**(16), 2771-2784.
78. Nabipour, H., Soltani, B., and Ahmadi Nasab, N. (2018) Gentamicin loaded $Zn_2(bdc)_2(dabco)$ frameworks as efficient materials for

drug delivery and antibacterial activity. *Journal of Inorganic and Organometallic Polymers and Materials*, **28**(3), 1206-1213.

79. Claes, B., Boudewijns, T., Muchez, L., Hooyberghs, G., Van der Eycken, E. V., Vanderleyden, J., Steenackers, H. P., and De Vos, D. E. (2017) Smart metal-organic framework coatings: triggered antibiofilm compound release. *ACS Applied Materials & Interfaces*, **9**(5), 4440-4449.
80. Lin, S., Liu, X., Tan, L., Cui, Z., Yang, X., Yeung, K. W. K., Pan, H., and Wu, S. (2017) Porous iron-carboxylate metal-organic framework: a novel bioplatform with sustained antibacterial efficacy and nontoxicity. *ACS Applied Materials & Interfaces*, **9**(22), 19248-19257.
81. Naseri, H., Sharifi, A., Ghaedi, M., Dashtian, K., Khoramrooz, S. S., Manzouri, L., Khosravanig, A. S., Pezeshkpoura, V., Sadri, F., and Askarinia, M. (2018) Sonochemical incorporated of cytosine in Cu-H_2bpdc as an antibacterial agent against standard and clinical strains of Proteus mirabilis with rsbA gene. *Ultrasonics Sonochemistry*, **44**, 223-230.
82. Bazer-Bachi, D., Assié, L., Lecocq, V., Harbuzaru, B., and Falk, V. (2014) Towards industrial use of metal-organic framework: Impact of shaping on the MOF properties. *Powder Technology*, **255**, 52-59.
83. Rubio-Martinez, M., Avci-Camur, C., Thornton, A. W., Imaz, I., Maspoch, D., and Hill, M. R. (2017) New synthetic routes towards MOF production at scale. *Chemical Society Reviews*, **46**(11), 3453-3480.
84. Hong, W. Y., Perera, S. P., and Burrows, A. D. (2015) Manufacturing of metal-organic framework monoliths and their application in CO_2 adsorption. *Microporous and Mesoporous Materials*, **214**, 149-155.
85. Valizadeh, B., Nguyen, T. N., and Stylianou, K. C. (2018) Shape engineering of metal-organic frameworks. *Polyhedron*, **145**, 1-15.
86. Rodríguez, H. S., Hinestroza, J. P., Ochoa-Puentes, C., Sierra, C. A., and Soto, C. Y. (2014) Antibacterial activity against Escherichia coli of Cu-BTC (MOF-199) metal-organic framework immobilized onto cellulosic fibers. *Journal of Applied Polymer Science*, **131**(19), 40815.
87. Wang, C., Qian, X., and An, X. (2015) In situ green preparation and antibacterial activity of copper-based metal-organic frameworks/cellulose fibers (HKUST-1/CF) composite. *Cellulose*, **22**(6), 3789-3797.
88. Neufeld, B. H., Neufeld, M. J., Lutzke, A., Schweickart, S. M., and Reynolds, M. M. (2017) Metal-organic framework material inhibits biofilm formation of *pseudomonas aeruginosa*. *Advanced Functional Materials*, **27**(34), 1702255.
89. Qian, L., Lei, D., Duan, X., Zhang, S., Song, W., Hou, C., and Tang, R. (2018) Design and preparation of metal-organic framework pa-

pers with enhanced mechanical properties and good antibacterial capacity. *Carbohydrate Polymers*, **192**, 44-51.

90. Miao, W., Wang, J., Liu, J., and Zhang, Y. (2018) Self-cleaning and antibacterial zeolitic imidazolate framework coatings. *Advanced Materials Interfaces,* **5**(14), 1800167.
91. Li, W., Zhang, Y., Li, Q., and Zhang, G. (2015) Metal-organic framework composite membranes: Synthesis and separation applications. *Chemical Engineering Science*, **135**, 232-257.
92. Mann, E. E., Rice, K. C., Boles, B. R., Endres, J. L., Ranjit, D., Chandramohan, L., Tsang, L. H., Smeltzer, M. S., Horswill, A. R., and Bayles, K. W. (2009) Modulation of eDNA release and degradation affects Staphylococcus aureus biofilm maturation. *PLoS ONE*, **4**(6), e5822.
93. Wang, J., Wang, Y., Zhang, Y., Uliana, A., Zhu, J., Liu, J., and Van der Bruggen, B. (2016) Zeolitic imidazolate framework/graphene oxide hybrid nanosheets functionalized thin film nanocomposite membrane for enhanced antimicrobial performance. *ACS Applied Materials & Interfaces*, **8**(38), 25508-25519.
94. Liu, M., Wang, L., Zheng, X., and Xie, Z. (2017) Zirconium-based nanoscale metal-organic framework/poly(ε-caprolactone) mixed-matrix membranes as effective antimicrobials. *ACS Applied Materials & Interfaces*, **9**(47), 41512-41520.

APPENDIX III

Supporting information publication Chapter 3

An Ag-loaded photoactive nano-Metal Organic Framework as a promising biofilm treatment

*Ana Arenas-Vivo,[a,b] Georgiana Amariei,[c] Sonia Aguado,[c] Roberto Rosal,[c] Patricia Horcajada [a] **

[a]Advanced Porous Materials Unit (APMU), IMDEA Energy Institute, Avda. Ramón de la Sagra 3, E-28935 Móstoles, Madrid, Spain

[b]Department of Inorganic Chemistry I, Chemical Sciences Faculty, Complutense University of Madrid, 28040 Madrid, Spain

[c] Department of Chemical Engineering, University of Alcalá, E-28871 Alcalá de Henares Madrid, Spain

*Corresponding autor E-mail: patricia.horcajada@imdea.org

Keywords: MIL-125NH_2, Ag nanoparticles, photo-active, biofilm treatment, biocide

III.I. Materials and Methods

III.I.i. Synthesis and characterization of AgNP@nanomil-125(Ti)NH_2 (AgNP@nanoMOF)

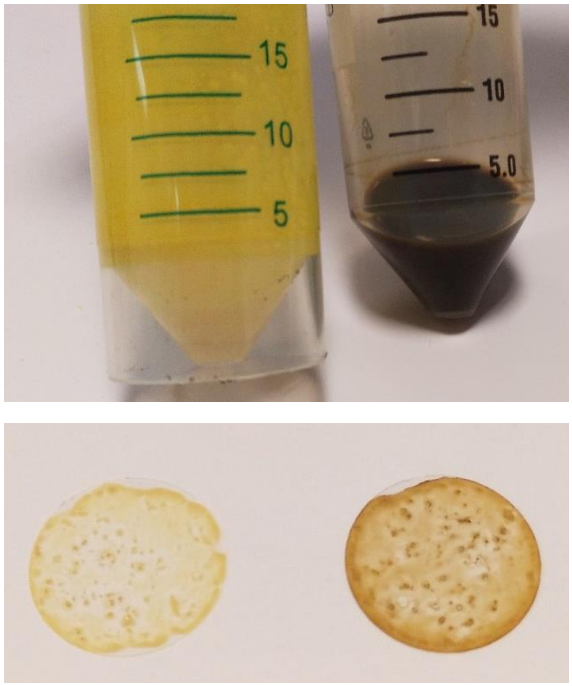

Figure S 1: Macroscopic view of the yellow nanoMOF (left) and brownish AgNP@nanoMOF composite (right). NP suspensions in ethanol (up) and thin film deposited over glass covers (down).

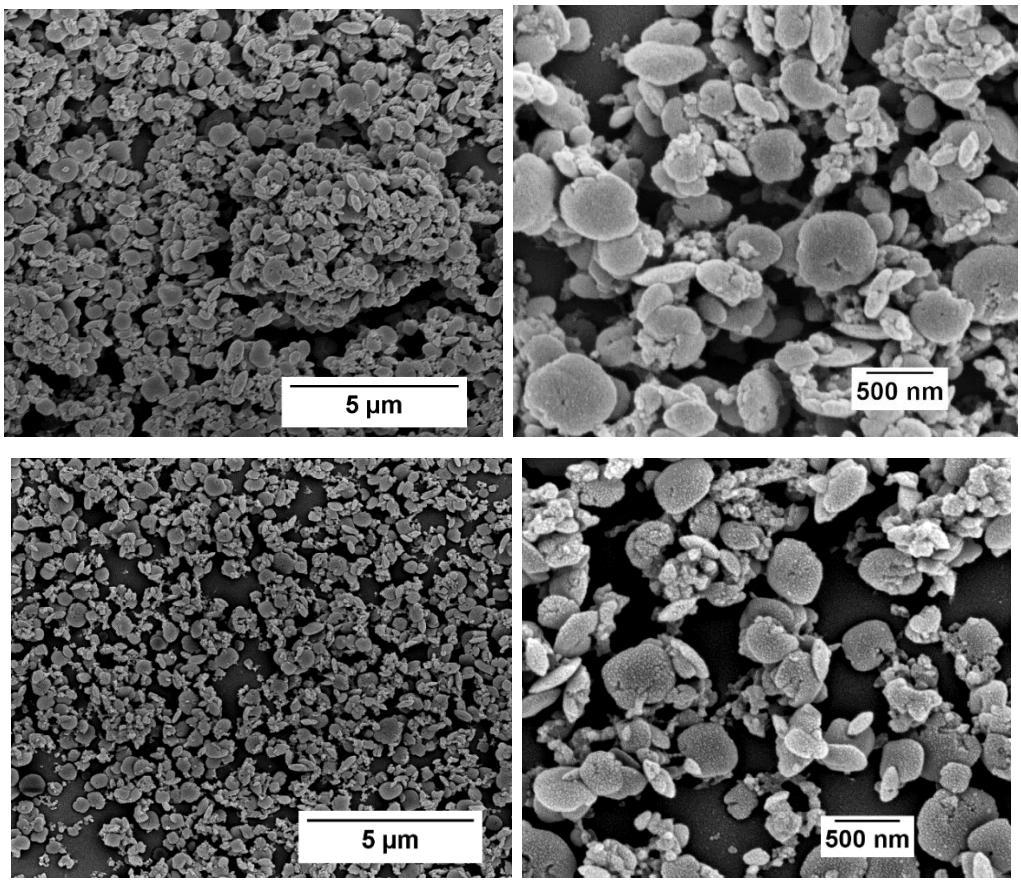

Figure S 2: SEM images of the surface of the cover glasses with the material deposited by drop casting: nanoMOF (top) thin film; AgNP@nanoMOF (bottom) thin film

III.I.ii. Materials characterization

All materials were fully characterized by using different solid-state techniques, including:

X-ray powder diffraction (XRPD) of the nanoMIL-125(Ti)NH_2 (nanoMOF) and the composite AgNP@nanoMIL-125(Ti)NH_2 (AgNP@nanoMOF), as well as the same materials deposited on the glass covers, were collected in an Empyrean PANalytical® powder diffractometer (PANalytical, Lelyweg, The Netherlands) in reflexion mode with a Cu Kα =1.5406 Å. The XR diagrams were carried out with a 2θ scan between 3-35° and 3-90° with a step size of 0.013° and a scanning speed of 0.1 $° \cdot s^{-1}$.

Fourier Transform Infrared Spectroscopy (FTIR) was performed in a Nicolet 6700 instrument (Thermo Scientific, Waltham, MA, USA) with the help of an ATR diamond accessory. **UV-Visible spectroscopy** of the solid materials was run in a Perkin Elmer® Lambda 1050 UV/vis/NIR (Perkin Elmer, Waltham, MA, USA).

Thermogravimetric analyses (TGA) were carried out in an SDT Q-600 thermobalance (TA Instruments, New Castle, De, USA) with a general heating profile from 30 to 600 °C with a heating rate of 5 °C · min^{-1}under air using a flux of 100 mL min^{-1}.

N_2 sorption isotherms *(77 K)* were done in an AUTO-SORB system (Quantachrome Instruments, Boynton Beach, FL, USA). Previous to the measurement, the sample was evacuated at 150 °C for 16 h. Specific surface area was determined by applying BET equation (Brunauer, Emmett & Teller) in the pressure interval P/P_o =0.01-0.3 (being P_0 the saturation pressure). Pore volume and pore size distribution were calculated by the NLDFT method (Non Localized Density Functional Theory) and the HK (Horvath-Kawazoe) methods, respectively.

Scanning electron microscopy (SEM) images of the surface of the deposited materials were obtained using a TM.100 tabletop SEM microscope (Hitachi, Japan, Tokyo) operating at 25 kV. The equipment also enabled the qualitative and semi-quantitative determination of the chemical elements present in the sample *via* Energy Dispersive X-ray Spectroscopy (EDS).

Transmission electron microscopy (TEM) images of both MOF and composite were taken with a Technai 20 TEM microscope (Philips, Amsterdam, the Netherlands) with a 200 kV acceleration voltage. For sample preparation, 1 mg of sample was dispersed in 10 mL of distilled water and sonicated with an ultrasound tip (UP400S, Hilscher, Teltow, Germany) at 20% amplitude for 20 sec. For observation, 1 μL of the prepared solution was dropped over a copper TEM support with a carbon mesh (Lacey Carbon, 300 mesh, Copper, approx. grid hole size: 63 μm, TED PELLA Redding, California, USA). Particle size was monitored via

Dynamic Light Scattering (DLS) and ξ-potential (ZP) was registered via Electrophoretic Light Scattering (ELS) using a Zetasizer Nano series Nano-ZS (Malvern Instruments, Worcestershire, UK). The particles were dispersed in the liquid media (methanol, ethanol, acetonitrile, and water) at a concentration of 0.1 mg mL^{-1} using an ultrasound tip (UP400S, Hilscher, Teltow, Germany) at 30% amplitude for 40 sec.

III.I.iii. Antifouling photo-bactericidal activity and bioanalytical procedures

The culture medium used in these studies is the bacteriological nutrient broth (NB) composed of: beef extract 5 g · L^{-1}, peptone 10 g · L^{-1}, NaCl 5 g · L^{-1},

pH=7-7.2. Bacterial growth was tracked by optical density at 600 nm, OD_{600}, with a Shimadzu UV-1800 spectrophotometer.

The antifouling capacity was assessed with SEM. Before imaging, the discs with the bacterial biofilm were washed twice with PBS, fixed in glutaraldehyde (2.5%) for 2 hours, and then dehydrated with gradient ethanol (30 %–100 %) and acetone. Each sample was dried with hexamethyldisilazane for 15 minutes prior to sputter coating with gold for SEM observation.

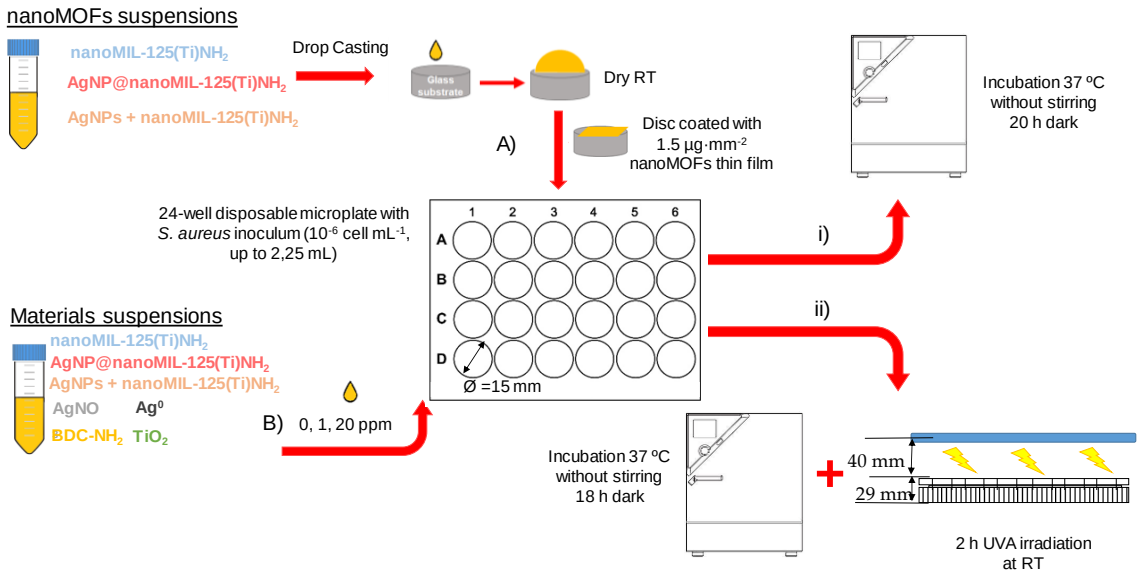

Scheme S 1: Procedure of the A) nanoMOFs thin films or B) Material suspensions in contact with S. aureus inoculums (10^6 cell mL^{-1}) for the antibacterial tests (i) in dark or (ii) dark followed by 2 h UVA irradiation.

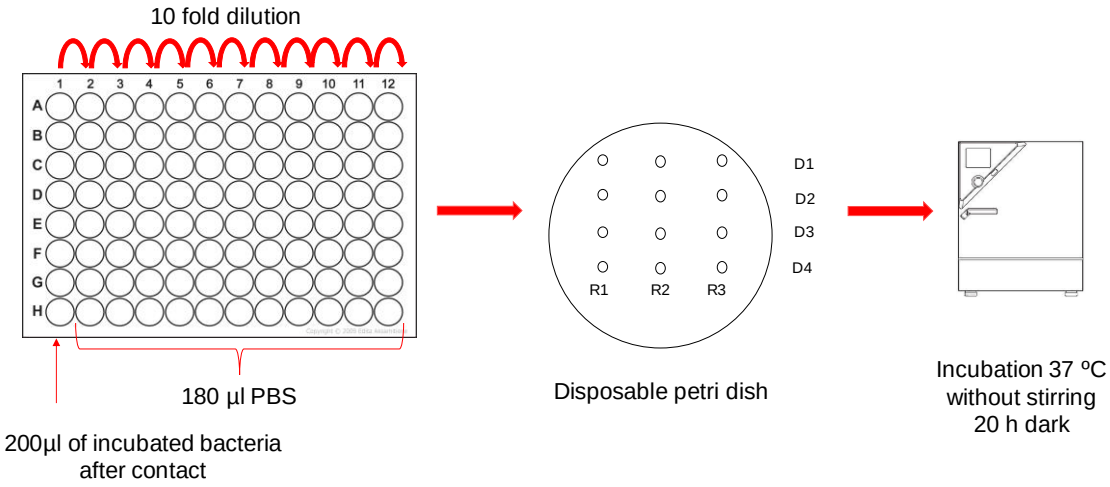

Scheme S 2: Preparation of the dilutions for the plate count of Colony Forming Units mL^{-1}

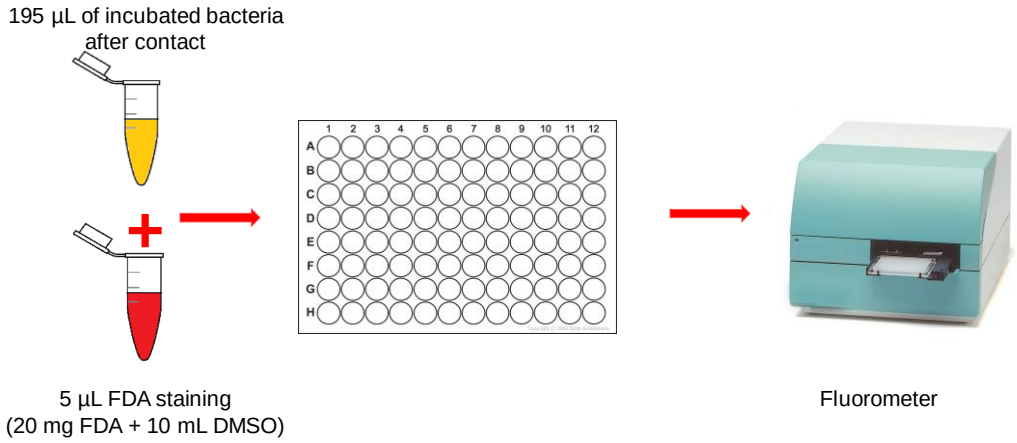

Scheme S 3: Preparation of the FDA staining prior to fluorescence emission

Bacterial Viability determined LIVE/DEAD staining with the help of confocal laser scanning microscopy (CLSM) differentiates viable and no-viability cells depending on its cell membrane integrity. While viable cells exhibit green fluorescence (Syto 9, live cells, excitation 480 nm/ emission 500 nm) non-viable bacteria have red fluorescence (propidium iodide, PI, dead cells, excitation 490 nm/ emission 635 nm. Samples were incubated with 50 µL of BacLight stain (a mixture of SYTO 9 and PI in DMSO, according to the manufacturer's recommendations) in the dark for 30 min at RT without stirring.

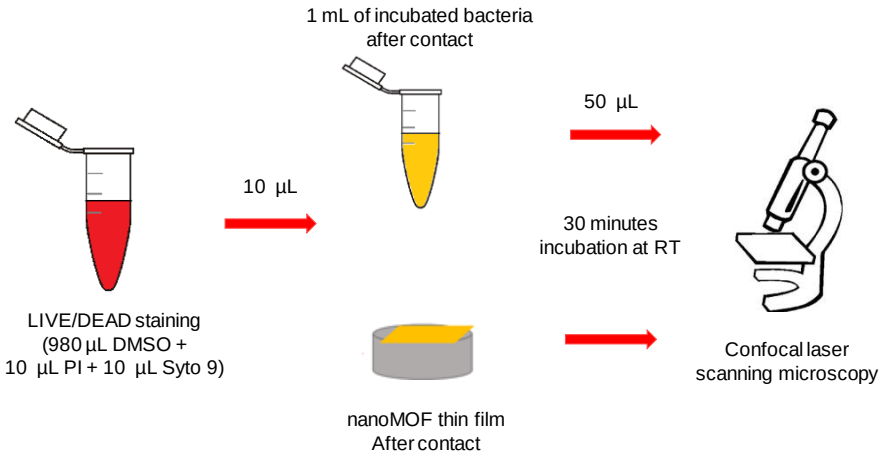

Scheme S 4: Preparation of the LIVE/DEAD staining prior to confocal microscopy imaging.

Green Biofilm Cell Stain was incubated with the samples for 30 min in dark at RT. Stained cells were visualized *via* CLSM using an excitation/emission maxima wavelength of 472/580 nm. The green emission observed identifies the biofilm bacteria cells with membrane integrity.

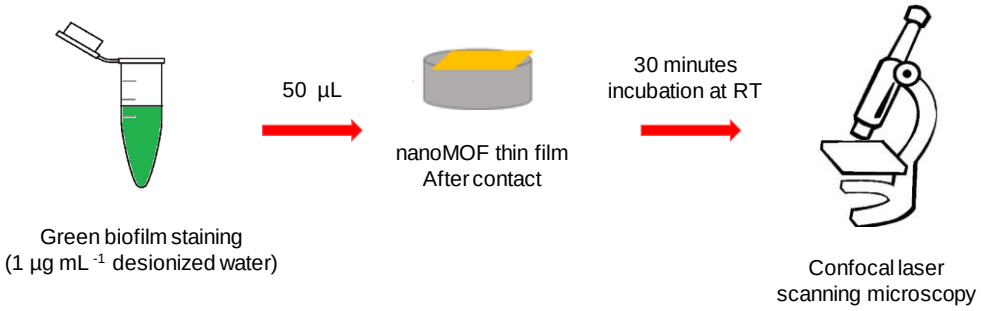

Scheme S 5: Preparation of the Green biofilm staining prior to confocal microscopy imaging.

III.I.iv. Stability of the MOF thin film in the culture broth

The amount of organic linker released, BDC-NH_2, was determined using a reversed phase high performance liquid chromatography (HPLC). Sunfire-C18 reverse-phase column (5 µm, 4.6 x 150 mm, Waters) was employed. For the quantification of all the chemical species, isocratic conditions were used. The flow rate was 1 $mL \cdot min^{-1}$, and the column temperature was fixed at 25 ºC. Before injection, the aliquot of the sample of interest was centrifuged (8150 x g RCF,10 min) to remove the precipitated species. After centrifugation, in all cases, the injection volume was 30 µL. The mobile phase was based on a mixture of 50:50 MeOH:buffer solution (0.04 M, pH = 2.5). The retention time and absorption maximum (λ) for BDC-NH_2 was 2.7 min and λ=228 nm. *Preparation of the buffer solution (0.04 M, pH = 2.5)*: 2.4 g (0.02 mol) of NaH_2PO_4 and 2.84 g (0.02 mol) of Na_2HPO_4 were dissolved in 1 L of MilliQ water. The pH was then adjusted to 2.5 with H_3PO_4 (≥ 85 %).

III.II. Complementary results and discussion

III.II.i. Synthesis and characterization of AgNP@nanoMOF

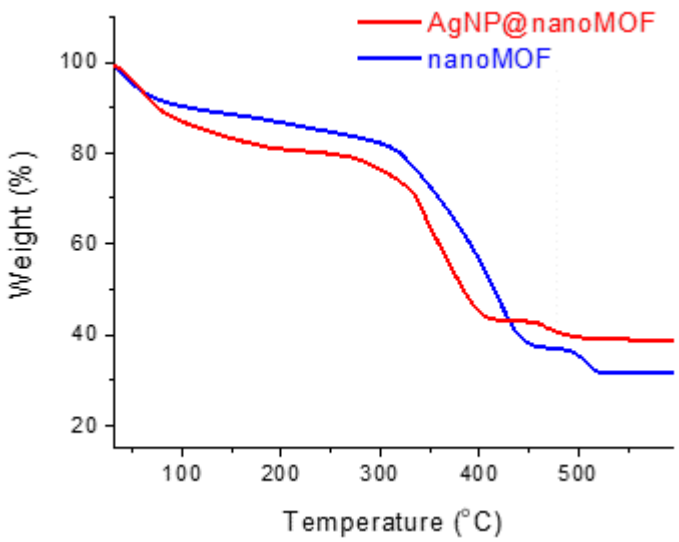

Figure S 3: TGA curves of nanoMOF (blue) and the AgNP@ nanoMOF (red).

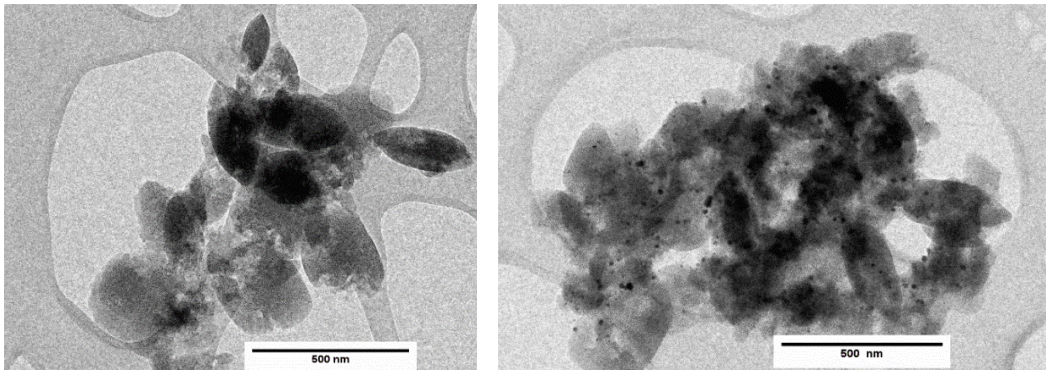

Figure S 4: TEM micrograph nanoMOF (left) and AgNP@nanoMOF (right) (scale bar: 500 nm).

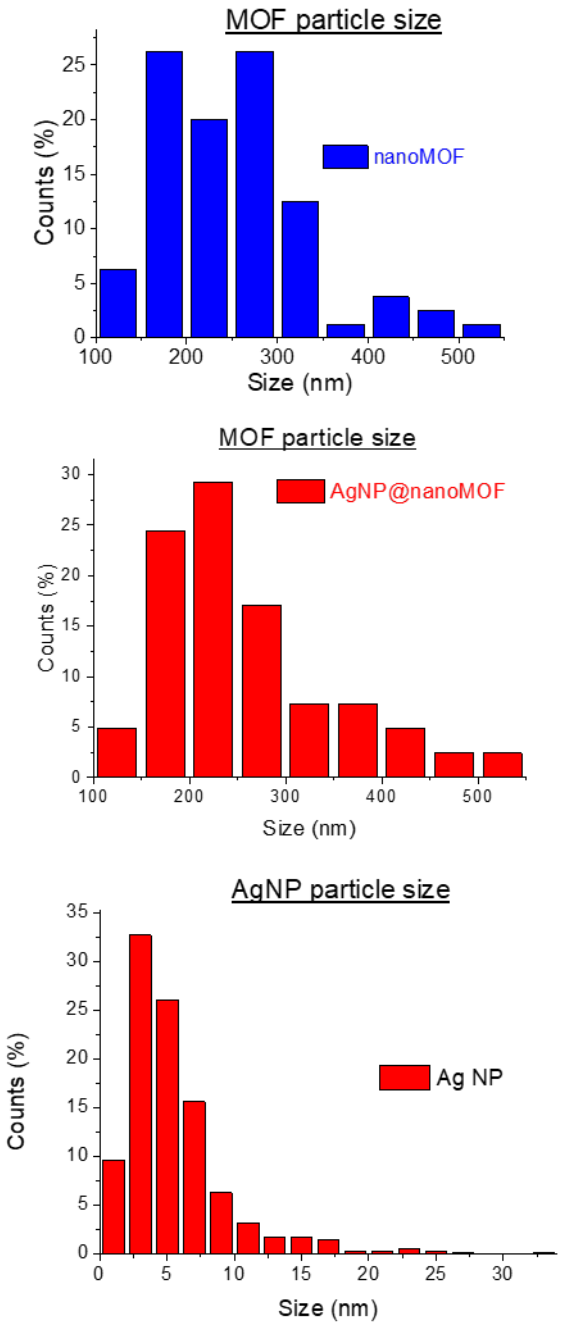

Figure S 5: Particle size distribution of nanoMOF (top, n=50) and AgNP@nanoMOF (middle, n=50) and AgNP (bottom, n=600) determined by TEM

Bearing in mind the potential applications (*e.g.* biology, catalysis), AgNP@nanoMOF dispersions should bear a good colloidal stability under the desired relevant conditions. For this reason, the hydrodynamic size and ζ-potential (when possible) of AgNP@nanoMOF were measured in different media (*e.g.*: water, methanol, ethanol and CH_3CN) and further compared with the nanoMOF (Table S 1). The hydrodynamic particle size of the composite was kept after the impregnation-reduction process, with s similar dimensions to the hosting material (239 ± 74 nm) and a relatively monodisperse distribution (Polydispersity Index (PdI) ~ 0.2),[1] in agreement with the particle size determined by TEM (see SI Figure S 5). In addition, the nanoMOF and the AgNP@nanoMOF were colloidally stable in their original alcoholic dispersion media (methanol, previously reported for the single nanoMOF,[2] and ethanol, required in the impregnation-reduction protocol stabilization) as their absolute surface charges were over 30 mV (-31 ± 8 mV and -38 ± 13 mV, respectively), value normally accepted to ensure colloidal stability by electrostatic repulsion. [3] In contrast, a larger particle size of the nanoMOF in aqueous solution (970 ± 455 nm) was found, which could be attributed to the NPs aggregation as a consequence of the almost neutrally charged surface (2 ± 3 mV). This phenomenon is however inexistent in the case of the composite, as the incorporation of AgNPs resulted in a more negative surface (-16 ± 4 mV *vs.* 2 ± 3 mV), which might help to stabilise the NPs in water (192 ± 98 nm).

Finally, in view of their specific antibacterial evaluation, the colloidal stability of nanoMOF and AgNP@nanoMOF was also assessed in a bacterial nutrient broth (NB; a complex medium composed by many organic and inorganic nutrients; see materials and methods 2.4). The presence of salts and proteins might strongly influence the colloidal stability of the nanoMOFs, as previously reported, [4] and might be the reason of change of surface charge in NB with respect to the alcoholic or aqueous solutions (Table S 1). Thus, both nanoMOF and AgNP@nanoMOF exhibited similar small particle sizes and ζ-potential values (~200 nm and -12 mV). This observation might suggest the formation of a protein corona or the modification of the solvation layer with different salts present in the NB, helping to the NPs colloidal stabilisation. As reported by Moore *et al.*, [5] when NPs are dispersed in culture media, proteins are strongly adsorbed on the surface forming the so-called protein corona, affecting the surface charge distribution and colloidal stability. In addition, the analysis of the colloidal stability of the AgNP@nanoMOF composite dispersed in the NB medium (determined up to 48 h, Figure S5) revealed that the composite average particle size remained within 180 ± 60 nm and an increment of the ξ-potential from -12 to -19 mV even within the first hour of contact, indicating the stabilization of the NPs with the salts and proteins present in the NB culture broth.

Table S 1: Particle size and ζ-potential values of the nanoMOF and AgNP@nanoMOF in different media.

NPs	Medium	Size (Ø, nm)	PdI	ζ-potential (ZP, mV)
nanoMOF	MeOH	230 ± 80	0.18	-31 ± 8
	H_2O	970 ± 455	0.25	2 ± 3
	NB	214 ± 101	0.29	-12 ± 1
	CH_3CN	313 ± 90	0.24	*
AgNP@nanoMOF	EtOH	239 ± 74	0.27	-38 ± 13
	H_2O	192 ± 98	0.25	-16 ± 4
	NB	191 ± 80	0.24	-12.6 ± 0.4

* not measured

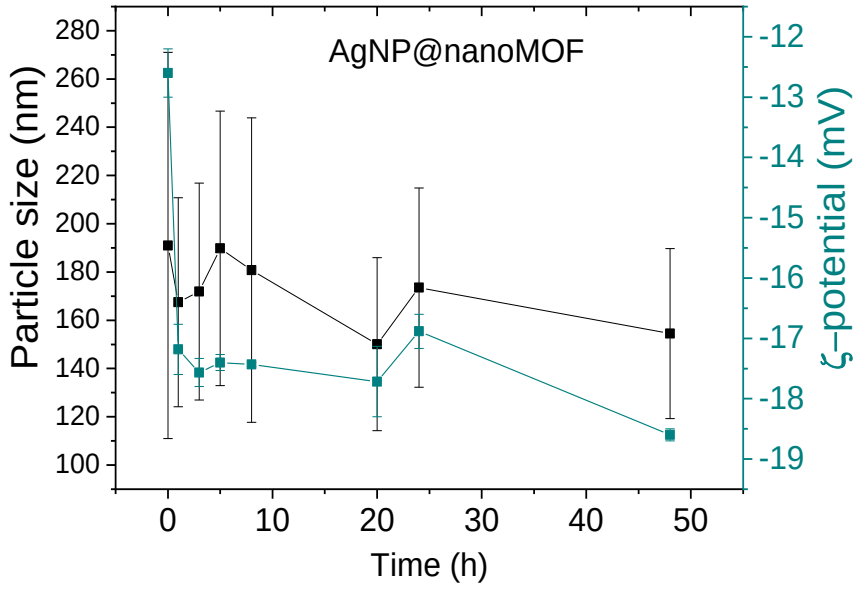

Figure S 6: Analysis of the colloidal stability with time of AgNP@nanoMOF composite dispersed in NB culture medium.

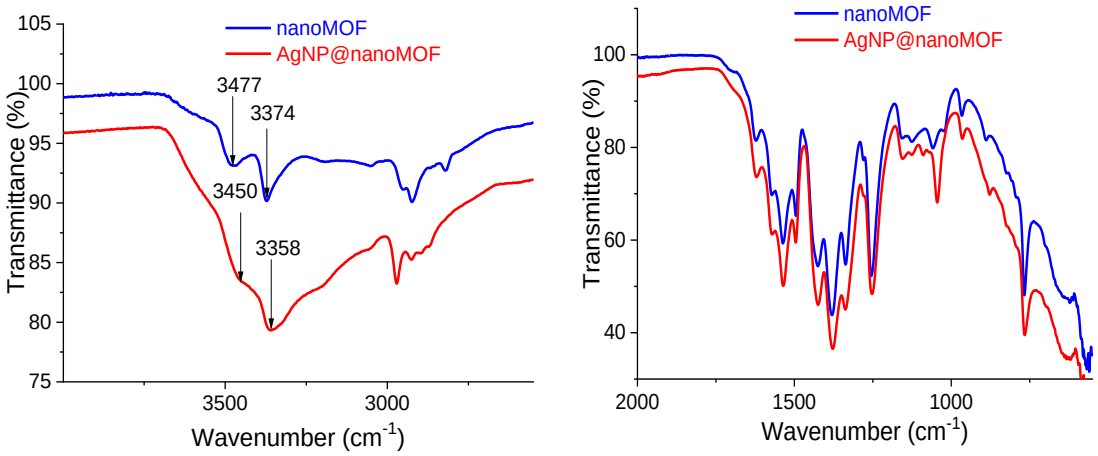

Figure S 7: FTIR spectra of nanoMOF (blue) and the AgNP@nanoMOF (red).

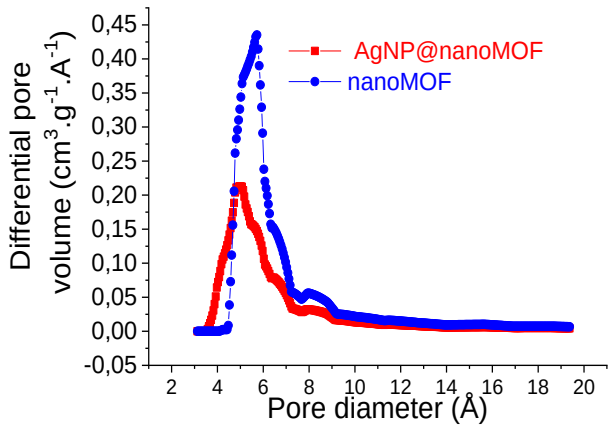

Figure S 8: HK Pore volume distribution of nanoMOF (blue) and the AgNP@nanoMOF (red).

III.II.ii. Antibacterial effect of AgNP@nanoMOF in suspension

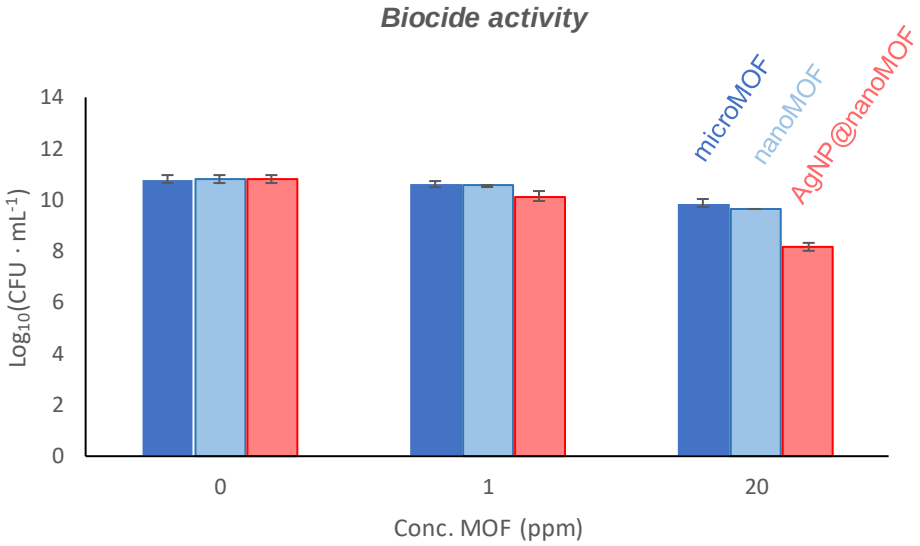

Figure S 9: Colony Forming Units mL^{-1} of culture broth (represented as the $Log_{10}(CFU)$) *of E. coli* planktonic bacteria in contact with a suspension of microMOF (dark blue), nanoMOF (blue), AgNP@nanoMOF (red), (Biocide activity).

Table S 2: Determination of planktonic *S. aureus* bacterial viability by plate count after 20 h in contact (in dark) with the different materials of study, expressed as CFU · mL^{-1}, inhibition % (with respect to the control CFU · mL^{-1}) and $Log_{10}(CFU \cdot mL^{-1})$

[MOF] (ppm)	Sample	CFU·mL^{-1}	Inhibition %	$Log_{10}(CFU \cdot mL^{-1})$
0	Control	4.97E+11	0.00	11.70
1	microMOF	4.47E+11	9.96	11.65
	nanoMOF	1.14E+11	77.08	11.06
	AgNP@nanoMOF	1.86E+10	96.25	10.27
	AgNP + nanoMOF	2.49E+11	49.86	11.40
20	microMOF	1.88E+11	62.12	11.27
	nanoMOF	1.52E+10	96.95	10.18
	AgNP@nanoMOF	7.75E+07	99.98	7.89
	AgNP + nanoMOF	8.47E+10	82.95	10.93
	$AgNO_3$	6.73E+10	86.46	10.83
	Ag^0	7.78E+10	84.34	10.89
	$BDC\text{-}NH_2$	2.48E+11	50.18	11.39
	TiO_2	2.33E+10	95.32	10.37

Table S 3: Determination of planktonic *E. coli* bacterial viability by plate count after 20 h in contact (in dark) with the different materials of study, expressed as CFU · mL^{-1}, inhibition % (with respect to the control CFU · mL^{-1}) and Log_{10}(CFU mL^{-1})

[MOF] (ppm)	Sample	CFU mL^{-1}	Inhibition %	Log_{10}(CFU · mL^{-1})
0	Control	6.43E+10	0.00	10.81
1	microMOF	3.98E+10	38.21	10.60
	nanoMOF	3.75E+10	41.69	10.57
	AgNP@nanoMOF	1.36E+10	78.91	10.13
20	microMOF	7.50E+09	88.34	9.88
	nanoMOF	4.53E+09	92.95	9.66
	AgNP@nanoMOF	1.58E+08	99.75	8.20

Table S 4: Determination of planktonic *S. aureus* bacterial viability by plate count after 18 h (in dark) + 2 h UVA in contact with the different materials of study, expressed as CFU · mL^{-1}, inhibition % (with respect to the control CFU · mL^{-1}) and Log_{10}(CFU · mL^{-1})

[MOF] (ppm)	Sample	CFU·mL^{-1}	Inhibition %	Log_{10}(CFU · mL^{-1})
0	Control	9.85E+09	0.00	9.99
1	nanoMOF	1.36E+09	86.22	9.13
	AgNP@nanoMOF	1.28E+07	99.87	7.11
	AgNP + nanoMOF	3.30E+09	66.46	9.52
20	nanoMOF	7.72E+07	99.22	7.89
	AgNP@nanoMOF	1.51E+04	99.9998	4.18
	AgNP + nanoMOF	1.09E+09	88.95	9.04
	$AgNO_3$	2.25E+08	97.72	8.35
	Ag^0	3.40E+08	96.55	8.53
	BDC-NH_2	7.24E+08	92.65	8.86
	TiO_2	2.81E+08	97.15	8.45

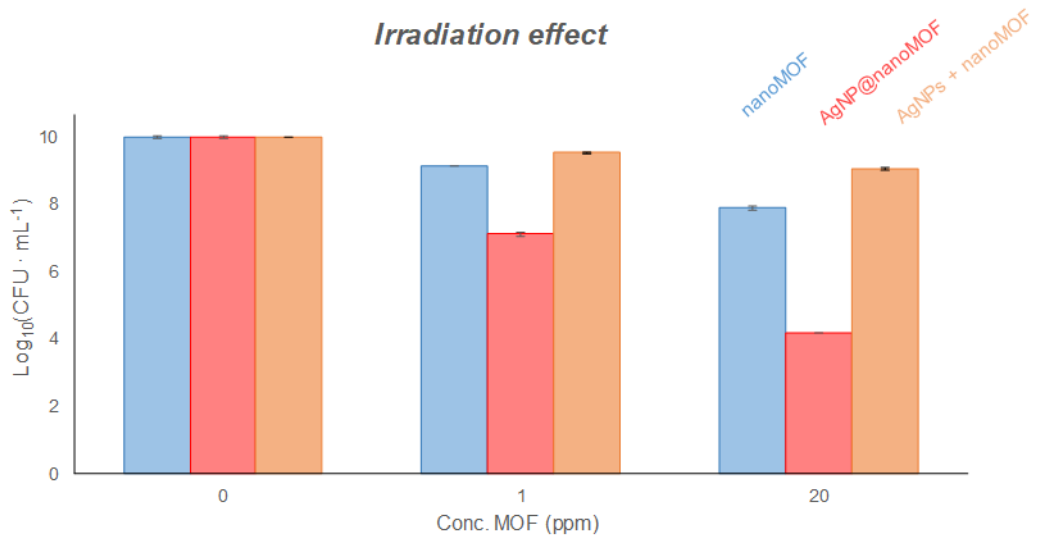

Figure S 10: Colony Forming Units mL^{-1} of culture broth (represented as the $Log_{10}(CFU)$) of *S. aureus* planktonic bacteria in contact with a suspension of nanoMOF (blue), AgNP@naoMOF (red), AgNP+nanoMOF(brown) after 18 h dark + 2 h of UVA irradiation, (Irradiation effect).

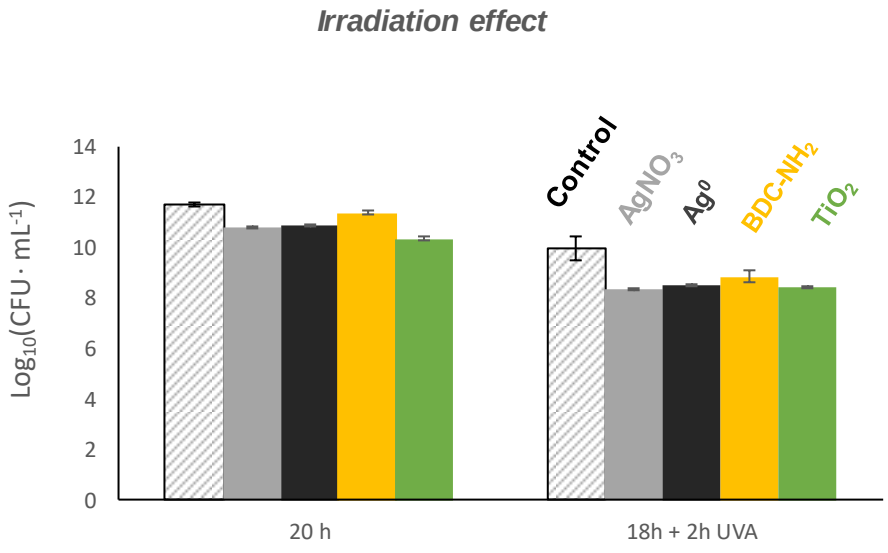

Figure S 11: *S. aureus* Colony Forming Units · mL^{-1} of culture broth (represented as the $Log_{10}(CFU)$) in contact with $AgNO_3$ (grey), Ag^0 (black), BDC-NH_2 (yellow) and TiO_2 (green) after 20 h of dark exposure and after 18 h dark + 2 h of UVA irradiation compared to the control (dashed bar).

Further analysis of the bacterial viability was carried out by the determination of the reduction of the bacterial enzymatic activity (Figure S12). On one side, when in contact with *S. aureus* in dark the 'physical' mixture AgNPs + nanoMOF showed almost no affection of the enzymatic activity when compared with the pristine nanoMOF, being even smaller (at 20 ppm, 4 *vs.* 15%). On the

other side, the inclusion of silver within the MOF, as in the case of the AgNP@nanoMOF composite, doubles the inhibition of the enzymatic activity (at 20 ppm, 37 *vs.* 15%; Figure S12). Moreover, the UVA irradiation duplicates the antibacterial effect, trend observed in previous results, overpassing the reduction of 80% of enzymatic activity (note that it is even higher than the one achieved by the irradiated silver controls). Additionally, similar trends were observed using the LIVE/DEAD staining (Figure S13): AgNP@nanoMOF almost doubled the biocide activity of nanoMOF (being the dead bacteria ratio 11 *vs.* 6 %, Figure S13), while the 'physical' mixture AgNPs + nanoMOF do not overpassed the dead bacteria of the control. Once again, UVA irradiation increased the bactericide effect of all samples.

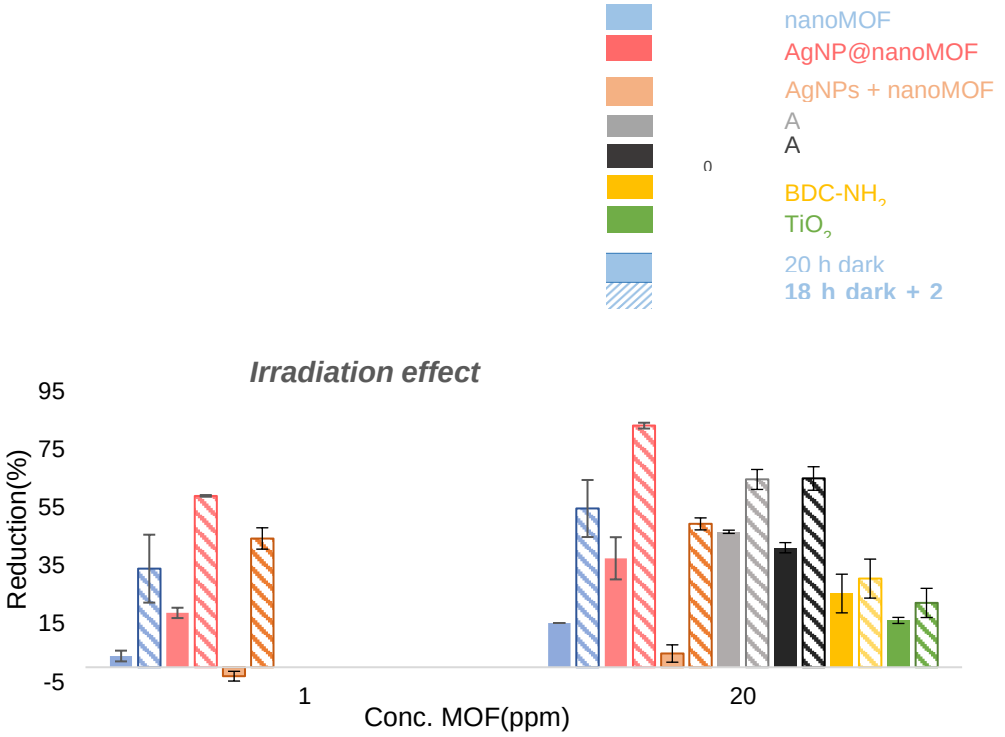

Figure S 12: Reduction (%) of enzymatic activity of planktonic *S. aureus* determined from FDA fluorescent emission (ex.:485 nm; em.: 538 nm) in contact nanoMOF (blue), AgNP@nanoMOF (red), AgNPs + nanoMOF (brown), $AgNO_3$ (grey), Ag^0 (black), BDC-NH_2 (yellow) and TiO_2 (green). *S. aureus* enzymatic activity inhibition in contact with MOF after 20 h of dark exposure and after 18 h dark + 2 h of UVA irradiation.

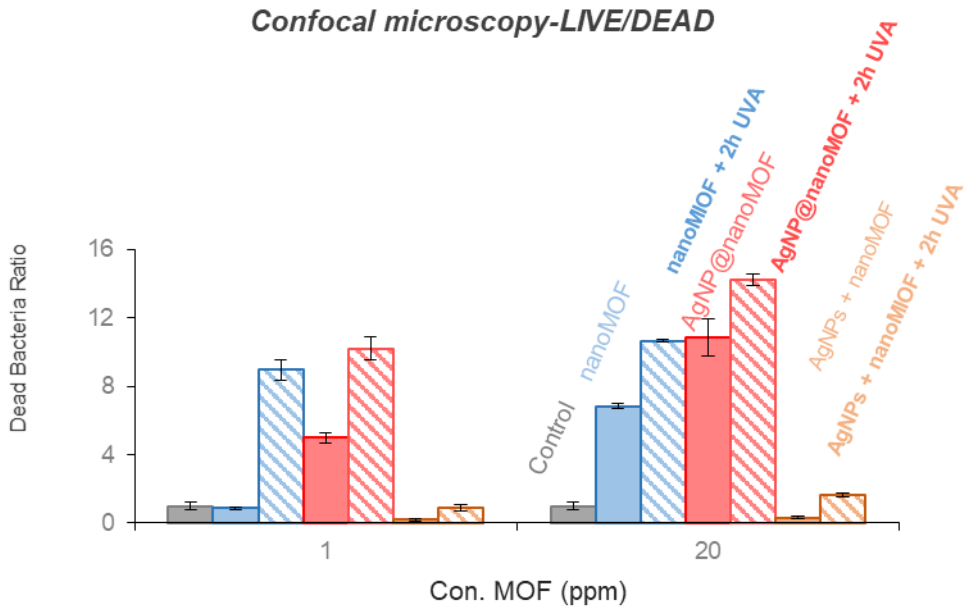

Figure S 13: Semi-quantitative analysis of the CLSM micrographs of planktonic *S. aureus* bacteria stained with LIVE/DEAD after contact with suspensions of nanoMOF (blue), AgNP@nanoMOF (red) and AgNPs + nanoMOF (brown). Comparison with and without irradiation. Results are presented as Dead Bacteria Ratio (% dead bacteria / % dead bacteria control).

III.II.iii. Biofilm treatment: Antifouling photo-bactericidal activity of AgNP@nanoMOF

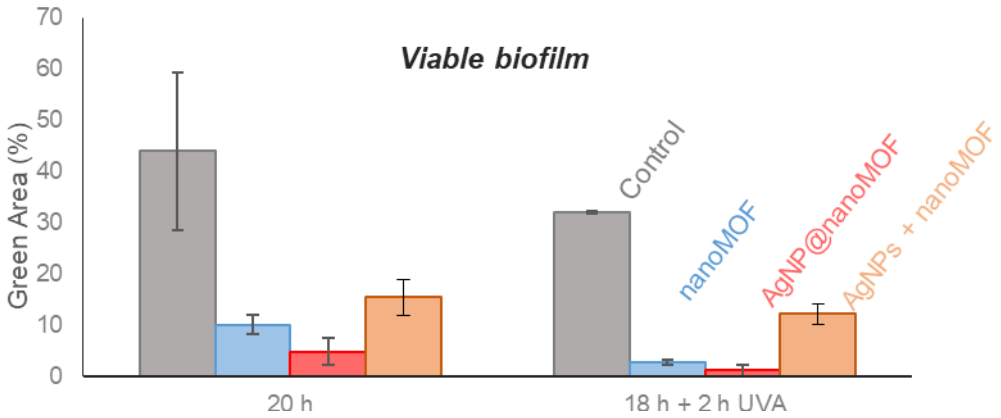

Figure S 14: Quantification of *S. aureus* biofilm on nanoMOF thin film (blue), AgNP@ nanoMOF thin film (red) and AgNPs + nanoMOF thin film (brown) by determination of the green areas marked by the FilmTracer FM 1-43 Green Biofilm Cell staining with the help of ImageJ.

Table S 5: Determination of planktonic and sessile *S. aureus* bacterial viability by plate count after 20 h (in dark), 18 h (in dark) + 2 h UVA or 18 h (in dark) + 2 h Vis in contact with the different materials of study, expressed as CFU · mL^{-1}, inhibition % (with respect to the control CFU · mL^{-1}) and Log_{10}(CFU · mL^{-1}).

		Planktonic bacteria			Sessile bacteria		
Contact time	Sample	CFU·mL^{-1}	Inhibition %	Log_{10}(CFU · mL^{-1})	CFU·mL^{-1}	Inhibition %	Log_{10}(CFU·mL^{-1})
20 h	Control	2.42E+09	0.0000	9.38	8.66E+08	0.0000	8.94
	nanoMOF	1.37E+09	43.3530	9.14	6.28E+08	27.5333	8.80
	Ag@nanoMOF	1.72E+08	92.8821	8.24	1.28E+08	85.2448	8.11
	Ag + nanoMOF	2.10E+09	13.4615	9.32	2.94E+08	66.0766	8.47
18 h + 2 h UVA	Control	3.03E+08	0.0000	8.48	7.84E+08	0.0000	8.89
	nanoMOF	3.31E+04	99.9891	4.52	4.47E+04	99.9943	4.65
	Ag@nanoMOF	1.44E+03	99.9995	3.16	9.56E+02	99.9999	2.98
	Ag + nanoMOF	7.65E+07	74.7379	7.88	1.98E+08	74.7831	8.30
18 h + 4 h VIS	Control	2.10E+10	0.00	10.32	2.95E+05	0.00	5.47
	nanoMOF	1.05E+10	49.75	10.02	1.70E+05	42.22	5.23
	Ag@nanoMOF	4.69E+08	97.76	8.67	4.92E+04	83.31	4.69

As AgNP@nanoMOF composite exhibited higher absorbance in the visible range (Figure 1), it has been considered interesting to determine the bacterial viability of both planktonic and sessile *S. aureus* after irradiation with visible range lamps (Figure S15). The same as with UVA irradiation, results exhibited the beneficial effect of the AgNPs in the composite as lower bacterial viability was determined by plate count. Although the final bacterial inhibition is lower compared to UVA samples (Table S5), it is still higher than the non-irradiated: AgNP@nanoMOF planktonic bacterial inhibition of 97.8% *vs.* 92.8% in dark. Despite the interesting photo-activity of the AgNP@nanoMOF under visible irradiation (where AgNPs act as an antenna), this mild bioactivity might be related with the lower ROS production in NB media after Visible irradiation (Figure S16).

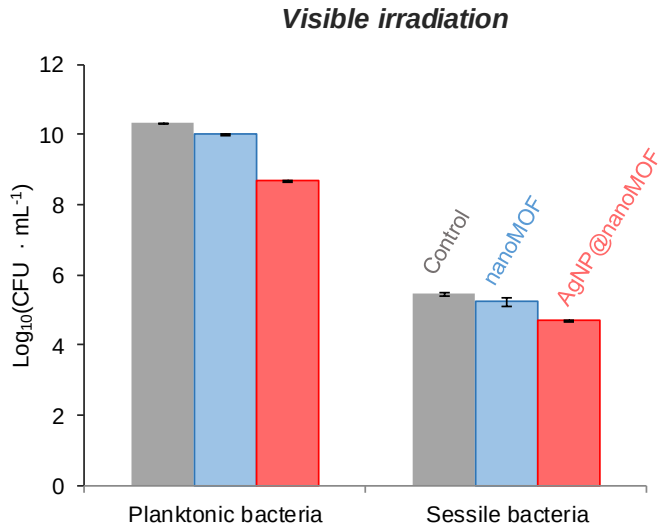

Figure S 15: Colony Forming Units · mL^{-1} culture (represented as the $Log_{10}(CFU)$) of the *S. aureus* suspension (planktonic bacteria; left) and S. aureus biofilm detached from the surface (sessile bacteria; right) in contact with nanoMOF (blue), AgNP@nanoMOF (red) thin films after 18 h + 4 h Vis irradiation compared with the control (grey).

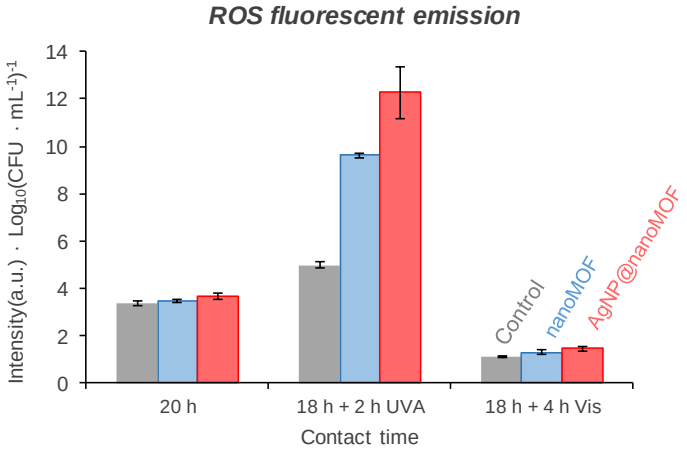

Figure S 16: Generation of Reactive Oxygen Species) of the *S. aureus* suspension (as determined by the ratio of the fluorescent emission with the $Log_{10}(CFU \cdot mL^{-1})$, ex.:495 nm; em.: 525 nm) in contact with nanoMOF (blue) and AgNP@nanoMOF (red) thin films over cover glasses after 20 h of dark exposure, after 18 h dark + 2 h of UVA irradiation and after 18 h + 4 h Vis irradiation, compared with the control (grey).

Table S 6: Determination of planktonic and sessile *E. coli* bacterial viability by plate count after 20 h (in dark) or18 h (in dark) + 2 h UVA contact with the different materials of study, expressed as CFU · mL^{-1}, inhibition % (with respect to the control CFU · mL^{-1}) and Log$_{10}$(CFU · mL^{-1}).

		Planktonic bacteria			Sessile bacteria		
Contact time	Sample	CFU · mL^{-1}	Inhibition %	Log$_{10}$(CFU · mL^{-1})	CFU · mL^{-1}	Inhibition %	Log$_{10}$(CFU · mL^{-1})
20 h	Control	2.96E+11	0.0000	11.47	1.38E+06	0.0000	6.14
	nanoMOF	1.90E+11	35.9595	11.28	4.54E+05	67.1095	5.66
	Ag@nanoMOF	1.07E+11	63.9280	11.03	2.91E+05	78.9103	5.46
18 h + 2 h UVA	Control	2.34E+10	0.0000	10.37	2.30E+05	0.0000	5.36
	nanoMOF	1.26E+10	46.2440	10.10	8.10E+03	96.4792	3.91
	Ag@nanoMOF	1.65E+09	92.9605	9.22	1.00E+02	99.9565	2.00

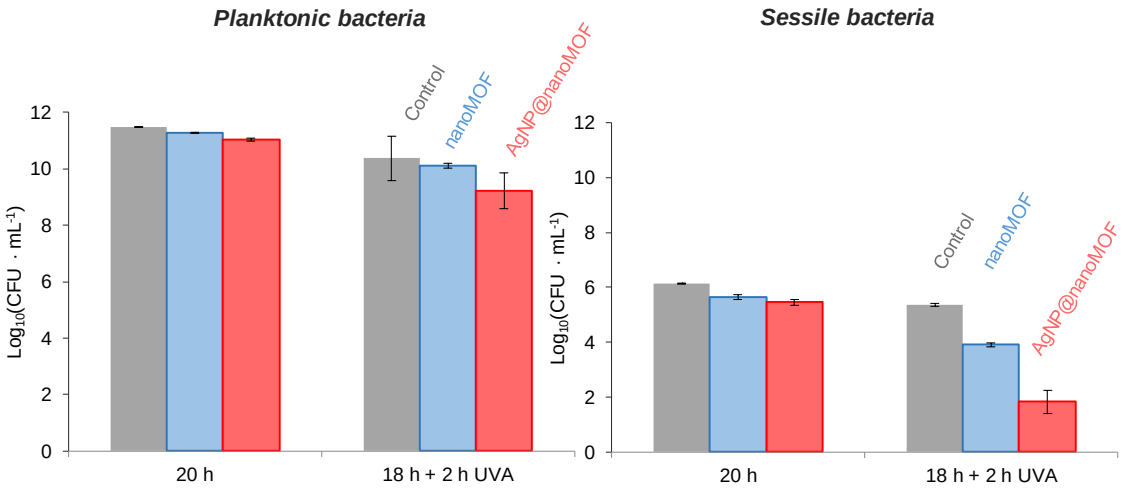

Figure S 17: Colony Forming Units · mL^{-1} culture (represented as the Log$_{10}$(CFU)) of the *E. coli* suspension (planktonic bacteria; left) and E. coli biofilm detached from the surface (sessile bacteria; right) in contact with nanoMOF (blue), AgNP@nanoMOF (red) thin films after 20 h of dark exposure and after 18 h dark + 2 h of UVA irradiation compared with the control (grey).

Supporting the previous experiments, the bacteria enzymatic activity reduction (FDA staining; see section 2.4 materials and methods) was determined for the planktonic *S. aureus* in the NB medium in contact with the nanoMOF and

AgNP@nanoMOF thin films in comparison with the bare glass covers and the ones coated with the AgNPs + nanoMOF 'physical' mixture. In agreement to CFU results, during the 20 h dark period of biofilm growth, all materials already reduce the enzymatic activity of the bacteria present in the culture broth (Figure S 18). It is noticeable the activity of the nanoMOF, reaching a 32 % of inhibition compared to the control cover glass, which evidences a non-negligible intrinsic bactericide effect. Once again, the thin film of AgNPs + nanoMOF 'physical' mixture seemed ineffective as the enzymatic activity reduction is within the range of the pristine MOF. Nevertheless, when the AgNPs are incorporated into the nanoMOF structure, the composite inhibition in dark doubles (60 *vs.* 32%). After 2 h UVA irradiation, the reduction of *S. aureus* enzymatic activity is 1.5 times higher in the thin films, having a final inhibition of 48% in the case of both the pristine nanoMOF and the physical mixture, and a 79% inhibition in the AgNP@nanoMOF composite. This enzymatic activity reduction fits well with the ROS production (Figure S 17) and the bacterial viability determined by plate counting (see Figure 4).

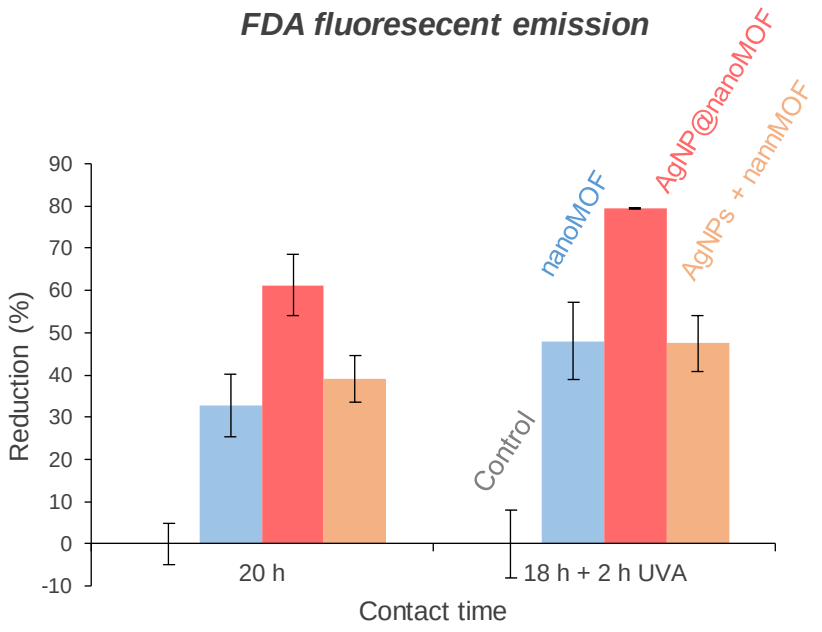

Figure S 18: Reduction (%) of enzymatic activity of the planktonic *S. aureus* determined from FDA fluorescent emission (ex.:485 nm; em.: 538 nm) in contact with nanoMOF (blue), AgNP@ nanoMOF (red) and AgNPs + nanoMOF (brown) thin films over cover glasses after 20 h of dark exposure and after 18 h dark + 2 h of UVA irradiation, compared with the control (grey).

As a complementary technique, LIVE/DEAD staining and confocal microscopy were finally used to analyse bacterial viability discriminating between alive (stained in green) or dead (stained in red) bacteria (see Figure S 16). The growth of *S. aureus* after the 20 h dark period is clear, observing an important amount of viable live bacteria in the bare control glass. However, bacteria cell

integrity was affected by the presence of the nanoMOF, appearing as yellowish or orange cells. It is generally accepted that yellow identifies still viable cells while orange are damaged cells, [6] what it means that the cells in contact with nanoMOF are partially dead. In the case of AgNP@nanoMOF, the composite seemed to cause important damages in the cell membrane, as almost all the bacteria appear red-stained or dead. In consonance, when the composite was exposed to 2 h-UVA irradiation, bacteria again appear with the red PI staining, showing cell impairment due to the disintegration of the bacterial membrane. On the contrary, when in contact with the 'physical' mixture AgNPs + nanoMOF thin film after 20 h in dark, can be seen a lot of bacteria still viable green stained and few of them red. Is only after UVA irradiation of the 'physical' mixture thin film when significant bacterial damage can be seen as bacteria appeared yellow and orange stained. Consequently, the biocide effect of the 'physical' mixture is lower compared to the one of the AgNP@nanoMOF composite. These results are in agreement with those of Green staining (Figure 3) and plate count (Figure 4).

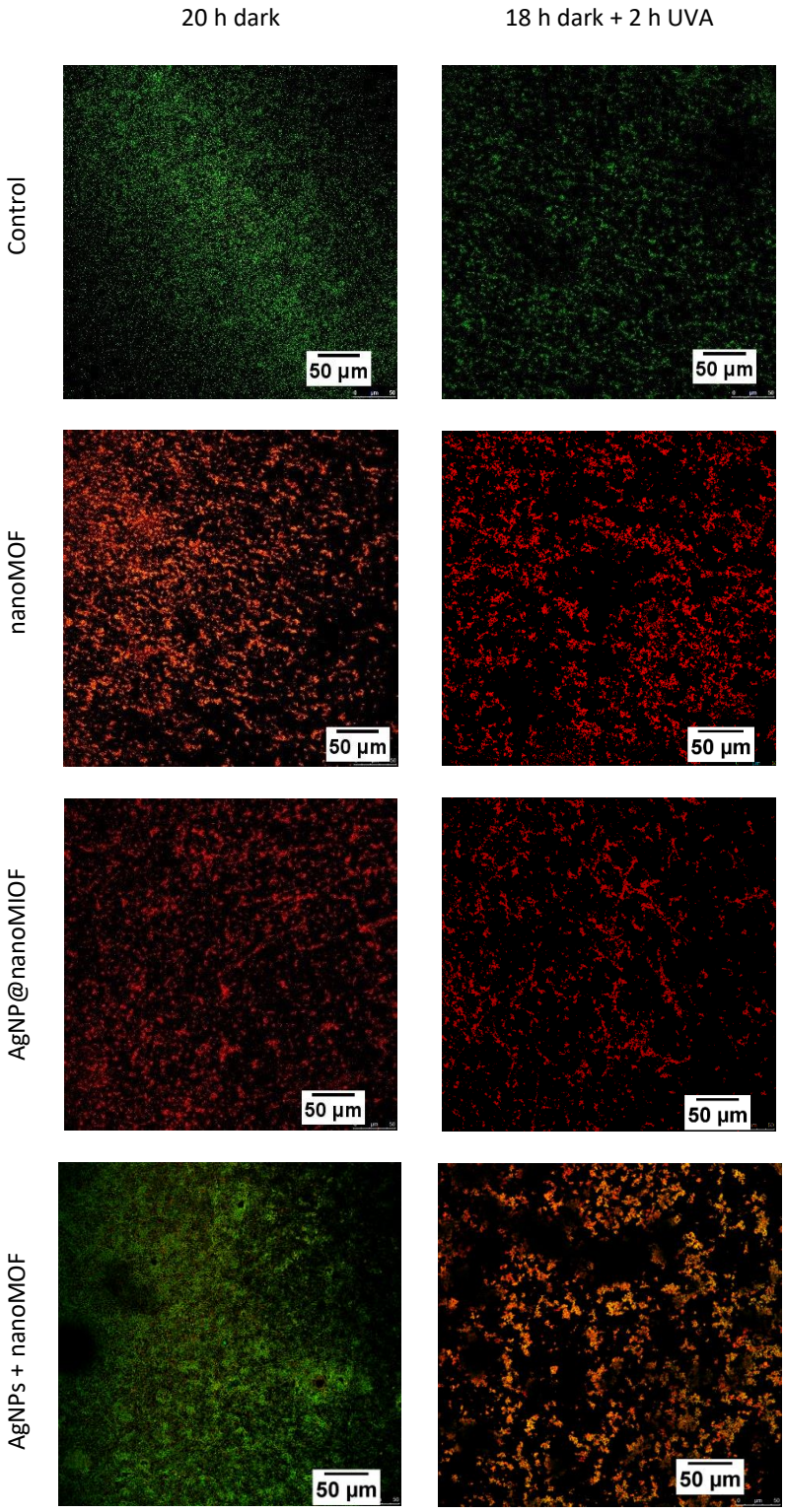

Figure S 19: LIVE/DEAD confocal micrographs of sessile *S. aureus* on top of cover glasses surface (left) after 20 h dark biofilm grown and (right) 18 h grown in dark plus 2 h UVA irradiation of the (top to bottom) positive control cover and the glass covered with nanoMOF thin film, AgNP@nanoMOF thin film and AgNPs + nanoMOF 'physical' mixture thin film

III.II.iv. AgNP@nanoMOF thin film chemical stability

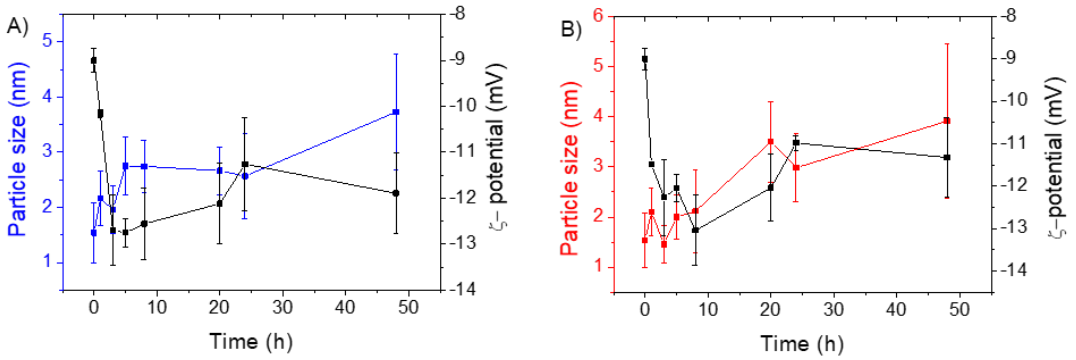

Figure S 20: Analysis of stability with time of the nanoMOF (A) and AgNP@nanoMOF (B) thin films coating over cover glasses in contact with NB culture medium at 37 °C during different periods of time. Determination of the particle size and ζ-potential with DLS.

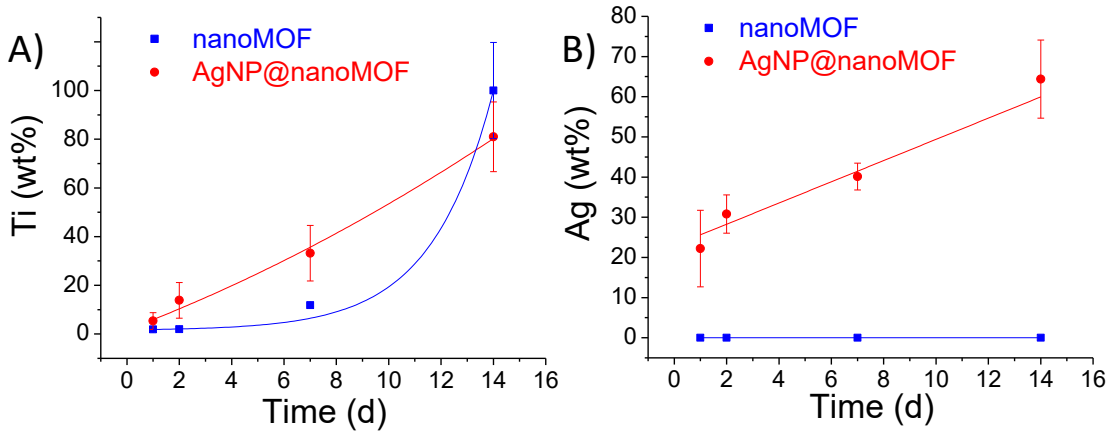

Figure S 21: NanoMOF degradation kinetics and metal release from the nanoMOF and AgNP@nanoMOF thin films on glass substrates in contact with the culture medium NB under accelerated degradation conditions incubated at 70°C. Ti (A) and Ag (B) release (expressed as wt.% of the total content) determined by ICP-OES

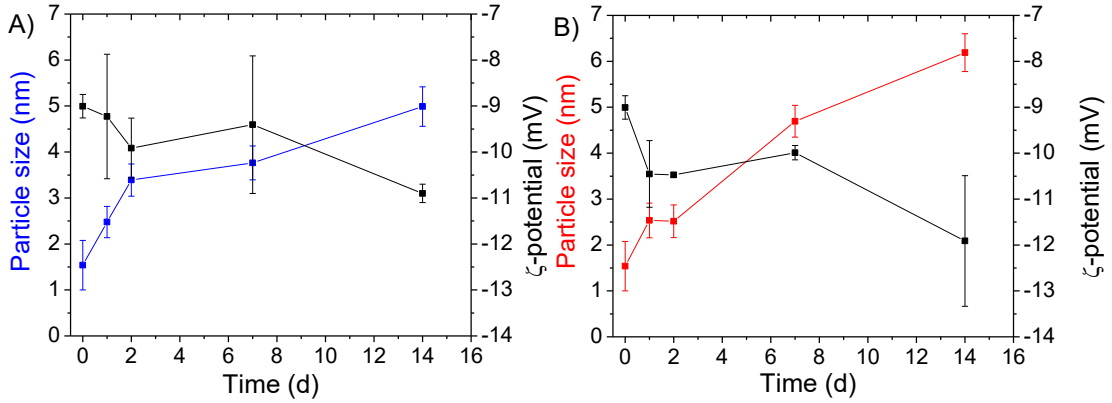

Figure S 22: Analysis of stability with time of the nanoMOF (A) and AgNP@nanoMOF (B) thin films coating over cover glasses in contact with NB culture medium under accelerated degradation conditions incubated at 70 °C during different periods of time. Determination of the particle size and ζ-potential with DLS.

Table S 7: Comparison of the chemical stability (Ag wt.% released after 24h) and MIC against planktonic (in suspension) *S. aureus* of different Ag-based MOF suspensions.

MOF	Ag wt.% released after 24 h	*S. aureus* MIC expressed by MOF concentration (ppm)	*S. aureus* MIC expressed by Ag concentration (ppm)	Reference
$[(AgL)NO_3]\cdot 2H_2O$	0.85 [*1]	297	38	7
$[(AgL)CF_3SO_3]\cdot 2H_2O$	1.03 [*1]	307	36	
$[(AgL)ClO_4]\cdot 2H_2O$	1.20 [*1]	293	37	
$Ag_3[C_7H_4O_5P]$	1.8 [*1]	26 [*3]	16 [*3]	8
[Ag(μ3-PTA=S)]n(NO3)n·nH2O	Not reported	20	6	9
$[Ag_4(\mu_4\text{-PTAL=S})(\mu_5\text{-PTA=S})(\mu_2\text{-}SO_4)_2(H_2O)_2]_n\cdot 2nH_2O$		40	16	
$[Ag_2(3\text{-NPTA})(bipy)_{0.5}(H_2O)]$	4.16 [*1]	20	8	10
$[Ag_2(O\text{-IPA})(H_2O)\cdot(H_3O)]$	2.5 [*1]	15	7.5	11
$[Ag_5(PYDC)_2(OH)]$	1.8 [*1]	20	12	
AgTAZ	3.3 [*2]	Not reported	Not reported	12
Ag@CuTCPP	41 ppm/5 h [*1]	6.25	Not reported	13
Penicillin	-	6.25	-	13
$C_{171}H_{173}Ag_{42}Cl_9O_{10}S_3$	Not reported	5	3.1	14
UiO66-2COOAg	Not reported	75	9	15
UiO67-bpdcAg		50	6.5	
AgNP@nanoMIL-125(Ti)NH_2	3.5 [*2]	20 [*4]	1.21 [*4]	This work

[*1] measured in distilled water

[*2] measured in the culture medium

[*3] Minimum Bactericidal concentration (MBC)

[*4] value higher than the 90% of the Minimum Inhibitory Concentration (> MIC_{90})

Table S 8: Inhibition of the Biofilm formation of *S. aureus* as MIC of several antibiotic in suspension.

Antibiotic	MIC (ppm)	Reference
Cefazolin	128	16
Azithromycin	128	16
Vancomycin	16	16
Oxacillin	128	16
Linezolid	128	16
AgNP@nanoMIL-125(Ti)NH_2	88*	This work

*MIC_{90} determined after 18h dark + 2 h UVA irradiation, concentration of the AgNP@nanoMIL-125(Ti)NH_2 thin film in contact with *S. aureus*,

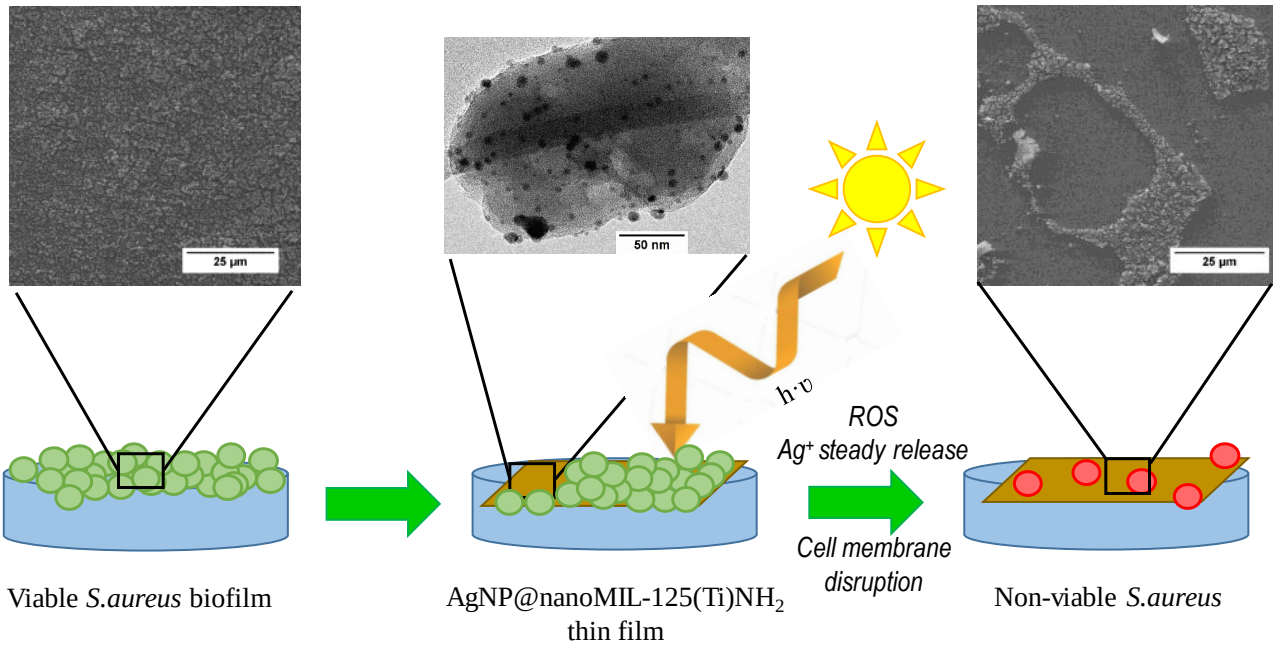

Scheme S 6: *S. aureus* biofilm treatment by AgNP@nanoMIL-125(Ti)NH2 thin film after UVA irradiation.

Bibliography

(1) Koppel, D. E. Analysis of Macromolecular Polydispersity in Intensity Correlation Spectroscopy: The Method of Cumulants. *J. Chem. Phys.* **1972**, *57* (11), 4814–4820. https://doi.org/10.1063/1.1678153.

(2) Vilela, S.; Salcedo-Abraira, P.; Colinet, I.; Salles, F.; de Koning, M.; Joosen, M.; Serre, C.; Horcajada, P. Nanometric MIL-125-NH2 Metal–Organic Framework as a Potential Nerve Agent Antidote Carrier. *Nanomaterials* **2017**, *7* (10), 321. https://doi.org/10.3390/nano7100321.

(3) Hunter, R. J. *Zeta Potential in Colloid Science : Principles and Applications*; Ottewi, R. H., Rowell, l R. L., Eds.; Academic Press: London, UK, 1988.

(4) Bellido, E.; Guillevic, M.; Hidalgo, T.; Santander-Ortega, M. J.; Serre, C.; Horcajada, P. Understanding the Colloidal Stability of the Mesoporous MIL-100(Fe) Nanoparticles in Physiological Media. *Langmuir* **2014**, *30* (20), 5911–5920. https://doi.org/10.1021/la5012555.

(5) Moore, T. L.; Rodriguez-Lorenzo, L.; Hirsch, V.; Balog, S.; Urban, D.; Jud, C.; Rothen-Rutishauser, B.; Lattuada, M.; Petri-Fink, A. Nanoparticle Colloidal Stability in Cell Culture Media and Impact on Cellular Interactions. *Chem. Soc. Rev.* **2015**, *44* (17), 6287–6305. https://doi.org/10.1039/C4CS00487F.

(6) Boulos, L.; Prévost, M.; Barbeau, B.; Coallier, J.; Desjardins, R. LIVE/DEAD® BacLight™: Application of a New Rapid Staining Method for Direct Enumeration of Viable and Total Bacteria in Drinking Water. *J. Microbiol. Methods* **1999**, *37* (1), 77–86. https://doi.org/10.1016/S0167-7012(99)00048-2.

(7) Liu, Y.; Xu, X.; Xia, Q.; Yuan, G.; He, Q.; Cui, Y. Multiple Topological Isomerism of Three-Connected Networks in Silver-Based Metal-Organoboron Frameworks. *Chem. Commun. (Camb).* **2010**, *46* (15), 2608–2610. https://doi.org/10.1039/b923365b.

(8) Berchel, M.; Gall, T. Le; Denis, C.; Hir, S. Le; Quentel, F.; Elléouet, C.; Montier, T.; Rueff, J.-M.; Salaün, J.-Y.; Haelters, J.-P.; et al. A Silver-Based Metal–Organic Framework Material as a 'Reservoir' of Bactericidal Metal Ions. *New J. Chem.* **2011**, *35* (5), 1000–1003. https://doi.org/10.1039/c1nj20202b.

(9) Jaros, S. W.; Smoleński, P.; Guedes da Silva, M. F. C.; Florek, M.; Król, J.; Staroniewicz, Z.; Pombeiro, A. J. L.; Kirillov, A. M. New Silver BioMOFs Driven by 1,3,5-Triaza-7-Phosphaadamantane-7-Sulfide (PTAĄS): Synthesis, Topological Analysis and Antimicrobial Activity. *CrystEngComm* **2013**, *15* (40), 8060–8064. https://doi.org/10.1039/c3ce40913a.

(10) Lu, X.; Ye, J.; Sun, Y.; Bogale, R. F.; Zhao, L.; Tian, P.; Ning, G. Ligand Effects on the Structural Dimensionality and Antibacterial Activities of Silver-Based Coordination Polymers. *Dalt. Trans.* **2014**, *43* (26), 10104–10113. https://doi.org/10.1039/c4dt00270a.

(11) Lu, X.; Ye, J.; Zhang, D.; Xie, R.; Feyisa, R.; Sun, Y.; Zhao, L.; Zhao, Q.; Ning, G. Silver Carboxylate Metal – Organic Frameworks with Highly Antibacterial Activity and Biocompatibility. *J. Inorg. Biochem.* **2014**, *138*, 114–121. https://doi.org/10.1016/j.jinorgbio.2014.05.005.

(12) Aguado, S.; Quirós, J.; Canivet, J.; Farrusseng, D.; Boltes, K.; Rosal, R. Antimicrobial Activity of Cobalt Imidazolate Metal – Organic Frameworks. *Chemosphere* **2014**, *113*, 188–192. https://doi.org/10.1016/j.chemosphere.2014.05.029.

(13) Ximing, G.; Bin, G.; Yuanlin, W.; Shuanghong, G. Preparation of Spherical Metal – Organic Frameworks Encapsulating Ag Nanoparticles and Study on Its Antibacterial Activity. *Mater. Sci. Eng. C* **2017**, *80*, 698–707. https://doi.org/10.1016/j.msec.2017.07.027.

(14) Zhang, S.-S.; Wang, X.; Su, H.-F.; Feng, L.; Wang, Z.; Ding, W.-Q.; Blatov, V. A.; Kurmoo, M.; Tung, C.-H.; Sun, D.; et al. A Water-Stable Cl@Ag $_{14}$ Cluster Based Metal–Organic Open Framework for Dichromate Trapping and Bacterial Inhibition. *Inorg. Chem.* **2017**, *56* (19), 11891–11899. https://doi.org/10.1021/acs.inorgchem.7b01879.

(15) Mortada, B.; Matar, T. A.; Sakaya, A.; Atallah, H.; Ali, Z. K.; Karam, P. Postmetalated Zirconium Metal Organic Frameworks as a Highly Potent Bactericide. **2017**, *56* (8), 4739–4744. https://doi.org/10.1021/acs.inorgchem.7b00429.

(16) Majidpour, A.; Fathizadeh, S.; Afshar, M.; Rahbar, M.; Boustanshenas, M.; Heidarzadeh, M.; Arbabi, L.; Moghadam, S. S. Dose-Dependent Effects of

Common Antibiotics Used to Treat Staphylococcus Aureus on Biofilm Formation. *Iran. J. Pathol.* **2017**, *12* (4), 362–370.

APPENDIX IV

Supporting information Chapter 4

IV.I. SiB association of AgNCs *via* photoreduction: protocol optimization

In the following is presented the sequential steps followed to refine the SiB association of AgNC to MIL-125-NH_2. Even the formation of AgNCs in solutions with capping agents is traditionally followed with UV-Vis measurements by the increase in absorbance (as SPR band disappears below 1-2 nm), this method was not viable to determine their association to MIL-125-NH_2.[1,2] As depicted in Figure AIV. 1 A), the synthesis in toluene reported by Maretti *et al.*,[3] with $AgCF_3COO$, I-2959 and cyclohexylamine, all in 2 mM concentration, there is increment in the absorption at 450 nm. Nevertheless, as MIL-125-NH_2 already has absorbance in the same region (see Figure 1 in Chapter 3 publication, section 3.3) it causes an interference hindering the observation of the AgNC. The UV-Vis absorbance spectra of the MOF (Figure AIV. 1 B) reflects an increment in the absorbance, also appreciable by the color change of the material, but with difficult direct correlation with AgNC formation. For this reason, synthesized samples were analyzed by TEM, which besides enabling AgNC size determination, provides information of its distribution and location with respect to the MIL-125-NH_2 support.

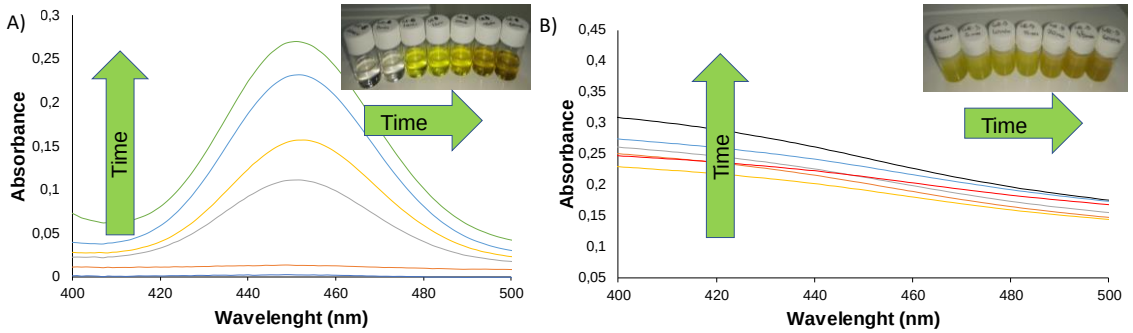

Figure AIV. 1: A) UV-Vis absorption spectra following the synthesis of AgNC with time stabilized by cyclohexylamine. B) UV-Vis absorption spectra following the synthesis of AgNC with time stabilized by MIL-125-NH_2

First attempts defined for the SiB association of the AgNC followed a procedure adapted from the previous bibliography.[3,4] All reagents, presynthesized microMOF (55 mg, 0.033 mmol, for synthesis refer to APPENDIX I I.II.ii MIL-125-NH_2 with micron particle size (microMOF)$AgCF_3COO$ (11,2 mg, 0.05 mmol; 70:30 weight ratio Ti:Ag, the maximum previously determined by chemical reduction) and I-2959 (5.7 mg, 0.025 mmol, 1:0.5 molar ratio with the Ag), were added to 100 mL of toluene under Ar atmosphere prior to irradiation in a photoreactor equipped with three actinic BL TL 6W/10 1FM Hg-lamps (Philips) connected in series with spectral emission in the UVA region (λ_{max} = 365nm), corresponding to a total irradiance of 40 $W \cdot m^{-2}$ under 400 nm. The design of the best synthetic strategy was optimized from this starting protocol considering several parameters (irradiation time, reagents addition, stirring, MOF:Ag ratio).

As there was no appreciable color change with naked eye, initial samples were irradiated with UVA during long periods of time: 30 min and 1 h. TEM analysis revealed that photoreduction time was excessive as the Ag was present in the form of NP larger than the pore size (Figure AIV. 2). Even more, after 1 h of irradiation these AgNPs were located outside the MOF, and their aggregation procured even Ag microparticles.

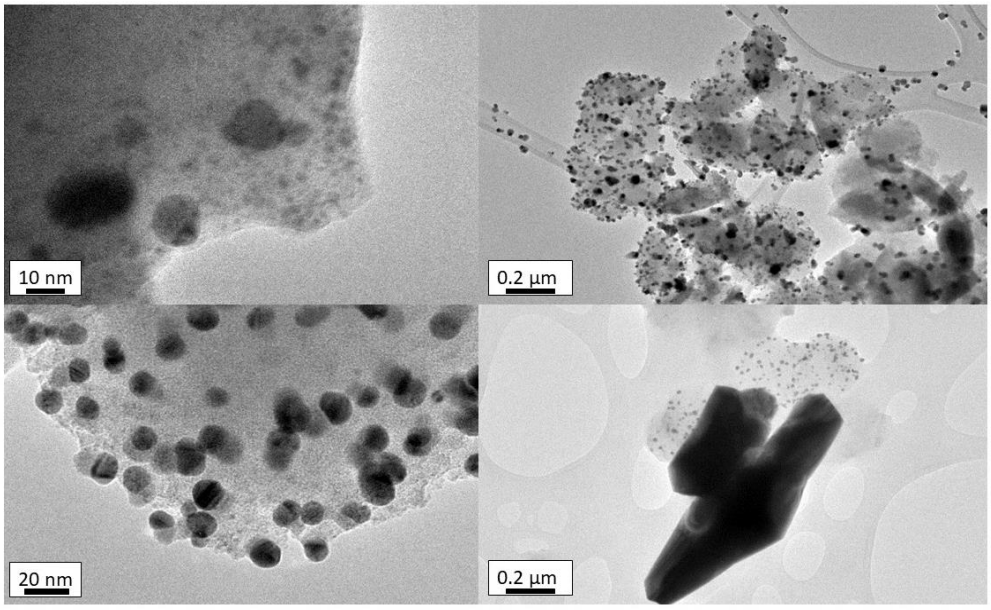

Figure AIV. 2: TEM micrographs of the AgNC@MIL-125-NH_2 analyzing the influence of photoreduction time: top, 30 min irradiation, bottom 1 h irradiation, showing some Ag microparticles with darker contrast.

In order to prevent particle aggregation and increase sample homogeneity, the MIL-125-NH_2 was first impregnated with $AgCF_3COO$ during 15 min in dark in Ar atmosphere prior to the addition of the photo-initiator and the irradiation time was reduced to 20 min. The change in the reagent addition in a stepwise manner (impregnation, then irradiation) led to a better distribution of the Ag species through the microMOF crystals than one-pot impregnation/irradiation (Figure AIV. 3). Nevertheless, even the sample presented a better control of particle size dispersion, the diameter was still bigger than the scouted AgNCs. Therefore, the photoinduced reduction of Ag should be done in sorter times.

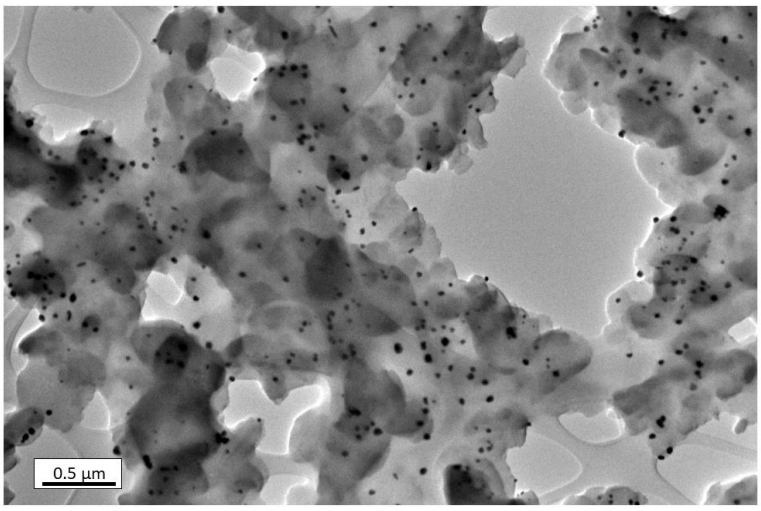

Figure AIV. 3: TEM micrographs of the AgNC@MIL-125-NH_2 analyzing the influence of the reagent addition in single step. Ag reduction was fast leading to NPs instead of NCs.

After reduction of the reaction time down to 1 min, samples exhibited a heterogeneous population of Ag nanospecies associated to the microMOF. As it can be observed in Figure AIV. 4, they were MIL-125-NH_2 crystals without associated silver, other crystals presented AgNPs and others presented a dense population of AgNCs. For overcoming these drawbacks, it was decided to keep stirring during the UVA irradiation to promote a more homogeneous AgNC@MIL-125-NH_2 composite and to reduce even more the photoreduction time down to just 15 s the prevent the aggregation of the NCs into NPs.

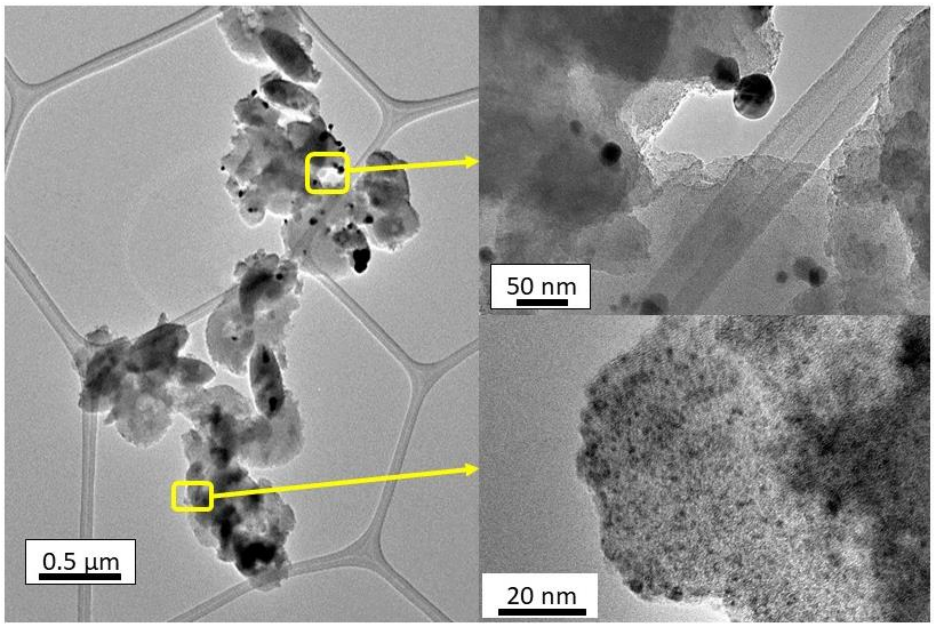

Figure AIV. 4: TEM micrographs of the AgNC@MIL-125-NH_2 in absence of stirring during photoreduction, showing heterogeneity through the sample having both AgNCs and AgNPs.

Finally, MOF:Ag proportion was also modulated to validate the SiB photoreduction of AgNC with adjustable silver content. For this, both TEM analysis (Figure AIV. 5) and TGA (Table AIV. 1) of the composites was carried out. The images presented AgNCs of ~1 nm with all Ti:Ag ratios. In addition, TGA confirmed the efficient association with high yields (>80 %), even higher than the previously obtained by chemical reduction (~60 %, see APPENDIX I section I.II SiB association of AgNPs *via* chemical reduction).

Briefing, could be concluded that for the photoinduced SiB association of AgNCs to MIL-125-NH_2: i) Ag growth was controlled by UVA irradiation time, requiring really short time (just 15 s) for AgNC formation; ii) monodispersed particle size was promoted by adjusting reagent addition in two steps, separating the impregnation with the silver salt and the addition of the photoinitiator; iii) homogeneous distribution of the AgNC through the microMOF crystals was

governed by stirring and iv) final Ag content associated to the MOF can be modulated varying the proportion of silver salt with respect to the MOF.

Table AIV. 1: Comparison of total Ag content in AgNC@MIL-125-NH_2 composites and impregnation-reduction yield with respect to the theoretically added silver, according to TGA (equipment error ± 0.2) results, with different Ti:Ag ratio

Ti:Ag (weight ratio) theoretical	**Ag (wt. %) by TGA in the** AgNC@MIL-125-NH_2 composites	**Yield (%)**
70:30	7.7	84
80:20	4.7	87
90:10	2.0	89

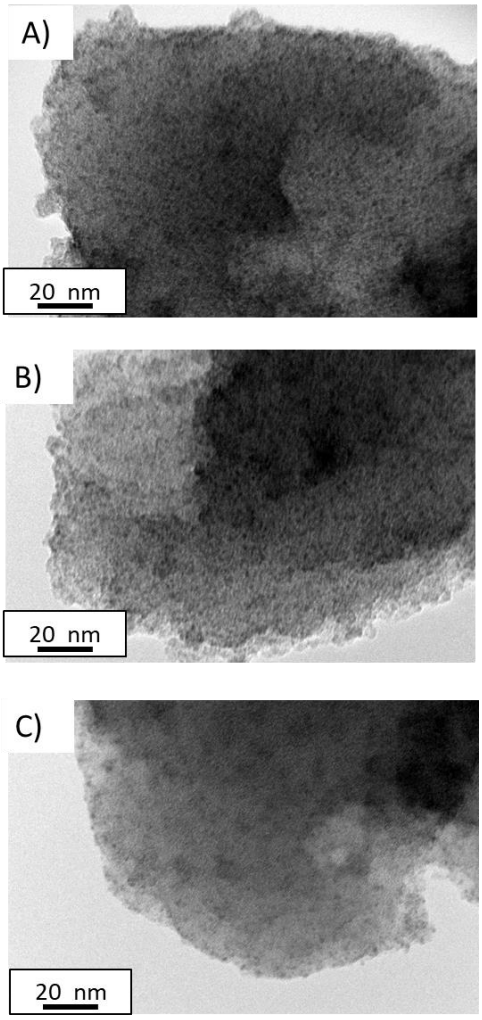

Figure AIV. 5: TEM micrographs of the AgNC@MIL-125-NH_2 showing the attainment of small AgNC with different Ti:Ag wt.% ratio: a) 70:30, b) 80:20 and c) 90:10

As a result, an ultrafast photoreduction protocol (only 20 min) was designed for the association of AgNCs supported on the porosity of MIL-125-NH_2. Recapitulating, in the optimized synthesis, the previously synthetized MIL-125-NH_2 (55 mg, 0.033 mmol) and $AgCF_3COO$ (11.2 mg, 0.05 mmol, final Ti:Ag wt.%. ratio of 70:30) were suspended in toluene (80 mL, 1 mol) in a round bottom flask, stirred for 15 min under Ar atmosphere and protected from ambient light. In parallel, I-2959 (5.7 mg, 0.025 mmol) was dissolved in toluene (20 mL, 0.25 mol). After the 15 min, the I-2959 solution was added to the MIL-125-NH_2/$AgCF_3COO$ solution drop by drop. The suspension was stirred for another 5 min in dark and under Ar atmosphere. Then, the mixture was irradiated under stirring for just 15 seconds. Suspension was exposed to UVA light in the previously described photoreactor. The obtained solid was recovered by filtration and washed with toluene (1x, 50 mL) and MeOH (4x, 50 mL). The AgNC@MIL-125-NH_2 composite was finally dried at RT and kept under darkness until use.

Bibliography

(1) Ledo, A.; Martı´nezmartı´nez, F.; Lo´pezlo´pez-Quintela, M. A.; Rivas, J. Synthesis of Ag Clusters in Microemulsions: A Time-Resolved UV-Vis and Fluorescence Spectroscopy Study. *Phys. B* **2007**, *398*, 273–277. https://doi.org/10.1016/j.physb.2007.05.010.

(2) Zhang, C.; Guo, Z.; Chen, G.; Zeng, G.; Yan, M.; Niu, Q.; Liu, L.; Zuo, Y.; Huang, Z.; Tan, Q. Green-Emitting Fluorescence Ag Clusters: Facile Synthesis and Sensors for Hg2+ Detection. *New J. Chem.* **2016**, *40* (2), 1175–1181. https://doi.org/10.1039/c5nj02268a.

(3) Maretti, L.; Billone, P. S.; Liu, Y.; Scaiano, J. C. Facile Photochemical Synthesis and Characterization of Highly Fluorescent Silver Nanoparticles. *J. Am. Chem. Soc.* **2009**, *131* (39), 13972–13980. https://doi.org/Doi 10.1021/Ja900201k.

(4) García-Bosch, N.; Liras, M.; Quijada-Garrido, I.; García, O. Multiamino Polymeric Capping of Fluorescent Silver Nanodots as an Effective Protective, Amphiphilic and PH/Thermo-Responsive Coating. *RSC Adv.* **2016**, *6* (72), 67643–67650. https://doi.org/10.1039/c6ra12024e.

APPENDIX V

Supporting information publication Chapter 4

Facile synthesis of an Agnanocluster@MOF composite and its superior visible-photocatalytic activity in continuous flow

Ana Arenas-Vivo,[a] Sara Rojas,[a] Iván Ocaña,[a] Ana Torres,[a] Marta Liras,[b,] Fabrice Salles,[c] Daniel Arenas-Esteban,[d] Sara Bals,[d] David Ávila,[e] Patricia Horcajada[a,*]*

[a] Advanced Porous Materials Unit, IMDEA Energy. Av. Ramón de la Sagra 3, 28935 Móstoles-Madrid, Spain.

[b] Photoactivated Process Unit, IMDEA Energy. Av. Ramón de la Sagra 3, 28935 Móstoles-Madrid, Spain.

[c] ICGM, Univ. Montpellier, CNRS, ENSCM, Montpellier, France.

[d] EMAT and NANOlab Center of Excellence, Univ. of Antwerp, Groenenborgenlaan 171, Antwerp 2020, Belgium.

[e] Department of Inorganic Chemistry, Chemical Sciences Faculty, Complutense University of Madrid, 28040 Madrid, Spain.

*Corresponding author E-mail: patricia.horcajada@imdea.org; marta.liras@imdea.org

V.I. Materials and Methods

All reactants were commercially obtained from Sigma-Aldrich (titanium(IV) isopropoxide (97%), sulfamethazine (SMT, ≥99%), 2-hydroxy-4′-(2-hydroxyethoxy)-2-methylpropiophenone (Irgacure-2959, I-2959, 98%)), Acros Organics (2-aminoterephtalic acid ($H_2BDC\text{-}NH_2$, 99%), silver trifluoroacetate ($AgCF_3COO$, 98%), 4-nitroaniline (4-NA, 98%), methylene blue (MB, pure)), Evonik (aeroxide ® TiO_2-P25)), Chemlab (*N*,*N*-dimethylformamide (DMF, 99.5%)), Labkem (methanol (MeOH)), and TCI ($NaBH_4$ (>95%), *p*-phenylendiamine (PPD, 98%)), and used without further purification.

Physicochemical characterization. Fourier transform infrared (FTIR) spectroscopic analyses were performed in a Nicolet 6700 (Thermo Scientific, USA) infrared spectrometer with the help of an attenuated total reflectance (ATR) diamond accessory. Nitrogen isotherms were obtained at 77 K using an AutosorbQ2 (Quantachrome Instruments, USA). Previous to the measurement, samples were evacuated at 150 °C for 16 h. Specific surface area was determined by applying Brunauer, Emmett & Teller equation (BET) in the relative pressure interval p/p_0 = 0.01-0.3 (being p_0 the saturation pressure). Pore volume and pore size distribution were calculated by the non-localized density functional theory (NLDFT) and the Horvath-Kawazoe (HK) methods, respectively. Routine X-ray powder diffraction (XRPD) patterns were collected using a conventional PANalytical Empyrean powder diffractometer (PANalytical Lelyweg, Netherlands, θ-2θ) using λCu $K_{\alpha 1}$, and $K_{\alpha 2}$ radiation (λ = 1.54051 and 1.54433 Å). The XRPD patterns were carried out with a 2θ scan between 3-35° and 3-90° with a step size of 0.013° and a scanning speed of 0.1 $° \cdot s^{-1}$. Thermogravimetric analyses (TGA) were carried out in an SDT Q-600 thermobalance (TA Instruments, New Castle, DE, USA) with a general heating profile from 30 to 600 °C with a heating rate of 5 $°C \cdot min^{-1}$ under air using a flux of 100 $mL \cdot min^{-1}$. Transmission electron microscopy (TEM) images were taken with a JEM 2100 (Jeol, Tokyo, Japan) with a 200 kV acceleration voltage (point resolution 0.25 nm). For sample preparation, 1 mg of sample was dispersed in 10 mL of distilled water and sonicated with an ultrasound tip (UP400S, Hilscher, Teltow, Germany) at 20% amplitude for 20 s. For observation, 1 μL of the prepared solution was dropped over a copper TEM support with a carbon mesh (lacey carbon, 300 mesh, copper, approx. grid hole size: 63 μm, TED PELLA Redding, California, USA). Particle size was monitored via counting with ImageJ software.[1] The mean particle size was statistically estimated ($n > 630$) *from TEM micrographs of the Agnancluster@MOF under optimized synthesis conditions.* Quantitative determination of Ag and Ti in the samples was done with inductively coupled

plasma-optical emission spectrometer (ICP-OES) Optima 3300 DV (Perkin Elmer, Waltham, MA, USA; digestion with HF and HNO_3); and energy dispersive X-ray analysis (EDS) coupled to the scanning electron microscopy Hitachi TM 1000 with tungsten applying 15 keV. UV-visible spectroscopic analysis of the solids and MB aqueous solutions were run in a Perkin Elmer® Lambda 1050 UV/vis/NIR (Perkin Elmer, Waltham, MA, USA).

High performance liquid chromatography (HPLC). Different organic molecules were analyzed by HPLC: the amount of 4-NA reacted and the PPD formed, the amount of degraded SMT, as well as the released $H_2BDC\text{-}NH_2$ linker were determined using a reversed phase HPLC Jasco LC-4000 series system, equipped with a PDA detector MD-4015 and a multisampler AS-4150 controlled by ChromNav software (Jasco Inc, Japan). A Purple ODS reverse-phase column (5 μm, 4.6 x 150 mm, Análisis Vínicos, Spain) was employed. For the quantification of all chemical species, isocratic conditions were used. The flow rate was 1 $mL \cdot min^{-1}$, and the column temperature was fixed at 298 K. In all cases, the injection volume was 30 μL. The mobile phase was based on a mixture of 50:50 MeOH:phosphate buffered solution (PBS; 0.04 M, pH = 2.5) for $H_2BDC\text{-}NH_2$ ligand analysis, with a retention time (rt) and an absorption maximum of 3.03 min and 228 nm, respectively. SMT was analyzed using a mixture of 35:65 acetonitrile:water, with a rt of 2.7 min and an absorption maximum of 263 nm. PPD was analyzed using a mixture of 80:20 PBS:MeOH (PBS, 0.04 M, pH = 8) with a rt of 2.5 min and an absorption maximum of 237 nm. 4-NA was analyzed using a mixture of 80:20 PBS:MeOH (PBS, 0.04 M, pH = 8) with a rt of 16 min and an absorption maximum of 380 nm.

Preparation of the phosphate buffered solution (0.04 M, pH = 2.5 and pH = 8): 0.02 mol (2.4 g) of NaH_2PO_4 and 0.02 mol (2.84 g) of Na_2HPO_4 were dissolved in 1 L of Milli-Q water. The pH was then adjusted to 2.5 with H_3PO_4 (≥ 85%) and to basic pH with NaOH 10 M.

V.II. HPLC conditions

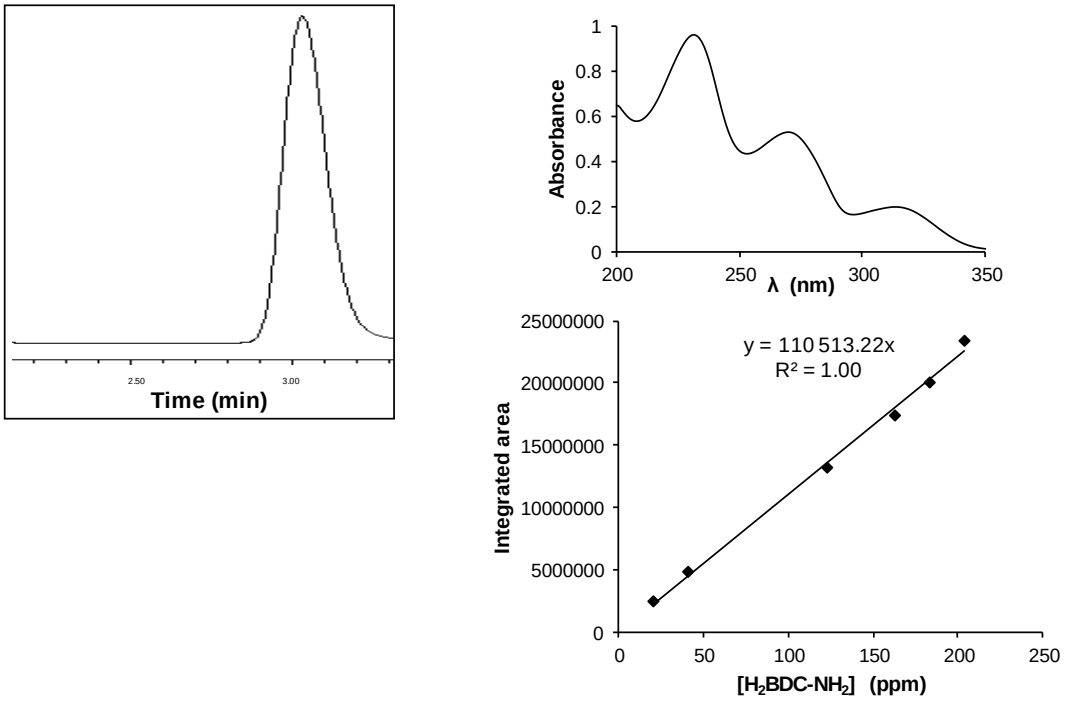

Figure AV. 1: Calibration plot of standard by HPLC method, and UV-vis spectra and chromatogram of H_2BDC-NH_2.

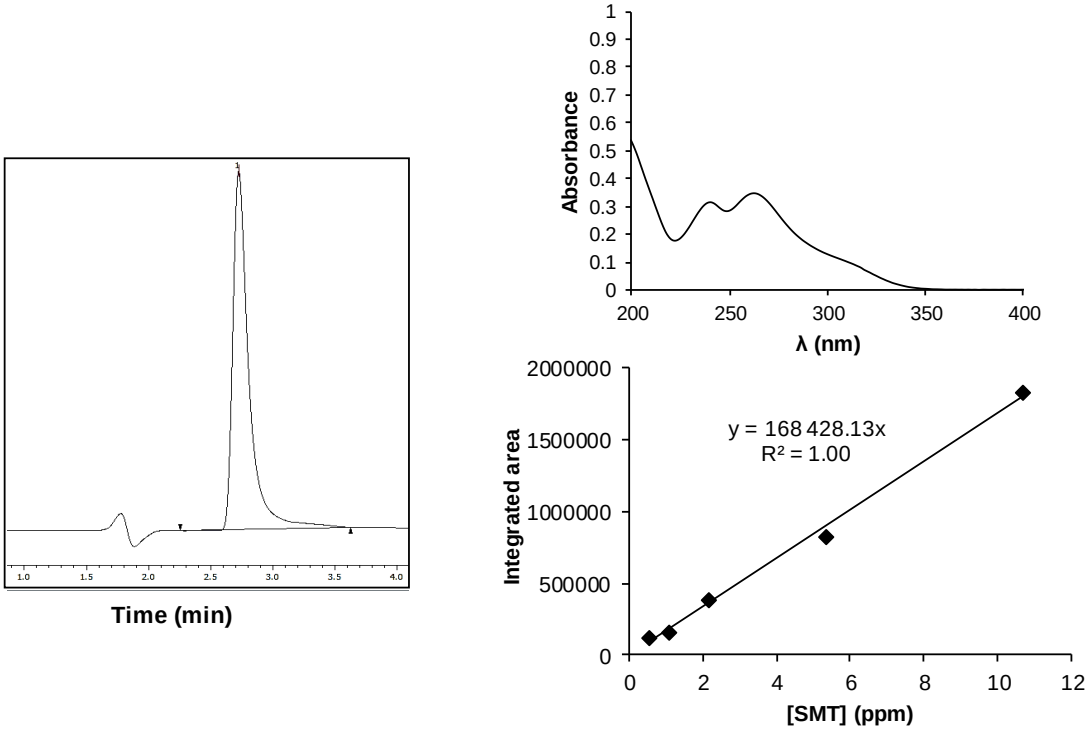

Figure AV. 2: Calibration plot of standard by HPLC method, and UV-vis spectra and chromatogram of SMT.

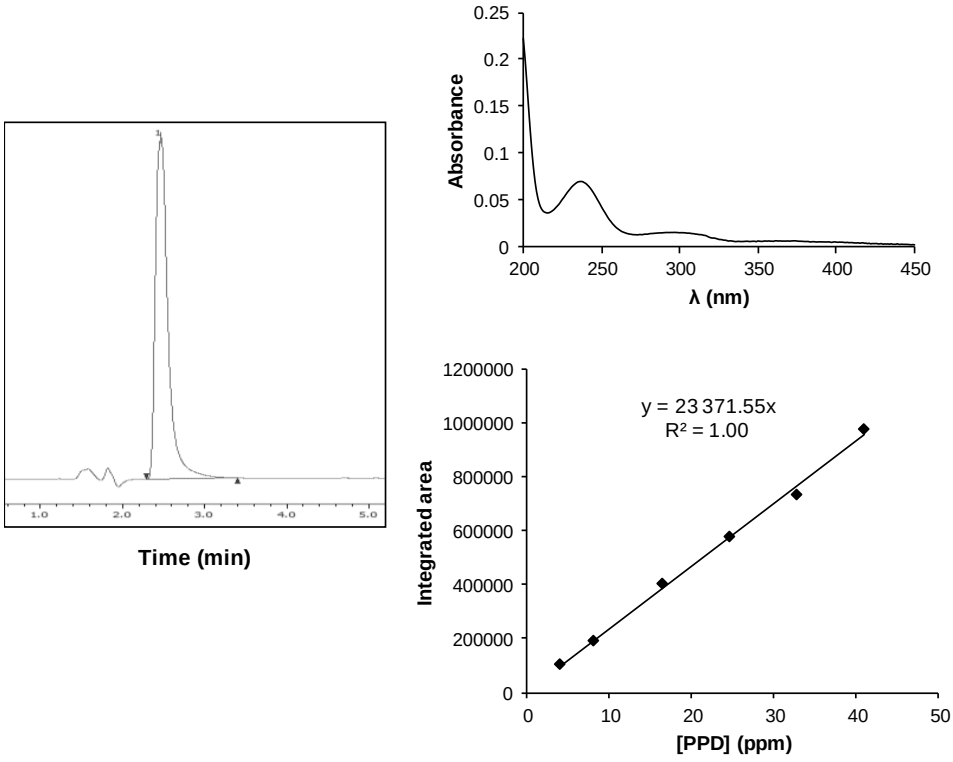

Figure AV. 3: Calibration plot of standard by HPLC method, and UV-vis spectra and chromatogram of PPD

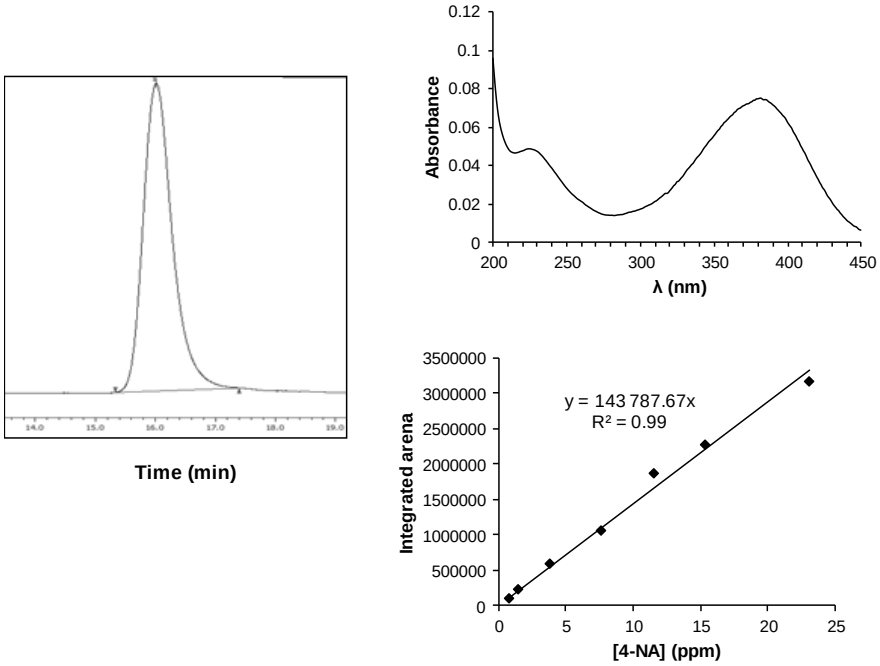

Figure AV. 4: Calibration plot of standard by HPLC method, and UV-vis spectra and chromatogram of 4-NA.

V.III. Photochemical synthesis and characterization of AgNC@MIL-125-NH_2

The synthesis of the MIL-125-NH_2 or $[Ti_8O_8(OH)_4(BDC\text{-}NH_2)_6]$ was performed following a similar experimental procedure previously described.[2] In a typical synthesis, $H_2BDC\text{-}NH_2$ (76 mmol, 13.75 g) was dissolved in a mixture of 200 mL of DMF (2.5 mol) and 50 mL of MeOH (1.25 mol) at RT under stirring. The mixture was placed in a round bottom flask equipped with a condenser and was warmed at 373 K under air. When the mixture reached the temperature of 373 K, titanium(IV) isopropoxide (50 mmol, 15 mL) was added and then, the MilliQ water (50.56 mmol, 0.91 mL). The mixture was kept under stirring and heated at 373 K for 72 h under air. The obtained yellow solid was filtered and washed in the filter twice with 100 mL of DMF at RT. The as-synthesized solid was dispersed at RT in DMF under stirring overnight (50 mL of DMF *per* 1 g of product). Then, the same procedure was repeated twice using MeOH instead of DMF. The MIL-125-NH_2 solid was finally dried at 373 K.

The immobilization of the Ag nanoclusters (AgNCs) in the porous structure of MIL-125-NH_2 was done following the inspiration of Maretti *et al.,*[3] and Garcia-Bosch *et al.*[4] In the optimized synthesis, the previously synthetized MIL-125-NH_2 (55 mg, 0.033 mmol) and $AgCF_3COO$ (11.2 mg, 0.05 mmol, final Ti:Ag wt. ratio of 21:1) were suspended in toluene (1 mol, 80 mL) in a round bottom flask, stirred for 15 min under Ar atmosphere and protected from ambient light. In parallel, I-2959 (0.025 mmol, 5.7 mg) was solved in toluene (0.25 mol, 20 mL). After the 15 min, the I-2959 solution was added to the MIL-125-NH_2/$AgCF_3COO$ solution drop by drop. The suspension was stirred for another 5 min in dark and under Ar atmosphere. Then, the mixture was irradiated under stirring for just 15 seconds. Suspension was exposed to UV light in a photoreactor equipped with three actinic BL TL 6W/10 1FM Hg-lamps (Philips) connected in series with spectral emission in the UV region ($\lambda_{max} = 365nm$), corresponding to a total irradiance of 40 $W \cdot m^{-2}$ under 400 nm.

The obtained solid was recovered by filtration and washed with toluene (1x, 50 mL) and MeOH (4x, 50 mL). The AgNC@MIL-125-NH_2 composite was finally dried at RT and kept under darkness until use. For comparison purposes, Ag-nanoparticles@MIL-125-NH_2 (AgNP@MIL-125-NH_2) keeping the Ti:Ag proportion was also synthesized following the procedure described by some of us (see **Section V.iV** for full experimental procedure).[5]

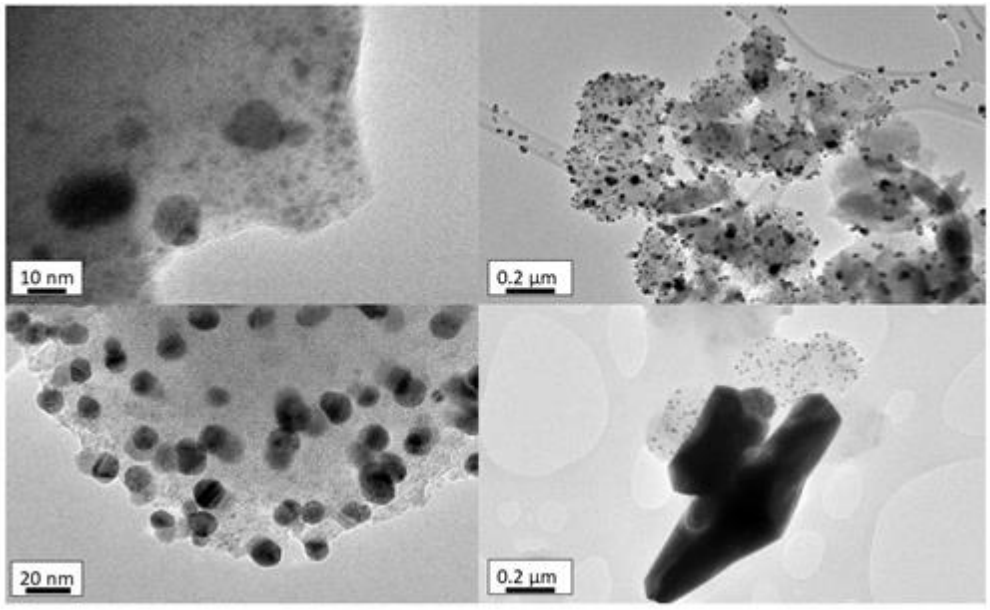

Figure AV. 5: TEM micrographs of the AgNC@MIL-125-NH_2 analyzing the influence of photoreduction time: top, 20 min irradiation, bottom 1 h irradiation, showing some Ag microparticles with darker contrast.

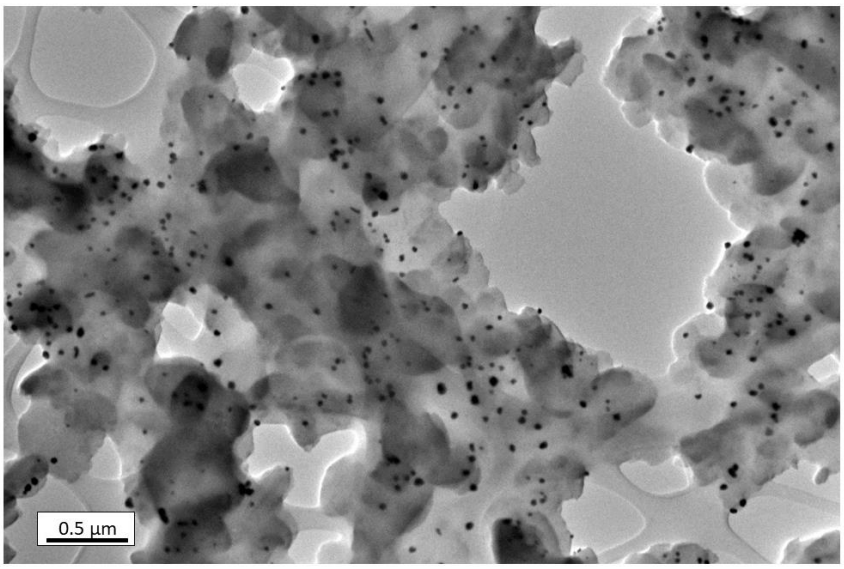

Figure AV. 6: TEM micrographs of the AgNC@MIL-125-NH_2 analyzing the influence of the reagent addition in single step. Ag reduction was fast leading to NPs instead of NCs.

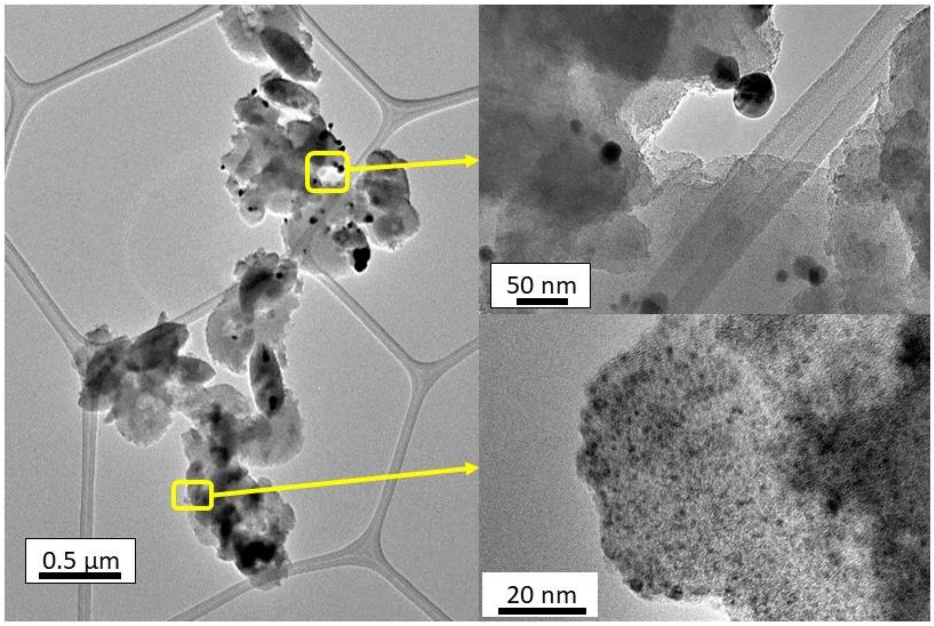

Figure AV. 7: TEM micrographs of the AgNC@MIL-125-NH_2 in absence of stirring during photoreduction, showing heterogeneity through the sample having both AgNCs and AgNPs.

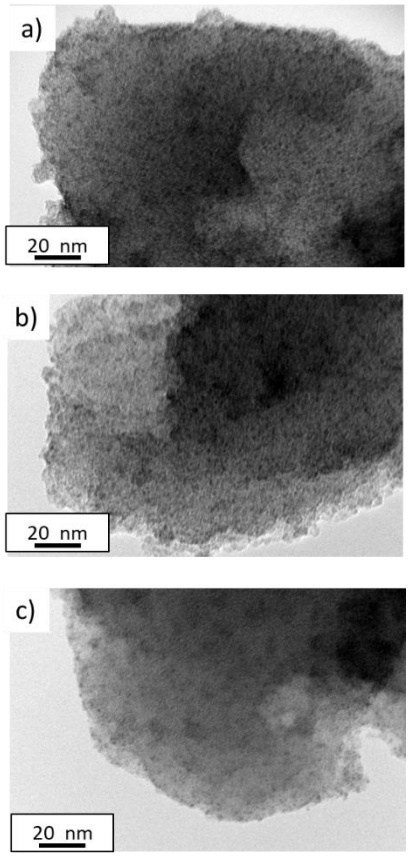

Figure AV. 8: TEM micrographs of the AgNC@MIL-125-NH_2 showing the attainment of small AgNC with different Ti:Ag wt. ratio: a) 21:1, b) 16:1, and c) 9:1.

Table AV. 1: Comparison of total Ag content in AgNC@MIL-125-NH_2 composites and impregnation-reduction yield with respect to the theoretically added silver, according to TGA (equipment error ± 0.2) results, with different Ti:Ag ratio

Ti:Ag (molar ratio) theoretical	**Ag (wt. %) by TGA in the AgNC@MIL-125-NH_2 composites**	**Yield (%)**
21:1	7.7	84
16:1	4.7	87
9:1	2.0	89

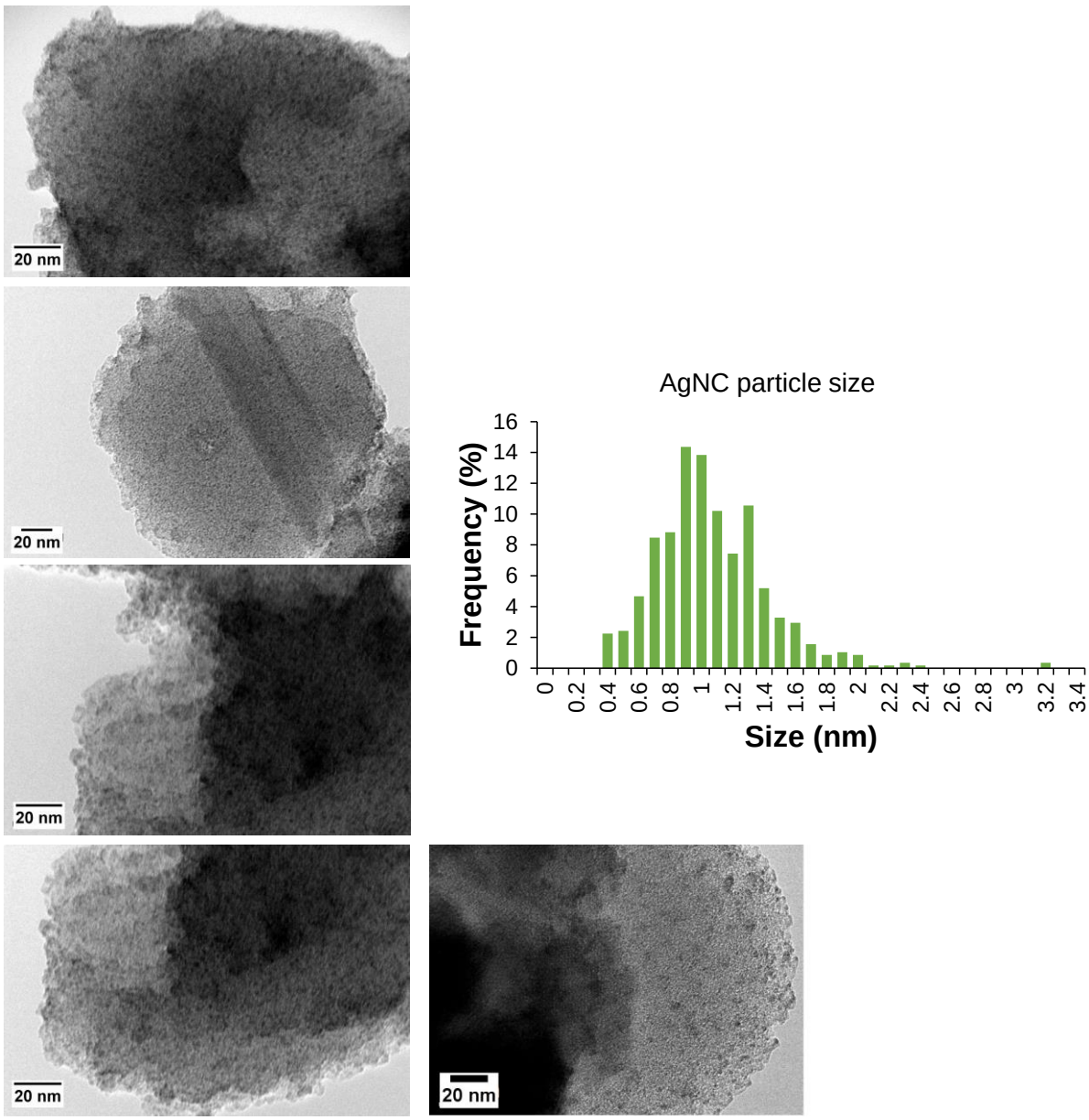

Figure AV. 9: Histogram with the AgNCs particle size distribution in the AgNC@MIL-125-NH_2 composite, synthesized with the optimum reaction protocol as determined by TEM (N>630, from the displayed 5 images and Figure 1 d).

High angle annular dark field-scanning transmission electron microscopy (HAADF-STEM) images for tomography reconstruction were acquired using an aberration corrected "cubed" FEI Titan 60–300 electron microscope operated at 300 kV. Due to the sensitivity of these materials under a focused beam, a "fast tomography" procedure was performed, using the Fischione model 2020 single-tilt tomography holder over a tilt range from −70° to +70°, with tilt increments of 2°.[6] The reconstruction of the tilt series was performed using the Astra Toolbox 1.8 for MATLAB 2018a.3 Visualization of the 3D reconstructions was performed using the Amira 5.4.0 software. Based on a careful segmentation, it is clear that the particles are present in the pores of the MOF. See attached movie.

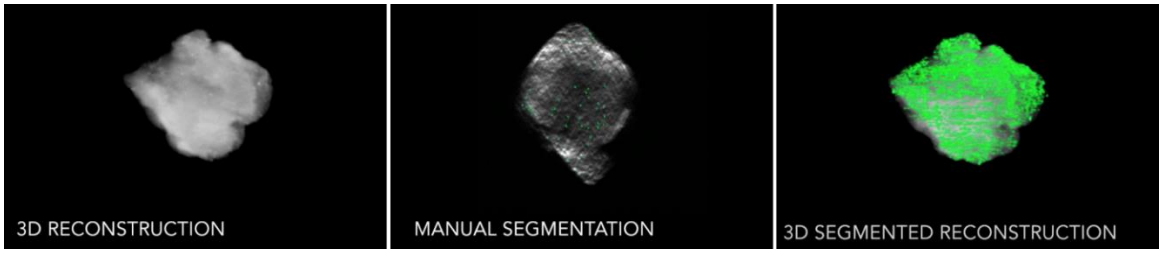

Figure AV. 10: HAADF-STEM manual orthoslices segmentation and 3D reconstruction of AgNC@MIL-125-NH_2.

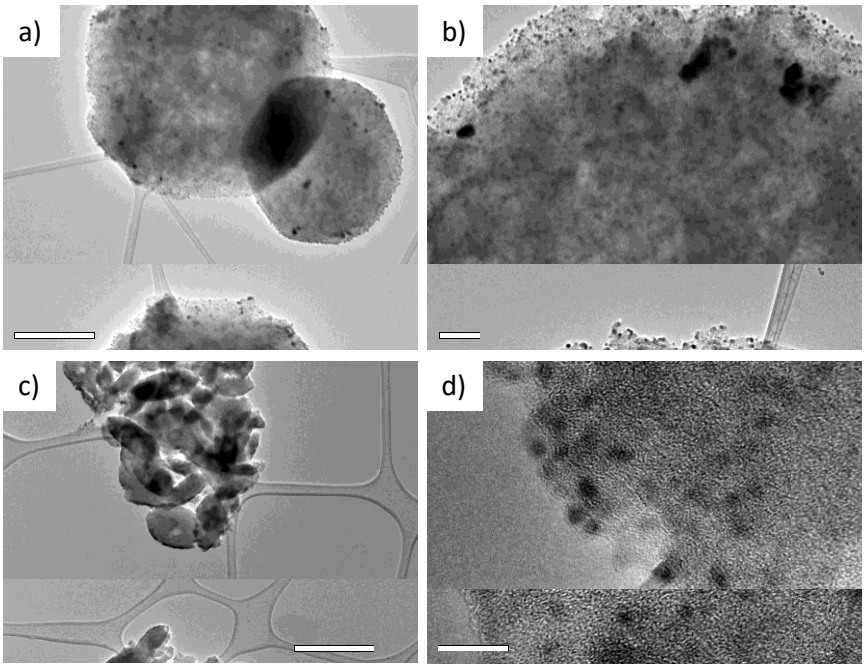

Figure AV. 11: TEM micrographs of the AgNC@MIL-125 (a, b) and AgNC@MIL-125-NH_2 materials (c, d) at different magnifications showing the influence of the NH_2 groups in the stabilization of AgNCs.

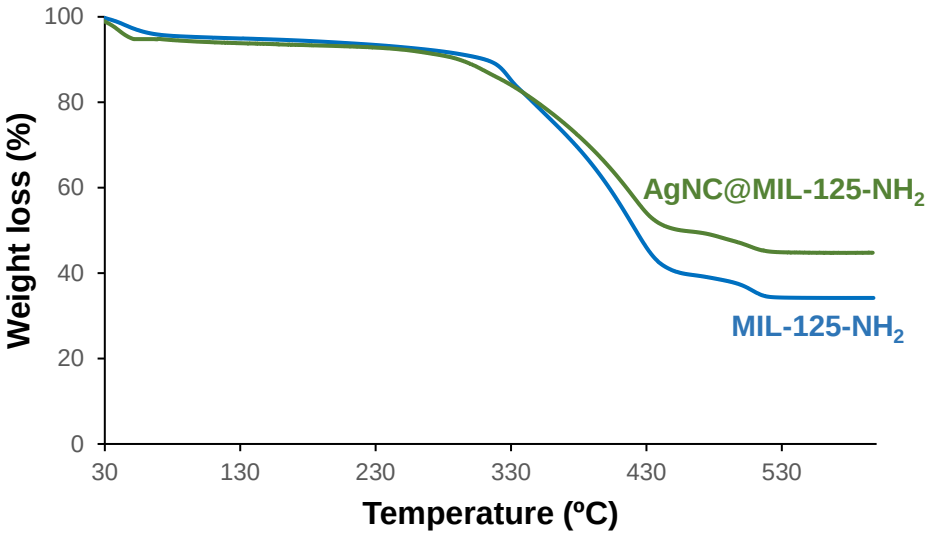

Figure AV. 12: TGA of MIL-125-NH_2 (blue) and AgNC@MIL-125-NH_2 (green).

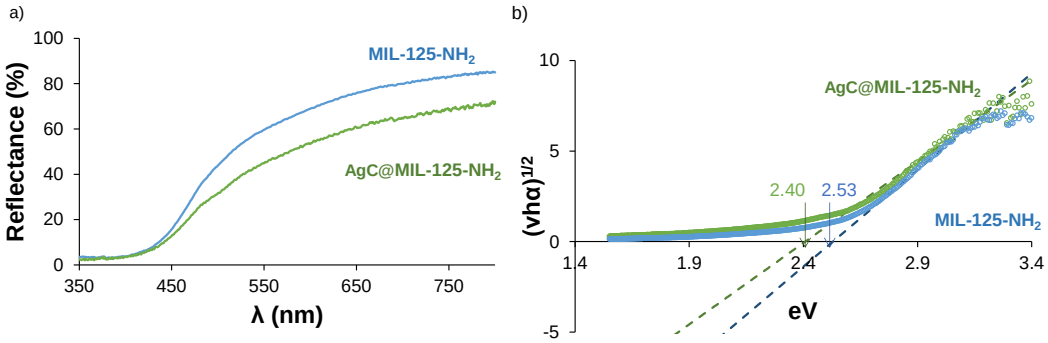

Figure AV. 13: a) Diffuse reflectance analysis, and b) band gap estimated form the Tauc plot[7] for direct allowed transition of MIL-125-NH_2 (blue) and AgNC@MIL-125-NH_2 (green).

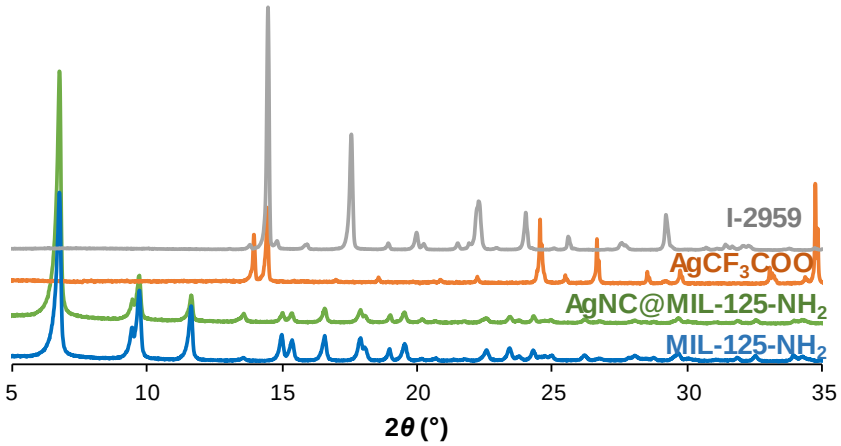

Figure AV. 14: XRPD patterns of AgNC@MIL-125-NH_2 composite (green) compared to the pristine MIL-125-NH_2 (blue), $AgCF_3COO$ (orange), and I-2959 (grey).

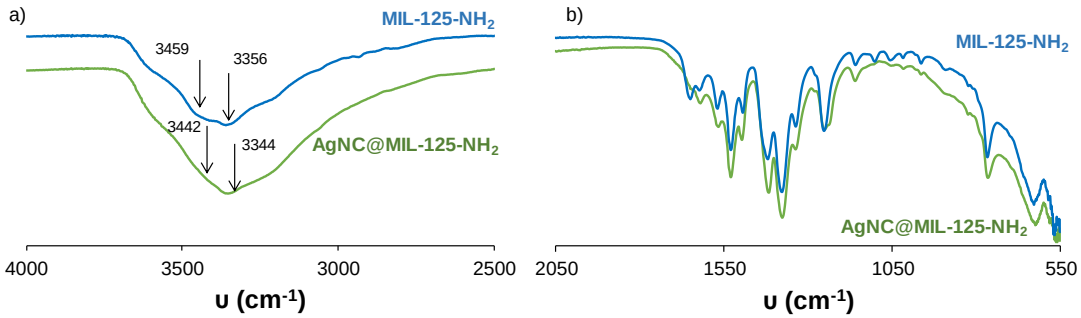

Figure AV. 15: FTIR spectra of MIL-125-NH_2 (blue) and AgNC@MIL-125-NH_2 (green).

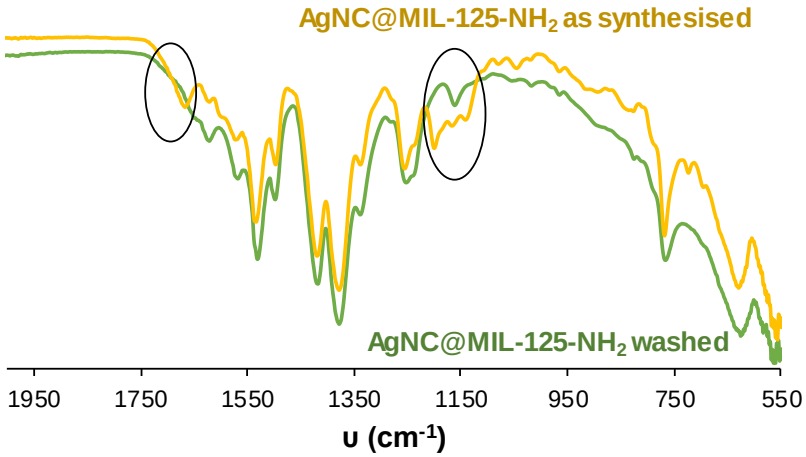

Figure AV. 16: FTIR spectra of AgNC@MIL-125-NH_2 as-synthesized (yellow) exhibiting extra vibrations of I-2959 (black circle) and AgNC@MIL-125-NH_2 after washing (green).

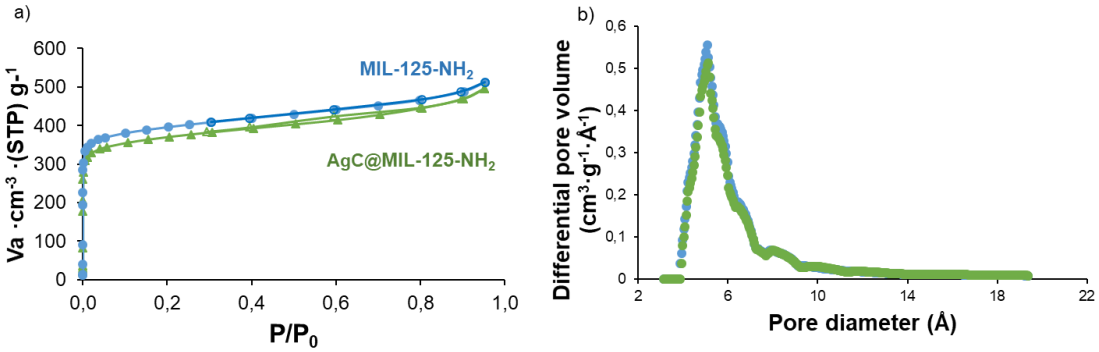

Figure AV. 17: a) N_2 sorption isotherms, and b) pore distribution with HK method of activated MIL-125-NH_2 (blue) and AgNC@MIL-125-NH_2 (green). Solid and empty symbols indicate adsorption and desorption branches, respectively.

V.IV. Photocatalytic degradation of emerging contaminants in water using AgNC@MIL-125-NH_2

The photocatalytic activity of AgNC@MIL-125-NH_2 and MIL-125-NH_2 was evaluated in terms of photodegradation of emerging organic contaminants (EOCs): a) MB as model dye, and b) SMT as challenging antibiotic. MB photodegradation capacity of these materials was further compared with TiO_2 and AgNP@MIL-125-NH_2, used here as reference materials. First, the stability of MB and SMT was studied under Vis light. It was verified that MB was not degraded (after 2 h, longer time than the experimental) and neither SMT (after 24 h) under Vis light irradiation.

Synthesis of AgNP@MIL-125-NH_2: The immobilization of the Ag nanoparticles was performed following an impregnation-reduction methodology previously reported by some of us, adapted to achieve equivalent amount of silver as in the AgNCs.[5] The previously synthetized MIL-125-NH_2 (250 mg, 0.15 mmol) was dispersed in 4 mL of a 0.1 M $AgNO_3$ solution (75 mg, 0.44 mmol) in CH_3CN by sonication (2 h) and stirred at RT for 16 h. The silver-impregnated MOF (Ag^+@MIL-125-NH_2) was recovered by centrifugation (10000 rpm/10 min), washed with CH_3CN to remove non-attached silver precursor, and dried at 100 °C overnight. Dried Ag^+@MIL-125-NH_2 was stirred under Ar atmosphere with 2 mL of absolute ethanol. For reduction, a 2 mL absolute ethanol solution of 0.06 M $NaBH_4$ (4.5 mg, 0.12 mmol) was added to the previous ethanol mixture dropwise and stirred for 10 min under Ar atmosphere. The composite AgNP@MIL-125-NH_2 was then recovered by centrifugation (10000 rpm/10 min), thoroughly washed with absolute ethanol, and dried at 100 °C.

These experiments were performed in a photoreactor equipped with a 300 W Xe lamp (Oriel Instruments OPS-A500) under open air at RT, with the samples stirred and placed at a fixed distance of 21 cm from the irradiation source. A 420 nm cutoff filter (Newport 20CGA-420 IJ342) was placed between the sample and the light source to eliminate the UV irradiation. It has to be pointed that prior to irradiation it is not necessary to stir the suspension until the adsorption-desorption equilibrium is reached. All experiments were performed at least in triplicate to ensure statistically reliable results.

A) MB

In a typical experiment, 5 mg of catalyst (TiO_2, AgNC@MIL-125-NH_2, AgNP@MIL-125-NH_2 or MIL-125-NH_2) was added to 10 mL of a MB (200 ppm, in the range of textile wastewater)[8] aqueous solution (tap water) in a 20 mL vial. Photodegradation reactions were performed under continuous stirring. At certain intervals (0, 5, 10, 20, 30, 40, 50, and 60 min), an aliquot of 250 µL was collected by centrifugation for analysis by UV-vis (MB) and HPLC (H_2BDC-NH_2) (V.II HPLC conditions). In addition, dark experiments were carried out under the same reaction conditions to evaluate the MB adsorption (Figure AV. 18). These experiments were performed in triplicate.

As mentioned, Figure AV. 21 shows that MB is not degraded under 60 min of Vis light irradiation (remaining ~95% of the initial concentration), demonstrating the need of a photocatalyst for the MB degradation. TiO_2 could not be considered as an efficient photocatalyst for decontamination as it exhibits a moderate activity (remaining ~80% of MB after 60 min). As its photoactivity is limited by the minor visible light absorption (E_g = 3.00 eV), MB removal probably comes from MB adsorption on the particles (TiO_2 S_{BET} = 35 - 65 $m^2 \cdot g^{-1}$).

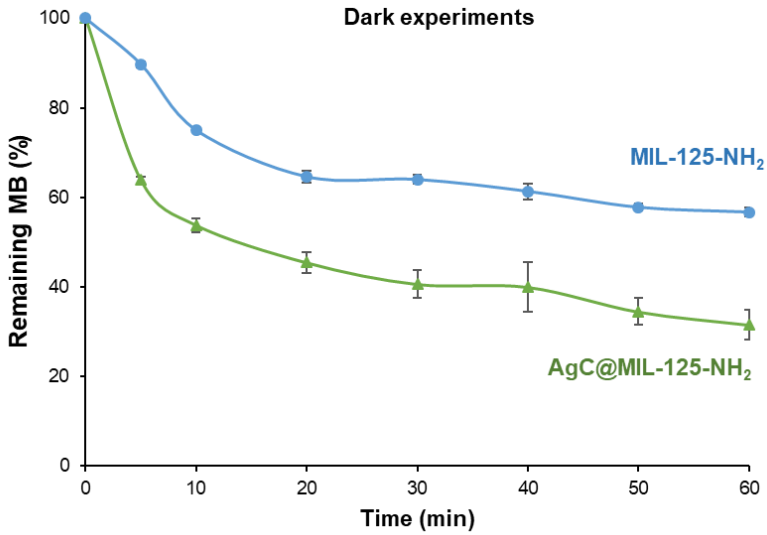

Figure AV. 18: MB adsorption kinetics in dark using AgNC@MIL-125-NH_2 (green triangles) and MIL-125-NH_2 (blue circles).

The MB photodegradation data using AgNC@MIL-125-NH_2 and MIL-125-NH_2 were fitted to a second order kinetics according to Eqn. (1).

$$\frac{1}{[C]} = \frac{1}{[C]_0} + kt \qquad \text{Eqn. (1)}$$

where $[C]$ and $[C]_0$ are the remaining amount of MB ($g \cdot mg^{-1}$) at the time t (min) and the initial MB concentration, respectively, and k is the second order kinetics constant ($g \cdot mg^{-1} \cdot min^{-1}$).

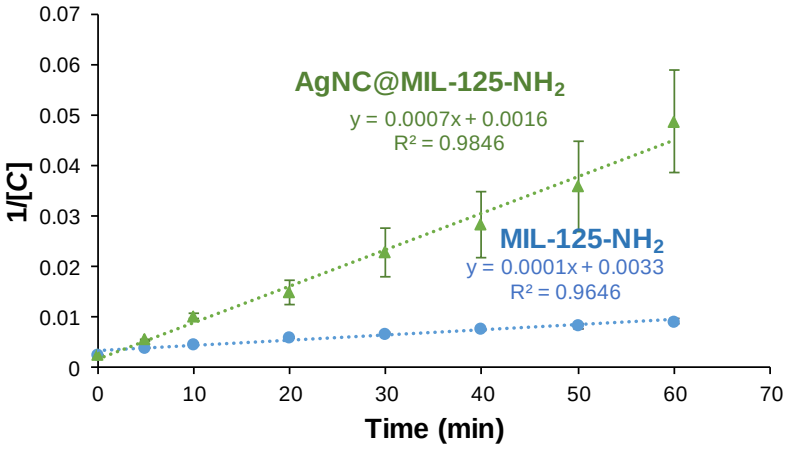

Figure AV. 19: Fitting of MB degradation data using MIL-125-NH_2 (blue circles) and AgNC@MIL-125-NH_2 (green triangles) to a second order kinetic.

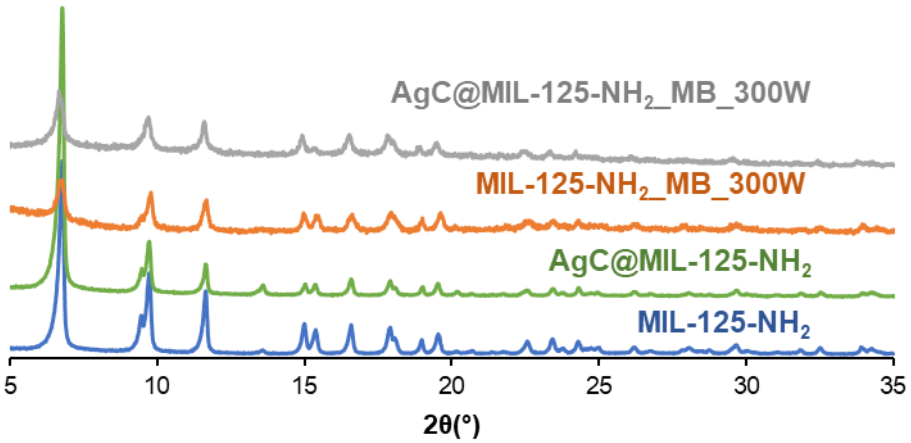

Figure AV. 20: XRPD patterns of the MIL-125-NH_2 and AgNC@MIL-125-NH_2 before (blue and green, respectively), and after being suspended in a MB tap aqueous solution under Vis irradiation for 1 h (MIL-125-NH_2_MB_300W (orange) and AgNC@MIL-125-NH_2_MB_300W (grey)).

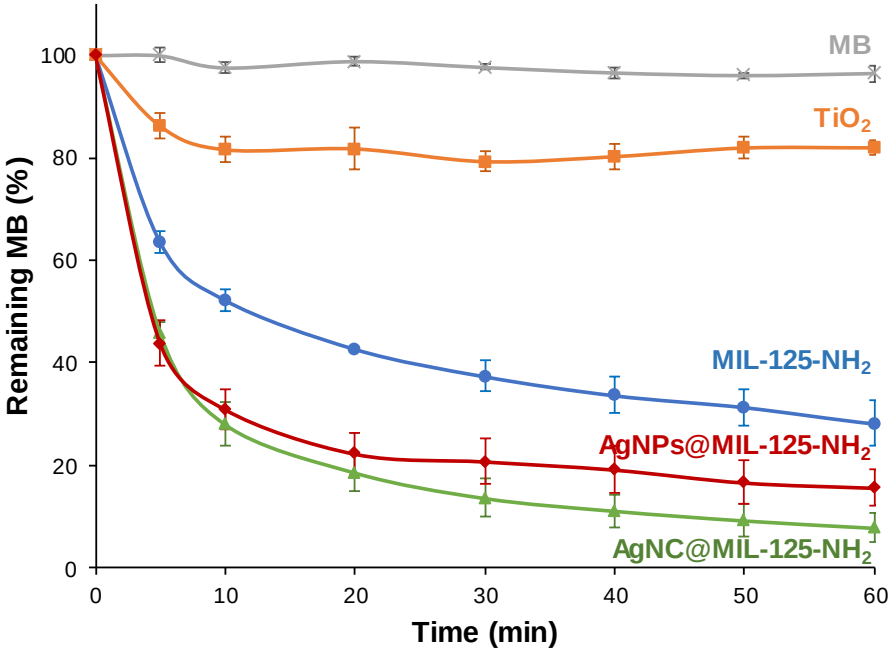

Figure AV. 21: MB photodegradation kinetics using AgNC@MIL-125-NH_2 (green triangles) and other materials as controls: AgNP@MIL-125-NH_2 (red diamonds), MIL-125-NH_2 (blue circles), TiO_2 (orange squares), and MB control without catalyst (grey crosses).

Table AV. 2: Comparison of degraded MB (%) using AgNC@MIL-125-NH_2 and other reported catalysts.

MOF based material	**MB degraded (%)**	**Time (min)**	**Kinetic model**	***K*** **(1st in min^{-1} / 2nd in $g \cdot mg^{-1} \cdot min^{-1}$)**	**Refs**
AgNC@MIL-125-NH_2	92	60	2nd	0.0007	This work
AgNPs@MIL-125-NH_2	84	60			This work
MIL-125-NH_2	72	60	2nd	0.0001	This work
TiO_2	18	60			This work
HPU-4@AgBr	95	60	ND	ND	[9]
Ag-MIL-125-AC	99.5	90	Pseudo 1st	0.1031	[10]
Ag_3PO_4@ MIL-125-NH_2	95	50	1st	0.089	[11]
Ag_3VO_4@MIL-125-NH_2	92	15	1st	0.0997	[12]
In-MOF	96	60	1st	0.0621	[13]
MIL-53(Fe)	11	40	1st	0.0036	[14]
Mn(dmtdc)	91	70	ND	ND	[15]
UiO-66-NH_2@ZnTCPc	68	120	Pseudo 1st	0.0168	[16]
ZIF-8	83	120	Pseudo 1st	0.0170	[17]
ZIF-8@Ag/AgCl	100	20	1st	0.1468	[18]

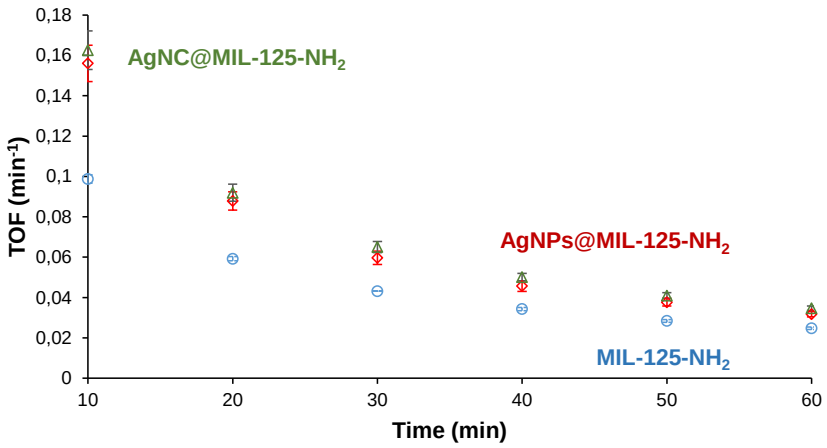

Figure AV. 22: TOF (min^{-1}) determination of MB photodegradation using AgNC@MIL-125-NH_2 (green triangles) AgNP@MIL-125-NH_2 (red diamonds) MIL-125-NH_2 (blue circles) as catalyst.

B) SMT

Static batch SMT photodegradation: In an 8 mL vial, 4 mg of AgNC@MIL-125-NH_2 or MIL-125-NH_2 were suspended in 4 mL of a SMT tap-aqueous solution (10 ppm, according with the concentration of SMT found in the environment).[19] Photodegradation reactions were performed under stirring. At certain intervals (0, 2, 5, 8, 12, 15, and 30 min), an aliquot of 100 µL was collected by centrifugation for HPLC analysis (SMT and H_2BDC-NH_2). These experiments were performed in triplicate.

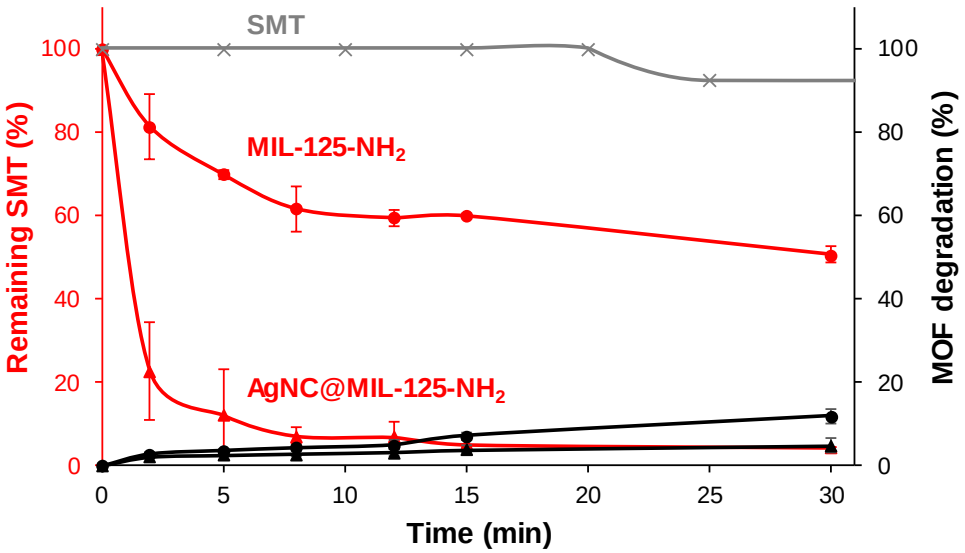

Figure AV. 23: Effect of time on the photodegradation of SMT using MIL-125-NH_2 (red circles, left y axis) or AgNC@MIL-125-NH_2 (red triangles) as photocatalyst. SMT (grey crosses, right x axis) without catalyst is included for comparison. MOF degradation over time is also represented (in black using circles and triangles, accordingly).

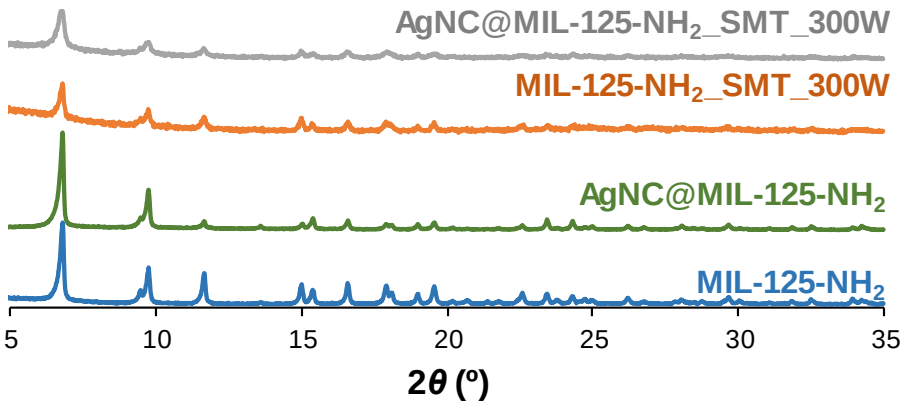

Figure AV. 24: XRPD patterns of the MIL-125-NH_2 and AgNC@MIL-125-NH_2 before (blue and green, respectively), and after being suspended in a SMT tap aqueous solution under Vis irradiation for 30 min (orange and grey, respectively; denoted as MIL-125-NH_2_SMT_300W and AgNC@MIL-125-NH_2_SMT_300W).

To shed some light on the SMT degradation kinetics and to gain further understanding on the involved mechanism, the first 10 min of SMT degradation were fitted to a second order kinetics according to Eqn. (1).

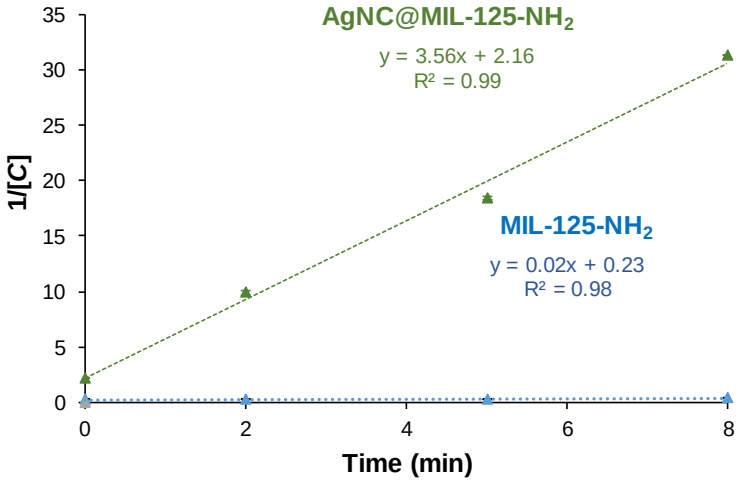

Figure AV. 25: Fitting of SMT degradation data using MIL-125-NH_2 (blue circles) and AgNC@MIL-125-NH_2 (green triangles) to a second order kinetics.

Table AV. 3: Comparison of degraded SMT values (% and $mg \cdot L^{-1} \cdot min^{-1}$) using AgNC@MIL-125-$NH_2$ and other MOF-based catalysts, as well as TiO_2.

MOF based material	**SMT degraded, % ($mg \cdot L^{-1} \cdot min^{-1}$)**	**Time (min)**	**Kinetic model**	***K*** **($g \cdot mg^{-1} \cdot min^{-1}$)**	**Refs**
AgNC@MIL-125-NH_2	96 (0.32)	30	2nd	3.56	This work
MIL-125-NH_2	49 (0.16)	30	2nd	0.02	This work
CUS@MIL-100(Fe)	100 (0.11)	180	ND	ND	[20]
PW_{12}@MFM-300(In)	98 (0.14)	120	ND	ND	[21]
MIL-53(Fe)@percarbonate	90 (83.50)	60	ND	ND	[22]
TiO_2	95 (0.08)	120	ND	ND	[23]

ND: no data reported

Continuous flow SMT photodegradation: A continuous flow reactor made of glass (length = 7.5 cm, T = 2.2 cm, volume = 10 mL) was employed to investigate SMT photodegradation through a continuous flow. In order to provide a suitable liquid and MOF distribution, before any test the reactor containing only 10 mg of AgNC@MIL-125-NH_2 powder was first conditioned with 10 mL of water (without SMT). Following the same experimental conditions as previously described at the beginning of this section, a SMT concentration of 10 $\mu g \cdot mL^{-1}$ and a distance of 21 cm between the light source and the reactor were used. Applying a NE-4000 dual-channel syringe pumping system (MicruX Technologies, Spain), a total volume of 120 mL of contaminated water were pumped into the reactor with a flow rate of 30 $mL \cdot h^{-1}$ (or *ca.* 80 $L \cdot m^{-2} \cdot h^{-1}$). The effluent was gathered at regular time intervals (10, 20, 25, 30, 35, 40, 50, 60, 70, 10, 110, 120, 130, 190, 220, and 240 min) and SMT and BDC-NH_2 concentration was quantified to evaluate the SMT elimination and the potential MOF degradation in a continuous mode. These experiments were performed in triplicate.

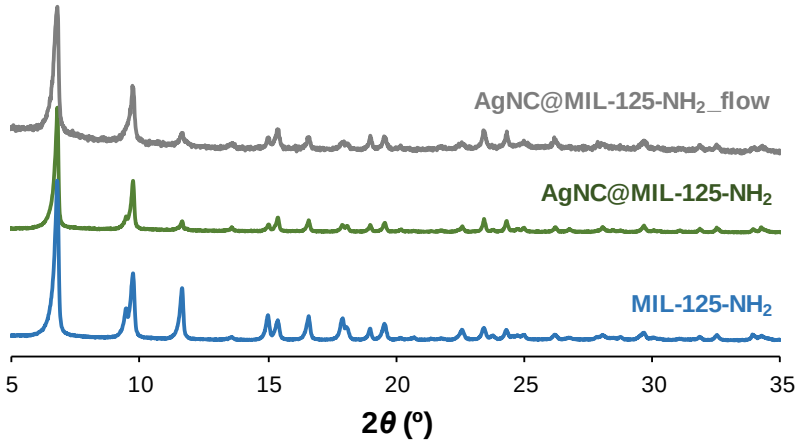

Figure AV. 26: XRPD patterns of the AgNC@MIL-125-NH_2 before and after being used in the continuous flow reactor under Vis irradiation for 4 h.

Monte Carlo simulations. In order to determine the main preferential adsorption sites available in the titanium terephthalate MIL-125-NH_2 structure for SMT guest molecules, force field-based Monte Carlo simulations were performed. For that purpose, the Metal-Organic Framework (MOF) crystal structure was taken from the literature and geometry-optimized.[24] Partial charges in the solid were then calculated using electronegativity equalization method,[25] while Lennard Jones parameters were taken from UFF to reproduce the van der Waals interactions.[26] Regarding the SMT molecules, Density Functional Theory (DFT) calculations were performed with $DMol^3$ to estimate the partial charges (**see Figure S28**) obtained from a geometry optimization using PW91 functional and DNP basis set and high convergence criteria and UFF was also used for Lennard-Jones parameters. The loading of the MOF by 1 or 2 SMT molecules (closed to the experimental loadings) were simulated by Monte Carlo (see **Figures S27**), using a temperature equal to 300 K, rigid solid and molecules structures and with a multi-cell (simulation box) large enough to consider a cut-off distance for Lennard Jones interactions equal to 12.5 Å. For a typical Monte Carlo calculation, $20 \cdot 10^6$ steps for both, equilibration and production processes, were used. From these calculations, it was therefore possible to extract the configuration of distribution of SMT molecules in the MOF pores and determine the plausible interactions.

After these calculations, the insertion of AgNCs in the MIL-125-NH_2 pores was investigated by Monte Carlo. For that purpose, previous structure and partial charges for MIL-125-NH_2 were used again and Ag nanoclusters (28 atoms) were considered without partial charge (Ag^0) and using UFF force field for Lennard Jones parameters. Monte Carlo simulations were performed in the same conditions than previously by imposing 7 Ag *per* unit-cell (which corresponded to the experimental Ag loading). From these calculations, it was thus possible to extract an Ag-loaded MIL-125-NH_2 and to run other calculations to study the loading of 1 or 2 SMT molecules in this new structure, following the same conditions than previously.

In each obtained structure, it was possible to calculate the textural properties (specific surface area for N_2, free pore volume), using the procedures developed by Düren *et al.*[27] (considering the center of a N_2 probe molecule rolling across the surface with a diameter equal to 3.681 Å) and Gubbins *et al.*[28] (probe size of 0 Å), respectively

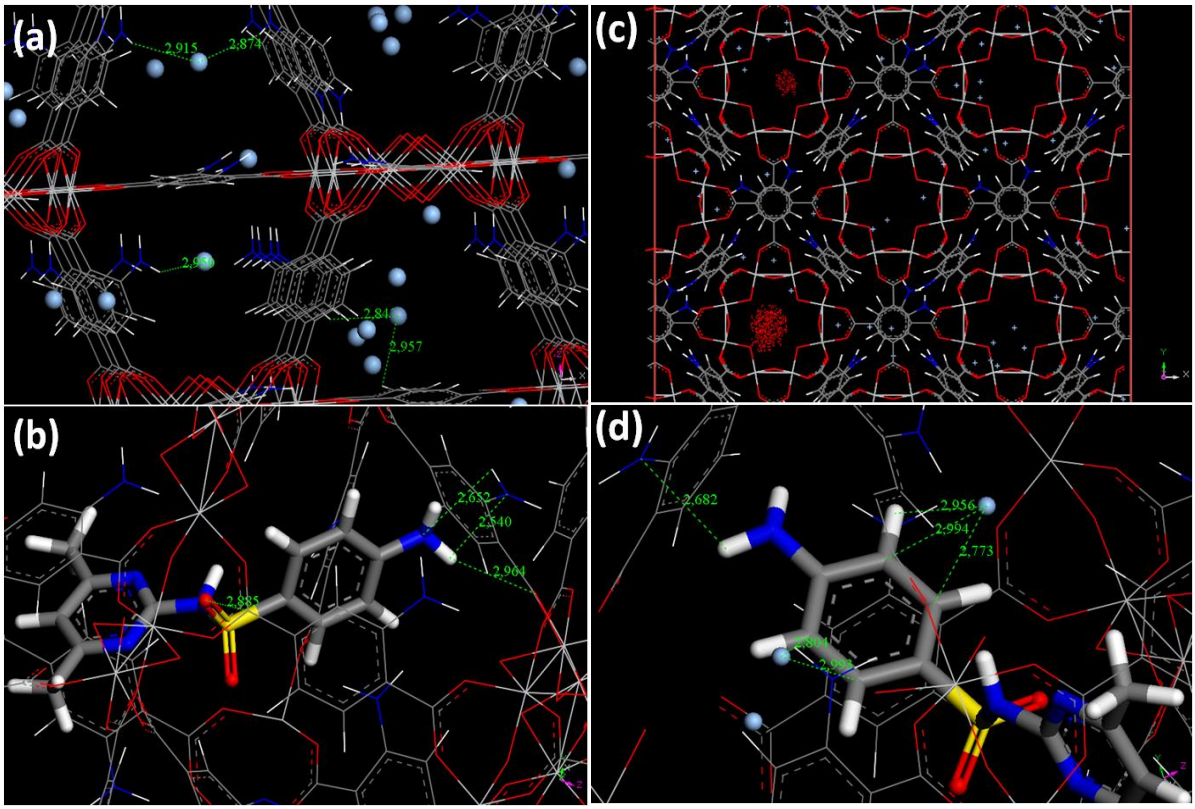

Figure AV. 27: Plausible structures extracted from Monte Carlo simulations for (a) AgNC@MIL-125-NH_2, (b) MIL-125-NH_2 containing 1 SMT molecule, (d) AgNC@MIL-125-NH_2 containing 1 SMT molecule. Figure (c) represents the 3D-energy plot for the presence of SMT in AgNC@MIL-125-NH_2

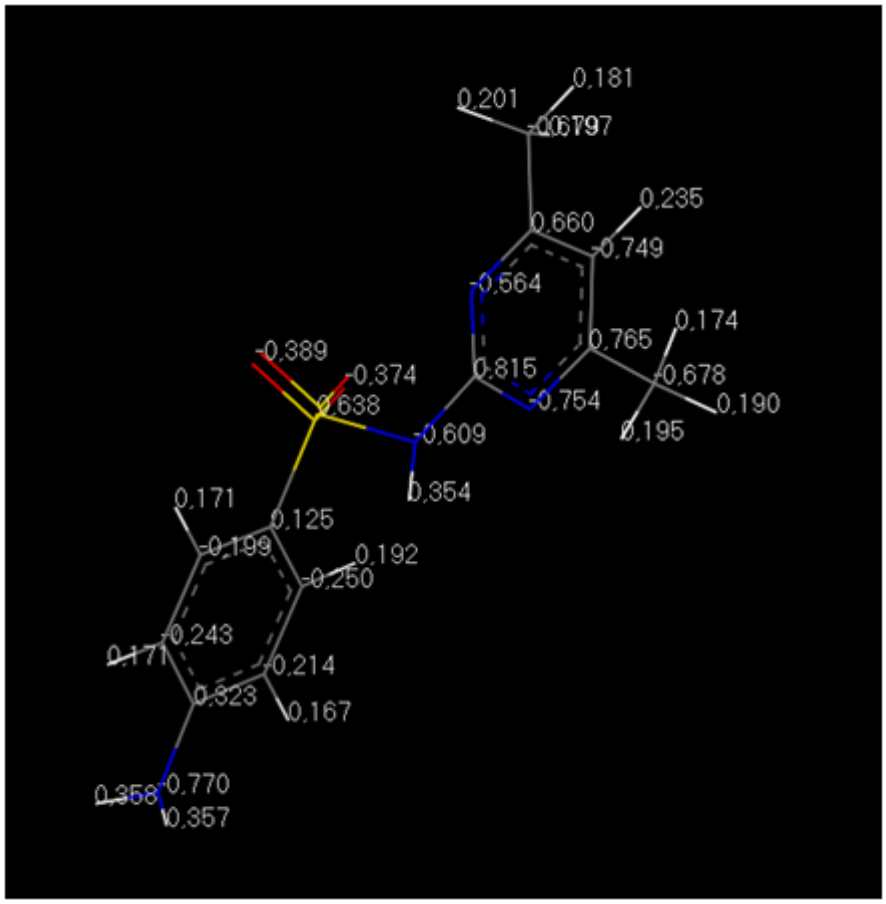

Figure AV. 28: Partial charges extracted from DFT calculations for SMT molecules (implemented in Monte Carlo simulations)

FTIR spectroscopy of SMT loaded materials

SMT-loaded materials AgNC@MIL-125-NH_2_SMT and MIL-125-NH_2_SMT were prepared by suspending 4 mg of AgNC@MIL-125-NH_2 or MIL-125-NH_2 into 4 mL of a SMT aqueous solution (10 ppm), following the same procedure as in the photodegradation experiments. The suspensions were kept under dark during all the experiment. After 24 h, the solids were centrifuged and recovered. The FTIR spectra of the SMT-loaded MIL-125-NH_2 confirmed a shift (from 3360 to 3376 cm^{-1} for the AgNC@MIL-125-NH_2; and from 3349 and 3446 cm^{-1} to 3386 and 3497 cm^{-1} for the MIL-125-NH_2, corresponding to the stretching ν_{asym}(N-H) and ν_{sym}(N-H) vibration bands of the –NH_2 groups in the MOF structure, respectively). These bands shift suggests the formation of interactions between SMT moieties and the –NH_2 group of MIL-125-NH_2. Additionally, in the case of the pristine MIL-125-NH_2, there is a shift associated to the carboxylate group found in the range of 1520-1650 cm^{-1} and 1280 to 1400 cm^{-1} for the ν_{asym} and ν_{sym} vibration bands, there is a red and blue shifts from 1534 to 1553 and 1339 to 1316 cm^{-1}, respectively. These variations are not found in the AgNC@MIL-125-NH_2 material, confirming the predictions of the simulation studies.

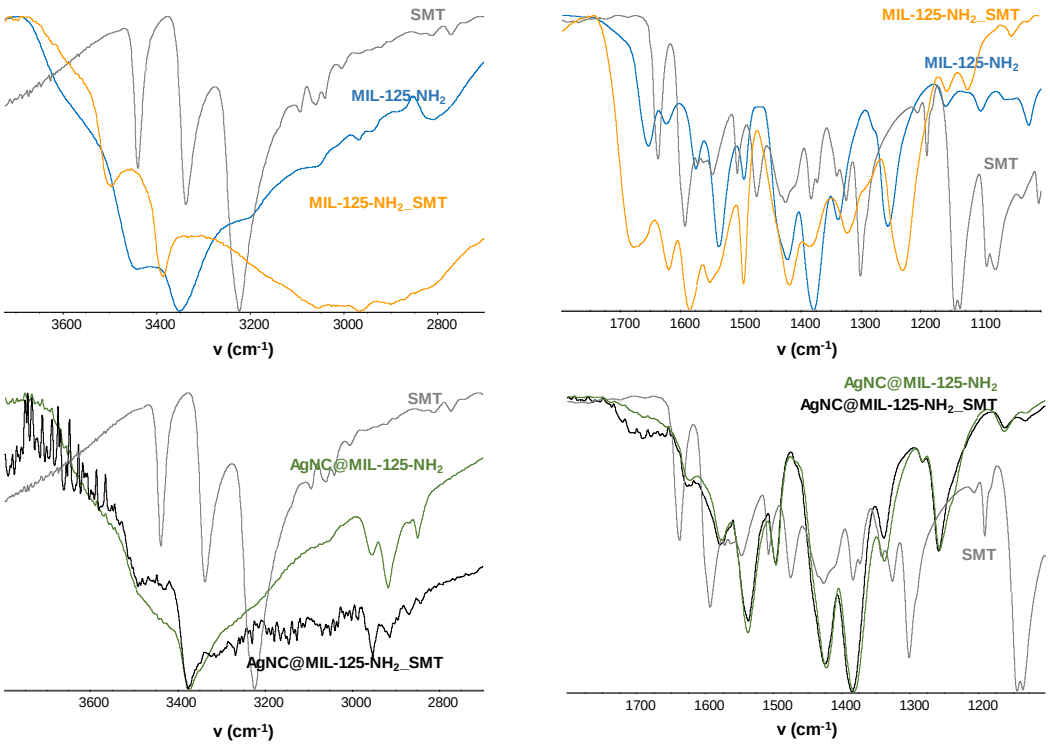

Figure AV. 29: FTIR spectra of the MIL-125-NH_2 (blue) and AgNC@MIL-125-NH_2 (green), and their corresponding SMT (MIL-125-NH_2_SMT (orange) and AgNC@MIL-125-NH_2_SMT (black)) loaded materials. The spectrum of free SMT has been included for comparison. All solids were previously dried overnight.

The breakthrough curve shape and breakthrough times are considered as the main factors to investigate the efficiency of the continuous flow reactors. Predictions of the breakthrough curve for the effluent is a requisite for the accurate design of a continuous contaminant elimination column.[29] The column data were fitted to the Thomas model (Origin Pro 2019b software was used for non-linear curve fitting). This model is one of the most general and widely used theoretical methods to describe column performance and its described following Eqn. (2)

$$\ln\left(\frac{Co}{Ct}-1\right)=\frac{K_{Th}q_oM}{F}-K_{Th}Cot \qquad \text{Eqn. (2)}$$

where Co is the inlet SMT concentration ($mg \cdot L^{-1}$); Ct is the effluent SMT concentration at time ($mg \cdot L^{-1}$); K_{Th} is the Thomas rate constant ($mL \cdot mg^{-1} \cdot min^{-1}$); q_o is the equilibrium of SMT uptake ($mg \cdot g^{-1}$); M is the mass of the absorbent (g); F is the inlet flow rate ($mL \cdot min^{-1}$); and t is the flow time (min).

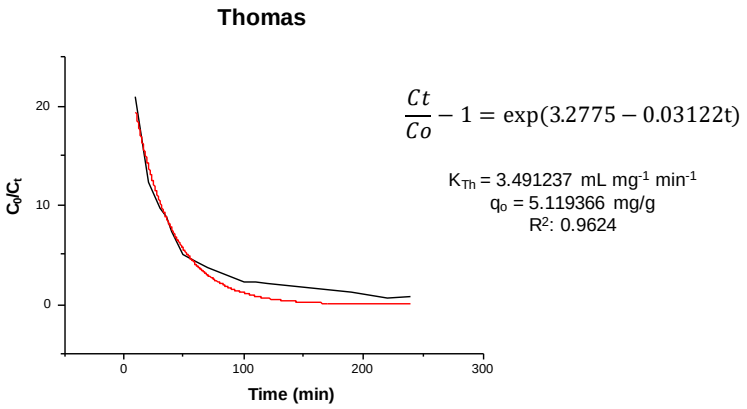

Figure AV. 30: Breakthrough curve (red) and fitting (black) of the data from the continuous water purification studies using the Thomas models at 298 K

V.V. Catalytic hydrogenation of 4-nitroaniline using AgNC@MIL-125-NH_2

In a typical experiment, 5 mg of AgNC@MIL-125-NH_2 or MIL-125-NH_2 were added to 15 mL of 4-NA in a tap water solution (2 mM), followed by the injection of 3.5 mL of a $NaBH_4$ aqueous solution (0.1 M). These tests were performed in dark and sealed to prevent H_2 loses. At certain intervals (0, 5, 10, 15, 20, and 30 min), an aliquot of 300 µL was filtered with a syringe filter (200 nm) and collected for

analysis by HPLC (4-NA, *p*-phenylendiamine-PPD, and $H_2BDC\text{-}NH_2$). These experiments were performed in triplicate.

The 4-NA degradation kinetics data during the first 30 min were fitted to a first order kinetics according to Eqn. (3).

$$Ln[C] = Ln[C]_0 + kt \qquad \text{Eqn. (3)}$$

where $[C]$ and $[C]_0$ are the remaining amount of 4-NA ($g \cdot mg^{-1}$) at the time t (min) and the initial 4-NA concentration, respectively, and k is the first order kinetics constant (min^{-1}).

In a first stage, the amount of $AgNC@MIL\text{-}125\text{-}NH_2$ catalyst required for the reaction was optimized. For an initial concentration of 4-NA of 0.2 mM considering reaction progress after 1 min, results revealed that catalyst concentrations below 3 mg were not enough (see Figure AV. 31**).** With only 20% of 4-NA remaining after 1 min, 5 mg of catalyst were considered as the best choice.

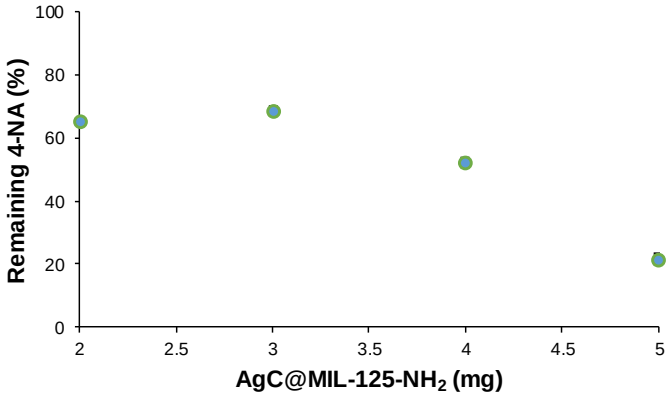

Figure AV. 31: Selection of amount of catalyst. Hydrogenation of 4-NA 0.2 mM.

As it can be seen in Figure AV. 32 reaction progress was easily followed by UV-Vis spectroscopy, by the transformation of the yellow 4-NA, with maximum absorbance at $\lambda_{4\text{-NA}} = 380$ nm, into the uncoloured PPD with $\lambda_{PPD} = 305$ nm. As the hydrogenation catalyzed by $AgNC@MIL\text{-}125\text{-}NH_2$ is relatively fast, the starting concentration of the 4-NA reagent was increased up to 2 mM to better follow the reaction kinetics. In addition, for better quantification of reagents and products, as well as catalyst stability under reaction conditions, periodic aliquots of the reaction media were taken during 30 min of the reaction and quantified by HPLC. Hydrogenation reaction was also carried out under the same conditions (4-NA 2 mM, 5 mg of catalyst) using $MIL\text{-}125\text{-}NH_2$ as a control of the AgNC catalytic activity (see article **Figure 5** in Chapter 4 section 4.2).

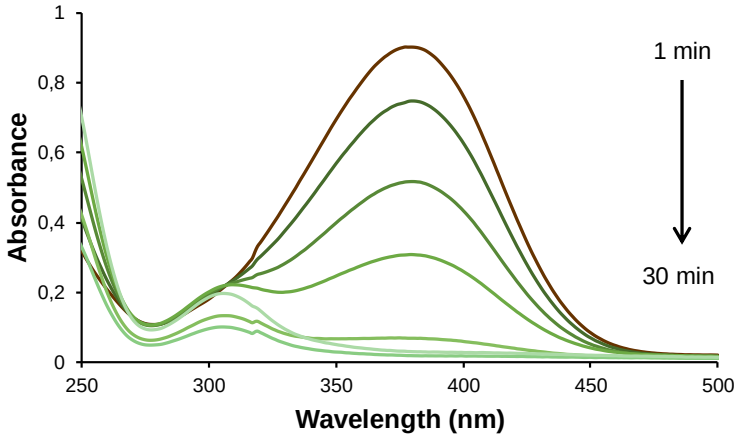

Figure AV. 32: UV-vis spectra of the hydrogenation of 4-NA (2 mM) upon addition of AgNC@MIL-125-NH_2 catalyst.

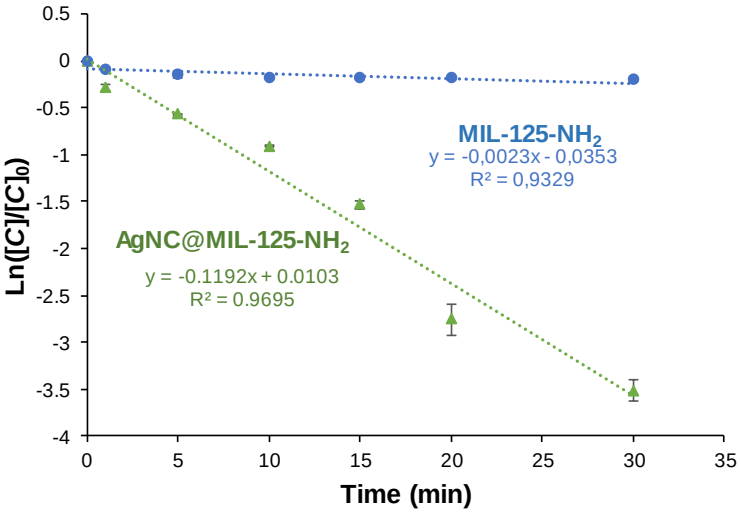

Figure AV. 33: Fitting to a first order kinetic of 4-NA hydrogenation data using AgNC@MIL-125-NH_2 (green triangle) and MIL-125-NH_2 (blue circle) as catalyst.

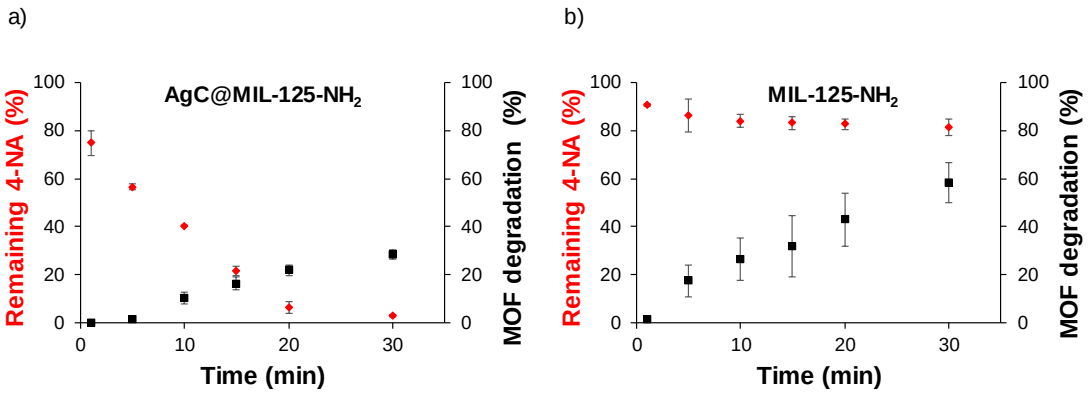

Figure AV. 34: AgNC@MIL-125-NH_2 stability followed by HPLC: H_2BDC-NH_2 leaching (black squares) during 4-NA hydrogenation (red diamonds).

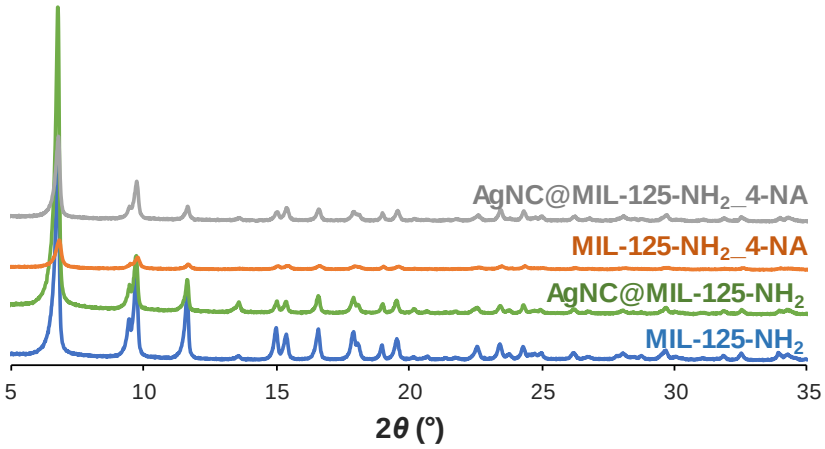

Figure AV. 35: XRDP patterns of the MIL-125-NH_2 and AgNC@MIL-125-NH_2 before (blue and green, respectively), and after being suspended as catalyst for 4-NA hydrogenation in dark for 30 min (MIL-125-NH_2_4-NA (orange) and AgNC@MIL-125-NH_2_4-NA (grey)).

Bibliography

(1) Abramoff, M. D.; Magalhaes, P. J.; Ram, S. J. Image Processing with ImageJ. *Biophotonics Int.* **2004**, *11*, 36–43.

(2) Moreira, M. A.; Santos, J. C.; Ferreira, A. F. P.; Loureiro, J. M.; Ragon, F.; Horcajada, P.; Yot, P. G.; Serre, C.; Rodrigues, A. E. Effect of Ethylbenzene in P-Xylene Selectivity of the Porous Titanium Amino Terephthalate MIL-125(Ti)-NH2. *Microporous Mesoporous Mater.* **2012**, *158*, 229–234. https://doi.org/10.1016/j.micromeso.2012.03.039.

(3) Maretti, L.; Billone, P. S.; Liu, Y.; Scaiano, J. C. Facile Photochemical Synthesis and Characterization of Highly Fluorescent Silver Nanoparticles. *J. Am. Chem. Soc.* **2009**, *131* (39), 13972–13980. https://doi.org/Doi 10.1021/Ja900201k.

(4) García-Bosch, N.; Liras, M.; Quijada-Garrido, I.; García, O. Multiamino Polymeric Capping of Fluorescent Silver Nanodots as an Effective Protective, Amphiphilic and PH/Thermo-Responsive Coating. *RSC Adv.* **2016**, *6* (72), 67643–67650. https://doi.org/10.1039/c6ra12024e.

(5) Arenas-Vivo, A.; Amariei, G.; Aguado, S.; Rosal, R.; Horcajada, P. An Ag-Loaded Photoactive Nano-Metal Organic Framework as a Promising Biofilm Treatment. *Acta Biomater.* **2019**, *97*, 490–500. https://doi.org/10.1016/j.actbio.2019.08.011.

(6) Vanrompay, H.; Skorikov, A.; Bladt, E.; Béché, A.; Freitag, B.; Verbeeck, J.; Bals, S. Fast versus Conventional HAADF-STEM Tomography of Nanoparticles: Advantages and Challenges. *Ultramicroscopy* **2021**, *221*, 113191. https://doi.org/10.1016/j.ultramic.2020.113191.

(7) Viezbicke, B. D.; Patel, S.; Davis, B. E.; Birnie, D. P. Evaluation of the Tauc Method for Optical Absorption Edge Determination: ZnO Thin Films as a Model System. *Phys. status solidi* **2015**, *252* (8), 1700–1710. https://doi.org/10.1002/pssb.201552007.

(8) Nibret, G.; Ahmad, S.; Rao, D. G.; Ahmad, I.; Shaikh, M. A. M. U.; Rehman, Z. U. Removal of Methylene Blue Dye from Textile Wastewater Using Water Hyacinth Activated Carbon as Adsorbent: Synthesis, Characterization and Kinetic Studies. *SSRN Electron. J.* **2019**, *26–28*, 1959–1969. https://doi.org/10.2139/ssrn.3358101.

(9) Li, H.; Li, Q.; He, X.; Xu, Z.; Wang, Y.; Jia, L. Synthesis of AgBr@MOFs Nanocomposite and Its Photocatalytic Activity for Dye Degradation. *Polyhedron* **2019**, *165*, 31–37. https://doi.org/10.1016/j.poly.2019.02.050.

(10) Abdelhameed, R. M.; Simões, M. M. Q.; Silva, A. M. S.; Rocha, J. Enhanced Photocatalytic Activity of MIL-125 by Post-Synthetic Modification with Cr ^{III} and Ag Nanoparticles. *Chem. - A Eur. J.* **2015**, *21* (31), 11072–11081. https://doi.org/10.1002/chem.201500808.

(11) Abdelhameed, R. M.; Maria, D.; Karmaoui, M. Engineering Highly Effective and Stable Nanocomposite Photocatalyst Based on NH2-MIL-125 Encirclement with Ag3PO4 Nanoparticles. *J. Photochem. Photobiol. A Chem.* **2018**, *351*, 50–58. https://doi.org/10.1016/j.jphotochem.2017.10.011.

(12) Emam, H. E.; Ahmed, H. B.; Gomaa, E.; Helal, M. H.; Abdelhameed, R. M. Doping of Silver Vanadate and Silver Tungstate Nanoparticles for Enhancement the Photocatalytic Activity of MIL-125-NH2 in Dye Degradation. *J. Photochem. Photobiol. A Chem.* **2019**, *383*, 111986–111998. https://doi.org/10.1016/j.jphotochem.2019.111986.

(13) Li, Q.; Xue, D. X.; Zhang, Y. F.; Zhang, Z. H.; Gao, Z.; Bai, J. A Dual-Functional Indium-Organic Framework towards Organic Pollutant Decontamination: Via Physically Selective Adsorption and Chemical Photodegradation. *J. Mater. Chem. A* **2017**, *5* (27), 14182–14189. https://doi.org/10.1039/c7ta02216f.

(14) Du, J. J.; Yuan, Y. P.; Sun, J. X.; Peng, F. M.; Jiang, X.; Qiu, L. G.; Xie, A. J.; Shen, Y. H.; Zhu, J. F. New Photocatalysts Based on MIL-53 Metal-Organic Frameworks for the Decolorization of Methylene Blue Dye. *J. Hazard. Mater.* **2011**, *190* (1–3), 945–951. https://doi.org/10.1016/j.jhazmat.2011.04.029.

(15) Fang, X. D.; Yang, L. B.; Dou, A. N.; Liu, Y. E.; Yao, J.; Xu, Q. Q.; Zhu, A. X. Synthesis, Crystal Structure and Photocatalytic Properties of a Mn (II) Metal-Organic Framework Based on a Thiophene-Functionalized Dicarboxylate Ligand. *Inorg. Chem. Commun.* **2018**, *96*, 124–127. https://doi.org/10.1016/j.inoche.2018.08.017.

(16) Liang, Q.; Zhang, M.; Zhang, Z.; Liu, C.; Xu, S.; Li, Z. Zinc Phthalocyanine

Coupled with UIO-66 (NH2) via a Facile Condensation Process for Enhanced Visible-Light-Driven Photocatalysis. *J. Alloys Compd.* **2017**, *690*, 123–130. https://doi.org/10.1016/j.jallcom.2016.08.087.

(17) Jing, H. P.; Wang, C. C.; Zhang, Y. W.; Wang, P.; Li, R. Photocatalytic Degradation of Methylene Blue in ZIF-8. *RSC Adv.* **2014**, *4* (97), 54454–54462. https://doi.org/10.1039/c4ra08820d.

(18) Fan, G.; Luo, J.; Guo, L.; Lin, R.; Zheng, X.; Snyder, S. A. Doping Ag/AgCl in Zeolitic Imidazolate Framework-8 (ZIF-8) to Enhance the Performance of Photodegradation of Methylene Blue. *Chemosphere* **2018**, *209*, 44–52. https://doi.org/10.1016/j.chemosphere.2018.06.036.

(19) Petrovic, M.; Verlicchi, P. Water Treatment Plants and Pharmaceutical Residues in Catalonia and Italy. *Contrib. to Sci.* **2014**, *10* (2), 135–150. https://doi.org/10.2436/cs.v10i2.139201.

(20) Tang, J.; Wang, J. Metal Organic Framework with Coordinatively Unsaturated Sites as Efficient Fenton-like Catalyst for Enhanced Degradation of Sulfamethazine. *Environ. Sci. Technol.* **2018**, *52*, 5367–5377. https://doi.org/10.1021/acs.est.8b00092.

(21) Li, G.; Zhang, K.; Li, C.; Gao, R.; Cheng, Y.; Hou, L.; Wang, Y. Solvent-Free Method to Encapsulate Polyoxometalate into Metal-Organic Frameworks as e Fficient and Recyclable Photocatalyst for Harmful Sulfamethazine Degrading in Water. *Appl. Catal. B Environ.* **2019**, *245*, 753–759. https://doi.org/10.1016/j.apcatb.2019.01.012.

(22) Li, R.; Chen, Z.; Cai, M.; Huang, J.; Chen, P.; Liu, G. Applied Surface Science Improvement of Sulfamethazine Photodegradation by Fe(III) Assisted MIL- 53(Fe)/Percarbonate System. *Appl. Surf. Sci.* **2018**, *457* (May), 726–734. https://doi.org/10.1016/j.apsusc.2018.06.294.

(23) Fukahori, S.; Fujiwara, T. Photocatalytic Decomposition Behavior and Reaction Pathway of Sulfamethazine Antibiotic Using TiO2. *J. Environ. Manage.* **2015**, *157*, 103–110. https://doi.org/10.1016/j.jenvman.2015.04.002.

(24) Zlotea, C.; Phanon, D.; Mazaj, M.; Heurtaux, D.; Guillerm, V.; Serre, C.; Horcajada, P.; Devic, T.; Magnier, E.; Cuevas, F.; et al. Effect of NH2 and CF3 Functionalization on the Hydrogen Sorption Properties of MOFs. *J. Chem. Soc. Dalt. Trans.* **2011**, *40* (18), 4879–4881. https://doi.org/10.1039/c1dt10115c.

(25) Rappé, A. K.; Goddard, W. A. Charge Equilibration for Molecular Dynamics Simulations. *J. Phys. Chem.* **1991**, *95* (8), 3358–3363.

https://doi.org/10.1021/j100161a070.

(26) Rappé, A. K.; Casewit, C. J.; Colwell, K. S.; Goddard, W. A.; Skiff, W. M. UFF, a Full Periodic Table Force Field for Molecular Mechanics and Molecular Dynamics Simulations. *J. Am. Chem. Soc.* **1992**, *114* (25), 10024–10035. https://doi.org/10.1021/ja00051a040.

(27) Düren, T.; Millange, F.; Férey, G.; Walton, K. S.; Snurr, R. Q. Calculating Geometric Surface Areas as a Characterization Tool for Metal - Organic Frameworks. *J. Phys. Chem. C* **2007**, *111* (42), 15350–15356. https://doi.org/10.1021/jp074723h.

(28) Gelb, L. D.; Gubbins, K. E. Pore Size Distributions in Porous Glasses: A Computer Simulation Study. *Langmuir* **1999**, *15* (2), 305–308. https://doi.org/10.1021/la9808418.

(29) Han, R.; Wang, Y.; Zhao, X.; Wang, Y.; Xie, F.; Cheng, J.; Tang, M. Adsorption of Methylene Blue by Phoenix Tree Leaf Powder in a Fixed-Bed Column: Experiments and Prediction of Breakthrough Curves. *Desalination* **2009**, *245* (1–3), 284–297. https://doi.org/10.1016/j.desal.2008.07.013.

APPENDIX VI

Supporting information publication Chapter 5

Phase selective microwave assisted synthesis of iron(III) aminoterephthalate MOFs

*Ana Arenas-Vivo,[1] David Ávila[2] and Patricia Horcajada[1]**

[1]Advanced Porous Materials Unit (APMU), IMDEA Energy Institute, Avda. Ramón de la Sagra 3, E-28935 Móstoles, Madrid, Spain

[2]Department of Inorganic Chemistry I, Chemical Sciences Faculty, Complutense University of Madrid, 28040 Madrid, Spain

* Corresponding author. E-mail address: patricia.horcajada@imdea.org

Keywords: microwave synthesis; metal-organic frameworks; porous solids; iron; aminoterephthalate; phase selection

VI.I. Microwave assisted solvothermal synthesis

Table AVI. 1: Letter codes for the resulting products of the following MW synthesis

Letter code	Resulting reaction product
A	MIL-53(Fe)-NH_2
B	MIL-88B(Fe)-NH_2
C	MIL-101(Fe)-NH_2
X	Amorphous
D	Fe_2O_3

Table AVI. 2: Mass, mol and molar ratios, and dispensed amounts for the MW investigation of the system $FeCl_3 \cdot 6H_2O$ / $H_2BDC\text{-}NH_2$ / HCl in **water** (V H_2O = 4 mL, T = 100 °C, t = 5 min). The resulting phases are indicated by the letter assigned in Table AVI. 1

Sample name	$FeCl_3 \cdot 6H_2O$ (mg)	$FeCl_3 \cdot 6H_2O$ (mmol)	$H_2BDC\text{-}NH_2$ (mg)	$H_2BDC\text{-}NH_2$ (mmol)	Ligand: Metal	[Fe] (M)	HCl 1 M (mL)	HCl: Fe	Result*
MW 1-01	21.6	0.08	14.48	0.08	1	0.02	0	0	C
MW 1-02	54	0.2	36.2	0.2	1	0.05	0	0	C + A
MW 1-03	108	0.4	72.4	0.4	1	0.1	0	0	A + C
MW 1-04	216	0.8	144.8	0.8	1	0.2	0	0	A
MW 1-05	54	0.2	36.2	0.2	1	0.05	0.05	0.25	C + A
MW 1-06	54	0.2	36.2	0.2	1	0.05	0.1	0.5	C + A
MW 1-07	54	0.2	36.2	0.2	1	0.05	0.15	0.75	A + C
MW 1-08	54	0.2	36.2	0.2	1	0.05	0.2	1	A

** In the case of mixture, the first letter is the major phase*

Table AVI. 3: Mass, mol and molar ratios, and dispensed amounts for the MW investigation of the system $FeCl_3 \cdot 6\ H_2O$ / $H_2BDC\text{-}NH_2$ / HCl in **water** (V H_2O = 4 mL, T= 150 °C, t= 5 min and $^{(\bullet)}$ t= 30 min). The resulting phases are indicated by the letter assigned in Table AVI. 1

Sample name	$FeCl_3 \cdot 6H_2O$ (mg)	$FeCl_3 \cdot 6H_2O$ (mmol)	$H_2BDC\text{-}NH_2$ (mg)	$H_2BDC\text{-}NH_2$ (mmol)	Ligand: Metal	[Fe] (M)	HCl 1 M (mL)	HCl: Fe	Result *
MW 2-01	21.6	0.08	14.48	0.08	1	0.02	0	0	C + A
MW 2-02	54	0.2	36.2	0.2	1	0.05	0	0	A + C
MW 2-03	108	0.4	72.4	0.4	1	0.1	0	0	A
MW 2-04$^{(\bullet)}$	108	0.4	72.4	0.4	1	0.1	0	0	A
MW 2-05	216	0.8	144.8	0.8	1	0.2	0	0	A
MW 2-06	54	0.2	36.2	0.2	1	0.05	0.1	0.5	C + A

** In the case of mixture, the first letter is the major phase*

Table AVI. 4: Mass, mol and molar ratios, and dispensed amounts for the MW investigation of the system $FeCl_3 \cdot 6\ H_2O$ / $H_2BDC\text{-}NH_2$ in **ethanol** (V EtOH = 4 mL. T= 150 °C. t= 5 min). The resulting phases are indicated by the letter assigned in Table AVI. 1

Sample name	$FeCl_3 \cdot 6H_2O$ (mg)	$FeCl_3 \cdot 6H_2O$ (mmol)	$H_2BDC\text{-}NH_2$ (mg)	$H_2BDC\text{-}NH_2$ (mmol)	Ligand: Metal	[Fe] (M)	HCl 1 M (mL)	HCl: Fe	Result
MW 3-01	21.6	0.08	14.48	0.08	1	0.02	0	0	B
MW 3-02	54	0.2	36.2	0.2	1	0.05	0	0	B
MW 3-03	108	0.4	72.4	0.4	1	0.1	0	0	B
MW 3-04	216	0.8	144.8	0.8	1	0.2	0	0	B

Table AVI. 5: Mass, mol and molar ratios, and dispensed amounts for the MW investigation of the system $FeCl_3 \cdot 6\ H_2O$ / $H_2BDC\text{-}NH_2$ in ethanol (V EtOH = 4 mL. T= 150 °C. t= 5 min). The resulting phases are indicated by the letter assigned in Table AVI. 1

Sample name	**$FeCl_3 \cdot 6H_2O$ (mg)**	**$FeCl_3 \cdot 6H_2O$ (mmol)**	**$H_2BDC\text{-}NH_2$ (mg)**	**$H_2BDC\text{-}NH_2$ (mmol)**	**Ligand: Metal**	**[Fe] (M)**	**HCl 1 M (mL)**	**HCl: Fe**	**Result**
MW 3-05	216	0.8	36.2	0.2	0.25	0.2	0	0	**B**
MW 3-06	216	0.8	72.4	0.4	0.5	0.2	0	0	**B**
MW 3-07	216	0.8	217.2	1.2	1.5	0.2	0	0	**B**
MW 3-08	216	0.8	289.6	1.6	2	0.2	0	0	**B**

Table AVI. 6: Mass, mol and molar ratios, and dispensed amounts for the MW investigation of the system $FeCl_3 \cdot 6\ H_2O$ / $H_2BDC\text{-}NH_2$ / in ethanol (V EtOH = 4 mL, [Fe]=0.1 M, ligand:metal 1:1). The resulting phases are indicated by the letter assigned in Table AVI. 1

Sample name	**$FeCl_3 \cdot 6H_2O$ (mg)**	**$FeCl_3 \cdot 6H_2O$ (mmol)**	**$H_2BDC\text{-}NH_2$ (mg)**	**$H_2BDC\text{-}NH_2$ (mmol)**	**Ligand: Metal**	**[Fe] (M)**	**T (°C)**	**Time (min)**	**Result**
MW 3-09	108	0.4	72.4	0.4	1	0.1	100	5	**B**
MW 3-10	108	0.4	72.4	0.4	1	0.1	100	10	**B**
MW 3-11	108	0.4	72.4	0.4	1	0.1	100	20	**C**
MW 3-12	108	0.4	72.4	0.4	1	0.1	100	30	**C**
MW 3-13	108	0.4	72.4	0.4	1	0.1	150	10	**B**
MW 3-14	108	0.4	72.4	0.4	1	0.1	150	20	**B**
MW 3-15	108	0.4	72.4	0.4	1	0.1	150	30	**B**
MW 3-16	108	0.4	72.4	0.4	1	0.1	180	5	**B**
MW 3-17	108	0.4	72.4	0.4	1	0.1	180	10	**D**
MW 3-18	108	0.4	72.4	0.4	1	0.1	180	20	**D**
MW 3-19	108	0.4	72.4	0.4	1	0.1	180	30	**D**

Table AVI. 7: Mass, mol and molar ratios, and dispensed amounts for the MW investigation of the system $FeCl_3 \cdot 6\ H_2O$ / $H_2BDC\text{-}NH_2$ in DMF (V DMF = 4 mL. T= 150 °C. ligand:metal=1:1). The resulting phases are indicated by the letter assigned in Table AVI. 1

Sample name	**$FeCl_3 \cdot 6H_2O$ (mg)**	**$FeCl_3 \cdot 6H_2O$ (mmol)**	**$H_2BDC\text{-}NH_2$ (mg)**	**$H_2BDC\text{-}NH_2$ (mmol)**	**Ligand: Metal**	**[Fe] (M)**	**T (°C)**	**Time (min)**	**Result***
MW 4-01	21.6	0.08	14.48	0.08	1	0.02	150	5	X
MW 4-02	54	0.2	36.2	0.2	1	0.05	150	5	**C + B**
MW 4-03	108	0.4	72.4	0.4	1	0.1	150	5	**B + C**
MW 4-04	216	0.8	144.8	0.8	1	0.2	150	5	**C+ A**
MW 4-05	21.6	0.08	14.48	0.08	1	0.02	150	30	**C**
MW 4-06	54	0.2	36.2	0.2	1	0.05	150	30	**C + B**
MW 4-07	108	0.4	72.4	0.4	1	0.1	150	30	**B + C**
MW 4-08	216	0.8	144.8	0.8	1	0.2	150	30	**A + C**

** In the case of mixture, the first letter is the major phase*

Table AVI. 8: Mass, mol and molar ratios, and dispensed amounts for the MW investigation of the system $FeCl_3 \cdot 6\ H_2O$ / $H_2BDC\text{-}NH_2$ / HCl in DMF (V DMF = 4 mL. T= 150 °C. t= 30 min). The resulting phases are indicated by the letter assigned in Table AVI. 1

Sample name	**$FeCl_3 \cdot 6H_2O$ (mg)**	**$FeCl_3 \cdot 6H_2O$ (mmol)**	**$H_2BDC\text{-}NH_2$ (mg)**	**$H_2BDC\text{-}NH_2$ (mmol)**	**Ligand: Metal**	**[Fe] (M)**	**HCl 1 M (mL)**	**HCl: Fe**	**Result***
MW 4-10	54	0.2	36.2	0.2	1	0.05	0	0	**C + B**
MW 4-11	54	0.2	36.2	0.2	1	0.05	0.1	0.5	**B**
MW 4-12	54	0.2	54.3	0.3	1.5	0.05	0	0	**C + B**
MW 4-13	54	0.2	54.3	0.3	1.5	0.05	0.1	0.5	**B**

** In the case of mixture, the first letter is the major phase*

VI.II. XRPD patterns

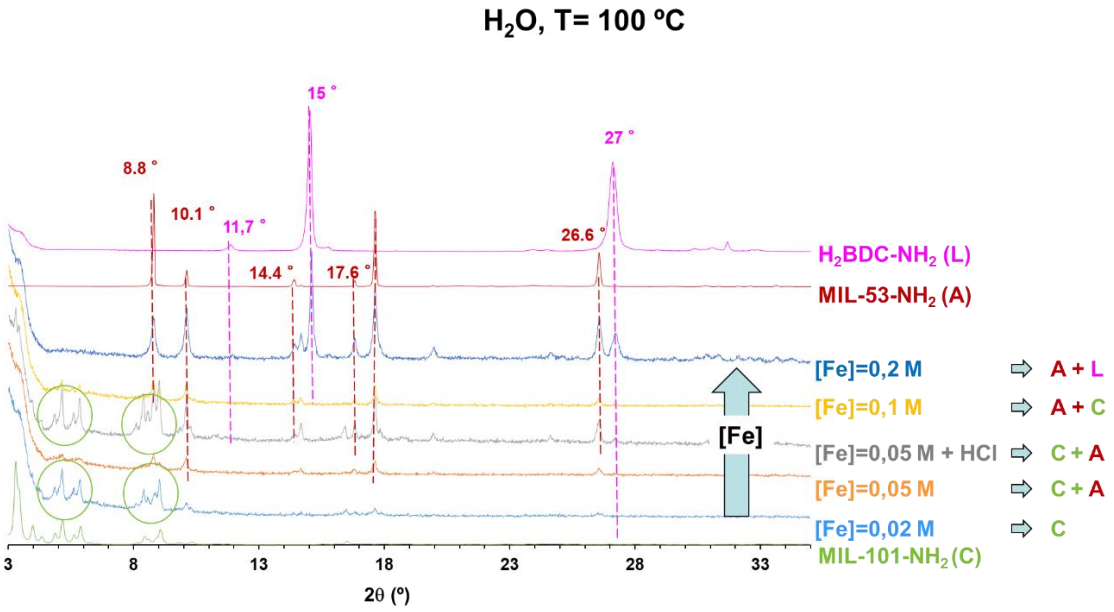

Figure AVI. 1: XRPD patterns for the MW investigation of the system $FeCl_3 \cdot 6\ H_2O$ / $H_2BDC\text{-}NH_2$ / HCl in **water** (V H_2O = 4 mL, T= 100 °C, t= 5 min) after activation with EtOH, compared to simulated MIL-101-NH_2 (green), MIL-53-NH_2 (red) and $H_2BDC\text{-}NH_2$ (pink)

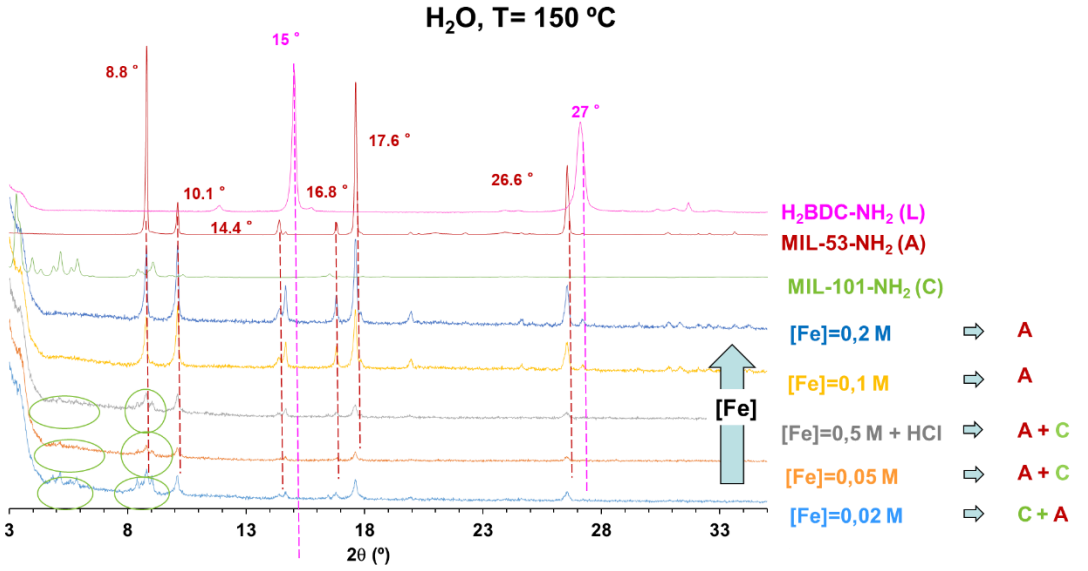

Figure AVI. 2: XRPD patterns for the MW investigation of the system $FeCl_3 \cdot 6\ H_2O$ / $H_2BDC\text{-}NH_2$ / HCl in **water** (V H_2O = 4 mL, T= 150 °C, t= 5 min) after activation with EtOH, compared to simulated MIL-101-NH_2 (green), MIL-53-NH_2 (red) and $H_2BDC\text{-}NH_2$ (pink)

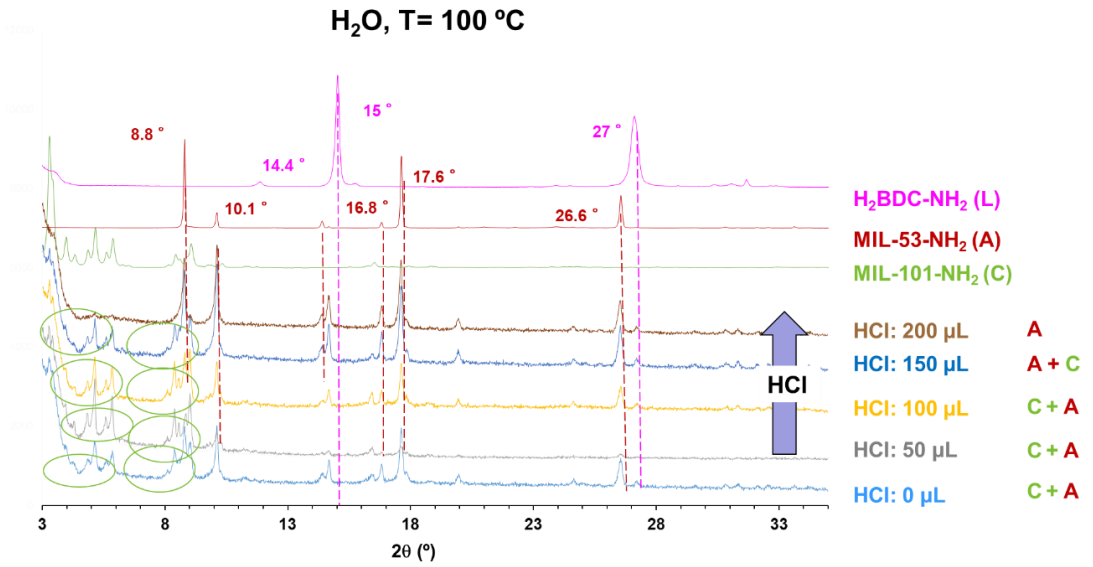

Figure AVI. 3: XRPD patterns for the MW investigation of the system $FeCl_3 \cdot 6\ H_2O$ / $H_2BDC\text{-}NH_2$ / HCl in **water** (V H_2O = 4 mL, T= 100 °C, t= 5 min, [Fe] = 0.05 M) after activation with EtOH, compared to simulated MIL-101-NH_2 (green), MIL-53-NH_2 (red) and $H_2BDC\text{-}NH_2$ (pink)

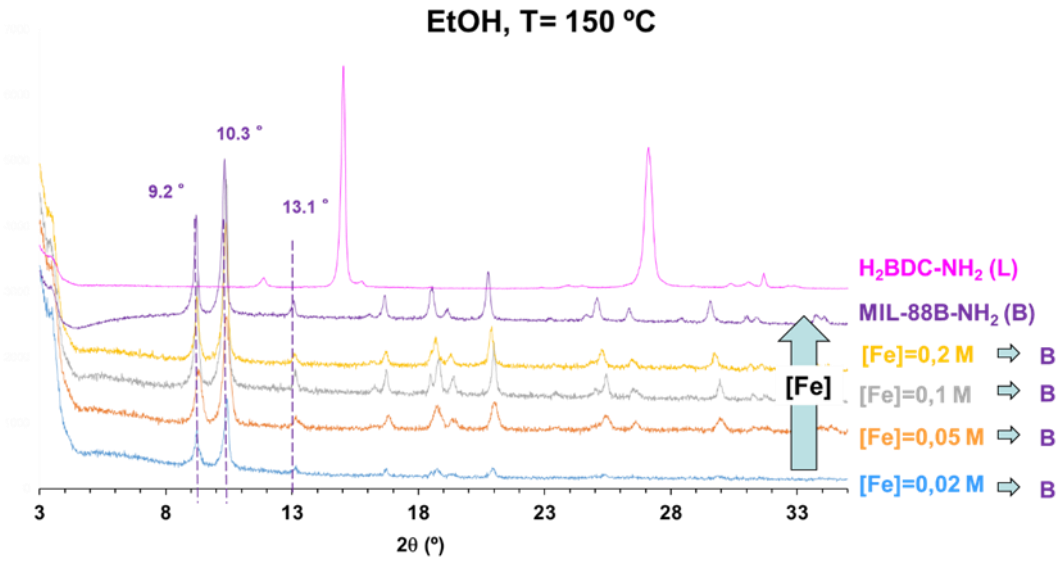

Figure AVI. 4: XRPD patterns for the MW investigation of the system $FeCl_3 \cdot 6\ H_2O$ / $H_2BDC\text{-}NH_2$ in **ethanol** (V EtOH = 4 mL, T= 150 °C, t= 5 min) after activation with EtOH, compared to simulated MIL-88B-NH_2 (purple) and $H_2BDC\text{-}NH_2$ (pink)

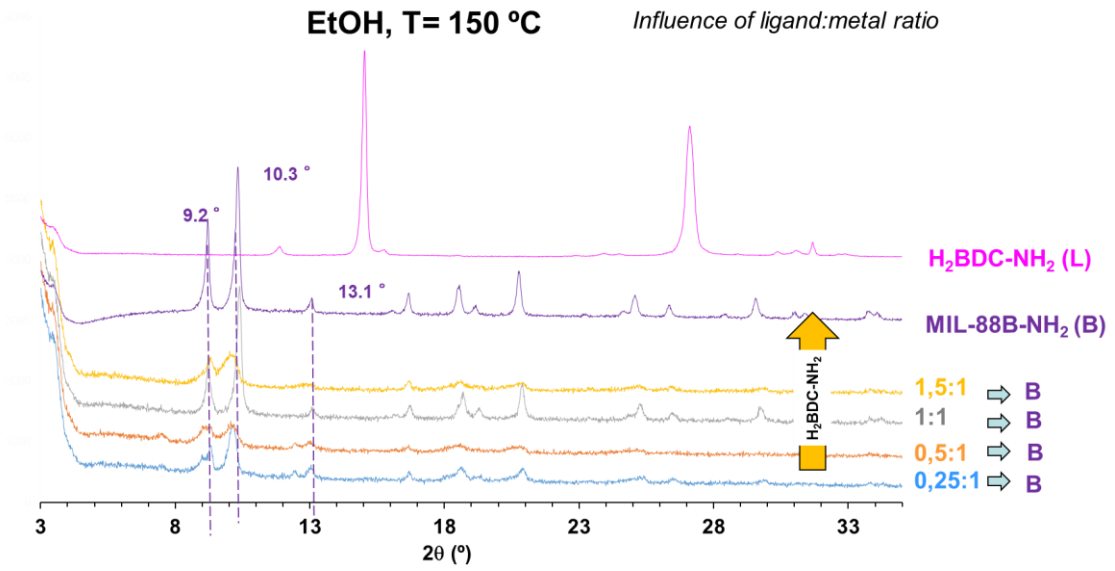

Figure AVI. 5: XPRD patterns for the MW investigation of the system $FeCl_3 \cdot 6\ H_2O$ / $H_2BDC\text{-}NH_2$ in **ethanol** (V EtOH = 4 mL, T= 150 °C, [Fe]= 0.2 M, t= 5 min) after activation with EtOH, compared to simulated MIL-88B-NH_2 (purple) and $H_2BDC\text{-}NH_2$ (pink)

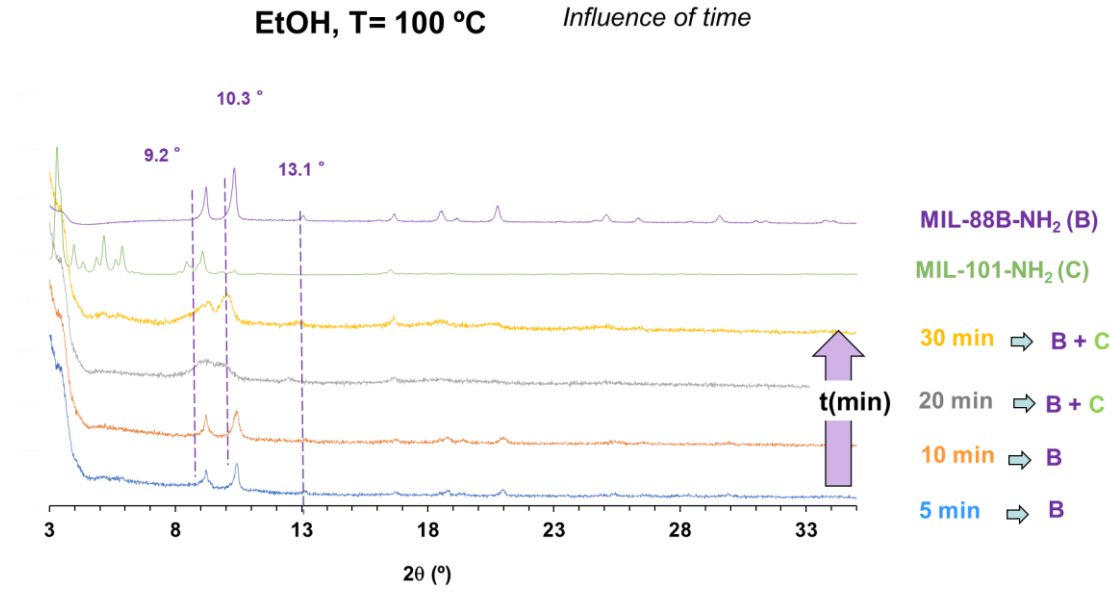

Figure AVI. 6: XRPD patterns for the MW investigation of the system $FeCl_3 \cdot 6\ H_2O$ / $H_2BDC\text{-}NH_2$ in **ethanol** (V EtOH = 4 mL, T= 100 °C, [Fe]= 0.1 M,) after activation with EtOH, compared to simulated MIL-88B-NH_2 (purple) and MIL-101-NH_2 (green).

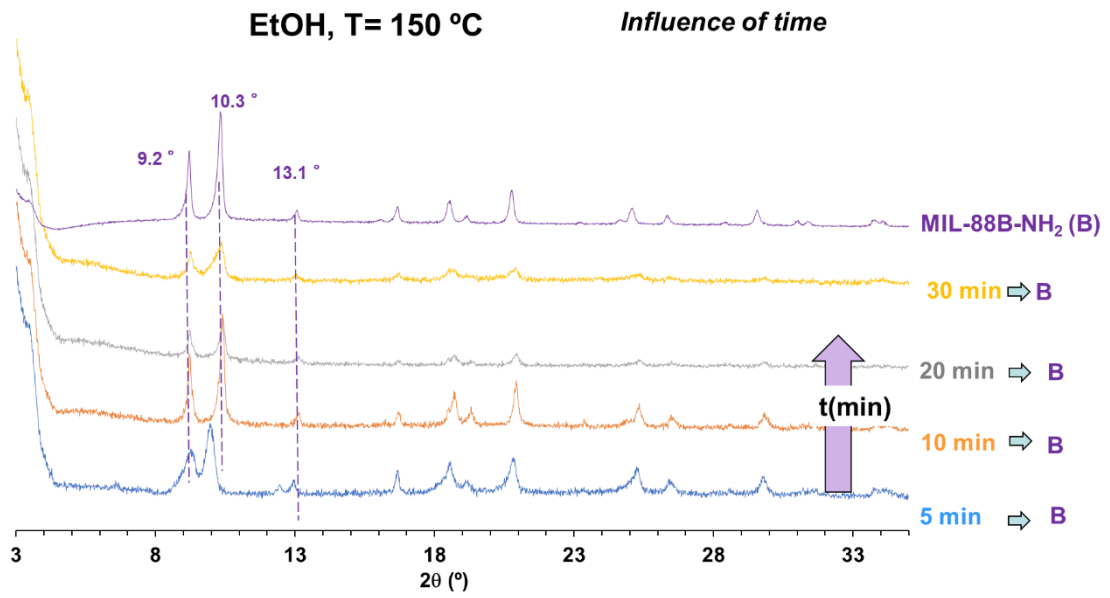

Figure AVI. 7: XRPD patterns for the MW investigation of the system $FeCl_3 \cdot 6\ H_2O$ / $H_2BDC\text{-}NH_2$ in **ethanol** (V EtOH = 4 mL, T= 150 °C, [Fe]= 0.1 M,) after activation with EtOH, compared to simulated MIL-88B-NH_2 (purple).

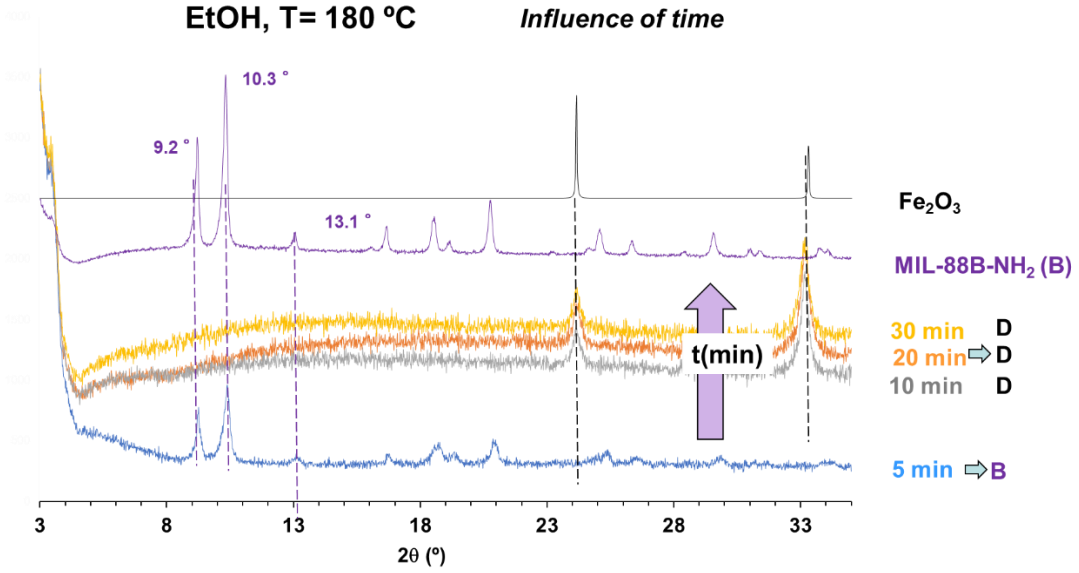

Figure AVI. 8: XRPD patterns for the MW investigation of the system $FeCl_3 \cdot 6\ H_2O$ / $H_2BDC\text{-}NH_2$ in **ethanol** (V EtOH = 4 mL, T= 180 °C, [Fe]= 0.1 M,) after activation with EtOH, compared to simulated MIL-88B-NH_2 (purple) and Fe_2O_3 (black).

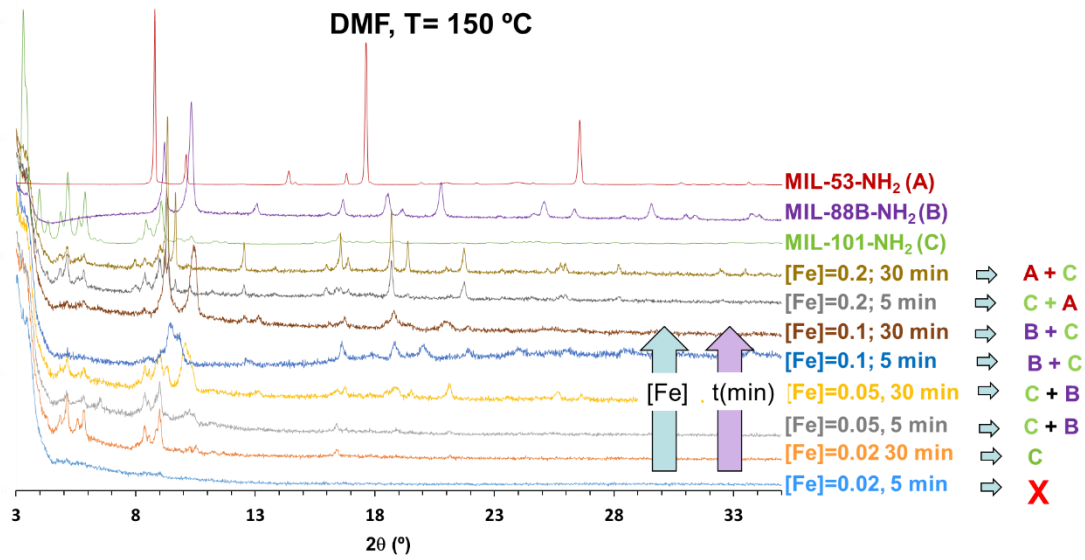

Figure AVI. 9: PXRD patterns for the MW investigation of the system $FeCl_3 \cdot 6\ H_2O$ / $H_2BDC\text{-}NH_2$ in **DMF** (V DMF = 4 mL, T= 150 °C, ligand:metal= 1:1) after activation with EtOH, compared to simulated MIL-88B-NH_2 (purple) and MIL-101-NH_2 (green).

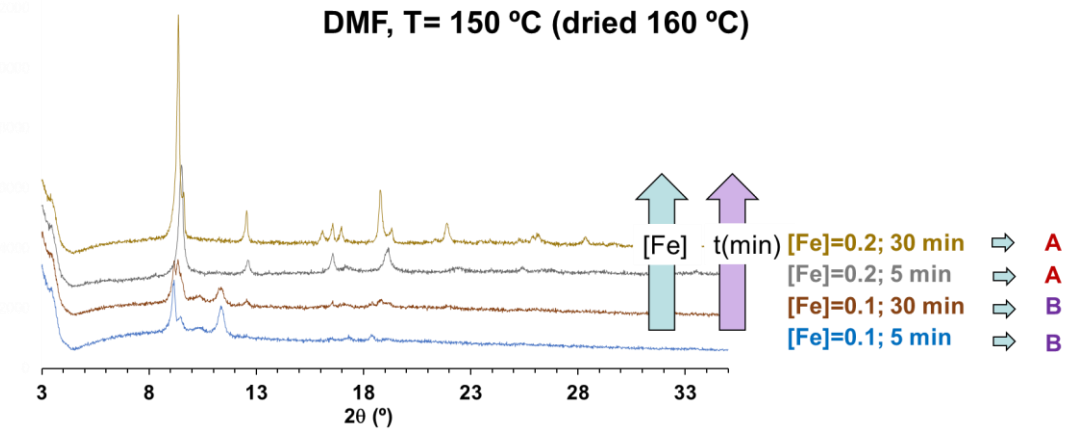

Figure AVI. 10: XRPD patterns for the MW investigation of the system $FeCl_3 \cdot 6\ H_2O$ / $H_2BDC\text{-}NH_2$ in **DMF** (V DMF = 4 mL, T= 150 °C, ligand:metal= 1:1) after activation with EtOH and dried at 160 ºC, for better discriminating between the different Fe-BDC-NH_2 MOF phases

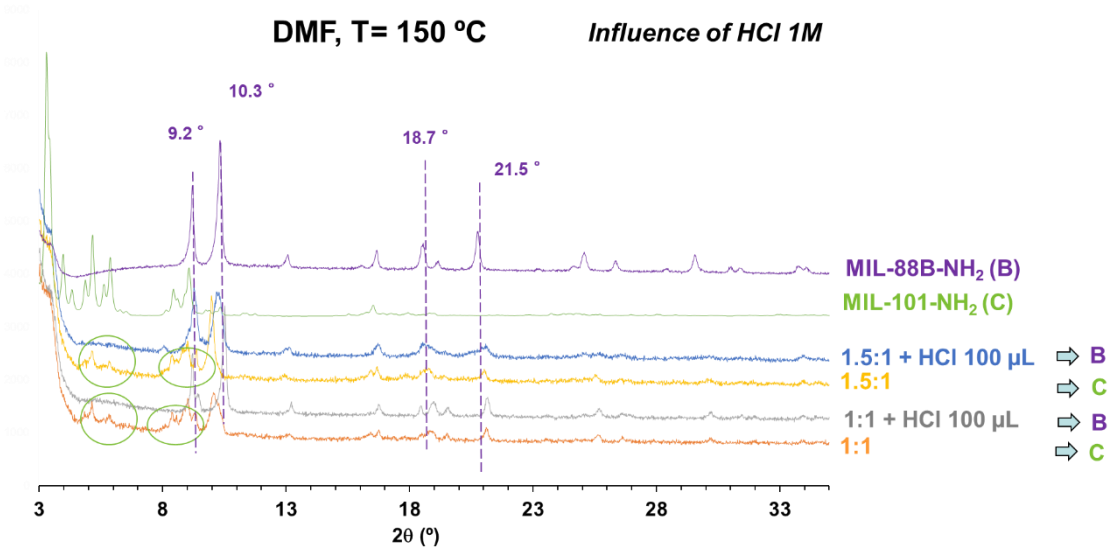

Figure AVI. 11: XRPD patterns for the MW investigation of the system $FeCl_3 \cdot 6\ H_2O$ / $H_2BDC\text{-}NH_2$ / HCl in **DMF** (V DMF = 4 mL, T= 150 °C, t= 30 min) after activation with EtOH, compared to simulated MIL-88B-NH_2 (purple) and MIL-101-NH_2 (green).

VI.III. Particle size and reaction yield

Table AVI. 9: Particle size and reaction yield for the MW investigation of the system $FeCl_3 \cdot 6\ H_2O$ / $H_2BDC\text{-}NH_2$ in **water** (V H_2O = 4 mL, **T= 100 °C**, t= 5 min)

[Fe] (M)	Particle size (Ø nm)	PdI	Yield (wt.%)	STY ($kg \cdot m^{-3} \cdot d^{-1}$)	Result
0.02	450 ± 200	0.25 ± 0.01	~100(*)	3850	**C**
0.05	190 ± 70	0.32 ± 0.01	~100(*)	5400	**C** + **A**
0.1	450 ± 150	0.20 ± 0.06	~100(*)	8700	**C** + **A**
0.2	260 ± 70	0.11 ± 0.02	70	10400	**A**

** remaining ligand found prior activation due to poor $H_2BDC\text{-}NH_2$ solubility in water*

Table AVI. 10: Particle size and reaction yield for the MW investigation of the system $FeCl_3 \cdot 6\ H_2O$ / $H_2BDC\text{-}NH_2$ in **water** (V H_2O = 4 mL, **T= 150 °C**, t= 5 min)

[Fe] (M)	Particle size (Ø nm)	PdI	Yield (wt.%)	STY ($kg \cdot m^{-3} \cdot d^{-1}$)	Result
0.02	300 ± 85	0.20 ± 0.11	~100(*)	2950	**C** + **A**
0.05	300 ± 90	0.37 ± 0.11	~100(*)	3900	**A** + **C**
0.1	325 ± 150	0.28 ± 0.03	60	4300	**A**
0.2	310 ± 120	0.30 ± 0.03	50	7000	**A**

** remaining ligand found prior activation due to poor $H_2BDC\text{-}NH_2$ solubility in water*

Table AVI. 11: Particle size and reaction yield for the MW investigation of the system $FeCl_3 \cdot 6\ H_2O$ / $H_2BDC\text{-}NH_2$ / HCl in **water** ([Fe] = 0.05 M, V H_2O = 4 mL, T= 100 °C, t= 5 min)

HCl (µL)	Particle size (Ø nm)	PdI	Yield (wt.%)	STY ($kg \cdot m^{-3} \cdot d^{-1}$)	Result
0	240 ± 100	0.35 ± 0.06	~100(*)	8500	**C** + **A**
50	480 ± 80	0.41 ± 0.05	~100(*)	8000	**C** + **A**
100	500 ± 100	0.50 ± 0.06	~100(*)	7500	**C** + **A**
150	590 ± 140	0.41 ± 0.06	~100(*)	7300	**A** + **C**
200	320 ± 110	0.39 ± 0.07	~100(*)	6500	**A**

** remaining ligand found prior activation due to poor $H_2BDC\text{-}NH_2$ solubility in water*

Table AVI. 12: Particle size and reaction yield for the MW investigation of the system $FeCl_3 \cdot 6\ H_2O$ / $H_2BDC\text{-}NH_2$ in **ethanol** (V EtOH = 4 mL, T= 150 °C, t= 5 min)

[Fe] (M)	Particle size (Ø nm)	PdI	Yield (wt.%)	STY ($kg \cdot m^{-3} \cdot d^{-1}$)	Result
0.02	300 ± 80	0.28 ± 0.12	~100	2050	**B**
0.05	250 ± 140	0.29 ± 0.09	85	3100	**B**
0.1	250 ± 80	0.12 ± 0.03	45	3300	**B**
0.2	210 ± 70	0.10 ± 0.02	40	6200	**B**

Table AVI. 13: Particle size and reaction yield for the MW investigation of the system $FeCl_3 \cdot 6\ H_2O$ / $H_2BDC\text{-}NH_2$ in **ethanol** (V EtOH = 4 mL, T= 150 °C, t= 5 min, [Fe]=0.2 M)

Ligand:metal	Particle size (Ø nm)	PdI	Yield (wt.%)	STY ($kg \cdot m^{-3} \cdot d^{-1}$)	Result
0.25:1	300 ± 85	0.15 ± 0.07	90	3200	**B**
0.5:1	290 ± 70	0.07 ± 0.05	60	4700	**B**
1:1	210 ± 70	0.10 ± 0.02	40	6200	**B**
1.5:1	270 ± 80	0.12 ± 0.06	35	5600	**B**

Table AVI. 14: Particle size and reaction yield for the MW investigation of the system $FeCl_3 \cdot 6\ H_2O$ / $H_2BDC\text{-}NH_2$ in **ethanol** (V EtOH = 4 mL, T= 100 °C, [Fe]=0.1 M)

Time (min)	Particle size (Ø nm)	PdI	Yield (wt.%)	STY ($kg \cdot m^{-3} \cdot d^{-1}$)	Result
5	220 ± 80	0.25 ± 0.05	95	16000	**B**
10	320± 80	0.34 ± 0.08	~100	10700	**B**
20	240 ± 80	0.28 ± 0.04	~100	6800	**C**
30	290 ± 70	0.20 ± 0.02	80	3500	**C**

Table AVI. 15: Particle size and reaction yield for the MW investigation of the system $FeCl_3 \cdot 6\ H_2O$ / $H_2BDC\text{-}NH_2$ in **ethanol** (V EtOH = 4 mL, T= 150 °C, [Fe]=0.1 M,)

Time (min)	Particle size (Ø nm)	PdI	Yield (wt.%)	STY ($kg \cdot m^{-3} \cdot d^{-1}$)	Result
5	250 ± 80	0.12 ± 0.03	40	3300	**B**
10	250 ± 100	0.16 ± 0.08	90	2600	**B**
20	250 ± 70	0.11 ± 0.01	60	2000	**B**
30	230 ± 60	0.07 ± 0.04	50	2100	**B**

Table AVI. 16: Particle size and reaction yield for the MW investigation of the system $FeCl_3 \cdot 6\ H_2O$ / $H_2BDC\text{-}NH_2$ in **DMF** (V DMF = 4 mL, T= 150 °C, ligand:metal=1:1)

[Fe] (M)	time (min)	Particle size (Ø nm)	PdI	Yield (wt.%)	STY ($kg \cdot m^{-3} \cdot d^{-1}$)	Result
0.02	5	-	-	-	-	x
	30	300 ± 80	0.12 ± 0.09	70	600	**C**
0.05	5	250 ± 60	0.14 ± 0.09	40	1500	**C** + **B**
	30	270 ± 80	0.26 ± 0.09	70	400	**C** + **B**
0.1	5	270 ± 70	0.08 ± 0.01	50	3500	**B** + **C**
	30	490 ± 150	0.20 ± 0.02	70	2300	**B** + **C**
0.2	5	230 ± 80	0.20 ± 0.01	20	6000	**C**+ **A**
	30	440 ± 60	0.20 ± 0.02	45	3800	**A** + **C**

Table AVI. 17: Particle size and reaction yield for the MW investigation of the system $FeCl_3 \cdot 6\ H_2O$ / $H_2BDC\text{-}NH_2$ / HCl in **DMF** (V DMF = 4 mL, T= 150 °C, t=30 min, [Fe]= 0.05)

Ligand:metal	HCl (µL)	Particle size (Ø nm)	PdI	Yield (wt.%)	STY ($kg \cdot m^{-3} \cdot d^{-1}$)	Result
1:1	0	270 ± 80	0.26 ± 0.09	70	400	**C** + **B**
	100	293 ± 100	0.34 ± 0.06	90	500	**B**
1.5:1	0	500 ± 150	0.18 ± 0.02	70	450	**C** + **B**
	100	600 ± 130	0.20 ± 0.09	~100	600	**B**

VI.IV. TEM

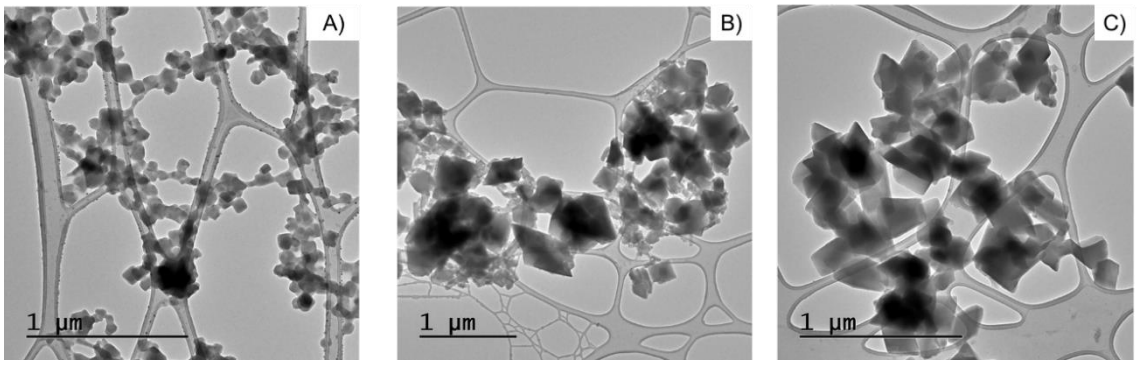

Figure AVI. 12: TEM micrographs for PXRD for the MW investigation of the system $FeCl_3 \cdot 6\ H_2O$ / $H_2BDC\text{-}NH_2$ / HCl in **water** (V H_2O = 4 mL, t= 5 min) after activation with EtOH: A) T= 100 °C, HCl 0.1 M = 0 µL; B) T= 100 °C, HCl 0.1 M = 100 µL; C) T= 150 °C, HCl 0.1 M = 0 µL

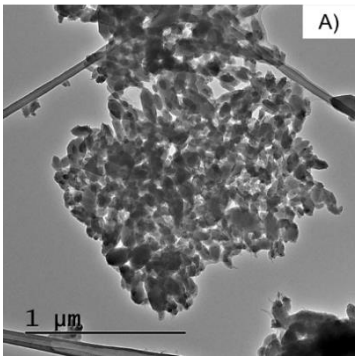

Figure AVI. 13: TEM micrographs for PXRD for the MW investigation of the system $FeCl_3 \cdot 6\ H_2O$ / $H_2BDC\text{-}NH_2$ in **ethanol** (V EtOH = 4 mL, t= 5 min T= 100 °C, [Fe]= 0.1 M) after activation with EtOH scale bar= 1 µm

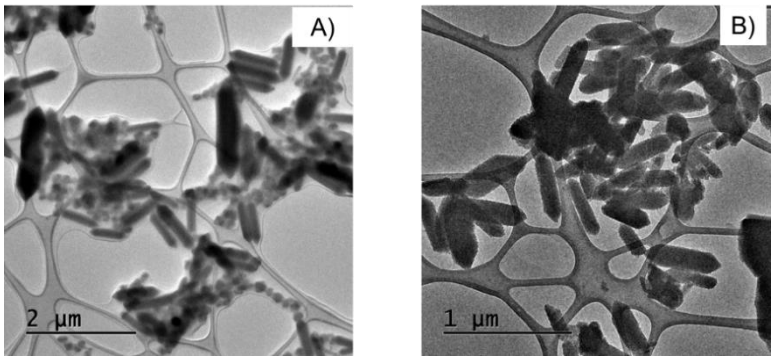

Figure AVI. 14: TEM micrographs for PXRD for the MW investigation of the system $FeCl_3 \cdot 6\ H_2O$ / $H_2BDC\text{-}NH_2$ / HCl in **DMF** (V DMF = 4 mL, t= 30 min, T= 100 °C, ligand:metal= 1:1) after activation with EtOH: A) HCl 0.1 M = 0 µL (scale bar= 2 µm); B) HCl 0.1 M = 100 µL (scale bar= 1 µm)

APPENDIX VII

Supporting information Chapter 6

VII.I. Materials and characterization techniques

Lipase from *Candida rugose* (*C-r*-lipase) (lyophilized powder, Type VII, nominal activity >> 700 U mg^{-1}), Amano Lipase from *Pseudomonas fluorescens* (*P-f*-lipase) (nominal activity ≥ 20,000 U · g^{-1}), *para*-nitrophenyl palmitate (*p*-NPP), bovine serum albumin (BSA) and Coomassie Brilliant Blue G-250, Fumaric acid, and iron(III) chloride hexahydrate were purchased from were supplied by Sigma Aldrich. A refined soybean oil was purchased from Mi Comestica Casera (Spain, ref.: ASJVB0118) mainly by palmitic acid (11 wt%, C16:0 A), stearic acid (5 wt.%, C18:0 A), oleic acid (24 wt.%, C18:1 A), linoleic acid (49 wt.% C18:2 A) and linolenic acid (7 wt.%, C18:3 A) (as determined by gas chromatography coupled to mass spectrometry following ISO 12966), (with average MW=920 g · mol^{-1} and density ρ=0.92 g · mL^{-1}.[1] The rest of reagents were purchased of ACS reagent grade from Merck.

Powder X-ray diffraction (PXRD) analysis was carried out on a PANalytical® Empyrean powder diffractometer (PANalytical, Lelyweg, The Netherlands) using a Cu Kα radiation (λ = 1.5406 Å) at 2θ ($\circ$) from 3 to 35 with a step of 0.013º and scanning rate of 0.1º · s^{-1}. Fourier transform infrared (FTIR) spectra were collected in the range 400–4000 cm^{-1} by a Thermo Nicolet 6700 FT-IR with an attenuated total reflectance (ATR) accessory instrument. Thermogravimetric analyses (TGA) were performed on a Q-600 thermobalance (TA Instruments, New Castle, De, USA). For this purpose, sample was heated in a continuous air flow (100 mL · min^{-1}) with a heating ramp rate of 5 °C · min^{-1} from 30 up to 600 °C. The scanning electron microscopy (SEM) images were taken on a Hitachi TM.100 tabletop SEM, equipped with a wolframium filament with a

constant voltage of 15 kV and a resolution of 200 nm and on a FEI/Philips XL-30 Field Emission ESEM. The UV-Vis spectra were recorded on a Perkin Elmer® Lambda 1050 UV/vis/NIR spectrophotometer (Perkin Elmer, Waltham, MA, USA).

VII.II. Biocatalyst preparation

VII.II.i. Lipase encapsulation and activity assay

Determination of protein content was carried out according to the Bradford Method.[2] It was an indirect measurement that evaluated the free lipases in the reaction media before and after encapsulation in MIL-88A.

Dye reagent was prepared as follows. Coomassie Brilliant Blue G-250 (100 mg) was dissolved in 50 mL 95 % ethanol. To this solution 100 mL 85 % (w/v) phosphoric acid was added. The resulting solution was diluted to a final volume of 1L. Final concentrations in the dye reagent were 0.01% (w/v) Coomassie Brilliant Blue G-250, 4.7% (w/v) ethanol, and 8.5% (w/v) phosphoric acid. Variation in absorbance (595 nm) after incubation for 5 min at R.T. was done in the UV-Vis SPECTROstar Omega (BMG Labtech, Ortenberg, Germany) using a 96 well plate filled with 200 μL of the dye reagent and 50 μL of the sample.

The enzyme encapsulation efficiency was determined by the following formula:

$$\text{Enzyme encapsulation efficiency \%} = (C_1V_1 - C_2V_2) * 100 / (C_1V_1) \qquad \text{Eqn (4)}$$

where C_1 and C_2 are the initial and final enzyme concentration, respectively, and V_1 and V_2 correspond to the volume of the enzyme solution used for encapsulation and the supernatant after encapsulation, respectively.

Activity of free and encapsulated lipases was evaluated by quantifying the relative ester hydrolysis of *p*-NPP promoted by the macromolecules:

***P-f*-lipase activity**: According to the method of Ye *et al.*, [3] ester hydrolysis was started by addition of 2 mg free lipase or 20 mg *P-f*-lipase@MIL-88A to the assay mixture, consisting of the following solutions: 0.5 mL of a 2 mM *p*-NPP solution in ethanol and 0.5 mL of a 0.1 M PBS pH = 7.0. The assay mixture was incubated at 32 °C under 400 rpm for 5 min. 0.5 mL of Na_2HCO_3 (0.5 M) were added to stop the reaction and after centrifugation (6000 rpm, 10 min), 0.5 mL of supernatant were taken and 10-fold diluted with deionized water to determine the

produced *p*-nitrophenol, measuring the increase in the absorption band intensity at 410 nm by UV-vis spectroscopy.

***C-r*-lipase activity**: Similarly, activity of free lipase and *C-r*-lipase@MIL-88A was carried out by monitoring the increase in the absorption band at 405 nm, which was promoted by the hydrolysis of *p*-NPP following the methodology reported in our group previous work.[4] The assay mixture consisted of 2 mL of the substrate solution and the free or encapsulated *C-r*-lipase. The substrate solution was a mixture of the following solutions: (30 mg p- NPP in 10 mL isopropanol; 0.1 g arabic gum and 0.4 mL of Triton X-100 in 90 mL 50mM phosphate buffer solution (PBS) of pH 7). The assay mixture was incubated at 37 °C for 5 min and the released p-nitro phenol was measured at 405 nm by UV-vis spectroscopy.

VII.II.ii. Synthetic protocol optimization

The MOF selected for enzyme immobilization, iron(III) fumarate MIL-88A, has a water-based synthesis protocol *a priori* compatible with the lipases to be encapsulated. Nevertheless, the previously reported synthesis of MIL-88A was considered harsh for the lipases,[5,6] and required adaptation for the attainment of lipase@MIL-88A composites. Lipase immobilization conditions in the MIL-88A were thoroughly studied by investigating the influence of different reaction parameters including temperature, reaction time, pH and lipase:MOF ratio.

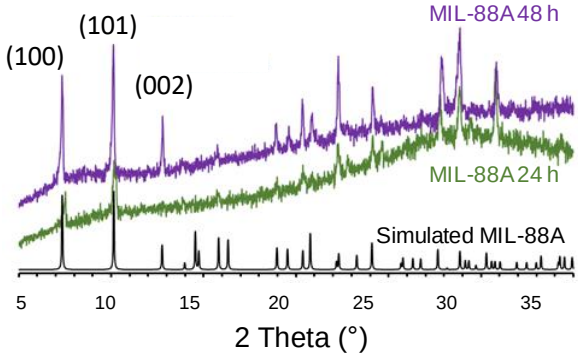

Figure AVII. 1:XRPD patterns of simulated MIL-88A and synthesized MIL-88A after 24 or 48 h.

Reaction temperature was first considered, as MIL-88A conventional synthesis requires high temperatures (65-100 ºC),[5,6] not compatible with the enzyme viability. Therefore, decrease of the temperature of reaction was overriding and preliminary attempts of MIL-88A synthesis were carried out at 50 °C for 24 and 48 h. While XRPD patterns after 24 h (Figure AVII. 1) revealed broad Bragg peaks consistent with the open form of MIL-88A structure, crystallinity was improved

after 48 h of reaction. However, both synthetic conditions resulted on total activity loss of the lipases due to the prolonged exposure to 50 °C.

To overcome this constrain, a first step in absence of the enzyme was included at a higher temperature for a very short time (65 °C during 10 min), which promoted the MOF formation, as evidenced by observing the main reflections of MIL-88A, together with a sharp diffraction peak at 2θ: 29°, corresponding to unreacted recrystallized fumaric acid (Figure AVII. 2). In a second stage, the preformed MOF was incubated with the *P-f*-lipase at 50 °C for 24 h. These reaction conditions led to a peak broadening, consistent with the formation of defects within the MOF crystals due to the presence of the enzyme (Figure AVII. 2), and to a significant decrease on the final activity of the bio-catalyst (from 0.97 to 0.13 mmol · L^{-1} of *p*-nitrophenol). Considering that the integrity (activity) of the free enzyme was confirmed at 50 ºC for 24 h, enzyme denaturalization might be here explained by the low pH of the reaction medium (pH = 2.4). This is in full agreement with the reported pH-stability of the *P-f*-lipase, within a 3-10 pH-range. [7] Therefore, the first step was settled to 65 °C during 10 min, but second step at 50 °C required additional optimization.

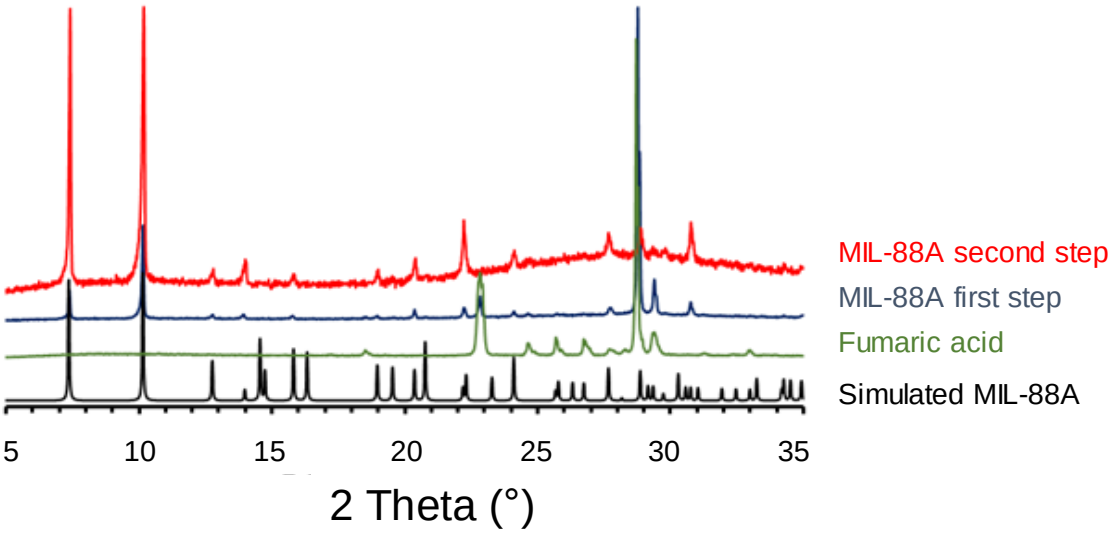

Figure AVII. 2: XRPD patterns of simulated MIL-88A (black) and the synthesized MIL-88A after the first (blue) and second step (red) of the synthetic protocol. Free fumaric acid is in green.

Role of the pH and time. Further optimization was carried out modifying the pH of the second reaction step. Previous studies demonstrated that an increase in the pH of the MIL-88A reaction accelerates its crystallization, [5] probably by a faster ligand deprotonation. So, the pH was increased (at 3, 4 or 5), reducing the reaction time to 2 h, regardless the pH value (Figure AVII. 3 A). Note that this effect might be beneficial for the *P-f*-lipase stability, not only for the less acidic pH but also for a shorter exposure to the reaction conditions.

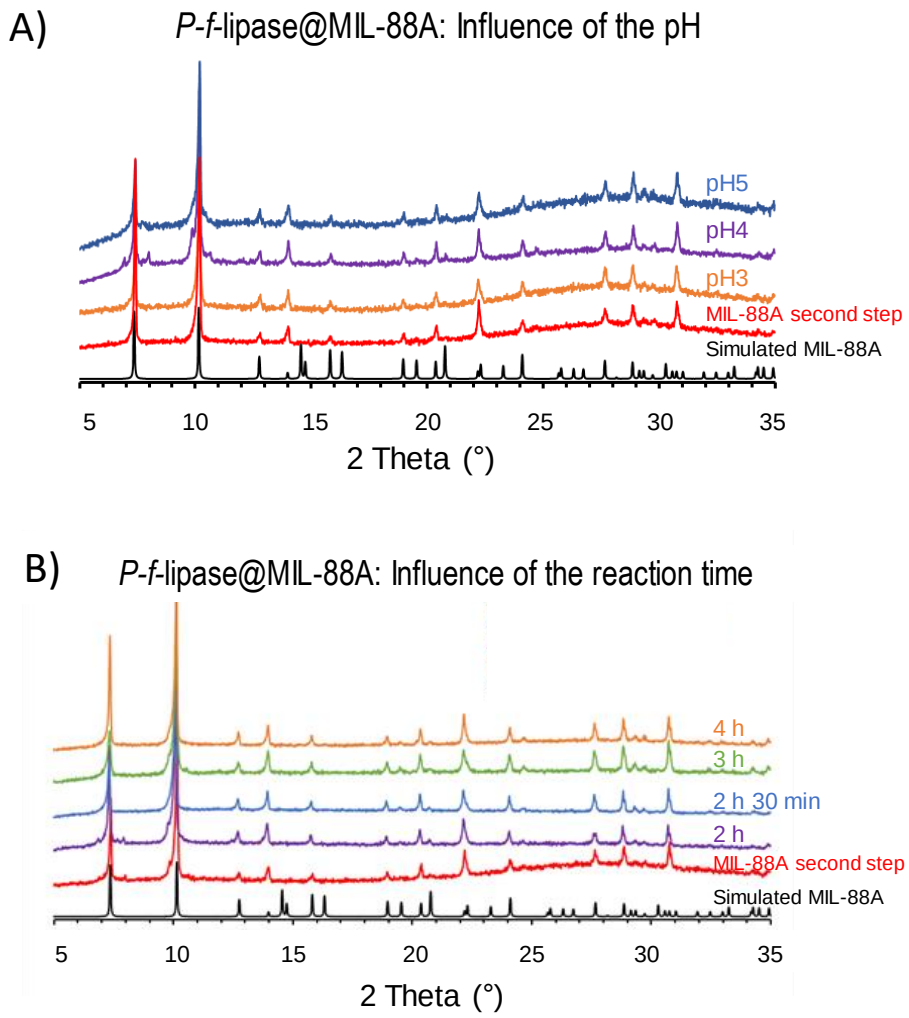

Figure AVII. 3: XRPD patterns of MIL-88A and *P-f*-lipaseMIL-88A evaluating in the second reaction step: A) the effect of the pH (3, 4 or 5) under fixed time (2 h) and B) the effect of the reaction time (2, 2.5, 3 or 4 h) under fixed pH = 3.

The loading of the lipase within the MIL-88A, estimated by Bradford Method, decreased with the increase of pH (Table AVII. 1A). Note that the catalytic activity of the biocomposites, determined by means of the *p*-NPP hydrolysis reaction, was lower than the free enzyme, which could be related with diffusional constraints. Interestingly, the biocatalytic activity also decreased with the pH increment in both the free and the encapsulated lipase, observing a maximum activity at pH 3 (Table AVII. 1 A). Additionally, longer reaction times (up to 4 h) did not lead to a significant increment in the activity or an improvement on MOF crystallinity (Table AVII. 1 B and Figure AVII. 3 B). Consequently, the optimized conditions selected for the second step reaction are 50 °C for 2 h at a pH=3 (Table AVII. 1).

Table AVII. 1:Encapsulation efficiency of the biocomposites and biocatalytic activity (estimated by *para*-nitrophenyl palmitate, *p*-NPP, hydrolysis)

A: as a function of the pH (conditions: 50 ºC, 2 h with 10 mg of lipase)			
Sample	pH	Encapsulation efficiency (%)[a]	Concentration of *p*-nitrophenol (mmol · L^{-1})
Free Lipase	3	-	0.97
P-f-lipase@MIL-88A	3	99.1 ± 0.5	0.86
Free Lipase	4	-	0.92
P-f-lipase@MIL-88A	4	91 ± 0.5	0.67
Free Lipase	5	-	0.84
P-f-lipase@MIL-88A	5	87.2 ± 0.6	0.56
B: as a function of time (conditions: 50ºC with 10 mg of lipase in pH=3)			
Sample	Time (h)	Encapsulation efficiency (%)[a]	Concentration of *p*-nitrophenol (mmol · L^{-1})
Free Lipase	2	-	0.97
P-f-lipase@MIL-88A	2	99.1 ± 0.5	0.86
Free Lipase	3	-	0.91
P-f-lipase@MIL-88A	3	92.1 ± 0.6	0.78
Free Lipase	4	-	0.82
P-f-lipase@MIL-88A	4	86.2 ± 0.5	0.67

[a] Values were calculated after washing, considering an initial lipase content of 10 mg.

Lipase: MOF ratio. With the aim to optimize the content of encapsulated lipase, different amounts of *P-f*-lipase were added in the second step reaction (5-20 wt.% with respect to the MIL-88A from the first step, see XRPD in Figure AVII. 4 A). Results concerning the efficiency of the encapsulation showed that the associated enzyme increased with the increment on the initial enzyme content (Table AVII. 2A), reaching a maximal loading at 15 wt.%. In contrast, despite the lower enzyme loading of 5 and 10 wt.% samples, they exhibited a higher catalytic activity (~7 g *p*-nitrophenol · g^{-1} lipase). If one expresses the catalytic activity as a function of the total biocatalyst weight, the 10 wt.%. biocomposite discloses a 2.5-fold higher activity than the 5 wt.%. sample (73 *vs.* 29 g *p*-nitrophenol · g^{-1} biocatalyst, respectively). As a result, the optimum amount of *P-f*-lipase to be immobilized in the second step was set to 10 wt.%.

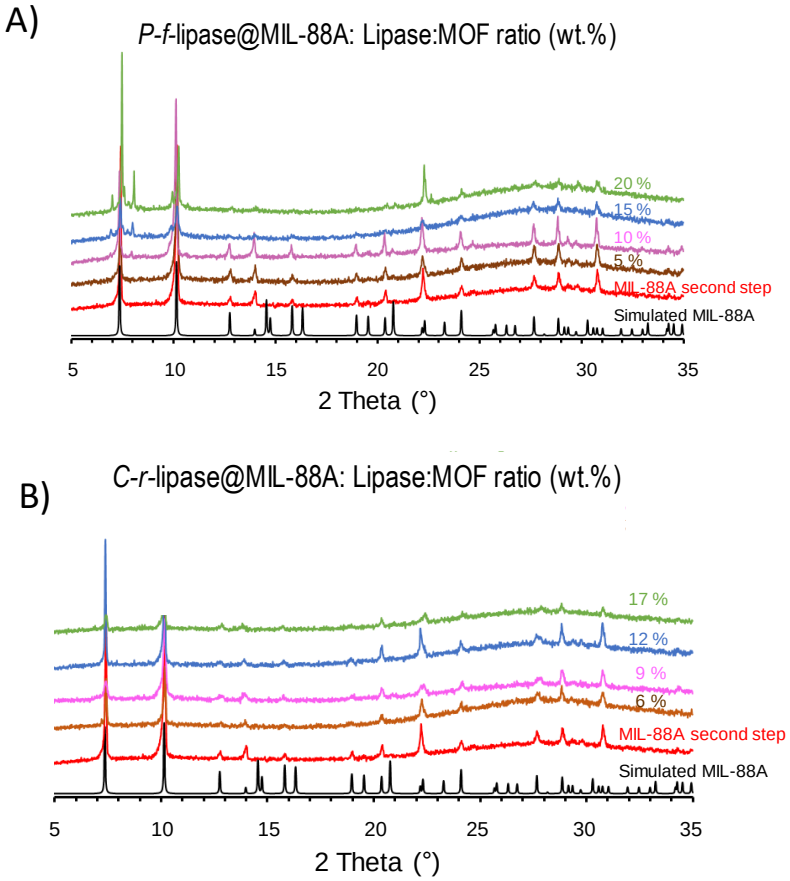

Figure AVII. 4: XRPD patterns of simulated MIL-88A, MIL-88A and lipase@MIL-88A composites with different *P-f*-lipase loadings (top) and with different *C-r*-lipase loadings (bottom).

It is of the interest of this work to consider other lipases for the synthesis of composites to catalyze the biodiesel transesterification and analyze the effect of the enzyme on the activity, hence *C-r*-lipase was also entrapped within the MIL-88A following a similar strategy (see XRPD Figure AVII. 4 B). Considering the different molecular weight from *P-f*-lipase and *C-r*-lipase (34 *vs.* 60 kDa), molar ratio was

optimized for the *C-r*-lipase. Whereas optimal molar ratio for *P-f*-lipase was 1.72×10^{-3} (corresponding to 10 or 17 wt.% for *P-f*-lipase or *C-r*-lipase, respectively) equal molar ratio for *C-r*-lipase (Table AVII. 2 B) led to a poor encapsulation efficiency (99.1 *vs.* 78.2 % for *P-f*-lipase and *C-r*-lipase, respectively) and the reduction of the catalytic activity. The heavier molecular weight of *C-r*-lipase, as well as the differences on their chemical nature (*i.e.* isoelectric point = 4.6-4.9 and 4.2 for *P-f*-lipase and *C-r*-lipase, respectively)[8,9] might affect the accessibility and/or interactions of the enzyme and the MOF.

Table AVII. 2: Optimization of the amount of lipase in the *P-f* and *C-r*-lipase@MIL-88A composite.

A: *P-f*-lipase@MIL-88A biocomposite			
Molar ratio (Lipase/MOF)	Weight % (mg lipase · 100 mg^{-1} MOF [a])	Encapsulation efficiency (%)[b] (loading wt.%)[c]	Activity (g *p*-nitrophenol · g^{-1} lipase)
8.64×10^{-4}	5	96.2 ± 0.5 (4.8 ± 0.5)	6.0
1.72×10^{-3}	**10**	**99.1 ± 0.5 (9.9 ± 0.5)**	**7.3**
2.58×10^{-3}	15	97.1 ± 0.6 (14.5 ± 0.4)	3.2
3.4×10^{-3}	20	78.5 ± 0.6 (15.7 ± 0.5)	2.6
B: *C-r*-lipase@MIL-88A biocomposite			
Molar ratio (Lipase/MOF)	Weight % (mg lipase · 100 mg^{-1} MOF [a])	Encapsulation efficiency (%)[b] (loading wt.%)[c]	Activity (g *p*-nitrophenol · g^{-1} lipase)
6.6×10^{-4}	6	91.3 ± 0.3 (5.5 ± 0.3)	6.0
8.82×10^{-4}	**9**	**95.2 ± 0.6 (8.6 ± 0.5)**	**7.4**
1.17×10^{-3}	12	91.8 ± 0.5 (11.0 ± 0.4)	5.8
1.72×10^{-3}	17	78.2 ± 0.3 (12.2 ± 0.4)	4.4

[a.] MIL-88A as synthesized and unreacted precursors from first step

[b.] Values were calculated after washing

[c.] Enzyme content with respect to the empty dehydrated MOF

By decreasing the *C-r*-lipase amount, a higher encapsulation efficiency (95 %) with a similar catalytic activity than the *P-f*-lipase@MIL-88 A (7.4 *vs.* 7.3 g *p*-nitrophenol · g^{-1} lipase) was found for the *C-r*-lipase@MIL-88 A biocatalyst, with an optimal content of 9 wt.% enzyme. The catalytic activity, expressed as a function of the total biocatalyst weight, reaches 60 g *p*-nitrophenol · g^{-1} biocatalyst.

After all this considerations, fully active *P-f*-lipaseMIL-88A and *C-r*-lipase@MIL-88A biocatalyst were synthesized using a simple two-steps *in situ* and soft green protocol (see Figure 6. 1). Therefore is was successfully validated a new BaS association procedure to a newly proposed MOF.

VII.II.iii. Biocatalyst characterization

Table AVII. 3: Particle size determined by SEM observation

Sample	Conditions	Average length (µm) (n=60)	Average thickness (µm) (n=60)
MIL-88A	1st step (10 min, 65 °C) (after washing)	1.7 ± 0.5	0.21 ± 0.07
MIL-88A	2nd step (pH=3, 2 h, 50 °C)	2.0 ± 0.5	0.24 ± 0.08
P-f-lipase@MIL-88A	pH=3 , 2 h, 50 °C	2.6 ± 0.3	0.6 ± 0.2
C-r-lipase@MIL-88A	pH=3 , 2 h, 50 °C	2.2 ± 0.4	0.5 ± 0.1

Effect of the pH on the lipase stability: In order to investigate the effect of the pH on the lipase stability and the protection provided by the MOF, the free (2 mg) or encapsulated lipases (20 mg lipase@MOF) were incubated in 2 mL of a 50 mM PBS solution at different pH values (from 2.0 to 5.0) at RT. After 2 h incubation, the material was recovered by centrifugation (6000 rpm, 10 min) and the residual relative activity was determined, as previously described in Section

IV.II.i. The acidity and alkalinity of the buffer solutions were varied by using either 0.1 M HCl or 0.1 M NaOH solutions.

VII.III. Biodiesel production

Methanolysis reactions were carried out in a round-bottom flask using 0.5 g of soybean oil, 100 mg of lipase@MIL-88A and water (varying from 5 to 15 wt.% the content based on oil weight) at mild temperatures (40-60 °C) during different times (12-60 h) in order to optimize the reaction conditions. During the reaction, methanol was added in two steps: at 0 and 6 h. Methannol:oil molar ratio was also varied (2:1, 4:1, 6:1 and 8:1). All reactions were carried out at least three times.

Pure product was separated from glycerol by adding 2 mL of *n*-hexane and 500 μL of methanol to the reaction mixture and centrifuging at 13000 rpm for 10 min. The biodiesel supernatant was dried in the oven at 65°C to evaporate solvents. Then, biodiesel with a 40-fold dilution in *n*-hexane was analyzed by gas chromatography coupled to mass spectrometry GC-MS. [10] To the mixture 300 μL of 1.0 mg/mL methyl margarate (C17:0 E) was added as the internal control.

GC-MS determination of biodiesel selectivity: The methyl esters produced in the transtereification reaction catalyzed by the lipase@MIL-88A biocatalyst were analyzed using GC-MS (Bruker SCION 436-GC; Electron energy 70 eV, Emission 300 V; He, flow rate: 1 $cm^3 \cdot min^{-1}$; Column WCOT fused silica 30 m x 0.25 mm ID x 0.25 μm), employing the NIST EI-MS spectra library (v2.0) with a minimum match score of 700 for the identification of the different compounds.

The injector temperature was set to 220 °C, the oven temperature followed a ramp: first, heating from 40 °C up to 70 °C with a 3 $°C \cdot min^{-1}$ rate, temperature was maintained at 70 °C for 5 min then, increased to 210 °C with 5 $°C \cdot min^{-1}$ heating ramp and finally, a slower ramp (1 $°C \cdot min^{-1}$) from 210 to 220 °C, being 220 °C the final oven temperature.

This qualitative determination enabled the determination of the biodiesel selectivity (%), defined by the transesterification activity, analyzing if the oil has been converted to fatty acid methyl esters (FAMEs) or if there is unwanted hydrolysis reaction (producing free fatty acids). Biodiesel selectivity was calculated by:

$$Biodiesel\ selectivity\ (\%) = \frac{A_{esters}}{A_{total}} \qquad \text{Eqn (5)}$$

where A_{esters} is the total area under the chromatogram corresponding only to ester products and A_{total} is the total area of both esters and fatty acids (C16 and C18).

Qualitative termination of the individual FAMEs produced, named here as Production was calculated by:

$$Production\ (\%) = \frac{A_{ester\ X}}{A_{total}} \qquad \text{Eqn (6)}$$

where $A_{ester\ X}$ is the total area under the chromatogram corresponding to a particular methyl ester product and A_{total} is the total area of both esters and fatty acids (C16 and C18).

The reusability of *P-f*-lipase@MIL-88A composite was investigated in the transesterification reaction of soybean oil with methanol under the optimal conditions with highest biocatalyst selectivity. At the end of the reaction, the biocatalyst was recovered by centrifugation (6000 rpm, 5 min), thoroughly washed with *n*-hexane and isobuthanol, and dried at RT before the following cycle of reaction. The structure of the recovered biocatalyst was monitored by PXRD and FTIR after the last cycle.

Bibliography

(1) Patzek, T. W. A First Law Thermodynamic Analysis of Biodiesel Production From Soybean. *Bull. Sci. Technol. Soc.* **2009**, *29* (3), 194–204. https://doi.org/10.1177/0270467609334022.

(2) Bradford, M. M. A Rapid and Sensitive Method for the Quantitation of Microgram Quantities of Protein Utilizing the Principle of Protein-Dye Binding. *Anal. Biochem.* **1976**, *72* (1–2), 248–254. https://doi.org/10.1016/0003-2697(76)90527-3.

(3) Ye, P.; Xu, Z.-K.; Che, A.-F.; Wu, J.; Seta, P. Chitosan-Tethered Poly(Acrylonitrile-Co-Maleic Acid) Hollow Fiber Membrane for Lipase Immobilization. *Biomaterials* **2005**, *26* (32), 6394–6403. https://doi.org/10.1016/J.BIOMATERIALS.2005.04.019.

(4) Rafiei, S.; Tangestaninejad, S.; Horcajada, P.; Moghadam, M.; Mirkhani, V.; Mohammadpoor-Baltork, I.; Kardanpour, R.; Zadehahmadi, F. Efficient Biodiesel Production Using a Lipase@ZIF-67 Nanobioreactor. *Chem. Eng. J.* **2018**, *334*, 1233–1241. https://doi.org/10.1016/J.CEJ.2017.10.094.

(5) Chalati, T.; Horcajada, P.; Gref, R.; Couvreur, P.; Serre, C. Optimisation of the Synthesis of MOF Nanoparticles Made of Flexible Porous Iron Fumarate MIL-88A. *J. Mater. Chem.* **2011**, *21* (7), 2220–2227. https://doi.org/10.1039/C0JM03563G.

(6) Serre, C.; Millange, F.; Surblé, S.; Férey, G. A Route to the Synthesis of Trivalent Transition-Metal Porous Carboxylates with Trimeric Secondary Building Units. *Angew. Chemie Int. Ed.* **2004**, *43* (46), 6285–6289. https://doi.org/10.1002/anie.200454250.

(7) Kulkarni, N.; Gadre, R. V. Production and Properties of an Alkaline, Thermophilic Lipase from Pseudomonas Fluorescens NS2W. *J. Ind. Microbiol. Biotechnol.* **2002**, *28* (6), 344–348. https://doi.org/10.1038/sj/jim/7000254.

(8) Ren, L.; Jia, H.; Yu, M.; Shen, W.; Zhou, H.; Wei, P. Enhanced Catalytic Ability of Candida Rugosa Lipase Immobilized on Pore-Enlarged Hollow Silica Microspheres and Cross-Linked by Modified Dextran in Both Aqueous and Non-Aqueous Phases. *Biotechnol. Bioprocess Eng.* **2013**, *18* (5), 888–896. https://doi.org/10.1007/s12257-013-0044-7.

(9) Kierkels, J. G. T.; Vleugels, L. F. W.; Geladé, E. T. F.; Vermeulen, D. P.; Kamphuis, J.; Wandrey, C.; van den Tweel, W. J. J. Pseudomonas Fluorescens Lipase Adsorption and the Kinetics of Hydrolysis in a Dynamic Emulsion System. *Enzyme Microb. Technol.* **1994**, *16* (6), 513–521. https://doi.org/10.1016/0141-0229(94)90023-X.

(10) Su, F.; Peng, C.; Li, G.-L.; Xu, L.; Yan, Y.-J. Biodiesel Production from Woody Oil Catalyzed by Candida Rugosa Lipase in Ionic Liquid. *Renew. Energy* **2016**, *90*, 329–335. https://doi.org/10.1016/J.RENENE.2016.01.029.

APPENDIX VIII

List of Publications

During the development of this thesis, AAV has participated as coauthor in 1 book chapter and 10 scientific papers (2 of them pending of submission), contributing as first author to 6 of them. It is interested to outstand that she has an h-index of 5 (Scopus Ana Arenas-Vivo, June 2021) and that all her published articles (besides the recently accepted publication in 2021, presented un Chapter 4), have been cited at least twice.

Book Chapter:

Authors: **Ana Arenas-Vivo** & Patricia Horcajada,
Title: Cepter 1: Antimicrobial Metal-Organic Frameworks;
Book: *Metal-Organic Frameworks* of Central West Publishing.
State: Published May 2019. ISBN: 978-1-925823-57-8

Scientific papers:

1. S. Rafiei,‡ **A. Arenas-Vivo**,‡ S. Tangestaninejad, M. Moghadam, M. Bahadoria, P. Horcajada, "Efficient and selective biodiesel production using a green lipase@MIL-88A biocatalyst", *Journal of American Chemistry Society* (Q1, IF:14.35)
   State: to be submitted
   ‡ Authors contributed equally to this work, co-first author

2. V. Celis-Arias,‡ **A. Arenas-Vivo**,‡ P. Horcajada, G. Amariei, R. Rosal, I. Izquierdo-Barba, M. Vallet Regi, E. Garrido, H. I. Beltrán, S. Loera-Serna, "Bactericidal effect of AgBDC MOF against *Escherichia coli* biofilm",*Acta Biomaterialia* (Q1, IF: 6.139)
State: to be submitted
‡ Authors contributed equally to this work, co-first author

3. **A. Arenas-Vivo**,† S. Rojas, I. Ocaña, A. Torres, M. Liras, F. Salles, D. Ávila P. Horcajada, "Facile synthesis of an Agnanocluster@MOF composite and its superior visible-photocatalytic activity in continuous flow", *Journal of materials Chemistry A,* **2021**, *Accepted Manuscript,* DOI: 10.1039/D1TA02251B (Q1, IF: 11.301)
State: Published
† First author

4. **A. Arenas-Vivo**,† D. Ávila, P. Horcajada, "Phase-selective microwave assisted synthesis of iron amino terephthalate MOFs", *Materials,* **2020**, *13*, 1469, DOI: 10.3390/ma13061469 (Q2, IF: 2.728, open access)
State: Published (cited by 3, Scopus Ana Arenas-Vivo, June 2021)
† First author

5. S. Quaresma; V. André, A. Antunes, S. Vilela, G. Amariei, **A. Arenas-Vivo**, R. Rosal, P. Horcajada, M.T. Duarte. "Novel antibacterial azelaic acid BioMOFs", *Crystal Growth & Design*, **2020,** *20* (1), 370-382, DOI: 10.1021/acs.cgd.9b01302 (Q1, IF:4.131)
State: Published (cited by 9, Scopus Ana Arenas-Vivo, June 2021)

6. S. Rojas, **A. Arenas-Vivo,** P. Horcajada, "Metal-organic frameworks: A novel platform for combined advanced therapies", *Coord. Chem. Rev.*, **2019**, *388*, 202-226, DOI: 10.1016/j.ccr.2019.02.032 (Q1: IF: 14.5)
State: Published (cited by 64, Scopus Ana Arenas-Vivo, April 2021)

7. C. Carrillo-Carrion, R. Martinez, M. F. Navarro, B. Pelaz, E. Polo, A. Olgiati, P. Taboada, M. G. Soliman, **A. Arenas-Vivo**, U. Catalan, S. Fernandez-Castillejo, R. Solà, W. Parak, P. Horcajada, R. Alvarez-Puebla and P. Pino, "Aqueous Stable Gold Nanostar/ZIF-8 Nanocomposites for Light Triggered Release of Active Cargo Inside Living Cells", *Angew. Chem., Int. Ed.*¸**2019,** *58*, 7078, DOI: 10.1002/ange.201902817 (Q1, IF: 12.102)

State: Published (cited by 40, Scopus Ana Arenas-Vivo, June 2021)

8. **A. Arenas-Vivo**,† G. Amariei, S. Aguado, R. Rosal, P. Horcajada, "An Ag-loaded photoactive nano-Metal-Organic Framework as promising biofilm treatment", *Acta Biomaterialia*, **2019**, *97*, 490-500, DOI: 10.1016/j.actbio.2019.08.011 (Q1, IF: 6.139)
State: Published (cited by 7, Scopus Ana Arenas-Vivo, June 2021)
† First author

9. M. F. Navarro Poupard, E. Polo, P. Taboada, **A. Arenas-Vivo**, P. Horcajada, B. Pelaz, P. del Pino, "Aqueous synthesis of copper(II)-imidazolate nanoparticles", *Journal: Inorg. Chem.*, **2018**, *57* (19), 12056-12065, DOI: 10.1021/acs.inorgchem.8b01612 (Q1, IF: 4.7)
State: Published (cited by 2, Scopus Ana Arenas-Vivo, June 2021)

10. **A. Arenas-Vivo**,† F.R. Beltrán, V. Alcázar, M.U. de la Orden, J. Martinez Urreaga, "Fluorescence labeling of high density polyethylene for identification and separation of selected containers in plastics waste streams. Comparison of thermal and photochemical stability of different fluorescent tracers", *Materials Today Communications*, **2017**, *12*, 125-132, DOI: 10.1016/j.mtcomm.2017.07.008 (Q2, IF: 2.678)
State: Published (cited by 5, Scopus Ana Arenas-Vivo, June 2021)
† First author

APPENDIX IX

Oral and poster communications in congresses

During the development of this thesis, AAV has participated and presented her results both in national congress (9 oral presentations and 3 posters) and international congress (2 oral presentations and 3 posters). Remarkably, AAV has also been awarded 2 times with the prize for the best oral presentation, in addition to a special mention in a scientific divulgation contest. Below are included the contributions, with the presenting author underlined

- Title: Antifouling photo-bactericidal combined effect of a Ag@nanoMOF
  Authors: A. Arenas-Vivo, G. Amariei, S. Aguado, R. Rosal, P. Horcajada
  Congress: Youg Researchers Day 2021, AEBIM
  Venue: Online congress
  Date: 12/07/2021
  Type of participation: Oral presentation **Awarded prize for the best 2020 publication by PhD member of AEBIN.**

- Title: Star MOFs: the return of the silver
  Authors: A. Arenas-Vivo, M. Liras, P. Horcajada
  Congress: 8th IMDEA Energy Annual Workshop of young researchers
  Venue: IMDEA Energy, Spain (National congress)
  Date: 13/12/2019
  Type of participation: Flash oral presentation **Awarded prize for the best flash oral presentation**

- Title: Antifouling photo-bactericidal combined effect of a Ag@nanoMOF
  Authors: A. Arenas-Vivo, G. Amariei, S. Aguado, R. Rosal, P. Horcajada
  Congress: IV QuimBioQuim Meeting
  Venue: CiQUS, Universidad de Santiago de Compostela, Spain (National congress)
  Date: 23/10/2019
  Type of participation: Poster

- Title: Selective green biodiesel production using a lipase@MIL-88A biocatalyst
  Authors: A. Arenas-Vivo, S. Rafiei, S. Tangestaninejad, M. Moghadam, M. Bahadoria, P. Horcajada
  Congress: II Brain Wars: the future is in your hands, divulgation contests
  Venue: Universidad Complutense de Madrid, Spain (National seminar)
  Date: 18/10/2019
  Type of participation: Oral presentation. **Awarded special mention for oral presentation**

- Title: Antifouling photo-bactericidal combined effect of a Ag@nanoMOF
  Authors: A. Arenas-Vivo, G. Amariei, T. Hidalgo, S. Aguado, R. Rosal, P. Horcajada
  Congress: Workshop on Layered materials
  Venue: Liblice Castle, Chech Republic (International congress)
  Date: 02/09/2019
  Type of participation: Poster

- Title: Especies activas asociadas a redes metal-orgánicas porosas
  Authors: A. Arenas-Vivo, P. Horcajada
  Congress: IV Simposio anual en Química avanzada
  Venue: Universidad Complutense de Madrid, Spain (National congress)
  Date: 16/07/2019
  Type of participation: Oral presentation

- Title: Selective green biodiesel production using a lipase@MIL-88A biocatalyst
  Authors: A. Arenas-Vivo, S. Rafiei, S. Tangestaninejad, M. Moghadam, M. Bahadoria, P. Horcajada
  Congress: XXXVII Reunión Bienal de la Real Sociedad Española de Química
  Partial Grant for inscription
  Venue: San Sebastian, Spain (National congress)

Date: 28/05/2019
Type of participation: Flash Oral presentation

- Title: A novel Ag-loaded photoactive nano-Metal-Organic Framework as promising biofilm treatment
  Authors: A. Arenas-Vivo, G. Amariei, S. Aguado, R. Rosal, P. Horcajada
  Congress: Jornadas de promoción de la investigación para estudiantes de ingeniería (Divulgation contest)
  Venue: Universidad Rey Juan Carlos de Madrid, Spain (National congress)
  Date: 05/04/2019
  Type of participation: Oral presentation. **Awarded the prize to the best communication**

- Title: Efficient and selective biodiesel production using a green lipase@MIL-88A biocatalyst
  Authors: A. Arenas-Vivo, M. Liras, P. Horcajada
  Congress: 7th IMDEA Energy Annual Workshop of young researchers
  Venue: IMDEA Energy, Spain (National congress)
  Date: 13/12/2018
  Type of participation: Poster and Flash oral presentation

- Title: Antifouling photo-bactericide combined effect of MOF thin film coatings
  Authors: A. Arenas-Vivo, G. Amariei, S. Aguado, R. Rosal, P. Horcajada
  Congress: Brain Wars: the future is in your hands, divulgation contests
  Venue: Universidad Complutense de Madrid, Spain (National seminar)
  Date: 19/10/2018
  Type of participation: Oral presentation

- Title: Antifouling photo-bactericide combined effect of a AgNP@nanoMOF
  Authors: A. Arenas-Vivo, G. Amariei, S. Aguado, R. Rosal, P. Horcajada
  Congress: XXVII International Material Research Conference
  Venue: Cancun, Mexico (International congress)
  Date: 18/08/2018
  Type of participation: Poster

- Title: Antifouling photo-bactericide combined effect of a AgNP@nanoMOF
  Authors: A. Arenas-Vivo, G. Amariei, S. Aguado, R. Rosal, P. Horcajada
  Congress: docMOF 2018, a PhD-run symposium
  Venue: Raitenhaslach, Germany (International congress)

Date: 01/05/2018
Type of participation: Oral Presentation

- Title: Association of active species to Metal-Organic Frameworks
  Authors: A. Arenas-Vivo, P. Horcajada
  Congress: Internal Seminar IMDEA Energy
  Venue: Móstoles, Madrid (National seminar)
  Date: 27/04/2018
  Type of participation: Oral Presentation

- Title: Antifouling photo-bactericide combined effect of a AgNP@nanoMOF
  Authors: A. Arenas-Vivo, G. Amariei, S. Aguado, R. Rosal, P. Horcajada
  Congress: 34th international GFZ congress
  Venue: Cabourg (Caen), France (International congress)
  Date: 27/03/2018
  Type of participation: Flash Oral Presentation and Poster

- Title: Metal Nanoparticles associated to Metal-Organic Frameworks
  Authors: A. Arenas-Vivo, P. Horcajada
  Congress: 6th IMDEA Energy Annual Workshop of young researchers
  Venue: IMDEA Energy, Spain (National congress)
  Date: 15/12/2017
  Type of participation: Poster and Flash oral presentation

APPENDIX X

CV

PROFILE & OBJECTIVE

I am a Chemical Engineer with plenty laboratory experience, especially in synthesis and characterization of nanomaterials and polymers. I am particularly interested in R&D in the materials field. I have an open-minded, creative, hard-working and friendly character. After leading groups in different context (industry, academia), I am a good communicator and I know how to work constructively under pressure and resolve conflicts collaboratively.

SKILLS

LANGUAGUES

Spanish: Native speaker.
English: Fluent. Advanced Certificate in English, C1. March 2012.
IELTS score 7.0. February 2014.
French: Intermediate. Diplôme d'Etudes en Langue Française; Delf B1. October 2009.

Ana Arenas Vivo

Chemical Engineer, Materials R&D specialty

EXPERIENCE

SIKA | R&D DEVELOPER
March 2021 – Present
New concrete admixtures formulation. Development and improvement of existent concrete admixtures formulas in order to improve their characteristics, manufacturing or to reduce costs. Testing under national and international standards. Production management and quality control.

ARCELORMITTAL | R&D ENGINEER
January 2020 – March 2021
Product design and development of new carbonaceous nanomaterials (graphite, graphene) from the revalorization of steelmaking process byproducts. Project leader for the scale-up of the pilot plant (kg per year) to industrial scale (T per year). Supervision of plant workers and technicians. Production management and quality control.

IMDEA ENERGY | PREDOCTORAL RESEARCHER
March 2017 – December 2019

Synthesis of Metal-Organic Frameworks (MOFs) as host material of active species (enzymes, metallic nanoparticles) for catalysis. Project leader (Fundación Iberdrola). Supervision of final year students (Bachelor and Master). Redaction of scientific reports and publications. Participation on divulgation events: conferences (3 international, 3 national), seminars

AYMING | JUNIOR CONSULTANT, R&D ADVISORY
October 2016 – December 2016

Identification and analysis of R&D projects. Management and project tracking. Preparation of documentation and proposals for direct financing channels and deductions on corporate income tax for our clients in diverse sectors (chemistry, automotive, industrial, cosmetic, bioengineering, banking).

COMPUTATION

Microsoft Office (Word, Excel, VBA Excel, Power Point, Project, Visio)
Matlab user level.
AspenTech user level.
CES Materials user level
Photoshop user level.
Programing languages: C, FORTRAN

PUBLICATIONS (selection)

- *Inorg. Chem.*, 57 (2018) 12056-12065
- *Coord. Chem. Rev.*, 388 (2019) 202-226
- *Angew. Chem.* 131 (2019) 7152-7156
- *Acta Biomat*, 97 (2019), 490-500
- *Cryst. Growth Des.* 20 (2020), 370-382
- Chapter 1 ISBN:978-1-925823-57-8
- *Materials*, 13 (2020), 1469

C/Caleruega 3, 10ºB, 28033
Madrid, España
anaarenasvivo@gmail.com
0034 679294586

EDUCATION

Ph.D. IN ADVANCED CHEMISTRY

Universidad Complutense de Madrid, 2017 – Present

Specialized in crystalline hybrid MOF nanomaterials and encapsulation of active species *in situ* and by diffusion. Develop at IMDEA Energy

MSc (Eng.) in ADVANCED ENGINEERING MATERIALS

University of Liverpool, School of Engineering, 2015 – 2016

Materials specialized materials with courses such as composites, 3D printing and chemical nanotechnology (1st of the class).

MSc (Eng.) in CHEMICAL ENGINEERING

Universidad Politécnica de Madrid, ETSII, 2014 – 2015

Completes the prior degree formation in general Chemical Engineering courses. Focus specialization in Materials and CAE modelling of polymer-based systems with the algorithms executed in FORTRAN language. Average score: 8.66/10 (1st of the class).

BSc (Eng.) in CHEMICAL ENGINEERING

Universidad Politécnica de Madrid, ETSII, 2010 – 2014

Average score: 8.19/10 (2nd of the class).

AWARDS AND RECOGNITIONS

- **Fundación Iberdrola 2017 Research Grant**. Principal Researcher (September 2017 - September 2018) Project: *"Metallic nano-objects associated to porous Metal-Organic Frameworks for chemical energy storage*"
- **Repsol Grant of Introduction to R&D** (November 2014-July 2015): One of the five select among 73 applicants. Project: "*Applications of molecular fluorescence spectroscopy in recycling plastics*", head of the research project.
- **Collaboration grant of the Spanish Ministry of Education, Culture and Sport** (2013-2014). Project: "*The impact of new pollutants in the recycling of PET*", in contribution to a major research of the Chemical Engineering and Environment Department (ETSII, UPM).

A. M. D. G.